Dissertations, Master's Theses and Master's Reports

2020

RATIOMETRIC NEAR-INFRARED FLUORESCENT PROBES FOR THE SENSITIVE DETECTION OF INTRACELLULAR pH AND BIO-THIOLS IN LIVE CELLS

Shuai Xia
Michigan Technological University, shuaix@mtu.edu

RATIOMETRIC NEAR-INFRARED FLUORESCENT PROBES FOR THE
SENSITIVE DETECTION OF INTRACELLULAR pH AND BIO-THIOLS IN LIVE
CELLS

By

Shuai Xia

A DISSERTATION

Submitted in partial fulfillment of the requirements for the degree of

DOCTOR OF PHILOSOPHY

In Chemistry

MICHIGAN TECHNOLOGICAL UNIVERSITY

2020

This dissertation has been approved in partial fulfillment of the requirements for the Degree of DOCTOR OF PHILOSOPHY in Chemistry.

Department of Chemistry

Dissertation Advisor: *Dr. Haiying Liu*

Committee Member: *Dr. Shiyue Fang*

Committee Member: *Dr. Tarun K. Dam*

Committee Member: *Dr. Xiaoqing Tang*

Department Chair: *Dr. John Jaszczak*

Table of Contents

Author Contribution Statement

All the research projects illustrated in this dissertation were under the guidance of the author's advisor Dr. Haiying Liu in the Department of Chemistry. There were seven chapters in this dissertation. The first introduction chapter and the last summary chapter were prepared freshly, and the other parts of this dissertation were edited and rearranged according to previous published peer-review papers by the author of this dissertation, to which the author's contributions would be detailly discussed as below.

Chapter 2 is based on a collaborative short communication which has already been published in "Chemical Communication 2018, 54 (55), 7625-7628". The author of this dissertation was in charge of the cellular confocal imaging part and involved partially in the optical property test. The novel dyes in this paper were synthesized by Dr. Yibin Zhang and the major optical measurement work was operated by Dr. Mingxi Fang. The computational calculation part was done by Dr. Rudy Luck. Dr. Haiying Liu and Dr. Rudy Luck were corresponding authors and they were responsible for finalizing the paper.

Chapter 3 is based on a collaborative original article which has already been published in "Sensors and Actuators B: Chemical 2018, 265, 699-708". The roles the author of this dissertation played were conducting cellular confocal imaging, performing half of the optical property task and preparing the leading compound for the synthesis. The fluorescent probes in this paper were synthesized by Dr. Jianbo Wang and the other optical measurement work was operated by Dr. Jianheng Bi. Dr. Haiying Liu, Dr. Fen-Tair Luo

and Dr. Marina Tanasova were corresponding authors and Dr. Haiying Liu was responsible for revising the draft.

Chapter 4 is based on a collaborative full article which has already been published published in "Journal of Materials Chemistry B 2019, 7 (2), 198-209". The contribution of the author of this dissertation to this project was conducting all the cellular confocal imaging part and examining a small portion of the optical properties. The fluorescent probes in this article were prepared by Dr. Jianbo Wang and most of the optical measurement work was done by Dr. Jianheng Bi and Dr. Mingxi Fang. The computational calculation part was done by Dr. Rudy Luck. Dr. Jianbo Wang, Dr. Rudy Luck, Dr. Hsien-Ming Lee and Dr. Haiying Liu were corresponding authors and they were responsible for revising the paper.

Chapter 5 is based on a collaborative full article which has already been published published in "ACS Applied Bio Materials. 2019, 2 (11), 4986-4997". For this project, the author of this dissertation investigated all the optical properties of the probes, conducted all the cellular confocal imaging part and further applied the fluorescent probes to Drosophila melanogaster. The fluorescent probes in this article were prepared by Dr. Yibin Zhang and the computational calculation part was done by Dr. Rudy Luck. Dr. Thomas Werner and his student Tessa Steenwinkel provided the Drosophila melanogaster for the *in vivo* test. Dr. Rudy Luck, Dr. Thomas Werner and Dr. Haiying Liu were corresponding authors and they were in charge of revising the draft.

Chapter 6 is based on a collaborative peer-review paper which has already been published in "ChemBioChem 2019, 20 (15), 1986-1994.". The contribution of the author of this dissertation to this article was conducting all the cellular confocal imaging part and applying the fluorescent probe to Drosophila melanogaster. The fluorescent probes in this article were prepared by Dr. Yibin Zhang and most of the optical measurement work was done by Dr. Mingxi Fang. The computational calculation part was operated by Dr. Rudy Luck. Dr. Thomas Werner and his student Tessa Steenwinkel performed *in vivo* test on Drosophila melanogaster. Dr. Haiying Liu, Dr. Rudy Luck and Dr. Thomas Werner were the corresponding authors and they made the revisions for the draft.

Acknowledgements

During my time in the chemistry department of Michigan Technological University, there were many people for whom I would like to show my sincere thanks for their continuing help and generous support whenever I had a tough time during my Ph.D. journey.

First, I would like to express my deepest and sincerest gratitude to Dr. Haiying Liu, my Ph.D. advisor, for the insightful advice, patient guidance and the continuing assistance during my Ph.D. time. Dr. Liu is a very smart and patient person who works very hard to organize all the papers for me. When I faced problems with the projects I was working on, he was always willing to help me. His passion, his confidence, his diligence and his full knowledge in my research field impressed me deeply and motivated me to keep on working as a productive scientist.

Second, I would like to also show my thanks to committee members of my dissertation: Dr. Shiyue Fang, Dr. Tarun K. Dam and Dr. Xiaoqing Tang, for their meaningful questions, generous support and valuable suggestions during my Ph.D. original research proposal, dissertation and oral defense. I also would like to acknowledge our current department chair Dr. John Jaszczak and former one Dr. Cary F. Chabalowski for their continuing support, suggestions and advice through my Ph.D. pursuits.

The published papers in my dissertation are all multi-author publications which indicates that all these projects involve collaborations. Therefore, I am really grateful to all

short to express how grateful I am to my beloved wife, Muxue (Snow) Zhang. Without her

support, understanding and encouragement, I would never have believed I could finish my

Ph.D. degree myself.

List of abbreviations

TPE:	Tetraphenylethylene
IPUAC:	The International Union of Pure and Applied Chemistry
NIR:	Near-infrared
RIR:	Restriction of intramolecular rotation
AIE:	Aggregation-induced emission
PET:	Photo-induced Electron Transfer
Cys:	Cysteine
HCY:	Homocysteine
GSH:	Glutathione
ICT:	Intramolecular Charge Transfer
ESIPT:	Excited State Intramolecular Proton Transfer
HBO:	2-(20-hydroxyphenyl)Benzoxazole
FRET:	Förster (Fluorescence) Resonance Energy Transfer
TBET:	Through Bond Energy Transfer

Abstract

In the past twenty years, fluorescence sensing and imaging based on fluorescent probes has been developed as an imperative technique due to the merits including excellent sensitivity, operational simplicity, instant time effectiveness and outstanding selectivity in the research areas such as mineralogy, gemology, biological medicine, materials and environmental engineering. Protons act as a significant role in a variety of pathological and physiological processes, and there are obvious differences in the pH among organelles: the pH in lysosomes is acid within the range of 4.5–5.5, whereas mitochondrial pH is basic that can be as high as 8.0. Abnormal intracellular pH is always an indication of a disrupted pH homeostasis in the whole cell. Furthermore, intracellular bio-thiols are vital to cell metabolism, which by either elevated or deficiency levels of bio-thiols will lead to some diseases. Possessing the advantages of avoiding systematic errors and undesirable photophysical properties of certain fluorophores, novel near-infrared ratiometric fluorescent sensors for the accurately monitoring intracellular pH and biothiols have become the spotlight in research topics.

Throughout this dissertation, we firstly have designed and synthesized two novel rhodamine-based dyes with high fluorescence quantum yield, good pH stability large Stokes shifts and excellent photostability by introducing an additional amino residue with fused rings into a classic rhodamine skeleton. We also have constructed a fluorescent sensor by incorporating a receptor to one of these dyes and applied it as an effective sensor for the quick and sensitive monitoring of lysosomal pH fluctuations. Then, we have

prepared two sets of ratiometric fluorescent probes for the sensitive detection of lysosomal pH values. The former series were based on π-conjugation modulation strategy, which was accomplished by conjugating a visible coumarin motif to a classic near-infrared hemicyanine skeleton via a vinyl linker. The lysosome-targeting goal was reached by introducing a morpholine ligand or a *o*-phenylenediamine group to the hemicyanine acceptor. For the latter series, we have obtained three near-infrared ratiometric fluorescent sensors containing a TPE as a donor and a rhodamine as an acceptor for the quantitative, sensitive and comparative analysis of lysosomal pH alterations through FRET and TBET approaches. Furthermore, we have prepared two near-infrared hybrid rhodol dyes for the ratiometric and sensitive visualization of pH value alterations in mitochondria taking advantage of conjugating typical hemicyanine fluorophores into a classic rhodol motif. Upon pH changes, a rhodol hydroxyl group in the probe acts as a spiropyran switch, resulting in the change of π-conjugation and the appearance of a new fluorescent peak. Due to the positive charge, these two novel rhodol dyes possessed the mitochondria-targeting property. In the end, besides the ratiometric fluorescent pH probes, we have reported a FRET-based fluorescent sensor for the ratiometric, selective and accurate detection of cysteine (Cys), which was achieved by linking a visible coumarin skeleton and a near-infrared rhodamine motif through a piperazine spacer. This probe could be used to monitor the intracellular cysteine concentration ratiometrically and be further applied for imaging of *Drosophila melanogaster larvae* to detect cysteine concentration alterations *in vivo*.

1 Introduction

1.1 Background of fluorescence spectroscopy

Fluorescence is one kind of luminescence and it is the emission of a longer wavelength of light by a molecule which has absorbed a shorter wavelength of radiation in most cases. The earliest observations of fluorescence were reported in the middle of 16th century by Bernardino de Sahagún from France and by Nicolás Monardes from Spain in a plant named as lignum nephriticum which was known as "kidney wood" in Latin.[1] The chemical active molecule responsible for the strong blue fluorescence was identified as matlaline (Figure 1.1) recently, which is the oxidation product of the one flavonoid that is found in lignum nephriticum.[2] In the early 19th century, a variety of fluorescent compounds were reported. In detail, in 1819, Edward D. Clarke from the University of Cambridge discovered the finer crystals of fluorite from Weardale possessed a dichroic character: the color by reflected light was a deep sapphire blue, whereas the color by transmitted light was an intense emerald green.[3] In 1822, the mineralogist R-J Haüy from France also mentioned the double-color effect of certain fluorite crystals. The reflected light was in violet color, however the transmitted light was described as the green color.[4] In 1833, Sir David Brewster described that chlorophyll was able to emit beautiful red fluorescence by green light excitation.[5] In the year of 1845, Sir John Herschel, a English polymath, obtained the quinine sulfate solution (Figure 1.1) and claimed that it was capable of emitting an extremely beautiful and vivid celestial blue light.[6] In the mid-19th century, the famous physicist and professor of mathematics George Gabriel Stokes made significant progresses toward fluorescent research. From his famous publication named as " On the

Refrangibility of Light" in 1852, he distinctly illustrated a universal phenomenon that he named dispersive reflection: the wavelength of the dispersed light was usually longer comparing to the wavelength of the original excitation radiation, which was later identified as Stokes shift.[7] In the next year, he started to define this phenomenon as fluorescence in his second paper.[8] However, there were always debates for the cold light between fluorescence and phosphorescence throughout the 19th century.

Matlaline   R =   **Quinine**
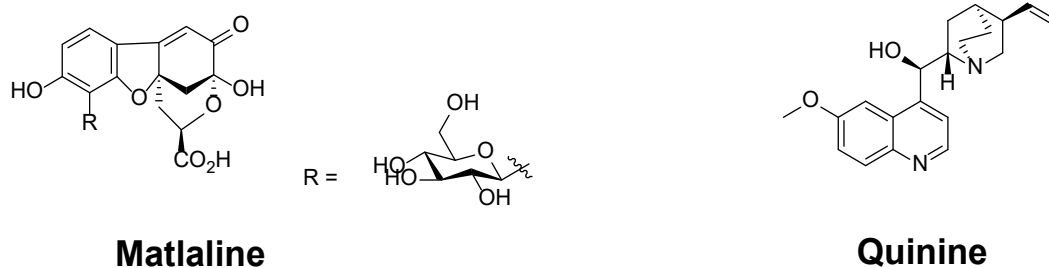
Figure 1.1. Structures of early discovered fluorescence compounds

Currently, the classic approach to clearly illustrate the mechanism of fluorescence is taking advantage of Jablonski diagram (Figure 1.2), which is named after Polish physicist Aleksander Jabłoński.[9] As we can conclude from Figure 1.2, the fluorophore receives energy under light irradiation and is excited from ground state to different vibrational levels on excited states of either S_1 or S_2 due to the excitation energy, which is followed by that the molecule quickly relaxes the energy to the lowest vibrational energy level of excited state S_1 through the fast processes such as vibrational relaxation ($\sim 10^{-12}$ S) and internal conversion ($\sim 10^{-12}$ S). Then the compound returns to different vibrational energy levels of ground state S_0 from the lowest vibrational state of S_1, releasing the energy by the means of the light, which is the whole process of fluorescence. Moreover, the fluorophore in the

2

lowest vibrational energy level of excited state S_1 could change spin via the intersystem crossing process ($\sim 10^{-8}$ S), leading to be converted to the triplet state T_1. The phosphorescence is the process transferred from T_1 state to different vibrational energy levels of ground states S_0 which is another kind of luminescence. Comparing to phosphorescence, the fluorescence possesses advantages such as higher energy transfer efficiency and shorter respond time.
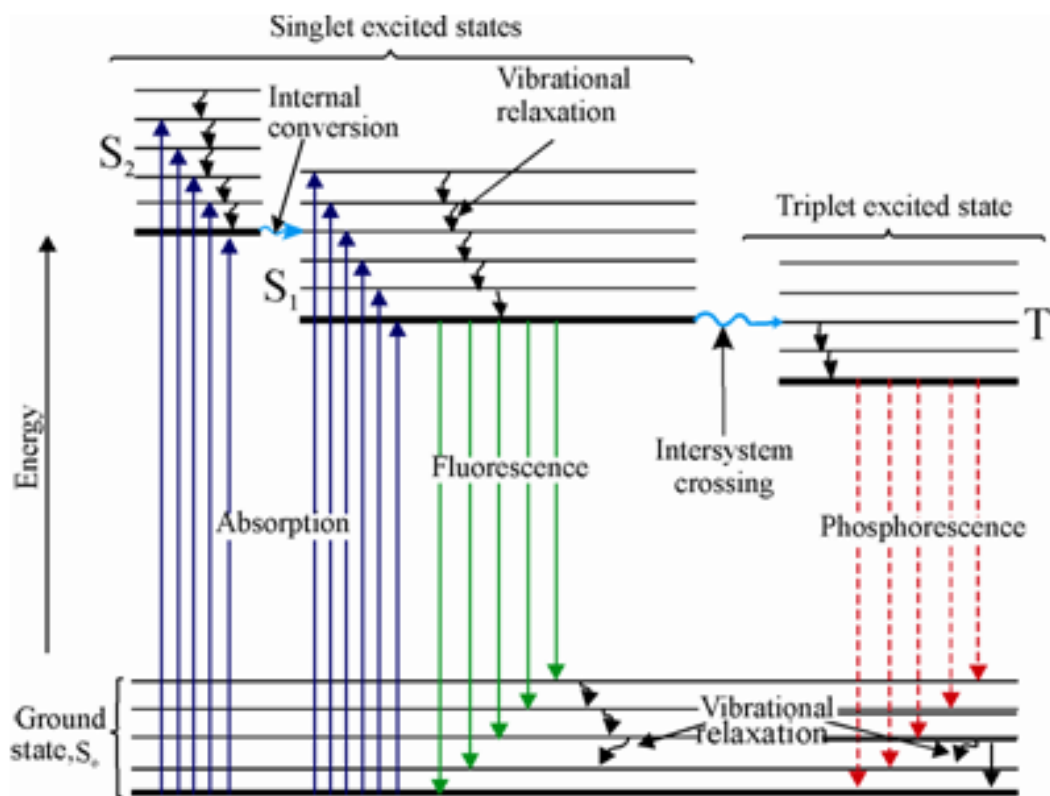
Figure 1.2. Illustration the differences between fluorescence and phosphorescence by Jablonski diagram.

Furthermore, we can also conclude from Jablonski diagram that the fluorescent emission wavelength is always longer than the radiation absorption wavelength since that

in most cases the energy of fluorescence is always less than the that of the excitation radiation. The fundamental characteristic parameters to describe the properties of a fluorescent active compound are shown as below:

i. Maximum absorption wavelength (λ_{abs}), maximum emission wavelength (λ_{em}) and Stokes shift

λ_{abs} and λ_{em} illustrate the wavelength for the maximum intensity of absorption peak and that of fluorescence emission peak, respectively. Stokes shift defines the shift between the λ_{abs} and λ_{em} and was created by the outstanding researcher George Gabriel Stokes who invented with the word fluorescence (Figure 1.3).
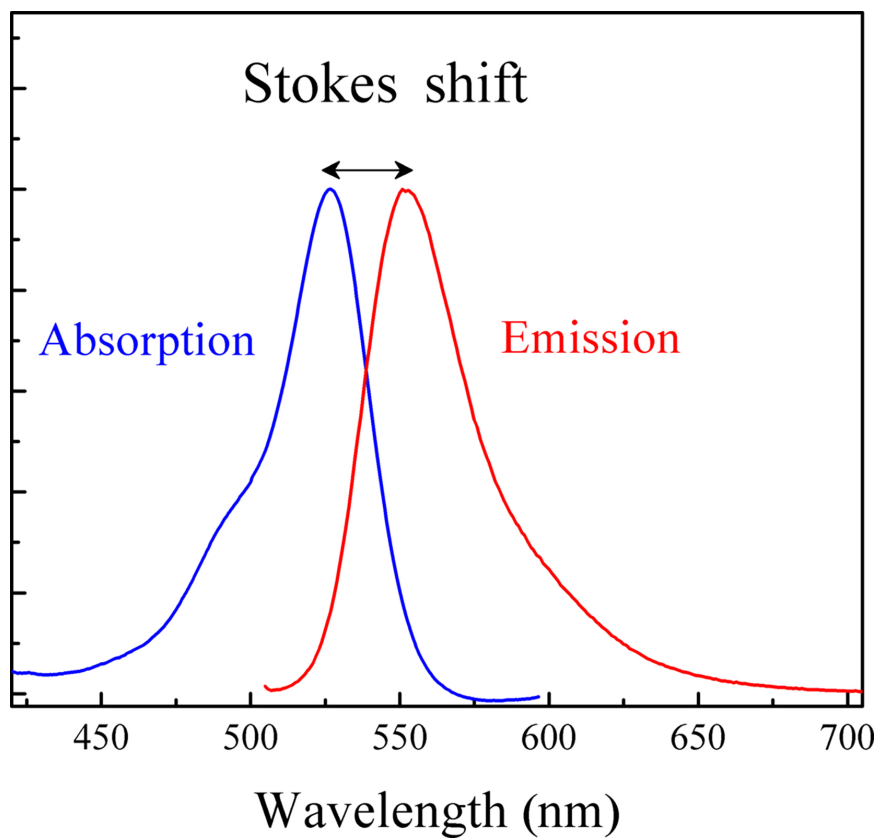
Figure 1.3. Stokes shift for the Rhodamine 6G

ii. **Molar extinction coefficient (ε)**

Molar extinction coefficient (ε), also regard as the molar attenuation coefficient, is the constant that describes how strongly a m olecule attenuates light at a certain wavelength. This constant is determined by Lambert-Beers law.

iii. **Fluorescence lifetime (τ)**

Fluorescence lifetime (τ) is the average time a fluorophore spends between staying at its lowest energy level of excited states and returning to the ground states through fluorescence radiation. The normal fluorescence lifetime of a fluorophore is at 10^9 second scale.

iv. **Fluorescence quantum yield (Φ$_F$)**

The fluorescence quantum yield (Φ$_F$), which is the unique property of a fluorophore, is the value of the photons emitted divided by the photons absorbed through the fluorescence process. Otherwise speaking, the quantum yield reveals the energy efficiency of the fluorophore.

1.2 Small molecules as fluorescent probes for detecting and labelling

The practical applications of fluorescence could be dated back to the mid of 19th century. In 1857, Edmond Becquerel proposed the concept of coating the inner surface of an electric discharge tube with a fluorescent material, resulting in the earliest utilization of fluorescence, namely fluorescent tube. Moreover, fluorescence has been recognized as a powerful analytical device detecting different concentrations of a variety of neutral or ionic

species. In 1868, the fluorescence analysis was firstly reported by Göppelsröder: the complex of morin with Al^{3+} produced a significant increase of fluorescence intensity, providing a straightforward approach for the detection of aluminum ions.[10] Since the 20th century, the fluorescence has been widely applied in areas such as mineralogy, staining dyes, gemology, medicine, biological detectors, chemical labeler, cosmic-ray detection, fluorescent lamps and most commonly, fluorescent probes. Possessing the advantages such as high sensitivity, a wide range of detecting concentrations, excellent specificity and outstanding accuracy, currently, fluorescent sensing and labelling is becoming a more and more popular technology that makes it feasible to do the things that were impossible before.[11] The fluorophores, which are fluorescent chemical compounds that possess different characteristics of fluorescent parameters, play a vital role in fluorescence sensing and labeling. As shown in Figure 1.4, tetraphenylethylene, coumarin, rhodamine, rhodol, hemicyanine and cyanine are the fluorophores this dissertation studies in the order from shortest wavelength to longest wavelength.
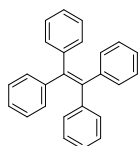
Tetraphenylethylene　　　　　　**Coumarin**　　　　　　**Rhodamine**
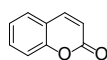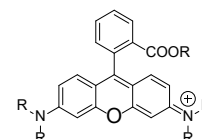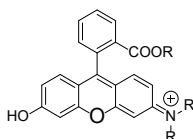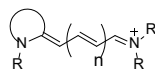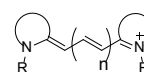
Rhodol　　　　　　**Hemicyanine**　　　　　　**Cyanine**

Figure 1.4. Structures of commonly reported fluorescent molecular skeleton

1.2.1 Commonly reported fluorescent molecular skeleton

a) Tetraphenylethylene

Tetraphenylethylene (TPE), the international union of pure and applied chemistry (IPUAC) name of which is 1,2,2-triphenylvinylbenzene, is the fluorophore that could emit short wavelength blue fluorescence. In addition, according to the Tang's et al report,[12] TPE exhibits the aggregation induced emission effect (AIE) and displays higher fluorescent intensity in aqueous solution than in organic solutions. The reason for this effect is that restriction of intramolecular rotation (RIR) results in the TPE to aggregate and perform higher emissive in aqueous system (Scheme 1.5). Our group has incorporated this AIE effect and uses TPE as the donor and Cy-7 as acceptor, achieving the goal to construct a novel fluorescent probe to detect intracellular pH ratiometrically with AIE effect.[13]
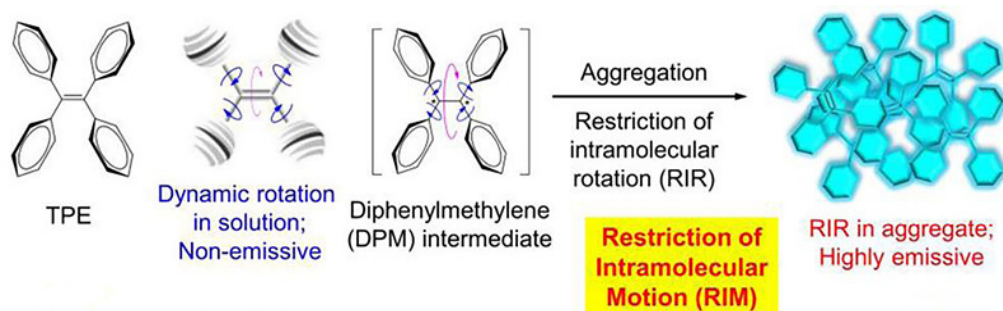
Figure 1.5. Structure of TPE and the illustration the process of its AIE properties

b) Coumarin

Coumarin was first discovered by A. Vogel from the tonka beans and by and N. J. B. G. Guibourt from the melilot flowers in 1820, independently.[14] Later in the 19th century, coumarin was synthesized and characterized as the structure consists of a fused pyrone and

benzene with the pyrone carbonyl group at position 2, and the coumarins skeleton now is regarded as 2*H*-chromen-2-one (Scheme 1.6). Coumarin is a colorless crystal with a sweet vanilla odor and a bitter taste.[15] As a fluorophore, coumarin is able to emit blue fluorescent with high quantum yield, and coumarin-derived fluorescent probes are usually constructed by adding an acetyl group in position 3 and a hydroxyl or an amino residue in position 7.
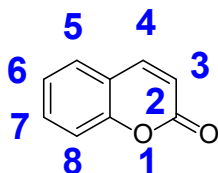
Figure 1.6. Structure of coumarin skeleton

c) Rhodamine

Rhodamines are the fluorophores that belongs to the family of xanthene of which the 3- and 6- positions are substituted with amino group. Possessing the metrics such as excellent photostability, good water solubility, perfect cell permeability and high quantum yield, rhodamine has been widely used as laser dyes, pigments, labeling agents, fluorescence lifetime test reagents as well as fluorescence standard compounds.[16] The most commonly reported rhodamine dyes are Rhodamine B, Rhodamine 101, Rhodamine 6G and Rhodamine 123 as shown in Figure 1.7. To point out, rhodamine families can serve as the chemosensors to detect different kinds of metal ions or pH *in vivo* or *in vitro* because the spirolactam ring could be attacked by the certain kinds of analytes to dramatically enhance the fluorescent intensity.[17] In the past 20 years, a lot of research groups have developed various of rhodamine-based fluorescent sensors for monitoring different species

and tuned the wavelength of rhodamine motif from visible region to near-infrared region.[18-20] Our group recently reported a novel ratiometric fluorescent probe using rhodamine as a donor which could be used as an efficient tool to sensitively detect intracellular pH.[21]
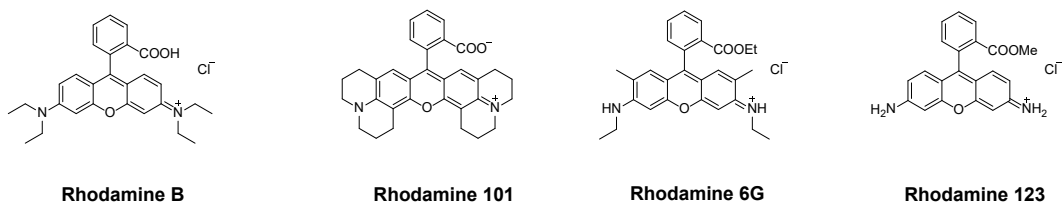
Figure 1.7. Structures of the common reported rhodamine.

d) Rhodol

As shown in Figure 1.8, the skeleton of rhodol dyes is a hybrid structure of fluorescein and rhodamine.[22] Rhodol fluorophores, which are also named as Rhodafluor,[23] possess the merits such as high molar extinction coefficients, perfect photostability, high quantum yields, and excellent solubility in various solvents, as well as low pH-dependence.[24] Even though rhodol dyes have lots of excellent photophysical advantages, the number of examples about the practical applications of rhodol motif is very limited due to the difficult synthetic approach.[25]
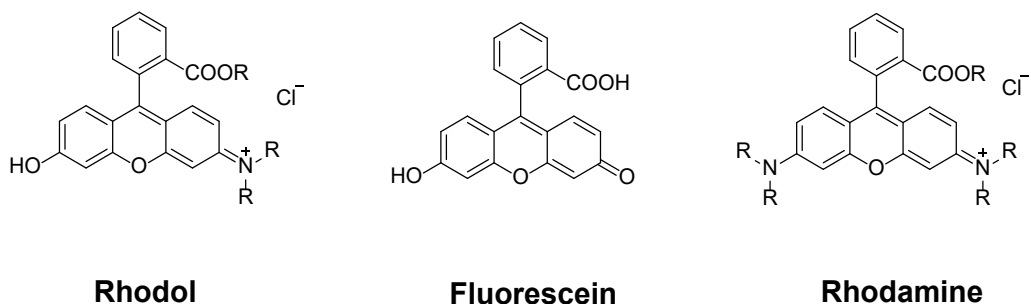
Figure 1.8. The comparison for the structures of Rhodol, Fluorescein and Rhodamine.

e) Hemicyanine and cyanine

Hemicyanine and cyanine belong to the family of polymethine group which has dominated the field of photography, labeling and other sophisticated areas of dye application since William C. H. G. discovered them in 1856.[26] As shown in Figure 1.4, the generic hemicyanine and cyanine dyes consist of two nitrogen centers, one of which is positively charged and the other of which is not charged. These two nitrogen centers are connected by a polymethine linker.[27] To exemplify, the differences between the hemicyanine and cyanine is that both the nitrogen atoms are in the aromatic system for cyanine fluorophore but only one aromatic nitrogen center for hemicyanine family.[28] Comparing to the conventional fluorophores such as coumarin, rhodamine and naphthalene, the hemicyanine and cyanine families own higher quantum yield, better water solubility and longer wavelength of absorption and emission spectrum.[29] Figure 1.9 displays the well-known examples of hemicyanine and cyanine compounds. The classic structures of Cy-3, Cy-5 and Cy-7 are named by combining the aberration of cyanine and the number of carbon atoms in the polymethine linker. We can conclude that absorption and emission peak wavelength will obtain red shift by around 100 nm when adding each 1, 2-vinyl moiety to polymethine linker, and another method to tune the spectrum is to introduce aromatic rings to enlarge the conjugation system.[30] The CS-2 NIR dye, a typical hemicyanine dye, was first reported by Weiying L. in 2012,[31] which itself could be served as fluorescent probe with spirolactam ring open-close mechanism that is similar to rhodamine derivatives. Our group has utilized cyanine and hemicyanine motif to construct various fluorescent probes which can sensitively detect different kinds of ions and pH.[32-34]
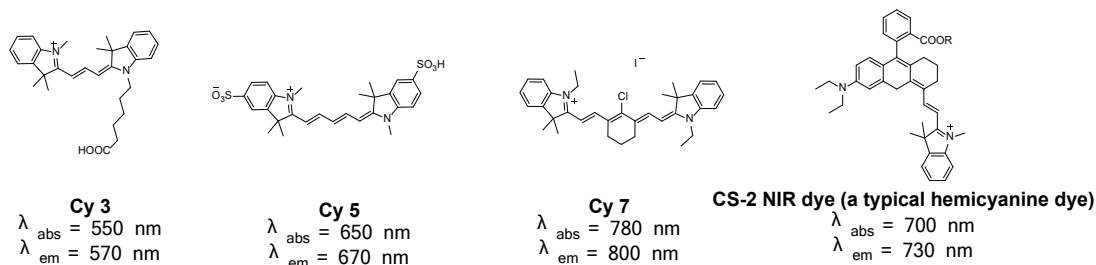
Figure 1.9. Examples of typical cyanine and hemicyanine dyes.

1.2.2 Demand and criteria for designing fluorescent probes

With those diversity of fluorophores at hand, it is of most importance to rationally design the fluorescent probes which are capable of sensing the analytes with good selectivity and sensitivity. The classic composition of a fluorescent probe includes three functional parts which are a fluorophore, a spacer and a receptor as shown in Figure 1.10. Specifically, the fluorophore is a fluorescent possessing skeleton that transfers the recognition between the receptor and the analyte into the alteration of fluorescence emission signal. The spacer, which is known as linker as well, acts as the bridge between the receptor and the fluorophore. The length of linker can be varied from a single bond to a long chain which is highly dependent on the mechanism of fluorescence sensing. The receptor, which is also regarded as binding site or chelator, is the recognition site with the analyte.[11] The modulation mechanisms of fluorescent sensors can be Intramolecular Charge Transfer (ICT), Photo-induced Electron Transfer (PET), Förster (Fluorescence) Resonance Energy Transfer (FRET) and Through Bond Energy Transfer (TBET) and so on which would result in fluorescent signal changes such as absorption wavelength, fluorescence emission wavelength, fluorescent peak intensity, fluorescence quantum yields, fluorescence lifetimes, and even anisotropies.[35]

11
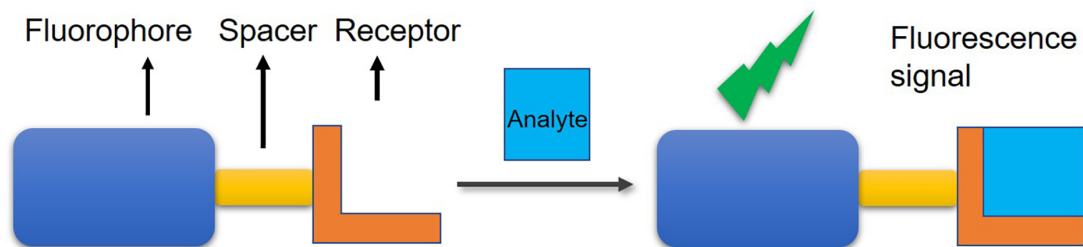
Figure 1.10. Illustration of the classic composition of a fluorescent probe

It is very important to rationally design the fluorescent probe with desired properties which will further impact its practical application. There are some fundamental demands and criteria that need to be met which will be shown as below.

a) **Selective response to analyte**: The first important demand that needs to be considered is that the fluorescent probe possesses the ability to selectively respond to the certain analyte without interference by the other compounds. Otherwise, we are not able to determine whether the fluorescent signal change is by the analyte or not which would further lead to the inaccurate analysis.

b) **Desired sensitivity to analyte**: Besides the selectivity, the sensitivity of the fluorescent probes against the analyte is also critical. Since the concentration of the analyte is at a certain range in the test system, the detecting limit of the fluorescent probe to the analyte must be within this certain range to guarantee the success for the analysis of this analyte.

c) **Alteration of fluorescent signals**: There are several kinds of fluorescent signal change such as the turn-on fluorescence signal (fluorescence enhancement), turn-off fluorescence signal (fluorescence quenching), fluorescent absorption and emission spectra shift, and fluorescent lifetime alterations. Among the approaches mentioned

12

above, the turn-on respond to analyte is the most favorable since it could dramatically increase the signal-to-noise ratio (S/N) and significantly reduce the level of difficulty in visualizing the actual fluorescence signal changes.

d) **Good stability**: One of the biggest disadvantages of fluorescent analysis is the weak stability against radiation and chemicals which significantly limit its practical applications. So great efforts are needed for designing the fluorescent probes with good photostability and chemostability.

e) **High water solubility and membrane permeability**: Because of the aqueous environment in live cells and animal tissues, it is highly desired to develop fluorescent probes with high water solubility for biological applications *in vivo* since. On the other hand, in order to pass through the cell membrane and go into the live cells, fluorescent probes should exhibit good permeability by incorporating some lipophilicity residues. However, fluorescent probes would easily accumulate and aggregate in the membrane of live cells membrane if fluorescent sensors contained too much hydrophobicity structures, resulting in extreme limitations of their applications.

f) **Tuning the wavelength to NIR region**: The near infrared region (NIR), which is defined between 650 nm and 900 nm, is a perfect detecting range for fluorescent probes. This is because the near infrared radiation not significantly reduces the photodamage but dramatically minimizes interferences by the light and absorbing scattering (Raman and Rayleigh).[36] Moreover, comparing to the conventional fluorescence, NIR light is able to penetrate deeper into biological tissues, which facilitates molecular fluorescent imaging progresses *in vivo*.[37] With such merits at hand, NIR is also called the "biological window".[38]

1.3 Strategies to design ratiometric fluorescent probes

Despite the conventional fluorescent fluorophores, such as coumarin, naphthalimide, rhodamine, fluorescein, rhodol, BODIPY, hemicyanine and cyanine, having been widely applied in labelling, bio-imaging, bio-sensing, disease diagnoses and environmental pollution detection,[39] there are still several critical drawbacks to them. First and foremost, measuring fluorescent emission only by a change of the fluorescence intensity at one peak could be affected by systematic errors, such as environmental changes around the fluorescent sensor (concentration, solution polarity, pH value, temperature, time and so on), localization of the probe, effective thickness of the cell in the optical beam, efficiency of the emission collection, and alterations of the laser radiation intensity. Second, some unfavorable photophysical characteristics of certain fluorophores would still restrain their potential applications.[40] To avoid the influences of such factors, a novel strategy has been invented to simultaneously record the fluorescence intensities at two channels and calculate the ratio of them, named as ratiometric measurement. In the development of ratiometric fluorescence sensing and labelling, several different approaches, including Internal Charge Transfer (ICT) mechainsim, Excited-State Intramolecular Proton Transfer (ESIPT) mechanism, Förster (Fluorescence) Resonance Energy Transfer (FRET) mechainism, Through-Bond Energy Transfer (TBET) mechanism, as well as π-conjugation modulation mechanism have been comprehensively studied in order to develop ratiometric fluorescent sensors and will be discussed in detail as follows.

1.3.1 ICT-based ratiometric fluorescent probes

The distinguishing feature of ratiometric fluorescent probes based on Internal charge transfer (ICT) mechanism is that the electron donor is conjugated to the electron acceptor through a π-conjugation, which have been extensively utilized for the detection of cation. ICT is a process that changes the overall charge distribution in a molecule. Typically, increased ICT effect would decrease the energy gap between the ground state and the excited state, leading to a significant red shift on both absorption band and fluorescence emission peak. The detailed mechanism of ICT-based ratiometric fluorescent probe is shown as Figure 1.11 and which can be divided into two situations: a) The electron-donating part interacts with an analyte, the electron-donating character of the fluorescent probe decreases, leading to a blue shift in the absorption and emission spectra; b) a dramatical red shift is observed when the ICT becomes more developed owing to the interaction of an analyte with the electron-accepting part.[41] Taking advantages of the ICT strategy, Valeur first reported ratiometric fluorescent probes for cation sensing in 2000.[42] Besides, the alterations in fluorescence lifetime and fluorescent quantum yield could also be observed due to ICT effect. Currently, numerous ratiometric fluorescent sensors based on ICT have been developed for ratiometrically detecting a variety of analytes.
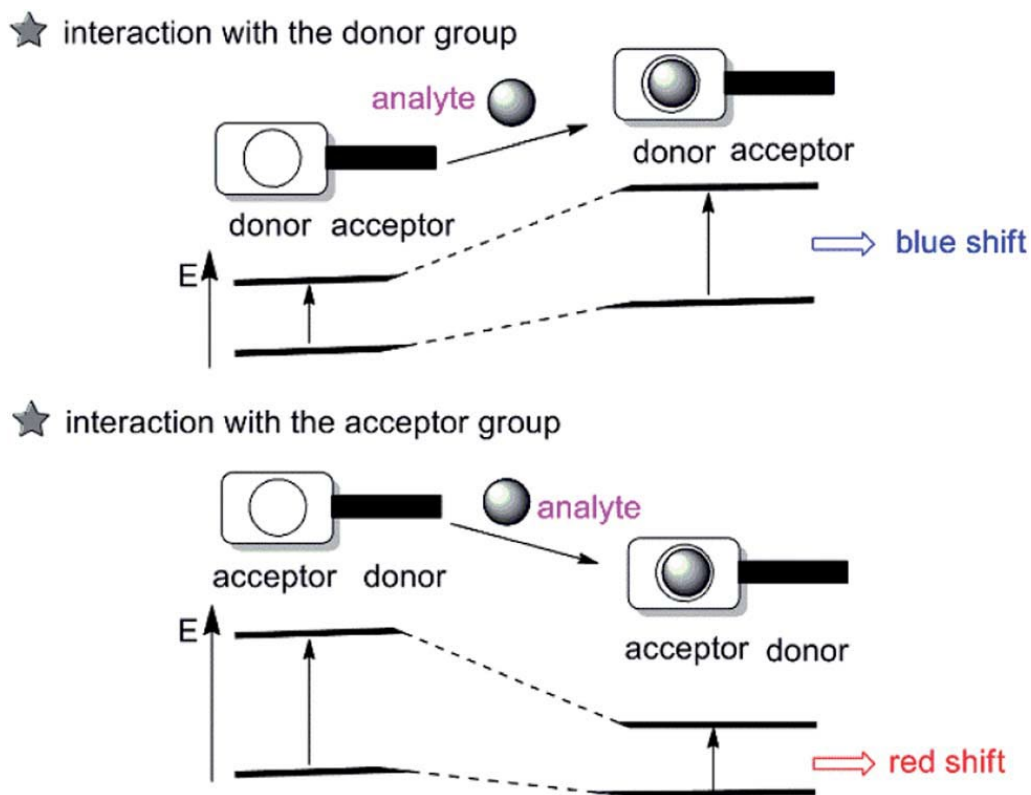
Figure 1.11. The mechanism of ratiometric fluorescent probes based on ICT effect

1.3.2 ESIPT-based ratiometric fluorescent probes

In ESIPT systems, protons in the excited state depart or join a fluorophore at different rates to that in the ground state. Typically, ESIPT is a quick process with reported time values ranging from 10^{-12} S to 10^{-13} S, which is faster than electron transfer process,.[43] In the excited state of a fluorophore, ESIPT characteristically involves a fast proton transfer from an amino or a hydroxyl residue to an imine nitrogen or a carbonyl oxygen unit. In 1982, Andrzej Mordziński and Anna Grabowska firstly reported the ESIPT process took place in 2-(20-hydroxyphenyl)benzoxazole (HBO).[44] In the ground state, due to intramolecular hydrogen bonding, HBO preferentially adopted the stable enol (E) form.

Under the excitation at 320 nm, the excited enol (E*) was quickly transferred to its excited keto (K*) tautomer through the ESIPT process within 10^{-12} S, which was responsible for an increased red fluorescence emission peak at 500 nm with a large Stokes shift. After decaying to the ground state, the keto (K) form reverted to the original enol (E) tautomer by a reverse proton transfer process. The other excited enol molecules of HBO that did not undergo ESIPT process were responsible for the emission band at the shorter 430 nm wavelength (Figure 1.12). However, ESIPT-based ratiometric fluorescent probes have proved limited in certain circumstances since non-analyte dependent fluorescence changes could be observed due to the simple protonation of the probe in aqueous solutions.
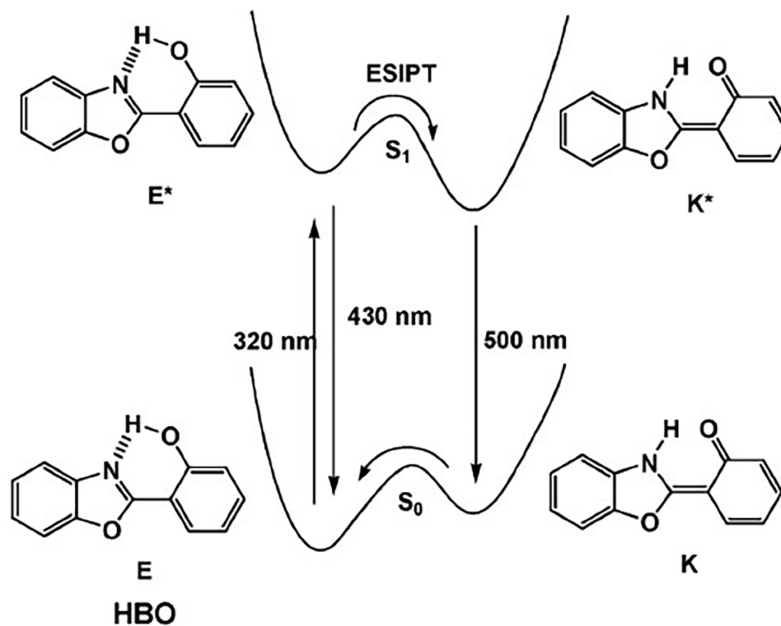
Figure 1.12. Illustration the process of ESIPT by the photophysical cycle of HBO.

1.3.3 FRET/TBET-based ratiometric fluorescent probes

Comparing with the ICT and ESIPT process which only contain one fluorophore motif in ratiometric fluorescent sensors, Förster (Fluorescence) Resonance Energy Transfer and Through Bond Energy Transfer (TBET) are the processes involving energy transfer between two different fluorescent skeletons that serve as a donor and an acceptor, respectively. Normally, fluorescent probes based on FRET processes are usually connected by a non-conjugated linker of which the energy transfer takes place through the space (Figure 1.13 a), and fluorescent probes based TBET are the ones which have a donor electronically connected to an acceptor via conjugated linkers. (Figure 1.13 b).
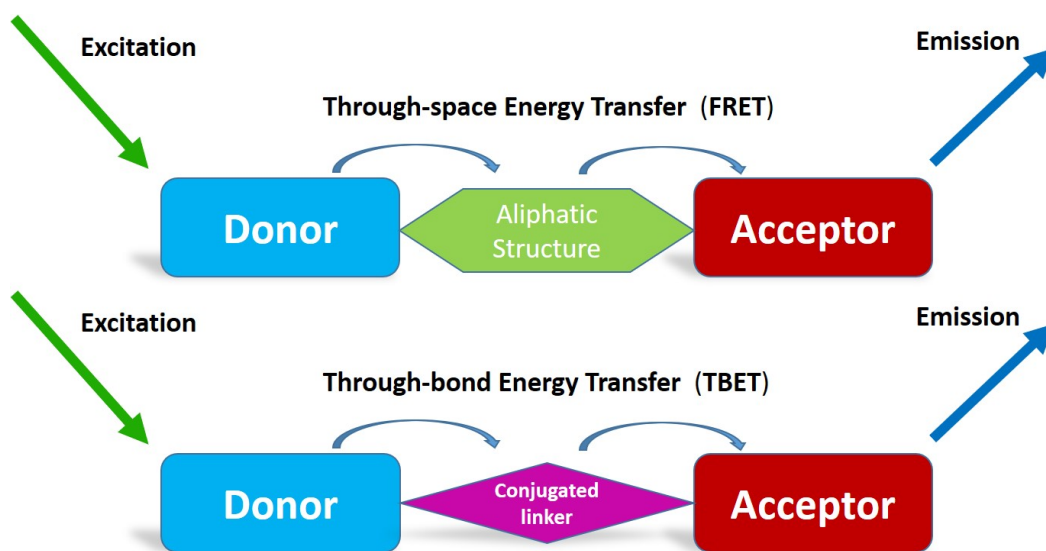
Figure 1.13. (a) Through-space (FRET) and (b) through-bond (TBET) energy transfer fluorescent probes structure

The occurrence of FRET process requires the following conditions: (1) the electron donor should have a high fluorescence quantum yield; (2) the acceptor fluorophore should have very strong absorbance at the donor excitation wavelength; (3) there should be an

appropriate alignment of the absorption and emission transition moments and their separation vector; (4) the typical distance between the electron donor and the acceptor electron should be no more than 10 nm through a non-radiative dipole–dipole coupling.[45] On the other hand, the requirements for the TBET-based fluorescent probe for the bio-imaging system are as follows: (1) there should be no overlap of the fluorescence donor emission peak with the fluorescence acceptor absorption band; (2) the acceptor fluorophore should possess high fluorescence quantum yield; (3) The linker between a donor and a acceptor must prevent them from becoming in the same plane for fear that the donor-acceptor system might behave as a single conjugated dye.[46] Since the year 2000, FRET and TBET processes have been the most favorable strategies for designing ratiometric fluorescent probes to detect cation, anions, amino acids, and the other biomarkers due to the merits such as high energy transfer efficiency, multiple donor-acceptor pair choices, and extremely high sensitivity to the analyte.[40]

1.3.4 π-Conjugation modulation-based ratiometric fluorescent probes

Besides the TBET and FRET approaches which consist of two fluorophores in the ratiometric system, there is another way to reach the ratiometric goal: namely, π-Conjugation modulation. The donor and the acceptor in the π-Conjugation modulation way are connected by SP^2 hybridized carbon-carbon bond, leading to their being coplanar.[47] Though possessing less energy transfer efficiency compared with TBET and FRET mechanisms, the π-Conjugation modulation are able to tune the fluorescence emission band to the NIR region, which is the perfect detecting window for the practical applications of fluorescent sensors.[48]

1.4 Advanced in ratiometric fluorescent probes as pH sensors

Protons play a significant part in various of physiological and pathological processes, like ion transport, receptor-mediated signal transduction, enzymatic activity, cell proliferation, endocytosis, homeostasis, and apoptosis. Generally, under normal physiological conditions, the pH of cytosolic and that of extracellular pH could be 7.2 and 7.4, respectively. Notably, there are obvious differences in the pH among organelles: the pH in lysosomes is acid within the range of 4.5–5.5, whereas mitochondrial pH is basic that can be as high as 8.0 (Figure 1.14). [49] In addition, abnormal intracellular pH would result in a disrupted pH homeostasis in the whole cell, resulting in cellular damages including inactivation of enzymes, disruption of membrane contractility, generation of free radicals, inappropriate cell apoptosis, as well as necrosis. Furthermore, abnormal pH is an indication for neurodegenerative or cardiopulmonary diseases such as Parkinson's, Alzheimer's and cancer.[50] Hence, it is extremely important for the precise detection the intracellular pH values, and fluorescent probes now have been regarded as one of the most powerful implements to monitor pH values. The first fluorescent pH probe was discovered by Roger Tsien in 1982 and was proven to be free from the interferences by the other ions such as Mn^{2+} in solution. This fluorescein-based probe displays very weak fluorescence at pH 3.56 and reveals a gradual fluorescent intensity increase as the pH increase, making it possible to monitor intracellular pH effectively.[51] Since then, a variety of small-molecule-based fluorescent sensors have been designed and constructed to monitor intracellular pH and only the typical ratiometric fluorescent pH probes will be discussed as later in this dissertation.

1.4.1 Ratiometric fluorescent probe to detect lysosomal pH

Lysosome is a membrane-bounded organelle existing in majority of the animal cells, which is responsible for receiving and degrading macromolecules that are from the cellular metabolism, such as proteins, DNA, and RNA. So, the lysosome is regarded as the waste disposal system of the cell.[52] The luminal pH of the lysosome ranges from 4.5 to 5.5. Due to the acidic pH in lysosome, strategies to selectively target lysosomes have been developed which incorporate the basic residue such as amino moiety into the fluorescent probe. Hence, fluorescent pH probes for targeting lysosome have been received more and more attention.

In 2014, Wan *et al.* developed the probe **1.1**, a original near-infrared ratiometric fluorescent sensor for detecting lysosomal pH, by incorporating a classic lysosome-targeting morpholine residue into a classic hemicyanine moiety (Figure 1.14a). The probe **1.1** displayed sensitive absorption (Figure 1. 14b) and fluorescence (Figure 1.14c) spectroscopic responses to alterations of pH values. Furthermore, the responding window of the probe **1.1** overlaps perfectly with the normal physiological pH region (pH 4.5–5.5) in lysosome, indicating that the probe **1.1** is an efficient and powerful tool for ratiometrically recognizing lysosomal pH values.[48]
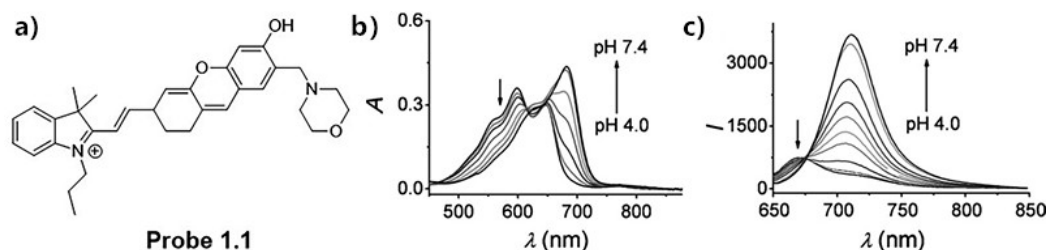
Figure 1.14. a) Structure of probe 1.1; b) absorption spectrum and c) fluorescent emission spectrum changes of probe **1.1** against pH

Jiang *et al.* discovered a fluorescent pH probe **1.2** to detect lysosomal pH value ratiometrically based on quinoline skeleton by introducing a dimethylethylamino residue as a lysosome-targeting ligand. The intensity of fluorescence peak decreased at 494 nm as pH values decreased, and a new fluorescence emission band appeared at 570 nm with a 76 nm red shift, enabling the efficient ratiometric detection of pH (Figure 1.15). In addition, probe **1.2** was proven to be localized in lysosome in living cells by co-stain study and was capable of ratiometrically detecting lysosomal pH fluctuation.[53]
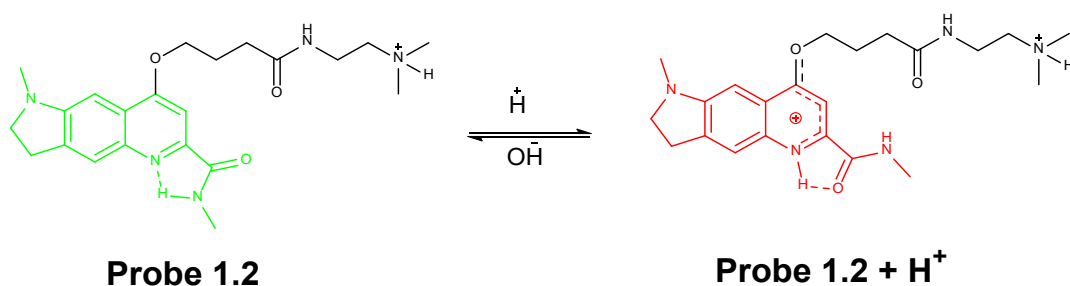
Probe 1.2   Probe 1.2 + H$^+$

Figure 1.15. The structure of probe **1.2** and its mechanism for reacting with proton.

Kimet *et al.* investigated a list of ratiometric two-photon fluorescent sensors on the basis of benzimidazole motif for the sensitive and selective detection of pH value in lysosome. Probe **1.3**, bearing dimethylethylamino residue as the lysosome-targeted unit, was assessed for ratiometrically detecting pH alterations in lysosomes (Figure 1.16). Gradual acidification prompted the emission peak of the probe **1.3** to shift from 448 nm to 490 nm with a pKa value of 5.82. Moreover, the probe **1.3** was able to effectively determine

the time-dependent increments in lysosomal pH values in HeLa cells treated with 5 mM

NH$_4$Cl with a small fluctuation of 0.1 pH unit.[54]
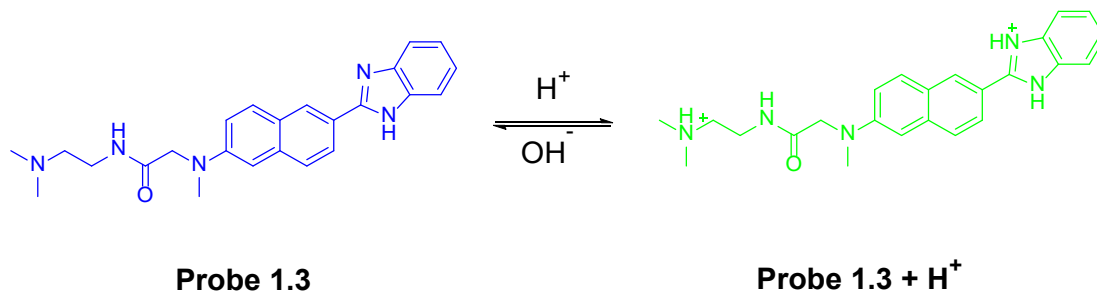
Figure 1.16. The structure of probe **1.3** and its pH responding mechanism.

Zhu *et al.* discovered two BODIPY-based fluorescent probes **1.4** and **1.5** through a

protonation-modulated ICT process. As shown in Figure 1.17, both two probes contained

morpholine group in order to target lysosome. For probe **1.4**, as pH value decreased from

6.83 to 0.82, the intensities of the main broad absorption band decreased gradually at 605

nm and another sharp band appeared at 558 nm which came from to the protonated form

of probe **1.4**. The alterations in the fluorescence spectra went in parallel with the absorption

spectra changes. With the pH value decreasing from 6.83 to 0.82, the intensity of near-

infrared emission band at 665 nm decreased gradually, which was accompanied by the

significant increase of fluorescence dual-band emissions at 515 nm and 569 nm. Similar

results were observed for the probe **1.5**. Thus they could be utilized for ratiometrically

detecting and imaging abnormal lysosome pH values.[55]

Lysosome Targeting
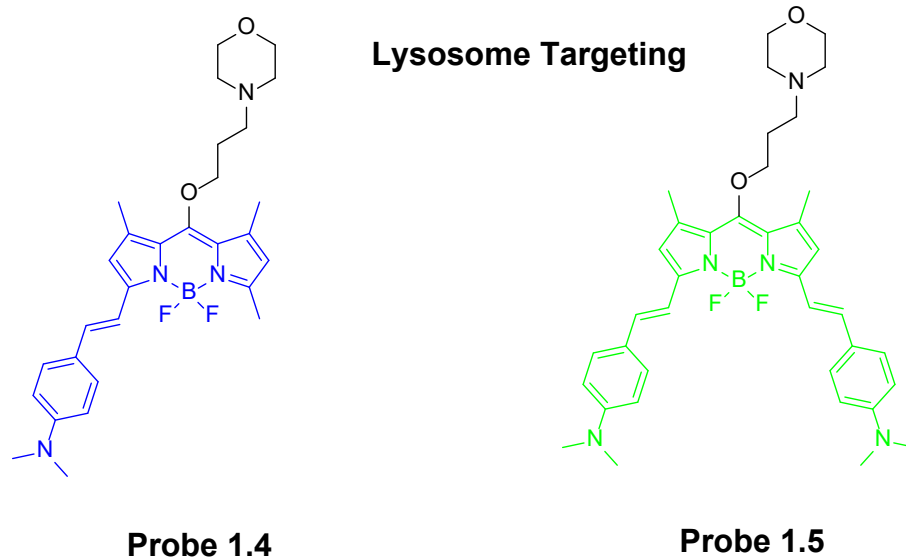
Probe 1.4

Probe 1.5

Figure 1.17. The structures of probe **1.4** and **1.5**

1.4.2 Ratiometric fluorescent probes to detect mitochondrial pH

The mitochondrion, with the plural form as mitochondria, is a double-membrane-bounded organelle found in most eukaryotic cells. As the ''energy factory'' of the cell, mitochondria are involved in many important metabolic functions including regulation of redox reactions and initiation of cellular apoptosis. In contrast with the acidic pH in lysosome, the pH value in the mitochondria is markedly alkaline with a value of approximately 8, which directly influences all biological processes in mitochondria. Therefore, the sensitive and accurate monitor of mitochondrial pH is highly demanded for understanding the critical role of mitochondrial biological events. Normally, in order to target mitochondria, the fluorescent probes should bear positive charge in the skeleton.

In 2015, Chen *et al.* developed a ratiometric fluorescent probe **1.6** (Scheme 1.18) via FRET mechanism for monitoring of mitochondrial pH by conjugating the pH-sensitive

fluorescein donor and pH-insensitive hemicyanine acceptor through an amide chain linker. The intrinsic ability of probe **1.6** to target mitochondria was originated from the cationic hemicyanine motif, which was further confirmed by a colocalization study with Mito-Tracker Deep Red 633. Besides mitochondria-targeting ability, the fluorescent probe **1.6** also could provide two different ratiometric sensing modes for pH values including the dual excitation mode and the dual excitation/dual emission mode. The fluorescent probe **1.6** possessed excellent reversible and linear ratiometric response within the pH range from 6.15 to 8.38, enabling it as a perfect sensor for ratiometically monitoring mitochondrial pH fluctuations in live cells.[56]
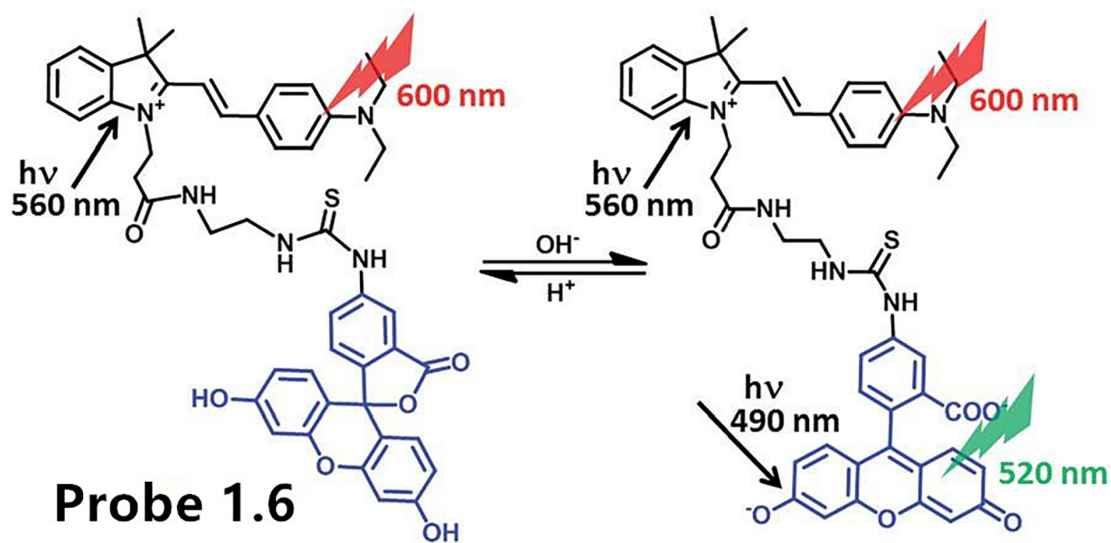
Figure 1.18. The structures of probe **1.6** and the mechanism of responding pH

In the same year, Li *et al.* obtained a hemicyanine-based fluorescent probe **1.7** with dual near-infrared fluorescence emission peaks, the fluorescence emission of which changed dramatically against pH alternation (Figure 1.19 a). As the pH decreased from 3.0 to 9.0, the intensity of the first fluorescence emission band decreased at 672 nm whereas

that of the second fluorescence emission peak at 748 nm enhanced (Figure 1.19 b). Interestingly, the intensity ratio between these two peaks for the probe **1.7** revealed an excellent linear ship among the physiology pH from 6.5 to 7.8 (Figure 1.20. c), making it possible for the quantitative analysis of mitochondrial pH fluctuations by the different stimulus through accurate ratiometric imaging. The probe **1.7** was well demonstrated a sensitive ratiometric fluorescent pH sensor not only *in vitro* but also *in vivo*, giving it possible for the further biological application.[57]
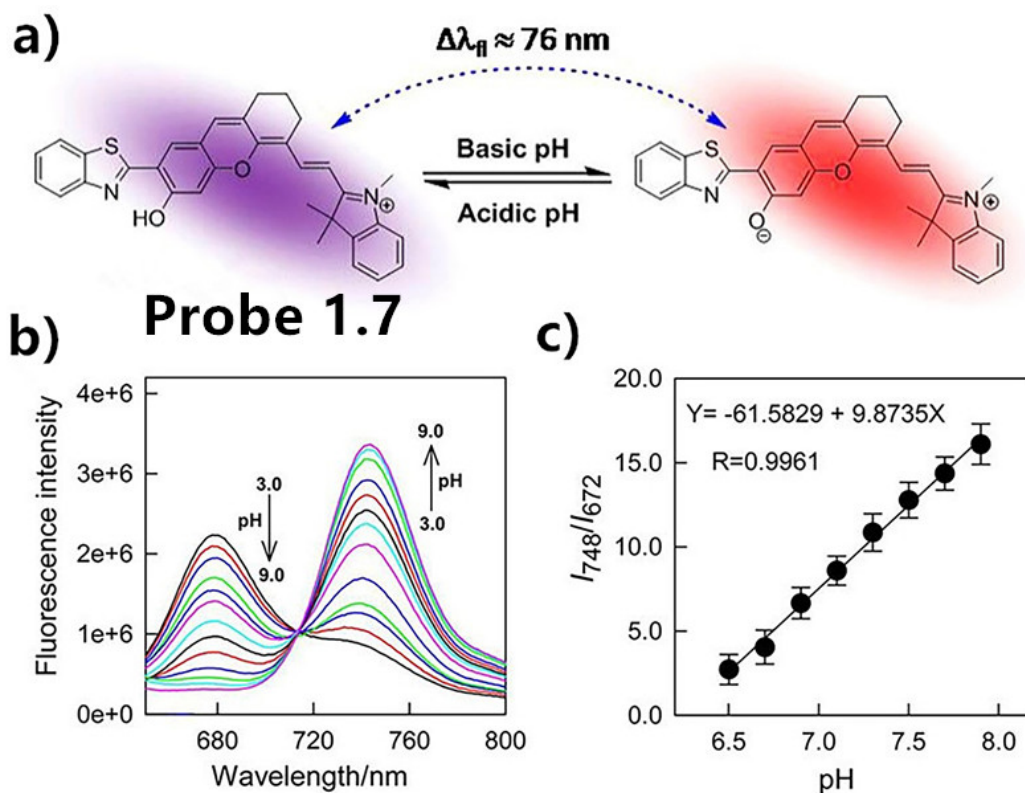
Figure 1.19. a) The structures of the probe **1.7** and its mechanism for monitoring pH; b) Fluorescence emission spectra of the probe **1.7** in buffer solution with pH decreasing from 3.0 to 9.0 under the excitation of 570 nm; c) The linear relationship for the ratio of I_{748}/I_{672} among the pH values ranging from 6.5 to 7.8.

Wu *et al.* presented the first ratiometric mitochondria-targeted fluorescent probe **1.8** on the basis of a pyridinium functioned 7-hydroxy coumarin skeleton for the real time detecting mitochondrial pH value in different live cells (Figure 1.20). Compared with commercially mitochondrial dyes, fluorescent probe **1.8** exhibited extraordinary pH sensitivity and excellent selectivity against biologically relevant anions, cations, amino acids as well as oxidative stress-associated redox reagents. What's more, possessing good biocompatibility, the probe **1.8** was further able to detect mitochondrial pH taking advantages the apporach of ratiometric fluorescence image.[58]
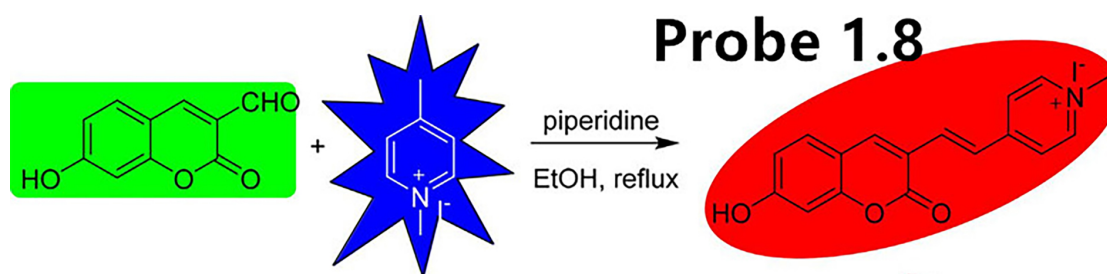
Figure 1.20. The synthesis routing to fluorescent probe **1.8.**

In 2019, Liu *et al.* constructed the fluorescent probe **1.9** by connecting a pH-sensitive naphthalimide fluorophore as a fluorescence donor and a mitochondria-targeting cyanine motif as a fluorescence acceptor through a FRET approach (Figure 1.21). Probe **1.9** showed excellent pH response, perfect mitochondria-targeting property, good selectivity and low cytotoxicity, which made probe **1.9** suitable for ratiometrically monitoring pH values in mitochondria of live cells. Furthermore, probe **1.9** was successfully utilized for the recognition of pH fluctuation in mitochondria under different stimulation reagents.[59]
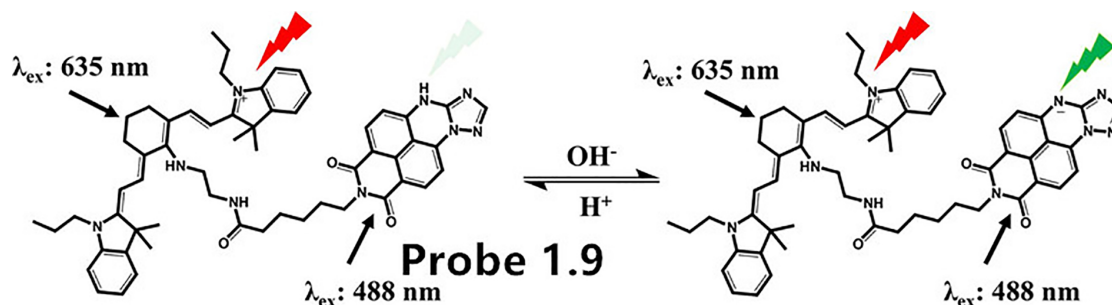
Figure 1.21. Mechanism of fluorescent probe **1.9.** for the ratiometric response to pH

1.5 Advanced in ratiometric fluorescent probes as biothiols sensors

Biothiols such as cysteine (Cys), glutathione (GSH) and homocysteine (Hcy) (Figure. 1.22), are tightly related with a number of important proteins and enzymes which are vital for the biological system. The endogenous concentrations of the biothiols suggest the functional state of the corresponding enzymes, and their abnormal levels have a close relationship with diseases.[60] Thus, with the powerful detection tool of ratiometric fluorescent probes at hand, it is of great importance to design fluorescent probes to monitor intracellular biothiols with a quick speed, good biorthogonality and excellent chemoselectivity.

Cysteine   **Homocysteine**   **Glutathione**
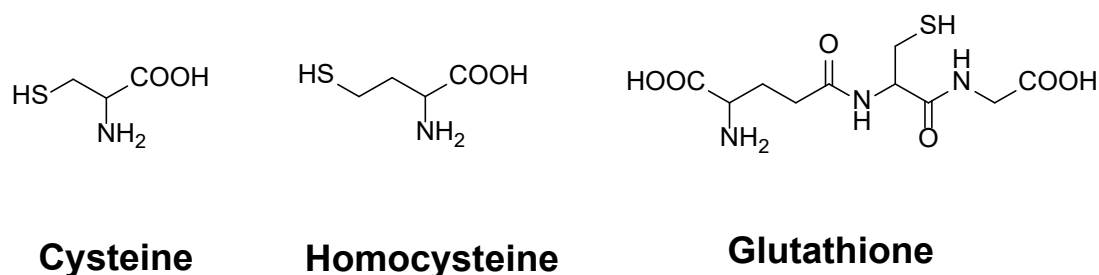
Figure 1.22. Chemical structures of Cys, Hcy and GSH

In 2015, Niu *et al.* developed a new ratiometric Cys-selective two-photon fluorescence sensor **1.10** which was able to be target mitochondria based on a typical merocyanine dye as a fluorescence motif and an acrylate residue as the biothiols reacting receptor. As we can see from Figure 1.23, the ratiometric sensing mechanism was an ICT process which involved a conjugating addition of cysteine (Cys) to acrylate residue from the blue fluorescent probe **1.10** to afford thioethers. This was followed by a nucleophilic intramolecular cyclization to give a 7-membered cyclic amide and a merocyanine compound which could emit green fluorescence. Besides, the fluorescent probe **1.10** not displayed the mitochondrial-targeting property but revealed a selective ratiometric detection of cysteine (Cys) concentrations over the other biothiols including hydrogen sulfide (H_2S),homocysteine (Hcy) or glutathione (GSH) in the live cells and tissues.[61]
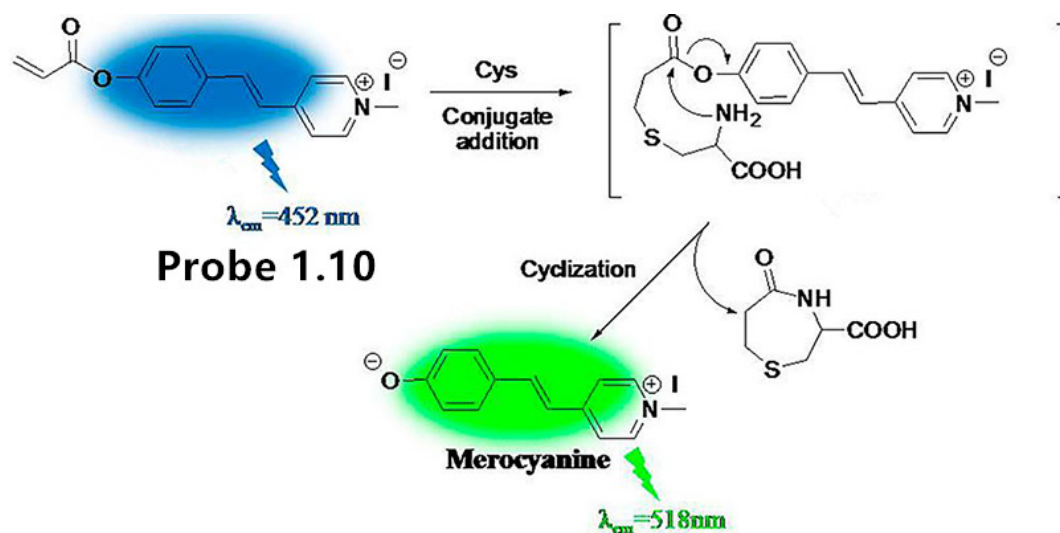
Figure 1.23. Plausible sensing mechanism of ratiometric probe **1.10** with cysteine

Fluorescent probe **1.11** was successfully designed and obtained for the ratiometric detecting of biothiols by Wang *et al.* based on a FRET approach. The probe **1.11** could be

divided into two components: one was rhodamine B motif serving as the acceptor and reference, and the other part was a substituted coumarin moiety donor acting as the biothiols responding receptor by introducing an acrylate residue. The detailed responding mechanism was on the basis of Michael addition with biothiols and followed by a nucleophilic intramolecular cyclization, leading to a sensitive and ratiometric response to biothiols (Figure 1.24). Furthermore, the probe **1.11** responded to Cys quickly within 10 min time window and possessed a limit of detection as low as 0.13 μM, suggesting that this sensor could selectively monitor intracellular Cys over the other biothiols.[62]
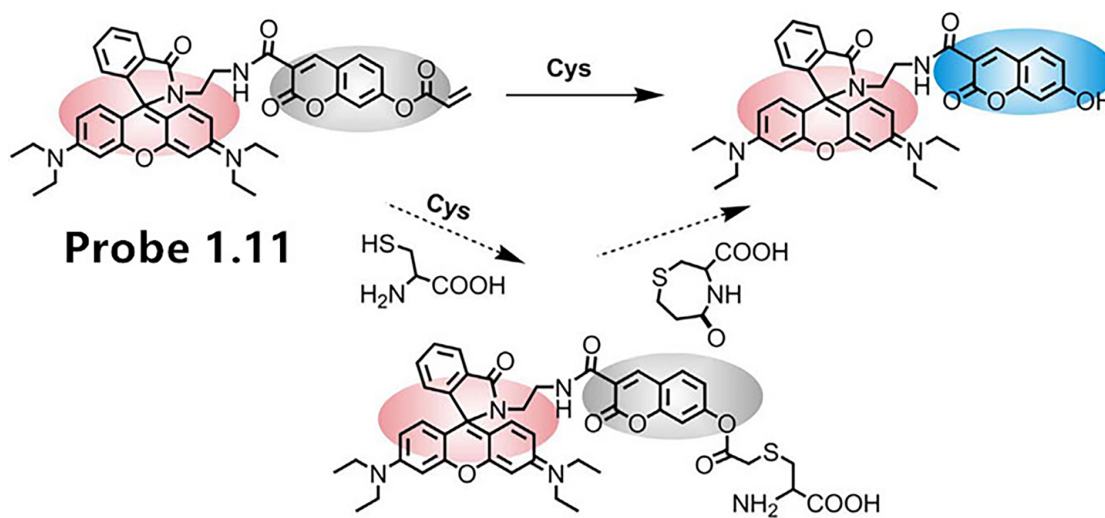
Figure 1.24. Proposed ratiometric sensing mechanism of probe **1.11** with Cys

To improve the selectivity of biothiols, Lin *et al.* employed an aromatic substituting−rearrangement approach to design and synthesize a novel Cys-specific fluorescent probe **1.12** based on a novel FRET coumarin−sulfonyl benzoxadiazole moiety (Figure 1.25), leading to the ratiometric discrimination of the other biothiols such as Hcy or GSH. Response of fluorescent probe **1.12** to Cys would generate a new yellow emission

peak at the wavelength of 580 nm, resulting in a 99 nm red shift and a 56.1-fold ratio increase for the yellow and blue channels.[63]
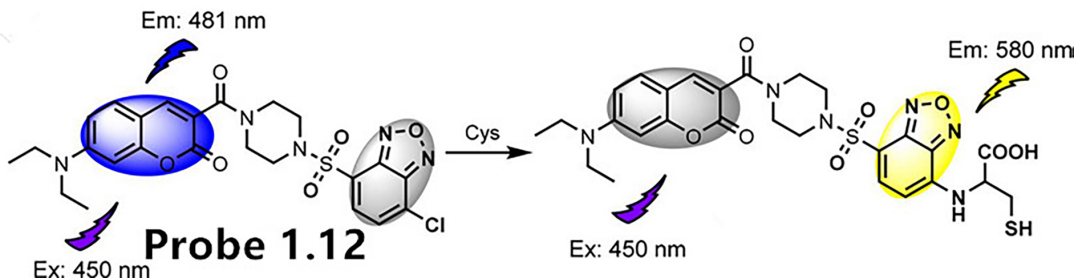
Figure 1.25. Design of ratiometric Cys-specific probe **1.12** based on FRET mechanism

In 2017, Gong *et al.* reported two fluorescent ratiometric BODIPY probes **1.13** (nonsymmetric) and **1.14** (symmetric) for selectively detecting GSH via an ICT process (Figure 1.26). The detailed detection mechanism was on the basis of an improved two-stage nucleophilic aromatic substitution of the nitrophenol residue from the probes **1.13** or **1.14** by GSH in buffer solution. Probe **1.13** could be used as a two-step ratiometric detection tool for three different concentration windows of GSH (0−6, 7−15, and 15−100 μM) with dramatical red shift in fluorescence peak and significant ratio alteration of fluorescent bands within 5 min time. On the contrary, probe **1.14** only displayed as a single-stage ratiometric fluorescent device for monitoring intracellular GSH.[64]
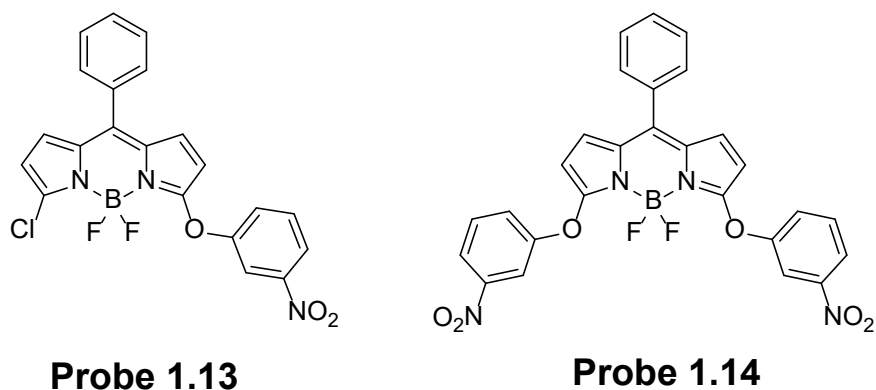
Figure 1.26. Structures of GSH-specific ratiometric fluorescent probes **1.13** and **1.14**

1.6 Research driving force, approaches and outline

1.6.1 Drawbacks of current fluorescent probe

Even with the fast development of fluorescent probes in the recent several decades, the current existing fluorescent probes are still far from satisfactory, which is definitely in need of improvement.

First at all, the absorption peaks and fluoresce emission bands for the majority of current fluorescent sensors lies within the ultraviolet region (200 – 400 nm) or visible light region (400 – 600 nm). The applications for the probes are severely affected due to the high energy for the radiations in these regions which may cause strong damage to the cells or tissues. In addition, the absorption and autofluorescence of biomolecules in cells or tissues are very strong which could not be omitted in UV/Vis regions, resulting in low signal-to-noise ratio. Furthermore, because of the strong absorption and light scattering in the UV/Vis range, it is extremely hard for the fluorescence to penetrate the tissues. These disadvantages will severely impede the practical application of the fluorescent probes.

Second, most of existing small-molecule-based fluorescent probes are intensity-based sensors which only emit one fluorescence emission channel. The main problem of these probes is that fluctuations in the concentration of probes, the environment of probe, and the intensity of the laser would cause the alterations of the corresponding fluorescent signal. Theoretically, this limitation could be removed by utilizing ratiometric fluorescent sensors possessing dual fluorescence channels. These probes allow the measurement of fluorescence intensity at two different bands. The ratio signals of ratiometric fluorescence probes would be free from interferences for the intensity-based probes.[65]

Third, since the structures of typical fluorophores are always including large π-conjugation systems and aromatic rings that are extremely hydrophobic, the water solubility is usually poor for the existing fluorescent probes, leading to the self-aggregation and fluorescence quenching in the aqueous system. This is the key fact that prevents the fluorescent probe from practical application.

1.6.2 Research approaches and plan

To overcome the drawbacks of current fluorescent sensors mentioned before, the main focuses of this dissertation are listed as below:

1) Designing and synthesizing new NIR fluorescent dyes with good water solubility, large Stokes shift, high quantum yield, and long wavelength emission.

2) Devising NIR ratiometric fluorescent probes with enhanced selectivity and sensitivity to monitor the pH changes in specific organelles in the live cells.

3) Introducing more bulky switches to the fluorophores so as to increase pK_a values of the pH fluorescent probe.s

4) Broadening the analytes to other species such as biothiols, enzymes and even oxygen levels in the cells and tissues.

In chapter 2, two novel dyes and one new fluorescent probe based on rhodamine moiety with good quantum yield, perfect water solubility and large Stokes shift were prepared by introducing fused rings to the amino residues of rhodamine moiety.

In chapters 3 and 4, we devised and synthesized two series of NIR ratiometric fluorescent probes to detect lysosomal pH variations by taking the advantages of the strategy as the π-modulation conjugation and the FRET or TBET, respectively.

In chapters 5, we presented two NIR ratiometric fluorescent probes which were able to detect pH fluctuations in mitochondria due to the positive charge in the molecule through the π-modulation conjugation approach.

Based on the contents in Chapters 3, 4 and 5, we subsequently designed and developed a neoteric FRET-based NIR fluorescent sensor for the sensitive and ratiometric recognition of biothiols in living cells and fruit flies that was discussed in detail in Chapter 6.

2 New near-infrared rhodamine dyes with large Stokes shifts for sensitive sensing of intracellular pH changes and fluctuations[66]

Yibin Zhang,[a,b] Shuai Xia,[a] Mingxi Fang,[a] Wafa Mazi,[a] Yanbo Zeng,[a] Taylor Johnston,[a] Adam Pap,[a] Rudy Luck[a]* and Haiying Liu[a]*

[a.] Department of Chemistry, Michigan Technological University, 1400 Townsend Drive, Houghton, MI 49931, USA. E-mail: hyliu@mtu.edu; rluck@mtu.edu

[b.] School of Chemistry and Chemical Engineering, Yangtze Normal University, Chongqing 408100, China

2.1 Introduction

Traditional rhodamine dyes such as rhodamines 6G, B and 101 have been widely used to develop fluorescent probes by introducing a variety of functional groups to form closed spirolactam on-off switches. This results in outstanding photophysical properties such as high molar extinction coefficients, excellent fluorescence quantum yields, great photostability and water solubility.[16, 67-72] The disadvantages of traditional rhodamine dyes include short fluorescence wavelengths with less than 600 nm absorptions and small Stokes shifts less than 35 nm, which may cause excitation wavelength interference, cellular damage and limit their biological applications.[16, 67-72] There have been recent reports on the tuning of traditional rhodamine dyes to the deep-red and near-infrared regions by extending π-conjugation of the xanthene ring, replacing the central oxygen atom by other elements such as N, C, S, Se, P, Si, Ge, Sn and Te in order to take advantage of NIR imaging features such as minimal tissue absorption, low background autofluorescence from biological samples, and deep tissue penetration.[73-87] Si-rhodamines and Ge-rhodamines and P-rhodamines show far-red and NIR emission while retaining the main advantages of the traditional rhodamine dyes such as high fluorescence quantum yields, excellent photostability and sufficient water solubility for biological imaging applications.[73-76, 78-81] Another very effective approach is to introduce the spirolactam fluorescence on–off switches to near-infrared hemicyanine dyes, which have shown some biological imaging applications.[76, 88-90] It is still very important to develop near-infrared rhodamine dyes with large Stokes shifts, high photostability and increased fluorescence to overcome excitation light interference for practical bioimaging applications.

In this communication, we tuned rhodamine emission to the near-infrared region by incorporating an additional amine group with fused rings to rhodamine dyes to enhance the electron donating ability of amine groups and improve the spectroscopic properties of the dyes. Rhodamine dyes **A** and **B** show near-infrared emission with large Stokes shifts, high molar absorptivity, excellent photostability, good hydrophilicity, and stable fluorescence under different pH conditions. Rhodamine dye **C** obtained by introducing o-phenylenediamine to rhodamine dye A shows fast and highly sensitive responses to cellular pH changes with significantly higher pKa of 5.4 related to spirolactam ring opening[91-95] because of larger steric hindrance between the o-phenylenediamine residue and xanethene moiety compared to traditional rhodamine dyes. Rhodamine dye **C** was successfully used to detect lysosomal pH changes, and pH fluctuations under oxidative stress and drug treatment (Scheme 2.1).
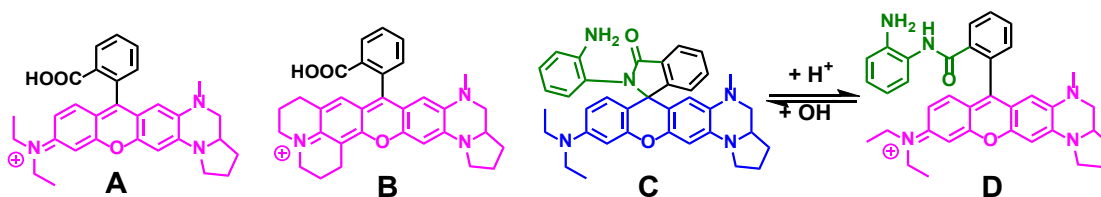
Scheme 2.1. Chemical structures of near-infrared rhodamine dyes (**A**, **B**, and **C**).

2.2 Method

Near-infrared rhodamine dyes **A** and **B** were prepared by a condensation reaction of 5-methyl-1,2,3,3a,4,5-hexahydropyrrolo[1,2-a]quinoxalin-8-ol (**4**) with either 2-(4-diethylamino-2-hydroxybenzoyl)benzoic acid (**5**) for **A**, or 2-[(2,3,6,7-tetrahydro-10-hydroxy-1H,5H-benzo[ij]quinolizin-9-yl)carbonyl]-benzoic acid (**6**) for **B** in trifloroacetic

acid under reflux (Scheme 2.2). Compound **4** was prepared according to a reported procedure.[96] Rhodamine dye **C** was prepared by introducing o-phenylenediamine to rhodamine dye **A** to form a non-fluorescent closed spirolactam ring structure through the condensation reaction of one amine group from o-phenylenediamine and the carboxylic acid on rhodamine dye **A** (Scheme 2.2).
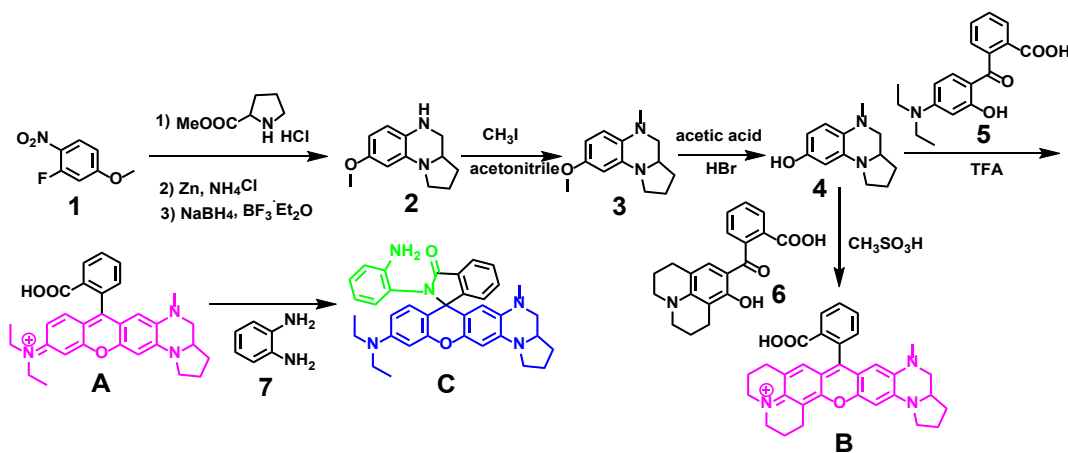
Scheme 2.2. Synthetic route to near-infrared rhodamine dyes **A**, **B** and **C**.

2.3 Results and discussions

2.3.1 Optical Properties

Rhodamine dye **A** spectra contain absorption and emission peaks at 575 and 648 nm respectively corresponding to a large Stokes shift of 73 nm (Figure 2.1). The absorption has a high molar absorptivity of 3.1×10^4 $M^{-1}cm^{-1}$, and a high fluorescence quantum yield of 22.6% in a pH 7.4 buffer containing 10% ethanol was measured. Rhodamine dye **B** spectra exhibit an absorption peak at 586 nm and an emission peak 644 nm with a slightly smaller Stokes shift of 58 nm compared to rhodamine **A** (Figure 2.2). Dye **B** displays a high molar absorptivity of 3.4×10^4 $M^{-1}cm^{-1}$, and, a slightly higher fluorescence quantum

38

yield to dye **A** of 25.1% under identical conditions. The fluorescence intensities of rhodamine dyes **A** and **B** increase with increases in the ratio of ethanol to water in solutions of ethanol and water (Figure S7-S8). Increases in the ethanol percentage reduce dye aggregation and fluorescence quenching and result in enhancement of dye fluorescence intensity. The fluorescence intensity and absorbance of rhodamine dyes **A** and **B** do not change much in different pH buffer solutions (Figure 2.1).
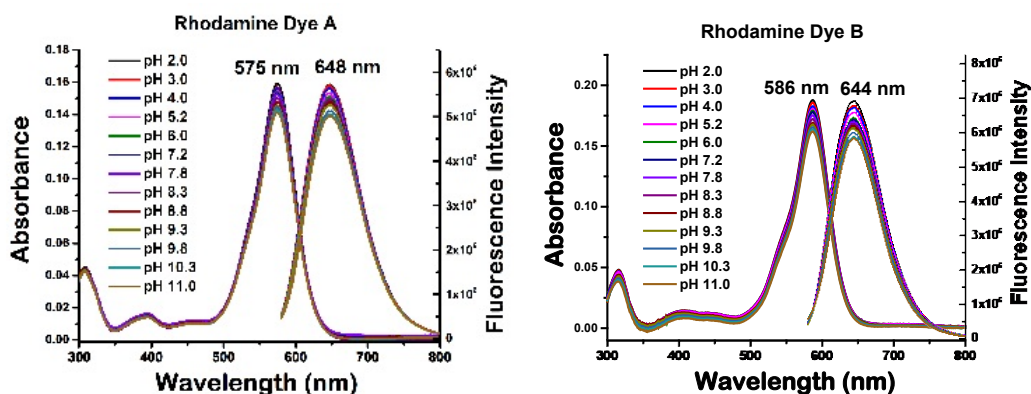
Figure 2.1. Absorption and fluorescence spectra of rhodamine dyes **A** and **B** in 10 mM buffers with excitation at 550 nm
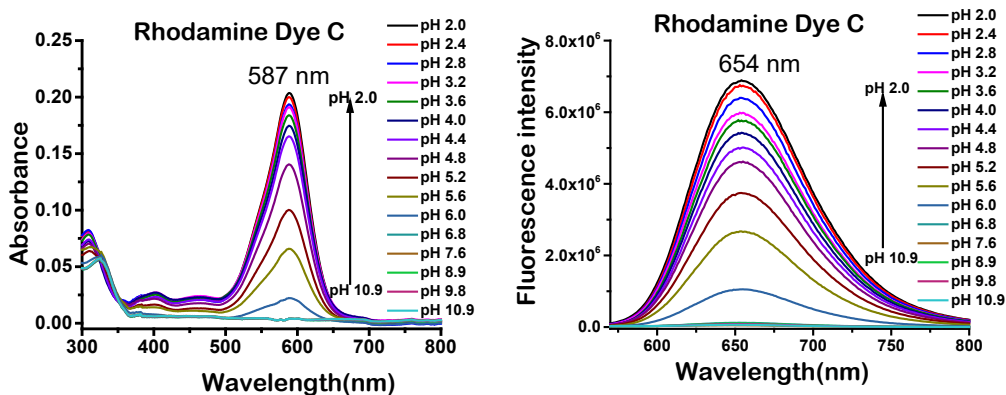
Figure 2.2. Absorption (left) and fluorescence (right) spectra of rhodamine dye **C** in 10 mM buffers with excitation at 550 nm.

Rhodamine dye **C** displays no absorption peak from 500 nm to 800 nm under neutral and basic pH conditions as the dye maintains a closed spirolactam ring structure. However, a stepwise decrease in pH value from 7.6 to 2.0 leads to a new absorption peak at 587 nm with corresponding increases in the intensity of this peak because of pH-activated spirolactam ring opening (Scheme 2.1).[91-95] Rhodamine dye **C** is non-fluorescent with the closed spirolactam ring form under basic and neutral conditions. However, a new fluorescence peak at 655 nm, corresponding to the aforementioned peak at 587 nm, which also increases with decreases in pH from 7.6 to 2.0 presumably due to significantly enhanced π-conjugation as the spirolactam ring opens under acidic conditions,[91-95] is obtained (Figure 2.2). A large Stokes shift of 68 nm for a pH 3.2 buffer is obtained. In addition, it displays a higher pK_a value of 5.4 related to spirolactam ring opening,[91-95] obtained using the Henderson–Hasselbach-type mass action equation (Figure S10).[91-94] This unusually higher pK_a value and very fast response to pH changes is due to the steric hindrance between the spriolactam moiety and the amine ring on the rhodamine backbone. A fluorescence quantum yield of 19.8 % with a molar absorptivity of $3.8\times10^4\,M^{-1}cm^{-1}$ in a 10 mM pH 3.2 buffer containing 10% ethanol is obtained. Rhodamine dye C is highly selective to reactions with protons at pH 3.2 compared to 50 µM solutions of different anions, cations, and amino acids according to selectivity experiments (Figures S12-S13).

2.3.2 Theoretical calculation

In order to confirm the nature of the electronic transitions obtained for rhodamine dyes **A-D**, theoretical studies (optimization, frequency and TD-DFT calculations) at the APFD[97]/6-311+G(2d, p)[98] level were conducted. Electronic transition maxima were calculated (expt.)

at 526 (575), 531 (586), 322 and 527 (587) nm for dyes **A-D** respectively (Figures S16, S22, S27 and S33) and these values are within an expected error range of 0.20–0.25 eV.[99] Full details are available as supporting information (Figure S14-S35). The results are best summarized in the form of difference density illustrations in Figure 3, which consists of subtracting the total density cube for the HOMO from that of the LUMO orbital that contributes the most to the UV-Vis transition as verified from the calculations.[99, 100] If both the HOMO and LUMO orbitals of a molecule are delocalized, there would not be great differences in color observed in these plots. The illustrations in Figure 2.3 reveal the movement of electron density towards the positively charged N atom (see Scheme 2.1) in dyes **A**, **B** and **D,** and clearly indicate that dye **C** has a greater difference in color than the other dyes. Finally, delocalization is restored in dye **D**, judging by the similar appear to the illustration for dyes **A** and **B**.
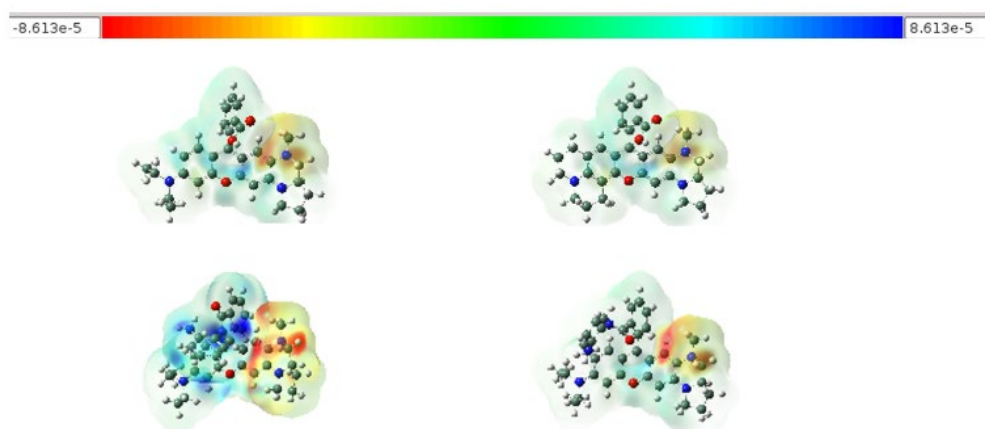
Figure 2.3. Difference density illustrations as iso-surfaces of rhodamine dyes **A** (top left), **B** (top right), **C** (bottom left) and **D** (bottom right). Red areas indicate values for the different density of -8.613e^{-5} and blue are for 8.613e^{+5}, see scale on top of illustration.

2.3.3 Photostability, cytotoxicity and cellular confocal imaging

Rhodamine dyes **A**, **B** and **C** show excellent photostability (Figures S11-S12) and very low cytotoxicity with cell viability of more than 80% at dye concentrations of 20 μM according to a standard MTS assay through 48 h incubation of HeLa cells with the rhodamine dyes (Figure S36). Lysosomes are the intracellular acidic organelles with pH values from 4.0 to 5.5. In order to test whether rhodamine **C** can target lysosomes in live cells, we co-stained HeLa cells with rhodamine dye **C** and lysotracker green, a lysosome specific dye. Confocal microscopic co-localization analysis of rhodamine dye **C** and lysotracker green gave the Pearson's coefficient value of 0.89 or higher, indicating that rhodamine dye C accumulates and becomes activated to engender fluorescence inside lysosomes in live cells (Figures 4 and S37). In addition, fluorescence of rhodamine dye **C** becomes brighter with increases of the dye concentrations (Figure 2.4). Next, we investigated whether rhodamine dye **C** could monitor intracellular pH changes by using H^+/K^+ ionophore nigericin to equilibrate the intracellular and extracellular pH values of HeLa and MCF7 human breast cells in media containing 5 μg/mL H^+/K^+ ionophore nigericin with different pH values from 3.0 to 7.5 (Figures 2.5 and S38).[91-94] Cellular fluorescence intensity of rhodamine dye **C** becomes brighter when pH decreases from 7.5 to 3.0 (Figure 2.5). It shows the same fluorescence responses to pH changes in buffer solutions and live cells with a higher pK_a value of 5.4 related to spirolactam ring opening[91-95] since its fluorescence can be observed at pH 6.5 in live cells (Figures 2.2, 2.5 and S38). The unusual pK_a value arise from considerable steric hindrance between o-phenylenediamine residue and bulky xanethene moiety compared with traditional rhodamine dyes (Scheme 2.1).
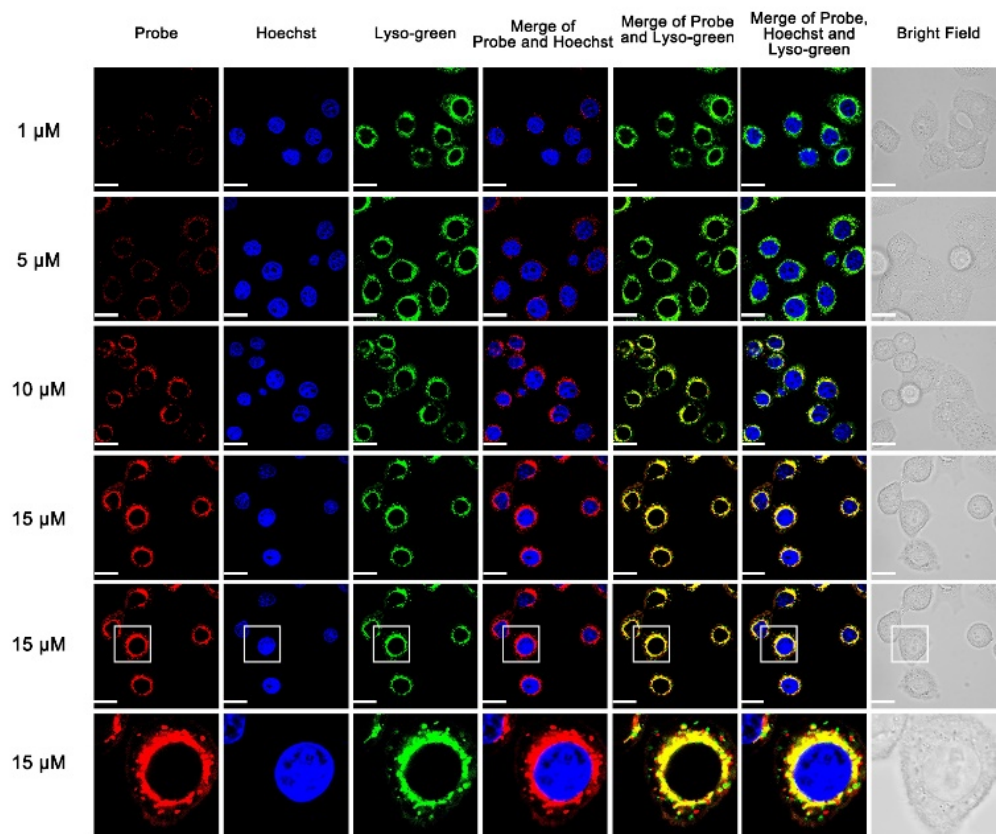
Figure 2.4. Acidity-activated turn-on cellular fluorescence of rhodamine dye **C** in lysosomes in HeLa cells. HeLa cells were cultured in media containing 1 µg/ml Hoechst stain, 1 µM Lysosensor green and rhodamine dye **C** with concentrations from 1 µM to 15 µM. The sixth row is the enlarged image of 15 µM rhodamine dye **C**. The images were obtained by confocal fluorescence microscopy with a scale bar of 20 µm. The filter sets used to image dye **C**, Hoechst and Lyso-green were excitation 559 nm and emission 675/50 nm, excitation 405 nm and emission 450/50 nm and excitation 488 nm and emission 550/50 nm, respectively.
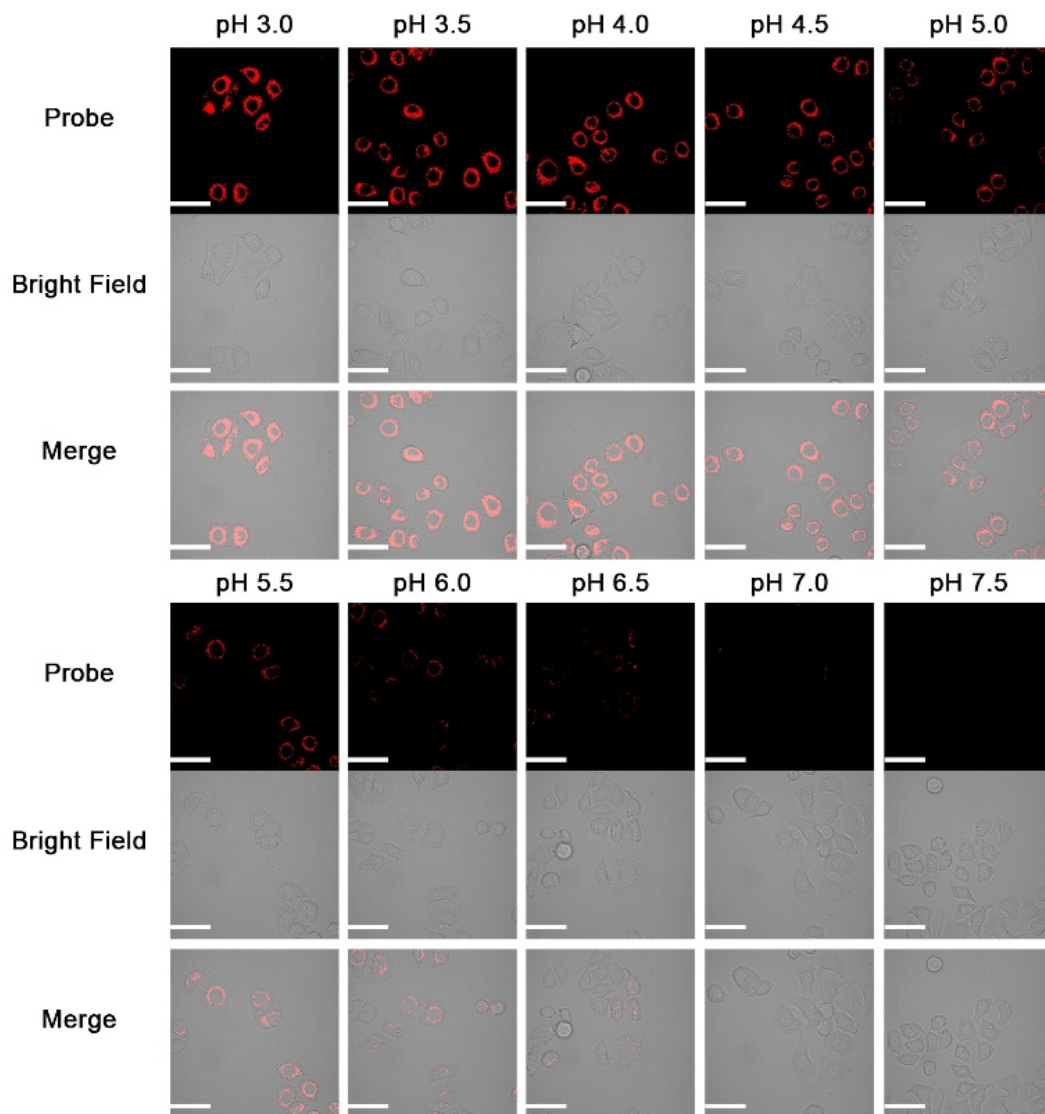
Figure 2.5. Cellular fluorescence intensities of 10 µM rhodamine dye **C** inside HeLa cells with different intracellular pH values, which was adjusted by using 5 µg/mL H^+/K^+ ionophore nigericin to equilibrate the intracellular and extracellular pH in media with different pH values. Confocal fluorescence microscopy was employed to collect the images with a scale bar of 50 µm. The filter sets used to image dye **C** was excitation 559 nm and emission 675/50 nm.

We further studied whether rhodamine dye **C** could be used to monitor lysosomal pH changes in HeLa cells. After incubation of HeLa cells with rhodamine dye **C**, the cells

show near-infrared fluorescence (Figure 2.6). 10 mM NH₄Cl treatment of HeLa cells causes a decrease of cellular fluorescence intensity because ammonium chloride treatment results in quick alkalification of the lysosomes, causing a pH increase (Figure 2.6). Treatment of HeLa cells with 100 μM hydrogen peroxide and *N*-ethylmaleimide also cause cellular fluorescence intensity decreases (Figure 2.6), indicating that lysosomal pH in live cells under oxidative stress increase because the oxidative stress under hydrogen peroxide redistributes H^+ ions from acidified lysosomes to cytosolic compartments by weakening proton ATPase, an enzyme that imports H^+ ions through ATP hydrolysis.[101-103] Treatment of HeLa with different concentrations of chloroquine also makes cellular fluorescence intensity decrease (Figure 2.7) because chloroquine functions as a lysosomotropic base to neutralize some proton ions in lysosomes in live cells. As a result, increases in chloroquine concentration results in gradual fluorescence decreases (Figure 2.7). These results convincing demonstrate that rhodamine dye **C** can accurately detect pH fluctuations in lysosomes.
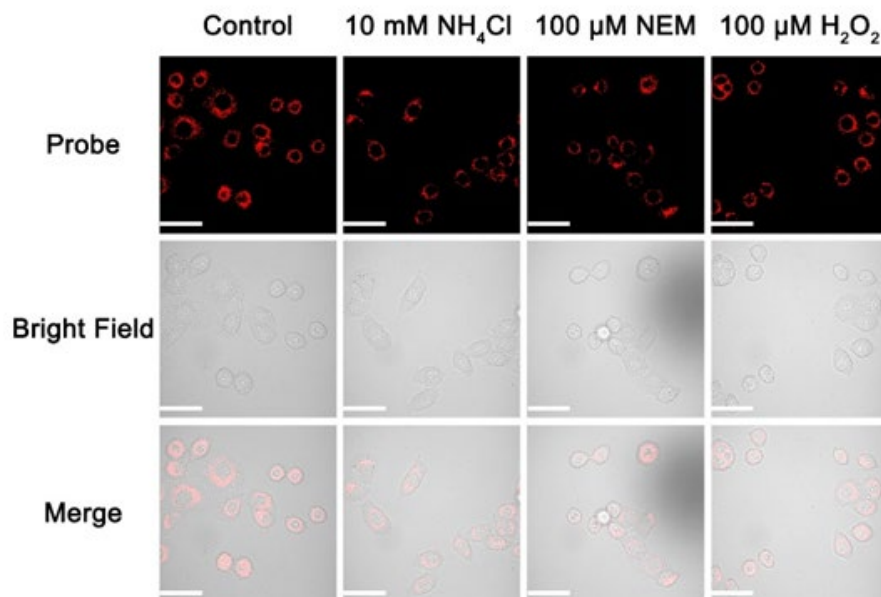
Figure 2.6. Cellular fluorescence intensities of 10 μM rhodamine dye **C** inside HeLa cells. Intact cells, and cells treated with 10 mM NH₄Cl, 100 μM NEM and 100 μM HClO, respectively. Confocal fluorescence microscopy was employed to collect the images with a scale bar of 50 μm. The filter sets used to image dye **C** was excitation 559 nm and emission 675/50 nm.
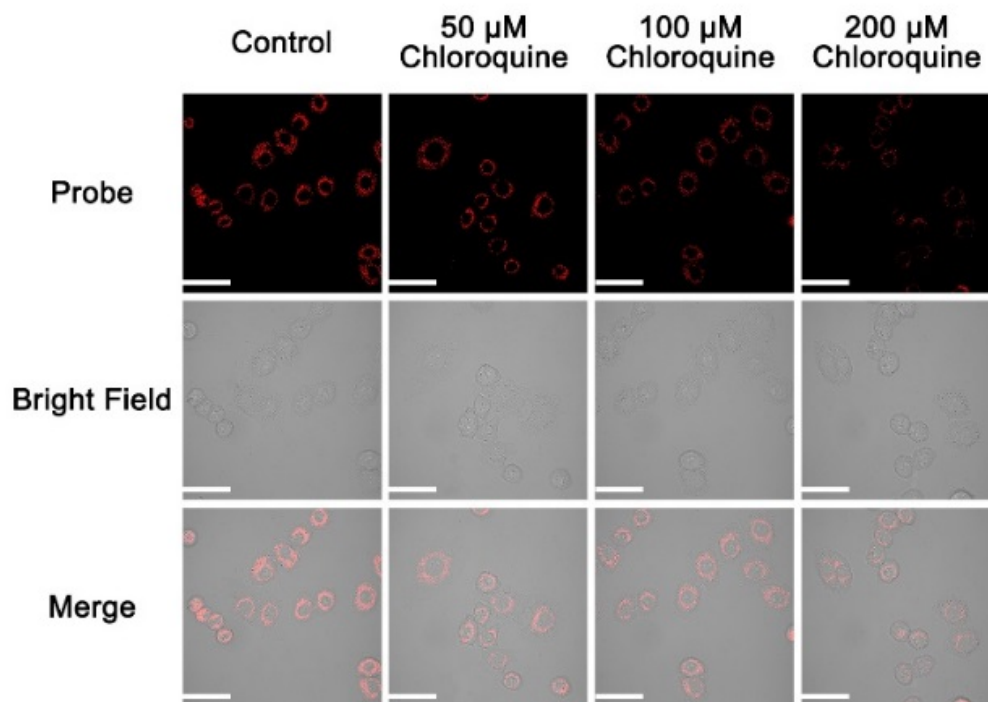
Figure 2.7. Cellular fluorescence intensities of 10 μM rhodamine dye **C** inside HeLa cells with different concentrations of chloroquine as a stimulant. Confocal fluorescence microscopy was used to collect the images with a scale bar of 50 μm. The filter sets used to image dye **C** was excitation 559 nm and emission 675/50 nm.

2.4 Conclusions

We developed new near-infrared rhodamine dyes with large Stokes shifts, excellent photostability and fluorescence brightness by integrating an additional amine group with fused rings to rhodamine dyes to increase the electron donating ability of amine groups. In addition, fluorescent probe (rhodamine dye **C**) with a higher pK_a value of 5.4 was prepared

46

as a useful molecular fluorescent tool in the study of pH-relevant biological processes for fast and sensitive detection of lysosomal pH changes and fluctuations under oxidative stress.

3 Fluorescent Probes Based on π-Conjugation Modulation between Hemicyanine and Coumarin Moieties for Ratiometric Detection of pH Changes in Live Cells with Visible and Near-infrared Channels[104]

Shuai Xia,[a] Jianbo Wang,[a,b*] Jianheng Bi,[a] Xiao Wang,[a] Mingxi Fang,[a] Tyler Phillips,[a] Aslan May,[a] Marina Tanasova,[a*] Fen-Tair Luo,[c*] and Haiying Liu[a*]

[a.] Department of Chemistry, Michigan Technological University, Houghton, MI 49931, E-mail: mtanasov@mtu.edu; hyliu@mtu.edu

[b.] College of Biological, Chemical Sciences and Engineering, Jiaxing University, Jiaxing 314001, China. E-mail: wjb4207@mail.ustc.edu.cn

[c.] Institute of Chemistry, Academia Sinica, Taipei, Taiwan 11529, Republic of China, E-mail: luoft@gate.sinica.edu.tw

3.1 Introduction

Ratiometric fluorescence imaging offers reliability in quantitative and comparative analyses and effectively overcome variations in the emission intensity, concentration, and compartmental localization of intensity-based fluorescent probes.[70, 72, 105-111] As a result, it has been commonly applied to study highly dynamic intracellular ion, voltage or pH changes. Common approaches to achieve ratiometric fluorescence imaging are to employ Forster Resonance Energy Transfer (FRET) or a through-bond energy transfer (TBET) from a fluorophore donor to a fluorophore acceptor.[112-114] The FRET strategy requires a spectral overlap between the donor emission and the acceptor absorption, which significantly limits choices of the donor and acceptor fluorophore pairs. In contrast, the TBET approach can effectively overcome this limitation, and offer multiple choices for the donor and acceptor fluorophore pairs. Other ratiometric fluorescent probes are based on π-conjugation modulation of fluorophores in response to analytes.[115-117] Most of the reported ratiometric fluorescent probes are based on Rhodamine acceptors in FRET and TBET strategies, which possess less than 600 nm in the acceptor emission. Therefore, it remains a challenging task, particularly for imaging of lysosomal pH in live cells, to develop ratiometric fluorescent probes with high turn-on fluorescence, large dynamic range, large pseudo-Stokes shifts, photodamage-free near-infrared imaging of living organisms, low autofluorescence interference from biological samples, and highly selective and sensitive ratiometric responses with well-defined dual excitation and emission capability. Although a number of fluorescent probes have been developed for pH detection,[83, 88, 89, 94, 116-139] pH ratiometric fluorescent probes are still limited, especially those with near-infrared emission.

In this paper, we present a simple but effective π-conjugation modulation strategy to construct fluorescent probes (**A** and **B**) for ratiometric detection of pH changes. The design of probe **A** is based on conjugating a coumarin fluorophore to a hemicyanine fluorophore via a vinyl connection and introducing a lysosome-targeting morpholine residue form a closed spirolactam structure of the hemicyanine (Scheme 3.1). In order to increase pK_a of the probe **B**, *o*-phenylenediamine residue was introduced to hemicyanine moiety. In neutral or basic condition, the probe shows very strong fluorescence of the coumarin fluorophore, and can effectively overcome blind fluorescence imaging encountered for typical intensity-based pH fluorescent probes. This outcome results from no fluorescence of the closed spirolactam structures of the hemicyanine moieties under basic and neutral pH conditions. Gradual decrease of pH from 7.4 to 2.0 causes ratiometric fluorescence responses of probes with the decrease in the coumarin fluorescence and increase in the hemicyanine fluorescence due to the acid-mediated opening of the spirolactam ring and the subsequent enhancement of π-conjugation. The probes show ratiometric response to pH changes in live cells with moderate decrease of the coumarin fluorescence and increase of hemicyanine fluorescence. This probe design strategy can offer a general approach to construct a variety of ratiometric fluorescent probes to detect biological thiols, metal ions, reactive oxygen and nitrogen species by introducing appropriate sensing ligands to the hemicyanine fluorophores with unique spirolactam ring structures.
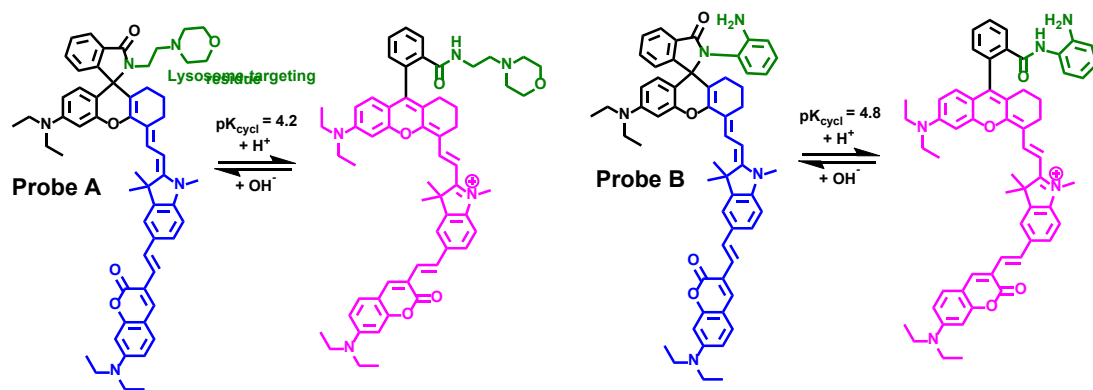
Scheme 3.1. Chemical structure response of fluorescent probes to pH changes with π-conjugation changes.

3.2 Materials and Methods

3.2.1 Instrumentation

400 MHz Varian Unity Inova NMR spectrophotometer instrument was employed to collect ^{1}H NMR and ^{13}C NMR spectra in CDCl$_3$ and CD$_3$OD solutions. Solvent residual peaks (^{1}H: δ 7.26 for CDCl$_3$, δ 3.31 for CD$_3$OD; ^{13}C: δ 77.3 for CDCl$_3$) were used as internal standards in ppm to define chemical shifts (δ) of intermediates and probe. Double focusing magnetic mass spectrometer, fast atom bombardment (FAB) ionization mass spectrometer, or matrix-assisted laser desorption/ionization time of flight mass spectrometer were used determine high-resolution mass spectrometer data (HRMS). Absorption and fluorescence spectra were conducted by using Per-kin Elmer Lambda 35 UV/VIS spectrometer and Jobin Yvon Fluoromax-4 spectrofluorometer, respectively.

3.2.2 Cell Culture and fluorescence imaging

HeLa cells were purchased from ATCC (Manassas, VA). Cells grown for a minimum of five passages were used in all experiments. The Cells were incubated in a 5% CO$_2$

humidified incubator at 37 °C and typically passaged with sub-cultivation of 1:3 every two days. For confocal imaging, HeLa cells were seeded into the 35 mm glass-bottom culture dishes (MatTek, MA) and allowed to grow for 1-2 days to reach 70–90% confluence. After 24 h of incubation, the cell culture medium was replaced by freshly prepared serum-free medium with 1, 5, 10, 20 μM of the probe **A** for 1 h. The cells were incubated further with 50 nM LysoTracker red (Thermo-Fisher) for 30 min to confirm the specific targeting of our probe **A** to lysosomes in HeLa cells. Live cell images were taken by a confocal fluorescence microscope (Olympus IX 81). The excitation wavelength of the coumarin is 405 nm and the images were collected at 500 – 550 nm (green channel) and 725 – 775 nm (NIR channel). The excitation wavelength of the hemicyanine dye is 635 nm and the images were collected at 725 – 775 nm (NIR channel). The excitation wavelength of the LysoTracker red is 559 nm and the images were collected at 575 – 625 nm.

3.2.3 Live cell fluorescence imaging at different intracellular pH values

HeLa cells were seeded into the 35 mm glass-bottom culture dishes (MatTek, MA) and allowed to grow for 1-2 days to reach 70–90% confluence. After 24 h of incubation, HeLa Cells were treated with probe **A** or **B** (15 μM concentrations) at 37 °C for 30 min, followed by rinsing twice with PBS buffer. Cells were then treated with nigericin (5 μg/mL) in buffers with pH values at 3.0, 4.0, 5.0, 6.0, and 7.0 for 30 min to equilibrate the intracellular and extracellular pH. Live cell images were taken by a confocal fluorescence microscope (Olympus IX 81).

3.2.4 Cell cytotoxicity assay

The cytotoxicity of the probe against HeLa cells was measured by using the standard MTS assay. Cells were seeded into the 96-well cell culture plate at 5×10^3/well in complete medium (DMEM containing 10% fetal bovine serum (FBS)). After growing for 24 h at 37 °C under 5% CO_2 and removal of the medium, cells were incubated with the probes with concentrations ranging from 0, 2, 5, 10, 15 to 20 µM in fresh culture medium, 100 µL/well) for 48 h at 37 °C under 5% CO_2. The probe solutions were replaced with the fresh culture medium (80 µL/well), and CellTiter 96® Aq$_{ueous}$ (20 µL/well) was added to evaluate cell viability. After incubation for 2 h, the cell viability was determined by measuring the light absorbance at 490 nm with a microplate reader (BioTek ELx800). Untreated cells were used as controls. Percent (%) cell viability was calculated by comparing the absorbance of the control cells to that of treated cells. Data were summarized as a plot where each data point represents an average of three wells.

3.2.5 Materials

Unless specifically indicated, all reagents and solvents were bought from commercial suppliers and were used without further purification. Compounds **3**, **4** and **8** were prepared and characterized according to the reported procedures (Supporting information).

Compound 5: To the mixture of compound **3** (0.48 g, 1 mmol) and **4** (0.42 g, 1 mmol) in Ac$_2$O (15 ml) was added KOAc (50 mg) and the reaction was heated at 60 °C for 1 h. The reaction mixture was concentrated under reduced pressure, and the residue partitioned between water (25 ml) and dichloromethane. The organic layer was separated, the combined organic extracts were dried over Na$_2$SO$_4$, filtered, and concentrated. The residue

was purified by flash column using dichloromethane and methanol to obtain the compound

4a as green solid (0.47 g, 58%).^{1}H NMR (400M, CD$_3$OD) δ 8.55 (d, J = 13.6 Hz, 1H),

8.15 (d, J = 5.6 Hz, 1H), 7.80 (d, J = 1.6 Hz, 1H), 7.69 – 7.66 (m, 2H), 7.61 (t, J = 7.2 Hz,

1H), 7.20 (d, J = 7.2 Hz, 1H), 7.02 (d, J = 8.4 Hz, 1H), 6.83 (s, 2H), 6.73 (s, 1H), 6.04 (d,

J = 13.6 Hz, 1H), 3.58 – 3.52 (q, J = 7.2 Hz, 4H), 3.52 (s, 3H), 2.67 – 2.65 (m, 2H), 2.37

– 2.34 (m, 2H), 1.81 – 1.78 (m, 2H), 1.76 (s, 6H), 1.23 (t, J = 7.2 Hz, 6H); ^{13}C NMR (100

MHz, CD$_3$OD) δ 171.3, 163.7, 156.5, 155.9, 152.7, 143.3, 143.1, 140.4, 137.5, 131.7,

131.3, 129.2, 128.9, 128.8, 121.1, 116.6, 114.2, 113.0, 112.1, 98.3, 95.3, 86.9, 44.9, 30.3,

27.5, 26.6, 24.2, 20.6, 11.6. HRMS (ESI): calculated for C$_{37}$H$_{38}$IN$_2$O$_3^+$ [M] $^+$, 685.1922;

found, 685.1920.

Compound 7: To the solution of compound **5** (350 mg, 0.5 mmol) in dry dichloromethane

(15 ml) was added dicyclohexylcarbodiimide (DCC) (103 mg, 0.5 mmol) and *N*-hydroxy-

succinimide (NHS) (69 mg, 0.6 mmol) under a nitrogen atmosphere at room temperature.

When the mixture was stirred for 30 min, 4-(2-aminoethyl)morpholine (compound **6**, 98

mg, 0.75 mmol) was added and the reaction was stirred overnight. After the mixture was

washed with water (2 × 20 mL), the organic layer was collected, dried over anhydrous

Na$_2$SO$_4$ and filtered. The filtrate was concentrated under reduced pressure. The residue was

purified by flash column chromatography using ethyl acetate and hexane as the eluent, to

afford probe as pray solid. (130 mg, 33%). ^{1}H NMR (400M, CDCl$_3$) δ 7.82 (d, J = 7.2 Hz,

1H), 7.46 – 7.36 (m, 5H), 7.14 (d, J = 7.2 Hz, 1H), 6.35 (t, J = 8.0 Hz, 1H), 6.33 – 6.28

(m, 2H), 6.25 – 6.22 (m, 1H), 5.35 (d, J = 12.8 Hz, 1H), 3.58 (t, J = 4.4 Hz, 4H), 3.44 –

3.38 (m, 1H), 3.34 – 3.30 (q, J = 7.2 Hz, 4H), 3.27 – 3.24 (m, 1H), 3.08 (s, 3H), 2.59 – 2.55

(m, 2H), 2.40 – 2.33 (m, 6H), 2.23 – 2.16 (m, 2H), 1.68 (s, 3H), 1.67 (s, 3H), 1.60 – 1.57

(m, 2H), 1.14 (t, J = 7.2 Hz, 6H); ^{13}C NMR (100 MHz, CDCl$_3$) δ 168.5, 156.7, 153.0, 151.7,

148.8, 148.0, 145.3, 141.7, 136.5, 132.3, 130.7, 128.9, 128.3, 123.6, 123.0, 121.4, 119.2,

108.6, 108.0, 105.5, 104.5, 97.9, 92.9, 80.5, 67.2, 66.9, 56.7, 53.7, 45.6, 44.6, 37.1, 29.4,

28.5, 28.4, 25.5, 23.2, 22.4, 12.7. HRMS (ESI): calculated for C$_{43}$H$_{50}$IN$_4$O$_3$ [M+H]$^+$,

797.2928; found, 797.2925.

Probe A: To the solution of compound **7** (70 mg, 89 µmol) in DMF (6 mL) were added

the palladium acetate (4 mg, 18 µmol), compound **8** (33 mg, 134 µmol), tri(*o*-

tolyl)phosphine (11 mg, 35 µmol), and Et$_3$N (3 ml). The mixture was heated at 90°C under

argon atmosphere overnight. After completion of the reaction (monitored by LC-MS), the

reaction was concentrated under reduced pressure and the residue purified by flash column

chromatography using dichloromethane and methanol as the eluent. Probe **A** was isolated

as red solid (46 mg, 56%). ^{1}H NMR (400M, CDCl$_3$) δ 7.83 (d, J = 7.2 Hz, 1H), 7.66 (s,

1H), 7.52 – 7.41 (m, 4H), 7.34 (d, J = 16.4 Hz, 1H), 7.27 – 7.24 (m, 2H), 7.17 – 7.15 (m,

1H), 7.02 (d, J = 16.4 Hz, 1H), 6.59 – 6.54 (m, 2H), 6.50 (d, J = 2.4 Hz, 1H), 6.34 – 6.32

(m, 1H), 6.26 – 6.23 (m, 1H), 5.38 (d, J = 12.4 Hz, 1H), 3.60 (t, J = 4.4 Hz, 4H), 3.43 –

3.38 (m, 5H), 3.37 – 3.32 (q, J = 7.2 Hz, 4H), 3.30 – 3.26 (m, 1H), 3.15 (s, 3H), 2.61 – 2.57

(m, 2H), 2.38 – 2.34 (m, 6H), 2.24 – 2.18 (m, 2H), 1.74 (s, 3H), 1.73 (s, 3H), 1.63 – 1.57

(m, 2H), 1.23 – 1.13 (m, 12H); ^{13}C NMR (100 MHz, CDCl$_3$) δ 168.5, 162.1, 157.7, 155.5,

153.0, 151.7, 150.3, 148.9, 148.1, 145.4, 139.8, 136.1, 130.2, 129.5, 128.9, 128.3, 127.9,

123.6, 123.0, 120.9, 119.5, 119.3, 119.2, 118.7, 109.5, 109.3, 108.6, 105.8, 105.4, 104.1,

97.9, 97.5, 92.9, 67.2, 66.9, 56.7, 53.7, 45.5, 45.1, 44.6, 37.1, 29.9, 29.5, 28.6, 28.5, 25.5,

23.2, 22.4, 12.7, 12.7. HRMS (ESI): calculated for $C_{58}H_{66}N_5O_5$ [M+H]$^+$, 912.5064; found, 912.5067.

Compound 9: To the solution of compound **7** (250 mg, 0.36 mmol) in 1,2-dichloroethane (20 mL) was added phosphorous oxychloride (220 mg, 1.46 mmol) under a nitrogen atmosphere. The reaction was refluxed for 2 h and the solvent was evaporated under vacuum. Dry acetonitrile (20 mL) was added to the residue, and followed by adding 1, 2-diaminobenzene (9) (0.12 g, 1.0 mmol) and triethylamine (0.5 mL). The mixture was stirred was stirred overnight. After the mixture was washed with water (2 × 20 mL), the organic layer was collected, dried over anhydrous Na_2SO_4, filtered and concentrated under reduced pressure. The residue was purified by flash column chromatography using ethyl acetate and hexane as the eluent, to afford probe as yellow solid (120 mg, 53%). ^{1}H NMR (400M, CDCl$_3$) δ 7.95 (d, J = 7.2 Hz, 1H), 7.51 – 7.45 (m, 2H), 7.40 (d, J = 8.4 Hz, 1H), 7.36 (s, 1H), 7.26 (d, J = 12.8 Hz, 1H), 7.22 (d, J = 7.6 Hz, 1H), 6.96 (t, J = 8.0 Hz, 1H), 6.65 (d, J = 8.0 Hz, 1H), 6.59 (d, J = 8.8 Hz, 1H), 6.53 (t, J = 6.4 Hz, 1H), 6.34 (d, J = 8.0 Hz, 1H), 6.30 (d, J = 8.8 Hz, 1H), 6.25 (s, 1H), 5.32 (d, J = 12.4 Hz, 1H), 3.79 (s, 2H), 3.36 – 3.31 (q, J = 7.2 Hz, 4H), 3.05 (s, 3H), 2.59 – 2.56 (m, 1H), 2.35 – 2.31 (m, 1H), 2.09 – 2.06 (m, 2H), 1.64 (s, 6H), 1.62 – 1.58 (m, 2H), 1.16 (t, J = 7.2 Hz, 6H); ^{13}C NMR (100 MHz, CDCl$_3$) δ 166.9, 156.4, 153.3, 152.2, 148.9, 148.0, 145.3, 144.1, 141.7, 136.5, 132.6, 131.6, 130.6, 128.8, 128.4, 123.4, 123.9, 123.5, 121.7, 118.9, 118.8, 118.1, 108.6, 108.0, 105.0, 98.2, 93.2, 80.4, 70.8, 45.6, 44.6, 29.5, 28.7, 28.4, 25.6, 24.1, 22.4, 12.9. MS (ESI): calculated for $C_{43}H_{44}IN_4O_2$ [M+H]$^+$, 775.2; found, 775.3.

Probe B: The procedure was similar to the way of synthesizing of the probe **A** using compound 7 (100 mg, 0.13 mmol) as starting materials and probe **B** was obtained as red solid (70 mg, 63%). ^{1}H NMR (400M, CDCl$_3$) δ 7.95 (d, J = 6.8 Hz, 1H), 7.64 (s, 1H), 7.54 – 7.45 (m, 3H), 7.40 (d, J = 1.6 Hz, 1H), 7.35 – 7.31 (m, 2H), 7.27 – 7.24 (m, 1H), 7.23 – 7.22 (m, 1H), 7.00 (d, J = 16.4 Hz, 1H), 6.99 – 6.95 (m, 1H), 7.66 (d, J = 7.6 Hz, 1H), 6.59 – 6.45 (m, 6H), 6.31 – 6.27 (m, 2H), 5.34 (d, J = 12.4 Hz, 1H), 3.78 (s, 2H), 3.42 – 3.37 (q, J = 7.2 Hz, 4H), 3.37 – 3.32 (q, J = 7.2 Hz, 4H), 3.11 (s, 3H), 2.60 – 2.57 (m, 1H), 2.35 – 2.31 (m, 1H), 2.08 – 2.05 (m, 2H), 1.69 (s, 6H), 1.63 – 1.58 (m, 2H), 1.21 – 1.16 (m, 12H); ^{13}C NMR (100 MHz, CDCl$_3$) δ 166.9, 162.0, 157.3, 155.4, 153.3, 152.3, 150.2, 148.9, 148.2, 145.4, 144.1, 139.7, 136.0, 132.6, 131.6, 130.2, 129.5, 128.7, 128.4, 127.8, 123.9, 123.5, 121.3, 119.2, 118.9, 118.6, 118.1, 109.5, 109.3, 108.5, 105.8, 104.6, 98.2, 97.5, 93.0, 70.9, 45.5, 45.1, 44.7, 29.5, 28.8, 28.5, 25.6, 24.1, 22.4, 12.9, 12.8. MS (ESI): calculated for $C_{58}H_{60}N_5O_4$ [M+H]$^+$, 890.5; found, 890.5.

3.3 Results and Discussions

3.3.1 Synthetic approach

The design and synthesis of the fluorescent probe **A** and **B** are outlined in Scheme **2**. The rational design was based on π-conjugation modulation between two fluorophores in response to pH to achieve ratiometric fluorescence responses of the probe to pH changes. We chose visible emissive coumarin and near-infrared emissive hemicyanine fluorophores to construct a ratiometric fluorescent probe because both fluorophores have excellent photostability, high molar absorption activity, and good fluorescence quantum yield.[73, 88, 89, 140] In order to specifically target lysosome in live cells, morpholine residue was

introduced to hemicyanine dye (**5**) to form a closed spirolactam ring structure, affording hemicyanine dye **7**. π-Conjugation between the coumarin and hemicyanine fluorophores via a vinyl connection was achieved by using a palladium-catalyzed Heck coupling reaction between iodo-functionalized hemicyanine (**7**) and vinyl-functionalized coumarin (**8**) so that the probe **A** could respond to pH changes through π-conjugation modulation between two fluorophores. Iodo-functionalized hemicyanine dye (**5**) was prepared by condensation reaction of compound **3** with 5-iodo-1,2,3,3-tetramethyl-3*H*-indol-1-ium iodide (**4**). In order to increase the pK$_a$ of probe **B**, 1,2-diaminobenzene residue was introduced to hemicyanine moiety to form a closed spirolactam ring by using the same approach as to prepare probe **A** (Scheme 3.2).
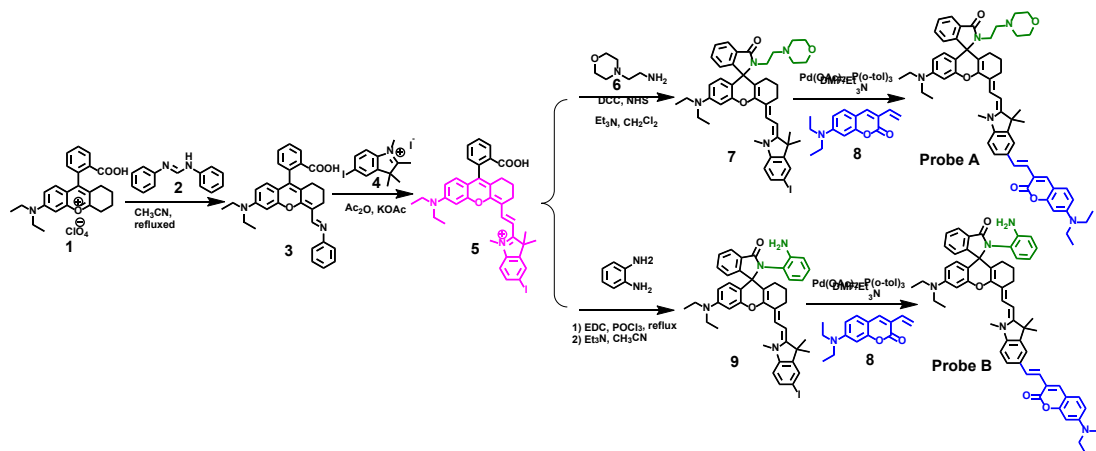
Scheme 3.2. Synthetic strategy to prepare a ratiometric fluorescent probes based on π-conjugation modulation between coumarin and hemicyanine dyes.

3.3.2 Optical responses of 7, probe A and probe B to pH changes

We investigated the pH influence on the absorption properties of the intermediate **7**, probes **A** and **B** in 10 mM citrate buffer containing 40% ethanol. At neutral or basic pH, intermediate **7** shows absorption peak at 380 nm with a closed spirolactam ring structure.

Increasing the acidity of the solution from pH 7.0 to 2.0 results in the appearance and increase of a new peak at 723 nm, corresponding to absorption of hemicyanine dye with a spirolactam ring opening structure. Hemicyanine absorption (715 nm) shows The 8 nm red-shift with the presence of the iodo group at hemicyanine dye.[88, 89] Under the neutral and basic conditions, probes **A** and **B** only display broad absorption peaks of coumarin moieties at 475 nm, and 450 nm because the hemicyanine moieties retain closed spirolactam ring structure (Figure 3.1). Decrease of pH from 7.0 to 2.5 leads to the appearance of new near-infrared absorption peaks at 745 nm and 735 nm for probes **A** and **B**, respectively. The intensity of the near-infrared absorption peak increases with pH decrease from 7.0 to 2.5. Compared with the reported absorption peak of typical hemicyanine dyes at 715 nm under acidic condition,[88, 89] π-conjugation of hemicyanine with coumarin causes red shifts in the absorption peaks of hemicyanine moieties by 22 nm for probe **A**, 12 nm for probe **B** at acidic pH, respectively. Furthermore, probes **A** and **B** molar display absorption coefficients of 4.1×10^4 and 3.3×10^4 $mol^{-1}cm^{-1}$ at pH 2.5 responding to the hemicyanine moiety absorption, respectively, indicating that conjugation of the coumarin dye to hemicyanine dye enhances molar absorptivity of the probes.
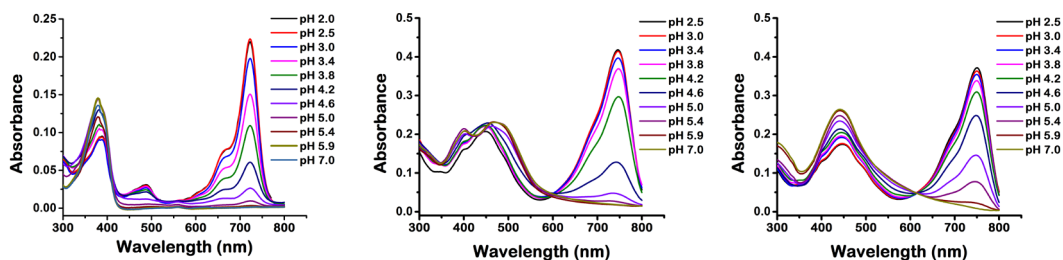
Figure 3.1. Absorbance spectra of 5 μM intermediate **7** (left), probe **A** (middle) and probe **B** (right) in 10 mM citrate buffer containing 40% EtOH.

We evaluated pH effect on fluorescence spectra of the probes **A** and **B** in 10 mM citrate buffer containing 40% ethanol. At pH 7.0, probes **A** and **B** shows no fluorescence of the hemicyanine moieties and fluorescence peak of coumarin moieties at 528 nm and 515 nm with fluorescence quantum yields of 26.0% and 23.5% at the excitation of 420 nm, respectively (Figure 3.2 and 3.3). However, probes **A** and **B** exhibit significant increase of hemicyanine fluorescence at 755 nm and 740 nm under excitation of 680 nm, respectively, because pH decrease from 7.0 to 2.5 promotes spirolactam ring opening of the hemicyanine moieties and significantly enhances π-conjugation of the probes. We employed the Henderson–Hasselbach-type mass action equation to calculate pK_{cycl} values of probes **A** and **B** related to the spirolactam ring opening of the hemicyanine moieties. The pH 4.2 and 4.8 were identified as the equilibrium pH for the spirolactam ring opening for probes **A** and **B**, respectively (Figure 3.4). Fluorescence quantum yields of coumarin and hemicyanine moieties at pH 3.0 were calculated to be 16.6% and 1.6% at excitation of 420 nm for probe **A**, and 16.0% and 1.3% for probe **B**, respectively. Fluorescence quantum yields of hemicyanine moieties at pH 3.0 is calculated to be 8.3% for probe **A**, and 7.9% for probe **B** at excitation of 680 nm. Both probes **A** and **B** also display ratiometric responses to pH changes from 7.0 to 2.5 with a moderate decrease in the coumarin fluorescence and increase in the hemicyanine fluorescence. We tested whether probes **A** and **B** could respond to pH changes reversibly by measuring fluorescence changes in the coumarin and hemicyanine fluorescence. Probes **A** and **B** displayed reversible responses to pH changes from pH 7.0 to pH 2.5 with ratiometric fluorescence changes in the hemicyanine over coumarin fluorescence (Figure S11).
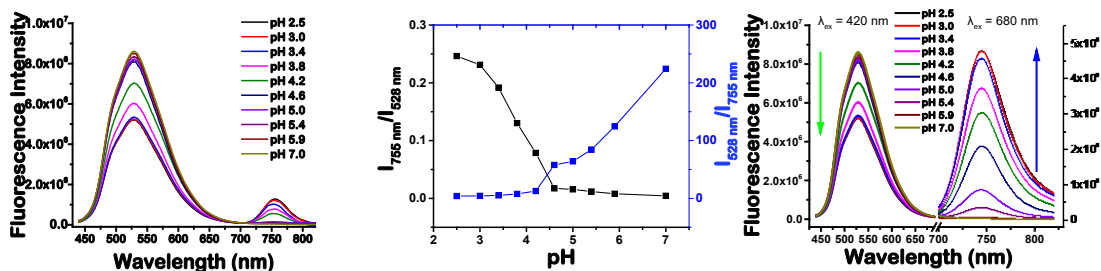
Figure 3.2. Fluorescence spectra of 5 μM probe **A** in 10 mM citrate buffer containing 40% EtOH at excitation of 420 nm (left), 420 nm (right) and 680 nm (right), respectively; pH dependent fluorescence ratios of hemicyanine acceptor ($I_{755\ nm}$) to coumarin donor ($I_{528\ nm}$) at excitation of 420 nm (middle).
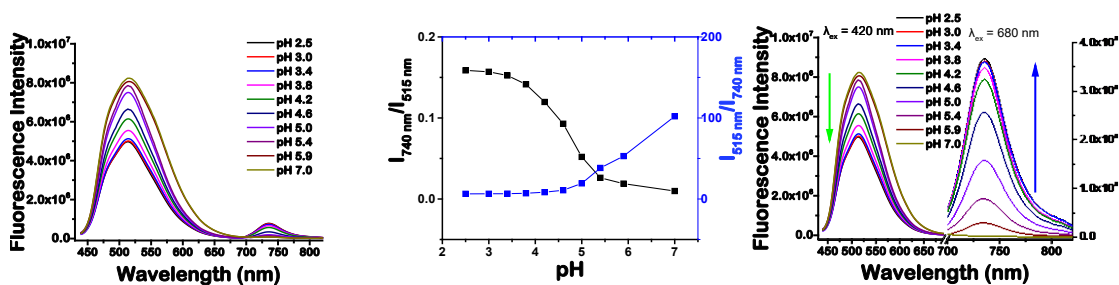
Figure 3.3. Fluorescence spectra of 5 μM probe **B** in 10 mM citrate buffer containing 40% EtOH at excitation of 420 nm (left), 420 nm (right) and 680 nm (right), respectively; pH dependent fluorescence ratios of hemicyanine acceptor ($I_{740\ nm}$) to coumarin donor ($I_{515\ nm}$) at excitation of 420 nm (middle).
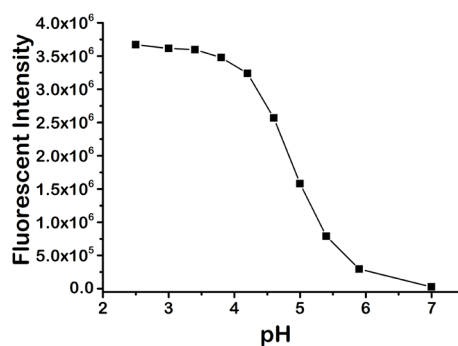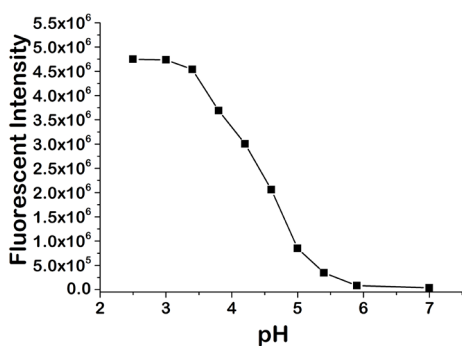
Figure 3.4. Plots of fluorescent intensity of 5 µM probe **A** (left) at 755 nm and probe **B** (right) at 740 nm versus pH at 680 nm excitation with three repeated measurements.

3.3.3 The selectivity of fluorescent probe A to the pH over metal ions.

We investigated the selectivity of the probes **A** and **B** to pH over 50 µM metal ions such as Zn^{2+}, Pb^{2+}, Fe^{2+}, Hg^{2+}, Cd^{2+}, Ca^{2+}, Mn^{2+}, Ni^{2+}, Mg^{2+}, Cu^{2+}, Co^{2+}, Na^+ and K^+ ions in 10 mM citrate buffer containing 40% ethanol (Figures S12-S15). The results show that the presence of different metal ions does not cause any significant fluorescence changes of the coumarin and hemicyanine moieties at both pH 7.6 and 2.4, indicating that the probes exhibit excellent selectivity to pH over metal ions.

3.3.4 Photostability of the fluorescent probes A and B.

We examined the photostability of probes **A** and **B** through their continuous excitation at 420 nm with 10-min intervals in 10 mM citrate buffers containing 5 µM probes **A** and **B** in 40% ethanol. Probe **A** shows good photostability with its coumarin fluorescence decrease by 1.0% at pH 7.6 and 2.5% at pH 2.4 and hemicyanine fluorescence decrease by 3.5% at pH 2.4 under 3-hour excitation at 420 nm (Figure S16). Probe **B** also displays excellent photostability with its coumarin fluorescence decrease by 1.3% at pH 7.6 and 2.1% at pH 2.4 and hemicyanine fluorescence decrease by 2.8% at pH 2.4 under 3-hour excitation at 420 nm (Figure S17).

3.3.5 Cytotoxicity of the fluorescent probes A and B.

The MTS assay was used to investigate the cytotoxicity of probes to live cells using HeLa cells (Figure 3.5). Incubation of HeLa cells with the different concentrations of probes **A**

and **B** showed that the cell viability was higher than 70% even at a concentration of 20 µM. Overall, the 15 µM test concentrations of probes **A** and **B** appear to be almost non-cytotoxic for HeLa cells.
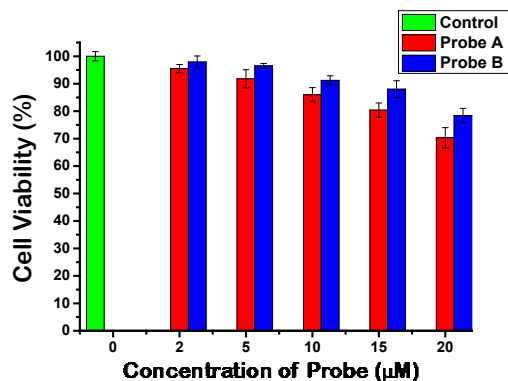
Figure 3.5. Cytotoxicity and cell proliferation of probes **A** and **B** conducted by MTS assay. HeLa cells were incubated with 2, 5, 10, 15, and 20 µM of probes for 48 h, and cell viability was measured by adding MTS reagent and measuring at 490 nm. The absorbance measured at 490 nm was directly proportional to the cell viability and was normalized to control cells in the absence of probes.

3.3.6 Fluorescence imaging of pH in live cells.

We studied whether probe **A** could image the intracellular pH by conducting live (HeLa) cell imaging with different probe concentrations. The morpholine residue was used to allow the probe to specifically target acidic lysosomes with pH around 4.5 in live cells. We incubated cells in the media containing probe and LysoTracker red to confirm whether our probe and LysoTracker red stay in the same cellular compartments. In HeLa cells, the probe **A** shows strong fluorescence of coumarin moiety and moderate fluorescence of hemicyanine moiety at 10 µM concentration with coumarin excitation at 420 nm. The probe exhibits stronger fluorescence of hemicyanine moiety with the same probe concentration

at hemicyanine excitation. Also, fluorescence intensities of both coumarin and hemicyanine moieties increase significantly with the probe concentration. The co-localization analysis of the probe with the commercial LysoTracker red based on the Pearson's coefficient gave a value of 0.85 or higher, indicating that probe **A** and LysoTracker Red exist in the same cellular compartment (Figure 3.6 and 3.7).
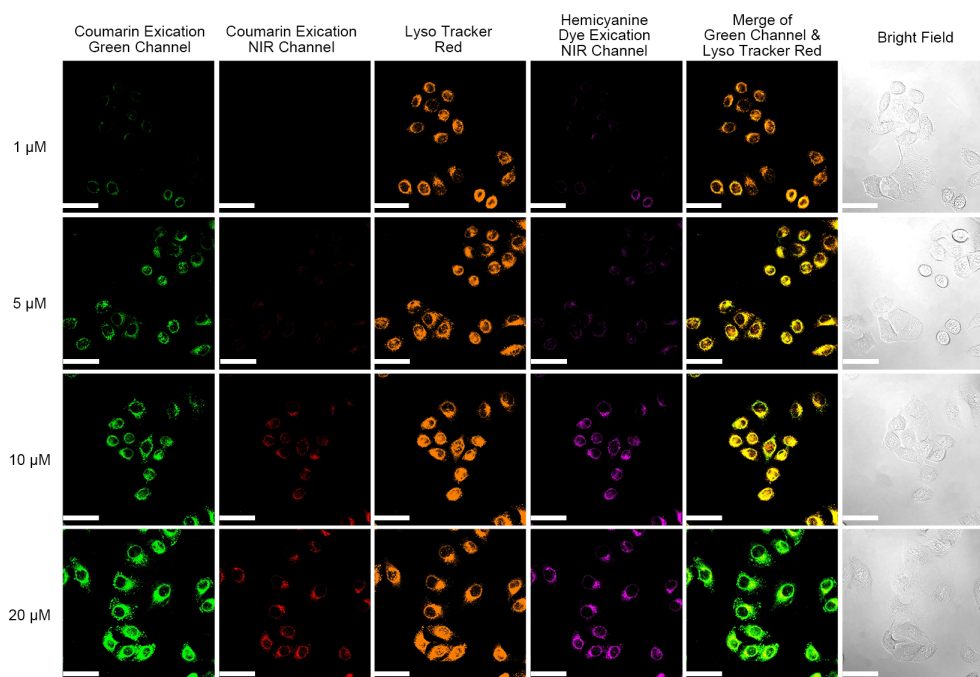
Figure 3.6. Fluorescence images of HeLa cells incubated with different concentrations of probe **A** in the presence of LysoTracker Red. Images were acquired using the confocal fluorescence microscope at 60 X magnification. Scale Bar: 50 µM
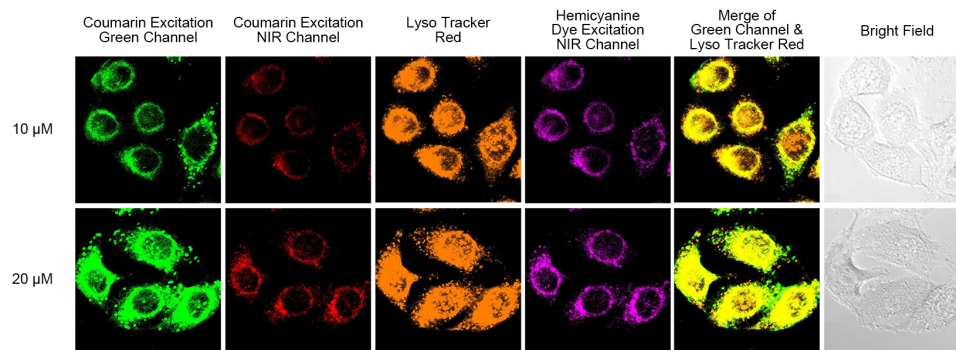
Figure 3.7. Enlarged fluorescence images of HeLa cells incubated with different concentrations of probe **A** in the presence of LysoTracker Red.

After demonstrating that the probe **A** selectively targets and stains lysosomes in live cells, we investigated whether the probe could respond to pH changes in live cells. We incubated HeLa cells with the probe in the media adjusted to pH values from 3.0 to 7.0 and used 5 µg/mL nigericin (H^+/K^+ ionophore) to equilibrate the intracellular and extracellular pH. After incubation, the very strong fluorescence of the coumarin moiety at pH 7.0 was observed. The presence of coumarin fluorescence allows overcoming blind fluorescence imaging spots at basic or neutral pH, an issue that most Rhodamine-based pH fluorescent probes encounter. Upon changing the pH from 7.0 to 3.0, ratiometric fluorescence response to pH changes was measured with the gradual coumarin fluorescence decrease and hemicyanine fluorescence increase at the excitation of 420 nm. The probe **A** also shows ratiometric responses to pH changes from 3.0 to 7.0 with fluorescence imaging color changes from yellow to deep green in the merge images of green and NIR fluorescence channels at excitation of the coumarin moiety. The fluorescence intensity of the hemicyanine moiety in the purple channel also gradually increased with the decrease in pH from 7.0 to 3.0 (Figure 3.8). Probe **B** displays similar ratiometric responses to pH changes in live cells as probe **A** does (Figure 3.9), but it possesses higher pK_a than probe **A** because moderate fluorescence intensity of hemicyanine moiety can still be observed at pH 6.0 (Figure 3.9). Increase of pK_a of probe **B** arises from introduction steric hindrance of o-phenylenediamine residue to hemicyanine moiety to form spirolactam structure.
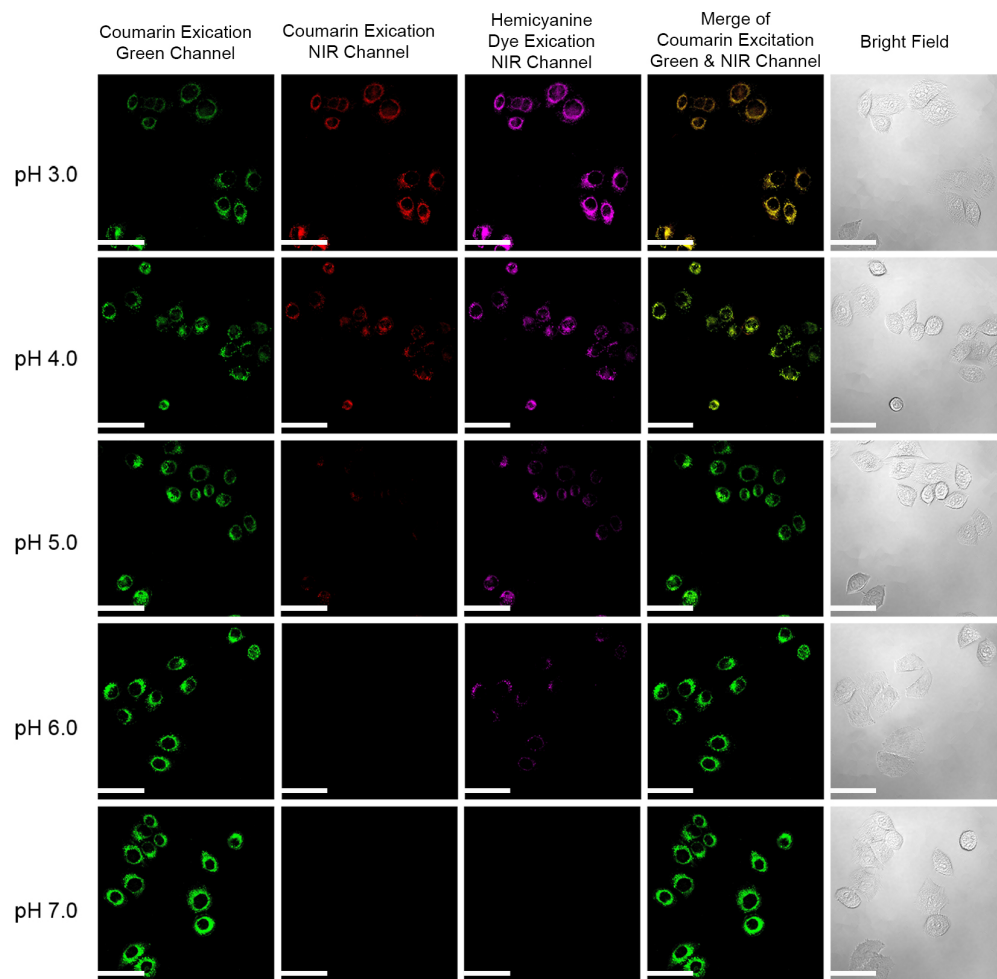
Figure 3.8. Fluorescence images of HeLa cells incubated with 15 µM fluorescent probe **A**. HeLa cells were incubated with 15 µM probe **A** at the pH ranging from pH 3.0 to 7.0 in presence of 5 µg/mL nigericin. Images were acquired using the confocal fluorescence microscope at 60 X magnification. Scale Bar: 50 µM
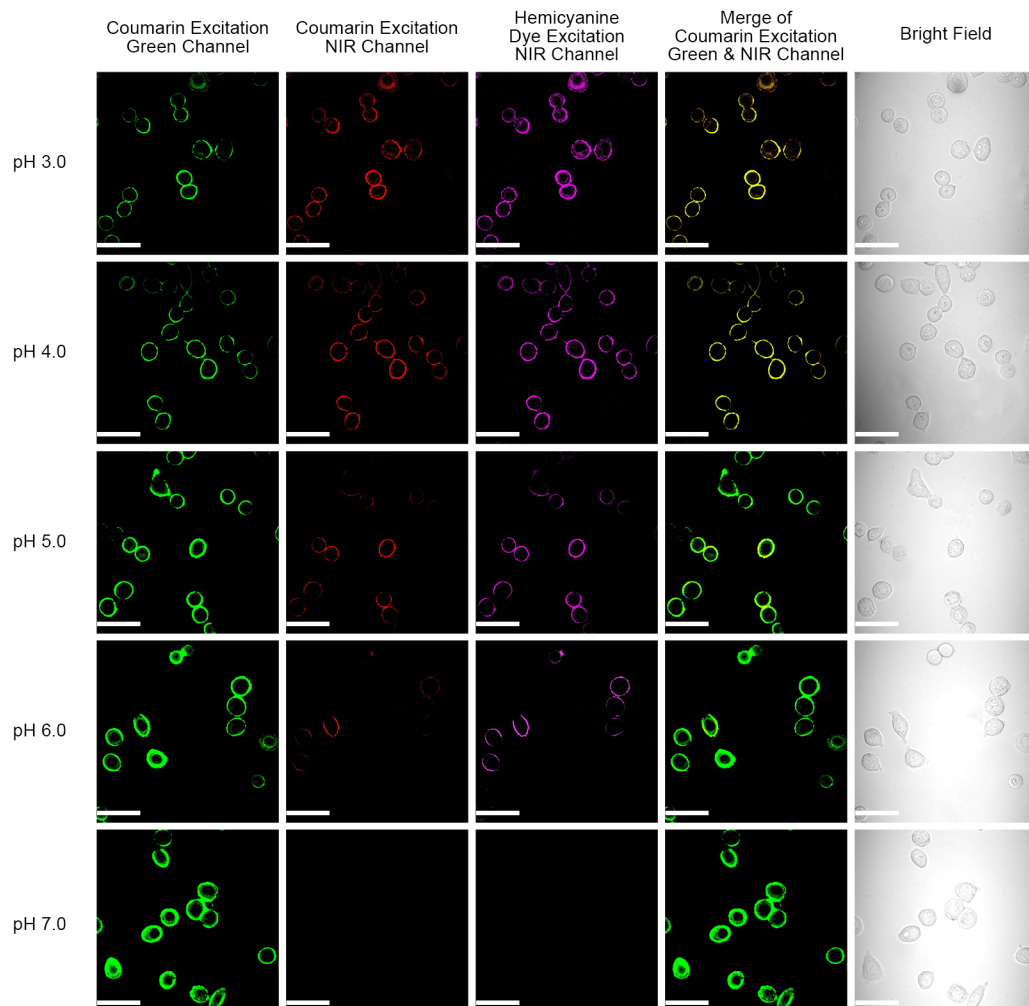
Figure 3.9. Fluorescence images of HeLa cells incubated with 15 µM fluorescent probe **B**. HeLa cells were incubated with 15 µM probe **B** at the pH ranging from pH 3.0 to 7.0 in presence of 5 µg/mL nigericin. Images were acquired using the confocal fluorescence microscope at 60 X magnification. Scale Bar: 50 µM
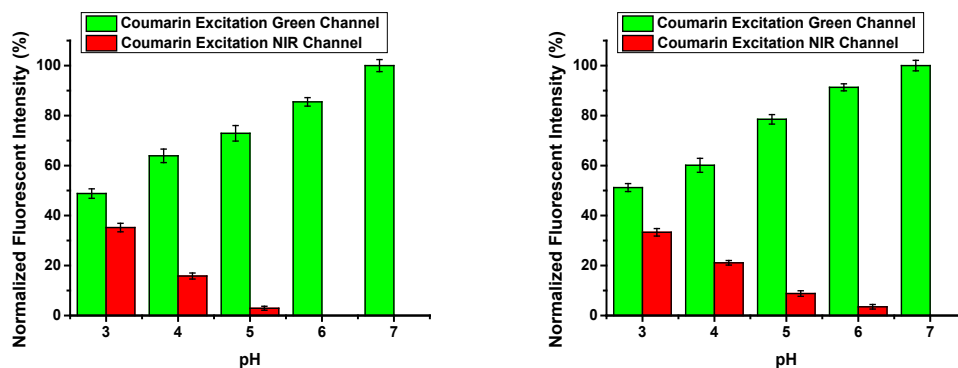
Figure 3.10 Fluorescence intensity of probe **A** (left) and probe **B** (right) in the HeLa cells obtained from statistical analysis of the confocal imaging in Figures 3.8 and 3.9.

3.4 Conclusion

In summary, we present two fluorescent probes with different pK_a values for ratiometric detection of pH changes in live cells by conjugating coumarin moiety to the near-infrared hemicyanine moiety through a vinyl connection and introducing morpholine and *o*-diaminebenzene residues to the hemicyanine to form a closed spirolactam structures, respectively. The probes show ratiometric fluorescence responses with coumarin fluorescence decreases and hemicyanine fluorescence increases to the pH changes from 7.0 to 3.0. The π-conjugation modulation between coumarin and hemicyanine moieties used in this probe design offers an effective way to construct a wide variety of ratiometric fluorescent probes to determine metal ions, biological thiols, reactive nitrogen and oxygen species after functionalization of the hemicyanine moiety with appropriate sensing ligands.

4 Near-infrared fluorescent probes based on TBET and FRET rhodamine acceptors with different pKa values for sensitive ratiometric visualization of pH changes in live cells[141]

Jianbo Wang,[*ab] Shuai Xia,[a] Jianheng Bi,[a] Yibin Zhang,[a] Mingxi Fang,[a] Rudy L. Luck,[*a] Yanbo Zeng,[ab] Tzu-Ho Chen,[cd] Hsien-Ming Lee[*c] and Haiying Liu[*a]

[a.] Department of Chemistry, Michigan Technological University, Houghton, MI 49931, E-mail: rluck@mtu.edu; hyliu@mtu.edu

[b.] College of Biological, Chemical Sciences and Engineering, Jiaxing University, Jiaxing 314001, China. E-mail: wjb4207@mail.ustc.edu.cn

[c.] Institute of Chemistry, and Chemical Biology and Molecular Biophysics, Academia Sinica, Taipei, Taiwan 11529, Republic of China, E-mail: leehm1@gate.sinica.edu.tw

[d.] Department of Chemistry, National Taiwan University, Taipei 10617, Taiwan, Republic of China

4.1 Introduction

Traditional rhodamine dyes have been widely used to develop fluorescent probes based on a spirocyclic ring-opening switch for detection of a variety of analytes such as cations, ATP, reactive oxygen, nitrogen and sulfur species. This is due to their excellent photophysical properties such as high absorption coefficient, excellent photostability and high fluorescence quantum yields in the visible region.[16, 67-72] To overcome environmental effects of probe concentration variation and uneven distribution, temperature, solvent polarity, and excitation light fluctuation on a single emission of traditional rhodamine dyes, different fluorophores as donors have been introduced to the rhodamine dyes as acceptors to achieve ratiometric fluorescence imaging with an integrated self-calibration capability of dual well-separated emissions. Naphthalimine, coumarin, dansyl, tetraphenylethene (TPE), fluorescein, and BODIPY derivatives have been used as FRET (fluorescence resonance energy transfer) or TBET (through-bond energy transfer) donors to construct fluorescent probes for ratiometric detection of various analytes. [70, 72] The ratiometric fluorescent probes with large pseudo-Stokes shifts can effectively eliminate a self-absorption property of traditional rhodamine dyes with very small Stokes shifts of less than 30 nm, and accomplish high resolution fluorescence imaging with low detection limits. However, fluorescence of these ratiometric sensing platforms is limited below 600 nm due to the distinctive emission of traditional rhodamine dyes. [1-7] In order to overcome this short wavelength emission disadvantage, many near-infrared rhodamine dyes have been developed to take advantage of unique near-infrared imaging features such as superior tissue penetration, significant reduced background fluorescence from biological samples, and low photodamage to tissues and dye photobleaching.[73-76, 78-81, 83, 92, 142-145] However,

ratiometric near-infrared fluorescent probes utilizing rhodamine dyes as acceptors for FRET and TBET have not been as well-developed.[95] Very recently, we reported three ratiometric fluorescent probes consisting of TPE and hemicyanine moieties, and demonstrated that the probe based on a TBET strategy showed excellent ratiometric responses to pH variations compared with probes based on a π-conjugation modulation strategy.[95] However, it is still challenging to construct near-infrared ratiometric fluorescent probes for accurate quantitative and comparative analyses of pH variations because it is not easy to select suitable donors to match the lower fluorescence quantum yields of infrared fluorescent dye acceptors compared with high fluorescence quantum yields of traditional rhodamine dyes as TBET or FRET acceptors.

In this paper, we develop three ratiometric near-infrared fluorescent probes (**A-C**) composed of TPE donors with reduced ACQ effects connected to near-infrared rhodamine acceptors to accomplish highly sensitive ratiometric detection of cellular pH variations utilizing a combined TBET and FRET strategy, see Scheme 4.1. Probe **A** bearing a lysosome-targeting morpholine residue possesses a pKa value of 4.4 which is related to spirolactam ring opening. In order to increase the pK_a values of the probes, bulky o-phenylenediamine and a derivative bearing tri(ethylene glycol)methyl ether residue were introduced to rhodamine acceptors to achieve higher pK_a values of 4.6 and 4.8 for probes **B** and **C**, respectively. TPE donors of probes **A-C** maintain aggregation-induced emission (AIE) properties[146] with reduced ACQ effects and under excitation at 405 nm show strong fluorescence peaks at 489 nm, 483 nm and 486 nm under neutral and basic conditions, respectively. Probes **A**, **B**, and **C** respond to pH changes from 7.58 to 2.38 in both buffers and living cells ratiometrically exhibiting a decrease in TPE fluorescence under 405 nm

excitation, and a concomitant increase of rhodamine fluorescence, and possess well-defined dual emissions and two Stokes shifts with large pseudo-Stokes shifts of 321 nm, 318 nm and 312 nm, respectively. Probes **A**, **B**, and **C** exhibit considerably large signal-to-background fluorescence increases of 365-, 131- and 1762-fold in term of fluorescence intensity ratios of TPE donor to rhodamine acceptor under stimulation of pH decreases from 7.58 to 3.18, respectively. The probes enable accurate double-checked ratiometric fluorescence imaging through the image co-localization of visible and near-infrared fluorescence channels and achieve quantitative analyses of intracellular pH changes. The success of these near-infrared ratiometric sensing platforms based on TPE donors will enable the expansion of a variety of ideal ratiometric fluorescent probes bearing different on-off spirolactam switches for detection of cations, reactive oxygen, nitrogen and sulfur species.
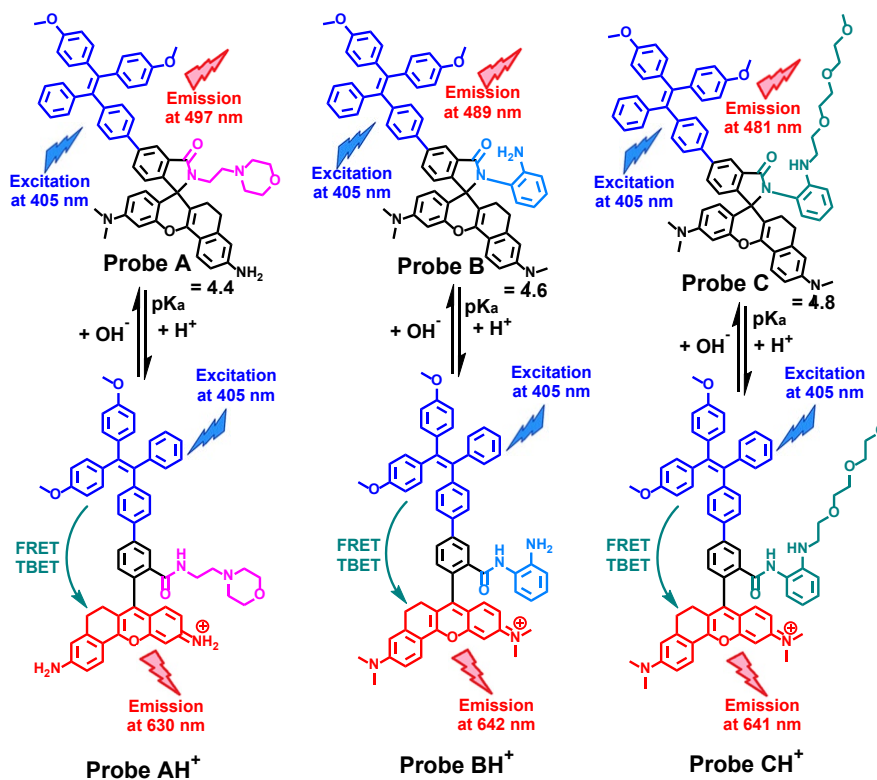
Scheme 4.1. Chemical structure response of fluorescent probes to pH changes with π-conjugation changes.

4.2 Materials and Methods

4.2.1 Instrumentation

Solvents and reagents were obtained from Sigma-Aldrich or Fisher scientific. Column chromatographic purification was conducted on silica gel (200-300 mesh) obtained from Sigma-Aldrich while thin-layer chromatography (TLC) analysis was conducted on silica gel plates obtained from Sigma-Aldrich. Intermediates. The fluorescent probes were characterized by a Varian Unity Inova NMR spectrophotometer at 400 MHz and 100 MHz to record ^{1}H NMR and ^{13}C NMR spectra in CDCl$_3$ or CD$_3$OD solutions, respectively. Either a double focusing magnetic mass spectrometer or a fast atom bombardment (FAB)

ionization mass spectrometer was used to determine high-resolution mass spectrometer data (HRMS). Absorption spectra were collected by employing a Perkin Elmer Lambda 35 UV/VIS spectrometer while fluorescence spectra were performed on a Jobin Yvon Fluoromax-4 spectrofluorometer.

4.2.2 Cell Culture and Cytotoxicity Assay

Standard MTS assay was employed to evaluate the probe cytotoxicity against HeLa cells. HeLa cells were cultured in modified Eagle's medium (DMEM, Gibco) in the presence of 10 % fetal bovine serum (FBS, fisher Scientific) under an atmosphere of 95% air and 5 % CO_2 at 37 °C. After the cells were further seeded into a 96-well plate (about 7×103 cells per well), and cultured for 24 hours, the cells were put in fresh culture medium containing probes **A, B**, or **C** at concentration levels of 0, 5, 10, 15 to 20 μM, and further incubated for 48 h at 37 °C under a 5% CO_2 humidified atmosphere. Cell viability was evaluated by incubating the cells in a fresh culture medium (80 μL) containing 20 μL CellTiter 96® Aqueous for another 2 h. Untreated cells were used as controls. The absorbance of the control cells in the absence of the probe was compared with that of the cells treated with the probe to determine the percentage of cell viability.

4.2.3 Probe application in cellular Imaging.

HeLa cells were seeded into 35 mm x 12 mm glass-bottom culture dishes and incubated for 24 h. Freshly prepared FBS-free medium containing probe **A**, **B** or **C** with concentrations ranging from 5, 10, 15, to 20 μM was used to replace the cell culture medium and the cells were further incubated for 1 h under a 5% CO_2 humidified

atmosphere. The cells were washed twice with PBS buffer before cellular imaging was conducted. In order to adjust intracellular pH values, the cells were washed with PBS buffer twice before they were incubated with 5 µg/mL nigericin in citric buffers for 30 minutes with pH ranging from 3.5, 4.0, 4.5, 5.0, 5.5, 6.0, 6.5 to 7.0 to achieve equilibration between the intracellular and extracellular pH. The cells were incubated for 10 min before they were washed with PBS buffer twice again for imaging. For an experiment under drug stimuli, HeLa cells were cultured in medium in the presence of different concentrations of chloroquine from 50 µM, 100 µM to 200 µM for 30 min. The cells were washed with PBS buffer twice after the medium was removed. A confocal fluorescence microscope (Olympus IX 81) was employed to collect cellular fluorescence images from 475 to 525 nm for blue fluorescence of TPE donor in the blue channel, and those from 650 to 700 nm for near-infrared fluorescence of the rhodamine acceptor in the red channel under TPE donor excitation at 405 nm. Near-infrared fluorescence images of the rhodamine acceptor from 650 to 700 nm in the green channel were collected under rhodamine acceptor excitation at 559 nm.

4.2.4 Materials

Unless specifically specified, all chemical reagents and solvents were obtained from commercial suppliers and used without further purification. The intermediates were synthesised and characterized and detailed information is listed as supporting information.

Synthesis of probe A: Compounds **5** (61 mg, 0.1 mmol), **6** (62 mg, 0.12 mmol), tetrakis(triphenylphosphine)palladium (10 mg, 8 µmol) and Na_2CO_3 (aq, 0.15 ml, 2M) was dissolved in a mixed solution of toluene/methanol (10/2 mL) and stirred at 85 °C for 24 h under

argon. After the solvents were removed by rotary evaporation, the residue was dissolved in ethyl acetate (20 ml) and washed with water (15 ml). The organic layer was collected, dried over Na_2SO_4, filtered and concentrated by rotary evaporation. The crude product was purified through flash column chromatography using an eluent of a mixed ethyl acetate and hexane solution (1:1, v/v) to yield the product (40 mg, 44%). ^{1}H NMR (400 MHz, CDCl$_3$) δ: 8.04 (d, J = 1.2 Hz, 1H), 7.65 – 7.62 (m, 3H), 7.54 – 7.51 (m, 1H), 7.46 – 7.43 (m, 2H), 7.38 (d, J = 8.4 Hz, 2H), 7.14 – 7.04 (m, 8H), 6.95 (t, J = 9.2 Hz, 3H), 6.65 – 6.61 (m, 4H), 6.46 – 6.44 (m, 2H), 6.32 (dd, J = 8.8 Hz, 2.4 Hz 1H), 3.73 (s, 3H), 3.72 (s, 3H), 3.56 (t, J = 4.4 Hz, 4H), 3.51 – 3.47 (m, 1H), 3.34 – 3.27 (m, 1H), 2.94 (s, 6H), 2.63 – 2.51 (m, 2H), 2.46 – 2.39 (m, 1H), 2.36 – 2.26 (m, 4H), 2.20 – 2.14 (m, 1H), 1.84 – 1.77 (m, 1H), 1.70 – 1.65 (m, 1H); ^{13}C NMR (100 MHz, CDCl$_3$) δ: 168.5, 158.4, 158.3, 152.8, 151.4, 150.2, 147.2, 147.1, 144.3, 144.1, 141.4, 140.7, 138.9, 138.5, 137.7, 136.5, 132.8, 132.3, 132.2, 131.6, 131.1, 129.0, 128.8, 128.7, 128.0, 126.6, 126.4, 123.9, 123.6, 121.1, 120.6, 114.3, 113.2, 112.7, 109.3, 106.6, 101.3, 99.0, 67.1, 66.3, 56.7, 55.3, 53.7, 40.6, 37.3, 28.5, 22.4. HRMS (ESI): calculated for $C_{60}H_{57}N_4O_5$ [MH]$^+$ 913.4329, found 913.4339.

Synthesis of probe B: Probe **B** was prepared according to synthesis of probe **A** by using compounds **10** (61 g, 0.1 mmol) and **6** (62 mg, 0.12 mmol), yielding the product (47 mg, 51%). ^{1}H NMR (400 MHz, CDCl$_3$) δ: 8.18 (d, J = 1.6 Hz, 1H), 7.71 (dd, J = 8.0 Hz, 1.6 Hz, 1H), 7.59 (d, J = 8.4 Hz, 1H), 7.44 (d, J = 8.4 Hz, 2H), 7.21 (d, J = 8.0 Hz, 1H), 7.11 – 7.07 (m, 8H), 7.01 – 6.92 (m, 5H), 6.72 (d, J = 8.0 Hz, 1H), 6.68 – 6.64 (m, 5H), 6.59 – 6.56 (m, 1H), 6.48 – 6.40 (m, 4H), 3.86 (s, 2H), 3.75 (s, 3H), 3.74 (s, 3H), 2.97 (s, 6H), 2.95 (s, 6H), 2.75 – 2.71 (m, 1H), 2.57 – 2.53 (m, 1H), 2.15 – 2.12 (m, 1H), 1.91 – 1.82 (m, 1H); ^{13}C NMR (100 MHz, CDCl$_3$) δ: 166.8, 158.3, 158.2, 153.1, 151.3, 150.8, 150.7, 147.2, 144.3, 144.1, 144.0, 141.4, 140.7, 138.8, 137.6, 136.5, 132.8, 132.2, 132.1, 131.6, 131.4, 129.0, 128.5, 127.9, 126.6, 124.2, 123.3, 121.6, 119.0,

118.7, 118.3, 113.3, 113.2, 111.5, 109.8, 109.2, 101.0, 99.1, 70.4, 55.4, 40.7, 40.6, 29.1, 22.3. HRMS (ESI): calculated for $C_{62}H_{55}N_4O_4$ [M+H]$^+$ 919.4223, found 919.4230.

Synthesis of probe C: Probe **C** was synthesized similar to the route used for probe **A** except compounds **12** (75 mg, 0.1 mmol) and **6** (62 mg, 0.12 mmol) were used to obtain the product (35 mg, 33%). ^{1}H NMR (400 MHz, CDCl$_3$) δ: 8.16 (s, 1H), 7.71 (d, J = 7.6 Hz, 1H), 7.55 (d, J = 8.4 Hz, 1H), 7.43 (d, J = 8.4 Hz, 2H), 7.20 (d, J = 8.0 Hz, 1H), 7.12 – 7.05 (m, 8H), 6.99 – 6.91 (m, 5H), 6.68 – 6.62 (m, 6H), 6.55 (d, J = 6.8 Hz, 1H), 6.45 – 6.39 (m, 4H), 3.74 (s, 3H), 3.73 (s, 3H), 3.63 – 3.52 (m, 8H), 3.44 – 3.42 (m, 2H), 3.29 (s, 3H), 3.18 – 3.14 (m, 2H), 2.94 (s, 12H), 2.87 – 2.83 (m, 1H), 2.57 – 2.49 (m, 1H), 2.07 – 2.03 (m, 1H), 1.92 – 1.85 (m, 1H). ^{13}C NMR (100 MHz, CDCl$_3$) δ: 166.9, 158.3, 158.2, 153.3, 151.3, 150.7, 150.3, 147.4, 145.3, 144.3, 144.1, 141.4, 140.7, 138.8, 137.6, 136.4, 132.7, 132.6, 132.1, 131.6, 131.3, 128.9, 127.9, 126.5, 126.3, 124.3, 123.3, 121.6, 118.7, 117.3, 113.3, 113.2, 112.4, 111.4, 109.8, 109.2, 100.7, 99.1, 94.6, 72.1, 70.9, 70.8, 70.5, 70.1, 59.2, 55.4, 43.4, 40.7, 40.6, 29.1, 22.7. HRMS (ESI): calculated for $C_{69}H_{68}N_4NaO_7$ [M+Na]$^+$ 1087.4986, found 1087.4977.

4.2.5 Computational Details

Initial structures for probes **A**, **B**, and **C** were obtained using the Chem3D program. These structures were then placed into Avogadro[147] and refined with the force field (UFF) calculations for an approximate starting geometry. Files suitable for Gaussian16 [148] were then generated and the molecules refined using density functional theory (DFT) with a hybrid functional using the TPSS functionals,[149, 150] and with initial electron basis set at the 6-31g(d,p) level and optimized to convergence. To obtain freq and excited state information, a split valence and triple zeta basis set for the atoms, namely TZVP was used.[151] Imaginary frequencies were not obtained in any of the frequency calculations. The

excited states were assessed on the basis of TD-DFT optimizations[152] in a Polarizable Continuum Model (PCM) of water.[153] Results were interpreted using GausViewfor all data and figures. Calculations of bond distances and angles were computed using Mercury.[154] The results of the calculations are given in detail in the Supporting Information.

4.3 Results and Discussions

4.3.1 Probe Design and Synthetic Approach

We selected TPE as a donor to take advantage of its unique AIE property,[155-163] and near-infrared rhodamines as acceptors due to their high molar absorptivity, excellent photostability and near-infrared emission.[87] Thus, a combined FRET and TBET strategy was utilized to construct ratiometric fluorescent probes for the sensitive sensing of cellular changes. Reacting 5-bromo-2-(4-(dimethylamino)-2-hydroxybenzoyl)benzoic acid (**1**) with 6-amino-1-tetralone (**2**) and also 6-(dimethylamino)-1-tetralone (**7**), afforded the bromo-functionalized near-infrared rhodamine dyes (**3** and **8**), respectively, Scheme 2. Fluorescent probe (**A**) bearing a lysosome-targeting morpholine residue was prepared by first coupling 4-(2-aminoethyl)morpholine (**4**) with the carboxylic acid residue of rhodamine derivative (**3**) to form a closed spirolactam structure (**5**), and then further reacting compound **5** with the TPE derivative (**6**) utilizing a palladium-catalyzed Suzuki coupling reaction. In order to enhance pK_a values of the probes related to spirolactam ring opening, o-phenylenediamine (**9**) and N1-(2-(2-(2-methoxyethoxy)ethoxy)ethyl)benzene-1,2-diamine (**11**) were introduced to the bromo-functionalized rhodamine derivative (**8**) forming rhodamine derivatives with closed spirolactam structures **10** and **12**, respectively. Fluorescent probes **B** and **C** were prepared by coupling the TPE derivative (**6**) with

compounds **10** and **12** through the palladium-catalyzed Suzuki coupling reaction, respectively, see Scheme 4.2.
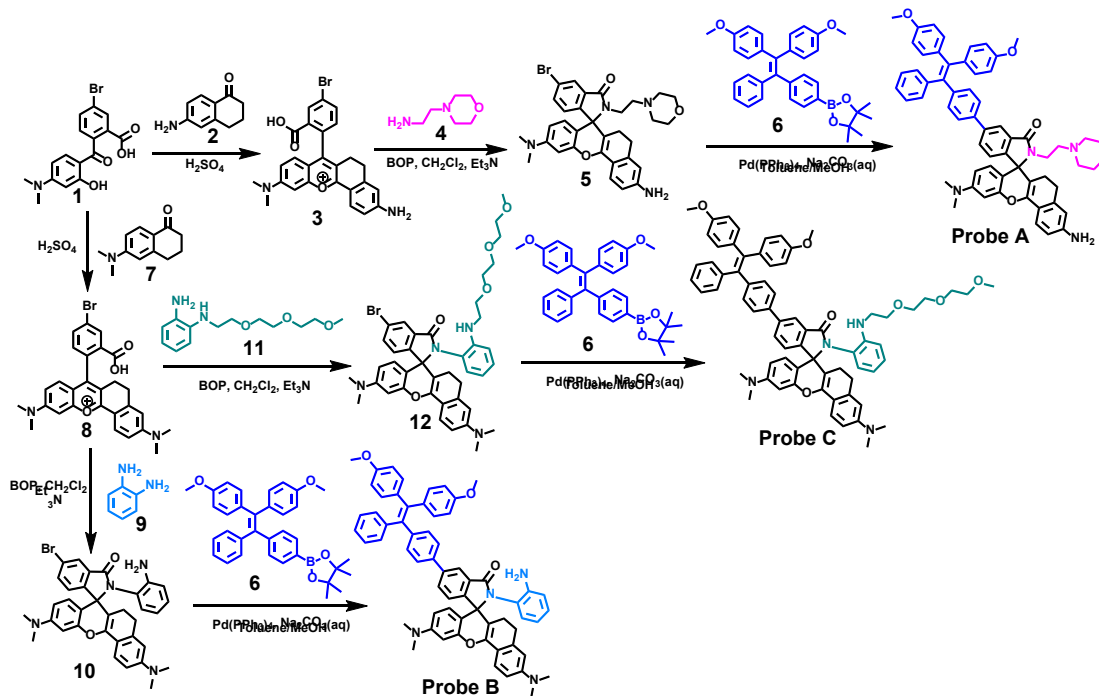
Scheme 4.2. Syntheses of probes **A-C**

4.3.2 Probe AIE properties

We investigated whether TPE donors on probes **A**, **B** and **C** retain aggregation-induced emission property to prevent ACQ effects (i.e., intermolecular π-π stacking). Increases in water percentages in mixed water and ethanol solutions from 0% to 99% resulted in only moderate absorbance decreases with probes **A**, **B**, and **C**. These absorptions were due to TPE donor absorption in probes containing closed spirolactam ring structures as this was under neutral pH conditions (Figure S17). However, increases in water percentage in mixed ethanol and water solutions from 0% and 80% result in significant fluorescence enhancement of TPE donors for probes **A**, **B**, and **C**, indicating that TPE donors possess

AIE properties (Figure S18). A picture of probe **A** with different water percentages in water and ethanol mixed solutions under UV radiation also shows that the fluorescence intensity of probe **A** increases with water percentage increases from 0% to 90% in the mixed solutions (Figure S19) presumably due to nano-aggregate formation, which was further confirmed by results of dynamic light scattering measurement (Figures S20-21). [155-163]

4.3.3 Probe optical responses to pH variations.

We studied probe absorption responses to pH variations in 10 mM citrate buffers containing 30% acetonitrile. Probes **A**, **B** and **C** show absorption peaks of TPE donors at 314 nm, 325 nm and 325 nm under neutral or basic pH conditions, respectively (Figure 4.1-4.3). As a result, functionalization of rhodamine acceptors with diamine benzene and its derivatives results in absorption red shifts of TPE donors because the benzene rings may partially conjugation with TPE donors. Gradual decreases in the pH from 7.58 to 3.2 results in the appearance and increase of two new absorption peaks, 425 and 585 nm, 445 and 607 nm, and 445 and 608 nm for each of probes **A**, **B**, and **C**, respectively. This is because acidic pH triggers the opening of the spirolactam ring on the rhodamine acceptors in the probes and, presumably significantly enhances π-conjugation of the rhodamine acceptors (Figure 4.1). The absorbance of the TPE donor attached to probe **A** decreases slightly in response to pH decreases from 7.58 to 3.2 (Figure 4.1) but those for probes **B** and **C** decrease moderately with corresponding pH changes (Figure 4.2-4.3).

We also investigated whether probes **A-C** would show ratiometric fluorescence responses to pH variations in citrate buffers containing 30% acetonitrile. Under excitation at 405 nm probe **A** displays only TPE fluorescence at 497 nm with a fluorescence quantum yield of

19.7% at pH 7.58 as the probe rhodamine acceptor preserves its closed spirolactam form at pH levels greater than 7.4. Probes **B** and **C** show similar fluorescence responses at pH levels of 7.58 as probe **A** and display fluorescence from the TPE donors at 490 nm and 485 nm with fluorescence quantum yields of 27.0% and 31.9%, respectively. Probe **A** exhibits ideal ratiometric fluorescence responses to pH variations as gradual decreases in pH levels from 7.58 to 3.19 result in dramatic decreases of the TPE donor fluorescence, with complete disappearance at pH 3.19, and proportional increases of rhodamine acceptor fluorescence at 630. Probe **A** exhibits well-defined visible and near-infrared fluorescence peaks, and possesses two Stokes shifts of 183 nm and 45 nm, corresponding to the TPE donor and rhodamine acceptor, respectively, and shows a big pseudo-Stokes shift of 316 nm (i.e., (rhodamine fluorescence 630 nm) – (TPE absorption 314 nm)). It offers remarkably ratiometric fluorescence responses to pH variations from 7.58 to 3.19, and achieves a significant 365-fold ratio increase in TPE donor fluorescence to the rhodamine acceptor fluorescence. This presumably occurs through highly efficient energy transfer from the TPE donor to the rhodamine acceptor based on a combined FRET and TBET mechanism, which was confirmed by the fact that the emission spectrum of the TPE donor overlaps significantly with the absorption spectrum of the rhodamine acceptor (Figure S22, left). Probe **A** with a pK_a of 4.4 related to spirolactam ring opening, has a fluorescence quantum yield of 22.4% with molar absorptivity of 5.8×10^4 $cm^{-1}M^{-1}$ at pH 3.2 under TPE excitation at 405 nm. In order to increase the pK_a value related to spirolactam ring opening, we introduced o-phenylenediamine and its derivative bearing tri(ethylene glycol)methyl ether residue to the rhodamine acceptors and formed closed spirolactam ring structures for probes **B** and **C**, respectively. Using an o-phenylenediamine derivative bearing tri(ethylene

glycol)methyl ether residue is also expected to significantly enhance the hydrophilicity of probe **C**. Probes **B** and **C** respond to pH changes ratiometrically as probe **A** does (Figures 2 and 3), but possess higher pK$_a$ values of 4.6 and 4.8, respectively. These pK$_a$ values were calculated using the Henderson–Hasselbalch equation (Figures S24-S26). [88, 89, 92-94] The increase in the pK$_a$ values for probes **B** and **C** may be ascribed to steric hindrance from the bulky o-phenylenediamine and its derivative bearing tri(ethylene glycol)methyl ether residues in the closed spirolactam structures. The highly sensitive ratiometric responses of probes **B** and **C** to pH variations also arise from highly efficient energy transfer through a combined FRET and TBET mechanism because their TPE donor emissions also overlaps significantly with their rhodamine acceptor absorptions (Figure S22, middle and right). They also provide considerably big signal-to-background fluorescence ratio increases to pH variation from 7.58 to 3.18 as probes **B** and **C** show 1762- and 131-fold ratio increases of TPE donor fluorescence to rhodamine acceptor fluorescence, respectively. Probe **B** shows a much more significant signal-to-background fluorescence ratio increase to pH variations because of the almost complete disappearance of TPE donor fluorescence at pH 3.19 (Figure 2, right). Probe **B** also displays dual well-separated fluorescence peaks at 490 nm and 642 nm, and exhibits two Stokes shifts of 165 nm and 35 nm with a large pseudo-Stokes shift of 317 nm. Probe **C** also shows two well-defined emission peaks at 485 nn and 642 nm, and possesses two Stokes shifts of 160 nm and 34 nm with a pseudo-Stokes shift of 317 nm. Probes **B** and **C** possess molar absorptivities of 5.4 x 10^4 cm^{-1}M^{-1} and 4.2 x 10^4 cm^{-1}M^{-1} with fluorescence quantum yields of 25.3% and 27.7% at pH 3.19 under TPE excitation at 405 nm, respectively. Additionally, probes **A**, **B**, and **C** possess fluorescence quantum yields of 23.5%, 26.2% and 28.0% at pH 3.19 under rhodamine

acceptor excitation at 555, 570 and 570 nm, respectively. This allows for the conclusion that the high energy transfer efficiencies of probes **A**, **B** and **C** from the TPE donors to the rhodamine acceptors are 95.3%, 96.6% and 98.9% with the combined TBET and FRET mechanism, respectively. The advantage to use TPE as donors is to achieve remarkable ratiometric fluorescence responeses of the probes to pH changes.
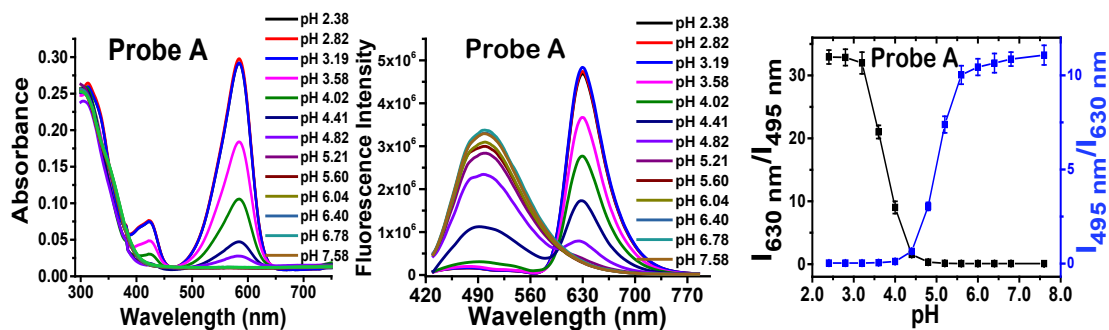
Figure 4.1. Absorption and fluorescence spectra of 10 μM probes **A** in 10 mM citrate buffers having pH ranges from 7.58 to 2.38 containing 30% acetonitrile under TPE excitation at 405 nm. Ratio between TPE donor fluorescence and rhodamine acceptor fluorescence versus pH values for probe.
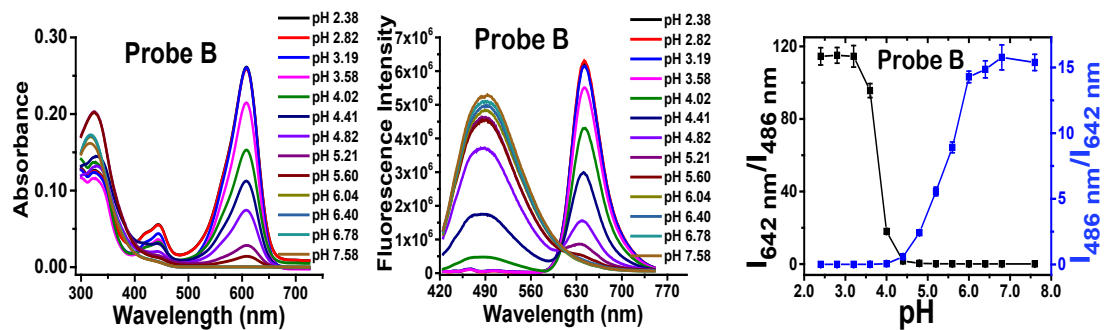
Figure 4.2. Absorption and fluorescence spectra of 10 μM probes **B** in 10 mM citrate buffers having pH ranges from 7.58 to 2.38 containing 30% acetonitrile under TPE excitation at 405 nm. Ratio between TPE donor fluorescence and rhodamine acceptor fluorescence versus pH values for probe.
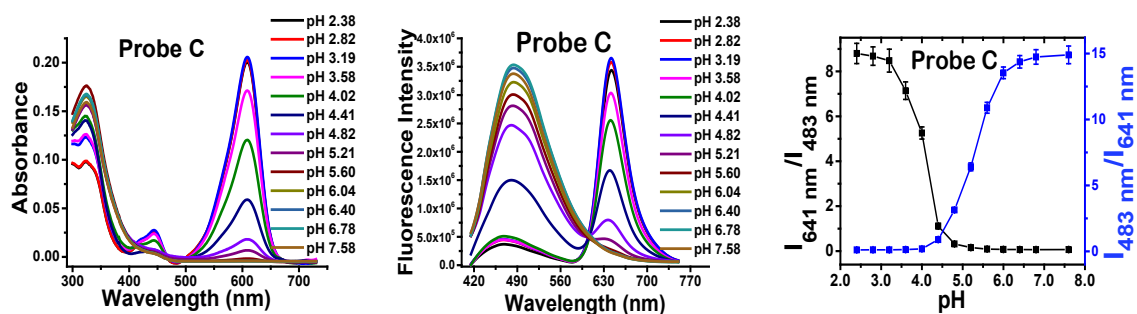
Figure 4.3. Absorption and fluorescence spectra of 10 μM probes **C** in 10 mM citrate buffers having pH ranges from 7.58 to 2.38 containing 30% acetonitrile under TPE excitation at 405 nm. Ratio between TPE donor fluorescence and rhodamine acceptor fluorescence versus pH values for probe.

4.3.4 Computational analysis.

In order to confirm the nature of the electronic transitions, theoretical studies (geometry optimization, frequency and TD-DFT calculations) at the TPSSH[164, 165]/TZVP[166] level were conducted for probes **A**, **B** and **C** and their protonated versions, namely, **AH+**, **BH+**, and **CH+**, which feature open spirolactam arrangements. There are some noteworthy changes in geometries of these structures upon protonation, see Figure 4.4. First, there are not significant differences in the torsion twist angles regarding the biphenyl moiety in the center of the structures as these ranges from -34.0 to -32.9, Figure 4.4.

Probe **A**

Probe **AH+**
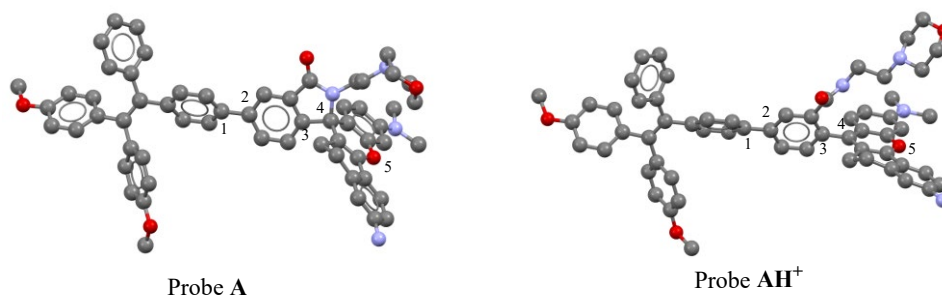
Molecule	C3-C4 (Å)	Torsion twist C1-C2 (°)	Bend C3-C4-O5 (°)	2-3 plane-4-5 plane
A	1.524	-33.4	134.3	88.7
AH$^+$	1.490	-33.5	178.2	71.3
B	1.521	-34.0	141.5	88.7
BH$^+$	1.490	-32.9	177.5	70.7
C	1.521	-33.2	142.1	89.5
CH$^+$	1.491	-32.7	177.5	72.8

Figure 4.4. Mercury[167] drawing of the optimized geometry for probe **A** (left) and probe **AH**$^+$ (right). H atoms are omitted for clarity. Grey: carbon; red: oxygen; blue: nitrogen. The labels apply to equivalent atom positions with the other probes which have different groups attached to the rhodamine moiety.

More significant is the increase in the angle labelled as C3-C4-O5 which goes from 134.3-178.2, 141.5-177.5 and 142.1-177.5° for probes **X** to **XH**$^+$, (**X** = **A**, **B**, **C**) respectively, Figure 4. This is also accompanied by a shortening of the bond distance between the atoms labelled C3 and C4 in Figure 4 from approximately 1.52 to 1.49 Å suggesting a multiple bond exists between these atoms in the protonated versions of the probes. These geometries would suggest that π-conjugation or TBET between TPE and rhodamine is difficult in probes **A**, **B** and **C** but that upon protonation and subsequent spirolactam ring opening, conjugation is possible, and this allows for the transmission of electron density from the TPE donor to the rhodamine acceptor as illustrated above in Figures 4.1-4.3.

There are several close transitions calculated for probes **A**, **B** and **C** which can be encapsulated by broad curves with maxima at 408 (exp 314), 370 (325) and 380 nm (325

nm) respectively, see Figures S54, S62 and S70, that are in reasonable agreement with the experimental data. The nature of the transition varies but the main contributors involve π to π^* transitions localized on the TPE end of the molecule, see Tables S3, S9 and S15, and corresponding Figure S55, S63 and S71. Data for experimental and electronic transitions for the probes in the protonated state are summarized in Table 1. It is noteworthy that good agreement between the calculated and experimentally obtained data was also noted with these compounds as the data in Table 1 illustrates. For probes $\mathbf{AH^+}$, $\mathbf{BH^+}$ and $\mathbf{CH^+}$, two transitions were obtained and illustrated graphically as Figures S58, S66 and S74, respectively. In Table 1, the lower energy transition labelled as Excited State (ES) 3 for $\mathbf{AH^+}$ and $\mathbf{BH^+}$ and ES 2 for $\mathbf{CH^+}$ mainly originates from π to π^* transitions localized on the rhodamine moieties, see Figures S58, S66 and S74 for corresponding LCAOs. The higher energy absorption consists of many individual transitions of which maxima of the curve suggests absorptions at 430 (expt. 425), 435 (445) and 435 nm (445 nm) for $\mathbf{AH^+}$, $\mathbf{BH^+}$ and $\mathbf{CH^+}$ respectively as illustrated in corresponding Figures S58, S66 and S74. Within these listings, significant contributions based on percentage contribution arise out of movement from the TPE to the rhodamine end of the probes as signified by transitions 237 → 243 and 242 → 244 for $\mathbf{AH^+}$, 238 → 244 and 243 → 245 for $\mathbf{BH^+}$ and 278 → 284 and 283 → 285 for $\mathbf{CH^+}$ as illustrated in the respective LCAO diagrams, Figures S59, S67 and S75.

Interestingly, the nature of the transitions can be also be gleaned from the different density illustrations for the excited states shown in Figure 4.5. The illustrations for probes $\mathbf{A}$, $\mathbf{B}$, and $\mathbf{C}$ for the excited states depict electron density moving from the ends of the molecule and ending up in the middle region as signified by the blue color in the middle. This is only

for one specific transition and recall there were many excited states contributing to the UV-Vis spectra. For the protonated probes, the illustrations in the middle for ES 3, illustrate π to π* transitions localized on the rhodamine end whereas those for ES 6 illustrate movement from the TPE to the rhodamine moieties.
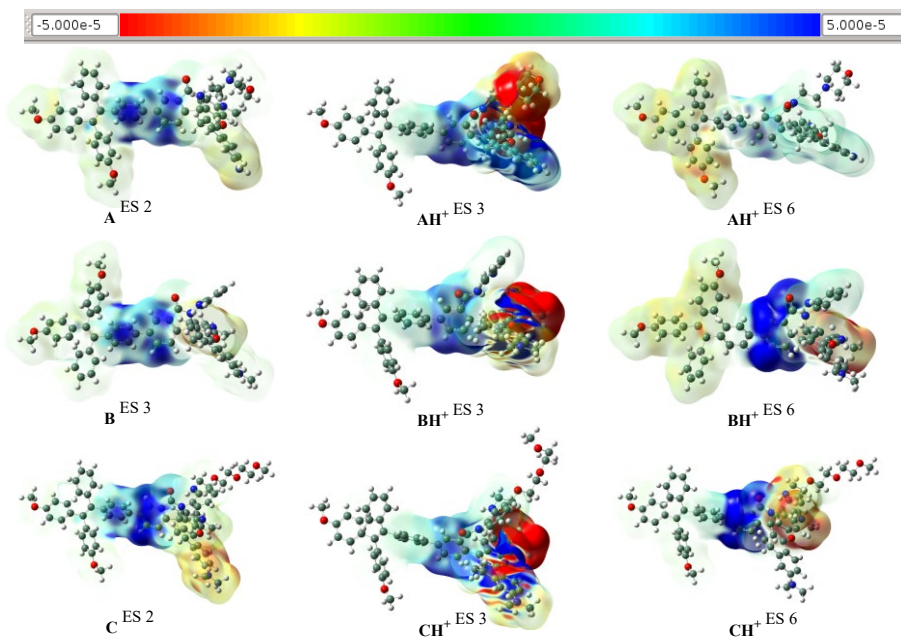
Figure 4.5. Difference density illustrations as isosurfaces of probes for the excited states indicated. Blue/red areas indicate values for the different density of $\pm 1.00e^{-5}$ for the middle column and $\pm 5.00e^{-5}$ for the outer ones, see scale on top of illustration.

Table 4.1. Calculated electronic transitions (nm), experimental data and corresponding oscillator strengths (f) and their percentage contribution to the UV/Vis spectra for the protonated probes.

Probe		Transition	Experiment (nm, eV)	Calculated (nm, eV)	f	%
AH^+	ES 3	240 → 243	585, 2.12	534, 2.32	0.6285	9.1
		241 → 243				88.9
	ES 5	237 → 243	425, 2.92	438, 2.83	0.3725	37.5
		238 → 243				51.1
		242 → 244				7.3
	ES 6	237 → 243	425, 2.92	423, 2.93	0.3465	33.2
		238 → 243				3.4
		242 → 244				61.4
BH^+	ES 3	241 → 244	607, 2.04	553, 2.24	0.8284	3.2
		242 → 244				95.0
	ES 5	238 → 244	445, 2.79	453, 2.74	0.2589	5.6
		239 → 244				83.6
		242 → 247				2.3
		243 → 245				2.8
	ES 6	237 → 244	445, 2.79	429, 2.89	0.4283	13.1
		243 → 245				83.9
CH^+	ES 2	281 → 284	608, 2.04	553, 2.24	0.8492	5.9
		282 → 284				92.2
	ES 5	277 → 284	445, 2.79	453, 2.74	0.2433	2.3
		278 → 284				7.7
		279 → 284				81.5
		282 → 287				2.1
		283 → 285				2.5
	ES 6	277 → 284	445, 2.79	430, 2.89	0.3205	41.4
		278 → 284				5.9
		283 → 285				51.3

4.3.5 Probe selectivity to pH over metal ions, anions, and amino acids.

We investigated potential interference of metal ions, anions and amino acids with fluorescence responses of the probes to pH at pH 7.6 or 2.4. The presence of 50 μM metal ions such as K^+, Mg^{2+}, Ca^{2+}, Al^{3+}, Ag^+, Mn^{2+}, Mn^{2+}, Ni^{2+}, Co^{2+}, Cu^{2+}, Zn^{2+}, Fe^{2+} or Fe^{3+} ions shows negligible influence of the probe TPE donor fluorescence and rhodamine

acceptor fluorescence in a buffer with pH 7.6 or 2.4 under excitation at 405, 555 or 570 nm (Figures S27-S35). These results show that probes **A-C** have excellent selectivity to pH over metal ions. The presence of 50 µM of different anions such as I^-, Br^-, NO^{2-}, S^{2-}, SO_3^{2-}, NO_3^-, SO_4^{2-}, HCO_2^{3-} or CO_3^{2-} ions doesn't lead to any significant interference with fluorescence responses of the probe TPE donor and rhodamine acceptor to pH 7.6 and 2.4 under excitation at 405, 555 or 570 nm (Figures S27-S35). In addition, 50 µM amino acids and biothiols such as DL-alanine, DL-arginine, L-cysteine, DL-leucine, DL-cystine, glycine, DL-proline, DL-methionine, DL-tyrosine, and reduced glutathione display insignificant influences on fluorescence responses of the probe donor and acceptor to pH at 7.6 and 2.4 under excitation at 405, 555 or 570 nm (Figures S27-S35). Therefore, probes **A-C** can provide promising approaches to investigate pH-related biological processes free from interference from the biological environment.

4.3.6 Probe reversibility and photostability to pH changes.

We studied whether probes **A-C** could respond to pH variations reversibly. Fluorescence of the probe TPE donors and rhodamine acceptors can well respond to pH changes from 2.4 to 7.6 reversibly under TPE donor excitation at 405 nm or rhodamine acceptor excitation at 555 nm or 570 nm (Figures S36-S38), indicating that probes **A-C** show reversible responses to pH changes.

We investigated the probe photostability under continuous probe excitation with 5-min intervals and through assessment of fluorescence intensity of the TPE donors or the rhodamine acceptors with every 10 min. Probes **A**, **B**, and **C** exhibit good photostability with TPE fluorescence decreases by 2.4%, 3.7%, and 2.8% in pH 7.6 citrate buffers,

rhodamine fluorescence decreases by 4.3%, 4.3% and 2.2% in pH 2.5 citrate buffer under 1-hour TPE excitation at 405 nm, and with rhodamine fluorescence decreases by 2.0%, 3.5% and 3.5% under 1-hour rhodamine excitation at 555 nm for probe **A**, and at 570 nm for probes **B** and **C**, respectively (Figure S39). TPE fluorescence of probes A, B, and C decrease by 7.5%, 9.5% and 5.5% in pH 7.6 citrate buffers under 3-hour TPE excitation at 405 nm while rhodamine fluorescence of probes **A**, **B**, and **C** decrease by 10%, 13% and 8.6% in pH 2.4 citrate buffer under 3-hour TPE excitation at 405 nm, and by 7.4%, 11% and 7.4% at pH 2.4 under 3-hour rhodamine excitation at 555 nm for probe A, and at 570 nm for probes B and C, respectively (Figure S39). The results indicate that the probes possess good photostability.

4.3.7 Cytotoxicity of the fluorescent probe.

We investigated the effect of the probes on the viability of HeLa cells with various probe concentrations ranging from 5 µM to 20 µM by using MTS assay to assess the cytotoxicity of the probes. No significant toxicity was observed with 20 µM probes **A-C** since the cell viability is greater than 82% at 20 µM probe concentration, indicating that the probes have a potential application in intracellular imaging of live cells because of their low cytotoxicity and good biocompatibility (Figure S40).

4.3.8 Probe applications in cellular imaging.

We investigated whether the probes could penetrate and stain the cells for potential cellular imaging applications. Three color channels were employed for these experiments: blue fluorescence channel from 475 to 525 nm under TPE donor excitation at 405 nm, and two

near-infrared fluorescence channels from 650 to 700 nm (pseudo-colored as red and green for clarity) under TPE donor excitation at 405 nm and under the rhodamine acceptor excitation at 559 nm, respectively. 15 µM probes **A-C** level show both strong cellular visible fluorescence intensities of the TPE donors in the first column and intense cellular near-infrared fluorescence of the rhodamine acceptors in the second column under TPE donor excitation at 405 nm (Figures S41-S43). In addition, they also display strong cellular near-infrared fluorescence intensities of rhodamine acceptors in the third column at 15 µM concentration level under the rhodamine excitation at 559 nm (Figures S41-S43). Increases of the probe concentrations significantly enhance fluorescence signals of both TPE donors in blue channel and rhodamine acceptors in red or green channel under the TPE donor excitation at 405 nm or under the rhodamine acceptor excitation at 559 nm. Probe **C** shows stronger donor and acceptor fluorescence intensities than probes **A** and **B** at the same probe concentration and pH levels because probe **C** possesses a higher pK_a value of 4.8 related to the spirolactam ring opening than probes **A** and **B**. These results demonstrate that the probes possess excellent cell membrane permeability. In order to prove probe potential targeting to lysosomes in live cells, we conducted collocalization correlation analysis by incubate HeLa cells with a near-infrared lysotracker[88] and probes A, B and C, respectively (Figure S44). The pearson's collocalization coefficients between donor excitation blue channel and near-infrared Lysotracker channel for probes **A, B** and **C** are 0.917, 0.896 and 0.934 respectively, indicating that our probes stay with near-infrared lysotracker together in lysosomes in live cells.

With these cellular imaging data in hand, we further investigated whether probes **A**, **B** and **C** could be applied in quantification of intracellular pH values. HeLa cells were incubated in a series of buffers with different pH values at 3.5, 4.0, 4.5, 5.5, 6.0, 6.5 and 7.0 in the presence of 5 µM nigericin (K^+/H^+ ionophore) to equilibrate the intracellular pH with external media.[168] Probe **A** responds to intracellular pH variations from 7.0 to 3.5 ratiometrically with gradual decreases in blue intracellular TPE donor emission in the first row, and gradual concomitant increases in near-infrared intracellular rhodamine acceptor emission (using red channel) in the second row under the TPE donor excitation at 405 nm. These observations match well with fluorescence spectral results in buffer solutions (Figure S45). In addition, near-infrared intracellular emission of the rhodamine acceptor (using green channel) in the third row also gradually increases under the rhodamine acceptor excitation at 559 nm when pH decreases from 7.0 to 3.5, which is also consistent with fluorescence spectral results in buffer solutions (Figure 24). The overlapped images in the first and second rows show dramatic color changes from deep blue, purple, pink to deep red when pH changes from 7.0 to 3.5, demonstrating that probe **A** can respond to pH changes in live cells ratiometrically (Figure S45). Probe **A** shows dual Stokes shifts of 177 nm and 48 nm with a big Stokes shift of 321 nm and possesses dual well-separated emissions under dual excitations (Figures 1 and S24). Overlapped images of the blue and green channels also show substantial color changes from deep blue, cyan, to deep green in the fifth row in responses to intracellular pH variations from 7.0 to 3.5 (Figure S45). Moreover, overlapped images of two near-infrared channels in the second and third rows under TPE donor and rhodamine acceptor excitations also show significant color changes from green, light yellow to deep yellow in responses to intracellular pH changes from 7.0

to 3.5 (Figure S45). These results convincing demonstrate that probe **A** can enable accurately double-checked fluorescence ratiometric sensing of intracellular pH changes through imaging colocalization of visible and near-infrared fluorescence channels. In addition, ratiometric images (red channel/blue channel) show significant color changes from strong brownish white to weakly brownish white upon intracellular pH changes from 3.5 to 6.0 (Figure S46). Probe **B** possesses a higher pKa value than probe **A** since the weak near-infrared fluorescence of probe **B** can be observed at pH 6.0 in the third row under the rhodamine excitation (Figure S47). Probe **C** also exhibits similar ratiometric fluorescence responses to pH variations in living cells, but possesses a higher pKa value related to the opening of the rhodamine acceptor spirolactam ring than probe B because the near-infrared fluorescence of probe **C** can be observed at pH 6.0 under TPE donor excitation (the second row), and at pH 6.5 (the third row) under the rhodamine excitation (Figure 4.6). The higher pKa values of probes **B** and **C** are due to significant steric hindrance in their spirolactam ring structures with bulky o-phenylenediamine and its derivative residues (Scheme 4.1). Statistical analysis of the confocal imaging data in Figures 8 also demonstrate that probes **A**, **B** and **C** show remarkable ratiometric fluorescence responses to intracellar pH variations from 7.0 to 3.5 with considerable fluorescence decreases of TPE donors, and concomitant increases of rhodamine acceptors (Figures 4.7, S48, S49 and S51), which is consistent with ratiometric fluorescence responses to pH variations in buffers (Figure 4.1-4.3).
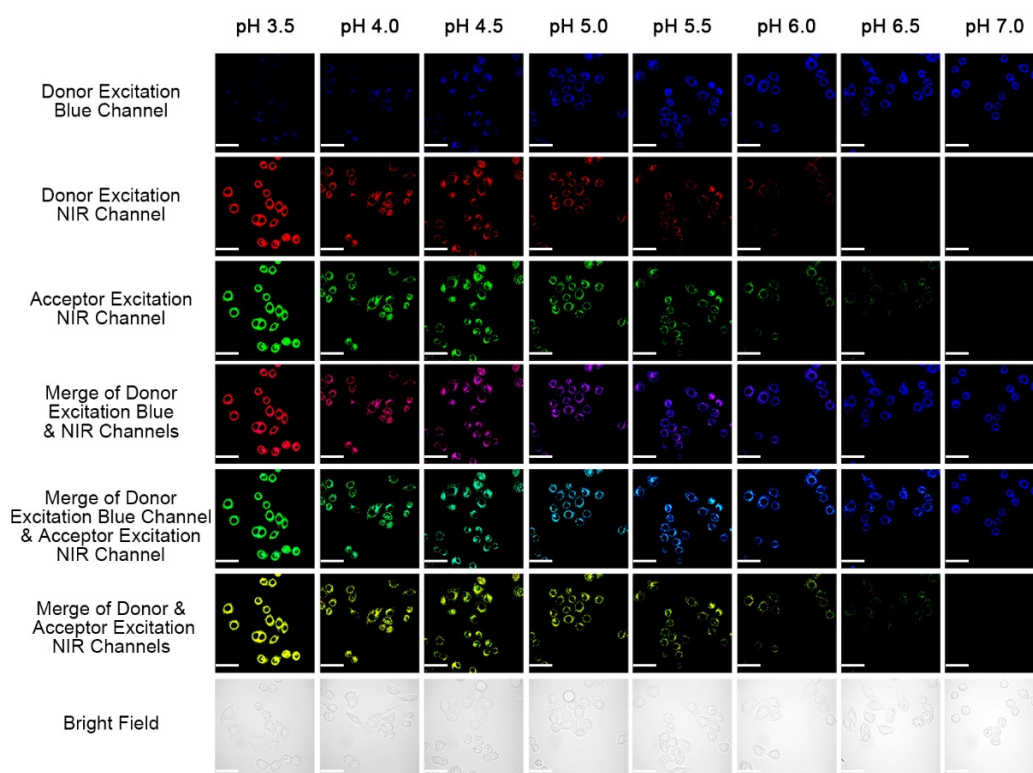
Figure 4.6. Cellular fluorescence images of 15 μM probes **C** incubated with HeLa cells in 10 mM citrate buffers having pH from 3.5 to 7.0 in the presence of 5 μg/mL nigericin. The blue channel in the first row was collected from 475 to 525 nm, and two NIR channels (pseudo-colored as red and green for clarity) in the second and third rows were collected from 650 to 700 nm under excitation of TPE donor and rhodamine acceptor at 405 nm and 559 nm, respectively. Confocal fluorescence microscope was employed to obtain fluorescence images at 60× magnification with scale bars of 50 μM.
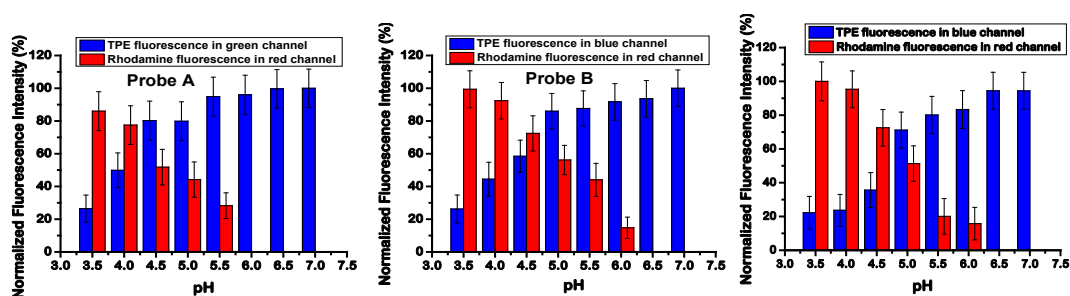
Figure 4.7. Cellular fluorescence intensities of TPE donors and rhodamine acceptors in probes **A** (left), **B** (middle) and **C** (right) in 10 mM citrate buffers with pH ranges from 3.5 to 7.0 having 5 μg/mL nigericin under TPE excitation at 405 nm. Statistical analysis of the confocal imaging data in Figures 4.5-4.7 generate the donor and acceptor fluorescence intensities of probes **A-C** in HeLa live cells.

We further applied probe **C** in monitoring pH fluctuations in live cells under drug stimulus. We treated HeLa cells with 100 and 200 μM chloroquine since chloroquine as a lysosomotropic agent can increase lysosomal pH by inhibiting autophagy and protein degradation (Figures 4.8 and S50).[120, 130, 169, 170] Compared with control cells without chloroquine treatment, the cellular blue fluorescence intensity of the TPE donor in the first column slightly increases, and cellular near-infrared fluorescence intensities of the rhodamine acceptor in the second and third columns decrease after the cells were treated with 100 and 200 μM chloroquine, indicating that the drug stimulus results in an increase in cellular pH. Fluorescence intensity of overlapped fluorescence images in the sixth columns also become weaker after chloroquine treatment of the cells. Overlapped images in the fourth column change colors from pink to blue with slightly pink under chloroquine stimulus while overlapped images in the fifth column also undergoes significant color changes from ice blue to azure blue. In addition, ratiometric images (red channel/blue channel) show significant color changes from reddish yellow to reddish blue before and after chloroquine stimulus (Figure S50). These results have convincingly demonstrated that the probe shows excellent performance in intracellular imaging of pH and its fluctuations.
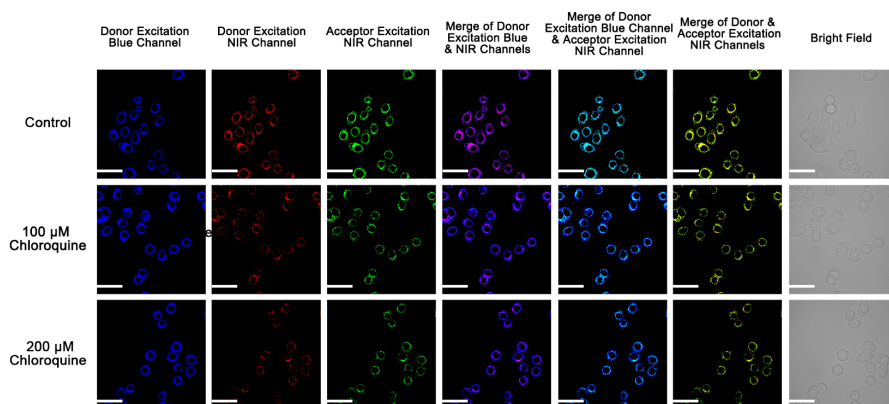
Figure 4.8. Cellular fluorescence images of 20 μM probes **C** incubated with HeLa cells in 10 mM citrate buffers with pH 7.4 in the absence and in the presence of 100 and 200 μM chloroquine. The blue channel in the first column was obtained from 475 to 525 nm, and two NIR channels (pseudo-colored as red and green for clarity) in the second and third columns were got from 650 to 700 nm under excitation of TPE donor and rhodamine acceptor at 405 nm and 559 nm, respectively. Confocal fluorescence microscope was used to acquire the images at 60× magnification with scale bars of 50 μM.

4.4 Conclusion

In summary, we have designed and synthesized three ratiometric fluorescent probes consisting of TPE donors and near-infrared acceptors in order to achieve sensitive, quantitative and comparative analyses of intracellular pH variations. Probes **A-C** with different pKa values have good photostability, excellent cell membrane permeability, biocompatibility, high selectivity, sensitivity, and remarkable ratiometric fluorescence responses to pH changes in both solutions and living cells. They are capable of visualizing intracellular minor pH fluctuations under drug stimulus. The probes allow for development of various ratiometric fluorescent probes for quantitative and comparative reliable analyses of cations, reactive nitrogen, oxygen and sulfur species by conjugating various biosensing groups into the near-infrared rhodamine acceptors.

5 Near-infrared Hybrid Rhodol Dyes with Spiropyran Switches for Sensitive Ratiometric Sensing of pH Changes in Mitochondria and Drosophila melanogaster first-instar larvae[171]

Yibin Zhang,[a‡] Shuai Xia,[a‡] Logan Mikesell,[a] Nick Whisman,[a] Mingxi Fang,[a] Tessa E. Steenwinkel,[b] Kai Chen,[c] Rudy L. Luck,[a*] Thomas Werner,[b*] and Haiying Liu[a*]

[a.] Department of Chemistry, and [b.] Department of Biological Sciences, Michigan Technological University, Houghton, MI 49931, E-mail: rluck@mtu.edu; twerner@mtu.edu; hyliu@mtu.edu

[c.] Molecular Imaging Center, Department of Radiology, Keck School of Medicine, University of Southern California, Los Angeles, CA 90033.

5.1 Introduction

Mitochondrial defects or dysfunctions are closely related to some cardiovascular and neurological diseases, such as Alzheimer's disease.[172-175] It is very important to precisely and quantitatively detect mitochondrial pH values because they are closely linked to the unique functions and biochemical processes of mitochondria.[176-180] Ideal fluorescent probes for pH sensing in mitochondria should be able to specifically target mitochondria, possess ratiometric sensing capability with two well-defined visible and near-infrared emissions, and effectively track mitophagy. Many rhodol-based probes have been developed,[2] and rhodol dyes hold exceptional photophysical advantages, including high fluorescent quantum yields, excellent photostability, pH sensitivity, and high absorption coefficients.[181, 182] In order to prevent cellular and tissue damage due to excitation using wavelengths less than 600 nm,[183-185] a variety of near-infrared rhodol dyes have been reported, where either the central oxygen atom has been substituted with N, C or Si atoms, or an additional amine has been incorporated for advantageous near-infrared imaging.[96, 144, 186-189] However, most of these probes are single-wavelength-based fluorophores without ratiometric sensing features, and they often register systematic errors, such as excitation light fluctuations, heterogeneous samples, probe concentration deviations, and varied localization in organelles in live cells.[96, 186-188, 190] Spiropyran molecular switches have been widely utilized in the design of optical probes because they respond reversibly to chemical stimuli through chemical structural changes.[191-194] Most optical probes are based on absorbance changes involving conversion between the spiropyran and hemicyanine forms due to an external stimulus, and many often lack ratiometric fluorescence responses because of non-fluorescent spiropyran forms.[191-196] Effective spiropyran switches with high

fluorescence are not yet fully developed in order to ratiometrically detect mitochondrial pH changes.

Here we present a simple but very effective way to prepare new proton-activated ratiometric near-infrared rhodol hydride dyes (probes **A-2** and **B-2**) for sensing pH changes by conjugating hemicyanine dyes into traditional rhodol dyes containing spiropyran molecular switches. The probes allow for ratiometric pH detection through π-conjugated modulation involving rhodol hydroxyl groups in the spiropyran switches under a pH stimulus. Acidic pH readily activates the breakdown of the hemiaminal ether moieties of the probes to produce indolenium moieties, extend rhodol π-conjugation, and lead to new fluorescence peaks with a considerable bathochromic shift to the near-infrared region for probes **A-1** and **B-1**, Chart 1. Moreover, under basic conditions, the free hydroxyl group of the rhodol fluorophore reacts as a nucleophile toward the indolenium moiety, forming a spiropyran switch, and leads to an emission at 563 nm for the rhodol fluorophores with significantly reduced π-conjugation, Chart 5.1. Gradual pH increases result in decreases of fluorescence peaks at 688 nm and 698 nm, as well as corresponding increases in the fluorescence peak at 563 nm for probes **A** and **B**, respectively. The probes undergo reversible structural transformations from hemicyanine configurations to spiropyran forms with significantly reduced π-conjugation upon pH increase. They demonstrate sensitive ratiometric sensing of pH variances in mitochondria and *D. melanogaster* first-instar larvae, and can monitor mitochondrial delivery to lysosomes during mitophagy, induced by cell nutrient starvation and drug treatment.
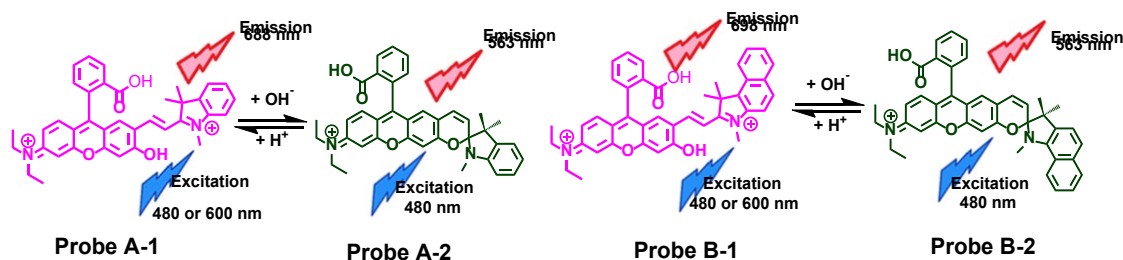
Chart 5.1. Probes **A** and **B** undergo reversible structural changes between closed spiropyran and opened hemicyanine forms upon pH changes.

5.2 Experimental Section

Instrumentation. ^{1}H NMR and ^{13}C NMR spectra of the fluorescent probes in CDCl3 solution were recorded using a Varian Unity Inova NMR spectrophotometer at 400 MHz and 100 MHz. Absorption spectra were collected with a Perkin Elmer Lambda 35 UV/VIS spectrometer, while fluorescence spectra were performed on a Jobin Yvon Fluoromax-4 spectrofluorometer.

Reagents. All solvents and chemical reagents were purchased from Fisher scientific or Sigma-Aldrich. The silica gel (200-300 mesh) from Sigma-Aldrich was used for column chromatographic purification, while silica gel plates from Sigma-Aldrich were employed to conduct thin-layer chromatography (TLC) analyses. The rhodol dye-bearing formyl group (**3**) was prepared and characterized according to a reported procedure.[197]

Synthesis of probe A. Compounds **3** (208 mg, 0.5 mmol) and **4** (150 mg, 0.5 mmol) were added to dry ethanol (10 mL) and were stirred at room temperature for 16 hours, Scheme 1. The mixture was concentrated under reduced pressure, diluted with dichloromethane, washed by water and brine, dried with anhydrous Na$_2$SO$_4$, filtered, and concentrated. The resulting residue was purified by using flash column chromatography gradient elution with

methanol to dichloromethane ratios increasing from 2% to 5%, affording probe **A-3** (70 mg, 26%). Probe **A-3**: ^{1}HNMR (300 MHz, CDCl$_3$) δ: 8.04 – 7.96 (m, 1H), 7.71 –7.56 (m, 3H), 7.11 – 7.27(m, 2H), 7.11 – 7.03 (m, 1H), 6.91 – 6.80 (m, 1H), 6.63 – 6.48 (m, 1H), 6.41 – 6.35 (m, 2H), 6.31(dd, J = 9.0, 2.6 Hz, 2H), 6.28 – 6.31 (m, 1H), 5.56 (dd, J = 10.2, 6.9 Hz, 1H), 3.33 (q, J = 7.1 Hz, 4H), 2.71 (d, J = 7.2 Hz, 3H), 1.28 (s, 3H), 1.13 – 1.20 (m, 6H), 1.12 (s, 3H).; ^{13}CNMR (75 MHz, CDCl$_3$) δ: 169.77, 156.21, 153.01, 149.67, 148.22, 136.76, 134.87, 129.56, 128.70, 127.74, 126.16, 125.01, 124.27, 121.80, 119.40, 118.56, 115.71, 111.65, 108.49, 107.12, 106.95, 105.28, 104.81, 102.76, 97.90, 52.40, 51.88, 44.73, 29.23, 26.43, 20.42, 12.85. LCMS (ESI): calculated for C$_{37}$H$_{35}$N$_2$O$_4$ [M]570.2, found [M+H] 571.3. HRMS (ESI):571.25865. Probe **A-1**: ^{1}HNMR (300 MHz, CDCl$_3$ + CF$_3$COOH) δ: 8.21 – 8.15 (m, 1H), 7.74 – 7.60 (m, 3H), 7.60 – 7.54 (m, 1H), 7.54 – 7.45 (m, 2H), 7.29 (s, 1H), 7.26 – 7.19 (m, 2H), 7.13 – 7.03 (m, 2H), 6.99 (dd, J = 9.8, 2.4 Hz, 1H), 6.91 (d, J = 2.4 Hz, 1H), 6.52 (d, J = 13.0 Hz, 1H), 3.70 (q, J = 7.3 Hz, 4H), 3.42 (d, J = 1.1 Hz, 3H), 1.45 (s, 3H), 1.29 – 1.42 (m, 6H), 1.24 – 1.35 (m, 3H), see Figures S1-S4.

Synthesis of probe B. Compounds **3** (208 mg, 0.5 mmol) and **7** (175 mg, 0.5 mmol) were added to dry ethanol (10 mL) and stirred at room temperature for 16 hours, Scheme 1. The mixture was concentrated under reduced pressure and diluted with dichloromethane. The product was washed with brine solution, dried with anhydrous Na$_2$SO$_4$, filtered, and concentrated. The resulting residue was purified by using a flash column chromatography gradient elution with methanol to dichloromethane ratios increasing from 2% to 5%, yielding probe **B-3** (86 mg, 28%). Probe **B-3**: ^{1}HNMR (300 MHz, CDCl$_3$) δ: 8.02 (d, J =

7.5 Hz, 1H), 7.94 – 7.91 (m, 1H), 7.82 – 7.78 (m, 1H), 7.77 – 7.73 (m, 1H), 7.67 – 7.59 (m, 2H), 7.41 – 7.37 (m, 1H), 7.24 – 7.18 (m, 2H), 6.97 (dd, J = 8.6, 4.6 Hz, 1H), 6.66 (d, J = 2.9 Hz, 1H), 6.55 – 6.48 (m, 2H), 6.42 (d, J = 4.1 Hz, 1H), 6.38 (d, J = 2.6 Hz, 1H), 6.33 – 6.30 (m, 1H), 5.66 – 5.62 (m, 1H), 3.32 (q, J = 7.1 Hz, 4H), 2.81 (d, J = 5.7 Hz, 3H), 1.63 (d, J = 1.6 Hz, 3H), 1.30 (s, 4H), 1.13 (t, J = 7.0 Hz, 6H).; ^{13}CNMR (75 MHz, CDCl$_3$) δ: 169.79, 156.56, 149.68, 146.03, 134.89, 129.67, 128.94, 126.52, 126.44, 125.03, 124.34, 121.73, 118.54, 115.64, 108.50, 106.31, 105.93, 105.26, 102.56, 97.89, 53.99, 44.73, 24.55, 22.03, 12.80. LCMS (ESI): calculated for C$_{41}$H$_{37}$N$_2$O$_4$ [M] 620.2, found [M+H] 621.3. HRMS (ESI):621.27428. Probe **B-1**: ^{1}HNMR (300 MHz, CDCl$_3$ + CF$_3$COOH) δ: 8.18 – 8.12 (m, 2H), 8.05 (d, J = 8.1 Hz, 1H), 7.85 – 7.75 (m, 3H), 7.62 – 7.56 (m, 2H), 7.47 (d, J = 7.5 Hz, 1H), 7.34 – 7.28 (m, 2H), 7.14 (d, J = 7.5 Hz, 1H), 7.03 (d, J = 9.8 Hz, 1H), 6.98 – 6.93 (m, 2H), 6.89 (d, J = 2.2 Hz, 1H), 6.61 (d, J = 13.0 Hz, 1H), 3.68 (d, J = 7.5 Hz, 4H), 3.53 (s, 3H), 1.63 (s, 3H), 1.36 (s, 3H), 1.36 – 1.23 (m, 6H), see Figures S5-S8.

Cell culture and cytotoxicity assay. HeLa cells were nurtured in DMEM (modified Eagle's medium, Gibco) supplemented with 10% FBS (fetal bovine serum, Fisher Scientific) at 3°C with 5% CO$_2$ humidified air, and then subcultured every 2-3 days until an 80 % confluence was attained. A cytotoxicity assay was carried out using a standard MTT assay against HeLa cells. The HeLa cells were seeded at a density of about 6000 cells per well in a 96-well plate, grown for 24 hours, followed by adding fresh culture medium containing probe **A** or **B** with different concentrations from 0, 5, 10, 20, 50 to 75 μM for further incubation of 48 hours. The cells were then incubated for 4 hours with 500 μg/mL

of tetrazolium salt (3-(4,5-dimethylthiazol-2-yl)-2,5-diphenyl tetrazolium bromide), which would be reduced to water-insoluble purple formazan by metabolically active cells. Dark purple crystals were dissolved with dimethylsulfoxide (DMSO), and the cell viability rate was determined by measuring the absorbance at 490 nm. The cell viability rate was calculated by $V_{rate} = (A − A_B)/(A_C − A_B) × 100\%$, where A is the absorbance of the experimental group, A_C is the absorbance of the control group (cell medium was used as control) and A_B is the absorbance of the blank group (no cells).

Cellular fluorescence imaging. HeLa cells were seeded in 35 mm confocal glass bottom dishes (MatTek) with $1×10^5$ cells per dish and cultured for 24 h before imaging. HeLa cells were incubated with 5 µM of probe **A** or **B** and either 10 µM Mito Tracker blue or 10 µM Lysosensor blue in normal medium in the presence of 1 % DMSO containing fetal bovine serum or the medium containing 1% DMSO without fetal bovine serum for 30 min and 2 h, followed by washing the cells twice with PBS buffer before imaging. HeLa cells were also incubated with probe **A** or **B** with 5 µM cyanine dye (IR-780) in normal cell culture medium for 30 min and washed twice with PBS buffer prior to imaging. For visualization of intracellular pH changes, HeLa cells were incubated in different pH citric buffers, containing nigericin (5 µg/mL) for 30 min to equilibrate the intracellular and extracellular pH.[88, 91, 93, 95, 198, 199] The cells were then incubated with 10 µM probe **A** or probe **B** for 15 min and then rinsed with FBS buffer twice before imaging. A confocal fluorescence microscope (Olympus IX 81, Olympus America Inc.) was used to obtain cell images. The cells were imaged with a 100x objective lens for the colocalization imaging experiments and with a 60x objective lens for the other imaging experiments. The fluorescence of

LysoSensor Blue or Mito Tracker Blue (blue channel) was measured from 425 nm to 475 nm under 405 nm excitation; the visible fluorescence (green channel) and near-infrared fluorescence (red channel) of the probes under 488 nm excitation were recorded from 525 nm to 575 nm, and from 650 nm to 750 nm, respectively. The near-infrared fluorescence of the probes (magenta channel) under excitation of 559 nm was recorded at 650−750 nm. The images were further processed with an Olympus FV10-ASW 3.1 viewer using Image Pro6 software.

***In vivo* experiments with *D. melanogaster* first-instar larvae.** A nine-well glass viewing dish was used to conduct fluorescence imaging of *D. melanogaster* first-instar larvae with probe **A**. The larvae were divided into four groups with ten freshly hatched first-instar larvae. The larvae in the first group were submerged in 500 μL PBS for 2 h for the blank control. The larvae in the second, third, and fourth groups were incubated with 10 μM probe **A** for 2 h in 500 μL of buffers with pH values 9.5, 7.4 and 5.0, respectively. Following incubation with probe **A** in the different buffer solutions, the larvae were washed thrice with PBS buffer and transferred with water onto microscope slides. Confocal fluorescence images were taken with an Olympus IX 81 microscope before the water dried on the slides. The fluorescence imaging protocol used for the *D. melanogaster* larvae was identical to how we imaged the cells.

5.3 Results and Discussion

5.3.1 Construction of Ratiometric Near-infrared Hydride Rhodol Dyes.

A formyl-functionalized rhodol dye (**3**) was reacted with 1,2,3,3-tetramethyl-3*H*-indolium iodide (**4**) and 1,2,3,3-tetramethyl-3*H*-benzo(e)indolium iodide (**5**) in ethanol at room temperature to form probes **A-3** and **B-3**, respectively, in order to introduce spiropyran switches into traditional rhodol dyes, Scheme 1. Rhodol derivative (**3**) was prepared by condensing 2-(4-diethylamino-2-hydroxybenzoyl)benzoic acid (**1**) with 4-(diethylamino)salicylaldehyde (**2**) in sulfuric acid at 100°C for two hours.[197] The probes **A-2**, and **B-2** under neutral and basic pH in aqueous solutions are composed of a rhodol fluorophore and *N,O*-disubstituted hemiaminal ether residue linked through a carbon-carbon double bonded connection, Chart 1. The incorporation of a hydroxyl group allows for variance in the π-conjugation of the rhodol dyes upon pH changes, which achieves sensitive ratiometric determination of pH changes, Chart 1. Under neutral and basic conditions, the free hydroxyl group acting as a nucleophile attacks the indolenium moiety, forming an *N,O*-disubstituted hemiaminal ether group and reduces π-conjugation. The rhodol fluorophore with a closed spiropyran configuration emits in the visible region, Chart 1. Under acidic pH conditions, breakdown of the hemiaminal ether residues occurs, generating indolenium moieties and considerably enhancing the π-conjugation in the rhodol fluorophores, resulting in a near-infrared emission with a bathochromic shift, Scheme 5.1.
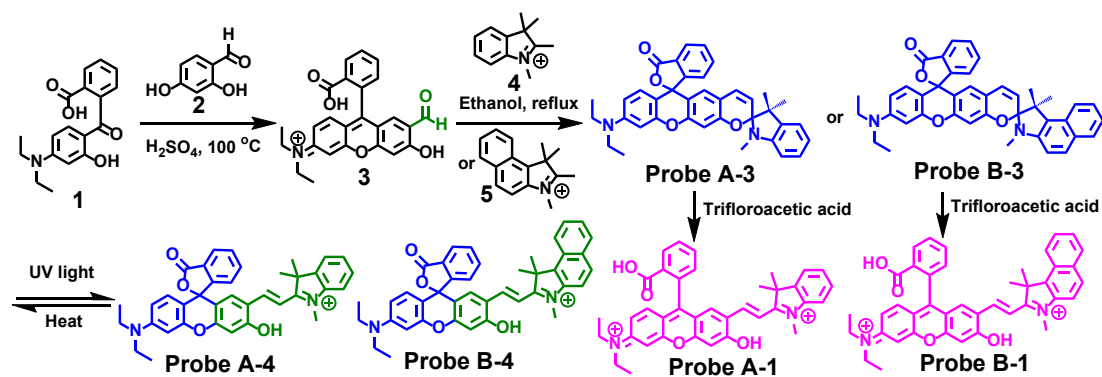
Scheme 5.1. Synthetic approach to the probe synthesis of near-infrared rhodol dyes (probes **A** and **B**) and their structural changes in trifluoracetic acid treatment or under UV radiation and heat treatment.

5.3.2 Optical Study of Probes in Organic Solvents.

Probes **A-3** and **B-3** are colorless in common organic solvents, such as tetrahydrofuran, dichloromethane, dimethylformamide, and DMSO, as the probes have closed forms of their spiropyran and spirolactone rings. The addition of trifluoroacetic acid to probes **A-3** and **B-3** in DMSO solution results in ring opening of both spiropyran and spirolactone configurations, leading to new absorption peaks at 546 nm and 542 nm (Figures S55 and S57), two fluorescence peaks at 575 and 706 nm for probe **A-1**, and 585 and 712 nm for probe **B-1**, (Figures S56 and S58) (Scheme 1). Probe **B-1** with more extended π-conjugation has both absorption and emission peaks occurring at longer wavelengths than probe **A-1**. All intermediates and probes were characterized by NMR and mass spectrometry, see supporting information.

Probes **A-3** and **B-3** are colorless without any significant absorption and emission peaks in DMSO solution (Figures S75, S80). Under UV radiation of 254 nm, a new broad absorption peak at 460 nm (Figure S75), and a new fluorescence peak at 523 nm appear

(Figure S76), increase with time and become maximized within 90 minutes for probe **A-3** (Figures S76-S78) because UV radiation transforms the closed spiropyran ring of the probe into the hemicyanine configuration as probe **A-4**, (Scheme 1). In addition, the probe with the opened hemicyanine configuration, i.e., **A-4**, can be reversibly converted into a probe with a closed spiropyran ring structure, i.e., **A-3**, if heated at 80°C (Scheme 1) (Figures S78-S79). Similar photolysis and heat effects to probe **A-3** were observed for probe **B-3** (Figures S80-S84), which shows longer absorption and emission peaks at 507 and 530 nm under UV radiation, respectively (Figures S83-S84), due to a more extended benzo(e)indolium π-conjugation in the opened hemicyanine configuration (Scheme 1). Probe **A-3** is almost colorless and shows extremely weak fluorescence at 582 nm in DMSO solution with a trace amount of water (Figure S85). However, addition of 10% water to DMSO solution of probe **A-3** causes significant fluorescence increase at 582 nm, indicating that water facilitates ring opening of spironolactone configuration of probe **A-3**, and leads to π-conjugation enhancement of probe **A-2**. These structural changes triggered by water were further confirmed by ^{1}H NMR spectra of probe **A-3** and **A-2** in DMSO-d_6 solution in the absence and presence of D_2O solution (Figures S86-S87).

5.3.3 Probe Optical Responses to pH Changes.

In aqueous solutions, spirolactone rings of the probes open as the bridging O atom is easily protonated (Chart 1). Upon excitation at 480 nm in pH 10.2 buffer, probes **A** and **B** produce similar sharp absorption peaks at 535 nm and fluoresce at the same wavelength of 558 nm, which indicates that both probes possess the same π-conjugation systems with closed spiropyran forms, i.e, probes **A-2** and **B-2**, at pH 10.2. Gradual decrease in the pH leads to

gradual decreases of the absorption peaks at 535 nm and gradual increases in new absorption peaks at 609 nm and 622 nm (Figures 5.1 and 5.2) for probes **A-1** and **B-1**, respectively (Chart 5.1) because acid converts the spiropyran rings into hemicyanine structures. Probe **B-1** displays a longer absorption wavelength at 622 nm due to better benzo(e)indolium π-conjugation with the opened hemicyanine configuration than probe **A-1** (Figure 2). Gradual pH decreases in solutions containing either probe **A** or **B** result in significant decreases of the fluorescence peaks at 558 nm and in considerable increases of a new near-infrared fluorescence peak at 688 nm or 698 nm under 480 nm excitation. This is because acidic pH activates breakdown of the *N,O*-disubstituted hemiaminal ether residues, leading to the opening of the spiropyran rings and converting the closed ring structures into a hemicyanine configurations with significantly enhanced π-conjugation (Chart 5.1). Under excitation at 480 nm, probe **A-1** has fluorescence quantum yields of 38.2% and 13.6%, corresponding to the emission peak at 558 nm at pH 10.2 and the near-infrared fluorescence peak at 688 nm at pH 3.6, respectively, see Section 3 of Supporting Information. Probe **B** displays similar ratiometric fluorescence sensing responses to pH decreases from 10.2 to 3.6 with decreases of visible fluorescence at 558 nm, as well as fluorescence increases of the near-infrared fluorescence peak at 698 nm (Figure 5.2). Probe **B-1** has a similar fluorescence peak at 558 nm with the closed spiropyran configuration at pH 10.2 to that for probe **A-1** but displays a slightly longer near-infrared fluorescence at 698 nm with the opened hemicyanine configuration, i.e., **B-2**, at pH 3.6. Probe **B** has a fluorescence quantum yield of 34.6% for the fluorescence peak at 558 nm in pH 10.2 buffer, and exhibits a fluorescence quantum yield of 10.1% in pH 3.6 buffer for the peak at 698 nm under 480 nm excitation. Near-infrared fluorescence of both probes increases

with pH decreases under 600 nm excitation (Figure 5.3). Additionally, probes **A** and **B** reversibly respond to pH variations related to opening of the probe spiropyran rings with average pKa values of 8.26 and 7.10, respectively (Figures S49-S54). The lower pKa value of probe **B** is due to the delocalization of a pair of unshared electrons from the nitrogen atom in the spiropyran ring into the naphthalene moiety, which requires a stronger acidic condition to protonate this nitrogen atom and open the ring.
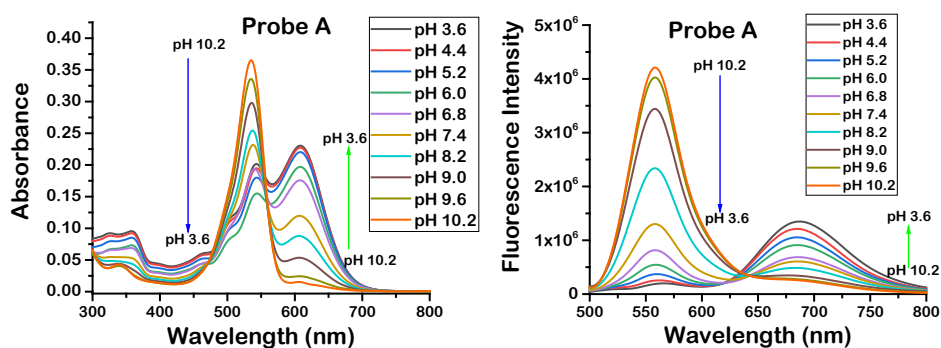
Figure 5.1. Absorption (left) and emission (right) spectra of 5 μM of probe **A** in different pH buffers containing 30% ethanol under 480 nm excitation
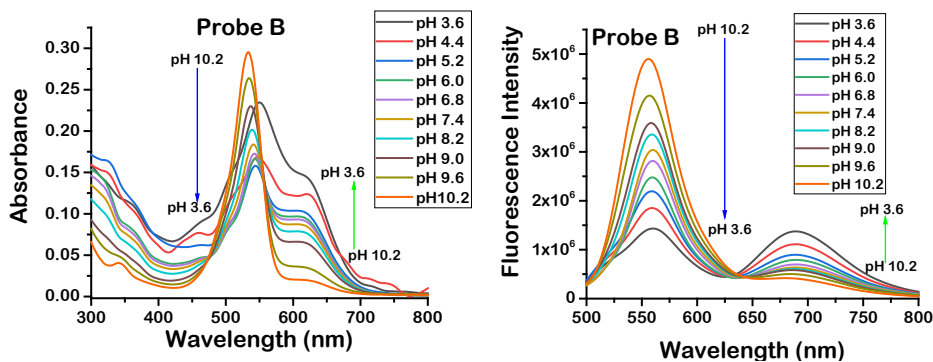
Figure 5.2. Absorption (left) and emission (right) spectra of 5 μM of probe **B** in different pH buffers containing 30% ethanol under 480 nm excitation.
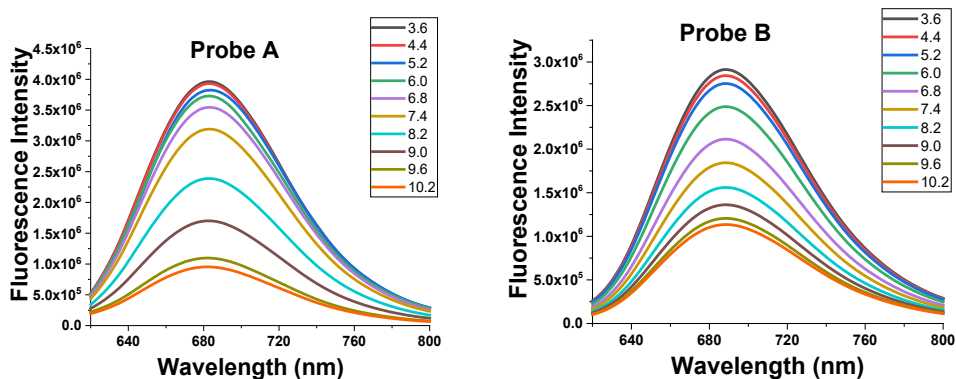
Figure 5.3. Fluorescence spectra of 5 µM of probes **A** (left) and **B** (right) in different pH buffers containing 30% ethanol under 600 nm excitation.

5.3.4 Computational Study of the Probes.

The aforementioned electronic transitions were investigated via theoretical calculations, where the structures of each molecule, i.e., **A-1-4** and **B-1-4**, depicted in Chart 1 and Scheme 1 were optimized, see supporting information Section 2 which includes procedural details. Absorptions were calculated in the UV range at 310 and 330 nm for **A-3** and **B-3**, respectively (Figures S20 and S39), whereas those for **A-4** and **B-4** were calculated to be at 450 and 473 nm (Figures S27 and S46). The calculations were also useful in tentatively assigning the ^{1}H NMR spectra for **A-3** (Figure S21) and **B-3** (Figure S40) and in assigning the resonance for the carbon atom in the lactone ring, as indicated in Figures S23 and S42, respectively. Of primary interest was the nature of the absorptions under the different pH environments. We found that the calculated absorptions were much lower than those measured experimentally, as listed in Table S25 for **A-1-2** and **B-1-2**. These calculated values are outside of the expected range[99] (i.e., < 0.25 eV), which may be ascribed to an underestimation of transition energies with the seven different functionals utilized. [200] However, the conformational and orbital information is useful because the trend in the absorptions is maintained. Structural optimizations reveal a major conformational change in the molecules, ranging from almost planar forms in **A-1** (Figure S9) and **B-1** (Figure S28) to bent forms in **A-2** (Figure S15) and **B-2** (Figure S34), with respect to the xanthene and hemicyanine sections. While the benzoic acid moieties in the rhodol section of the

molecule are almost perpendicular to the xanthene plane at **A-1** (75°), **A-2** (83°), **B-1** (65°), and **B-2** (82°), the hemicyanine moieties in **A-1** and **B-1** are attached to the rhodol section via C to C atom single bonds, which have torsion angles of -19° and -30°, respectively. In **A-2** and **B-2**, this linkage is in the form of the spiropyran ring, which results in angles between the xanthene and hemicyainine planes of 79° and 83°, respectively (Figure 5.4).

These different geometries result in the observable transitions in **A-1** and **B-1** consisting of HOMO→LUMO orbitals, whereas those for **A-2** and **B-2** consist of HOMO-1→LUMO orbitals (Figures S47 and S48). The drawings in Figure 2 illustrate that the HOMOs in probes **A-1** and **B-1** involve π-orbitals from the xanthene and hemicyanine sections of both molecules, judging from the movement of electron density from the red sections of the molecule to the blue. Notably, in **A-1**, the charge transfer occurs from the left end of the xanthene ring (i.e., the part involving the diethyl ammonium moiety) to the right. In **B-1**, the origin is at the right end, i.e., the hemicyanine section. In **A-2** and **B-2**, the charge transfer is equivalent (HOMO-1→LUMO) and involves primarily π-orbitals on the xanthene section of the molecule (Figure 5.4), probably because of the conformation noted previously. Here, the HOMOs consists of orbitals localized on the hemicyanine section of the molecules, see Figure S47 for **A-2** and Figure S48 for **B-2**.
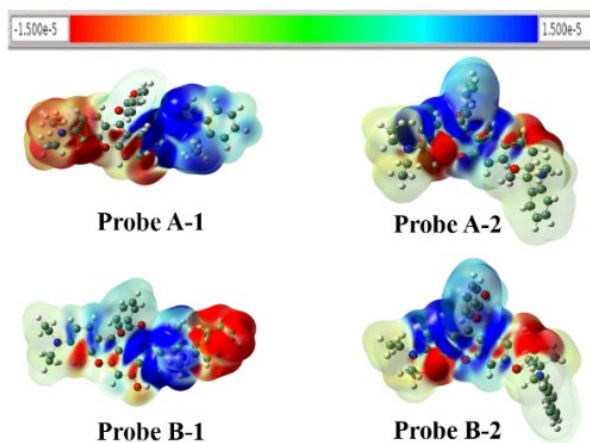
Figure 5.4. Current density difference illustrations as iso-surfaces of probes **A-1** (top left), **A-2** (top right), **B-1** (bottom left), and **B-2** (bottom right). Red areas represent values for the various densities of $-1.500e^{-5}$ and blue are for $1.500e^{-5}$, see scale on top of illustration.

5.3.5 The Probe-Selective and -Reversible Responses to pH, Photostability, and Cytotoxicity.

Probe cytotoxicity and selectivity in the presence of potential interfering biological molecules and ions were investigated. We measured fluorescence spectra of probe **A** or **B** in the presence of 100 μM metal ions (Al^{3+}, Ca^{2+}, Co^{2+} Cu^{2+}, Fe^{3+}, K^+, Mg^{2+}, Mn^{2+}, Ni^{2+}, and Zn^{2+}), 100 μM anions (CN^-, $S_2O_3^{2-}$, HSO_3^-, SO_3^{2-}, ClO^-, HCO_3^-, CO_3^{2-}, S^{2-}, NO_3^-, PO_4^{3-}, SO_4^{2-}, Cl^-), 100 μM various amino acids, and biothiols (100 μM cysteine, 100 μM homocysteine and 10 mM GSH) in pH 3.8, 7.5 or 9.9 buffers, (Figures S59-S70). These ions and molecules do not significantly change the fluorescence ratios, indicating that the probes can detect the intracellular pH without interference caused by intracellular biological molecules and ions. Furthermore, the probes show selective responses to pH values in the absence and presence of reactive oxygen and nitrogen species, such as 50 μM nitric oxide (NO), peroxynitrite ($ONOO^-$), sodium peroxide, and 100 μM hydrogen peroxide (Figures S71-S72). The probes also show good photostability throughout 2 hours of excitation at 480 nm and 550 nm (Figures S88-S91). In addition, probes **A** and **B** exhibit reversible florescence responses to pH changes between 4.0 and 10.0 (Figures S73-S74). The cytotoxicity of the probes was investigated with an MTT cell viability assay. The results in Figure S92 show that the probes are nontoxic and allow high cell-proliferation rates even under high probe concentrations.

5.3.6 Cellular Fluorescence Imaging in Mitochondria.

Being positively charged, the probes should be able to selectively target mitochondria with negative electric potentials across their inner membranes through electrostatic interactions. To test this hypothesis, we conducted intracellular localization tests of the probes via

colocalization experiments with organelle trackers, such as Lysosensor blue, mitochondria-targeting cyanine dye (IR-780), and Mito Tracker blue (a cationic fluorescent probe that accumulates specifically in mitochondria), using HeLa cells in normal culture medium. As expected, cellular fluorescent intensity increases with the probe concentration increases in probes **A** and **B** (Figures 5.5 and S93). The observed high Pearson correlation coefficients (at more than 0.95) of probes **A** and **B** with cyanine IR-780 dye confirm that the probes selectively stain mitochondria in live cells. The Pearson correlation coefficients of probes **A** and **B** (channel I) with Mito Tracker blue in HeLa cells during 30 minutes of incubation in normal medium containing FBS are high at 0.95 and 0.97, respectively (Top of Figure 5.6, Figures S95, S96 (**A**) and S111, S112 (**B**)). In contrast, lower Pearson correlation coefficients of 0.67 and 0.35 are observed for probes **A** and **B** (channel I) with Lysosensor blue in HeLa cells in 30-min cell incubation in normal medium containing FBS, respectively (Bottom of Figure 5.6, Figures S97, S98 (**A**) and S113, S114 (**B**)). Upon an increase of the incubation time to 2 hours, the average Pearson correlation coefficients of probes **A** and **B** (channel I) with Mito Tracker blue are 0.95 and 0.94, respectively (Figures S99, S100 (**A**) and S115, S116 (**B**)), while the average Pearson correlation coefficients of probes **A** and **B** (channel I) with Lysosensor blue increase to 0.69 and 0.51, respectively (Figures S101, S102 (**A**) and S117, S118 (**B**)). These high Pearson correlation coefficients of probes **A** and **B** with Mito Tracker blue convincingly demonstrate that the probes stay in mitochondria in live cells in normal medium.
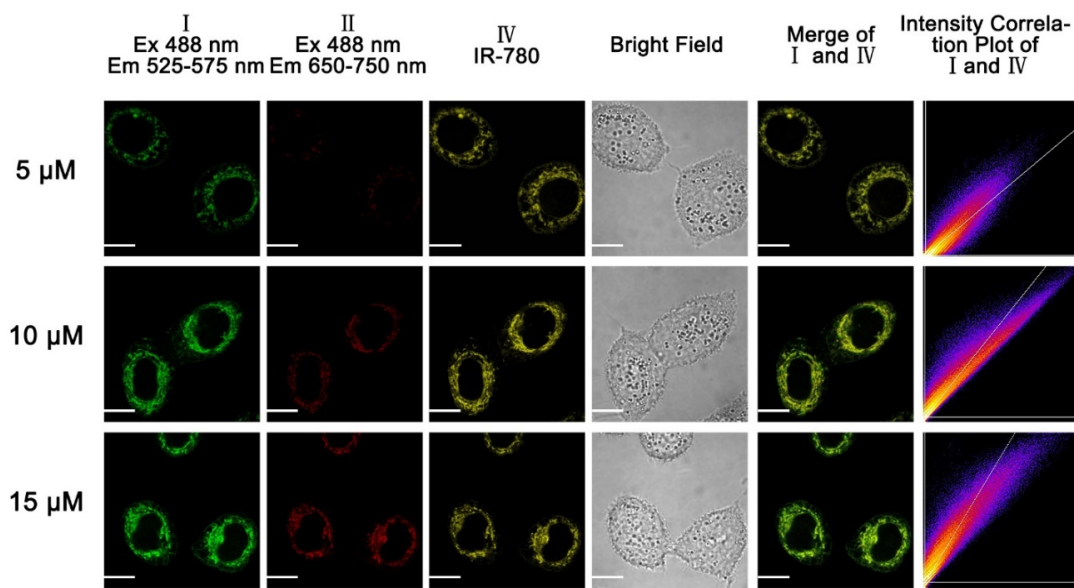
Figure 5.5. Fluorescence imaging of HeLa cells with probe **A** under excitation at 488 nm and 559 nm, 5 µM of cyanine dye (IR-780) under excitation at 630 nm in normal medium in the presence of FBS with 30 minutes of incubation. Scale bar: 20 µm.
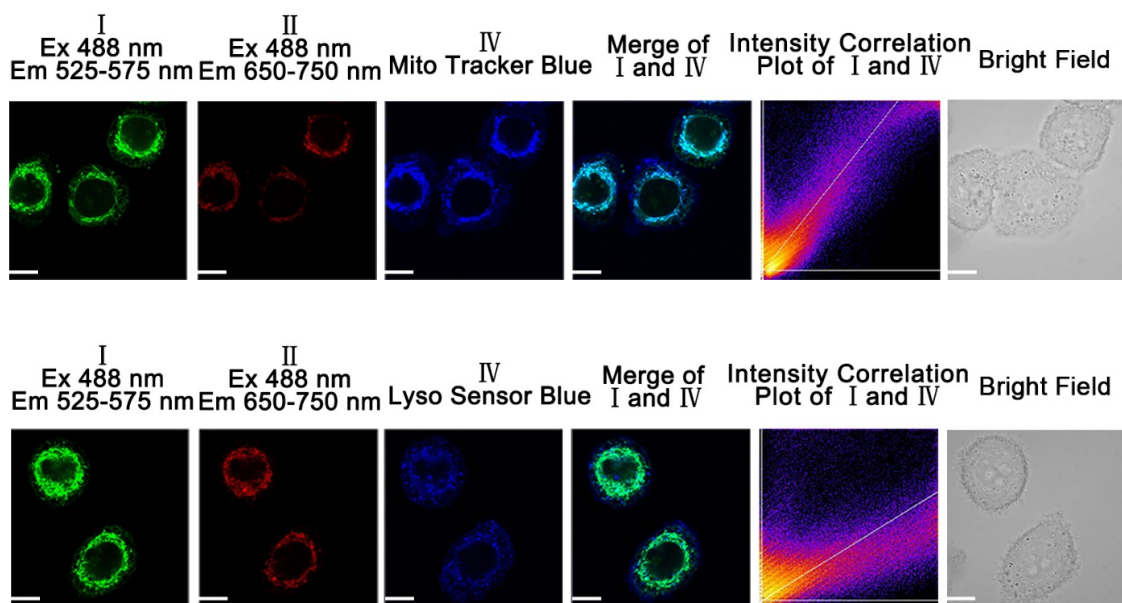
Figure 5.6. Fluorescence imaging of HeLa cells with 5 µM of probe **A**, 10 µM Mito Tracker blue (upper) or 10 µM Lysosensor blue (bottom) under excitation at 405 nm in normal medium in the presence of FBS at 30-min incubation. Scale bar: 20 µm.

In order to further confirm that the probes selectively accumulate in mitochondria in live cells, we further treated HeLa cells with an uncoupler of mitochondrial oxidative phosphorylation, i.e., carbonyl cyanide 4-(trifluoromethoxy) phenylhydrazone (FCCP), to disrupt the mitochondrial membrane potential resulting in acidification of mitochondria. HeLa cells were incubated with either probe **A** or **B** for 30 minutes in a normal cell culture medium and then subjected for an additional 20 min incubation with FCCP dissolved in PBS buffer. We observed a visible fluorescence decrease and near-infrared fluorescence increase with dramatic color changes in the ratio images of the near-infrared channel II divided by the visible channel I from blue to green for probe **A** (Figures 5.7 and S94). These results indicate that FCCP treatment leads to apparent acidification of mitochondria because of the disruption of the mitochondrial membrane potential caused by FCCP treatment, further confirming that the probes stay in mitochondria before the FCCP treatment.
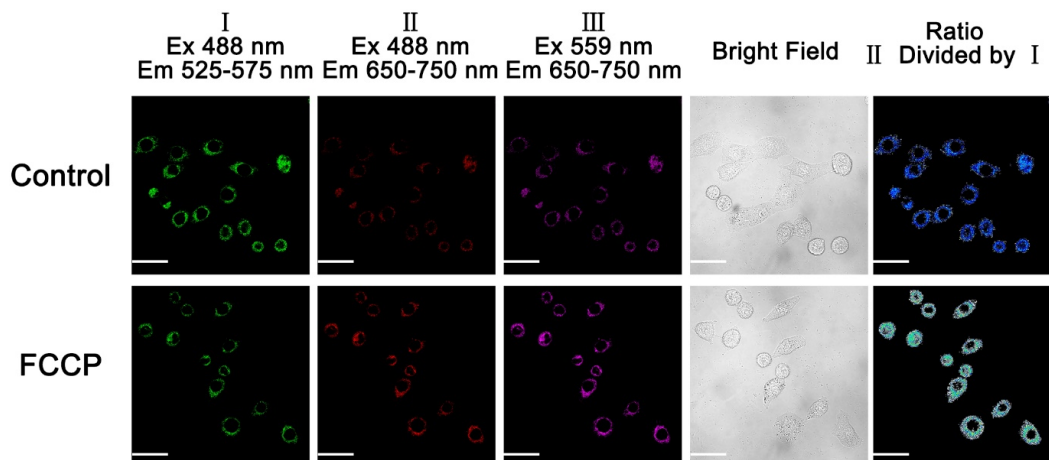
Figure 5.7. Fluorescence imaging of HeLa cells with 3.0 µM of probe **A** in normal medium with 20-min incubation under excitation at 488 nm and 559 nm as control experiment after FCCP treatment. The FCCP treatment was further conducted as follows: Cells were

incubated with probe A for 20 minutes in normal medium and further incubated with 20 µM of FCCP for 20 additional minutes. The cells were washed before the confocal imaging was conducted. Scale bar: 50 µm.

5.3.7 Mitophagy Caused by Cell Nutrient Starvation.

Starvation is well-known to induce mitophagy[201] and we then determined if the probes can illuminate the mitophagy process that occurs from nutrient starvation. During mitophagy, lysosomes infuse into defective mitochondria producing acidic autolysosomes, resulting in a decrease in the pH value inside mitochondria.[201] Probe **A** was incubated with HeLa cells in serum-free medium at different incubation times. Our cellular imaging results during nutrient starvation show that incubation times from 10 minutes to three hours cause a gradual decrease in the visible fluorescence in the green channel and a gradual increase of the near-infrared fluorescence in the red channel under 488 nm excitation (Figure 5.8). A significant color change in the merged images of visible and near-infrared fluorescence from deep green to brown color is also observed (Figure 5.8), indicating that the probe fluorescence changes in the visible and near-infrared channels are related to mitophagy induced by nutrient starvation. Probes **A** and **B** remain in mitochondria within 30 minutes of incubation of HeLa cells in serum-free medium. This is evident as probes **A** and **B** (channel I) with Mito tracker blue in HeLa cells show high Pearson correlation coefficients of 0.92 and 0.91, respectively (Figures 5.9 upper, S103 (**A**), S104 (**A**) and S119, S120 (**B**)), while they have lower Pearson correlation coefficients of 0.44 and 0.46 with Lysosensor blue, respectively (Figures 5.9, lower, S93 (**B**), and S109 (**A**)). During a 2-hour incubation in serum-free medium, the fluorescence images of probes **A** and **B** (channel I) with Lysosensor blue in HeLa cells show high Pearson correlation coefficients of 0.93 and 0.93,

respectively (Bottom of Figure 5.10, Figures S109 (**A**), S110 (**A**) and S125, S126 (**B**)). In contrast, fluorescence images of probes **A** and **B** (channel I) with Mito Tracker blue have lower Pearson correlation coefficients of 0.44 and 0.46 respectively in the 30 minute (Figures S105, S106 (**A**) and Figures S121, S122 (**B**)) and 0.49 and 0.58 respectively for the 2-hour incubation during cell starvation (Figures 5.10, S107, S108 (**A**) and S123, S124 (**B**)). These results indicate that the probes were localized to acidic autolysosomes during mitophagy caused by cell starvation after the 2-hour incubation period. These results demonstrate that the probes can be used to track the mitophagy process induced by nutrient starvation (Figures 5.8-5.10, S103-S126).
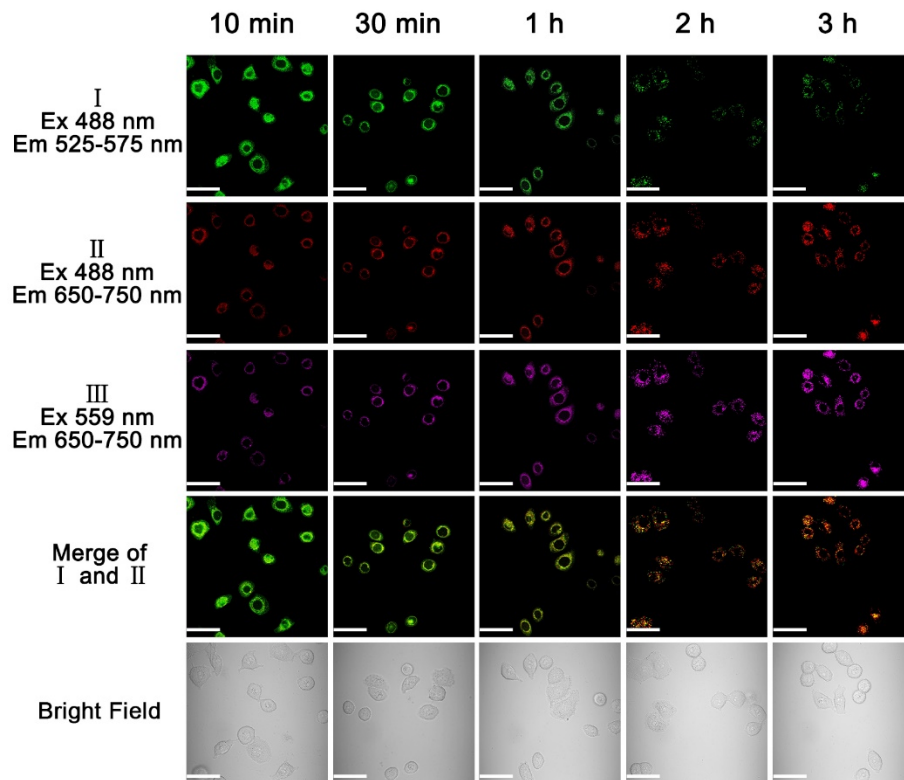
Figure 5.8. Fluorescence imaging of HeLa cells incubated with 10 μM of probe **A** in serum-free medium under excitation at 488 nm and 559 nm with a scale bar of 50 μm.

117
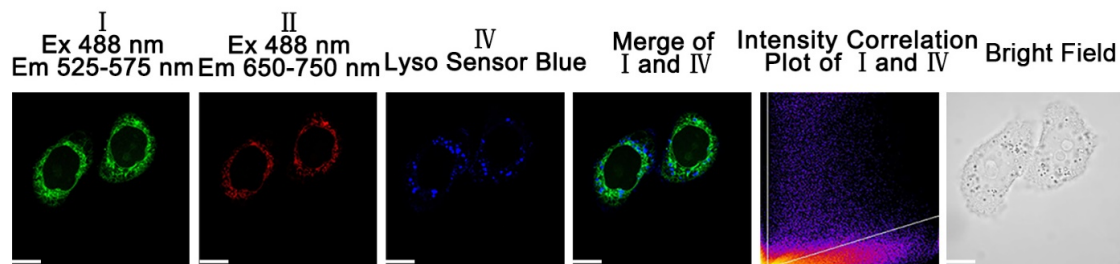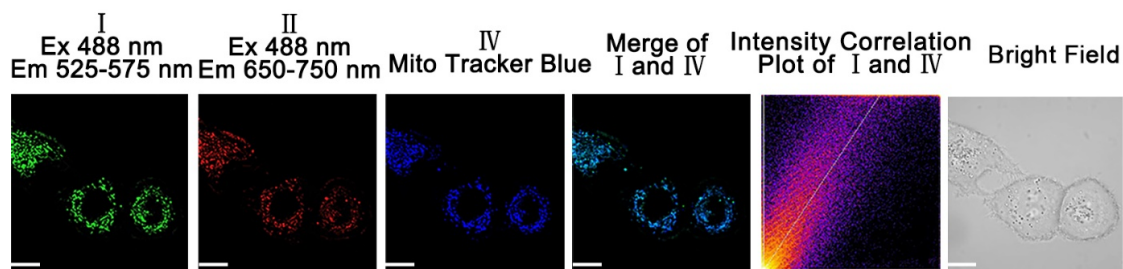
Figure 5.9. Fluorescence imaging of HeLa cells with 5 µM of probe **A**, 10 µM Mito Tracker blue (top, Ex 405 nm) and 10 µM Lysosensor blue (bottom, Ex 405 nm) in serum-free medium for 30-min incubation. Scale bar: 20 µm.
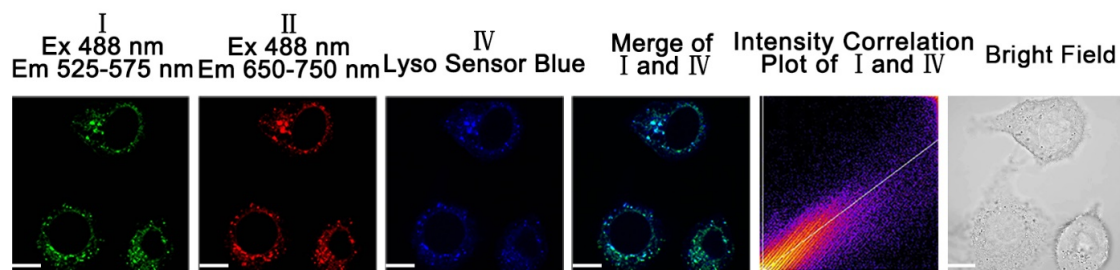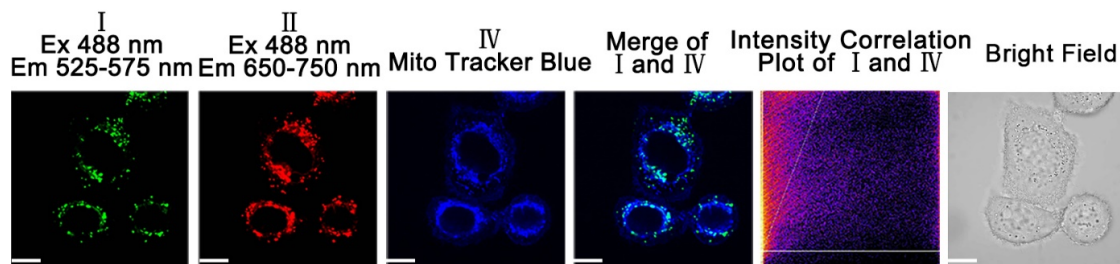
Figure 5.10. Fluorescence imaging of HeLa cells with 5 µM of probe A, 10 µM Mito Tracker blue (top, Ex 405 nm), or 10 µM Lysosensor blue (bottom, Ex 405 nm) in serum-free medium for 2-hour incubation. Scale bar: 20 µm.

We also used rapamycin to induce mitophagy in normal culture medium and determined if probes **A** and **B** can be used to track mitophagy induced by this drug. Fluorescence images display significant increases in the cellular near-infrared fluorescence and decreases in the cellular visible fluorescence with substantial color changes from blue to green. These results indicate that probe **A** is located within the autolysosomes formed by fusing damaged mitochondria with lysosomes during mitophagy, due to the rapamycin treatment (Figures 5.11 and S127). As a consequence of this localization, the probe effectively detects mitochondrial acidification during mitophagy caused either by nutrient starvation or drug treatment with rapamycin (Figures 5.8-5.11).
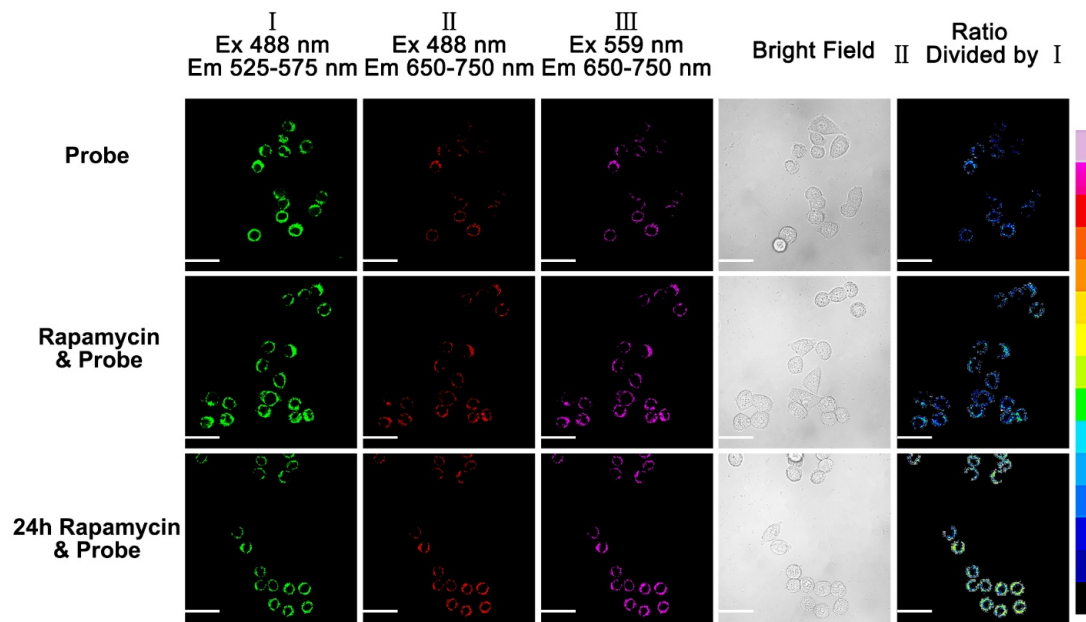
Figure 5.11. Fluorescence images of HeLa cells incubated with 3.5 μM of probe **A** and rapamycin (100 nM) in normal culture medium after a 1h-incubation time with probe **A** under excitation of 488 nm and 559 nm with scale bars of 50 μm. Images from top to bottom: probe **A** only (top), probe **A** and rapamycin (middle), cells incubated with rapamycin for 24 h and then further incubated with probe **A** for one hour (bottom).

5.3.8 Visualization of Intracellular pH Changes.

We further tested if the probes can detect intracellular pH changes ratiometrically in mitochondria by incubating HeLa cells with probe **A** or **B**, using buffers with different pH values in the presence of 5 μM K$^+$/H$^+$ ionophore nigericin, which is used to achieve an equilibration between the pH of the external buffer and the intra-cellular pH value.[88, 91, 93, 95, 198, 199] A gradual decrease of the intracellular pH from 10.0 to 3.0 lead to a visible fluorescence decrease and a corresponding near-infrared fluorescence increase at 488 nm excitation for probe **A**, Figures 5.12, S128-S132. The merged cellular images of the visible and near-infrared fluorescence of probe **A** in the third column undergoes significant changes from a deep green to brown and then finally a deep red upon cellular pH changes from 10.0 to 3.0. Similar fluorescence ratiometric responses of probe **B** under these conditions were observed (Figure S131 and S132). We further conducted colocalization experiments of probe **A** and **B** with Mito Tracker blue or Lysosensor blue with intracellular pH 5.0 and 6.0 (Figures 5.13, S133-S139). The Pearson correlation coefficients of probe **B** (channels I, II, and III) with Mito Tracker blue (channel IV) in HeLa cells are high at 0.97, 0.96, and 0.98 after a 2-h incubation of probe **B** and Mito Tracker blue with HeLa cells in pH 6.0 normal medium, containing FBS and 5 μM nigericin, respectively (Figure 5.13). This is clearly depicted in the overlapped cellular images and the scatter plots, indicating that probe **B** stays in mitochondria in live cells after a 2-h probe incubation with HeLa cells in pH 6.0 normal medium containing 5 μM nigericin. Similar high Pearson correlation coefficients of probe **A** with Mito Tracker blue were also obtained under pH 5.0 or 6.0 (Figures S133 and S135). These results demonstrate that probes **A** and **B** can effectively detect pH changes in mitochondria ratiometrically (Figures 12, 13, S133-S139) and that

they can be utilized for the visualization of mitophagy processes induced by cell starvation (Figure 5.7).

Reactive oxygen species (ROS) come from mitochondria inside most mammalian cells, are produced due to mitochondrial damage in a variety of pathologies and play a very important role in redox signaling from mitochondria to the rest of the cell. We also used probe **A** to detect pH fluctuations in live cells under oxidative stress. Hydrogen peroxide treatment of HeLa cells results in a cellular fluorescence decrease in the near-infrared channel and a fluorescence increase in the visible channel over time, indicating that pH increases over time in mitochondria due to the H_2O_2 treatment (Figure S140), which is consistent with what was reported in the literature.[180]

Additionally, we conducted photobleaching studies in HeLa cells by confocal fluorescence microscopy. Cellular visible and near-infrared fluorescence intensities decrease slightly during a 240-second photobleaching experiment, as detected by confocal fluorescence microscopy (Figures S141-S144), indicating that the probes show photostability in live cells and this confirms our *in vitro* results (Figures S85-S88).

5.3.9 Fluorescence imaging of *D. melanogaster* first-instar larvae.

For the first time, we demonstrated the feasibility of imaging pH changes in the model organism *D. melanogaster*. We incubated first-instar larvae of *D. melanogaster* with probe **A** in buffer solutions of three different pH values for 2 hours, after which we conducted fluorescent confocal microscopy (Figure 5.13). The larvae incubated at pH 9.5 containing probe **A** showed strong visible fluorescence in the green channel and extremely weak near-

infrared fluorescence in channels II and III under excitation at 488 nm and 559 nm. A decrease of the pH to 7.4 and then to 5.0 lead to a strong decrease of the visible fluorescence of the gut tissue in channel I and a considerable near-infrared fluorescence increase in channels II and III under the same excitation conditions (Figure 5.13), which is consistent with the fluorescence responses of probe **A** to pH changes in buffer solutions (Figure 5.1).
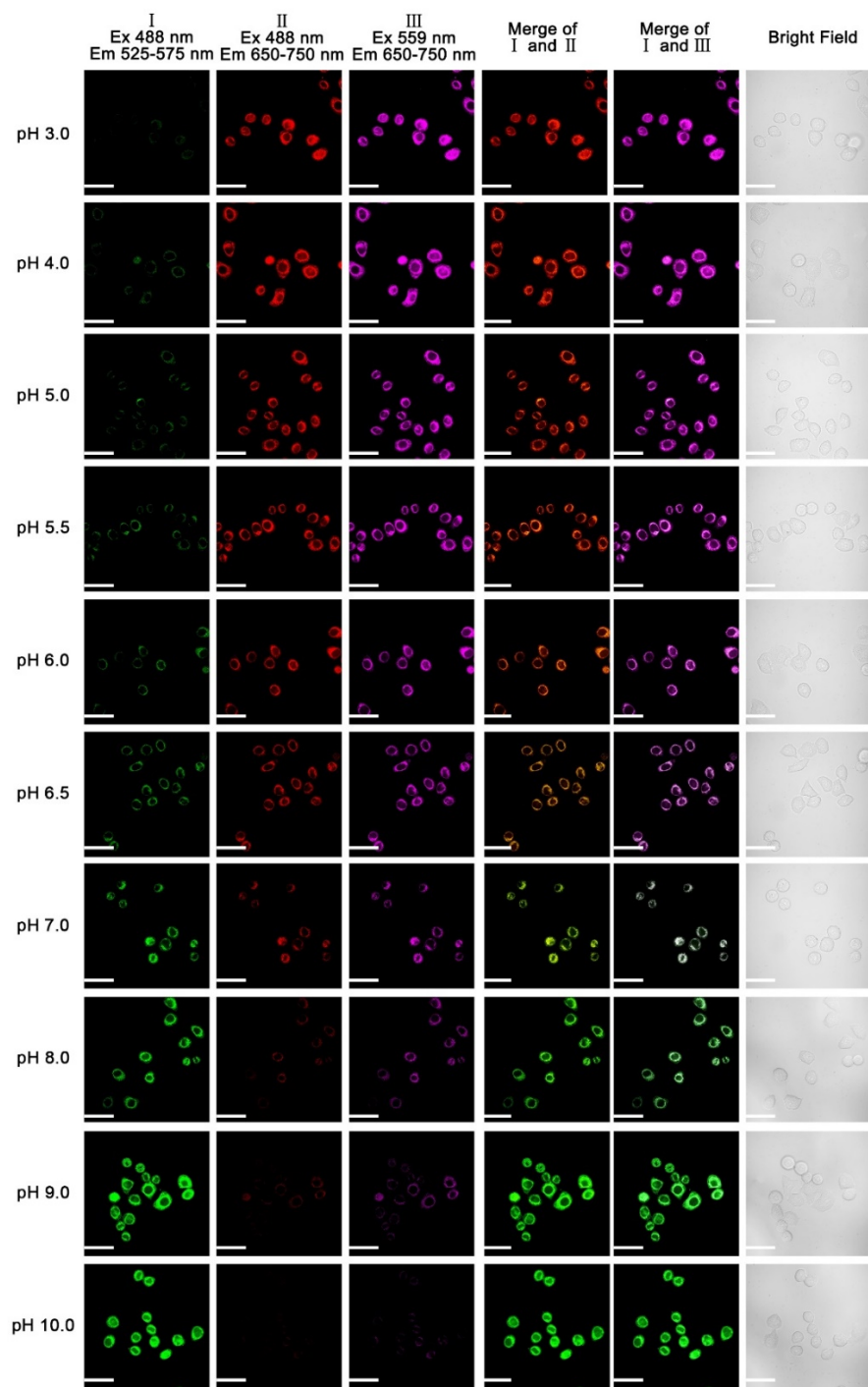
Figure 5.11. Fluorescence images of HeLa cells incubated with 10 μM of probe **A** in different pH buffers containing 5 μM nigericin. Scale bar: 50 μm.
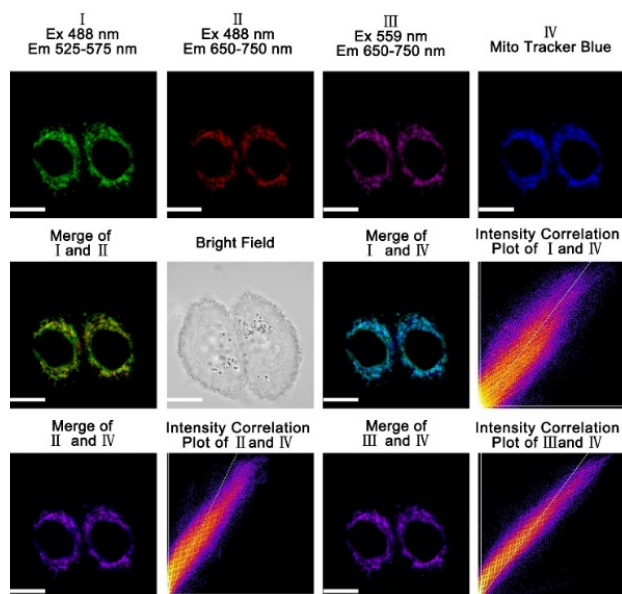
Figure 5.12. Fluorescence images of HeLa cells incubated with 5 µM of probe **B** in pH 6.0 buffer containing 5 µM nigericin and 10 µM Mito Tracker blue (Ex 405 nm). Scale bar: 10 µm. Pearson correlation coefficient between channel I and channel IV: 0.97. Pearson correlation coefficient between channel II and channel IV: 0.96. Pearson correlation coefficient between channel III and channel IV: 0.98.
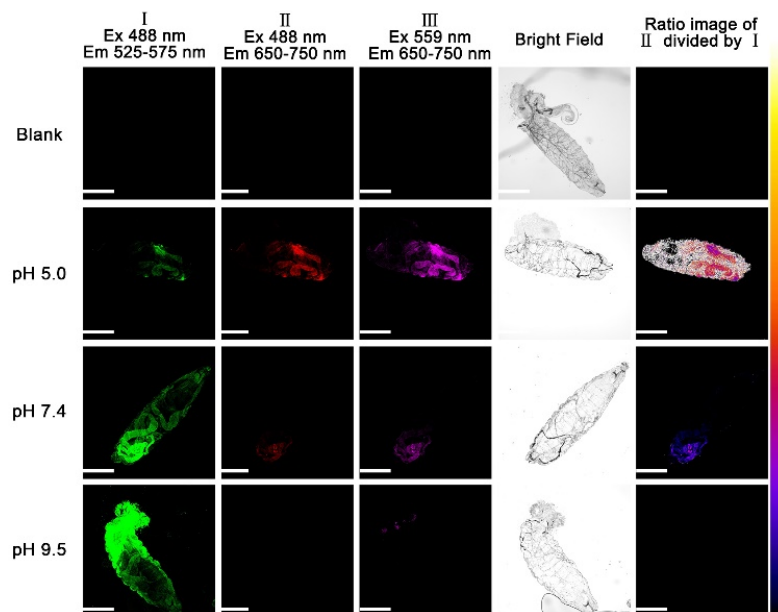
Figure 5.13. Fluorescence images of *D. melanogaster* first-instar larvae incubated with 10 µM probe **A** in different pH buffers for 2 hours. Scale bar: 200 µm.

5.4 Conclusion

Near-infrared ratiometric rhodol-based fluorescent probes have been developed by incorporating molecular spiropyran switches into traditional rhodol dyes for ratiometric sensing of pH changes in mitochondria and visualization of mitophagy processes induced by cell nutrient starvation and drug treatment. Probe **A** was also successfully used to image pH changes in *D. melanogaster* first-instar larvae for the first time based on a literature survey. The probes display quick fluorescence sensing responses to pH changes in near-infrared and visible channels and possess good selectivity, high sensitivity, low cytotoxicity, excellent cell permeability, and very useful ratiometric features to overcome systematic errors of intensity-based probes.

6 A FRET-based Near-infrared Fluorescent Probe for Ratiometric Detection of Cysteine in Mitochondria[202]

Shuai Xia,[a] Yibin Zhang,[a] Mingxi Fang,[a] Logan Mikesell,[a] Tessa E. Steenwinkel,[b] Shulin Wan,[a] Tyler Philips,[a] Rudy L. Luck,[a*] Thomas Werner,[b*] and Haiying Liu[a*]

[a.] Department of Chemistry, Michigan Technological University, Houghton, MI 49931, E-mail: rluck@mtu.edu; hyliu@mtu.edu

[b.] Department of Biological Sciences, Michigan Technological University, Houghton, MI 49931, E-mail: twerner@mtu.edu

6.1 Introduction

Biothiols, such as cysteine (Cys), homocysteine (Hcy), and glutathione (GSH) exert important roles in redox homeostasis, metabolism, protein synthesis, signal transduction, post-translational modification, and metabolism [203-207]. Biothiols deficiency is associated with different disorders such as liver damage, lethargy, neurotoxicity, slow growth, hematopoiesis, skin lesions, and neurodegenerative diseases, such as Alzheimer's and Parkinson's disease [206, 207]. Many fluorescent probes have been developed to detect biothiols [72, 204, 208-214]. Most of them are intensity-based probes and suffer from systematic errors caused by variations in probe concentration, radiation light fluctuations, and different functioning locations and environments within cells [72, 208-210]. Ratiometric fluorescent probes have been developed to overcome systematic errors by introducing built-in internal fluorophores and utilizing foster resonance energy transfer (FRET) or through-bond energy transfer (TBET) strategies [215, 216]. The near-infrared fluorophores take advantage of unique ratiometric and near-infrared imaging features such as deep-tissue penetration, low cellular and tissue fluorescence background, and reduction of probe photobleaching [215, 217]. However, ratiometric fluorescent probes for cysteine detection with near-infrared emissions are currently limited to a few examples [218, 219]. Herein, we detail a near-infrared fluorescent probe for ratiometric selective detection of Cys and Hcy over GSH in live cells by employing coumarin as a donor and near-infrared rhodamine as an acceptor with a piperazine-tethered spacer based on the FRET strategy. We chose coumarin and near-infrared rhodamine derivative because of their excellent optical properties including outstanding photostability, high absorption coefficients, and high fluorescence quantum yields.[220] Ratiometric fluorescence sensing of Cys and Hcy is achieved by

manipulating π-conjugation changes of the rhodamine acceptor with a phenyl thioester molecular switch in response to biothiols because the phenyl thioester rapidly binds to Cys and Hcy through a substitution reaction with the phenyl thioester, and a formation of spirolactam ring configurations (Scheme 1). In the absence of Cys or Hcy and when excited at 440 nm, probe **A** shows two well-defined fluorescence peaks with weak fluorescence of the coumarin donor, and strong fluorescence of the rhodamine acceptor, presumably because of highly efficient energy transfer from the coumarin donor to the rhodamine acceptor. Gradual addition of Cys results in a significant fluorescence decrease from the rhodamine acceptor and a corresponding fluorescence increase from the coumarin donor because the formation of the non-fluorescent spirolactam closed ring structure occurs on the rhodamine acceptor and the reaction with Cys results in fluorescence quenching of the rhodamine acceptor. This also effectively prevents energy transfer from the coumarin donor to the rhodamine acceptor. The probe displays less sensitive ratiometric fluorescence responses to Hcy and insignificant responses to glutathione (Scheme 6.1). The probe has been applied to determine cysteine concentration changes in HeLa cells, and Drosophila melanogaster larvae.
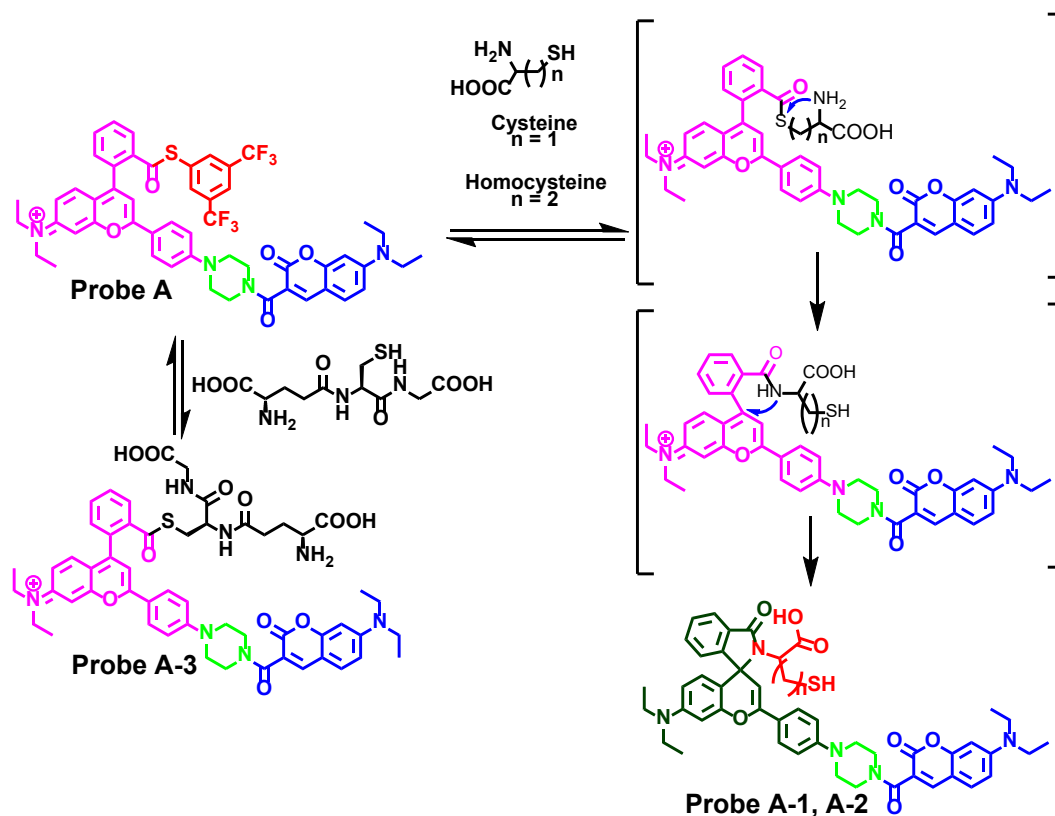
Scheme 6.1. Fluorescent probe **A** and its structural responses to biothiols

6.2 Results and Discussion

6.2.1 Synthesis

The synthetic routine for probe A is shown in Scheme 2. 7-(dethylamino)coumarin-3-carboxylic acid (**2**) was coordinated to 4′-piperazinoacetophenone (**1**) through an amide bond, affording compound **3**. A near-infared rhodamine derivative bearing coumarin donor (**5**) was prepared by condensation of compound 3 with 2-(4-diethylamino-2-hydroxybenzoyl)benzoic acid (4) in sulfuric acid at high temperature.[221, 222] Our approach effectively overcomes a challenging separation issue in preparing a highly polar near-infrared rhodamine derivative bearing a piperazine residue.[220] Probe **A** was prepared by introducing the biothiol-sensing switch of a phenyl thioester to the rhodamine acceptor by

coupling 3,5-bis(trifluoromethyl)benzenethiol (**6**) with dye intermediate (**5**). We chose dye

5 to develop ratiometric fluorescent probe **A** for cysteine because it has much greater

fluorescence quantum yield than those of other near-infrared coumarin hybrid dyes.[92]

Probe **A** was characterized by NMR and high-resolution mass spectrometries (Figures S1-

S5).
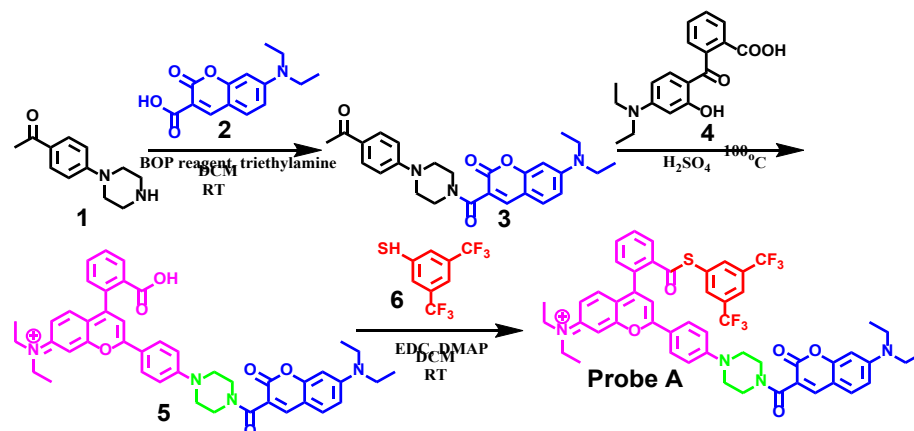
Scheme 6.2. Synthesis route to prepare probe **A**

6.2.2 Optical responses of Probe A to cysteine

Probe **A** shows two strong well-defined absorption peaks at 420.7 nm and 606.9 nm,

corresponding to the absorption wavelengths of the coumarin donor and the rhodamine

acceptor, respectively (Figure 6.1a). Gradual addition of Cys leads to a gradual decrease in

the rhodamine acceptor absorbance and almost no change in coumarin donor absorbance

because of the formation of a closed spirolactam ring on the rhodamine acceptor, which

significantly reduces rhodamine π-conjugation. The probe displays two well-defined

fluorescence peaks with strong fluorescence for the rhodamine acceptor at 645 nm and a

weak fluorescence peak for the coumarin donor at 467 nm in the absence of Cys (Figure

6.1b) because of the high-efficiency energy transfer from the coumarin donor to the

rhodamine acceptor. The energy transfer efficiency of the coumarin donor to the rhodamine acceptor was calculated to be 95.1%. The probe shows a large pseudo-Stokes shift of 224 nm, i.e., the difference between the coumarin absorption and the rhodamine fluorescence peaks. Upon gradual addition of Cys, the probe shows a gradual decrease in rhodamine acceptor fluorescence and a concomitant gradual increase in coumarin donor fluorescence. This sensitive ratiometric change in the fluorescence response of the probe to Cys arises from a suppressed energy transfer from the coumarin donor to the rhodamine acceptor due to the formation of a closed spirolactam ring on the rhodamine acceptor, after it reacts with Cys (Scheme 6.1). The fluorescence intensity ratios of rhodamine to coumarin increase from 0.235 to 4.237 with a final enhancement factor of 18-fold upon Cys addition. The probe shows similar ratiometric responses to Hcy with much smaller changes in absorbance and a fluorescence decrease of the rhodamine acceptor, as well as a fluorescence increase of the coumarin donor (Figure S6). This observation was further confirmed by the fluorescence spectra of the probe in the absence and presence of Cys and Hcy under rhodamine acceptor excitation at 560 nm (Figures S7, S8). Probe **A** also exhibits insignificant responses to GSH because the reaction of the probe with GSH maintains the same thioester bond without changing the π-conjugation of the rhodamine acceptor to affect energy transfer efficiency from the coumarin donor to the rhodamine acceptor. The reaction products of the probe with Cys, Hcy, and GSH were confirmed by mass spectrometry (Figures S9-S11).
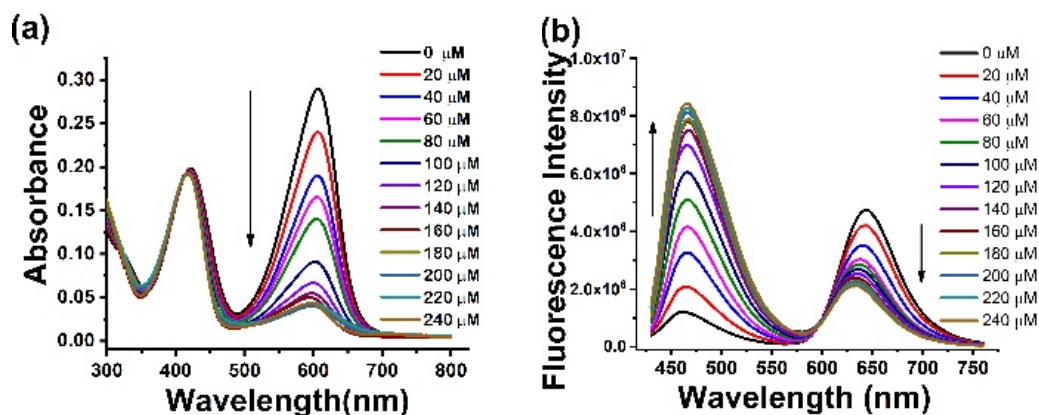
Figure 6.1. (a) Absorption and (b) fluorescence spectra of 5 μM probe **A** in the absence and presence of various concentrations of Cys in pH 7.4 buffer containing 30% ethanol at excitation of 440 nm.

6.2.3 Theoretical calculations

We also examined the electronic properties of probe **A** and its reaction products with Cys and GSH with theoretical calculations conducted, using an exchange correlation (xc) functional DFT/TPSSH [150] and with atoms defined at the split-valence triple-ζ plus polarization function (TZVP[223]) implemented, using the Gaussian 16[224] suite of programs. Interestingly, reasonable agreement between theoretical and experimental data were obtained; for probe A, calculated (expt.) at 552 (607), 393 (421); A-1 393 (421); A-3 563, 393 nm. These values are within the expected error range of 0.20–0.25 eV.[99] Full details are available in the Supporting Information.(Fig. S12-S23) The isolated nature of the transitions can be observed in difference density illustrations exemplified in Figure 2. In probe A, the ES2 transition at 552 nm has a 95.9% contribution from the rhodamine moiety, and at 393 nm, i.e., ES8, 88.4% are contributed from a transition localized on the coumarin sector. A-1 has only one transition with a significant oscillator strength, and this was localized on the coumarin moiety with a 96.4% contribution. For A-3, ES2 (Figure 6.2) is

localized on the rhodamine moiety at 95.2%, but for ES10, 17.3% are due to a transition from the coumarin to the rhodamine moiety, while 5.2% are from an LCAO on rhodamine to coumarin, and 74.4% are localized solely on the coumarin. The results of the calculations confirm that for probe A, excitation at 440 nm (Figure 6.1), leading to fluorescence from the rhodamine moiety, is not occurring as a consequence of orbital transmission.
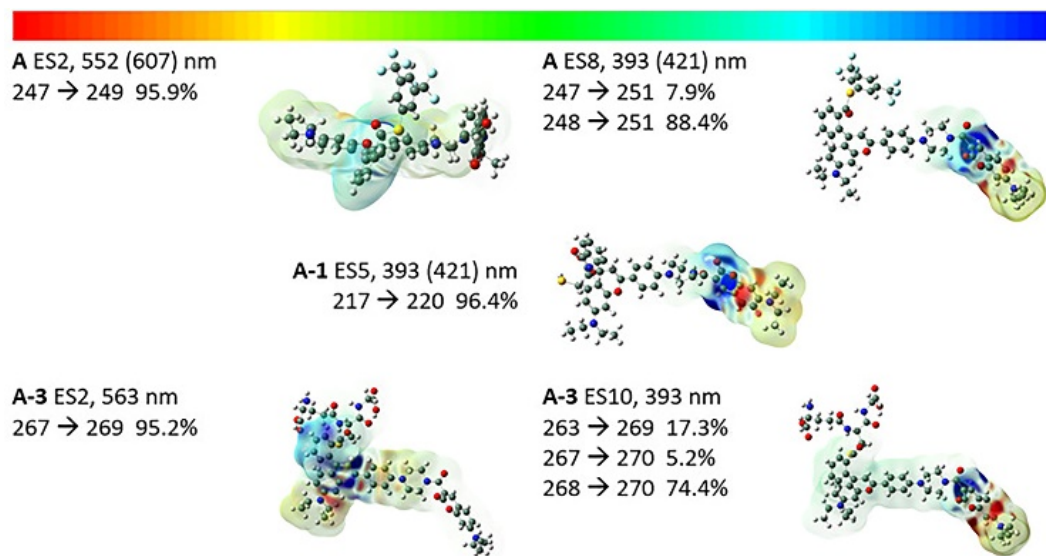
Figure 6.2. Current density difference illustrations as iso-surfaces of the probes A, A-1, and A-3, as indicated for the excited states (ES) and the calculated (and experimental) wavelengths. The composition of specific ES, together with percentage contributions, are indicated. Drawings of the numbered LCAOs are available in the Supporting Information. Red areas indicate values for the different density of $-5.000e^{-5}$ and blue are for $5.000e^{-5}$, see image scale on top of the illustration.

6.2.4 Kinetic and thermodynamic study

Probe **A** responds quickly to Cys and Hcy as the fluorescence ratio values of the rhodamine acceptor to the coumarin donor plateaus within 20 minutes in the presence of 30

equivalents of Cys or Hcy (Figure 6.3a). The pseudo-first-order rate constants (k) for Cys and Hcy were determined as 0.08572 ± 0.00622 min^{-1} and 0.07364 ± 0.00630 min^{-1}, respectively (Figure S24). The reaction rate constant for Hcy is lower than that of Cys due to that the facile five-membered ring Cys attack intermediate is more favored than intramolecular attack by amino group through a six-membered ring compound for Hcy. The fluorescence ratio values of the rhodamine acceptor to the coumarin donor show a linear relationship with Cys concentrations from 25 μM to 150 μM at 20 min, with a detection limit of 1.5×10^{-6} M (Figure 6.3b, Figure S25b). Furthermore, the detection limit of Hcy is calculated to be 1.3×10^{-5} M (Figure S25a) which is much higher than that of Cys, indicating that probe **A** could serve as the ratiometric fluorescent tool to selectively detect Cys over other biothiols.
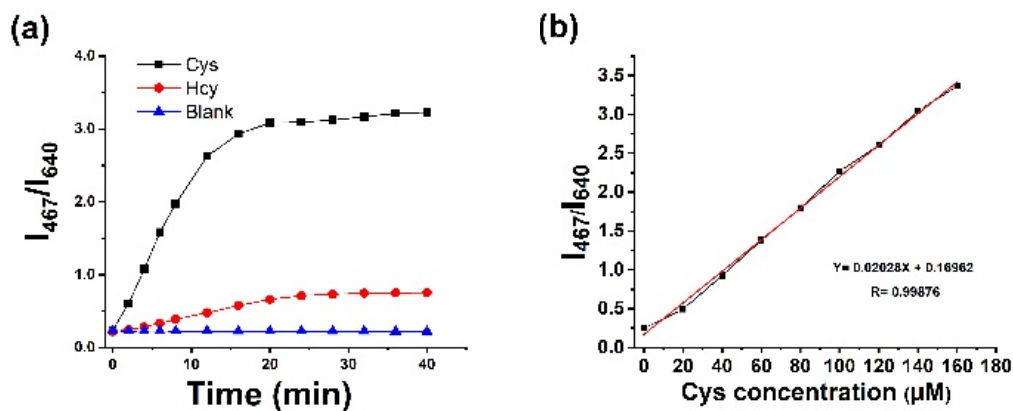
Figure 3. (a) Reaction time responses of 5 μM probe **A** to 30 equiv. Cys and Hcy in pH 7.4 buffers containing 30% ethanol at excitation of 440 nm. (b) Linear relationship of the fluorescence intensity ratio of the rhodamine acceptor to the coumarin donor fluorescence to Cys concentration in pH 7.4 buffers containing 30% ethanol at excitation of 440 nm for 20 min.

6.2.5 Selectivity, photostability and pH effects

We also investigated probe selectivity to Cys or Hcy in the presence of different biological species, such as amino acids (Figure S26), anions (Figure S27), and cations (Figure S28). The results suggest that the probe displays high selectivity to Cys and Hcy over other species. We further evaluated the photostability of the fluorescent probe **A** in a time-dependent fluorescence experiment. Within 2 h of illumination at 400 nm, the fluorescence ratio between the coumarin donor and rhodamine acceptor exhibited a very small change with less than 8% of decrease compared to the initial intensity (Figure S29). At 2 h excitation at 560 nm, the fluorescent intensity of rhodamine acceptor showed even less than 5% of decrease (Figure S30). Thus, the probe **A** is highly resistant to photo-bleaching and with good photostability. We also studied the effect of pH on cysteine sensing in physiological ranges. The results presented in Figures S31 and S32 indicate that there are small and insignificant changes in the probe fluorescence, and more important, fluorescence responses of the probe to cysteine are not significantly affected by pH from 5.0 to 8.5. Therefore, probe **A** accurately senses cysteine within this pH range from 5.0 to 8.5.

6.2.6 Cell viability and confocal imaging for HeLa cells

We further investigated probe cytotoxicity to HeLa cells by standard MTT assays. The cell viability is more than 90% at the treatment of 50 μM of probe **A** (Figure S33), affirming that the probe **A** displays low cytotoxicity toward HeLa cells. As probe **A** is positively charged, we suspected that it may target mitochondria through electrostatic interactions with negative electric potentials across the inner mitochondrial membranes. In order to test

this hypothesis, we carried out intracellular colocalization experiments by co-staining HeLa cells with the probe and a mitochondria-targeting cyanine dye (IR-780). Strong cellular fluorescence of the probe's rhodamine acceptor was observed under 405 nm and 559 nm excitation, and weak fluorescence of the probe's coumarin donor was observed under 405 nm excitation (Figure 6.4). The weak fluorescence of the donor is due to the low intracellular Cys concentration in live cells. The Pearson colocalization coefficient of the probe with a cyanine dye (IR-780) is high at 0.94, indicating that the probe **A** stays in mitochondria with the cyanine dye IR-780.
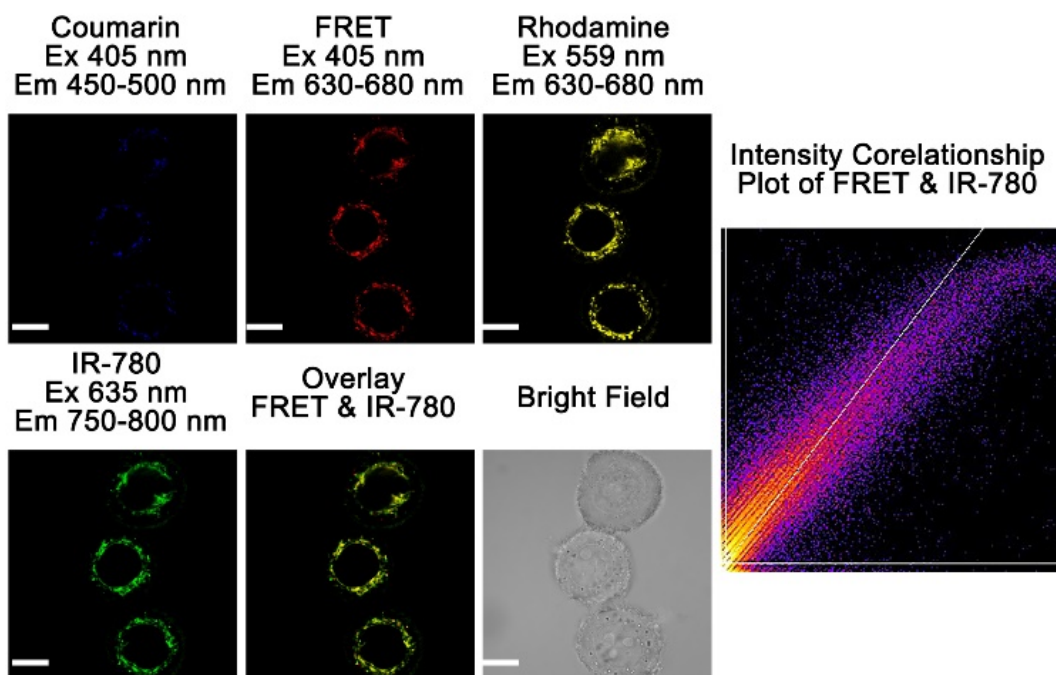
Figure 6.4. Fluorescence imaging of HeLa cells with 5 µM probe **A** under 405 nm or 559 nm excitation, and 10 µM cyanine dye (IR-780) under 635 nm excitation. Scale bar: 20 µm.

We investigated whether the probe can detect Cys in live cells by using 10 μM of the probe to incubate with HeLa cells at 37 °C for 30 min. Both blue fluorescence from the coumarin donor and near-infrared fluorescence (red and yellow channels) were observed (Figure 6.5). However, when HeLa cells were incubated with different concentrations of Cys from 100 μM to 500 μM under the coexistence of endogenous Cys, followed by further incubation of the cells with probe **A**, cellular blue fluorescence of the coumarin donor significantly increases proportionally with increased Cys concentration, while the near-infrared fluorescence from the rhodamine acceptor decreases significantly. In addition, overlapped images of fluorescence in blue and red channels undergo significant color changes from pink to blue, when the Cys concentration is increased from 100 μM to 500 μM. Ratiometric images of the probe (where coumarin fluorescence is divided by rhodamine fluorescence) under considerable color changes from bluish red to white before and after cysteine treatment (Figure S34). These suggest that exogenous cysteine transported to mitochondria further reacts with the probe in mitochondria resulting in a closed spirolactam ring structure in the rhodamine acceptor, leading to increases of coumarin fluorescence and decreases of rhodamine fluorescence under cysteine treatment. The cellular fluorescence responses of the probe to Cys are similar to the fluorescence spectra responses in aqueous solution (Figure 6.1). We also conducted a control experiment by pre-treating HeLa cells with 1.0 mM NEM (*N*-ethylmaleimide) to remove intracellular endogenous biothiols, before the cells were incubated with the probe. A slight decrease of blue fluorescence of the probe's coumarin donor was observed with a significant increase of near-infrared fluorescence of the probe's rhodamine acceptor in the red and yellow channels. This indicates that NEM treatment causes a decrease of biothiols concentration due to an addition reaction of NEM

with a mercapto group on the endogenous biothiols (Figure 6.5). We also investigated whether probe **A** could detect Hcy in HeLa cells. Similar results to cysteine sensing in HeLa cells were observed (Figure S34) which is in agreement with fluorescence responses of the probe to Hcy in buffer solutions (Figure 6.3).
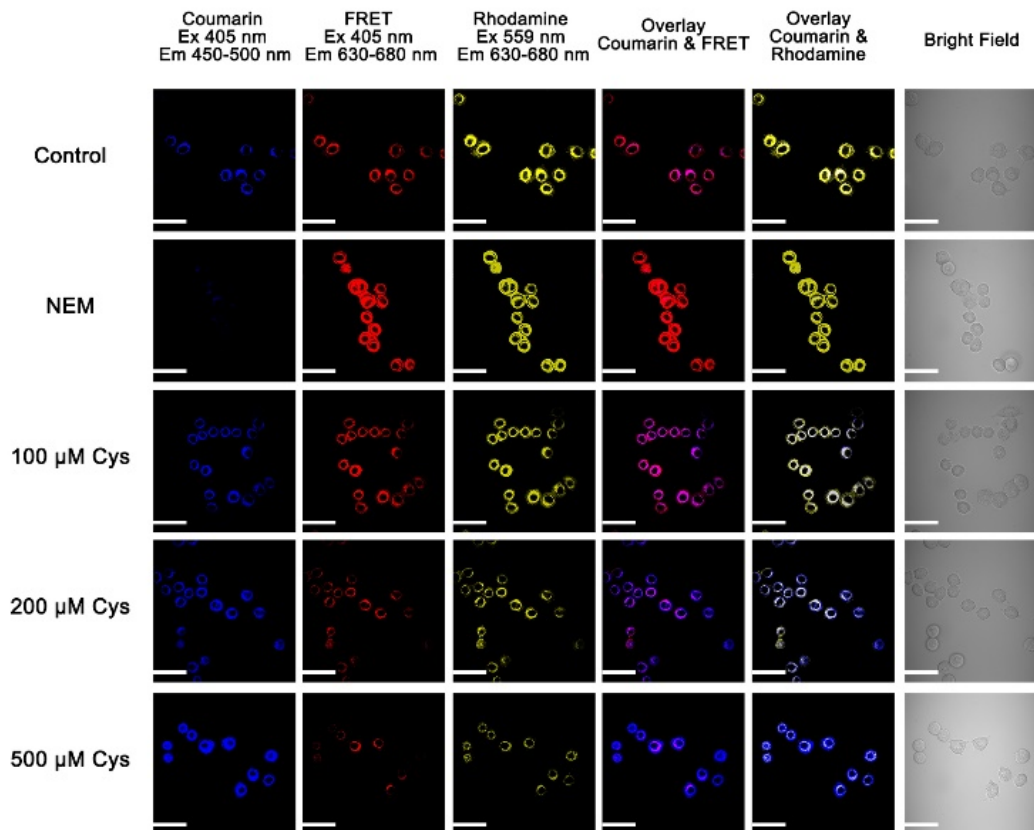
Figure 6.5. Fluorescence imaging of HeLa cells with 10 µM probe **A** in the absence and presence of different concentrations of Cys or under NEM treatment. Scale bar: 50 µm.

We further studied concentration changes of Cys on HeLa cells that were oxidatively-stress-induced by applying different concentrations of hydrogen peroxide (Figure 6.6). Gradual increases of hydrogen peroxide from 20 µM to 100 µM lead to a significant decrease of cellular blue fluorescence from the coumarin donor, and a considerable

increase of cellular near-infrared fluorescence of the rhodamine acceptor in the red and yellow channels under 405 nm and 559 nm excitation. Additionally, ratiometric images of the blue channel over the red channel also undergo significant color changes from bluish pink to an extremely weak blue. This is due to decreases in cysteine concentration under oxidative stress, when the hydrogen peroxide concentration is increased from 20 μM to 100 μM. Hydrogen peroxide converts the mercapto group on cysteine into a disulfide group through oxidation, resulting in concentration decreases of endogenous cysteine in live cells. As a result, coumarin fluorescence decreases in the blue channel and near-infrared rhodamine fluorescence in the red channel increases under oxidative stress with hydrogen peroxide treatment (Figure 6.6).
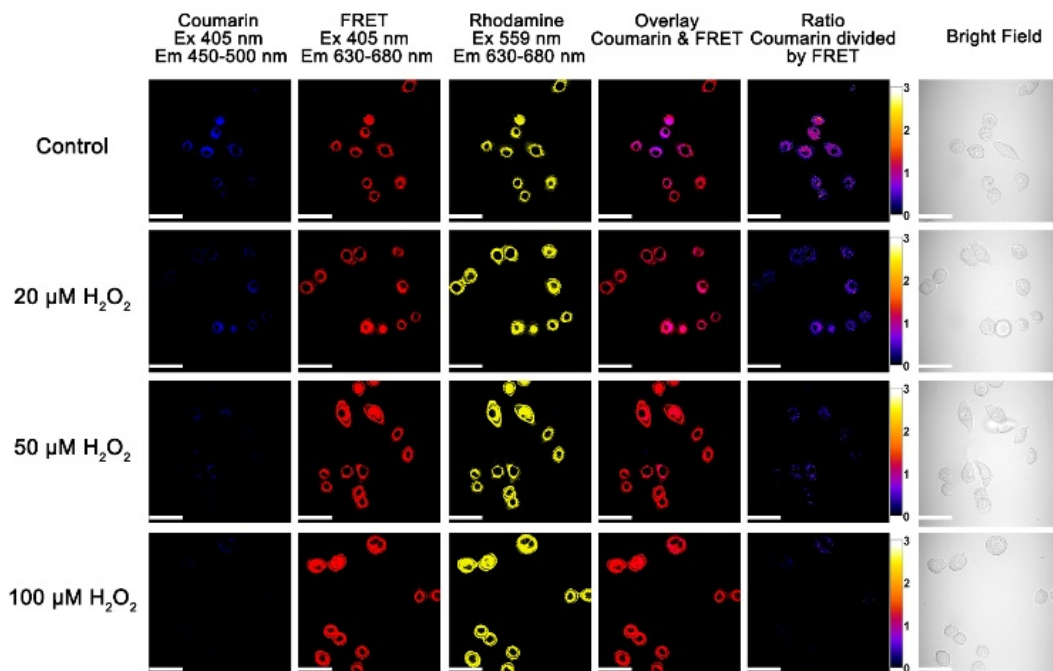
Figure 6.6. Fluorescence imaging of HeLa cells with 10 μM probe **A** before and after hydrogen peroxide treatment. Scale bar: 50 μm. Ratiometric images were obtained by using the ImageJ.

The endogenous Cys concentration decreases under oxidative stress in the presence of nitric oxide can effectively oxidize biothiols. Moreover, we studied intracellular Cys concentration changes under the stimulus of lipopolysaccharide (LPS), as it was reported that lipopolysaccharide treatment can generate nitric oxide and create oxidative stress in live cells to oxidize biothiols [225]. LPS treatment of HeLa cells results in a decrease in coumarin fluorescence and an increase rhodamine fluorescence due to a decrease in endogenous cysteine concentration due to cysteine oxidation by nitric oxide. Ratiometric images of the blue channel over the red channel undergo dramatic color changes from reddish blue to weak blue before and after LPS treatment (Figure 6.7). These results convincingly demonstrate that the probe possesses high cell permeability and is capable of detecting intracellular Cys changes ratiometrically with visible and near-infrared channels (Figures. 6.5-6.7).
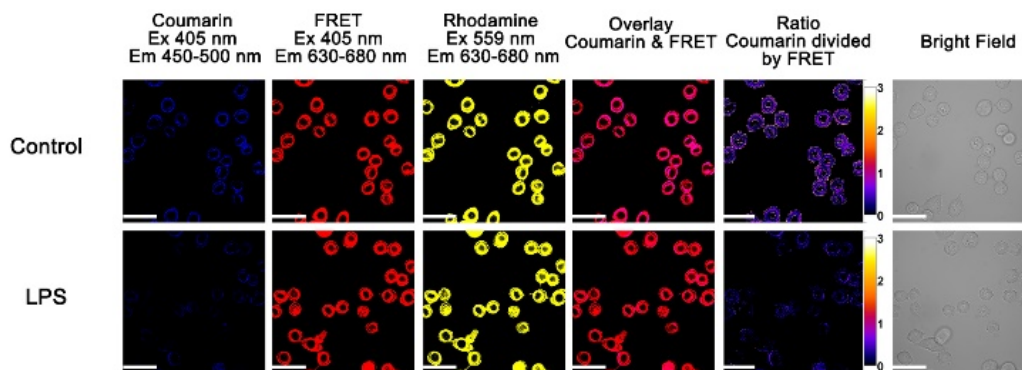
Figure 6.7. Fluorescence imaging of HeLa cells with 10 µM probe **A** before and after lipopolysaccharide (LPS) treatment with scale bars of 50 µm. Ratiometric images were obtained by using the ImageJ.

6.2.7 *In vivo* experiments with *Drosophila melanogaster* first-instar larvae

Finally, we conducted fluorescence imaging of live *Drosophila melanogaster* first-instar larvae in the absence and presence of different concentrations of cysteine (Figure 6.8). *Drosophila melanogaster* does not have a fluorescence background and it possesses a very low cysteine concentration since probe **A** reveals very weak fluorescence from the coumarin donor and highly intense fluorescence from the rhodamine acceptor. The probe locates in the epidermis and tracheae (Figure 6.8). However, gradual increases of incubation Cys concentrations with the larvae result in increases of coumarin fluorescence and decreases of the rhodamine acceptor fluorescence because intake cysteine into the larvae further reacted with the probe resulting in a closed non-fluorescent spirolactam ring of the rhodamine acceptor, preventing effective FRET from coumarin donor to the rhodamine acceptor (Figure 8). The probe coumarin fluorescence in blue channel decreases and rhodamine near-infrared fluorescence in red and yellow channel increases after the larvae was first incubated with cysteine and the probe, and then further treated with hydrogen peroxide (Figure S37). This suggests that hydrogen peroxide treatment also reduces cysteine concentration in the larvae. These results indicate that probe **A** can be successfully applied to live tissues in order to detect Cys concentrations.
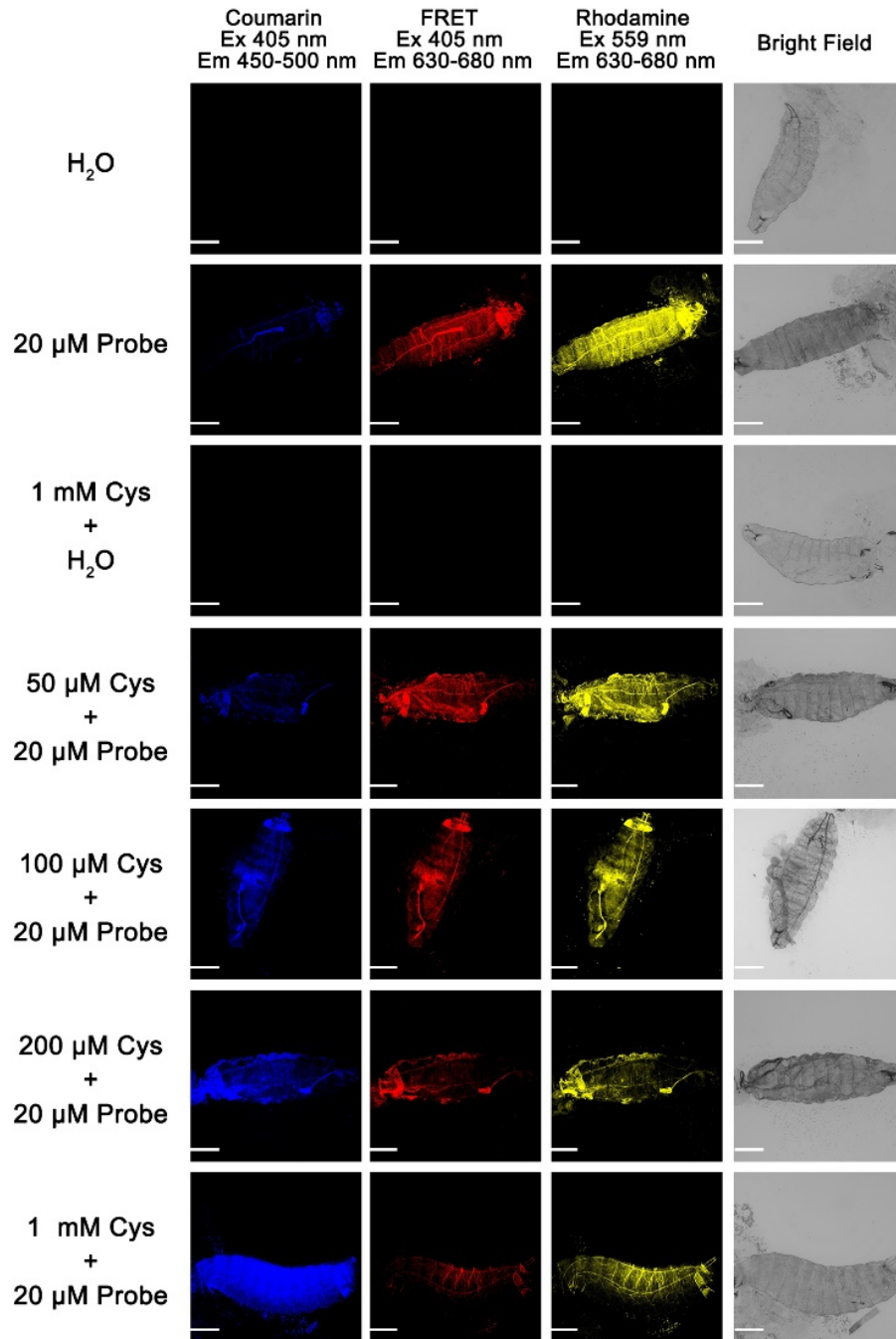
Figure 6.8. Fluorescence imaging of *Drosophila melanogaster* first-instar larvae with 20 µM probe **A** in the absence and presence of different concentrations of cysteine. Scale bar: 200 µm

6.3 Conclusions

We have developed a fluorescent probe **A** based on coumarin as a donor and near-infrared rhodamine acceptor for the sensitive ratiometric Cys detection. The probe offers ratiometric detection of Cys concentration and fluctuation in live cells with a self-calibration capability under oxidative stress through hydrogen peroxide and LPS treatment and can be utilized for the visualization of cysteine changes in *Drosophila melanogaster* larvae in the visible and near-infrared channels.

6.4 Experimental Section

Instruments and chemicals: A 400 MHz Inova NMR spectrometer was employed to record ^{1}H NMR spectra at 400 MHz and ^{13}C NMR spectra at 100 MHz. Chemical shifts (δ) of intermediates and probes were determined by using internal standards in ppm from solvent residual peaks (^{1}H: δ 7.26 for CDCl$_3$, δ 2.50 for DMSO-d$_6$; ^{13}C: δ 77.3 for CDCl$_3$). High-resolution mass spectra were recorded on an electrospray ionization mass spectrometer. Absorption spectra were obtained using a Perkin-Elmer Lambda 35 UV/VIS spectrometer and conventional fluorescence spectra were obtained using a Jobin Yvon Fluoromax-4 spectrofluorometer. IR spectra were obtained using a Perkin Elmer FT-IR Spectrometer. The MTT assay was performed on a BioTek ELx800 absorbance microplate reader. An Olympus IX81 inverted microscope was used for cellular imaging. All reagents and solvents were purchased from commercial source and used without further purification.

Optical measurement method: The UV-vis absorption spectra of probe **A** in the presence of thiols, for the first-order kinetic plot and to establish selectivity, photostability and linear

ratio relationship measurements were obtained in the range 300 to 800 nm with increments of 1 nm. The corresponding fluorescence spectra were collected at the excitation wavelength of either 400 nm for donor or 560 nm for acceptor excitation. The concentration of the probe in each sample was 5 μM. Cresyl violet (Φ_f = 0.56 in EtOH) as a fluorescence standard was used as the reference standard to determine the fluorescence quantum yields of probe **A** in ethanol and buffer solutions. Quinine sulfate (Φ_f = 0.546 in 1N H_2SO_4) as a standard was used as the reference standard to determine the fluorescence quantum yield of probe **A** after reaction with thiols. All samples and references were freshly prepared under similar conditions. The fluorescence quantum yields were calculated using the following equation:

$$\Phi_X = \Phi_{st}(Grad_X/Grad_{st})(\eta_X^2/\eta_{st}^2)$$

Where the subscripts '*st*' and '*X*' stand for standard and test, respectively, Φ is the fluorescence quantum yield, "*Grad*" means the gradient from the plot of integrated fluorescence intensity versus absorbance and η is the refractive index of the solvent.

Cell culture and MTT cytotoxicity assay: HeLa cells were cultured in Dulbecco's Modified Eagle's medium (DMEM, Gibco) containing 10% fetal bovine serum (FBS, Fisher Scientific) at 37°C in the humid atmosphere containing 5% CO_2. HeLa cells were subcultured at 80% confluence using 0.25% trypsin (w/v) (Fisher Scientific) every other day. A standard MTT assay was applied to determine the cytotoxicity of probe **A**. In detail, the cells were seeded in 96-well plates at an initial density of 4000 cells per well, with 100 μL DMEM medium per well. After seeding for 24 hours on the 96 well plate, the medium

was replaced by different concentrations of probe **A** (0, 5, 10, 15, 25, 50 μM solutions in fresh culture medium, 100 μL/well) for 48 h. After that, the cells were incubated for 4 hours with the tetrazolium salt dye (3- (4,5-dimethylthiazol-2-yl)-2,5-diphenyl tetrazolium enbromide) at a final concentration of 500 μg/mL whereupon metabolically active cells reduced the dye to the water insoluble purple formazan dye. The dark purple crystals were dissolved with DMSO and the cell viability rate determined by measuring absorbance at 490 nm (BioTek ELx800). The cell viability rate was calculated by $V_{rate} = (A - A_B)/(A_C - A_B) \times 100\%$, where A is the absorbance of the experimental group, A_C is the absorbance of the control group (cell medium used as control) and A_B is the absorbance of the blank group (no cells). Data were illustrated graphically, with each data point calculated from an average of three wells.

Cell confocal microscopy imaging: Cells were seeded in confocal glass bottom dishes with 10^5 cells per dish and cultured for 24 h. Probe **A** was added to each dish and cultured for 30 minutes. Cells were then washed with PBS (pH 7.4) twice, and 1 mL of PBS was then added before imaging. The fluorescence of probe **A** was determined based on excitation with a 405 nm or 559 nm laser with emission spectra collected between 450−500 or 630−680 nm respectively. The fluorescence of cyanine dye IR-780 channel was determined under 635 nm excitation and its emission collected between 750 and 800 nm. A confocal fluorescence microscope (Olympus IX 81) was used to take images of the HeLa cell and an Olympus FV10-ASW 3.1 viewer, Image *J* and Image Pro 6 were used to process the image data.

In vivo **experiments with *Drosophila melanogaster* first-instar larvae:** In order to test the probe in *Drosophila melanogaster*, we used a nine-well glass viewing dish. We treated the larvae in four different ways: 1) larvae were submerged in 500 µL of distilled water for four hours and washed three times in 500 µL of distilled water for the negative control. 2) Larvae were incubated in 20 µM probe for two hours and washed three times with 500 µL of distilled water. 3) larvae were submerged in 500 µL of 1 mM cysteine for two hours, washed three times in 500 µL of distilled water, and incubated for an additional two hours in distilled water. 4) larvae were submerged in 500 µL of 50 µM, 100 µM, 200 µM and 1mM cysteine for two hours, respectively, washed three times in 500 µL of distilled water, incubated for an additional two hours in 20 µM probe, and then washed three times in 500 µL of distilled water. For each sample, 10 freshly hatched first-instar larvae were used. After the incubation, the larvae were transferred with water onto a microscope slide and then covered with a cover slip. The larvae were then immediately analyzed by confocal microscopy (Olympus IX 81). The confocal microscopy conditions of the channels were identical to those utilized for the HeLa cells images.

Synthesis of 3-(4-(4-acetylphenyl)piperazine-1-carbonyl)-7-(diethylamino)-2*H*-chromen-2-one (Compound 3): A mixture of 1-(4-(piperazin-1-yl)phenyl)ethan-1-one (312 mg, 3 mmol), 7-(diethylamino)-2-oxo-2*H*-chromene-3-carboxylic acid (861 mg, 3.3 mmol), BOP reagent (1.46 g, 3.3 mmol) and trimethylamine (1 mL) in 20 mL anhydrous dichloromethane was stirred for 8 hours at room temperature, see Scheme 2. The mixture was then washed by water and then brine, dried with anhydrous Na_2SO_4, filtered and evaporated under reduced pressure. The resulting residue was purified by flash column

chromatography under gradient elution with hexanes/ethyl acetate (1:1) to yield compound **3** as a yellow solid. ^{1}HNMR (300 MHz, chloroform-*d*) δ 7.89 – 7.78 (m, 3H), 7.27 (d, *J* = 6.7 Hz, 1H), 6.83 (d, *J* = 6.8 Hz, 2H), 6.56 (dd, *J* = 6.6, 1.8 Hz, 1H), 6.46 – 6.40 (m, 1H), 3.85 (s, 2H), 3.52 (d, *J* = 12.2 Hz, 2H), 3.39 (q, *J* = 5.2 Hz, 8H), 2.48 (s, 3H), 1.21 – 1.13 (m, 6H).^{13}CNMR (75 MHz, chloroform-*d*) δ 196.63, 165.27, 159.32, 157.46, 153.89, 151.93, 145.81, 130.55, 128.19, 115.79, 113.99, 109.63, 107.89, 97.04, 47.23, 45.26, 42.25, 26.52, 12.75. LCMS(ESI): calculated for $C_{26}H_{29}N_3O_4[M]^+$ 447.2, found 448.1$[M+H]^+$

Synthesis of *N*-(4-(2-carboxyphenyl)-2-(4-(4-(7-(diethylamino)-2-oxo-2*H*-chromene-3-carbonyl)piperazin-1-yl)phenyl)-7*H*-chromen-7-ylidene)-N-ethylethanaminium (Compound 5): After compound **3** (447 mg, 1 mmol) and compound **4** (313 mg, 1 mmol) were added to methanesulfonic acid (6 mL), the reaction mixture stirred at 100°C for 6 hours under an argon atmosphere, see Scheme 2. The mixture was then added to 20 mL water and extracted with dichloromethane (3 × 100 mL). The organic layers were collected, dried over Na_2SO_4, and evaporated under reduced pressure. The mixture was purified by flash column chromatography dichloromethane/menthol (40:1) to yield compound **5** [226] as a blue solid.

Synthesis of fluorescent probe A: Compound **5** (75.3 mg, 0.1 mmol), compound **6** (26.9 mg, 0.11 mmol), EDC (21 mg, 0.11 mmol), DMAP (13.4 mg, 0.11 mmol) were each added to 20 mL anhydrous dichloromethane. This was stirred for 8 hours at room temperature. The mixture was then washed with water, then brine, dried with anhydrous Na_2SO_4, filtered and then evaporated to dryness under reduced pressure. The resulting residue was purified by flash column chromatography using a mixture of dichloromethane/methanol (30:1) as

eluent to give probe **A** as a blue solid, see Scheme 2. ^{1}H NMR (300 MHz, chloroform-*d*) δ 8.24 – 8.09 (m, 3H), 7.93 – 7.84 (m, 2H), 7.86 – 7.73 (m, 2H), 7.71 – 7.63 (m, 3H), 7.46 (s, 1H), 7.33 – 7.25 (m, 2H), 7.13 – 6.94 (m, 4H), 6.59 (dd, *J* = 6.7, 1.8 Hz, 1H), 6.46 (d, *J* = 2.4 Hz, 1H), 3.87 (s, 2H), 3.77 – 3.51 (m, 9H), 3.42 (q, *J* = 7.1 Hz, 4H), 1.31 (t, *J* = 5.0 Hz, 6H), 1.21 (t, *J* = 5.0 Hz, 6H).^{13}C NMR (75 MHz, chloroform-*d*) δ 188.70, 166.97, 165.53, 159.50, 159.38, 158.22, 157.54, 155.05, 154.92, 152.07, 145.99, 135.71, 134.88, 133.74, 132.87, 132.53, 131.61, 131.20, 130.25, 129.25, 127.62, 117.32, 115.51, 114.87, 114.39, 109.73, 109.49, 107.98, 97.14, 46.27, 45.28, 42.20, 12.82, 12.76. LCMS(ESI): calculated for $C_{52}H_{47}F_6N_4O_5S$ [M]$^+$953.31659, found 953.31607.

Summary and outlook of the dissertation

In summary for this dissertation, we chose the fluorescent probes as the approach for the efficient detection of intracellular pH and biothiols since they exhibited merits including outstanding selectivity, quick response, low limits of detection and good cell compatibility. The whole dissertation could be separated into three parts: A) Developing novel rhodamine dyes and incorporating pH switch to them as the fluorescent probe to detect intracellular pH fluctuation; B) Designing and synthesizing near-infrared and ratiometric fluorescent probes to monitor lysosomal or mitochondrial pH; C) Presenting a novel FRET-based near-infrared fluorescent probe to ratiometrically detect intracellular levels of biothiols and visualize cysteine concentration fluctuation *in vivo*.

In chapter two, our goal was to develop novel structure of rhodamine with improved spectroscopic properties. To reach this goal, we introduced an additional fused-ring amino residue into a rhodamine skeleton to afford two novel dyes. These two new rhodamine dyes displayed fluorescence emissions in the near-infrared region with large Stokes shift, outstanding photostability, high molar extinction coefficient, increased fluorescence quantum yield, perfect hydrophilicity, and excellent pH stability, because the amino residue possessed enhanced electron-donating abilities. Besides, by employing an *o*-phenylenediamine switch to one of the dyes, a novel near-infrared rhodamine-based pH probe was obtained with sensitive and quick responses to intracellular pH alterations. To point out, this fluorescent probe possessed a much higher pK_a of 5.4 compared to the traditional rhodamine probes due to the larger steric hindrance between the xanthene motif and the *o*-phenylenediamine receptor. This rhodamine-based fluorescent probe was applied

successfully to efficiently detect pH in the lysosomes and monitor pH fluctuations by different stimulations.

In chapters three and four, we aimed to develop ratiometric fluorescent lysosome-targeting pH probes with good cell membrane permeability and high pK_a. For chapter three, we presented two ratiometric fluorescent probes by connecting a green fluorescent coumarin donor to a classic near-infrared hemicyanine acceptor through a vinyl linker based on π- conjugation modulation mechanism. Bearing with lysosome targeting group morpholine and *o*-diaminebenzene, respectively, these two probes showed ratiometric fluorescence responses to the pH changing from7.0 to 3.0 as the intensity of coumarin fluorescence decreased and the intensity of NIR hemicyanine fluorescence increased. As in chapter four, we developed three ratiometric fluorescent probes containing TPE moiety as a fluorescence donor and rhodamine skeleton as a fluorescence acceptor through TBET and FRET approaches to reach the goals of quantitative, sensitive and selective analyses of lysosomal pH variations. Due to the steric hinder, the probe bearing *o*-diaminebenzene residue possessed higher pK_a which would be applied for detecting fluctuations of lysosomal pH with higher efficiency.

In chapter five, our objective was to design and synthesize ratiometric fluorescent sensors to detect mitochondrial pH. Thus, we attached two different positive-charged hemicyanine fluorophores into a typical rhodol skeleton to give two NIR hybrid rhodol fluorescent sensors for the sensitive ratiometric visualization of mitochondrial pH alterations. Upon pH value decreasing, the hydroxyl group in the rhodol skeleton of these two probes switched from spiropyran form to open ring form which resulted in an enlarged

150

π-conjugation system, leading to dual fluorescence emission peaks alternating ratiometrically not only *in vitro* but also *in vivo*.

In chapter six, our target was to apply ratiometric fluorescent sensors to detect intracellular biothiols efficiently. In order to reach this, based on FRET mechanism, we chose a visible emission coumarin as a fluorescence donor and a NIR rhodamine as a fluorescence acceptor through a piperazine linker as to obtain an original ratiometric fluorescent sensor to sensitively monitor intracellular Cys levels.

Despite the progress we made to acquire fluorescent probes with enhanced spectroscopy properties, more efforts are still needed for the further development of the new fluorescent sensors. Therefore, the outlooks of this dissertation are as follows: First and foremost, the common drawback of the fluorescent probe method is the issue of bad photostability which means the fluorescence emission quenches quite a lot after a long time of strong radiation. Thus, we need to rationally design and synthesize the novel fluorescent dyes with improved photostability. Second, the fluorescent probes are the small molecules which are always having solubility issues in aqueous systems that severely impact the practical applications of them. The approaches we can adopt to overcome this disadvantage include: a) introduce hydrophilic residues such as the ethylene glycol chain; b) conjugate the fluorescent probe with water-soluble polymer residue to construct fluorescent macromolecules; c) combine the fluorescent probe with nano materials together to possess some exclusive properties. With improved water solubility, it is promising to employ the fluorescent probes to visualize different animal tissues, such as fruit flies, mice, zebra fishes and even monkeys. Last but not the least, the fluorescent probes could only play the

151

role of sensors in the medical field, not having the ability to treat the disease. Therefore, it is vital to combine the clinical drug with the fluorescent imaging approach to reach the goal of detecting and curing simultaneously.

.

Reference List

1.   Valeur, B.; Berberan-Santos, M. N., A Brief History of Fluorescence and Phosphorescence before the Emergence of Quantum Theory. *Journal of Chemical Education* **2011,** *88* (6), 731-738.

2.   Acuña, A. U.; Amat-Guerri, F.; Morcillo, P.; Liras, M.; Rodríguez, B., Structure and Formation of the Fluorescent Compound of Lignum nephriticum. *Organic Letters* **2009,** *11* (14), 3020-3023.

3.   Clark., D. E., *Annals of Philosophy* **1819,** *14*, 34-36.

4.   Haüy, R.-J., *Traité de Minéralogie.* 2nd ed.; 1822; Vol. 1.

5.   Brewster, D., XIX. On the Colours of Natural Bodies. *Transactions of the Royal Society of Edinburgh* **1834,** *12* (2), 538-545.

6.   Herschel, J. F. W., *Philosophical Transactions* **1845**, 143-145, 147-153.

7.   Stokes, G. G., XXX. On the change of refrangibility of light. *Philosophical Transactions of the Royal Society of London* **1852,** *142*, 463-562.

8.   Stokes, G. G., XVI. On the change of refrangibility of light.—No. II. *Philosophical Transactions of the Royal Society of London* **1853,** *143*, 385-396.

9.   Jablonski, A., Efficiency of Anti-Stokes Fluorescence in Dyes. *Nature* **1933,** *131* (3319), 839-840.

10.   Göppelsröder, F., *Journal für praktische Chemie* **1868,** *104*, 10–27.

11.   Demchenko, A. P., *Introduction to Fluorescence Sensing.* Spinger: 2015.

12.   Mei, J.; Leung, N. L. C.; Kwok, R. T. K.; Lam, J. W. Y.; Tang, B. Z., Aggregation-Induced Emission: Together We Shine, United We Soar! *Chemical Reviews* **2015,** *115* (21), 11718-11940.

13.   Fang, M.; Xia, S.; Bi, J.; Wigstrom, T. P.; Valenzano, L.; Wang, J.; Mazi, W.; Tanasova, M.; Luo, F.-T.; Liu, H., A cyanine-based fluorescent cassette with aggregation-induced emission for sensitive detection of pH changes in live cells. *Chemical Communications* **2018,** *54* (9), 1133-1136.

14.   Cao, D.; Liu, Z.; Verwilst, P.; Koo, S.; Jangjili, P.; Kim, J. S.; Lin, W., Coumarin-Based Small-Molecule Fluorescent Chemosensors. *Chemical Reviews* **2019,** *119* (18), 10403-10519.

15.   Ieri, F.; Pinelli, P.; Romani, A., Simultaneous determination of anthocyanins, coumarins and phenolic acids in fruits, kernels and liqueur of Prunus mahaleb L. *Food Chemistry* **2012,** *135* (4), 2157-2162.

16.   Beija, M.; Afonso, C. A. M.; Martinho, J. M. G., Synthesis and applications of Rhodamine derivatives as fluorescent probes. *Chem. Soc. Rev.* **2009,** *38* (8), 2410-2433.

17.   Lavis, L. D., Teaching Old Dyes New Tricks: Biological Probes Built from Fluoresceins and Rhodamines. **2017,** *86* (1), 825-843.

18.   Yang, X.-F.; Guo, X.-Q.; Zhao, Y.-B., Development of a novel rhodamine-type fluorescent probe to determine peroxynitrite. *Talanta* **2002,** *57* (5), 883-890.

19.   Peng, T.; Chen, X.; Gao, L.; Zhang, T.; Wang, W.; Shen, J.; Yang, D., A rationally designed rhodamine-based fluorescent probe for molecular imaging of peroxynitrite in live cells and tissues. *Chemical Science* **2016,** *7* (8), 5407-5413.

20.   Sunnapu, O.; Kotla, N. G.; Maddiboyina, B.; Singaravadivel, S.; Sivaraman, G., A rhodamine based "turn-on" fluorescent probe for Pb(ii) and live cell imaging. *RSC Advances* **2016,** *6* (1), 656-660.

21.   Zhang, Y.; Bi, J.; Xia, S.; Mazi, W.; Wan, S.; Mikesell, L.; Luck, R. L.; Liu, H., A Near-Infrared Fluorescent Probe Based on a FRET Rhodamine Donor Linked to a Cyanine Acceptor for Sensitive Detection of Intracellular pH Alternations. *Molecules* **2018,** *23* (10), 2679.

22.   Lee, L. G.; Berry, G. M.; Chen, C.-H., Vita blue: A new 633-nm excitable fluorescent dye for cell analysis. **1989,** *10* (2), 151-164.

23.   Burdette, S. C.; Lippard, S. J., The Rhodafluor Family. An Initial Study of Potential Ratiometric Fluorescent Sensors for Zn2+. *Inorganic Chemistry* **2002,** *41* (25), 6816-6823.

24.   Whitaker, J. E.; Haugland, R. P.; Ryan, D.; Hewitt, P. C.; Haugland, R. P.; Prendergast, F. G., Fluorescent rhodol derivatives: Versatile, photostable labels and tracers. *Analytical Biochemistry* **1992,** *207* (2), 267-279.

25.   Peng, T.; Yang, D., Construction of a Library of Rhodol Fluorophores for Developing New Fluorescent Probes. *Organic Letters* **2010,** *12* (3), 496-499.

26.   Williams, C. G., XXVI.—Researches on Chinoline and its Homologues. *Transactions of the Royal Society of Edinburgh* **1856,** *21* (3), 377-401.

27.   Winkle, M. R.; Ronald, R. C., Regioselective metalation reactions of some substituted (methoxymethoxy)arenes. *The Journal of Organic Chemistry* **1982,** *47* (11), 2101-2108.

28.   He, L.; Lin, W.; Xu, Q.; Ren, M.; Wei, H.; Wang, J.-Y., A simple and effective "capping" approach to readily tune the fluorescence of near-infrared cyanines. *Chemical Science* **2015,** *6* (8), 4530-4536.

29.   Mishra, A.; Behera, R. K.; Behera, P. K.; Mishra, B. K.; Behera, G. B., Cyanines during the 1990s: A Review. *Chemical Reviews* **2000,** *100* (6), 1973-2012.

30.   James, N. S.; Chen, Y.; Joshi, P.; Ohulchanskyy, T. Y.; Ethirajan, M.; Henary, M.; Strekowsk, L.; Pandey, R. K., Evaluation of polymethine dyes as potential probes for near infrared fluorescence imaging of tumors: part - 1. *Theranostics* **2013,** *3* (9), 692-702.

31.   Yuan, L.; Lin, W.; Yang, Y.; Chen, H., A Unique Class of Near-Infrared Functional Fluorescent Dyes with Carboxylic-Acid-Modulated Fluorescence ON/OFF Switching: Rational Design, Synthesis, Optical Properties, Theoretical Calculations, and Applications for Fluorescence Imaging in Living Animals. *Journal of the American Chemical Society* **2012,** *134* (2), 1200-1211.

32.   Wang, J.; Xia, S.; Bi, J.; Fang, M.; Mazi, W.; Zhang, Y.; Conner, N.; Luo, F.-T.; Lu, H. P.; Liu, H., Ratiometric Near-Infrared Fluorescent Probes Based On Through-Bond Energy Transfer and π-Conjugation Modulation between Tetraphenylethene and Hemicyanine Moieties for Sensitive Detection of pH Changes in Live Cells. *Bioconjugate Chemistry* **2018,** *29* (4), 1406-1418.

33.   Bi, J.; Fang, M.; Wang, J.; Xia, S.; Zhang, Y.; Zhang, J.; Vegesna, G.; Zhang, S.; Tanasova, M.; Luo, F.-T.; Liu, H., Near-infrared fluorescent probe for sensitive detection of Pb(II) ions in living cells. *Inorganica Chimica Acta* **2017,** *468*, 140-145.

34.   Vegesna, G. K.; Janjanam, J.; Bi, J.; Luo, F.-T.; Zhang, J.; Olds, C.; Tiwari, A.; Liu, H., pH-activatable near-infrared fluorescent probes for detection of lysosomal pH inside living cells. *Journal of Materials Chemistry B* **2014,** *2* (28), 4500-4508.

35.   Lakowicz, J. R., *Topics in Fluorescence Spectroscopy*. Springer 2002; Vol. 2.

36.   Gao, X.; Cui, Y.; Levenson, R. M.; Chung, L. W. K.; Nie, S., In vivo cancer targeting and imaging with semiconductor quantum dots. *Nature Biotechnology* **2004,** *22* (8), 969-976.

37.   Frangioni, J. V., In vivo near-infrared fluorescence imaging. *Current Opinion in Chemical Biology* **2003,** *7* (5), 626-634.

38.   Weissleder, R., A clearer vision for in vivo imaging. *Nature Biotechnology* **2001,** *19* (4), 316-317.

39.   Lavis, L. D.; Raines, R. T., Bright Ideas for Chemical Biology. *ACS Chemical Biology* **2008,** *3* (3), 142-155.

40.   Fan, J.; Hu, M.; Zhan, P.; Peng, X., Energy transfer cassettes based on organic fluorophores: construction and applications in ratiometric sensing. *Chemical Society Reviews* **2013,** *42* (1), 29-43.

41.   Liu, M.; Yu, X.; Li, M.; Liao, N.; Bi, A.; Jiang, Y.; Liu, S.; Gong, Z.; Zeng, W., Fluorescent probes for the detection of magnesium ions (Mg2+): from design to application. *RSC Advances* **2018,** *8* (23), 12573-12587.

42.   Valeur, B.; Leray, I., Design principles of fluorescent molecular sensors for cation recognition. *Coordination Chemistry Reviews* **2000,** *205* (1), 3-40.

43.   Berezin, M. Y.; Achilefu, S., Fluorescence Lifetime Measurements and Biological Imaging. *Chemical Reviews* **2010,** *110* (5), 2641-2684.

44.   Mordziński, A.; Grabowska, A., Intramolecular proton transfer in excited benzoxazoles. *Chemical Physics Letters* **1982,** *90* (2), 122-127.

45.   dos Remedios, C. G.; Moens, P. D. J., Fluorescence Resonance Energy Transfer Spectroscopy Is a Reliable "Ruler" for Measuring Structural Changes in Proteins: Dispelling the Problem of the Unknown Orientation Factor. *Journal of Structural Biology* **1995,** *115* (2), 175-185.

46.   Jiao, G.-S.; Thoresen, L. H.; Burgess, K., Fluorescent, Through-Bond Energy Transfer Cassettes for Labeling Multiple Biological Molecules in One Experiment. *Journal of the American Chemical Society* **2003,** *125* (48), 14668-14669.

47.   Zhang, J.; Zhu, S.; Valenzano, L.; Luo, F.-T.; Liu, H., BODIPY-based ratiometric fluorescent probes for the sensitive and selective sensing of cyanide ions. *RSC Advances* **2013,** *3* (1), 68-72.

48.   Wan, Q.; Chen, S.; Shi, W.; Li, L.; Ma, H., Lysosomal pH Rise during Heat Shock Monitored by a Lysosome-Targeting Near-Infrared Ratiometric Fluorescent Probe. *Angewandte Chemie International Edition* **2014,** *53* (41), 10916-10920.

49.   Hou, J.-T.; Ren, W. X.; Li, K.; Seo, J.; Sharma, A.; Yu, X.-Q.; Kim, J. S., Fluorescent bioimaging of pH: from design to applications. *Chemical Society Reviews* **2017,** *46* (8), 2076-2090.

50.   Izumi, H.; Torigoe, T.; Ishiguchi, H.; Uramoto, H.; Yoshida, Y.; Tanabe, M.; Ise, T.; Murakami, T.; Yoshida, T.; Nomoto, M.; Kohno, K., Cellular pH regulators: potentially promising molecular targets for cancer chemotherapy. *Cancer Treatment Reviews* **2003,** *29* (6), 541-549.

51.   Rink, T. J.; Tsien, R. Y.; Pozzan, T., Cytoplasmic pH and free Mg2+ in lymphocytes. **1982,** *95* (1), 189-196.

52.   Luzio, J. P.; Pryor, P. R.; Bright, N. A., Lysosomes: fusion and function. *Nature Reviews Molecular Cell Biology* **2007,** *8* (8), 622-632.

53.   Li, G.; Zhu, D.; Xue, L.; Jiang, H., Quinoline-Based Fluorescent Probe for Ratiometric Detection of Lysosomal pH. *Organic Letters* **2013,** *15* (19), 5020-5023.

54.   *Annals of Philosophy*. London., 1812; Vol. v.1 (1812).

55.   Zhu, M.; Xing, P.; Zhou, Y.; Gong, L.; Zhang, J.; Qi, D.; Bian, Y.; Du, H.; Jiang, J., Lysosome-targeting ratiometric fluorescent pH probes based on long-wavelength BODIPY. *Journal of Materials Chemistry B* **2018,** *6* (27), 4422-4426.

56.   Chen, Y.; Zhu, C.; Cen, J.; Bai, Y.; He, W.; Guo, Z., Ratiometric detection of pH fluctuation in mitochondria with a new fluorescein/cyanine hybrid sensor. *Chemical Science* **2015,** *6* (5), 3187-3194.

57.   Li, Y.; Wang, Y.; Yang, S.; Zhao, Y.; Yuan, L.; Zheng, J.; Yang, R., Hemicyanine-based High Resolution Ratiometric near-Infrared Fluorescent Probe for Monitoring pH Changes in Vivo. *Analytical Chemistry* **2015,** *87* (4), 2495-2503.

58.   Wu, M.-Y.; Li, K.; Liu, Y.-H.; Yu, K.-K.; Xie, Y.-M.; Zhou, X.-D.; Yu, X.-Q., Mitochondria-targeted ratiometric fluorescent probe for real time monitoring of pH in living cells. *Biomaterials* **2015,** *53*, 669-678.

59.   Liu, X.; Wang, L.; Bing, T.; Zhang, N.; Dihua, S., A Mitochondria-Targeted Ratiometric Fluorescent pH Probe. *ACS Applied Bio Materials* **2019,** *2* (3), 1368-1375.

60.   Niu, L.-Y.; Chen, Y.-Z.; Zheng, H.-R.; Wu, L.-Z.; Tung, C.-H.; Yang, Q.-Z., Design strategies of fluorescent probes for selective detection among biothiols. *Chemical Society Reviews* **2015,** *44* (17), 6143-6160.

61.   Niu, W.; Guo, L.; Li, Y.; Shuang, S.; Dong, C.; Wong, M. S., Highly Selective Two-Photon Fluorescent Probe for Ratiometric Sensing and Imaging Cysteine in Mitochondria. *Analytical Chemistry* **2016,** *88* (3), 1908-1914.

62.   Wang, F.; Feng, C.; Lu, L.; Xu, Z.; Zhang, W., A ratiometric fluorescent probe for rapid and sensitive detection of biothiols in fetal bovine serum. *Talanta* **2017,** *169*, 149-155.

63.   He, L.;   Yang, X.;   Xu, K.; Lin, W., Improved Aromatic Substitution– Rearrangement-Based Ratiometric Fluorescent Cysteine-Specific Probe and Its Application of Real-Time Imaging under Oxidative Stress in Living Zebrafish. *Analytical Chemistry* **2017,** *89* (17), 9567-9573.

64.	Gong, D.; Han, S.-C.; Iqbal, A.; Qian, J.; Cao, T.; Liu, W.; Liu, W.; Qin, W.; Guo, H., Fast and Selective Two-Stage Ratiometric Fluorescent Probes for Imaging of Glutathione in Living Cells. *Analytical Chemistry* **2017,** *89* (24), 13112-13119.

65.	Yuan, L.; Lin, W.; Zheng, K.; Zhu, S., FRET-Based Small-Molecule Fluorescent Probes: Rational Design and Bioimaging Applications. *Accounts of Chemical Research* **2013,** *46* (7), 1462-1473.

66.	Zhang, Y.; Xia, S.; Fang, M.; Mazi, W.; Zeng, Y.; Johnston, T.; Pap, A.; Luck, R. L.; Liu, H., New near-infrared rhodamine dyes with large Stokes shifts for sensitive sensing of intracellular pH changes and fluctuations. *Chemical Communications* **2018,** *54* (55), 7625-7628.

67.	Kaur, B.; Kaur, N.; Kumar, S., Colorimetric metal ion sensors - A comprehensive review of the years 2011-2016. *Coord. Chem. Rev.* **2018,** *358*, 13-69.

68.	Sivaraman, G.; Iniya, M.; Anand, T.; Kotla, N. G.; Sunnapu, O.; Singaravadivel, S.; Gulyani, A.; Chellappa, D., Chemically diverse small molecule fluorescent chemosensors for copper ion. *Coord. Chem. Rev.* **2018,** *357*, 50-104.

69.	Gupta, A.; Kumar, N., A review of mechanisms for fluorescent "turn-on" probes to detect Al3+ ions. *Rsc Advances* **2016,** *6* (108), 106413-106434.

70.	Zhang, R. Q.; Yan, F. Y.; Huang, Y. C.; Kong, D. P.; Ye, Q. H.; Xu, J. X.; Chen, L., Rhodamine-based ratiometric fluorescent probes based on excitation energy transfer mechanisms: construction and applications in ratiometric sensing. *RSC Adv.* **2016,** *6* (56), 50732-50760.

71.	Zhu, H.; Fan, J. L.; Wang, B. H.; Peng, X. J., Fluorescent, MRI, and colorimetric chemical sensors for the first-row d-block metal ions. *Chem. Soc. Rev.* **2015,** *44* (13), 4337-4366.

72.	Yuan, L.; Lin, W. Y.; Zheng, K. B.; Zhu, S. S., FRET-Based Small-Molecule Fluorescent Probes: Rational Design and Bioimaging Applications. *Accounts of Chemical Research* **2013,** *46* (7), 1462-1473.

73.	Zheng, Q. S.; Lavis, L. D., Development of photostable fluorophores for molecular imaging. *Curr. Opin. Chem. Biol.* **2017,** *39*, 32-38.

74.	Ikeno, T.; Nagano, T.; Hanaoka, K., Silicon-substituted Xanthene Dyes and Their Unique Photophysical Properties for Fluorescent Probes. *Chem. Asian J.* **2017,** *12* (13), 1435-1446.

75.	Umezawa, K.; Citterio, D.; Suzuki, K., New Trends in Near-Infrared Fluorophores for Bioimaging. *Anal. Sci.* **2014,** *30* (3), 327-349.

76.   Yuan, L.; Lin, W. Y.; Zheng, K. B.; He, L. W.; Huang, W. M., Far-red to near infrared analyte-responsive fluorescent probes based on organic fluorophore platforms for fluorescence imaging. *Chem. Soc. Rev.* **2013,** *42* (2), 622-661.

77.   Liu, C.; Jiao, X. J.; Wang, Q.; Huang, K.; He, S.; Zhao, L. C.; Zeng, X. S., A unique rectilinearly pi-extended rhodamine dye with large Stokes shift and near-infrared fluorescence for bioimaging. *Chem. Commun.* **2017,** *53* (77), 10727-10730.

78.   Mao, Z. Q.; Jiang, H.; Song, X. J.; Hu, W.; Liu, Z. H., Development of a Silicon-Rhodamine Based Near-Infrared Emissive Two-Photon Fluorescent Probe for Nitric Oxide. *Anal. Chem.* **2017,** *89* (18), 9620-9624.

79.   Grimm, J. B.; Muthusamy, A. K.; Liang, Y. J.; Brown, T. A.; Lemon, W. C.; Patel, R.; Lu, R. W.; Macklin, J. J.; Keller, P. J.; Ji, N.; Lavis, L. D., A general method to fine-tune fluorophores for live-cell and in vivo imaging. *Nat. Methods* **2017,** *14* (10), 987-994.

80.   Grimm, J. B.; Brown, T. A.; Tkachuk, A. N.; Lavis, L. D., General Synthetic Method for Si-Fluoresceins and Si-Rhodamines. *ACS Cent. Sci.* **2017,** *3* (9), 975-985.

81.   Zhang, H. X.; Liu, J.; Liu, C. L.; Yu, P. C.; Sun, M. J.; Yan, X. H.; Guo, J. P.; Guo, W., Imaging lysosomal highly reactive oxygen species and lighting up cancer cells and tumors enabled by a Si-rhodamine-based near-infrared fluorescent probe. *Biomaterials* **2017,** *133*, 60-69.

82.   Niu, G. L.; Liu, W. M.; Zhou, B. J.; Xiao, H. Y.; Zhang, H. Y.; Wu, J. S.; Ge, J. C.; Wang, P. F., Deep-Red and Near-Infrared Xanthene Dyes for Rapid Live Cell Imaging. *J. Org. Chem.* **2016,** *81* (17), 7393-7399.

83.   Niu, G. L.; Zhang, P. P.; Liu, W. M.; Wang, M. Q.; Zhang, H. Y.; Wu, J. S.; Zhang, L. P.; Wang, P. F., Near-Infrared Probe Based on Rhodamine Derivative for Highly Sensitive and Selective Lysosomal pH Tracking. *Anal. Chem.* **2017,** *89* (3), 1922-1929.

84.   Zhou, X. Q.; Lai, R.; Beck, J. R.; Li, H.; Stains, C. I., Nebraska Red: a phosphinate-based near-infrared fluorophore scaffold for chemical biology applications. *Chem. Commun.* **2016,** *52* (83), 12290-12293.

85.   Niu, G. L.; Liu, W. M.; Wu, J. S.; Zhou, B. J.; Chen, J. H.; Zhang, H. Y.; Ge, J. C.; Wang, Y.; Xu, H. T.; Wang, P. F., Aminobenzofuran-Fused Rhodamine Dyes with Deep-Red to Near-Infrared Emission for Biological Applications. *J. Org. Chem.* **2015,** *80* (6), 3170-3175.

86.   Chai, X. Y.; Cui, X. Y.; Wang, B. G.; Yang, F.; Cai, Y.; Wu, Q. Y.; Wang, T., Near-Infrared Phosphorus-Substituted Rhodamine with Emission Wavelength above 700 nm for Bioimaging. *Chem_Eur J.* **2015,** *21* (47), 16754-16758.

87.   Gong, Y. J.; Zhang, X. B.; Mao, G. J.; Su, L.; Meng, H. M.; Tan, W. H.; Feng, S. L.; Zhang, G. S., A unique approach toward near-infrared fluorescent probes for bioimaging with remarkably enhanced contrast. *Chem. Sci.* **2016,** *7* (3), 2275-2285.

88.   Zhang, S. W.; Chen, T. H.; Lee, H. M.; Bi, J. H.; Ghosh, A.; Fang, M. X.; Qian, Z. C.; Xie, F.; Ainsley, J.; Christov, C.; Luo, F. T.; Zhao, F.; Liu, H. Y., Luminescent Probes for Sensitive Detection of pH Changes in Live Cells through Two Near-Infrared Luminescence Channels. *ACS Sens.* **2017,** *2* (7), 924-931.

89.   Vegesna, G. K.; Janjanam, J.; Bi, J. H.; Luo, F. T.; Zhang, J. T.; Olds, C.; Tiwari, A.; Liu, H. Y., pH-activatable near-infrared fluorescent probes for detection of lysosomal pH inside living cells. *J. Mater. Chem. B* **2014,** *2* (28), 4500-4508.

90.   Yuan, L.; Lin, W. Y.; Yang, Y. T.; Chen, H., A Unique Class of Near-Infrared Functional Fluorescent Dyes with Carboxylic-Acid-Modulated Fluorescence ON/OFF Switching: Rational Design, Synthesis, Optical Properties, Theoretical Calculations, and Applications for Fluorescence Imaging in Living Animals. *J. Am. Chem. Soc.* **2012,** *134* (2), 1200-1211.

91.   Fang, M. X.; Xia, S.; Bi, J. H.; Wigstrom, T. P.; Valenzano, L.; Wang, J. B.; Mazi, W.; Tanasova, M.; Luo, F. T.; Liu, H. Y., A cyanine-based fluorescent cassette with aggregation-induced emission for sensitive detection of pH changes in live cells. *Chem. Commun.* **2018,** *54* (9), 1133-1136.

92.   Fang, M. X.; Adhikari, R.; Bi, J. H.; Mazi, W.; Dorh, N.; Wang, J. B.; Conner, N.; Ainsley, J.; Karabencheva-Christova, T. G.; Luo, F. T.; Tiwari, A.; Liu, H. Y., Fluorescent probes for sensitive and selective detection of pH changes in live cells in visible and near-infrared channels. *J. Mater. Chem. B* **2017,** *5* (48), 9579-9590.

93.   Zhang, J. T.; Yang, M.; Mazi, W. F.; Adhikari, K.; Fang, M. X.; Xie, F.; Valenzano, L.; Tiwari, A.; Luo, F. T.; Liu, H. Y., Unusual Fluorescent Responses of Morpholine-Functionalized Fluorescent Probes to pH via Manipulation of BODIPY's HOMO and LUMO Energy Orbitals for Intracellular pH Detection. *ACS Sens.* **2016,** *1* (2), 158-165.

94.   Zhang, J. T.; Yang, M.; Li, C.; Dorh, N.; Xie, F.; Luo, F. T.; Tiwari, A.; Liu, H. Y., Near-infrared fluorescent probes based on piperazine-functionalized BODIPY dyes for sensitive detection of lysosomal pH. *J. Mater. Chem. B* **2015,** *3* (10), 2173-2184.

95.   Wang, J. B.; Xia, S.; Bi, J. H.; Fang, M. X.; Mazi, W. F.; Zhang, Y. B.; Conner, N.; Luo, F. T.; Lu, H. P.; Liu, H. Y., Ratiometric Near-Infrared Fluorescent Probes Based On Through Bond Energy Transfer and pi-Conjugation Modulation between Tetraphenylethene and Hemicyanine Moieties for Sensitive Detection of pH Changes in Live Cells. *Bioconjugate Chem.* **2018,** *29* (4), 1406-1418.

96.   Chen, W.; Xu, S.; Day, J. J.; Wang, D. F.; Xian, M., A General Strategy for Development of Near-Infrared Fluorescent Probes for Bioimaging. *Angew. Chem. Int. Ed.* **2017,** *56* (52), 16611-16615.

97.   Austin, A.; Petersson, G. A.; Frisch, M. J.; Dobek, F. J.; Scalmani, G.; Throssell, K., A Density Functional with Spherical Atom Dispersion Terms. *J. Chem. Theory Comput.* **2012,** *8* (12), 4989-5007.

98.   Turq, P.; Lantelme, F.; Friedman, H. L., BROWNIAN DYNAMICS - ITS APPLICATION TO IONIC-SOLUTIONS. *J. Chem. Phys.* **1977,** *66* (7), 3039-3044.

99.   Adamo, C.; Jacquemin, D., The calculations of excited-state properties with Time-Dependent Density Functional Theory. *Chem. Soc. Rev.* **2013,** *42* (3), 845-856.

100.   Foresman, J. B.; Frisch, Æ., *Exploring Chemistry with Electronic Structure Methods*. Gaussian, Inc.: Wallingford, CT USA, 2015.

101.   Pan, W.; Wang, H. H.; Yang, L. M.; Yu, Z. Z.; Li, N.; Tang, B., Ratiometric Fluorescence Nanoprobes for Subcellular pH Imaging with a Single-Wavelength Excitation in Living Cells. *Anal. Chem.* **2016,** *88* (13), 6743-6748.

102.   Li, G. P.; Zhu, D. J.; Xue, L.; Jiang, H., Quinoline-Based Fluorescent Probe for Ratiometric Detection of Lysosomal pH. *Org. Lett.* **2013,** *15* (19), 5020-5023.

103.   Ohgaki, R.; van Ijzendoorn, S. C. D.; Matsushita, M.; Hoekstra, D.; Kanazawa, H., Organellar Na+/H+ Exchangers: Novel Players in Organelle pH Regulation and Their Emerging Functions. *Biochemistry* **2011,** *50* (4), 443-450.

104.   Xia, S.; Wang, J.; Bi, J.; Wang, X.; Fang, M.; Phillips, T.; May, A.; Conner, N.; Tanasova, M.; Luo, F.-T.; Liu, H., Fluorescent probes based on π-conjugation modulation between hemicyanine and coumarin moieties for ratiometric detection of pH changes in live cells with visible and near-infrared channels. *Sensors and Actuators B: Chemical* **2018,** *265*, 699-708.

105.   Kawagoe, R.; Takashima, I.; Uchinomiya, S.; Ojida, A., Reversible ratiometric detection of highly reactive hydropersulfides using a FRET-based dual emission fluorescent probe. *Chem. Sci.* **2017,** *8* (2), 1134-1140.

106.   Zhang, Y. Y.; Li, S. L.; Zhao, Z. W., Using Nanoliposomes To Construct a FRET-Based Ratiometric Fluorescent Probe for Sensing Intracellular pH Values. *Anal. Chem.* **2016,** *88* (24), 12380-12385.

107.   Jia, X. T.; Chen, Q. Q.; Yang, Y. F.; Tang, Y.; Wang, R.; Xu, Y. F.; Zhu, W. P.; Qian, X. H., FRET-Based Mito-Specific Fluorescent Probe for Ratiometric Detection and Imaging of Endogenous Peroxynitrite: Dyad of Cy3 and Cy5. *J. Am. Chem. Soc.* **2016,** *138* (34), 10778-10781.

108.   Song, G. J.; Bai, S. Y.; Dai, X.; Cao, X. Q.; Zhao, B. X., A ratiometric lysosomal pH probe based on the imidazo 1,5-a pyridine-rhodamine FRET and ICT system. *RSC Adv.* **2016,** *6* (47), 41317-41322.

109.   Zhang, Y. R.; Meng, N.; Miao, J. Y.; Zhao, B. X., A Ratiometric Fluorescent Probe Based on a Through-Bond Energy Transfer (TBET) System for Imaging HOCl in Living Cells. *Chem. Eur. J.* **2015,** *21* (52), 19058-19063.

110.   He, L. W.; Dong, B. L.; Liu, Y.; Lin, W. Y., Fluorescent chemosensors manipulated by dual/triple interplaying sensing mechanisms. *Chem. Soc. Rev.* **2016,** *45* (23), 6449-6461.

111.   Fan, J. L.; Hu, M. M.; Zhan, P.; Peng, X. J., Energy transfer cassettes based on organic fluorophores: construction and applications in ratiometric sensing. *Chem. Soc. Rev.* **2013,** *42* (1), 29-43.

112.   Dimura, M.; Peulen, T. O.; Hanke, C. A.; Prakash, A.; Gohlke, H.; Seidel, C. A. M., Quantitative FRET studies and integrative modeling unravel the structure and dynamics of biomolecular systems. *Curr. Opin. Struct. Biol.* **2016,** *40*, 163-185.

113.   Rowland, C. E.; Brown, C. W.; Medintz, I. L.; Delehanty, J. B., Intracellular FRET-based probes: a review. *Methods and Applications in Fluorescence* **2015,** *3* (4).

114.   Kumar, N.; Bhalla, V.; Kumar, M., Resonance energy transfer-based fluorescent probes for Hg2+, Cu2+ and Fe2+/Fe3+ ions. *Analyst* **2014,** *139* (3), 543-558.

115.   Zhang, J.; Zhu, S.; Valenzano, L.; Luo, F.-T.; Liu, H. Y., BODIPY-based Ratiometric Fluorescent Probes for Sensitive and Selective Sensing of Cyanide Ion. *RCS Advances* **2012,** *3*, 68-72.

116.   Wan, Q. Q.; Chen, S. M.; Shi, W.; Li, L. H.; Ma, H. M., Lysosomal pH Rise during Heat Shock Monitored by a Lysosome-Targeting Near-Infrared Ratiometric Fluorescent Probe. *Angew. Chem. Int. Ed.* **2014,** *53* (41), 10916-10920.

117.   Li, Y. H.; Wang, Y. J.; Yang, S.; Zhao, Y. R.; Yuan, L.; Zheng, J.; Yang, R. H., Hemicyanine-based High Resolution Ratiometric near-Infrared Fluorescent Probe for Monitoring pH Changes in Vivo. *Anal. Chem.* **2015,** *87* (4), 2495-2503.

118.   Diwu, Z. J.; Chen, C. S.; Zhang, C. L.; Klaubert, D. H.; Haugland, R. P., A novel acidotropic pH indicator and its potential application in labeling acidic organelles of live cells. *Chem. Biol.* **1999,** *6* (7), 411-418.

119.   Lv, H. S.; Liu, J.; Zhao, J.; Zhao, B. X.; Miao, J. Y., Highly selective and sensitive pH-responsive fluorescent probe in living Hela and HUVEC cells. *Sens. Actuator B-Chem.* **2013,** *177*, 956-963.

120.   Zhu, H.; Fan, J. L.; Xu, Q. L.; Li, H. L.; Wang, J. Y.; Gao, P.; Peng, X. J., Imaging of lysosomal pH changes with a fluorescent sensor containing a novel lysosome-locating group. *Chem. Commun.* **2012,** *48* (96), 11766-11768.

121.   Li, Z.; Song, Y. L.; Yang, Y. H.; Yang, L.; Huang, X. H.; Han, J. H.; Han, S. F., Rhodamine-deoxylactam functionalized poly styrene-alter-(maleic acid) s as lysosome activatable probes for intraoperative detection of tumors. *Chem. Sci.* **2012,** *3* (10), 2941-2948.

122.   Ying, L. Q.; Branchaud, B. P., Selective labeling and monitoring pH changes of lysosomes in living cells with fluorogenic pH sensors. *Bioorg. Med. Chem. Lett.* **2011,** *21* (12), 3546-3549.

123.   Smith, D. G.; McMahon, B. K.; Pal, R.; Parker, D., Live cell imaging of lysosomal pH changes with pH responsive ratiometric lanthanide probes. *Chem. Commun.* **2012,** *48* (68), 8520-8522.

124.   Ma, L. J.; Cao, W. G.; Liu, J. L.; Deng, D. Y.; Wu, Y. Q.; Yan, Y. H.; Yang, L. T., A highly selective and sensitive fluorescence dual-responsive pH probe in water. *Sens. Actuator B-Chem.* **2012,** *169*, 243-247.

125.   Galindo, F.; Burguete, M. I.; Vigara, L.; Luis, S. V.; Kabir, N.; Gavrilovic, J.; Russell, D. A., Synthetic macrocyclic peptidomimetics as tunable pH probes for the fluorescence imaging of acidic organelles in live cells. *Angew. Chem. Int. Ed.* **2005,** *44* (40), 6504-6508.

126.   DePedro, H. M.; Urayama, P., Using LysoSensor Yellow/Blue DND-160 to sense acidic pH under high hydrostatic pressures. *Anal. Biochem.* **2009,** *384* (2), 359-361.

127.   Hasegawa, T.; Kondo, Y.; Koizumi, Y.; Sugiyama, T.; Takeda, A.; Ito, S.; Hamada, F., A highly sensitive probe detecting low pH area of HeLa cells based on rhodamine B modified beta-cyclodextrins. *Biorg. Med. Chem.* **2009,** *17* (16), 6015-6019.

128.   Lin, H. J.; Herman, P.; Kang, J. S.; Lakowicz, J. R., Fluorescence lifetime characterization of novel low-pH probes. *Anal. Biochem.* **2001,** *294* (2), 118-125.

129.   Wang, L.; Xiao, Y.; Tian, W. M.; Deng, L. Z., Activatable Rotor for Quantifying Lysosomal Viscosity in Living Cells. *J. Am. Chem. Soc.* **2013,** *135* (8), 2903-2906.

130.   Dong, B. L.; Song, X. Z.; Wang, C.; Kong, X. Q.; Tang, Y. H.; Lin, W. Y., Dual Site-Controlled and Lysosome-Targeted Intramolecular Charge Transfer-Photoinduced Electron Transfer-Fluorescence Resonance Energy Transfer Fluorescent Probe for Monitoring pH Changes in Living Cells. *Anal. Chem.* **2016,** *88* (7), 4085-4091.

131.   Wang, Q. Q.; Zhou, L. Y.; Qiu, L. P.; Lu, D. Q.; Wu, Y. X.; Zhang, X. B., An efficient ratiometric fluorescent probe for tracking dynamic changes in lysosomal pH. *Analyst* **2015,** *140* (16), 5563-5569.

132.   Zhang, J. T.; Yang, M.; Mazi, W.; Adhikari, K.; Fang, M. X.; Xie, F.; Valenzano, L.; Tiwari, A.; Luo, F. T.; Liu, H. Y., Unusual Fluorescent Responses of Morpholine-Functionalized Fluorescent Probes to pH via Manipulation of BODIPY's HOMO and LUMO Energy Orbitals for Intracellular pH Detection. *ACS Sens.* **2016,** *1* (2), 158-165.

133.   Schaferling, M., Nanoparticle-based luminescent probes for intracellular sensing and imaging of pH. *Wiley Interdisciplinary Reviews-Nanomedicine and Nanobiotechnology* **2016,** *8* (3), 378-413.

134.   Grossi, M.; Morgunova, M.; Cheung, S.; Scholz, D.; Conroy, E.; Terrile, M.; Panarella, A.; Simpson, J. C.; Gallagher, W. M.; O'Shea, D. F., Lysosome triggered near-infrared fluorescence imaging of cellular trafficking processes in real time. *Nature Communications* **2016,** *7*.

135.   Song, X. B.; Hu, M. Y.; Wang, C.; Xiao, Y., Near-infrared fluorescent probes with higher quantum yields and neutral pK(a) values for the evaluation of intracellular pH. *RSC Adv.* **2016,** *6* (73), 69641-69646.

136.   Li, P.; Xiao, H. B.; Cheng, Y. F.; Zhang, W.; Huang, F.; Zhang, W.; Wang, H.; Tang, B., A near-infrared-emitting fluorescent probe for monitoring mitochondrial pH. *Chem. Commun.* **2014,** *50* (54), 7184-7187.

137.   Hou, J. T.; Ren, W. X.; Li, K.; Seo, J.; Sharma, A.; Yu, X. Q.; Kim, J. S., Fluorescent bioimaging of pH: from design to applications. *Chem. Soc. Rev.* **2017,** *46* (8), 2076-2090.

138.   Yin, J.; Hu, Y.; Yoon, J., Fluorescent probes and bioimaging: alkali metals, alkaline earth metals and pH. *Chem. Soc. Rev.* **2015,** *44* (14), 4619-4644.

139.   Shi, W.; Li, X. H.; Ma, H. M., Fluorescent probes and nanoparticles for intracellular sensing of pH values. *Methods and Applications in Fluorescence* **2014,** *2* (4).

140.   Barot, K. P.; Jain, S. V.; Kremer, L.; Singh, S.; Ghate, M. D., Recent advances and therapeutic journey of coumarins: current status and perspectives. *Med. Chem. Res.* **2015,** *24* (7), 2771-2798.

141.   Wang, J.; Xia, S.; Bi, J.; Zhang, Y.; Fang, M.; Luck, R. L.; Zeng, Y.; Chen, T.-H.; Lee, H.-M.; Liu, H., Near-infrared fluorescent probes based on TBET and FRET rhodamine acceptors with different pKa values for sensitive ratiometric visualization of pH changes in live cells. *Journal of Materials Chemistry B* **2019,** *7* (2), 198-209.

142.   Chen, Y. C.; Zhang, W. J.; Cai, Y. J.; Kwok, R. T. K.; Hu, Y. B.; Lam, J. W. Y.; Gu, X. G.; He, Z. K.; Zhao, Z.; Zheng, X. Y.; Chen, B.; Gui, C.; Tang, B. Z., AIEgens for dark through-bond energy transfer: design, synthesis, theoretical study and application in ratiometric Hg2+ sensing. *Chem. Sci.* **2017,** *8* (3), 2047-2055.

143.   Ren, T. B.; Xu, W.; Zhang, W.; Zhang, X. X.; Wang, Z. Y.; Xiang, Z.; Yuan, L.; Zhang, X. B., A General Method To Increase Stokes Shift by Introducing Alternating Vibronic Structures. *J. Am. Chem. Soc.* **2018,** *140* (24), 7716-7722.

144.   Ren, T. B.; Xu, W.; Jin, F. P.; Cheng, D.; Zhang, L. L.; Yuan, L.; Zhang, X. B., Rational Engineering of Bioinspired Anthocyanidin Fluorophores with Excellent Two-Photon Properties for Sensing and Imaging. *Anal. Chem.* **2017,** *89* (21), 11427-11434.

145.   Chen, T. H.; Zhang, S. W.; Jaishi, M.; Adhikari, R.; Bi, J. H.; Fang, M. X.; Xia, S.; Luck, R. L.; Pati, R.; Lee, H. M.; Luo, F. T.; Tiwari, A.; Liu, H. Y., New Near-Infrared Fluorescent Probes with Single-Photon Anti-Stokes-Shift Fluorescence for Sensitive Determination of pH Variances in Lysosomes with a Double-Checked Capability. *ACS Applied Bio Materials* **2018**, DOI: 10.1021/acsabm.8b00020.

146.   Xu, B.; Chi, Z.; Li, H.; Zhang, X.; Li, X.; Liu, S.; Zhang, Y.; Xu, J., Synthesis and Properties of Aggregation-Induced Emission Compounds Containing Triphenylethene and Tetraphenylethene Moieties. *The Journal of Physical Chemistry C* **2011,** *115* (35), 17574-17581.

147.   Hanwell, M. D.; Curtis, D. E.; Lonie, D. C.; Vandermeersch, T.; Zurek, E.; Hutchison, G. R., Avogadro: an advanced semantic chemical editor, visualization, and analysis platform. *J. Cheminform.* **2012,** *4*.

148.   Frisch, M. J.; Trucks, G. W.; Schlegel, H. B.; Scuseria, G. E.; Robb, M. A.; Cheeseman, J. R.; Scalmani, G.; Barone, V.; Mennucci, B.; Petersson, G. A.; Nakatsuji, H.; Caricato, M.; Li, X.; Hratchian, H. P.; Izmaylov, A. F.; Bloino, J.; Zheng, G.; Sonnenberg, J. L.; Hada, M.; Ehara, M.; Toyota, K.; Fukuda, R.; Hasegawa, J.; Ishida, M.; Nakajima, T.; Honda, Y.; Kitao, O.; Nakai, H.; Vreven, T.; Montgomery, J. A.; Peralta, J., J. E. ; Ogliaro, F.; Bearpark, M.; Heyd, J. J.; Brothers, E.; Kudin, K. N.; Staroverov, V. N.; Kobayashi, R.; Normand, J.; Raghavachari, K.; Rendell, A.; Burant, J. C.; Iyengar, S. S.; Tomasi, J.; Cossi, M.; Rega, N.; Millam, J. M.; Klene, M.; Knox, J. E.; Cross, J. B.; Bakken, V.; Adamo, C.; Jaramillo, J.; Gomperts, R.; Stratmann, R. E.; Yazyev, O.; Austin, A. J.; Cammi, R.; Pomelli, C.; Ochterski, J. W.; Martin, R. L.; Morokuma, K.; Zakrzewski, V. G.; Voth, G. A.; Salvador, P.; Dannenberg, J. J.; Dapprich, S.; Daniels, A. D.; Farkas, Ö.; Foresman, J. B.; Ortiz, J. V.; Cioslowski, J.; Fox, D. J., *Gaussian 16*. Gaussian, Inc.: Wallingford CT, 2016. , 2016.

149.   Staroverov, V. N.; Scuseria, G. E.; Tao, J. M.; Perdew, J. P., Comparative assessment of a new nonempirical density functional: Molecules and hydrogen-bonded complexes. *J. Chem. Phys.* **2003,** *119* (23), 12129-12137.

150.   Tao, J. M.; Perdew, J. P.; Staroverov, V. N.; Scuseria, G. E., Climbing the density functional ladder: Nonempirical meta-generalized gradient approximation designed for molecules and solids. *Phys. Rev. Lett.* **2003,** *91* (14).

151.   Schafer, A.; Huber, C.; Ahlrichs, R., FULLY OPTIMIZED CONTRACTED GAUSSIAN-BASIS SETS OF TRIPLE ZETA VALENCE QUALITY FOR ATOMS LI TO KR. *J. Chem. Phys.* **1994,** *100* (8), 5829-5835.

152.   Casida, M. E.; Jamorski, C.; Casida, K. C.; Salahub, D. R., Molecular excitation energies to high-lying bound states from time-dependent density-functional response theory: Characterization and correction of the time-dependent local density approximation ionization threshold. *J. Chem. Phys.* **1998,** *108* (11), 4439-4449.

153.   Cances, E.; Mennucci, B.; Tomasi, J., A new integral equation formalism for the polarizable continuum model: Theoretical background and applications to isotropic and anisotropic dielectrics. *J. Chem. Phys.* **1997,** *107* (8), 3032-3041.

154.   Macrae, C. F.; Bruno, I. J.; Chisholm, J. A.; Edgington, P. R.; McCabe, P.; Pidcock, E.; Rodriguez-Monge, L.; Taylor, R.; van de Streek, J.; Wood, P. A., Mercury CSD 2.0 - new features for the visualization and investigation of crystal structures. *J. Appl. Crystallogr.* **2008,** *41*, 466-470.

155.   Mei, J.; Hong, Y. N.; Lam, J. W. Y.; Qin, A. J.; Tang, Y. H.; Tang, B. Z., Aggregation-Induced Emission: The Whole Is More Brilliant than the Parts. *Adv. Mater.* **2014,** *26* (31), 5429-5479.

156.   Qian, J.; Tang, B. Z., AIE Luminogens for Bioimaging and Theranostics: from Organelles to Animals. *Chem* **2017,** *3* (1), 56-91.

157.   Hu, R.; Leung, N. L. C.; Tang, B. Z., AIE macromolecules: syntheses, structures and functionalities. *Chem. Soc. Rev.* **2014,** *43* (13), 4494-4562.

158.   Ding, D.; Li, K.; Liu, B.; Tang, B. Z., Bioprobes Based on AIE Fluorogens. *Acc. Chem. Res.* **2013,** *46* (11), 2441-2453.

159.   Kwok, R. T. K.; Leung, C. W. T.; Lam, J. W. Y.; Tang, B. Z., Biosensing by luminogens with aggregation-induced emission characteristics. *Chem. Soc. Rev.* **2015,** *44* (13), 4228-4238.

160.   Feng, G. X.; Liu, B., Multifunctional AIEgens for Future Theranostics. *Small* **2016,** *12* (47), 6528-6535.

161.   Hu, F.; Liu, B., Organelle-specific bioprobes based on fluorogens with aggregation-induced emission (AIE) characteristics. *Org. Biomol. Chem.* **2016,** *14* (42), 9931-9944.

162.   Liang, J.; Tang, B.; Liu, B., Specific light-up bioprobes based on AIEgen conjugates. *Chem. Soc. Rev.* **2015,** *44* (10), 2798-2811.

163.   Liu, H. Y.; Fang, M. X.; Xia, S. H.; Bi, J. H.; Wigstrom, T. P.; Valenzano, L.; Wang, J. B.; Mazi, W.; Tanasova, M.; Luo, F.-T., A Cyanine-based Fluorescent Cassette with Aggregation-induced Emission for Sensitive Detection of pH Changes in Live Cells. *Chemical Communications (Cambridge)* **2018**, 10.1039/C7CC08986D.

164.   Tao, J.; Perdew, J. P.; Staroverov, V. N.; Scuseria, G. E., Climbing the Density Functional Ladder: Nonempirical Meta--Generalized Gradient Approximation Designed for Molecules and Solids. *Phys. Rev. Lett.* **2003,** *91* (14), 146401.

165.   Staroverov, V. N.; Scuseria, G. E.; Tao, J.; Perdew, J. P., Comparative assessment of a new nonempirical density functional: Molecules and hydrogen-bonded complexes. *The Journal of Chemical Physics* **2003,** *119* (23), 12129-12137.

166.   Schäfer, A.; Huber, C.; Ahlrichs, R., Fully optimized contracted Gaussian basis sets of triple zeta valence quality for atoms Li to Kr. *The Journal of Chemical Physics* **1994,** *100* (8), 5829-5835.

167.   Macrae, C. F.; Bruno, I. J.; Chisholm, J. A.; Edgington, P. R.; McCabe, P.; Pidcock, E.; Rodriguez-Monge, L.; Taylor, R.; van de Streek, J.; Wood, P. A., Mercury CSD 2.0 - New Features for the Visualization and Investigation of Crystal Structures *J. Appl. Crystallogr.* **2008,** *41*, 466-470.

168.   Wei, Y. F.; Cheng, D.; Ren, T. B.; Li, Y. H.; Zeng, Z. B.; Yuan, L., Design of NIR Chromenylium-Cyanine Fluorophore Library for "Switch-ON" and Ratiometric Detection of Bio-Active Species In Vivo. *Anal. Chem.* **2016,** *88* (3), 1842-1849.

169.   Mahon, G. J.; Anderson, H. R.; Gardiner, T. A.; McFarlane, S.; Archer, D. B.; Stitt, A. W., Chloroquine causes lysosomal dysfunction in neural retina and RPE: Implications for retinopathy. *Curr. Eye Res.* **2004,** *28* (4), 277-284.

170.   Wu, L. L.; Li, X. L.; Huang, C. S.; Jia, N. Q., Dual-Modal Colorimetric/Fluorescence Molecular Probe for Ratiometric Sensing of pH and Its Application. *Anal. Chem.* **2016,** *88* (16), 8332-8338.

171.   Zhang, Y.; Xia, S.; Mikesell, L.; Whisman, N.; Fang, M.; Steenwinkel, T. E.; Chen, K.; Luck, R. L.; Werner, T.; Liu, H., Near-Infrared Hybrid Rhodol Dyes with Spiropyran Switches for Sensitive Ratiometric Sensing of pH Changes in Mitochondria and Drosophila melanogaster First-Instar Larvae. *ACS Applied Bio Materials* **2019,** *2* (11), 4986-4997.

172.   Zielonka, J.; Joseph, J.; Sikora, A.; Hardy, M.; Ouari, O.; Vasquez-Vivar, J.; Cheng,   G.;   Lopez,   M.;   Kalyanaraman,   B.,   Mitochondria-Targeted

Triphenylphosphonium-Based Compounds: Syntheses, Mechanisms of Action, and Therapeutic and Diagnostic Applications. *Chem. Rev.* **2017,** *117* (15), 10043-10120.

173.   Lin, M. T.; Beal, M. F., Mitochondrial dysfunction and oxidative stress in neurodegenerative diseases. *Nature* **2006,** *443* (7113), 787-795.

174.   Vasquez-Trincado, C.; Garcia-Carvajal, I.; Pennanen, C.; Parra, V.; Hill, J. A.; Rothermel, B. A.; Lavandero, S., Mitochondrial dynamics, mitophagy and cardiovascular disease. *Journal of Physiology-London* **2016,** *594* (3), 509-525.

175.   Cadonic, C.; Sabbir, M. G.; Albensi, B. C., Mechanisms of Mitochondrial Dysfunction in Alzheimer's Disease. *Molecular Neurobiology* **2016,** *53* (9), 6078-6090.

176.   Liu, Y.; Zhou, J.; Wang, L. L.; Hu, X. X.; Liu, X. J.; Liu, M. R.; Cao, Z. H.; Shangguan, D. H.; Tan, W. H., A Cyanine Dye to Probe Mitophagy: Simultaneous Detection of Mitochondria and Autolysosomes in Live Cells. *J. Am. Chem. Soc.* **2016,** *138* (38), 12368-12374.

177.   Xu, W.; Zeng, Z. B.; Jiang, J. H.; Chang, Y. T.; Yuan, L., Discerning the Chemistry in Individual Organelles with Small-Molecule Fluorescent Probes. *Angewandte Chemie-International Edition* **2016,** *55* (44), 13658-13699.

178.   Chen, Y. C.; Zhu, C. C.; Cen, J. J.; Bai, Y.; He, W. J.; Guo, Z. J., Ratiometric detection of pH fluctuation in mitochondria with a new fluorescein/cyanine hybrid sensor. *Chemical Science* **2015,** *6* (5), 3187-3194.

179.   Sarkar, A. R.; Heo, C. H.; Xu, L.; Lee, H. W.; Si, H. Y.; Byun, J. W.; Kim, H. M., A ratiometric two-photon probe for quantitative imaging of mitochondrial pH values. *Chemical Science* **2016,** *7* (1), 766-773.

180.   Cao, L. X.; Zhao, Z. S.; Zhang, T.; Guo, X. D.; Wang, S. Q.; Li, S. Y.; Li, Y.; Yang, G. Q., In vivo observation of the pH alternation in mitochondria for various external stimuli. *Chem. Commun.* **2015,** *51* (97), 17324-17327.

181.   Lee, M. H.; Sessler, J. L.; Kim, J. S., Disulfide-Based Multifunctional Conjugates for Targeted Theranostic Drug Delivery. *Accounts of Chemical Research* **2015,** *48* (11), 2935-2946.

182.   Han, J. Y.; Burgess, K., Fluorescent Indicators for Intracellular pH. *Chem. Rev.* **2010,** *110* (5), 2709-2728.

183.   Fu, W.; Yan, C. X.; Guo, Z. Q.; Zhang, J. J.; Zhang, H. Y.; Tian, H.; Zhu, W. H., Rational Design of Near-Infrared Aggregation-Induced-Emission Active Probes: In Situ Mapping of Annyloid-beta Plaques with Ultrasensitivity and High-Fidelity. *J. Am. Chem. Soc.* **2019,** *141* (7), 3171-3177.

184.   Yan, C. X.; Guo, Z. Q.; Shen, Y. Y.; Chen, Y.; Tian, H.; Zhu, W. H., Molecularly precise self-assembly of theranostic nanoprobes within a single-molecular framework for in vivo tracking of tumor-specific chemotherapy. *Chem. Sci.* **2018,** *9* (22), 4959-4969.

185.   Yan, C. X.; Guo, Z. Q.; Liu, Y. J.; Shi, P.; Tian, H.; Zhu, W. H., A sequence-activated AND logic dual-channel fluorescent probe for tracking programmable drug release. *Chem. Sci.* **2018,** *9* (29), 6176-6182.

186.   Roth, A.; Li, H.; Anorma, C.; Chan, J., A Reaction-Based Fluorescent Probe for Imaging of Formaldehyde in Living Cells. *J. Am. Chem. Soc.* **2015,** *137* (34), 10890-10893.

187.   Zhang, S. W.; Adhikari, R.; Fang, M. X.; Dorh, N.; Li, C.; Jaishi, M.; Zhang, J. T.; Tiwari, A.; Pati, R.; Luo, F. T.; Liu, H. Y., Near-Infrared Fluorescent Probes with Large Stokes Shifts for Sensing Zn(II) Ions in Living Cells. *ACS Sens.* **2016,** *1* (12), 1408-1415.

188.   Grzybowski, M.; Taki, M.; Yamaguchi, S., Selective Conversion of P=O-Bridged Rhodamines into P=O-Rhodols: Solvatochromic Near-Infrared Fluorophores. *Chemistry-a European Journal* **2017,** *23* (53), 13028-13032.

189.   Yuan, L.; Lin, W. Y.; Zhao, S.; Gao, W. S.; Chen, B.; He, L. W.; Zhu, S. S., A Unique Approach to Development of Near-Infrared Fluorescent Sensors for in Vivo Imaging. *J. Am. Chem. Soc.* **2012,** *134* (32), 13510-13523.

190.   Li, X. H.; Gao, X. H.; Shi, W.; Ma, H. M., Design Strategies for Water-Soluble Small Molecular Chromogenic and Fluorogenic Probes. *Chem. Rev.* **2014,** *114* (1), 590-659.

191.   Shao, N.; Jin, J. Y.; Wang, H.; Zheng, J.; Yang, R. H.; Chan, W. H.; Abliz, Z., Design of Bis-spiropyran Ligands as Dipolar Molecule Receptors and Application to in Vivo Glutathione Fluorescent Probes. *J. Am. Chem. Soc.* **2010,** *132* (2), 725-736.

192.   Castet, F.; Rodriguez, V.; Pozzo, J. L.; Ducasse, L.; Plaquet, A.; Champagne, B., Design and Characterization of Molecular Nonlinear Optical Switches. *Acc. Chem. Res.* **2013,** *46* (11), 2656-2665.

193.   Yildiz, I.; Deniz, E.; Raymo, F. M., Fluorescence modulation with photochromic switches in nanostructured constructs. *Chem. Soc. Rev.* **2009,** *38* (7), 1859-1867.

194.   Barman, S.; Das, J.; Biswas, S.; Maiti, T. K.; Singh, N. D. P., A spiropyran-coumarin platform: an environment sensitive photoresponsive drug delivery system for efficient cancer therapy. *Journal of Materials Chemistry B* **2017,** *5* (21), 3940-3944.

195.   Shiraishi, Y.; Sumiya, S.; Hirai, T., Highly sensitive cyanide anion detection with a coumarin-spiropyran conjugate as a fluorescent receptor. *Chem. Commun.* **2011,** *47* (17), 4953-4955.

196.   Su, T.; Cheng, F. R.; Cao, J.; Yan, J. Q.; Peng, X. Y.; He, B., Dynamic intracellular tracking nanoparticles via pH-evoked "off-on" fluorescence. *Journal of Materials Chemistry B* **2017,** *5* (17), 3107-3110.

197.   Zhang, Y.; Ma, L.; Tang, C.; Pan, S.; Shi, D.; Wang, S.; Li, M.; Guo, Y., A highly sensitive and rapidly responding fluorescent probe based on a rhodol fluorophore for imaging endogenous hypochlorite in living mice. *Journal of Materials Chemistry B* **2018,** *6* (5), 725-731.

198.   Zhang, Y. B.; Xia, S.; Fang, M. X.; Mazi, W.; Zeng, Y. B.; Johnston, T.; Pap, A.; Luck, R. L.; Liu, H. Y., New near-infrared rhodamine dyes with large Stokes shifts for sensitive sensing of intracellular pH changes and fluctuations. *Chem. Commun.* **2018,** *54* (55), 7625-7628.

199.   Chen, T. H.; Zhang, S. W.; Jaishi, M.; Adhikari, R.; Bi, J. H.; Fang, M. X.; Xia, S.; Luck, R. L.; Pati, R.; Lee, H. M.; Luo, F. T.; Tiwari, A.; Liu, H. Y., New Near-Infrared Fluorescent Probes with Single-Photon Anti-Stokes-Shift Fluorescence for Sensitive Determination of pH Variances in Lysosomes with a Double-Checked Capability. *ACS Applied Bio Materials* **2018,** *1* (3), 549-560.

200.   Jacquemin, D.; Wathelet, V.; Perpète, E. A.; Adamo, C., Extensive TD-DFT Benchmark: Singlet-Excited States of Organic Molecules. *Journal of Chemical Theory and Computation* **2009,** *5* (9), 2420-2435.

201.   Eiyama, A.; Kondo-Okamoto, N.; Okamoto, K., Mitochondrial degradation during starvation is selective and temporally distinct from bulk autophagy in yeast. *FEBS Lett.* **2013,** *587* (12), 1787-1792.

202.   Xia, S.; Zhang, Y.; Fang, M.; Mikesell, L.; Steenwinkel, T. E.; Wan, S.; Phillips, T.; Luck, R. L.; Werner, T.; Liu, H., A FRET-Based Near-Infrared Fluorescent Probe for Ratiometric Detection of Cysteine in Mitochondria. *ChemBioChem* **2019,** *20* (15), 1986-1994.

203.   Yue, Y. K.; Huo, F. J.; Ning, P.; Zhang, Y. B.; Chao, J. B.; Meng, X. M.; Yin, C. X., Dual-Site Fluorescent Probe for Visualizing the Metabolism of Cys in Living Cells. *J. Am. Chem. Soc.* **2017,** *139* (8), 3181-3185.

204.   Lim, C. S.; Masanta, G.; Kim, H. J.; Han, J. H.; Kim, H. M.; Cho, B. R., Ratiometric Detection of Mitochondrial Thiols with a Two-Photon Fluorescent Probe. *J. Am. Chem. Soc.* **2011,** *133* (29), 11132-11135.

205.   Liu, J.; Sun, Y. Q.; Huo, Y. Y.; Zhang, H. X.; Wang, L. F.; Zhang, P.; Song, D.; Shi, Y. W.; Guo, W., Simultaneous Fluorescence Sensing of Cys and GSH from Different Emission Channels. *J. Am. Chem. Soc.* **2014,** *136* (2), 574-577.
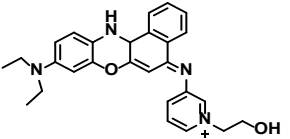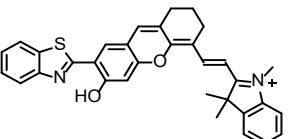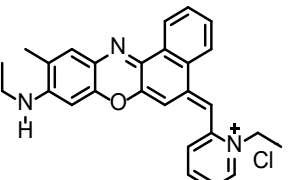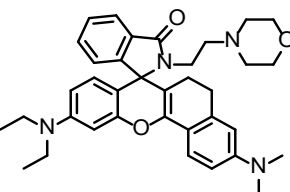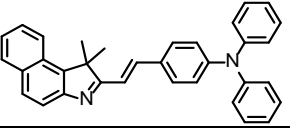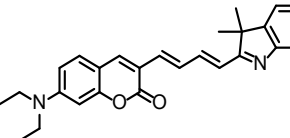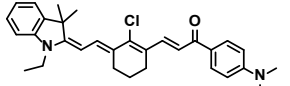
206.   Zhang, S.; Ong, C. N.; Shen, H. M., Critical roles of intracellular thiols and calcium in parthenolide-induced apoptosis in human colorectal cancer cells. *Cancer Lett.* **2004,** *208* (2), 143-153.

207.   Townsend, D. M.; Tew, K. D.; Tapiero, H., Sulfur containing amino acids and human disease. *Biomed. Pharmacother.* **2004,** *58* (1), 47-55.

208.   Zhang, J. J.; Wang, J. X.; Liu, J. T.; Ning, L. L.; Zhu, X. Y.; Yu, B. F.; Liu, X. Y.; Yao, X. J.; Zhang, H. X., Near-Infrared and Naked-Eye Fluorescence Probe for Direct and Highly Selective Detection of Cysteine and Its Application in Living Cells. *Anal. Chem.* **2015,** *87* (9), 4856-4863.

209.   Chen, X.; Zhou, Y.; Peng, X. J.; Yoon, J., Fluorescent and colorimetric probes for detection of thiols. *Chem. Soc. Rev.* **2010,** *39* (6), 2120-2135.

210.   Jung, H. S.; Chen, X. Q.; Kim, J. S.; Yoon, J., Recent progress in luminescent and colorimetric chemosensors for detection of thiols. *Chem. Soc. Rev.* **2013,** *42* (14), 6019-6031.

211.   Yang, X. P.; Liu, W. Y.; Tang, J.; Li, P.; Weng, H. B.; Ye, Y.; Xian, M.; Tang, B.; Zhao, Y. F., A multi-signal mitochondria-targeted fluorescent probe for real-time visualization of cysteine metabolism in living cells and animals. *Chem. Commun.* **2018,** *54* (81), 11387-11390.

212.   Liu, Y.; Yu, D. H.; Ding, S. S.; Xiao, Q.; Guo, J.; Feng, G. Q., Rapid and Ratiometric Fluorescent Detection of Cysteine with High Selectivity and Sensitivity by a Simple and Readily Available Probe. *Acs Applied Materials & Interfaces* **2014,** *6* (20), 17543-17550.

213.   Xue, S. H.; Ding, S. S.; Zhai, Q. S.; Zhang, H. Y.; Feng, G. Q., A readily available colorimetric and near-infrared fluorescent turn-on probe for rapid and selective detection of cysteine in living cells. *Biosens. Bioelectron.* **2015,** *68*, 316-321.

214.   Huang, Y. L.; Zhou, Q.; Feng, Y.; Zhang, W.; Fang, G. S.; Fang, M.; Chen, M.; Xu, C. Z.; Meng, X. M., Rational design of a ratiometric two-photon fluorescent probe for real-time visualization of apoptosis. *Chem. Commun.* **2018,** *54* (74), 10495-10498.

215.   He, L. W.; Yang, X. L.; Xu, K. X.; Lin, W. Y., Improved Aromatic Substitution Rearrangement-Based Ratiometric Fluorescent Cysteine-Specific Probe and Its Application of Real-Time Imaging under Oxidative Stress in Living Zebrafish. *Anal. Chem.* **2017,** *89* (17), 9567-9573.

216.   Niu, W. F.; Guo, L.; Li, Y. H.; Shuang, S. M.; Dong, C.; Wong, M. S., Highly Selective Two-Photon Fluorescent Probe for Ratiometric Sensing and Imaging Cysteine in Mitochondria. *Anal. Chem.* **2016,** *88* (3), 1908-1914.
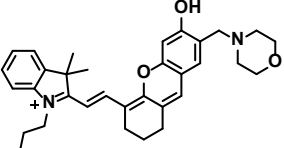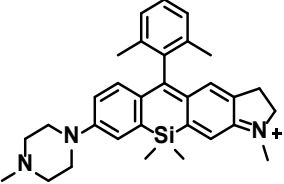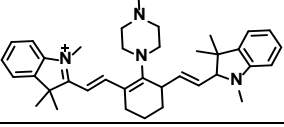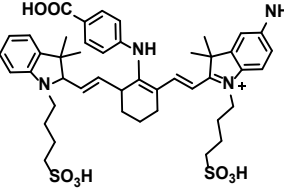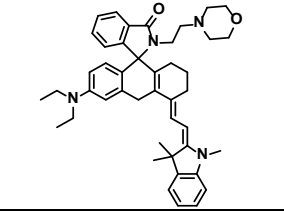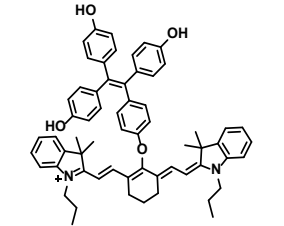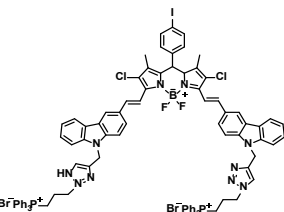
217.   Ren, T. B.; Zhang, Q. L.; Su, D. D.; Zhang, X. X.; Yuan, L.; Zhang, X. B., Detection of analytes in mitochondria without interference from other sites based on an innovative ratiometric fluorophore. *Chem. Sci.* **2018,** *9* (24), 5461-5466.

218.   Lv, H. M.; Yang, X. F.; Zhong, Y. G.; Guo, Y.; Li, Z.; Li, H., Native Chemical Ligation Combined with Spirocyclization of Benzopyrylium Dyes for the Ratiometric and Selective Fluorescence Detection of Cysteine and Homocysteine. *Anal. Chem.* **2014,** *86* (3), 1800-1807.

219.   Qi, S. J.; Liu, W. M.; Zhang, P. P.; Wu, J. S.; Zhang, H. Y.; Ren, H. H.; Ge, J. C.; Wang, P. F., A colorimetric and ratiometric fluorescent probe for highly selective detection of glutathione in the mitochondria of living cells. *Sensors and Actuators B-Chemical* **2018,** *270*, 459-465.

220.   Cheng, D.; Pan, Y.; Wang, L.; Zeng, Z. B.; Yuan, L.; Zhang, X. B.; Chang, Y. T., Selective Visualization of the Endogenous Peroxynitrite in an Inflamed Mouse Model by a Mitochondria-Targetable Two-Photon Ratiometric Fluorescent Probe. *J. Am. Chem. Soc.* **2017,** *139* (1), 285-292.

221.   Wang, J. B.; Xia, S.; Bi, J. H.; Zhang, Y. B.; Fang, M. X.; Luck, R. L.; Zeng, Y. B.; Chen, T. H.; Lee, H. M.; Liu, H. Y., Near-infrared fluorescent probes based on TBET and FRET rhodamine acceptors with different pK(a) values for sensitive ratiometric visualization of pH changes in live cells. *Journal of Materials Chemistry B* **2019,** *7* (2), 198-209.

222.   Zhang, Y. B.; Bi, J. H.; Xia, S.; Mazi, W.; Wan, S. L.; Mikesell, L.; Luck, R. L.; Liu, H. Y., A Near-Infrared Fluorescent Probe Based on a FRET Rhodamine Donor Linked to a Cyanine Acceptor for Sensitive Detection of Intracellular pH Alternations. *Molecules* **2018,** *23* (10).

223.   Schäfer, A.; Horn, H.; Ahlrichs, R., Fully optimized contracted Gaussian basis sets for atoms Li to Kr. **1992,** *97* (4), 2571-2577.

224.   Frisch, M. J.; Trucks, G. W.; Schlegel, H. B.; Scuseria, G. E.; Robb, M. A.; Cheeseman, J. R.; Scalmani, G.; Barone, V.; Petersson, G. A.; Nakatsuji, H.; Li, X.; Caricato, M.; Marenich, A. V.; Bloino, J.; Janesko, B. G.; Gomperts, R.; Mennucci, B.; Hratchian, H. P.; Ortiz, J. V.; Izmaylov, A. F.; Sonnenberg, J. L.; Williams-Young, D.; Ding, F.; Lipparini, F.; Egidi, F.; Goings, J.; Peng, B.; Petrone, A.; Henderson, T.; Ranasinghe, D.; Zakrzewski, V. G.; Gao, J.; Rega, N.; Zheng, G.; Liang, W.; Hada, M.; Ehara, M.; Toyota, K.; Fukuda, R.; Hasegawa, J.; Ishida, M.; Nakajima, T.; Honda, Y.; Kitao, O.; Nakai, H.; Vreven, T.; Throssell, K.; Montgomery, J. A., Jr; Peralta, J. E.; Ogliaro, F.; Bearpark, M. J.; Heyd, J. J.; Brothers, E. N.; Kudin, K. N.; Staroverov, V. N.; Keith, T. A.; Kobayashi, R.; Normand, J.; Raghavachari, K.; Rendell, A. P.; Burant, J. C.; Iyengar, S. S.; Tomasi, J.; Cossi, M.; Millam, J. M.; Klene, M.; Adamo, C.; Cammi, R.; Ochterski, J. W.; Martin, R. L.; Morokuma, K.; Farkas, O.; Foresman, J. B.; Fox, D. J. *Gaussian 16, Revision A.03*, Gaussian, Inc.: Wallingford CT, 2016.
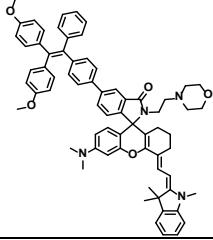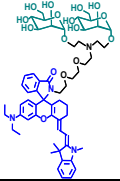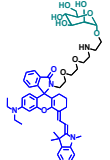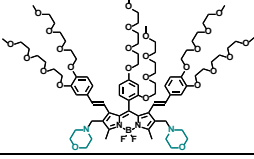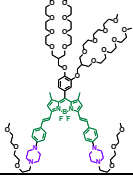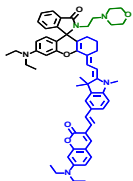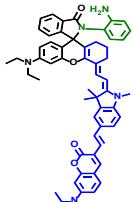
225.   Vegesna, G. K.; Sripathi, S. R.; Zhang, J. T.; Zhu, S. L.; He, W. L.; Luo, F. T.; Jahng, W. J.; Frost, M.; Liu, H. Y., Highly Water-Soluble BODIPY-Based Fluorescent Probe for Sensitive and Selective Detection of Nitric Oxide in Living Cells. *Acs Applied Materials & Interfaces* **2013,** *5* (10), 4107-4112.

226.   Cheng, D.; Pan, Y.; Wang, L.; Zeng, Z.; Yuan, L.; Zhang, X.; Chang, Y.-T., Selective Visualization of the Endogenous Peroxynitrite in an Inflamed Mouse Model by a Mitochondria-Targetable Two-Photon Ratiometric Fluorescent Probe. *Journal of the American Chemical Society* **2017,** *139* (1), 285-292.
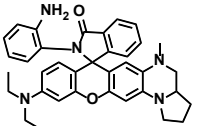
Appendix A Supporting Information for Chapter 2

1. Summary of near-infrared fluorescent probes for detection of pH.

Probe structure	Molar Absorption Coefficients (M^{-1} cm^{-1})	Absorbance Maxima (nm)	Emission Maxima (nm)	fluorescence Quantum Yields	solvent	pK$_a$
	33000	630	723	0.01	phosphate buffer containing 0.1% DMSO	7.1
	130000	608	672	0.17	phosphate buffer	7.2
	34200	612	641	1.1	phosphate buffer	2.4
	-	580	650	0.24	40 mM BR buffer	5.04
	72800	546	655	0.22	ethanol/ water (2/1, v/v)	4.40
	54500	572	722	0.026	acetonitrile– buffer (v/v, 3 : 7) solution	3.93
	30000	529	680	0.01	phosphate buffer	6.3

		681	708	0.16	phosphate buffer	5.0
	25000	605	683	0.18	phosphate buffer	6.1
	130000	759	789	0.03	phosphate buffer	5.5
		771	691	0.05	DMSO	4.71
		720	739	0.08	B-R buffer	4.98
		775	794	0.068	aqueous solution containing 30% ethanol	7.4
	58600	700	733	0.53	Ethanol	-

Structure						
	23600	715	737	0.0678	Citrate buffer containing 30% ethanol	4.9
	3.0 x 10⁴	713	740	0.081 at pH 4.4	Citrate phosphate buffer containing 1% ethanol	6.1
	3.0 x 10⁴	713	740	0.084 at pH 4.4	Citrate phosphate buffer containing 1% ethanol	5.8
		565	652	0.0032 at pH 7.4	Buffer with 1% DMSO	6.2
	4.46 x 10⁴ at pH 4.46	671	716	0.07 at pH 4.5	Buffer	3.57
	4.1×10⁴ at pH 2.5	745	755	0.083 at pH 3.0	buffer containing 40% ethanol	4.2
	3.3×10⁴ at pH 2.5	735	740	0.079 at pH 3.0	buffer containing 40% ethanol	4.8

	3.8×10⁴ at pH 3.2	587	654	0.198 at pH 3.2	Buffer containing 10% ethanol	5.4

2. Synthetic route to near-infrared rhodamine dyes A, B and C.

We showed how to prepare rhodamine dyes A-C and characterize the products by NMR and Mass spectrometer.

Scheme SA.1. Synthetic approach to prepare rhodamine dyes A-C.

Synthesis of rhodamine dye A: After compounds **4** (204 mg, 1 mmol) and 5 (313 mg, 1 mmol) were added to trifluoroacetic acid (10 ml), the mixture was heated under reflux and stirred for 8 hours. When the reaction was cooled down to room temperature, the solvent was removed under reduced pressure. The resulting residue was purified by using flash column chromatography gradient elution with methanol ratio to dichloromethane from 0% to 10%. The rhodamines **A** was obtained as blue solid. ^{1}H NMR (400 MHz, CD$_3$OD) δ 8.30 (d, J = 7.7 Hz, 1H), 7.82 (t, J = 7.5 Hz, 1H), 7.75 (t, J = 7.5 Hz, 1H), 7.36 – 7.38 (m, 1H), 7.09 (d, J = 7.8 Hz, 1H), 6.97 (d, J = 9.3 Hz, 1H), 6.91 (s, 1H), 6.73 (s, 1H), 5.96 (d, J = 3.4 Hz, 1H), 3.57 – 3.74 (m, 4H), 2.77 – 2.91 (m, 2H), 2.67 (s, 3H), 2.22 – 2.26 (m, 3H), 2.02 – 2.07 (m, 2H), 1.56 – 1.59 (m, 2H), 1.26 (t, J = 7.1 Hz, 6H).; ^{13}C NMR (100 MHz, CDCl$_3$) δ 171.02, 160.32, 159.12, 157.60, 150.96, 139.80, 138.66, 135.10, 134.17, 133.60, 119.25, 117.17, 106.78, 98.50, 62.26, 56.65, 49.21, 42.21, 33.70, 26.74, 15.65. LCMS(ESI): calculated for C$_{30}$H$_{32}$N$_3$O$_3$ [M]$^+$482.2, found 482.5.

Synthesis of rhodamine dye B: Rhodamine **B** was prepared in the same way for synthesis of rhodamine **A** by using compounds **4** (337 mg, 1 mmol) and **6** (313 mg, 1 mmol),

affording the product as blue solid. ^{1}H NMR (400 MHz, CDCl$_3$) δ: 8.18 (d, J = 7.4 Hz, 1H), 7.68 (q, J = 6.6 Hz, 2H), 7.32 – 7.23 (m, 1H), 6.72 (d, J = 6.5 Hz, 1H), 6.67 (s, 1H), 6.02 (d, J = 2.9 Hz, 1H), 3.71 – 3.84 (m, 2H), 3.45 – 3.55 (m, 4H), 3.08 – 2.96 (m, 2H), 2.62 – 2.69 (m, 7H), 2.27 – 2.16 (m, 2H), 2.06 (d, J = 5.9 Hz, 3H), 1.96 – 1.83 (m, 2H), 1.62 – 1.47 (m, 2H).; ^{13}C NMR (100 MHz, CDCl$_3$) δ: 155.92, 154.36, 151.61, 149.71, 145.91, 135.44, 134.25, 131.03, 130.50, 129.97, 125.53, 123.79, 114.50, 104.74, 103.83, 94.28, 58.11, 52.60, 50.50, 47.66, 38.35, 29.84, 27.61, 22.90, 20.85, 19.96. LCMS(ESI): calculated for C$_{32}$H$_{32}$N$_3$O$_3$ [M]$^+$506.2, found 506.5.

Synthesis of rhodamine dye C: After 1,2-diaminobenzene (324 mg, 3 mmol), rhodamines **A** (482 mg, 1 mmol), BOP reagent (530 mg, 1.2 mmol) and triethylamine(2 mL) were added to dry DCM (15 ml), the mixture was stirred at room temperature for 16 hours. Then the mixture was diluted with DCM, washed with water and brine, dried with anhydrous Na$_2$SO$_4$, filtered and concentrated in vacuo. The resulting residue was purified by using flash column chromatography gradient elution with methanol ratio to dichloromethane from 0% to 5%. The rhodamines **C** was obtained as blue solid. ^{1}H NMR (400 MHz, CDCl$_3$) δ: 7.95 (d, J = 7.5, Hz, 1H), 7.67 – 7.56 (m, 2H), 7.24 – 7.16 (m, 1H), 6.89 (d, J = 7.7, 1H), 6.57 (d, J = 8.1, 2H), 6.42 – 6.16 (m, 3H), 6.04 – 5.89 (m, 2H), 5.78 (s, 1H), 3.74 – 3.65 (m, 1H), 3.32 (d, J = 5.3 Hz, 5H), 3.14 (s, 1H), 2.47 (s, 3H), 2.25 – 2.37 (m, 1H), 1.81 – 2.02 (m, 3H), 1.22 – 1.43 (m, 2H), 1.11 (t, J = 7.0 Hz, 6H).; ^{13}C NMR (100 MHz, CDCl$_3$) δ: 167.26, 154.33, 152.76, 149.06, 137.94, 133.04, 132.98, 131.82, 128.77, 128.69, 128.58, 128.35, 124.43, 122.76, 121.48, 117.28, 116.62, 107.97, 97.95, 96.64, 69.89, 57.03, 54.67, 47.46, 44.22, 38.93, 30.16, 23.53, 11.76. LCMS(ESI): calculated for C$_{36}$H$_{38}$N$_5$O$_2$ [M]$^+$572.3, found 572.5.

3. ^{1}H and ^{13}C NMR spectra of near-infrared dyes A, B, and C.
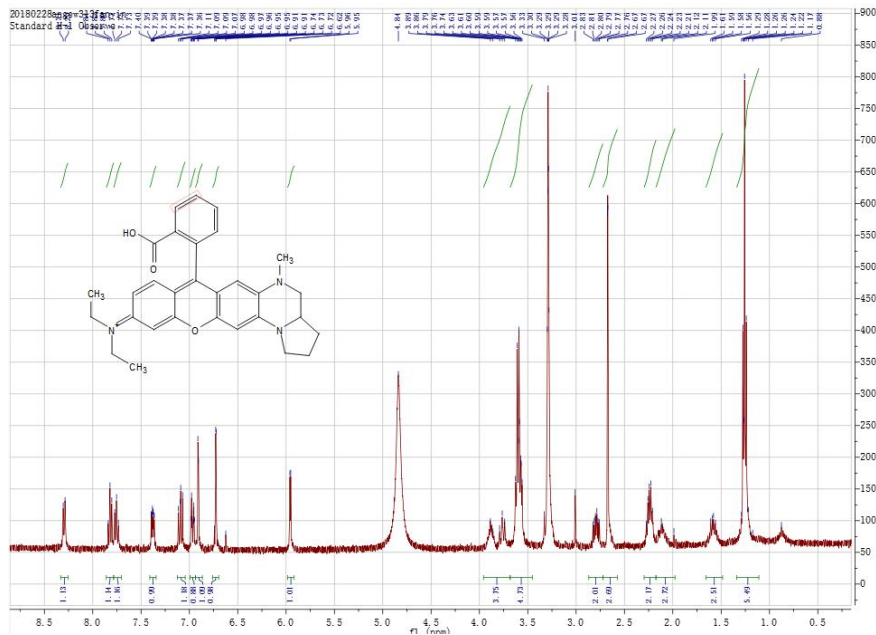

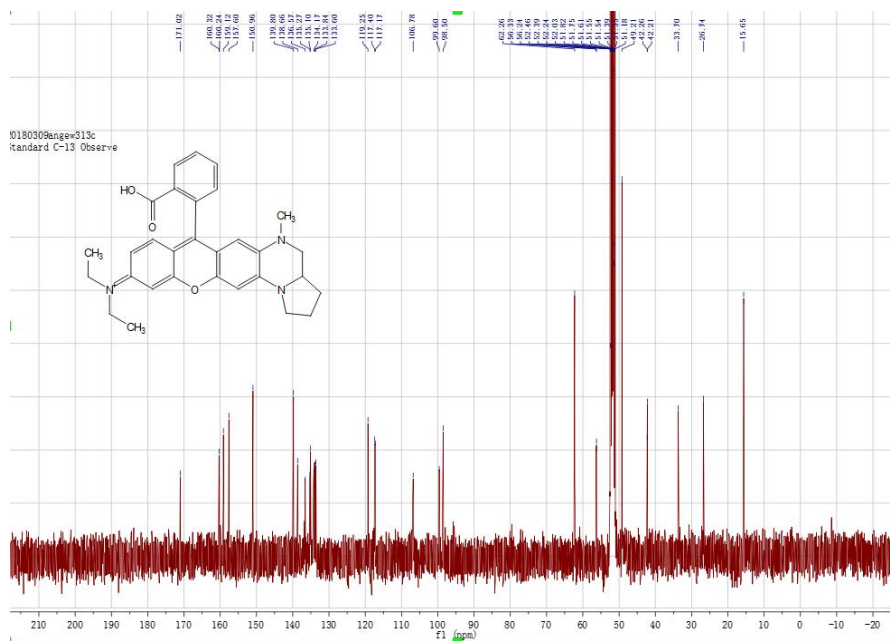**Figure S A.1**. ^{1}H NMR spectrum of rhodamine dye **A** in CD$_3$OD solution.

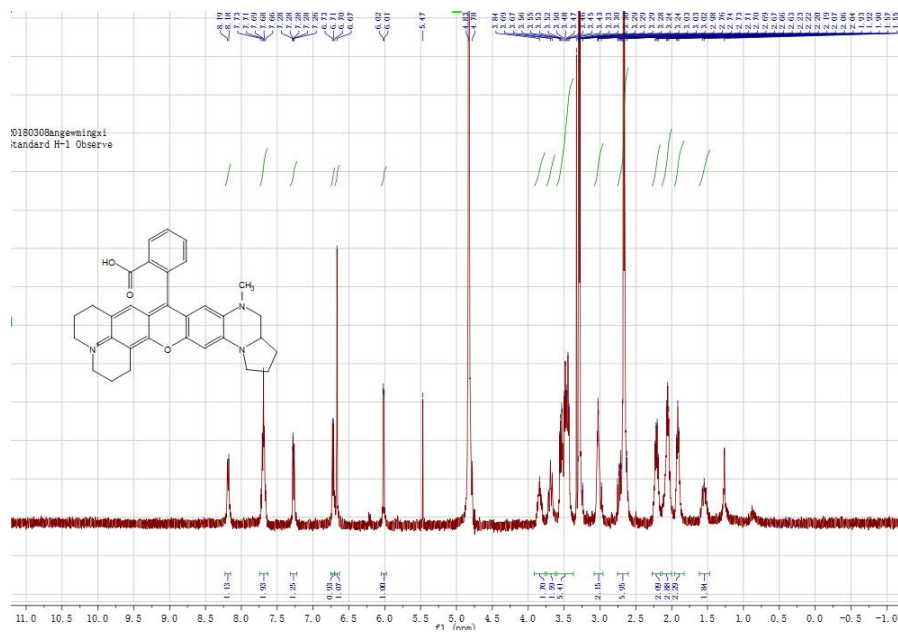**Figure S A.2**. ^{13}C NMR spectrum of rhodamine dye **A** in CD$_3$OD solution.

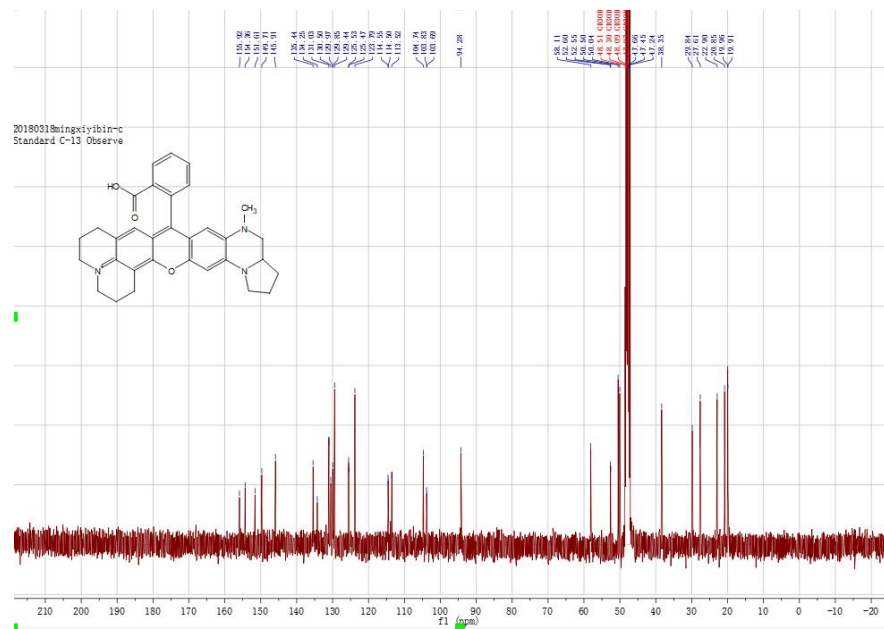**Figure S A.3**. ^{1}H NMR spectrum of rhodamine dye **B** in CD$_3$OD solution.

Figure S A.4. ^{13}C NMR spectrum of rhodamine dye **B** in CD$_3$OD solution.

Figure S A.5. ^{1}H NMR spectrum of rhodamine dye **C** in CD$_3$OD solution.

Figure S A.6. ^{13}C NMR spectrum of rhodamine dye **C** in CD$_3$OD solution.

4. A fluorescence standard and calculation of fluorescence quantum yields of the rhodamine dyes

We chose a near-infrared rhodamine dye shown below as a fluorescent standard to calculate fluorescence quantum yields of rhodamine dyes A, B and C.

Near-infrared rhodamine dye as a fluorescence standard
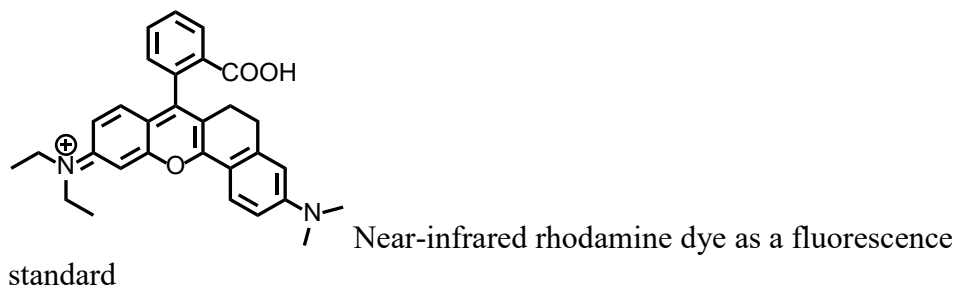
The UV-Vis absorption spectra of rhodamine **A**, **B** and **C** were collected in the range from 300 to 800 nm with increments of 1 nm. For the buffers, we prepared Citrate-phosphate buffer from pH 2.0 to pH 7.8, and carbonate-bicarbonate buffer for pH 8.8 to pH 11. Their corresponding fluorescence spectra were collected at the excitation wavelength of 550 nm with increments of 1 nm. The excitation and emission slit widths were set to 5 nm. A near-infrared rhodamine dye above was utilized as a reference standard to calculate the fluorescence quantum yields of rhodamine **A**, **B**, and **C** in ethanol and buffer solutions. The standard dye with a fluorescence quantum yield 37% in pH 7.4 PBS buffer with 10% ethanol was used. The absorbance was kept between 0.05 and 0.1 in order to obtain optimized data. All the samples and references were freshly prepared under identical conditions. The fluorescence quantum yields were calculated according to literature[4] using the equation below:

$$\phi_X = \phi_{st}(Grad_X / Grad_{st})(\eta_X^{\,2} / \eta_{st}^{\,2})$$

Where Φ is the fluorescence quantum yield, the subscripts 'st' and 'X' stand for standard and test, respectively, "Grad" represents the gradient from the plot of integrated fluorescence intensity versus absorbance and η is the refractive index of the solvent.

We investigated effect of ethanol percentage in water-ethanol mixed solution on dye fluorescence intensity (Figure S7-S9). Increase of ethanol percentages from 1% to 60% causes the dye fluorescence intensity increases to reduce dye aggregation in aqueous solutions.
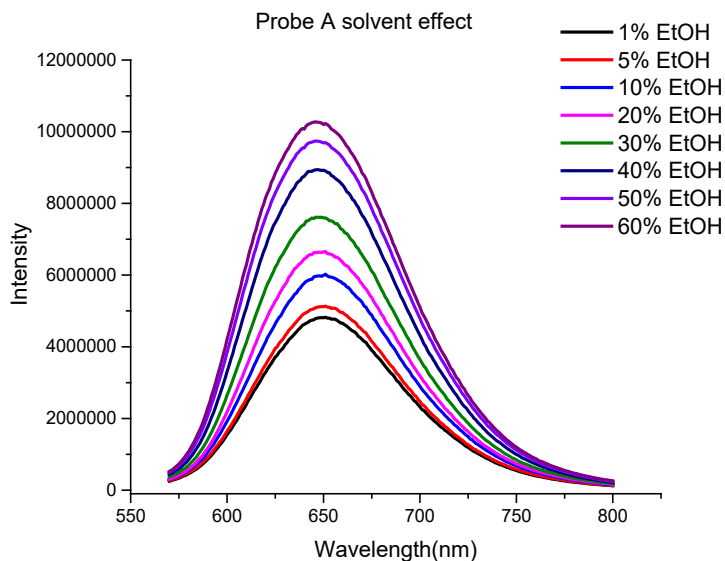

Figure S A.7. Fluorescence spectra of rhodamine dye **A** in 10 mM pH 7.4 buffers with different percentages of ethanol in ethanol and water mixed solution.
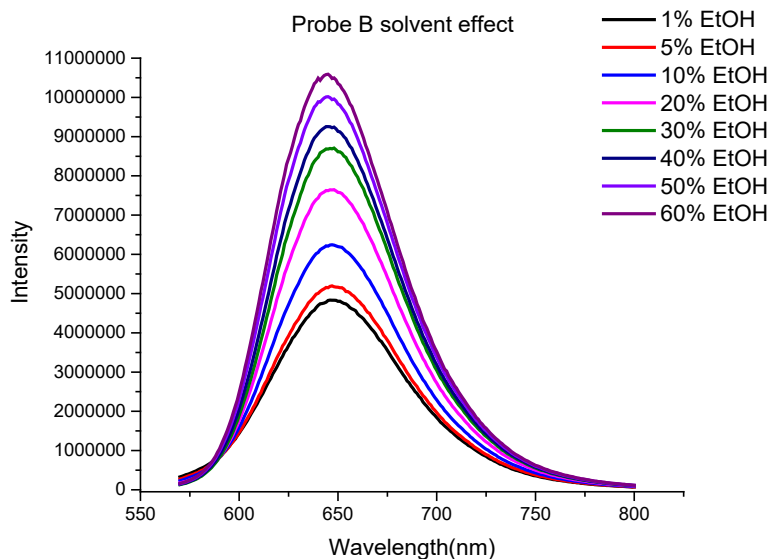

Figure S A.8. Fluorescence spectra of rhodamine dye **B** in 10 mM pH 7.4 buffers with different percentages of ethanol in ethanol and water mixed solution.
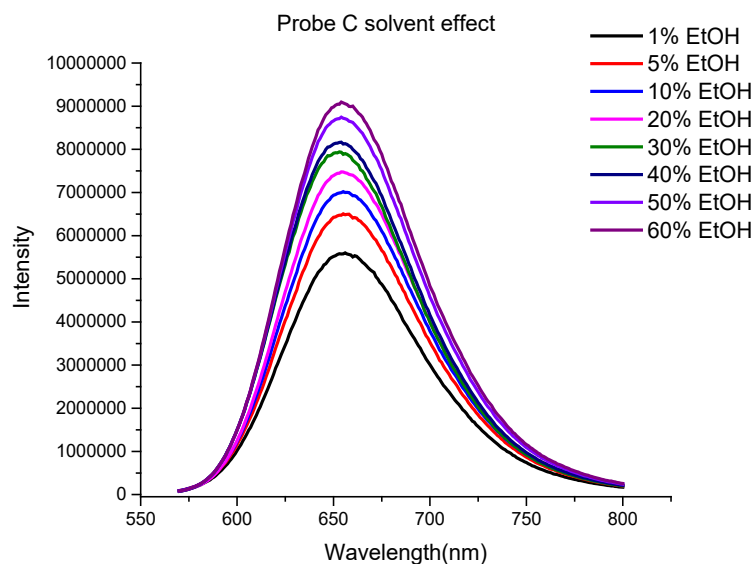
Figure S A.9. Fluorescence spectra of rhodamine dye **C** in 10 mM pH 2.4 buffers with different percentages of ethanol in ethanol and water mixed solution.

5. Determination of pK$_a$ by fluorometric titration

pK$_a$ of rhodamine dye **C** was obtained by using the equation below through fluorometric titration as a function of pH, which was obtained by using the fluorescence spectra. The expression of the steady-state fluorescence intensity F as a function of the proton concentration has been extended for the case of n: 1 complex between H$^+$ and a fluorescent dye.

$$F = \frac{F_{\min}[H^+]^n + F_{\max}K_a}{K_a + [H^+]^n}$$

$F_{\min}$ and $F_{\max}$ stand for the fluorescence intensities at maximal and minimal H$^+$ concentrations, respectively while n is apparent stoichiometry of H$^+$ binding to the rhodamine dye C. Nonlinear fitting of equation expressed above to the fluorescence titration data was plotted as a function of H$^+$ concentration.
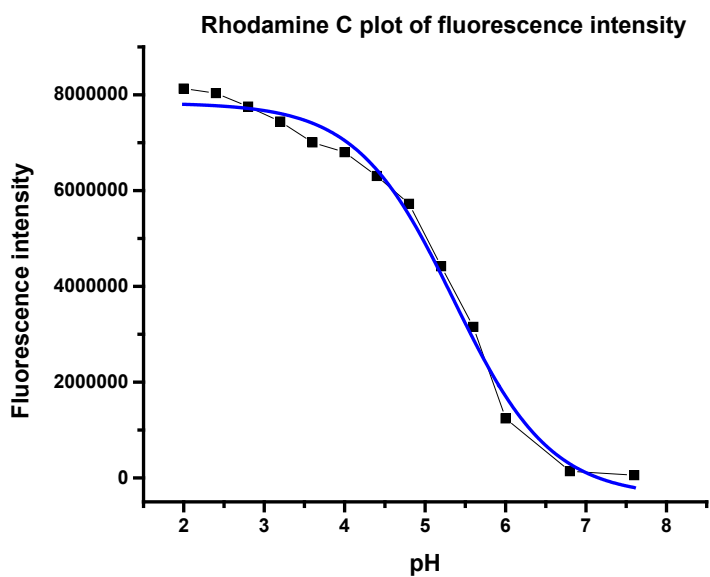
Figure S A.10. Plot curve of fluorescence intensity of rhodamine dye C versus pH

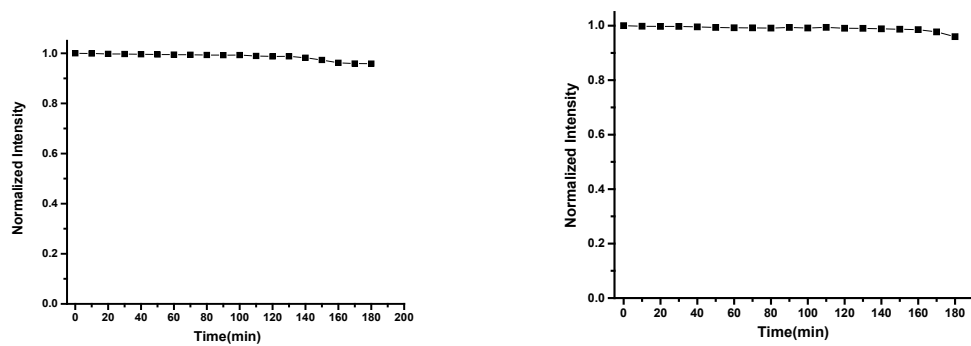# 6. Dye stability and selectivity

Figure S A.11. Fluorescence intensity of rhodamine dyes **A** (left) and **B** (right) versus excitation time in 10 mM pH 5.0 buffers
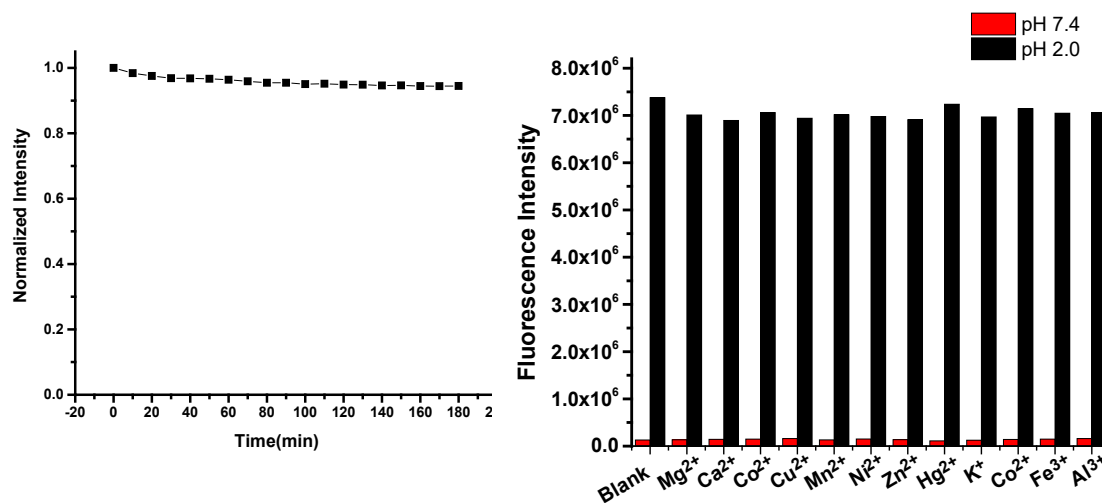
Figure S A.12. Fluorescence intensity of rhodamine dye **C** versus excitation time in 10 mM pH 2.0 buffer (left), and fluorescence responses (right) of rhodamine dye **C** to different metal ions in 10 mM buffers at pH 7,4 and 2.0 under excitation of 550 nm.
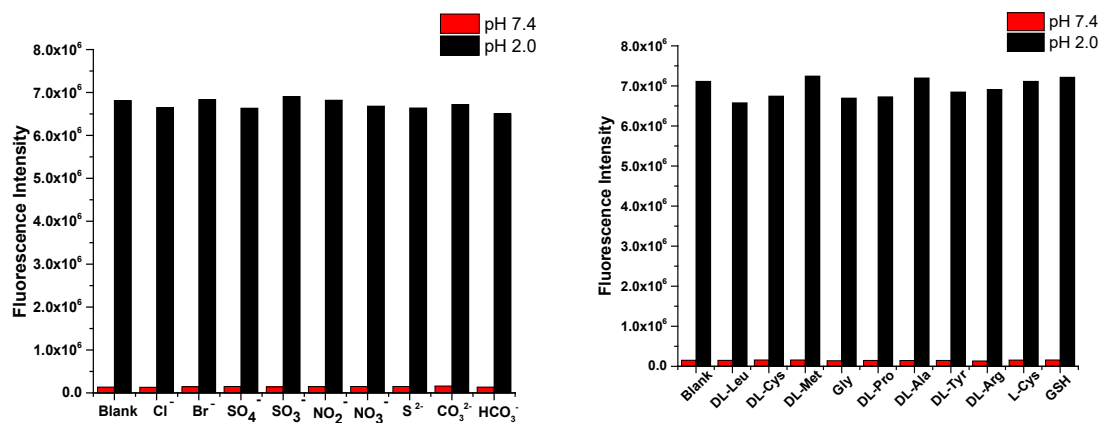

Figure S A.13. Fluorescence responses of rhodamine dye **C** to different anions and amino acids in 10 mM buffers at pH 7,4 and 2.0 under excitation of 550 nm.

7. Computationally derived structures for rhodamine dyes A-D.

The structures of rhodamine probes A-D were constructed using Avogadro and GaussView. Structures were initially optimized using the capabilities within these aforementioned programs. Calculations were then conducted using density functional theory (DFT) with spherical atom dispersion terms, namely APFD, with all electron basis sets at the 6-311+G(2d, p) level implemented using the Gaussian16 suite of programs for the full geometry optimization and frequency calculations of the probes. Imaginary frequencies were not obtained in any of the frequency calculations. The first six excited states were assessed on the basis of TD-DFT optimizations in a Polarizable Continuum Model (PCM) of water. Results were interpreted using Chemissian for the UV-plots and GausView for all other data and figures. The diagrams and listings of atomic positions from the calculations are listed sequentially for rhodamine dyes A-D below and all data are within the PCM matrix of water.
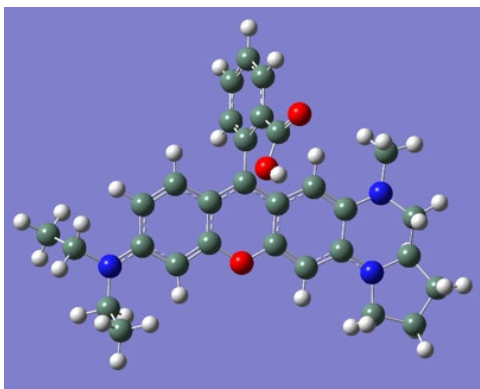

Figure S A.14. Drawing of rhodamine dye A with atoms represented as spheres of arbitrary size (H-white, C-grey, N-blue and O-red) using the GaussView program.

Table S1. Atomic coordinates for rhodamine dye A.

Row	Symbol	X	Y	Z
1	C	2.9186	-1.43723	-0.31593
2	C	1.627969	-1.97698	-0.22453
3	C	0.532581	-1.14906	-0.24277
4	C	0.660267	0.258562	-0.33456
5	C	1.970222	0.794538	-0.40591
6	C	3.089058	0.002094	-0.40136
7	C	-0.50134	1.033538	-0.31166
8	C	-1.75166	0.405999	-0.2268
9	C	-1.81101	-1.00644	-0.16436
10	C	-2.99162	-1.70334	-0.07567
11	H	-2.93883	-2.78101	-0.01166
12	C	-4.21905	-1.01167	-0.03746
13	C	-4.17397	0.418345	-0.07861
14	C	-2.99116	1.086681	-0.16733
15	N	4.371741	0.500232	-0.48887
16	N	3.996547	-2.22124	-0.33075
17	C	-5.46609	-3.12009	-0.01831
18	C	-6.66708	-0.97413	0.183902
19	C	5.407718	-0.30638	0.134967
20	C	5.355802	-1.69853	-0.44251
21	C	6.179658	-2.76461	0.260388
22	O	-0.67735	-1.74405	-0.16973
23	C	4.551324	1.931599	-0.41117
24	H	5.628165	-1.65344	-1.50543
25	C	-0.41184	2.50711	-0.41402
26	C	0.091567	3.319675	0.61159
27	C	-0.78135	3.095913	-1.62116
28	C	0.224673	4.691458	0.405626
29	C	-0.65954	4.46529	-1.8117
30	H	-1.15595	2.465755	-2.42059
31	C	-0.15434	5.266983	-0.7959
32	C	0.511527	2.807088	1.941343
33	O	1.344485	3.347713	2.632377
34	O	-0.14253	1.702128	2.316864
35	H	0.209544	1.426127	3.176885
36	C	-7.28865	-0.59408	-1.15275
37	H	-8.25278	-0.10424	-0.99639
38	H	-6.64291	0.089628	-1.70869
39	H	-7.45427	-1.48012	-1.77067
40	H	2.071821	1.868971	-0.46185
41	H	1.476886	-3.04622	-0.16029
42	H	-2.99153	2.170122	-0.19892
43	H	-5.09163	0.989328	-0.05336
44	H	3.991592	2.427257	-1.20661
45	H	5.606896	2.160578	-0.55035
46	H	4.224802	2.343549	0.554111
47	C	3.98075	-3.66511	-0.1208
48	C	5.460254	-4.05129	-0.14631
49	H	6.125656	-2.61749	1.34403
50	H	7.228148	-2.74221	-0.03846
51	N	-5.39376	-1.6671	0.037769
52	H	-7.33168	-1.64392	0.734323
53	H	-6.53323	-0.09881	0.821374
54	H	-6.43092	-3.37591	-0.46193
55	H	5.28586	-0.34378	1.227718
56	H	6.377026	0.143106	-0.0819
57	H	5.671473	-4.8902	0.517067
58	H	5.75547	-4.34168	-1.1581
59	H	-0.95497	4.903802	-2.75882
60	H	-0.05601	6.3372	-0.93978
61	H	0.62142	5.298949	1.210812
62	H	3.515945	-3.88396	0.846699
63	H	3.398617	-4.16693	-0.89843
64	C	-5.32474	-3.77154	1.35089
65	H	-4.36092	-3.53297	1.806236
66	H	-6.11189	-3.42898	2.027122
67	H	-5.40223	-4.85783	1.262586
68	H	-4.70934	-3.49068	-0.71261

HOMO

LUMO

Figure S A.15. The HOMO and LUMO for rhodamine dye A.
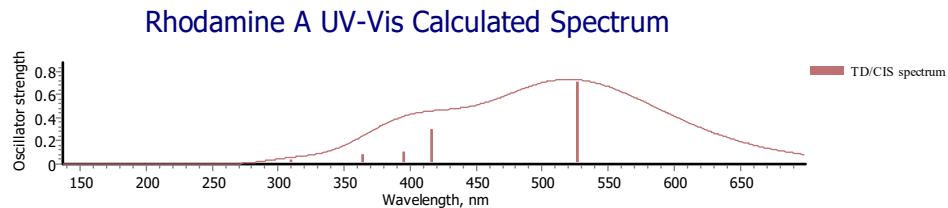
Energy[nm]	Oscillator Strength
526.3186	0.7013
416.0985	0.2919
394.9695	0.0981
363.4748	0.0816
318.7845	0.0118
309.9002	0.0366

Figure S A.16. Calculated UV-Vis spectrum for rhodamine dye **A** and listing of peak positions with oscillator strengths. This represents a HOMO-LUMO transition.
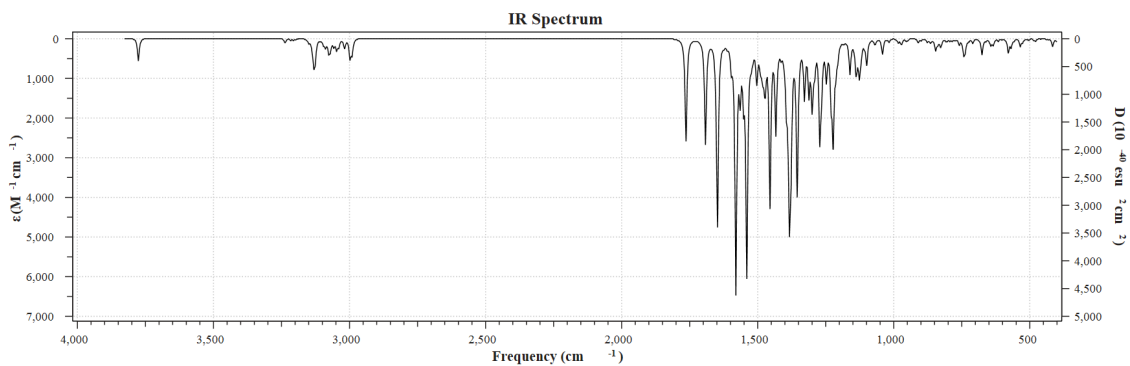
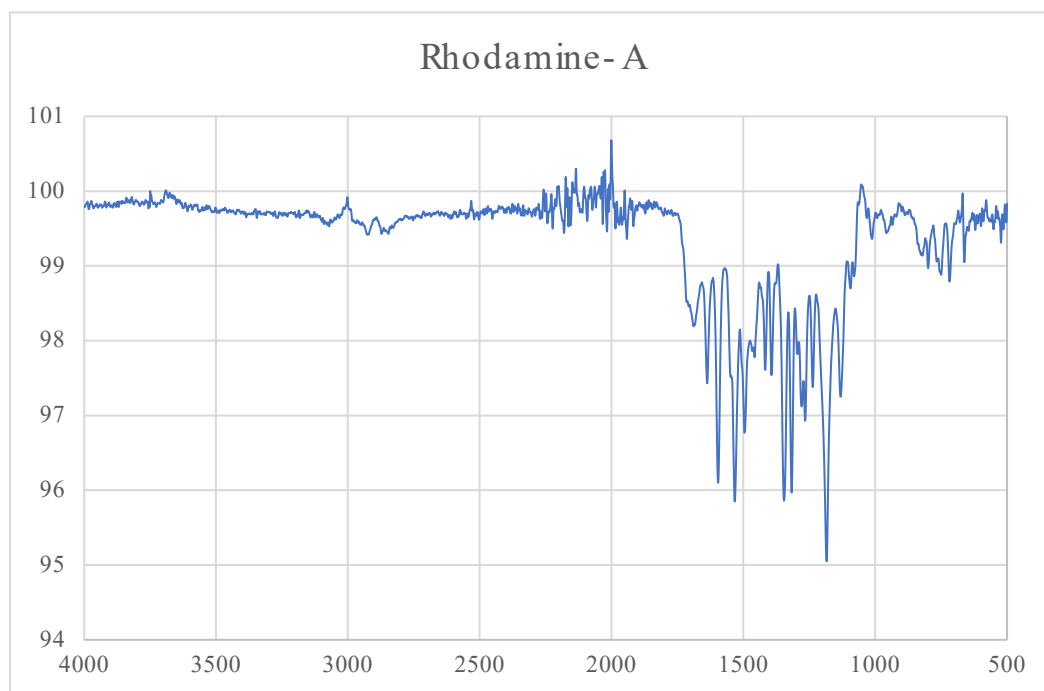**Figure S A.17**. Calculated FTIR spectrum of rhodamine dye **A**.

Figure S A.18. The solid state FTIR spectrum of rhodamine dye **A**.
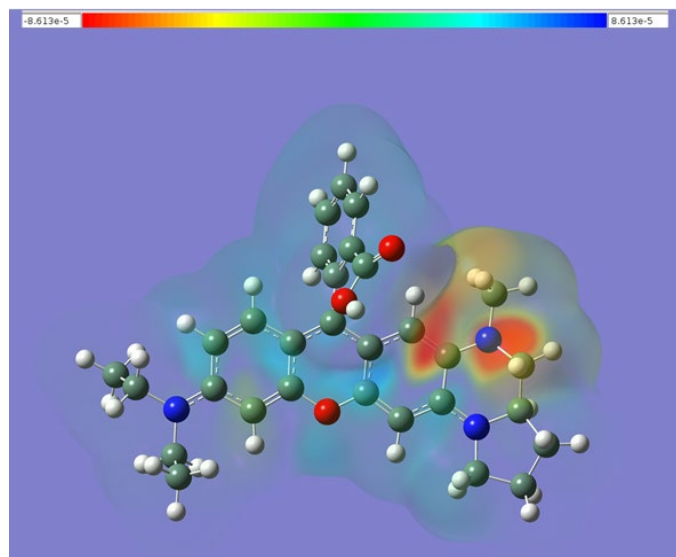
Figure S A.19. Current density difference plot for rhodamine dye **A** obtained by subtracting the SCF (ground state) density from the CI (excited state) density using the Cubegen program in GaussView.
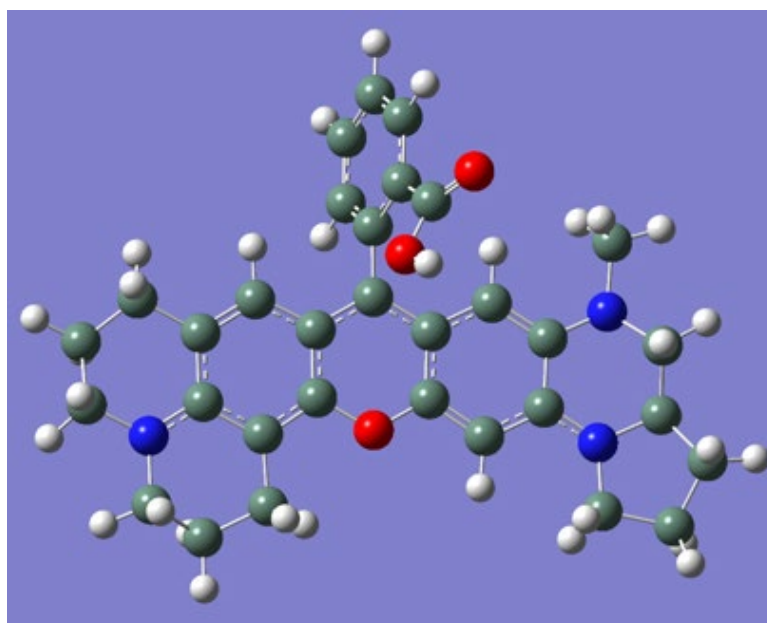

Figure S A.20. Drawing of rhodamine dye B with atoms represented as spheres of arbitrary size (H-white, C-grey, N-blue and O-red) using the GaussView program.

Table S2. Atomic coordinates for rhodamine dye B.

| Row	Symbol	X	Y	Z
1	C	3.106163	-1.29763	-0.26362
2	C	1.843912	-1.89282	-0.14255
3	C	0.70959	-1.11683	-0.17906
4	C	0.770031	0.288652	-0.31919
5	C	2.052011	0.882301	-0.42338
6	C	3.207119	0.142983	-0.40294
7	C	-0.43003	1.007281	-0.30985
8	C	-1.64694	0.326526	-0.19197
9	C	-1.64156	-1.08457	-0.08506
10	C	-2.7865	-1.84448	0.020606
11	C	-4.03243	-1.17526	0.052413
12	C	-4.07086	0.260066	-0.01203
13	C	-2.90963	0.959409	-0.14165
14	N	4.465047	0.698149	-0.52281
15	N	4.221965	-2.03071	-0.25781
16	C	-5.16632	-3.31311	0.386049
17	C	-4.01214	-3.97565	-0.33699
18	H	-4.01532	-5.04724	-0.1256
19	H	-4.14765	-3.85344	-1.4166
20	C	-2.70126	-3.34279	0.0994
21	C	5.540524	-0.03342	0.126084
22	C	5.553473	-1.44819	-0.39669
23	C	6.430156	-2.44418	0.344494
24	O	-0.46967	-1.76328	-0.07317
25	C	4.57586	2.138266	-0.49409
26	H	5.82192	-1.43099	-1.46157
27	C	-0.4103	2.479135	-0.46296
28	C	0.071658	3.348397	0.525805
29	C	-0.82566	3.010069	-1.68211
30	C	0.13793	4.717244	0.272478
31	C	-0.77075	4.376271	-1.91999
32	H	-1.18411	2.336587	-2.45307
33	C	-0.28685	5.234183	-0.94027
34	C	0.537478	2.901302	1.863856
35	O	1.360378	3.500078	2.518295
36	O	-0.06281	1.785167	2.29229
37	H	0.317098	1.55635	3.154362
38	C	-6.48255	-1.23361	0.262825
39	H	2.103311	1.957617	-0.51832
40	H	1.742742	-2.96501	-0.03991
41	H	-2.9489	2.042014	-0.19387
42	C	-5.38855	0.973902	0.087679
43	H	3.985707	2.579848	-1.29935
44	H	5.617908	2.41291	-0.65193
45	H	4.238666	2.566471	0.460538
46	C	4.275058	-3.46272	0.013006
47	C	5.771222	-3.77957	-0.00356
48	H	6.373499	-2.25488	1.421457
49	H	7.475365	-2.38481	0.039042
50	N	-5.18325	-1.87878	0.145272
51	H	-5.10504	-3.50365	1.466278
52	H	-6.12139	-3.71289	0.040571
53	H	5.424206	-0.03428	1.220241
54	H	6.486559	0.453265	-0.11272
55	H	6.024279	-4.57862	0.69359
56	H	6.076714	-4.09849	-1.00367
57	H	-1.10158	4.768613	-2.87567
58	H	-0.24043	6.302347	-1.12094
59	H	0.519374	5.369169	1.049848
60	H	3.823743	-3.663	0.991105
61	H	3.715734	-4.02523	-0.73969
62	H	-1.87553	-3.69938	-0.52042
63	H	-2.46358	-3.64466	1.127095
64	C	-6.51052	0.102074	-0.44959
65	H	-5.33251	1.927176	-0.44336
66	H	-5.59078	1.212107	1.139825
67	H	-7.48388	0.573416	-0.29616
68	H	-6.3856	-0.05477	-1.52624
69	H	-7.22097	-1.91572	-0.16424
70	H	-6.73518	-1.10662	1.324611

HOMO   LUMO

Figure S A.21. The HOMO and LUMO for rhodamine dye **B**.

Rhodamine B UV-Vis Calculated Spectrum
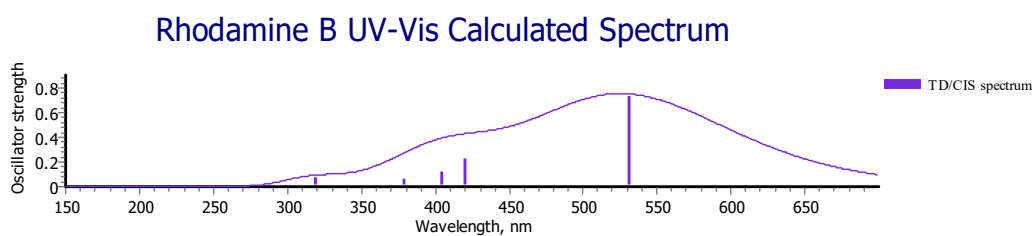
Energy[nm]	Oscillator Strength
530.6436	0.7265
420.0314	0.2276
403.8727	0.1180
378.6607	0.0533
325.7616	0.0227
319.0717	0.0652

Figure S A.22. Calculated UV-Vis spectrum for rhodamine dye **B** and listing of peak positions with oscillator strengths. This represents a HOMO-LUMO transition.
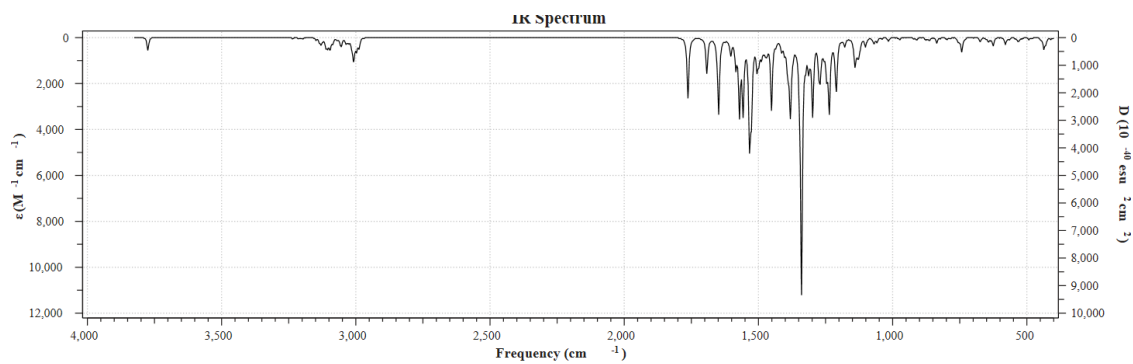
Figure S A.23. Calculated FTIR spectrum of rhodamine dye **B**.
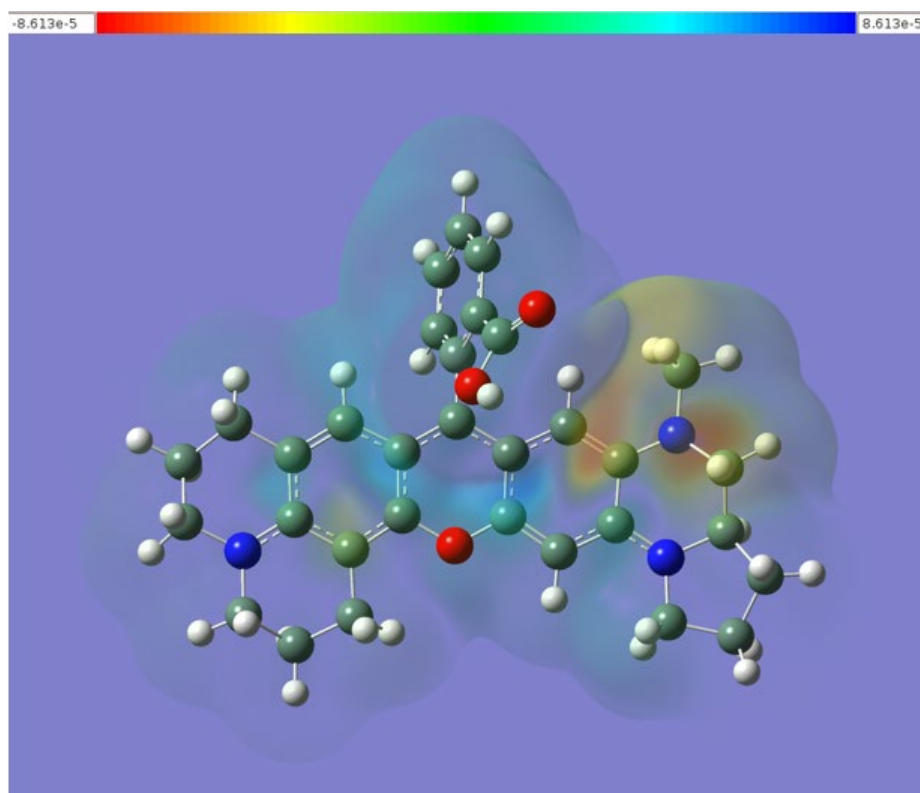
Figure S A.24. Current density difference plot for rhodamine dye B obtained by subtracting the SCF (ground state) density from the CI (excited state) density using the Cubegen program in GaussView.
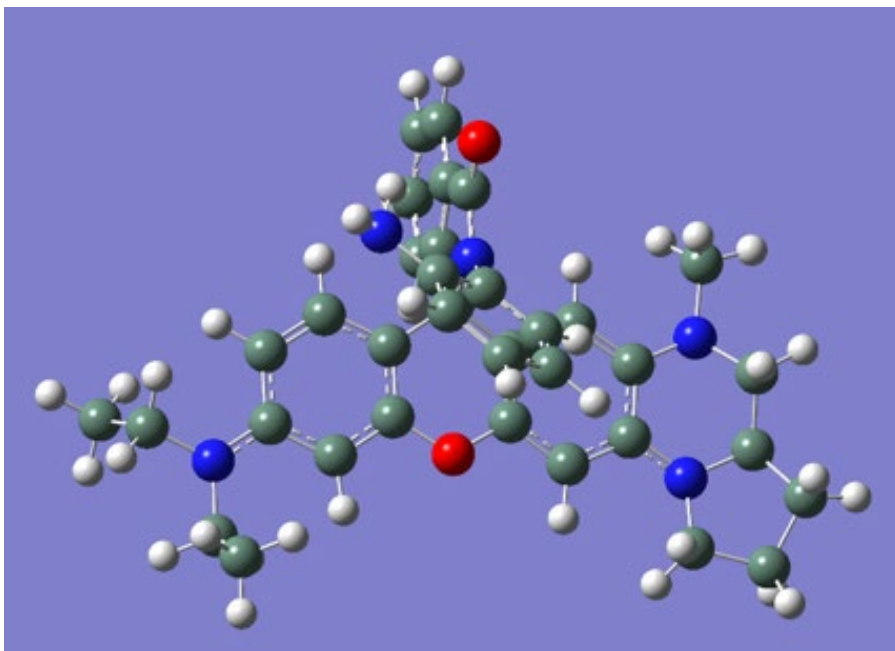
Figure S A.25. Drawing of rhodamine dye C with atoms represented as spheres of arbitrary size (H-white, C-grey, N-blue and O-red) using the GaussView program.

**Table S3**. Atomic coordinates for rhodamine dye C.

Row	Symbol	X	Y	Z
1	C	3.284816	-1.22417	-0.7192
2	C	2.027323	-1.82252	-0.71884
3	C	0.872419	-1.05217	-0.63431
4	C	0.933231	0.324225	-0.54501
5	C	2.198981	0.924916	-0.52696
6	C	3.370976	0.200555	-0.6184
7	C	-0.29928	1.141932	-0.28719
8	C	-1.53141	0.321362	-0.54674
9	C	-1.47319	-1.06412	-0.64862
10	C	-2.61175	-1.84575	-0.78317
11	C	-3.88569	-1.25897	-0.83039
12	C	-3.94788	0.15374	-0.74668
13	C	-2.79961	0.898497	-0.60147
14	N	4.639399	0.787641	-0.61952
15	N	4.424509	-1.96102	-0.8261
16	C	-4.95353	-3.45249	-1.14283
17	C	-4.88168	-4.22596	0.169251
18	C	5.656324	-0.03537	0.01343
19	C	5.747923	-1.3575	-0.71504
20	C	6.565372	-2.43974	-0.02375
21	O	-0.30013	-1.76008	-0.61837
22	C	4.716403	2.192365	-0.29444
23	H	6.15106	-1.17046	-1.7203
24	C	-0.29141	2.446101	-1.04437
25	C	-0.32214	3.518865	-0.17284
26	C	-0.25199	2.646056	-2.41243
27	C	-0.3192	4.829759	-0.62511
28	C	-0.24864	3.956039	-2.88049
29	H	-0.22471	1.806205	-3.09892
30	C	-0.28157	5.039351	-1.9974
31	C	-0.36524	3.00944	1.212669
32	O	-0.45333	3.662524	2.251394
33	N	-0.31542	1.655195	1.127038
34	C	-6.34143	-1.43182	-0.87972
35	H	2.242044	2.000788	-0.40892
36	H	1.925196	-2.89781	-0.79606
37	H	4.133469	2.780268	-1.00605
38	H	5.755675	2.513167	-0.3672
39	H	4.350749	2.416286	0.719886
40	C	4.457084	-3.40087	-0.63364
41	C	5.949341	-3.7234	-0.57867
42	H	6.411011	-2.38127	1.059311
43	H	7.634636	-2.34873	-0.22206
44	N	-5.01635	-2.016	-0.95977
45	H	-5.84364	-3.75043	-1.70384
46	H	-4.10347	-3.69864	-1.7849
47	H	5.427557	-0.20882	1.077694
48	H	6.61472	0.48332	-0.0448
49	H	6.156575	-4.60275	0.03275
50	H	6.330536	-3.91839	-1.58549
51	H	-0.22004	4.142373	-3.94921
52	H	-0.27748	6.05017	-2.39124
53	H	-0.34581	5.657826	0.075204
54	H	3.950685	-3.66829	0.30453
55	H	3.945733	-3.92668	-1.44657
56	C	-6.87014	-0.94888	-2.22529
57	H	-7.01002	-2.19281	-0.46749
58	H	-6.33665	-0.61762	-0.15056
59	H	-6.91912	-1.77449	-2.94039
60	H	-6.22373	-0.1759	-2.64791
61	H	-7.87584	-0.53303	-2.11855
62	H	-5.75969	-4.02029	0.787447
63	H	-3.99422	-3.94825	0.742891
64	H	-4.84441	-5.30248	-0.01858
65	H	-2.47428	-2.9176	-0.83399
66	H	-4.8984	0.667019	-0.80328
67	H	-2.88251	1.978284	-0.52375
68	C	-0.43513	0.768777	2.222952
69	C	0.589556	-0.13773	2.48223
70	C	0.455105	-1.10444	3.467227
71	C	-0.71817	-1.14972	4.213669
72	C	-1.72553	-0.2252	3.993891
73	C	-1.60723	0.755431	3.001357
74	N	-2.63996	1.644998	2.757529
75	H	-2.62856	-0.25219	4.597308
76	H	1.258446	-1.80869	3.653239
77	H	-0.84436	-1.90065	4.987427
78	H	1.496469	-0.07916	1.892058
79	H	-2.33335	2.583324	2.534044
80	H	-3.34001	1.661749	3.485865
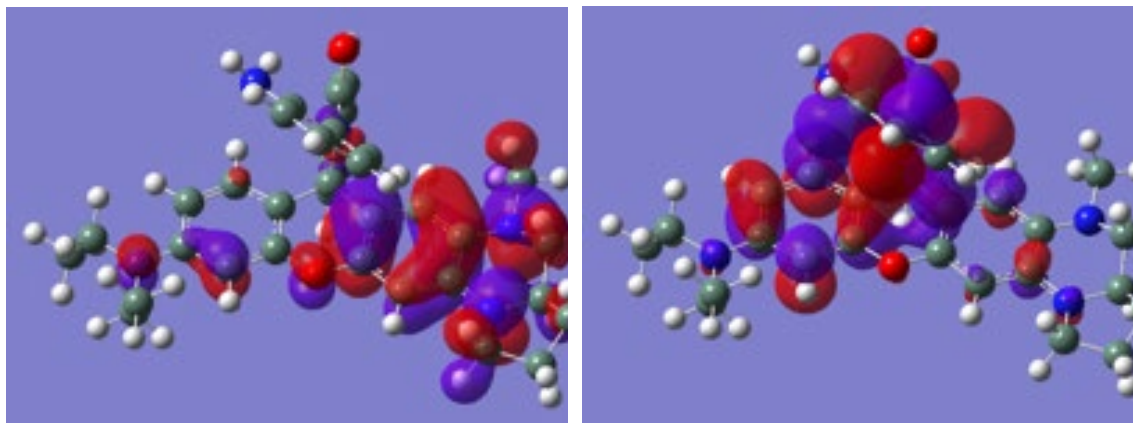
HOMO

LUMO

Figure S A.26. The HOMO and LUMO+4 (see Fig. S31) for rhodamine dye **C**.
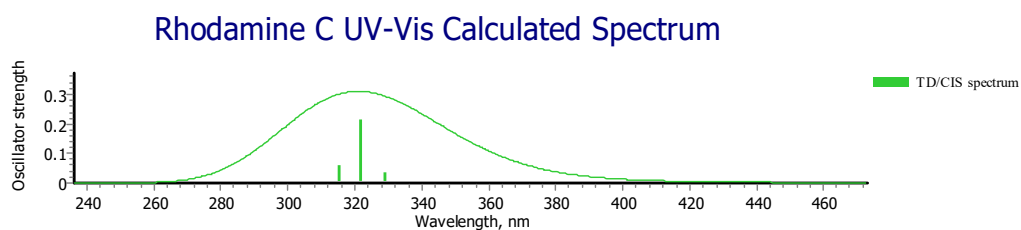
Energy[nm]	Oscillator Strength
400.2094	0.0038
358.5761	0.0014
328.9509	0.0354
321.7795	0.2127
315.2746	0.0568
309.0890	0.0100

Figure S A.27. Calculated UV-Vis spectrum for rhodamine dye C and listing of peak positions with oscillator strengths. This represents a HOMO-LUMO+4 transition.
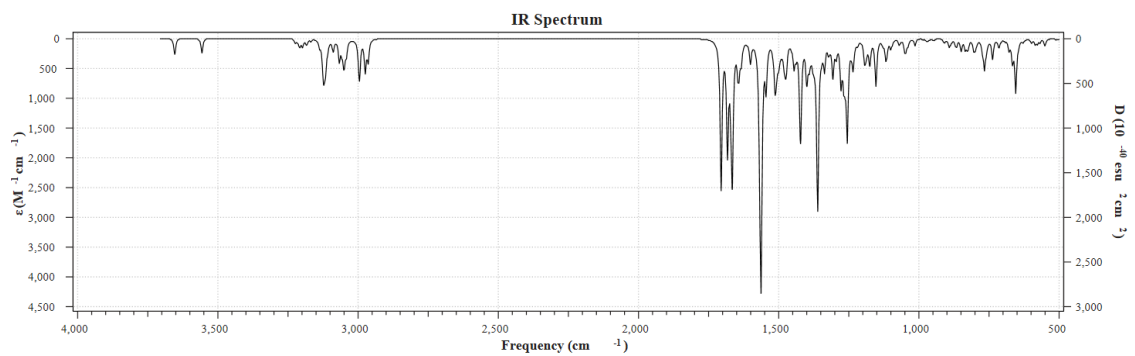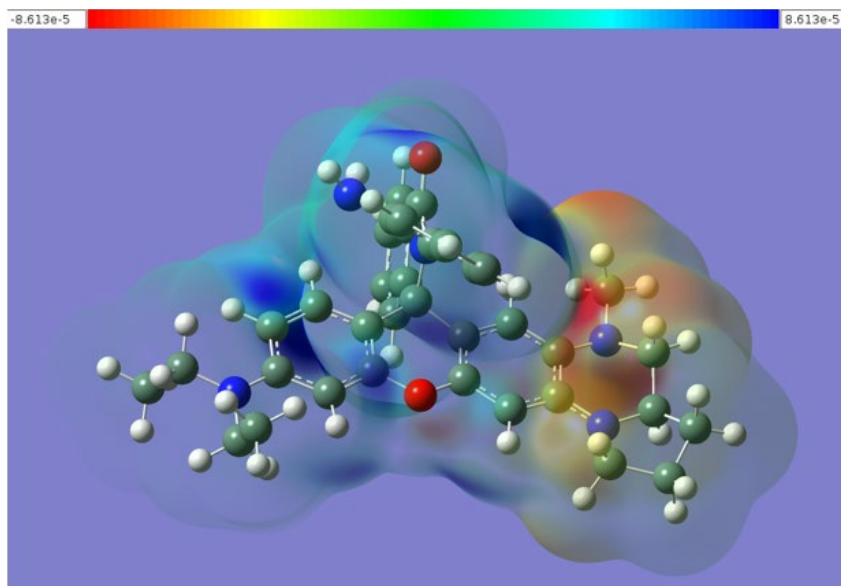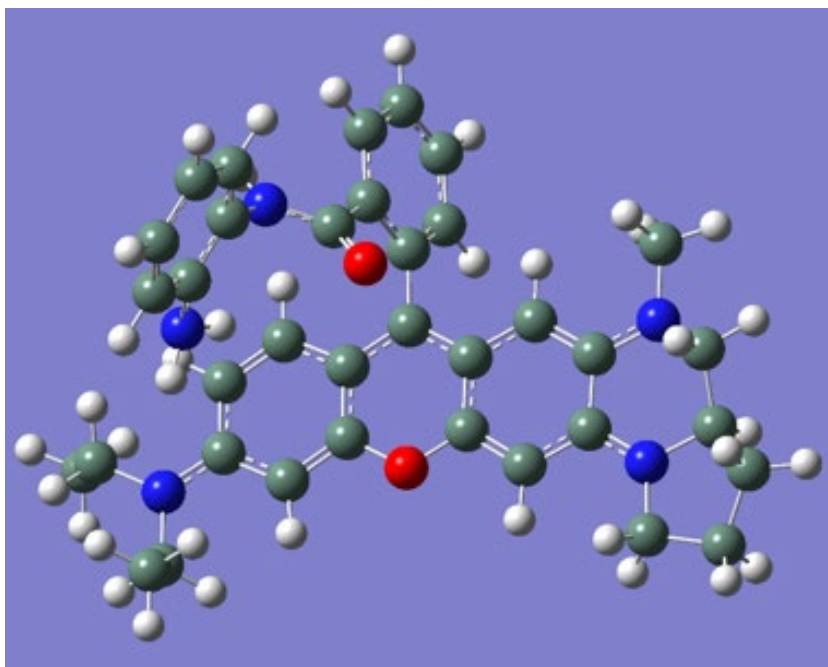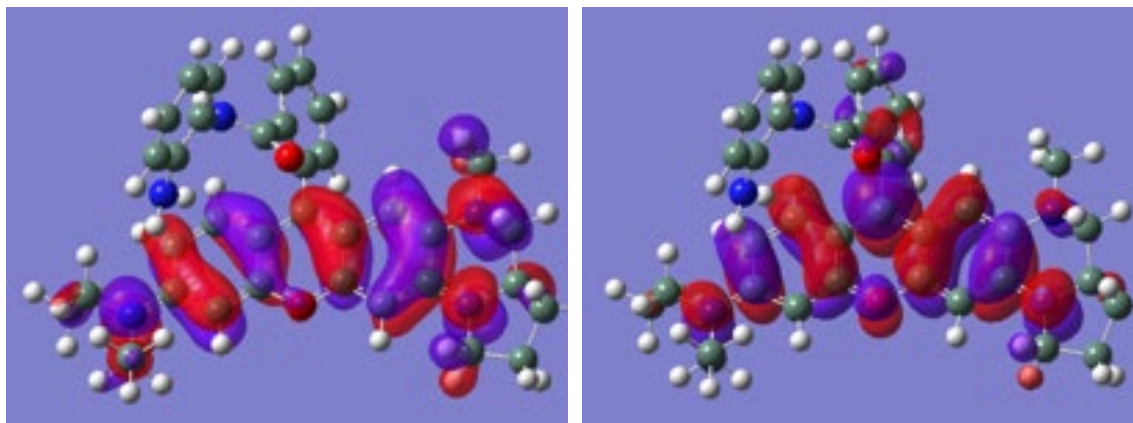
IR Spectrum

Figure S A.28. Calculated FTIR spectrum of rhodamine dye **C**.
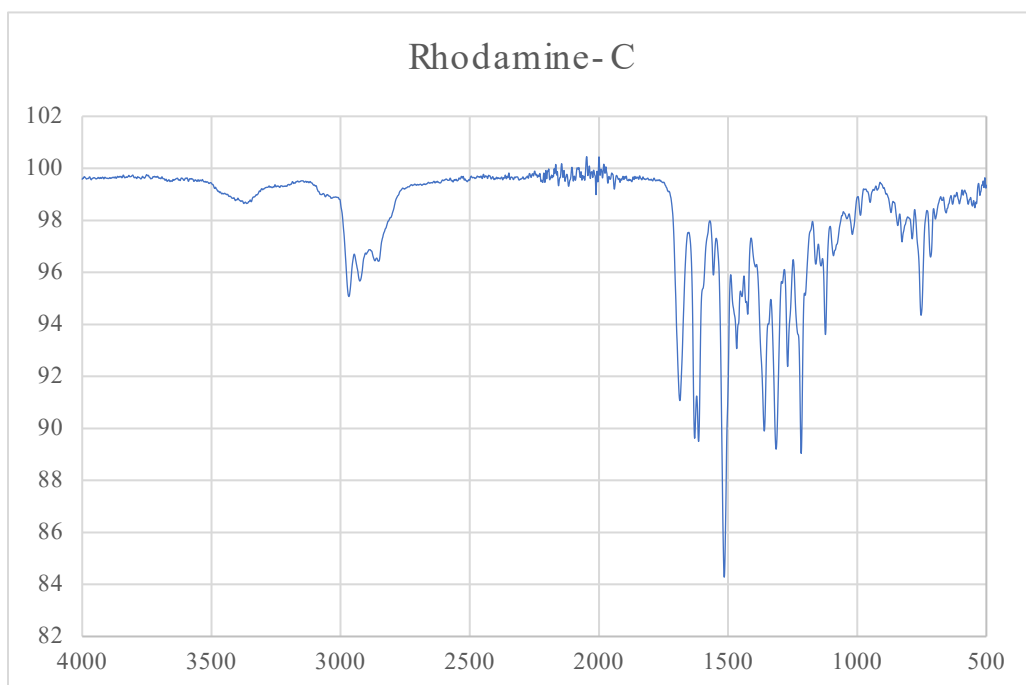
Rhodamine-C

Figure S A.29. The solid state FTIR spectrum of rhodamine dye **C**.

Figure S A.30. Current density difference plot for rhodamine dye **C** obtained by subtracting the SCF (ground state) density from the CI (excited state) density using the Cubegen program in GaussView.

Figure S A.31. Drawing of rhodamine dye **D** with atoms represented as spheres of arbitrary size (H-white, C-grey, N-blue and O-red) using the GaussView program.

Table S4. Atomic coordinates for rhodamine dye D.

Row	Symbol	X	Y	Z					
					41	C	-6.7879	2.785306	1.776552
1	C	-3.96667	1.075092	0.215158	42	H	-6.81071	0.832774	2.727992
2	C	-2.80188	1.853575	0.282925	43	H	-8.22643	1.119353	1.700565
3	C	-1.62549	1.376776	-0.23899	44	N	4.048404	3.138825	-0.69547
4	C	-1.5401	0.097209	-0.84356	45	H	4.721331	5.057011	-0.35853
5	C	-2.70804	-0.70503	-0.85088	46	H	2.987108	4.893219	-0.29779
6	C	-3.90706	-0.25753	-0.3601	47	H	-5.65153	-1.00101	1.647543
7	C	-0.30448	-0.32198	-1.33263	48	H	-6.93618	-1.29959	0.463025
8	C	0.798757	0.544237	-1.26034	49	H	-6.96638	3.288007	2.727262
9	C	0.655869	1.793089	-0.61482	50	H	-7.36913	3.303445	1.009172
10	C	1.704132	2.662022	-0.42649	51	H	-0.88428	-3.44236	-4.70165
11	C	2.987545	2.33611	-0.90889	52	H	0.438634	-5.1591	-3.49463
12	C	3.127737	1.113096	-1.63822	53	H	1.392036	-4.64275	-1.27566
13	C	2.078392	0.257274	-1.7912	54	H	-4.65976	2.786335	2.288538
14	N	-5.06594	-1.00407	-0.39017	55	H	-5.02541	3.638335	0.778494
15	N	-5.12934	1.530324	0.680485	56	C	5.750968	3.195146	-2.50102
16	C	3.91896	4.409849	0.002187	57	H	6.079662	3.226836	-0.36717
17	C	4.000209	4.256805	1.515546	58	H	5.527152	1.684423	-0.95706
18	C	-6.03392	-0.71849	0.655411	59	H	5.658031	4.278615	-2.60946
19	C	-6.36477	0.752505	0.62497	60	H	5.091586	2.724901	-3.2343
20	C	-7.15594	1.301403	1.800637	61	H	6.780696	2.917077	-2.73835
21	O	-0.54326	2.177318	-0.12289	62	H	4.955	3.813941	1.80973
22	C	-4.97654	-2.38278	-0.81143	63	H	3.200043	3.615265	1.891889
23	H	-6.88125	0.982072	-0.31652	64	H	3.913955	5.231993	2.000594
24	C	-0.1268	-1.67075	-1.90954	65	H	1.512011	3.574462	0.120156
25	C	0.62739	-2.63739	-1.23197	66	H	4.07886	0.851936	-2.08027
26	C	-0.66299	-1.97031	-3.15682	67	H	2.219713	-0.665	-2.34307
27	C	0.829431	-3.88546	-1.81202	68	C	2.996937	-2.61643	1.682186
28	C	-0.45975	-3.22052	-3.72849	69	C	2.927693	-3.71784	2.523688
29	H	-1.23293	-1.2131	-3.68468	70	C	3.462163	-3.66947	3.803119
30	C	0.284917	-4.17931	-3.0558	71	C	4.064594	-2.48997	4.233825
31	C	1.129713	-2.34794	0.147618	72	C	4.138474	-1.38612	3.401216
32	O	0.404756	-1.83877	0.99249	73	C	3.608341	-1.42625	2.104517
33	N	2.42051	-2.68953	0.38187	74	N	3.736871	-0.35155	1.251708
34	C	5.400764	2.760896	-1.08488	75	H	4.613536	-0.47283	3.747205
35	H	-2.62483	-1.70365	-1.25587	76	H	3.40511	-4.53363	4.455258
36	H	-2.81696	2.837728	0.731649	77	H	4.483002	-2.42823	5.233615
37	H	-4.55305	-2.44451	-1.81565	78	H	2.438781	-4.61547	2.158196
38	H	-5.97966	-2.80576	-0.84244	79	H	3.845418	0.550243	1.690932
39	H	-4.35873	-2.98963	-0.13445	80	H	3.106923	-0.3271	0.46332
40	C	-5.30506	2.785972	1.403323	81	H	2.969534	-3.0574	-0.38197

201

HOMO   LUMO

Figure S A.32. The HOMO and LUMO for rhodamine dye **D**.
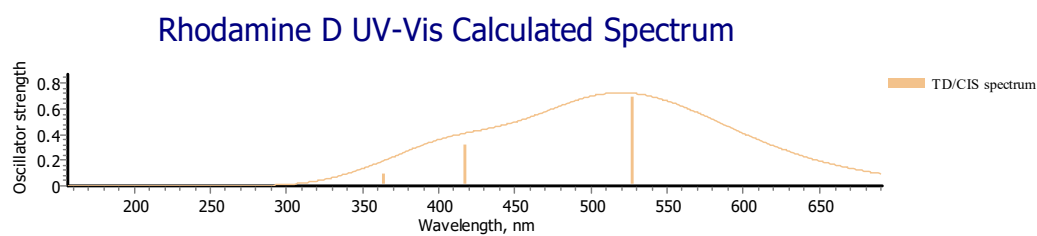
Energy[nm]	Oscillator Strength
526.8554	0.6902
454.2569	0.0059
417.6966	0.3179
363.9976	0.0905
351.2518	0.0095
321.0047	0.0102

Figure S A.33. Calculated UV-Vis spectrum for rhodamine dye **D** and listing of peak positions with oscillator strengths. This represents a HOMO-LUMO transition.
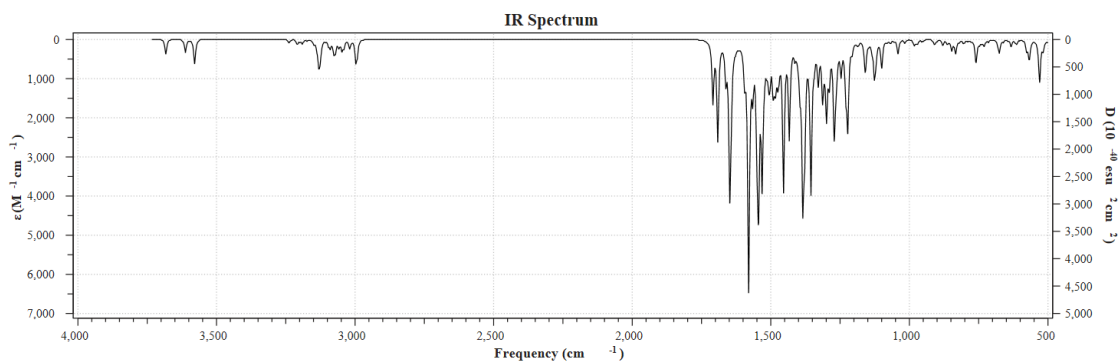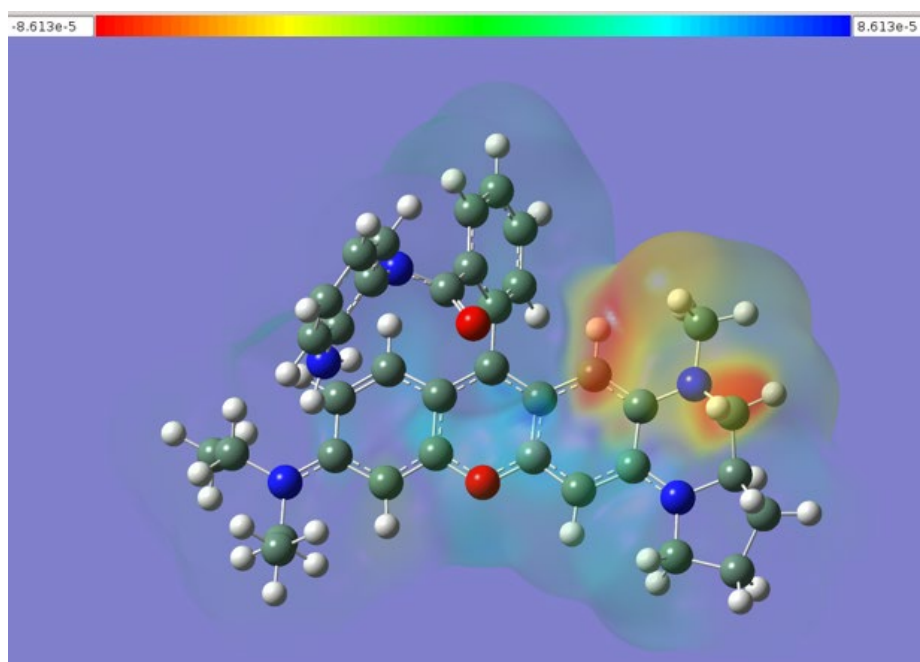
Figure S A.34. Calculated FTIR spectrum of rhodamine dye **D**.

Figure S A.35. Current density difference plot for rhodamine dye **D** obtained by subtracting the SCF (ground state) density from the CI (excited state) density using the Cubegen program in GaussView.

8. Cytotoxicity of the rhodamine dyes

We used a standard MTS assay to investigate cytotoxicity of the rhodamine dyes **A**, **B** and **C**. The results show that the dyes have very low cytotoxicity.
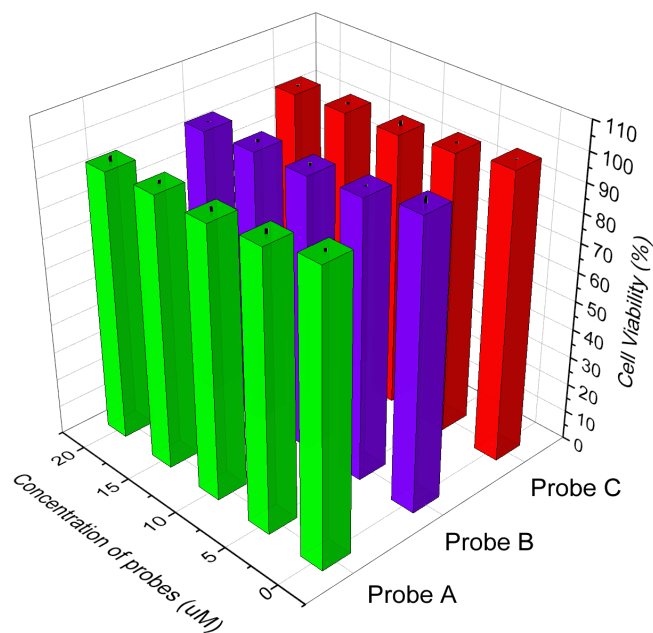
Figure S A.36. Cytotoxicity of rhodamine dyes **A**, **B**, and **C** through standard MTS assay by incubation of HeLa cells with 5, 10, 15, 20 μM of rhodamine dye **A**, **B**, or **C** for 48 hours, respectively. The cell viability is directly related to the absorbance at 490 nm.

9. Cell culture and fluorescent imaging

Cell Culture and Cytotoxicity Assay. MCF7 cells and HeLa cells were purchased at ATCC (Manassas,VA) and were cultured in RPMI 1640 medium (Gibco) and modified Eagle's medium (DMEM, Gibco) in the presence of 10 % fetal bovine serum (FBS, fisher Scientific) under 5 % CO_2 at the temperature, respectively. Standard MTS assay was employed to test the cytotoxicity of rhodamine dyes **A**, **B** and **C** against HeLa cell line. After the cells were further seeded into in a 96-well plate (about 7×10^3 cells per well) and were further incubated for 24 hours. The HeLa cells were put in the fresh culture medium containing probes **A**, **B**, or **C** with concentration from 0, 5, 10, 15 to 20 µM, and further incubated for 48 h at 37 °C in 5% CO_2 humidified atmosphere, followed by further incubating the cells in a fresh culture medium (80 µL) containing 20 µL CellTiter 96® Aq$_{ueous}$ for another 2 h. Untreated cells were used as controls. The cell viability was determined by making the comparison of the 490 nm absorption between the control cells in the absence of the probe with that of the cells treated with the probe.

Rhodamine dye C applications in cellular Imaging. HeLa cells were seeded into 35 mm x 12 mm glass-bottom culture dishes and incubated for 24 h. When freshly prepared FBS-free medium containing rhodamine dye **C** with concentrations ranging from 1, 5, 10, to 15 µM was used to replace the cell culture medium, the cells was further incubated for 30 min under 5% CO_2 humidified atmosphere. Hoechst and Lysosensor green were added to the solution as the final concentration of 1 µg/ml and 1 µM to incubate another 30 min, respectively. The cells were rinsed with PBS buffer twice again before imaging. To adjust intracellular pH values, the cells were washed with PBS buffer twice before they were treated with 5 µg/mL nigericin in citric buffers with different pH values from 3.0, 3.5, 4.0, 4.5, 5.0, 5.5, 6.0, 6.5, 7.0, 7.5 to equilibrate the intracellular and extracellular pH for 30 min. The

cells were incubated with rhodamine dye **C** for 30 min before they were rinsed with PBS buffer twice again for imaging. For the experiment for monitoring lysosomal pH changes, HeLa cells were cultured in medium in the absence and in the presence of 10 mM NH_4Cl, 100 µM NEM (*N*-ethylmaleimide), and 100 µM H_2O_2 before incubating with rhodamine dye **C** for another 30 min. For an experiment under drug stimulation, HeLa cells were cultured in medium in the presence of different concentrations of chloroquine from 50 µM, 100 µM to 200 µM for 30 min followed by incubation with rhodamine dye **C** with another 30 min. Confocal fluorescence microscope (Olympus IX 81) was employed to collect cellular fluorescence images from 425 to 475 nm for blue fluorescence of Hoechst under excitation at 405 nm, from 525 to 575 nm for green fluorescence of Lysosensor green under excitation at 488 nm, and from 650 to 700 nm for red fluorescence of rhodanmine dye **C** under the excitation at 559 nm.

Lysosensor green was used to determine whether rohodamine dye **C** was located in lysosomes in live cells (Figure S37). Confocal microscopic co-localization analysis of rhodamine dye **C** and lysotracker green gave the Pearson's coefficient value of 0.89 or higher, indicating that rhodamine dye **C** accumulates and becomes activated to engender fluorescence in lysosomes in live cells (Figure S37).
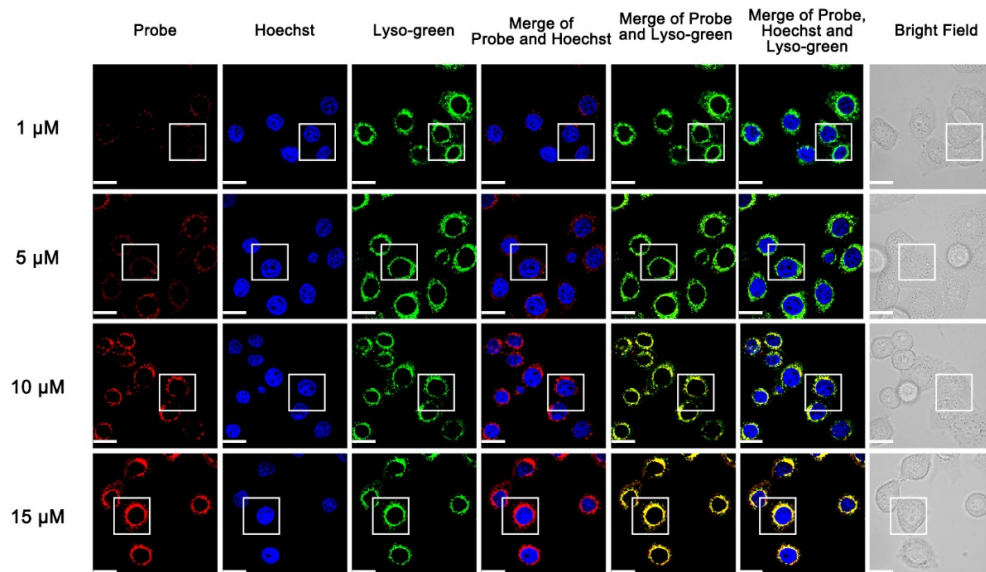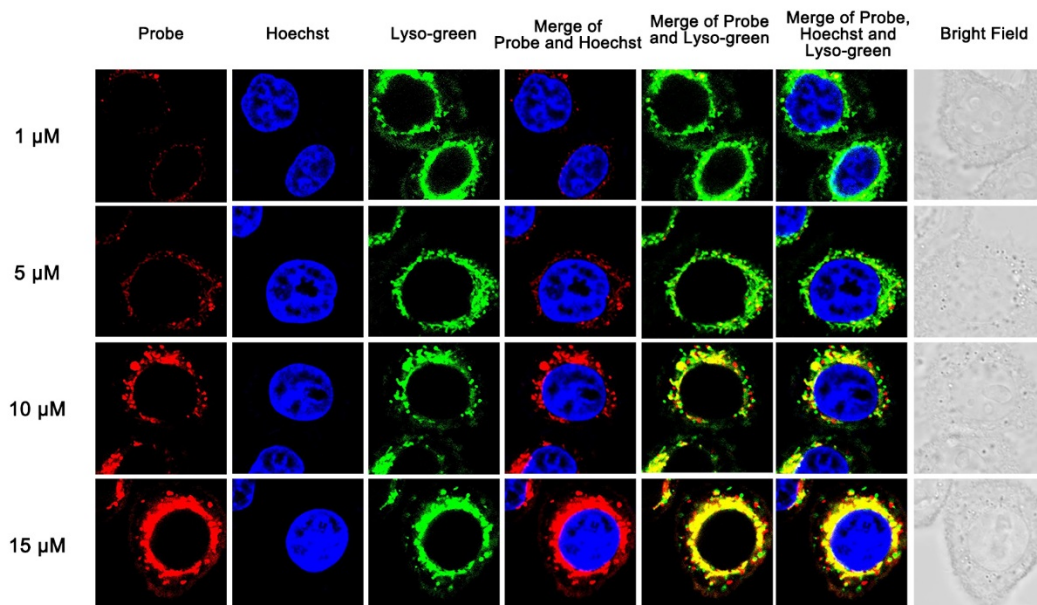
Figure S A.37. Enlarged acidity-activated turn-on cellular fluorescence of rhodamine dye **C** in lysosomes in HeLa cells. HeLa cells were cultured in media containing 1 µg/ml Hoechst stain, 1 µM Lysosensor green and rhodamine dye **C** with different concentrations. The images were obtained by confocal fluorescence microscopy with a scale bar of 20 µm. The filter sets used to image dye **C**, Hoechst and Lyso-green were excitation 559 nm and emission 675/50 nm, excitation 405 nm and emission 450/50 nm and excitation 488 nm and emission 550/50 nm, respectively.
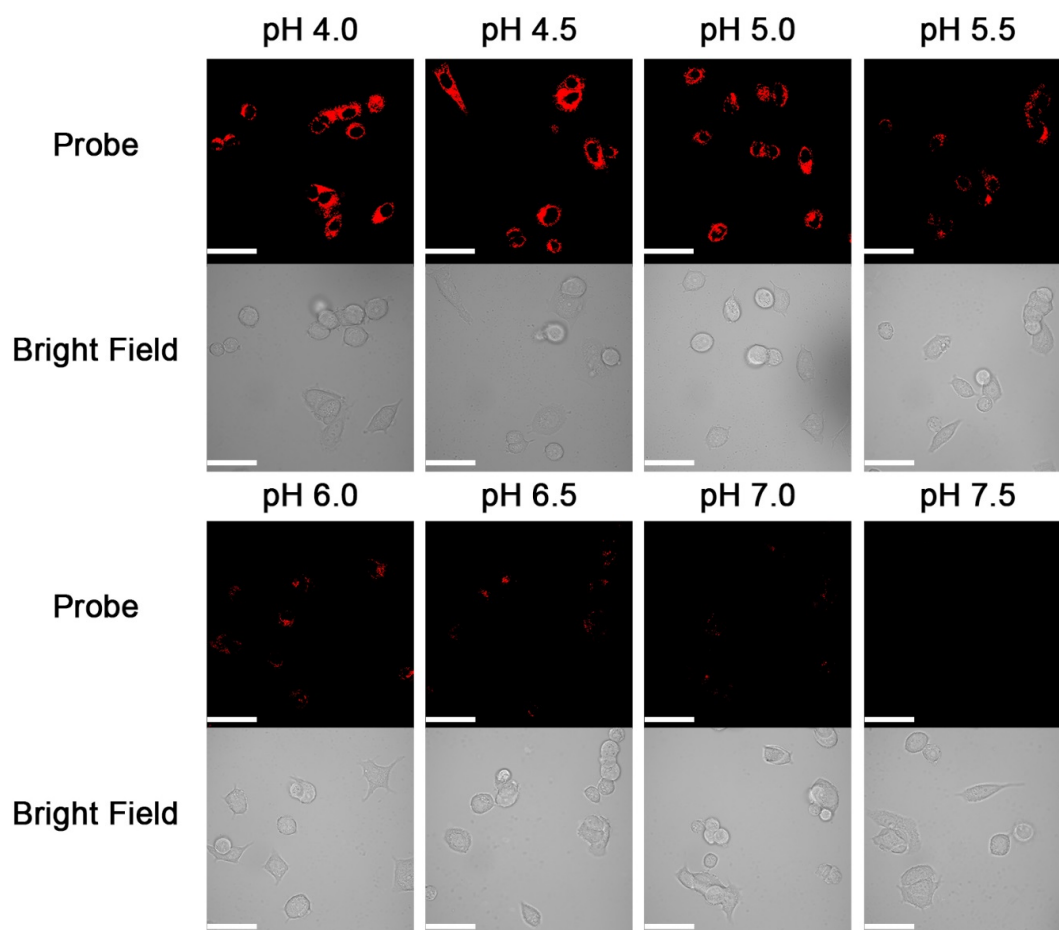
Figure S A.38. Cellular fluorescence intensities of 10 µM rhodamine dye **C** inside MCF7 cells with different intracellular pH values, which was adjusted by using 5 µg/mL H^+/K^+ ionophore nigericin to equilibrate the intracellular and extracellular pH in media with different pH values. Confocal fluorescence microscopy was employed to collect the images with a scale bar of 50 µm. The filter sets used to image dye C was excitation 559 nm and emission 675/50 nm.

Appendix B   Supporting Information for Chapter 3

1. Instruments and Materials

400 MHz Varian Unity Inova NMR spectrophotometer instrument was used to obtain ^{1}H NMR and ^{13}C NMR spectra in CDCl$_3$ and CD$_3$OD solutions. Chemical shifts (δ) are set in ppm relative to solvent residual peaks (^{1}H: δ 7.26 for CDCl$_3$, δ 3.31 for CD$_3$OD; ^{13}C: δ 77.3 for CDCl$_3$) as internal standards. High-resolution mass spectrometer data (HRMS) were measured with fast atom bombardment (FAB) ionization mass spectrometer, double focusing magnetic mass spectrometer or matrix assisted laser desorption/ionization time of flight mass spectrometer. Absorption and fluorescence spectra were obtained by using Per-kin Elmer Lambda 35 UV/VIS spectrometer and Jobin Yvon Fluoromax-4 spectrofluorometer, respectively. Unless specifically indicated, all reagents and solvents were obtained from commercial suppliers and used without further purification. Compounds **3**, **4** and **8** were prepared according to the reported procedures.

We report a ratiometric fluorescent probe based on π-conjugation modulation between coumarin and hemicyanine moieties for sensitive ratiometric detection of pH changes in live cells by monitoring visible and near-infrared fluorescence changes. In a π-conjugation modulation strategy, a coumarin dye was conjugated to a near-infrared hemicyanine dye via a vinyl connection while lysosome-targeting morpholine residue was introduced to the hemicyanine dye to form a closed spirolactam ring structure. The probe shows only visible fluorescence of the coumarin moiety under physiological and basic conditions because the hemicyanine dye retains its closed spirolactam ring structure. However, decrease of pH to acidic condition causes spirolactam ring opening, and significantly enhances π-conjugation within the probe, thus generating a new near-infrared fluorescence peak of the hemicyanine at 760 nm. Moreover, the probe displays ratiometric fluorescence response to pH with increases of the coumarin fluorescence and decreases of the hemicyanine fluorescence when pH changes from 7.4 to 2.5. The probe is fully capable of imaging pH changes in live cells with good ratiometric responses in visible and near-infrared channels, and effectively avoids fluorescence blind spots under neutral and basic pH conditions - an issue that typical intensity-based pH fluorescent probes run into. The probe design platform reported herein can be easily applied to prepare a variety of ratiometric fluorescent probes for detection of biological thiols, metal ions, reactive oxygen and nitrogen species by introducing appropriate functional groups to hemicyanine dye.
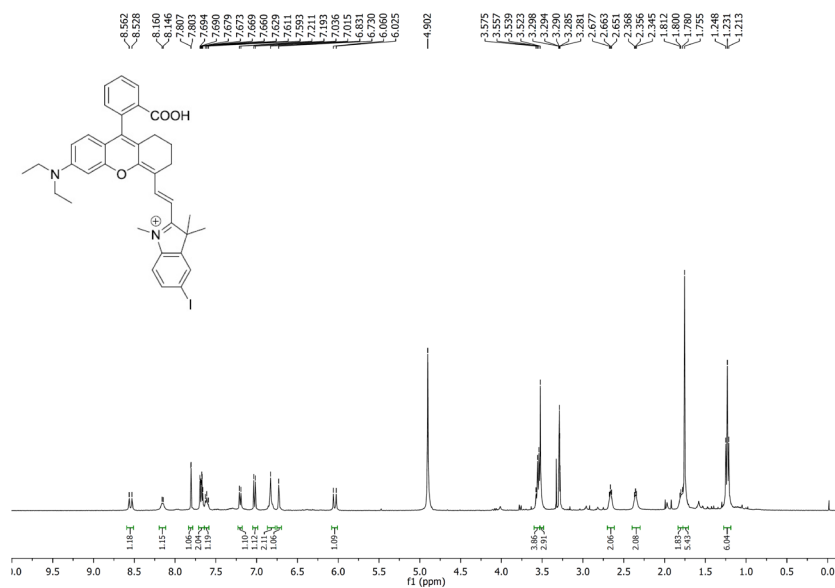
2. ¹H and ¹³C NMR spectra of intermediates and probe

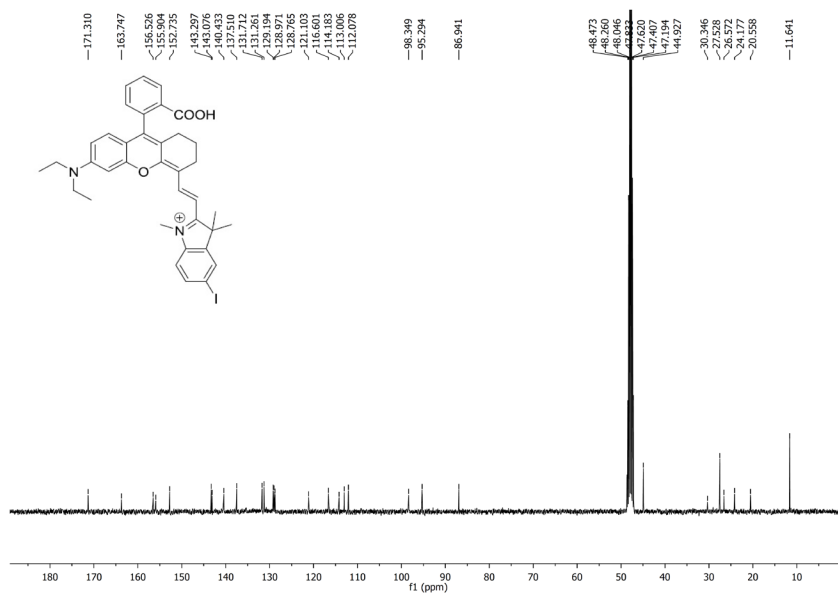**Figure S B.1**. ¹H NMR spectrum of compound **5** in CD₃OD

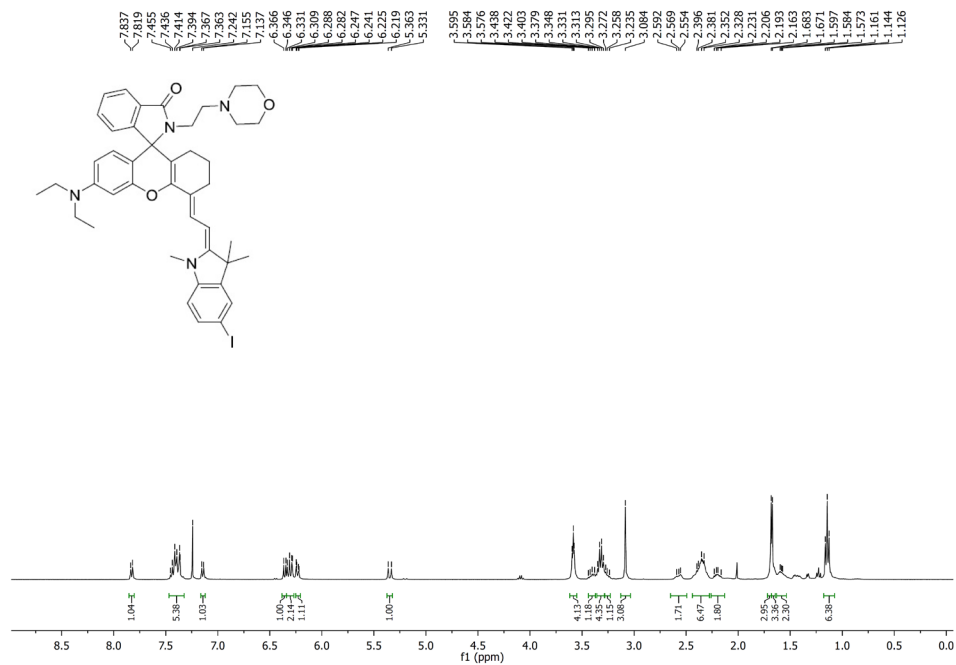**Figure S B.2**. ¹³C NMR spectrum of compound **5** in CD₃OD solution.

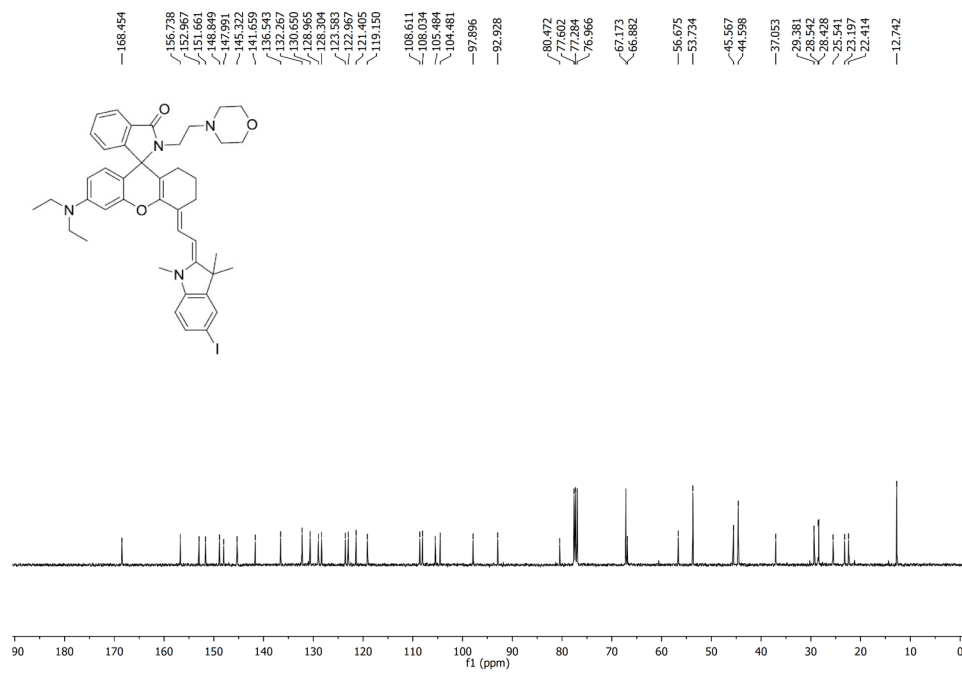**Figure S B.3**. ^{1}H NMR spectrum of compound **6** in CDCl$_3$ solution.

Figure S B.4. ^{13}C NMR spectrum of compound **6** in CDCl$_3$ solution.

Figure S B.5. ^{1}H NMR spectrum of fluorescent probe **A** in CDCl$_3$ solution.

Figure S B.6. ^{13}C NMR spectrum of fluorescent probe **A** in CDCl$_3$ solution.

Figure S B.7. ^{1}H NMR spectrum of compound **9** in CDCl$_3$ solution.

Figure S B.8. ^{13}C NMR spectrum of compound **9** in CDCl$_3$ solution.

213
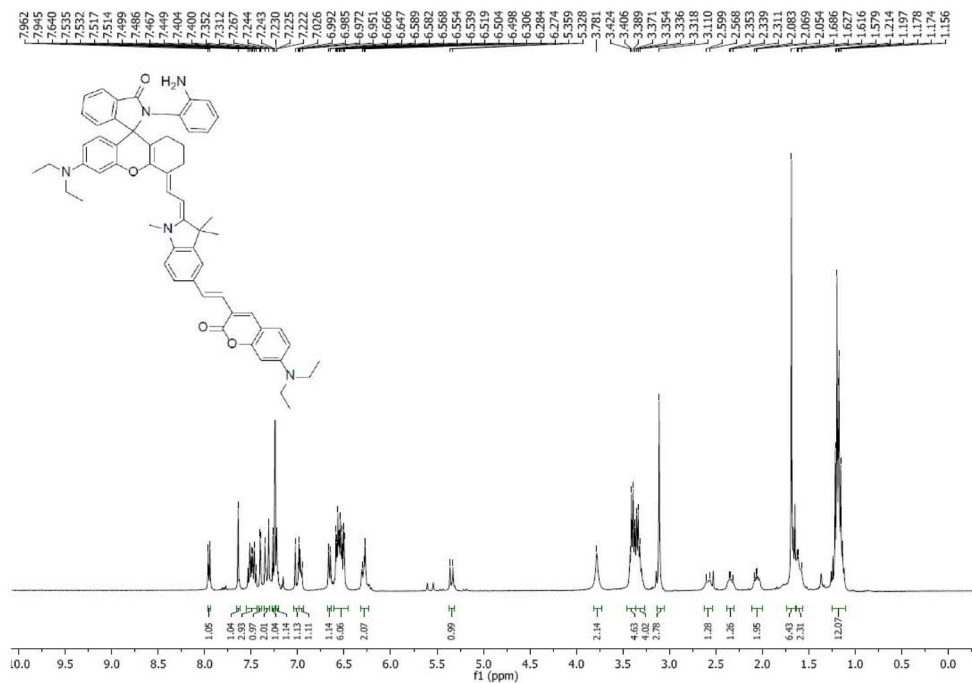
Figure S B.9. ^{1}H NMR spectrum of fluorescent probe **B** in CDCl$_3$ solution.
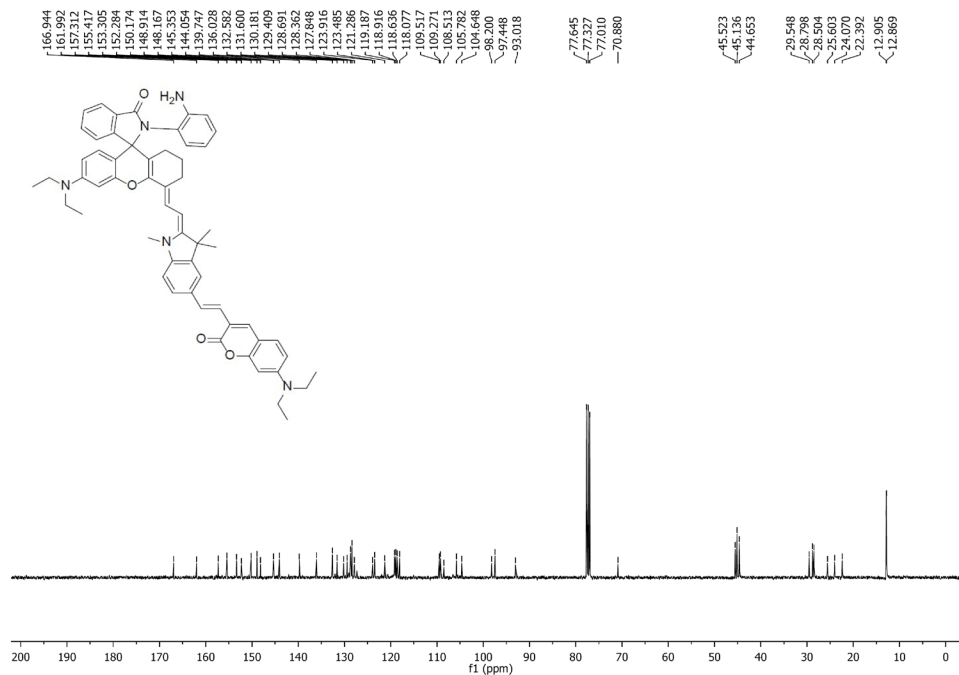
Figure S B.10. ^{13}C NMR spectrum of fluorescent probe **B** in CDCl$_3$ solution.

3. Optical Measurement

All absorbance spectra and emission spectra were obtained at room temperature using a standard 1 cm path length quartz fluorescence cuvette. All spectra were obtained 10 minutes after samples were freshly made. The probe concentration was 5 μM for each measurement. For the selectivity measurement, all metal ion solutions were freshly made, and all the metal ion concentrations in testing samples were controlled at 40 μM. The slit widths of excitation and emission of fluorescence measurements were both set to 5 nm. The quantum yields were calculated according to reference reported. Fluorescence quantum yields were calculated by measuring fluorescence of fluorophores of the known quantum yield with the same experimental parameters (excitation wavelength and slit width). The samples and the reference solutions were freshly prepared under identical conditions. The fluorescence quantum yields were calculated using the following equation:

$$\Phi_X = \Phi_{st}(Grad_X/Grad_{st})(\eta_X^2/\eta_{st}^2)$$

Where the subscripts '*st*' and '*X*' stand for standard and test, respectively, Φ is the fluorescence quantum yield, "*Grad*" represents the gradient from the plot of integrated fluorescence intensity versus absorbance and η is the refractive index of the solvent.

Rhodamine 6G (0.95 in ethanol) was used as standard to calculate quantum yield of coumarin moiety, and a typical hemicyanine dye (S1) (0.41 in ethanol) was used as standard to calculate quantum yield of hemicyanine moiety.
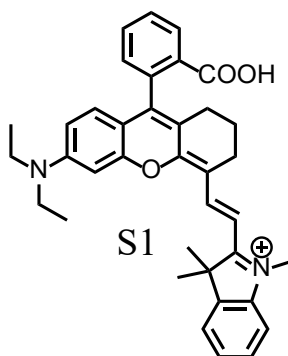
4. Determination of pK_a by fluorometric titration

The constant K_a of probe **A** was determined in buffer solutions by fluorometric titration as a function of pH using the fluorescence spectra. The expression of the steady-state fluorescence intensity F as a function of the proton ion concentration has been extended for the case of a n: 1 complex between H$^+$ and a fluorescent probe, which is expressed by the equation below:

$$F = \frac{F_{min}[\text{H}^+]^n + F_{max}K_a}{K_a + [\text{H}^+]^n}$$

F_{min} and F_{max} stand for the fluorescence intensities at maximal and minimal H$^+$ concentrations, respectively, and n is apparent stoichiometry of H$^+$ binding to the probe which affects the fluorescent change. Nonlinear fitting of equation expressed above to the fluorescence titration data recoded as a function of H$^+$ concentration with K_a and n as free adjustable parameters yields the estimated apparent constant of K_a.

5. Optical measurement data for the intermediate 7, and probes A and B
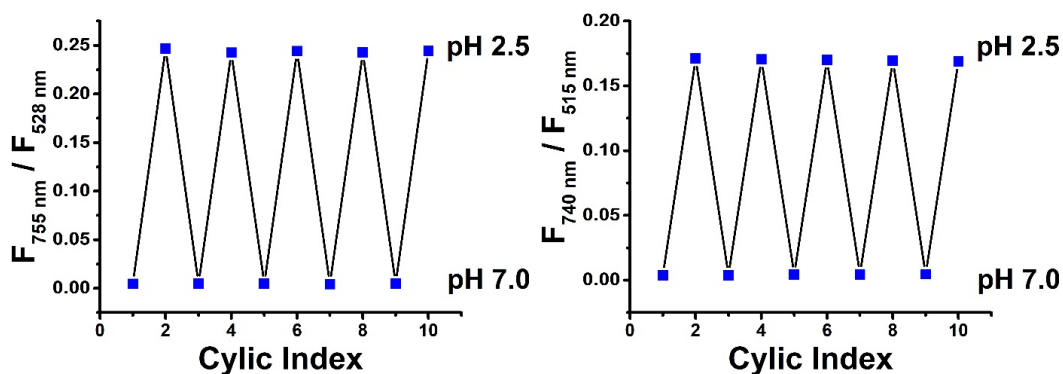
Figure S B.11. Reversible ratiometric fluorescence responses of 5 μM probes **A** (left) and **B** (right) to pH changes in 10 mM citrate buffer at excitation of 420 nm.
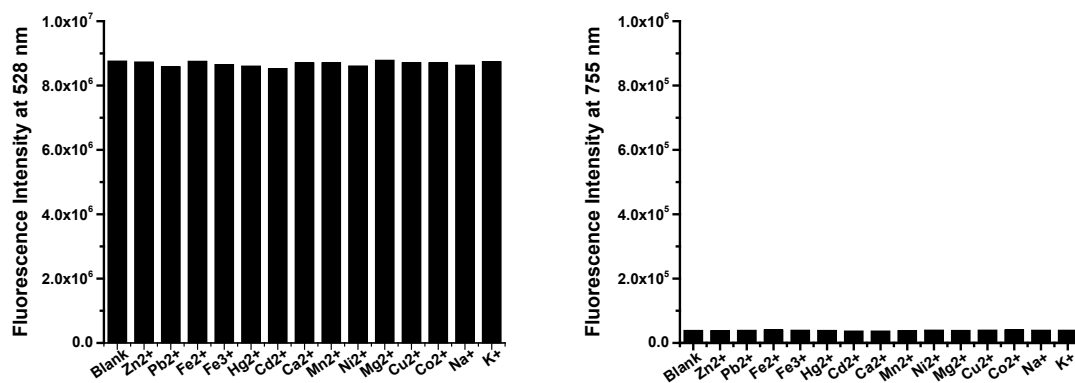
Figure S B.12. Fluorescence responses of the probe coumarin and hemicyanine fluorescence at 528 nm (left) and 755 nm (right) to pH 7.6 over different 50 μM metal ions in 10 mM citrate buffer containing 5 μM probe **A** and 40% ethanol at excitation of 420 nm, respectively.
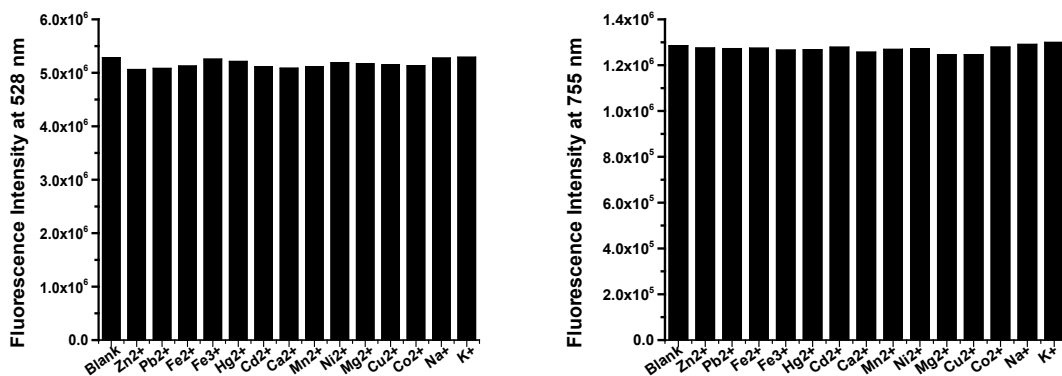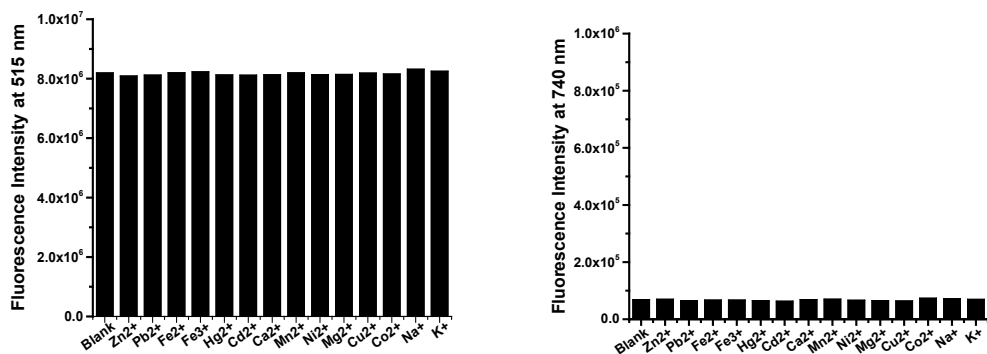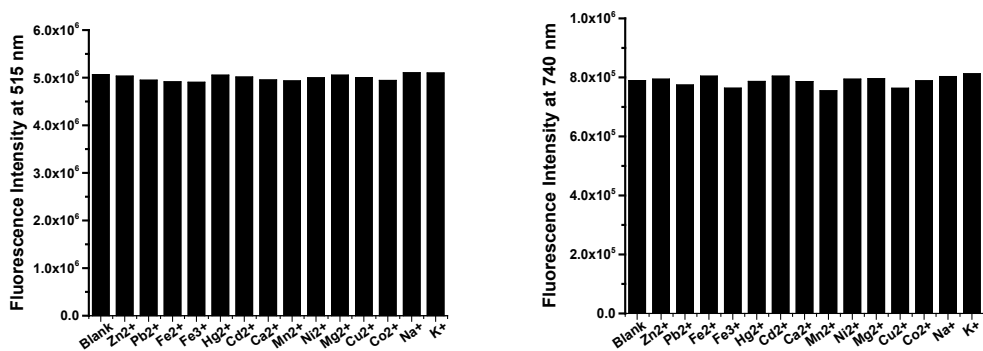

Figure S B.13. Fluorescence responses of the probe coumarin and hemicyanine fluorescence at 528 nm (left) and 755 nm (right) to pH 2.4 over different 50 μM metal ions in 10 mM citrate buffer containing 5 μM probe **A** and 40% ethanol at excitation of 420 nm, respectively.

Figure S B.14. Fluorescence responses of the probe coumarin and hemicyanine fluorescence at 515 nm (left) and 740 nm (right) to pH 7.6 over different 50 μM metal ions in 10 mM citrate buffer containing 5 μM probe **B** and 40% ethanol at excitation of 420 nm, respectively.
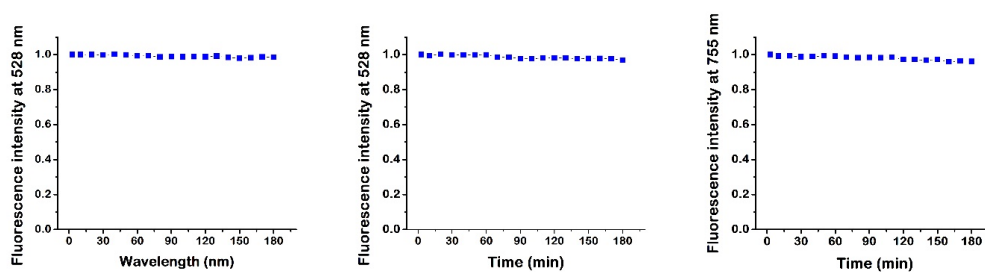

Figure S B.15. Fluorescence responses of the probe coumarin and hemicyanine fluorescence at 515 nm (left) and 740 nm (right) to pH 2.4 over different metal ions in 10

mM citrate buffer containing 5 μM probe **B** and 40% ethanol at excitation of 420 nm, respectively.

Figure S B.16. Normalized fluorescence intensity of coumarin fluorescence at pH 7.6 (left) and 2.4 (middle) and hemicyanine fluorescence at pH 2.4 (right) in 10 mM citrate buffer containing 5 μM probe **A** and 40% ethanol at excitation of 420 nm.
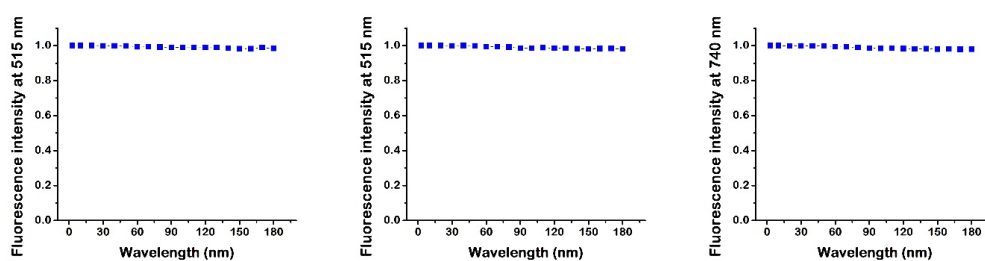

Figure S B.17. Normalized fluorescence intensity of coumarin fluorescence at pH 7.0 (left) and 2.4 (middle) and hemicyanine fluorescence at pH 2.4 (right) in 10 mM citrate buffer containing 5 μM probe **B** and 40% ethanol at excitation of 420 nm.

6. Enlarged fluorescence images of Hela cells incubated with different concentrations of probe A in the presence of Lyso Tracker Red.
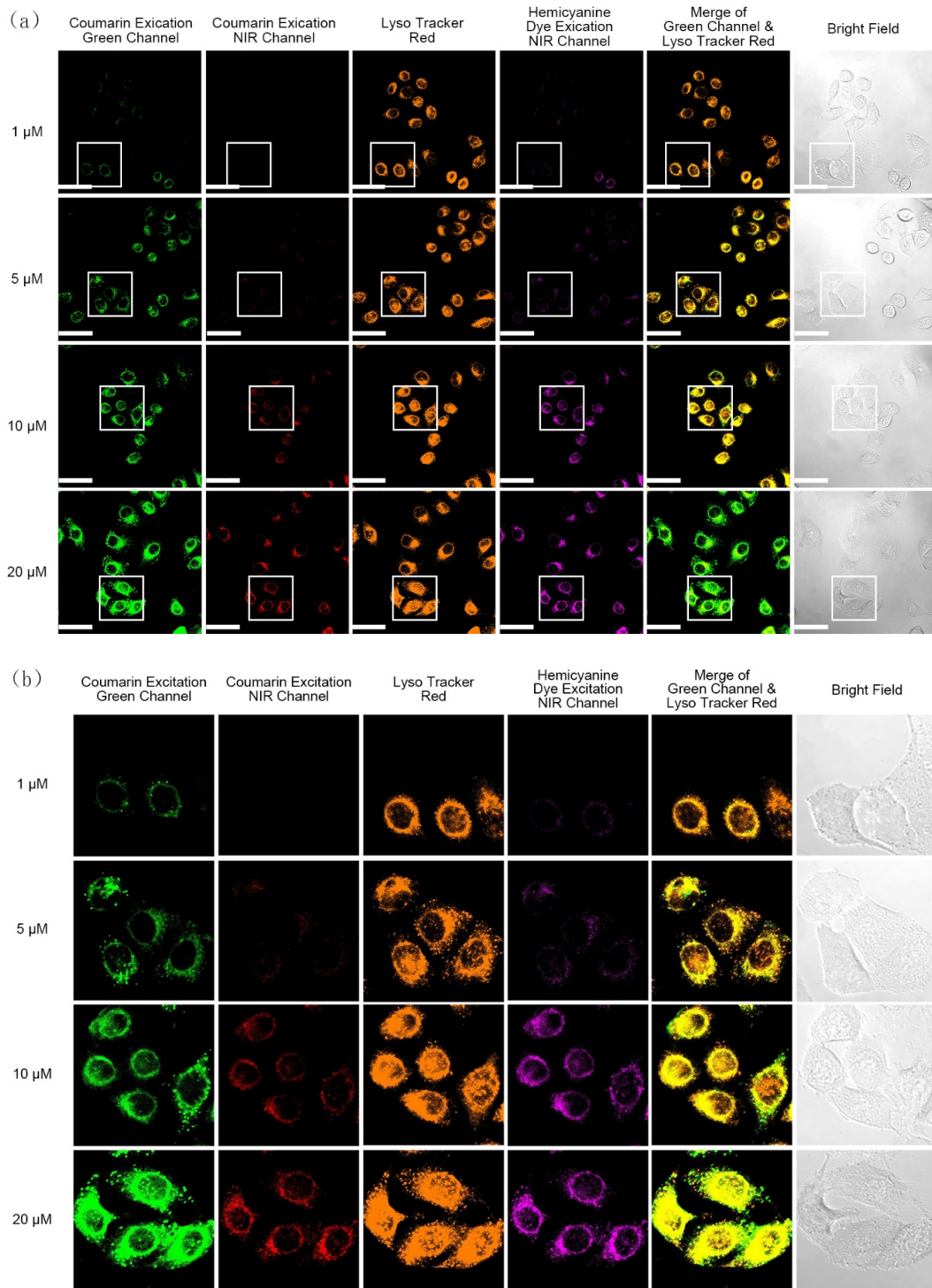
Appendix C   Supporting Information for Chapter 4

1. Instruments and Materials

Solvents and reagents were obtained from Sigma-Aldrich or Fisher scientific. Column chromatographic purification was conducted on silica gel (200-300 mesh) obtained from Sigma-Aldrich while thin-layer chromatography (TLC) analysis was conducted in silica gel plates obtained from Sigma-Aldrich. Compound **1**, **6**, and **7** were prepared according to the reported procedures. Intermediates and the fluorescent probes were characterized by Varian Unity Inova NMR spectrophotometer at 400 MHz and 100 MHz to record ^{1}H NMR and ^{13}C NMR spectra in CDCl$_3$ or CD$_3$OD solutions, respectively.   Double focusing magnetic mass spectrometer or fast atom bombardment (FAB) ionization mass spectrometer was used to determine high-resolution mass spectrometer data (HRMS). Absorption spectra were collected by employing Per-kin Elmer Lambda 35 UV/VIS spectrometer while fluorescence spectra were performed on Jobin Yvon Fluoromax-4 spectrofluorometer.

Synthesis of compound 3: Compound **2** (0.35 g, 2.2 mmol) was slowly put to solution of compound **1** (0.8 g, 2.2 mmol) in H$_2$SO$_4$ (10 ml) at 0 °C. The reaction was stirred for 3 h at 100 °C. After reaction completed, the mixture was poured into the ice-water and HClO$_4$ (1 ml) was added. The precipitate was formed, filtrated and purified by column chromatography employing methanol/dichloromethane/ (1:10, v/v) to afford compound **3** as blue solid (1.0 g, 79%). ^{1}H NMR (CD$_3$OD/CDCl$_3$, 400 MHz) δ: 8.32 (s, 1H), 8.03 (d, *J* = 6.4 Hz, 1H), 7.80 (d, *J* = 8.0 Hz, 1H), 7.38 (s, 1H), 7.09 (d, *J* = 8.0 Hz, 1H), 6.99 (s, 1H), 6.96 – 6.93 (m, 2H), 6.69 (d, *J* = 8.4 Hz, 1H), 6.50 (s, 1H), 3.21 (s, 3H), 3.20 (s, 3H), 2.82 (m, 2H), 2.57 (m, 2H); HRMS: calculated for C$_{26}$H$_{22}$BrN$_2$O$_3$$^+$ [M-ClO$_4$]$^+$ 489.0808, found 489.0813.

Synthesis of compound 8: The procedure for compound **8** was the same as synthesis of compound **3** using compound **1** (0.8 g, 2.2 mmol) and compound **2** (0.42 g, 2.2 mmol) as starting materials. The produce was obtained as blue solid (1.1 g, 82%).^{1}H NMR

(CD₃OD/CDCl₃, 400 MHz) δ: 8.22 (s, 1H), 7.99 (d, J = 9.2 Hz, 1H), 7.63 (d, J = 8.0 Hz, 1H), 7.17 (s, 1H), 6.89 (d, J = 7.6 Hz, 1H), 6.76 – 6.74 (m, 2H), 6.66 (d, J = 9.2 Hz, 1H), 6.42 (s, 1H), 3.11 (s, 3H), 3.10 (s, 3H), 3.10 (s, 3H), 3.09 (s, 3H), 2.84 – 2.75 (m, 2H), 2.52 – 2.45 (m, 2H); HRMS: calculated for $C_{28}H_{26}BrN_2O_3^+$ [M-ClO₄]⁺ 517.1127, found 517.1130.
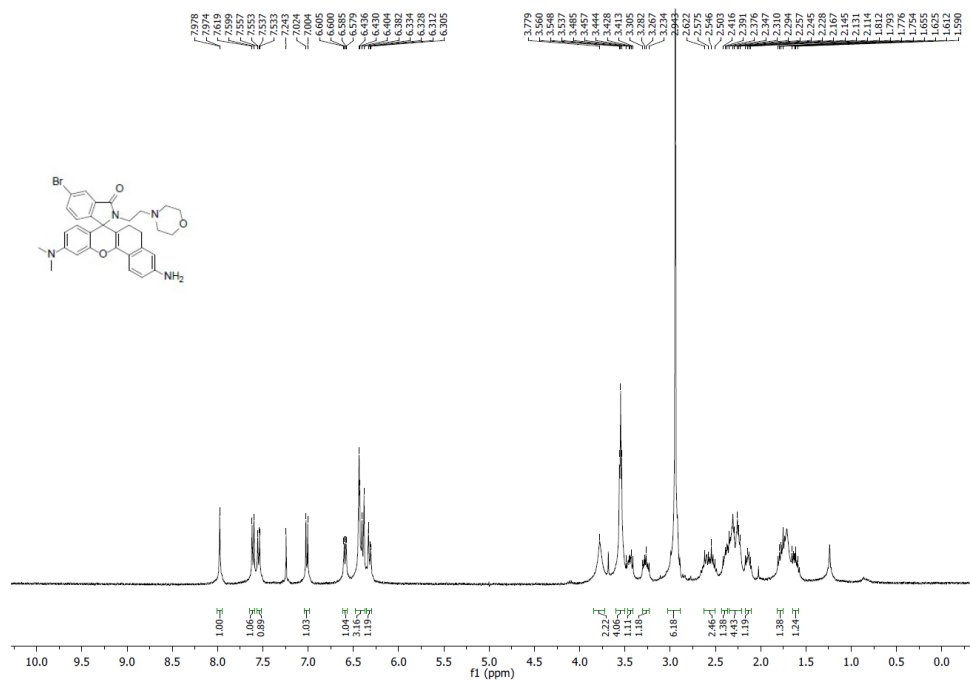
Synthesis of compound 5: Compound **3** (0.36 g, 0.6 mmol) and BOP reagent (0.33 g, 0.75 mmol) was put to dry dichloromethane (15 ml). After the mixture was stirred for 30 min, compound **4** (0.1 g, 0.75 mmol) and Et₃N (0.5 ml) were further added to the mixture, and the reaction was conducted overnight. When the mixture was washed with water (10 ml *2), the organic layer was collected, dried over Na₂SO₄, and filtered. After the filtrate was concentrated under reduced pressure, the residue was purified by column chromatography using hexane /ethyl acetate (1:1, v/v) to yield the product as grey yellow solid (0.18 g, 50%). ¹H NMR (400 MHz, CDCl₃) δ: 7.97 (d, J = 1.6 Hz, 1H), 7.61 (d, J = 8.0 Hz, 1H), 7.54 (dd, J = 8.0 Hz, 1.6 Hz, 1H), 7.01 (d, J = 8.0 Hz, 1H), 6.59 (dd, J = 8.0 Hz, 2.0 Hz, 1H), 6.44 – 6.38 (m, 3H), 6.32 (dd, J = 8.8 Hz, 2.4 Hz, 1H), 3.78 (s, 2H), 3.55 (t, J = 4.8 Hz, 4H), 3.49 – 3.41 (m, 1H), 3.31 – 3.23 (m, 1H), 2.94 (s, 6H), 2.62 – 2.50 (m, 2H), 2.42 – 2.38 (m, 1H), 2.34 – 2.23 (m, 4H), 2.17 – 2.11 (m, 1H), 1.81– 1.75 (m, 1H), 1.65 – 1.59 (m, 1H); ¹³C NMR (100 MHz, CDCl₃) δ: 166.9, 152.8, 151.5, 150.2, 147.3, 138.4, 135.4, 134.1, 128.8, 126.2, 125.3, 123.7, 122.6, 120.4, 114.3, 112.7, 109.3, 105.7, 100.6, 98.9, 67.1, 66.5, 56.6, 53.7, 40.5, 37.3, 28.4, 21.3. HRMS (ESI): calculated for $C_{32}H_{24}BrN_4O_3$ [M+H]⁺ 600.1814, found 600.1807.

Synthesis of compound 9: A mixture of 1, 2-diaminobenzene (1.0 g, 9.25 mmol), 1-chloro-2-[2-(2-methoxyethoxy)ethoxy]ethane (2.0 g, 11 mmol), KI (0.46 g, 2.8 mmol) and K₂CO₃ (2.56 g, 18.5 mmol) in dry DMF (15 ml) was heated for 24 h at 100 °C. After the reaction was filtered, the solvent was removed from the filtrate. The residue was purified by column chromatography employing methanol /dichloromethane (1:20, v/v) to afford the product as colorless oil (0.5 g, 21%). ¹H NMR (400 MHz, CDCl₃) δ: 6.79 – 6.75 (m, 1H), 6.70 – 6.64 (m, 4H), 3.72 (t, J = 5.2 Hz, 2H), 3.66 – 3.65 (m, 4H), 3.64 – 3.63 (m, 2H), 3.55 – 3.52 (m, 2H), 3.36 (s, 3H), 3.27 (t, J = 5.2 Hz, 2H); ¹³C NMR (100 MHz, CDCl₃) δ:
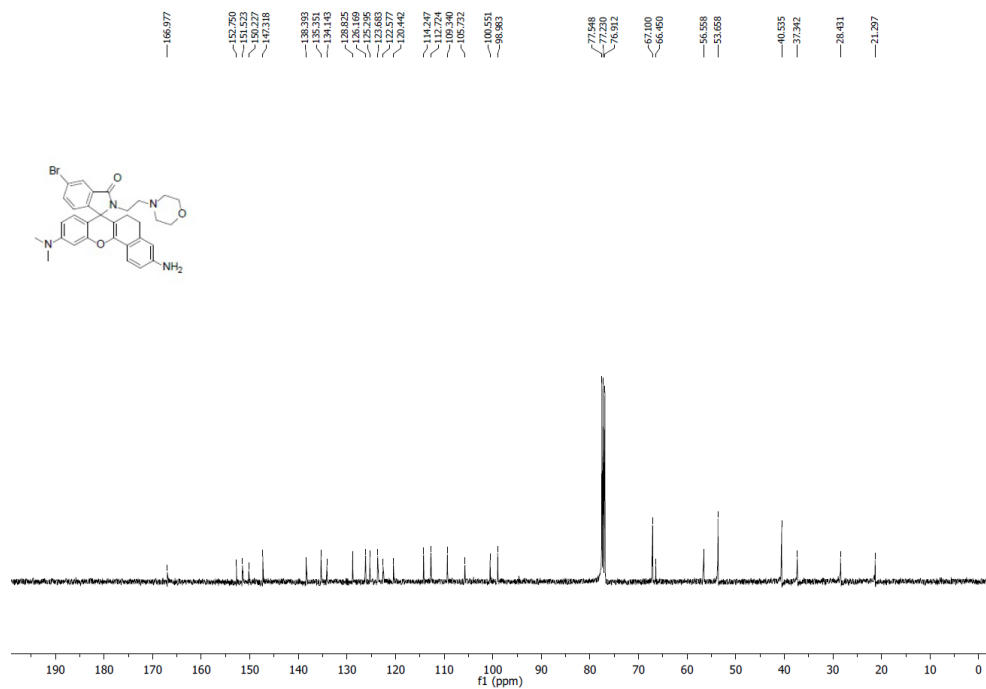
137.4, 135.2, 120.4, 119.2, 116.4, 112.7, 72.2, 70.9, 70.8, 70.6, 70.0, 59.3, 44.3. HRMS (ESI): calculated for $C_{13}H_{22}N_2NaO_3$ [M+Na]$^+$ 277.1528, found 277.1536.

Synthesis of compound 10: The procedure for compound **10** was the same as synthesis of compound **5** using compound **8** (0.31 g, 0.5 mmol) and compound **9** (0.15 g, 0.6 mmol) as starting materials. The product was obtained as grey yellow solid (0.17 g, 45%). ^{1}H NMR (400 MHz, CDCl$_3$) δ: 8.06 (s, 1H), 7.62 (dd, J = 8.0 Hz, 2.0 Hz, 1H), 7.54 (d, J = 8.4 Hz, 1H), 7.07 (d, J = 8.0 Hz, 1H), 7.02 (d, J = 8.0 Hz, 1H), 6.64 – 6.54 (m, 4H), 6.45 – 6.39 (m, 4H), 3.60 – 3.59 (m, 8H), 3.53 – 3.51 (m, 2H), 3.39 (s, 3H), 3.17 – 3.16 (m, 2H), 2.95 (s, 12H), 2.58 – 2.51 (m, 2H), 2.20 – 1.96 (m, 1H), 1.89 – 1.84 (m, 1H); ^{13}C NMR (100 MHz, CDCl$_3$) δ: 166.7, 153.4, 151.4, 150.8, 150.2, 145.1, 135.7, 133.8, 129.1, 128.7, 126.8, 126.0, 125.7, 125.3, 123.4, 122.7, 118.4, 117.9, 117.5, 112.4, 111.4, 111.1, 109.8, 109.3, 99.6, 99.1, 71.9, 70.7, 70.5, 70.3, 69.9, 59.4, 43.5, 40.7, 40.6, 29.0, 22.7. HRMS (ESI): calculated for $C_{41}H_{45}BrN_4NaO_5$ [M+Na]$^+$ 775.2471, found 775.2461.
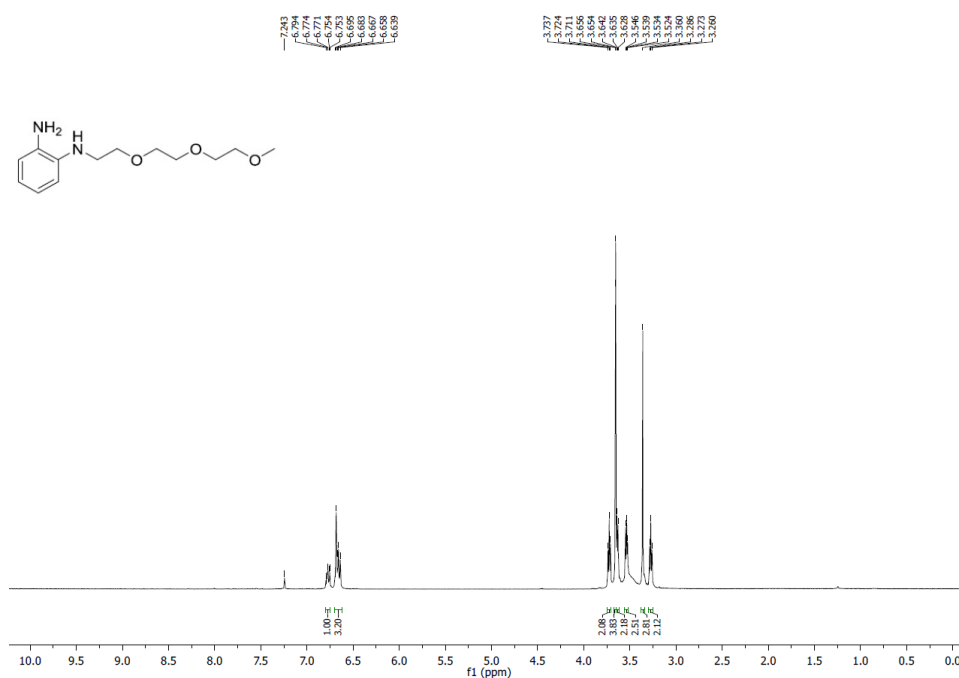
Synthesis of compound 12: The procedure for compound **12** was the same as synthesis of compound **5** using compound **8** (0.31 g, 0.5 mmol) and 1,2-diaminobenzene (65 mg, 0.6 mmol) as starting material. The product was obtained as grey yellow solid (0.12 g, 40%). ^{1}H NMR (400 MHz, CDCl$_3$) δ: 8.14 (s, 1H), 7.62 (d, J = 8.4 Hz, 1H), 7.58 (d, J = 8.8 Hz, 1H), 7.33 (dd, J = 6.0 Hz, 2.8 Hz, 1H), 7.08 (d, J = 8.0 Hz, 1H), 6.92 (t, J = 8.0 Hz, 1H), 6.67 (d, J = 8.4 Hz, 1H), 6.62 (d, J = 8.0 Hz, 1H), 6.57 (d, J = 8.4 Hz, 1H), 6.48 – 6.40 (m, 4H), 3.85 (s, 2H), 2.95 (s, 6H), 2.94 (s, 6H), 2.77 – 2.71 (m, 1H), 2.59 – 2.53 (m, 1H), 2.11 – 2.08 (m, 1H), 1.87 – 1.81 (m, 1H); ^{13}C NMR (100 MHz, CDCl$_3$) δ: 165.4, 153.1, 151.4, 150.8, 147.5, 144.0, 138.4, 135.7, 133.6, 128.8, 126.7, 125.7, 123.4, 123.1, 122.7, 119.0, 118.4, 118.3, 111.4, 109.8, 109.3, 100.0, 99.1, 70.7, 40.7, 40.6, 29.0, 22.3. HRMS (ESI): calculated for $C_{34}H_{32}BrN_4O_2$ [M+H]$^+$ 607.1709, found 607.1701.
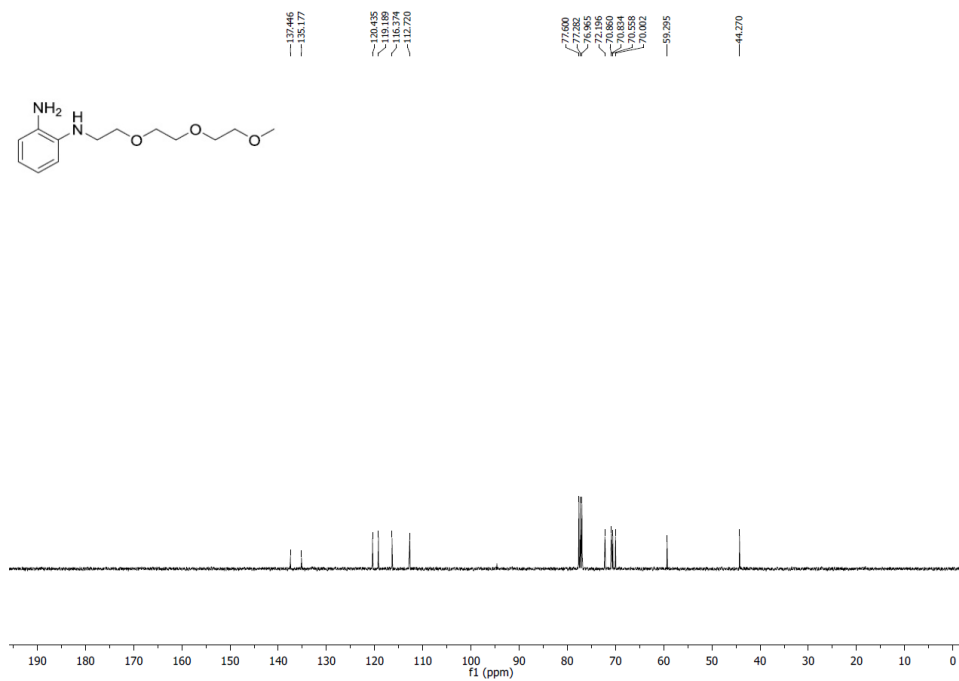
2. ^{1}H and ^{13}C NMR spectra of intermediates and the probes

- **Figure S C.1**. ^{1}H NMR spectrum of compound **3** in CD$_3$OD/CDCl$_3$ solution.

- **Figure S C.2**. ^{1}H NMR spectrum of compound **8** in CD$_3$OD/CDCl$_3$ solution.

- **Figure S C.3**. ^{1}H NMR spectrum of compound **5** in CDCl$_3$ solution.

- **Figure S C.4**. ^{13}C NMR spectrum of compound **5** in CDCl$_3$ solution.

- **Figure S C.5**. ^{1}H NMR spectrum of compound **9** in CDCl$_3$ solution.

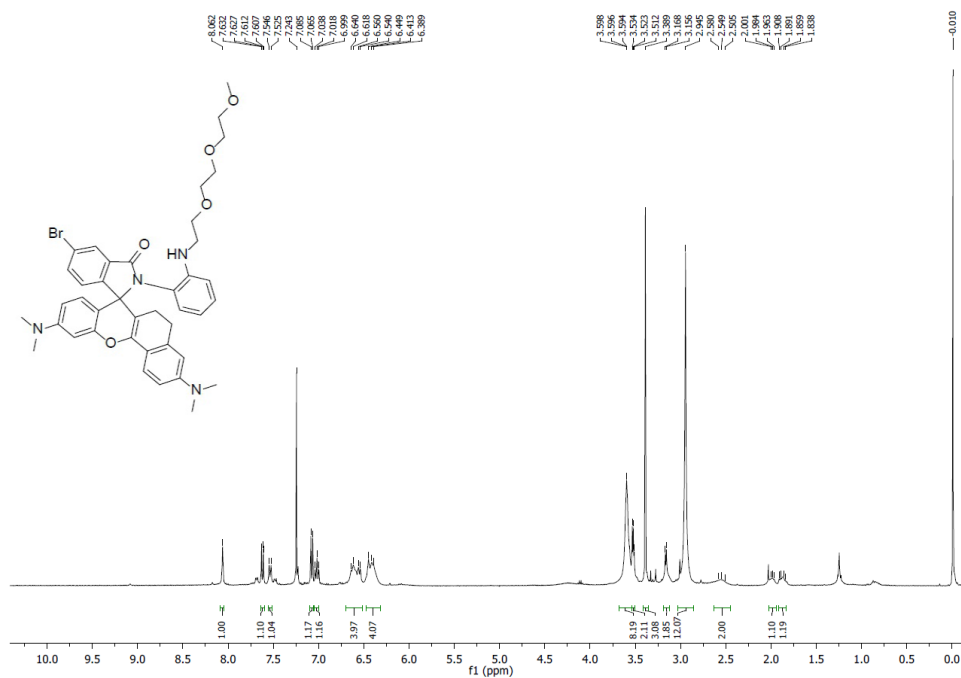- **Figure S C.6**. ^{13}C NMR spectrum of compound **9** in CDCl$_3$ solution.

Figure S C.7. ^{1}H NMR spectrum of compound **10** in CDCl$_3$ solution.

Figure S C.8. ^{13}C NMR spectrum of compound **10** in CDCl$_3$ solution.

Figure S C.9. ^{1}H NMR spectrum of probe **12** in CDCl$_3$ solution.

Figure S C.10. ^{13}C NMR spectrum of probe **12** in CDCl$_3$ solution.

Figure S C.11. ^{1}H NMR spectrum of probe **A** in CDCl$_3$ solution.

Figure S C.12. ^{13}C NMR spectrum of probe **A** in CDCl$_3$ solution.

Figure S C.13. ^{1}H NMR spectrum of probe **B** in CDCl$_3$ solution.

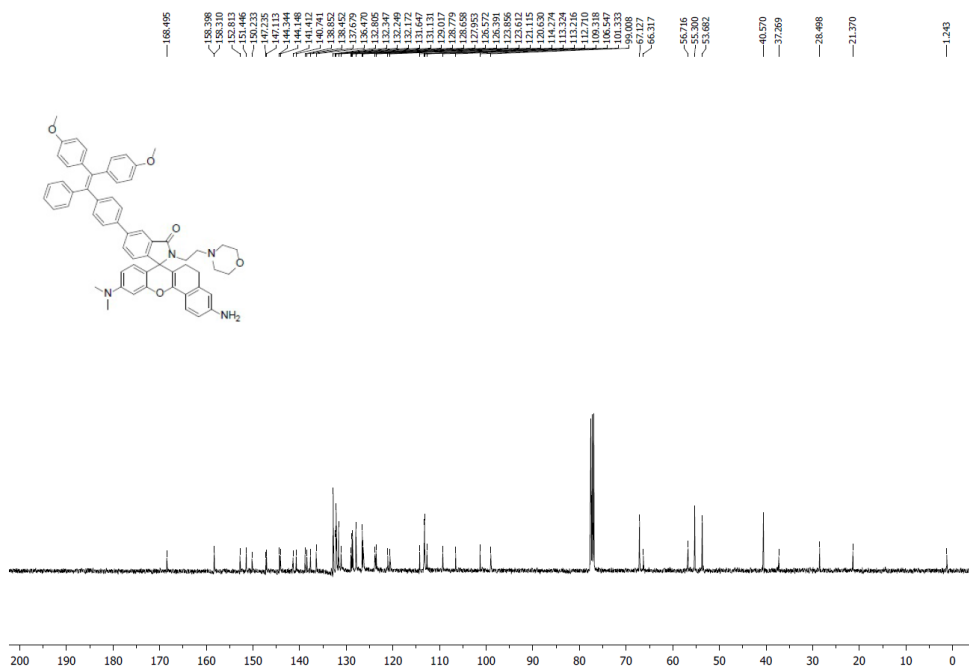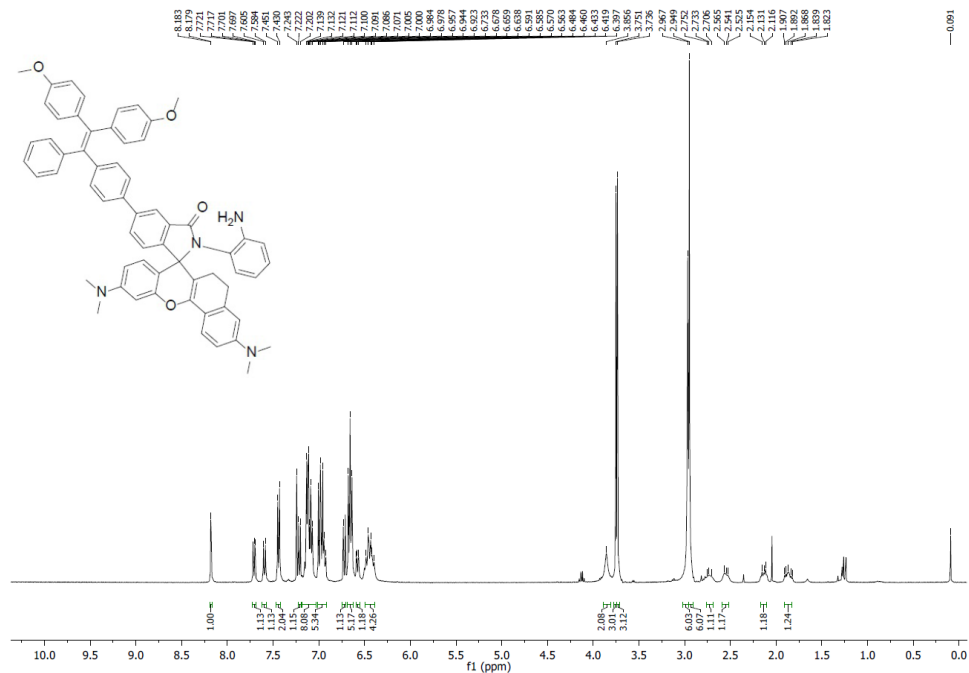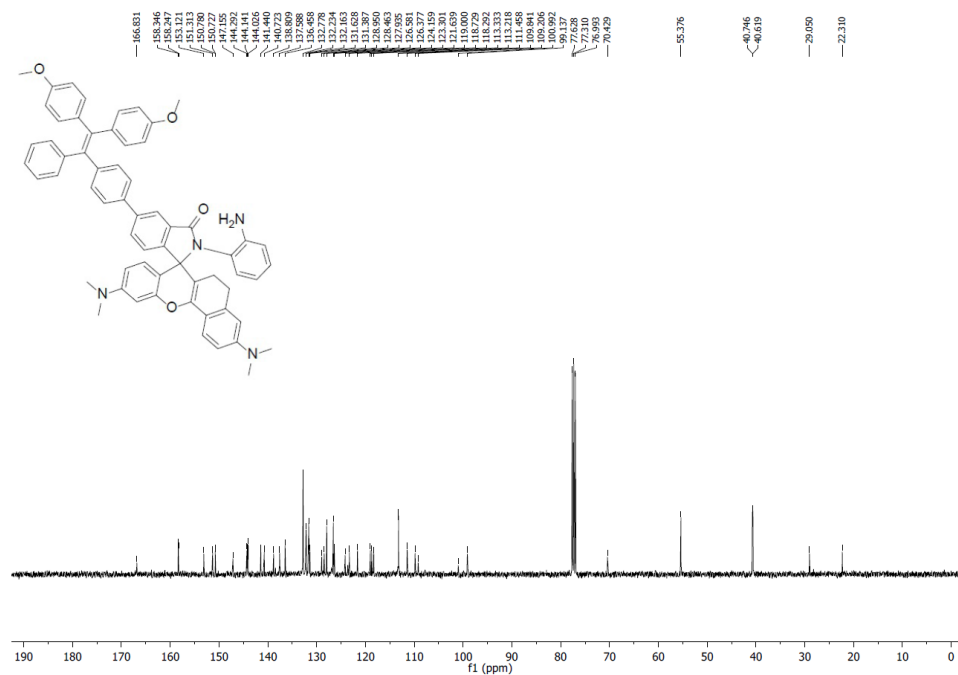**Figure S C.14**. ^{13}C NMR spectrum of probe **B** in CDCl$_3$ solution.

230

Figure S C.15. ¹H NMR spectrum of probe **C** in CDCl₃ solution.

Figure S C.16. ¹³C NMR spectrum of probe **C** in CDCl₃ solution.

3. Investigate Aggregation-induced Emission of the Probes.

Figure S C.17. Absorption spectra of probes A, B, and C with water percentages from 1% to 99% in ethanol and water mixtures.

Figure S C.18. Fluorescence spectra of 10 µM probes A, B, and C with different water percentages from 1% to 80% in ethanol and water mixtures.

Figure S C.19. A photo of probe A with different water percentages from 0% to 99% in water and ethanol mixed solutions under UV radiation (365 nm).

4. Dynamic Light Scattering Measurement

We investigate nanoparticles sizes of probe **A** in mixed ethanol and water solutions with different water percentages by conducting dynamic light scattering measurement through Coulter NP4plus, Beckman Coulter, Fllerton, CA. The measurements are carr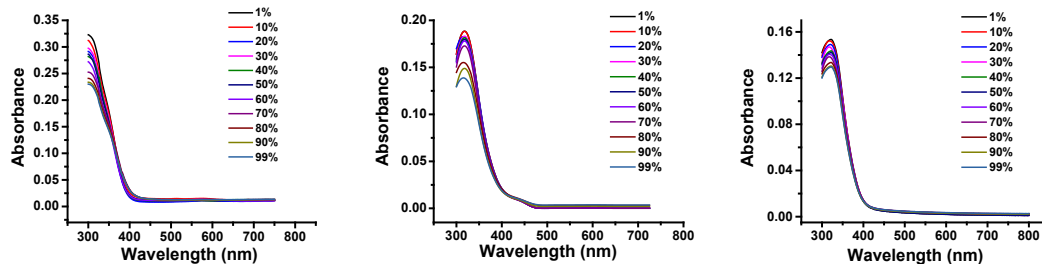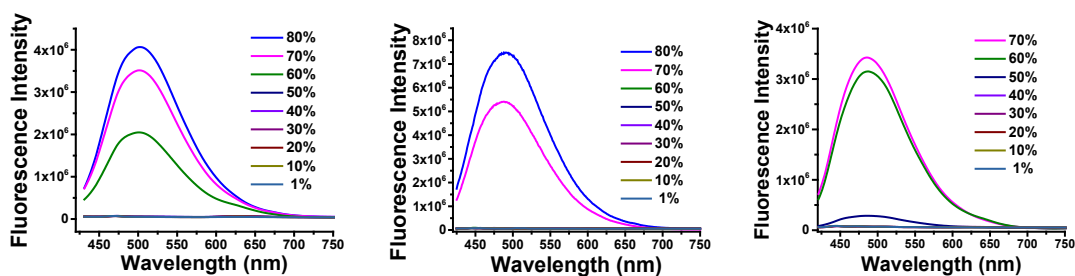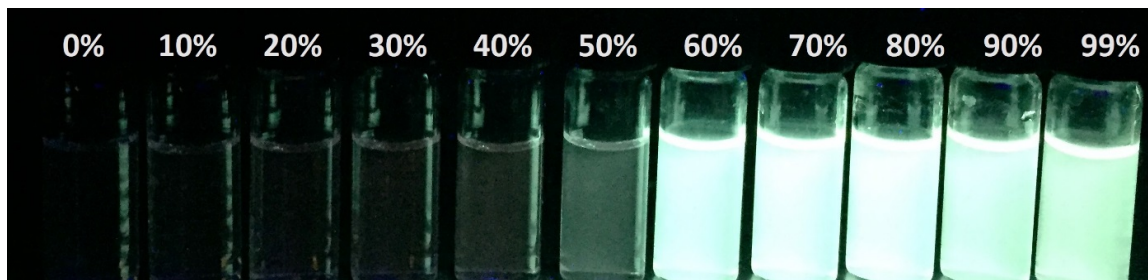ied out with scattering angles of 90 degree at room temperature of 25 ºC. There is not obvious dynamic light scattering peak related to formation of nanoparticles of probe **A** in ethanol solution (Figure S20). However, increase of water percentage to 80% causes aggregation of probe A in the solution as dynamic light scattering peaks were observed with large nanoparticles of 7422 nm (Figure S21).

Unimodal Results Summary

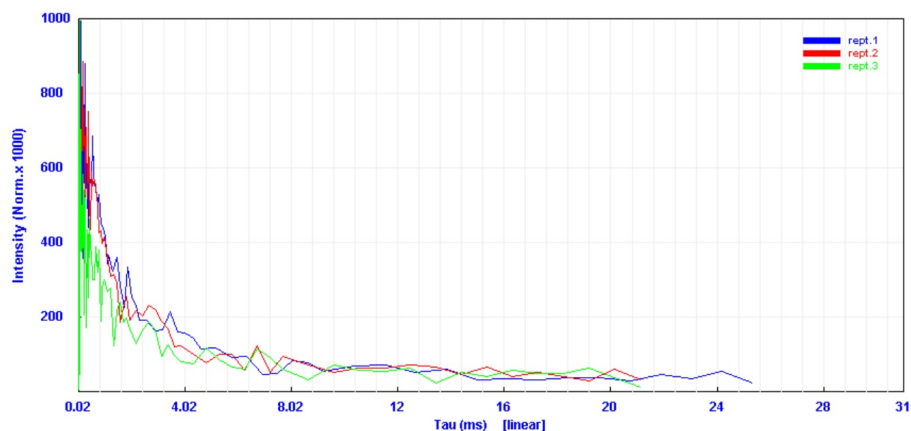| Rept#.	Mean (nm)	P.I.	Diff.Coef (m²/s)	Counts/s	Baseline Error	Overflow
Rept.1	744.3	-2.512	4.81e-13	1.17e+05	0.38%	0
Rept.2	0.0	-203.628	-1.74e-13	1.42e+05	0.40%	0
Rept.3	127.6	1.305	2.80e-12	1.55e+05	0.08%	0
Average	290.6 ± 325.02	-68.278 ± 95.720				

Figure S C.20. Dynamic light scattering measurement data of 5 µM in ethanol solution.

Unimodal Results Summary

Rept#.	Mean (nm)	P.I.	Diff.Coef (m²/s)	Counts/s	Baseline Error	Overflow
Rept.1	6306.2	0.473	5.14e-14	1.56e+06	8.79%	0
Rept.2	8145.1	-0.152	3.98e-14	1.48e+06	2.95%	0
Rept.3	7816.0	-0.194	4.15e-14	1.47e+06	1.23%	0
Average	7422.4 ± 800.65	0.042 ± 0.305				

Figure S C.21. Dynamic light scattering measurement data of 5 µM in ethanol solution containing 80% water.

5. Calculation of fluorescence quantum yields of the probes

Fluorescence quantum yields of the probes were calculated according to literature[3] using the equation below.

$$\phi_x = \phi_{st} \frac{\eta_x^2 \, A_{st} I_x}{\eta_{st}^2 \, A_x I_{st}}$$

ϕ represents fluorescence quantum yield. I_x is integration of sample's fluorescence spectra at specific excitation wavelength. A is the absorbance at the specific excited wavelength while the absorbances at the wavelength of excitation is optimally kept in between 0.02 and 0.05. η is the refractive index of solvents which were used for optical measurements, and the subscripts x and st stand for the probe and a reference compound of known fluorescence quantum yield, respectively.

Fluorescence quantum yields of the probe rhodamine acceptors were calculated at pH 2.8 using a near-infrared rhodamine dye (Standard) as a standard with a fluorescence quantum yield 37% in pH 7.4 PBS buffer with 10% ethanol. Compound **1** was synthesized according to the procedure in literature[2]. Rhodamine 6G with fluorescence quantum yield of 95% in ethanol was used as standard to calculate quantum yields of TPE donor parts.

6. Determination of pKa by fluorometric titration

The constant K_a of probe**s** were obtained by fluorometric titration as a function of pH using the fluorescence spectra. The expression of the steady-state fluorescence intensity F as a function of the proton concentration has been extended for the case of a n: 1 complex between H^+ and a fluorescent probe, which is expressed by the equation below:

$$F = \frac{F_{min}[\text{H}^+]^n + F_{max}K_a}{K_a + [\text{H}^+]^n}$$

F_{min} and F_{max} are the fluorescence intensities at maximal and minimal H^+ concentrations, respectively, and n is apparent stoichiometry of H^+ binding to the probe which affects the fluorescent change. Nonlinear fitting of equation expressed above to the fluorescence titration data recoded as a function of H^+ concentration with K_a and n as free adjustable parameters yields the estimated apparent constant of K_a.

7. TPE donor Emission spectra at pH 7.6, and rhodamine acceptor absorption spectra at pH 3.2
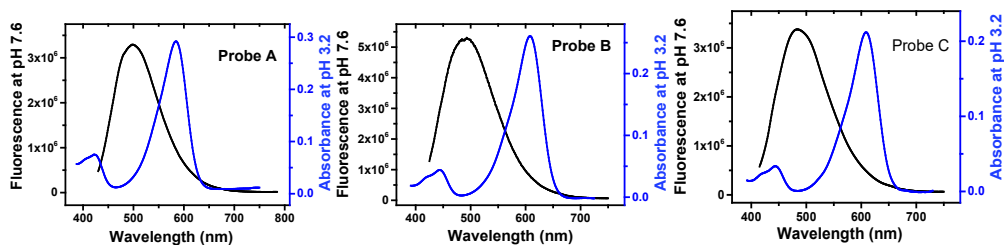
Figure S C.22. TPE donor fluorescence spectra of probes **A** (left), **B** (middle) and **C** (right) in 10 mM pH 7.6 citrate buffers and rhodamine acceptor absorption spectra of probes **A** (left), **B** (middle) and **C** (right) in 10 mM pH 3.2 citrate buffers.

8. Probe optical responses to pH changes.
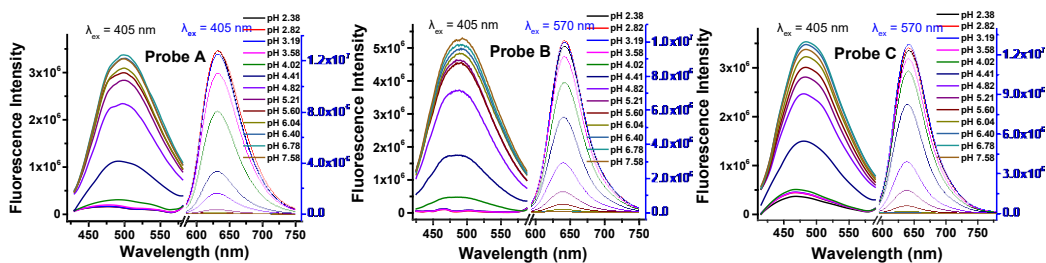
Figure S C.23. Fluorescence spectra (left) of probes **A** (left), **B** (middle) and **C** (right) in 10 mM citrate buffers under TPE excitation at 405 nm and rhodamine excitation at 570 nm.

9. Fluorescence spectra of the probes under rhodamine excitation
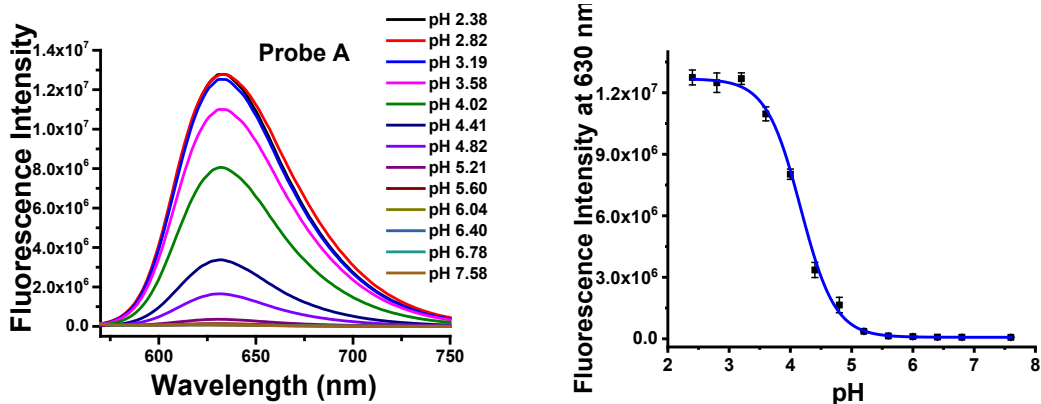
Figure S C.24. Fluorescence spectra (left) of probe **A** in 10 mM citrate buffers under rhodamine excitation of 550 nm, and plot (right) of fluorescence intensity versus pH.
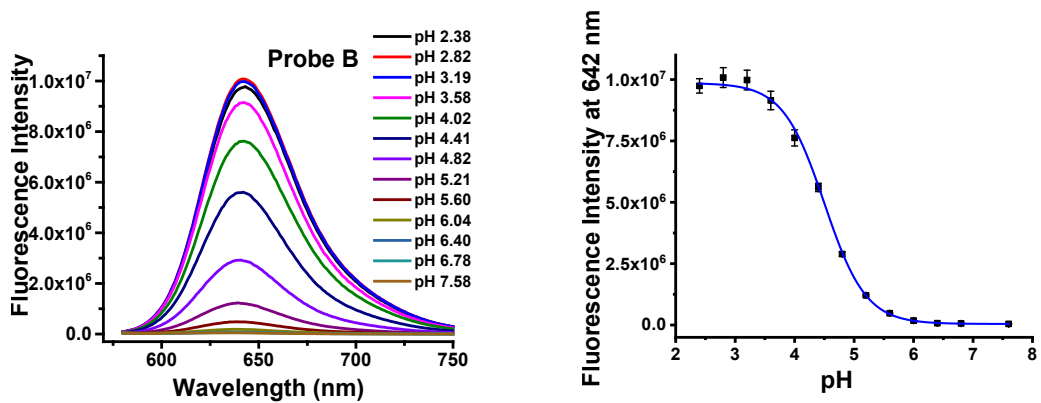
Figure S C.25. Fluorescence spectra (left) of probe **B** in 10 mM citrate buffers under rhodamine excitation of 570 nm, and plot (right) of fluorescence intensity versus pH.
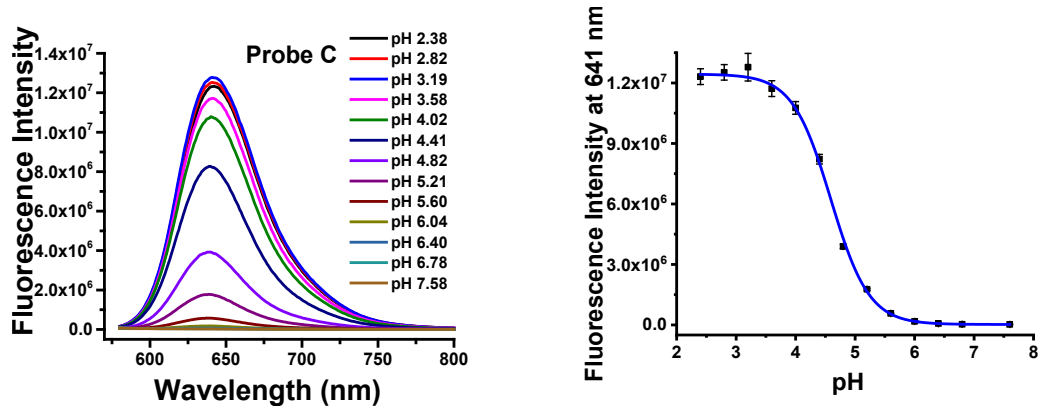
Figure S C.26. Fluorescence spectra (left) of probe **C** in 10 mM citrate buffers under rhodamine excitation at 570 nm, and plot (right) of fluorescence intensity versus pH.

10. Probe selectivity to pH over cations, anions, and amino acids

Figure S C.27. TPE donor fluorescence intensity of probe **A** at 489 nm in 10 mM citrate buffers with pH 7.58 or 2.38 containing 50 μM different cations, anions, amino acids or biothiols under excitation at 405 nm

Figure S C.28. Rhodamine fluorescence intensity of probe **A** at 630 nm in 10 mM citrate buffers with pH 7.58 or 2.38 containing 50 µM different cations, anions, amino acids or biothiols under excitation at 405 nm.

Figure S C.29. Rhodamine acceptor fluorescence intensity of probe **A** at 630 nm in buffers with pH 7.58 or 2.38 containing 50 µM different cations, anions, amino acids or biothiols under excitation at 555 nm.
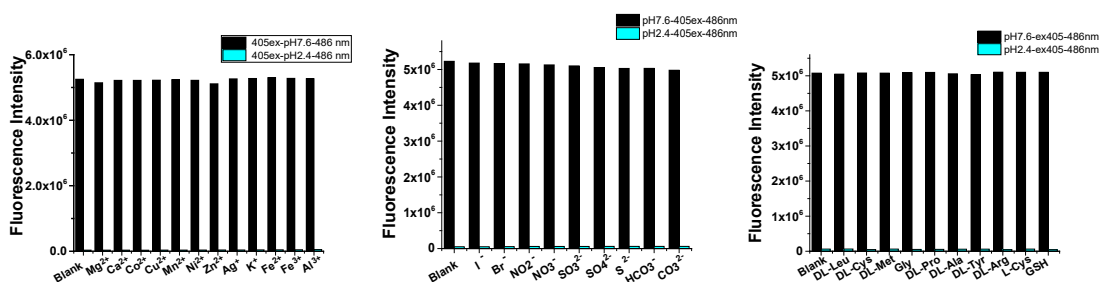
Figure S C.30. TPE donor fluorescence intensity of probe **B** at 486 nm in 10 mM citrate buffers with pH 7.58 or 2.38 containing 50 µM different cations, anions, amino acids, or biothiols under excitation at 405 nm.
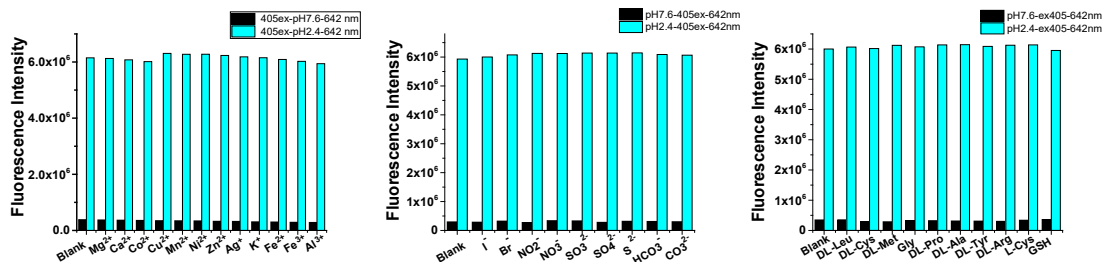
Figure S C.31. Rhodamine acceptor fluorescence intensity of probe **B** at 642 nm in 10 mM citrate buffers with pH 7.58 or 2.38 containing 50 µM different cations, anions, amino acids, or biothiols under excitation at 405 nm.
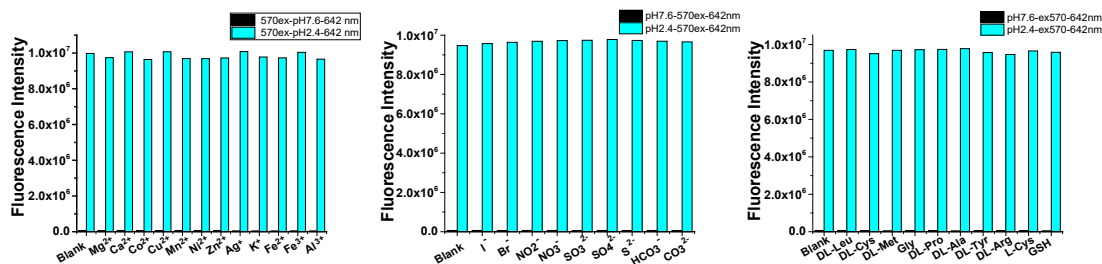
Figure S C.32. Rhodamine acceptor fluorescence intensity of probe **B** at 642 nm in buffers with pH 7.58 or 2.38 containing 50 µM different cations, anions, amino acids or biothiols under excitation at 570 nm.
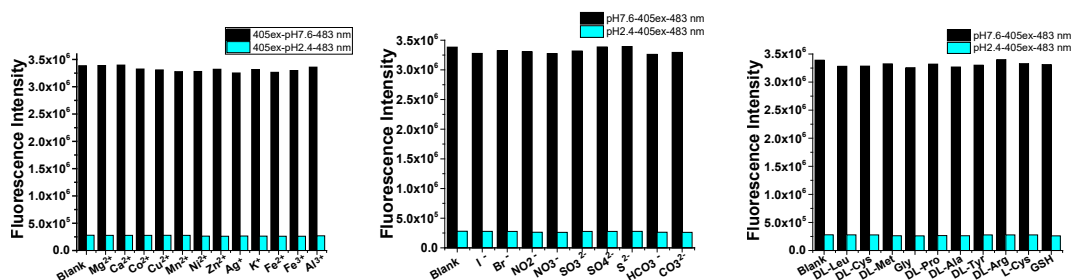
Figure S C.33. TPE donor fluorescence intensity of probe **C** at 483 nm in 10 mM citrate buffers with pH 7.58 or 2.38 containing 50 µM different cations, anions, amino acids or biothiols under excitation at 405 nm.
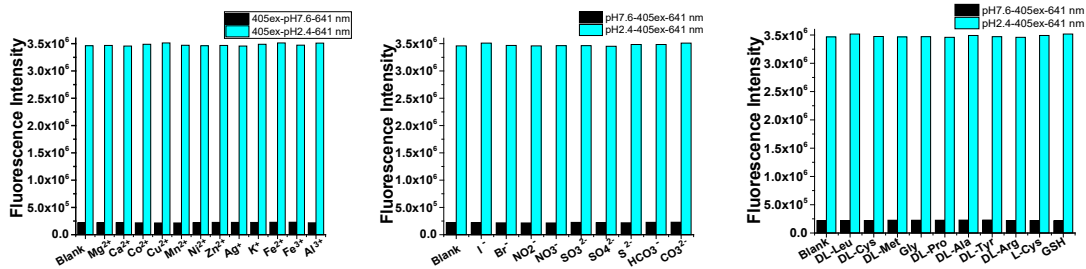
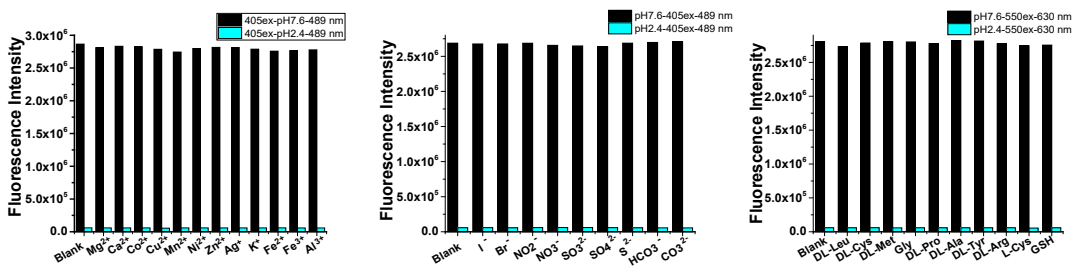**Figure S C.34**. Rhodamine fluorescence intensity of probe **C** at 641 nm in 10 mM citrate buffers with pH 7.58 or 2.38 containing 50 µM different cations, anions, amino acids or biothiols under excitation at 405 nm.

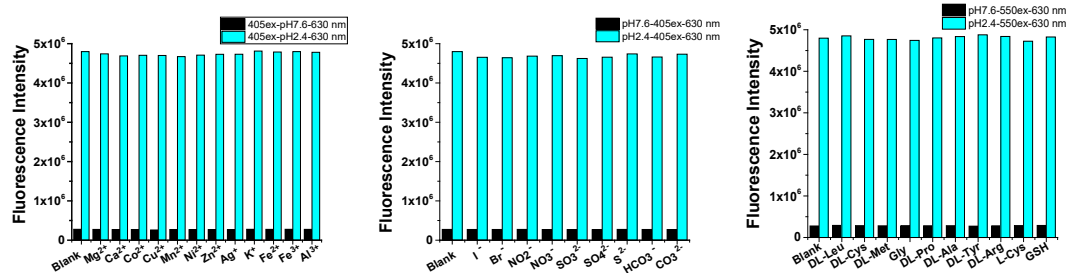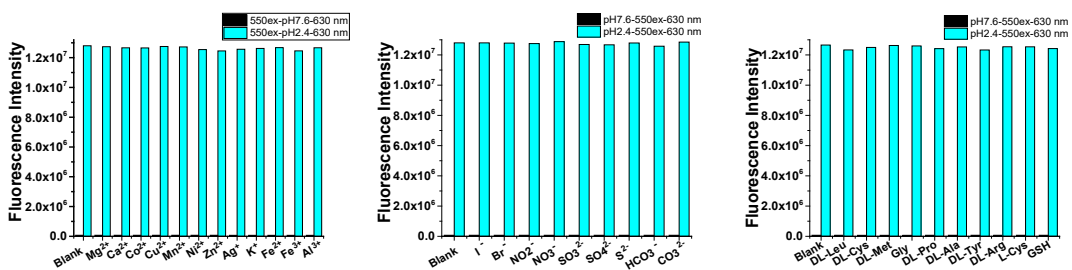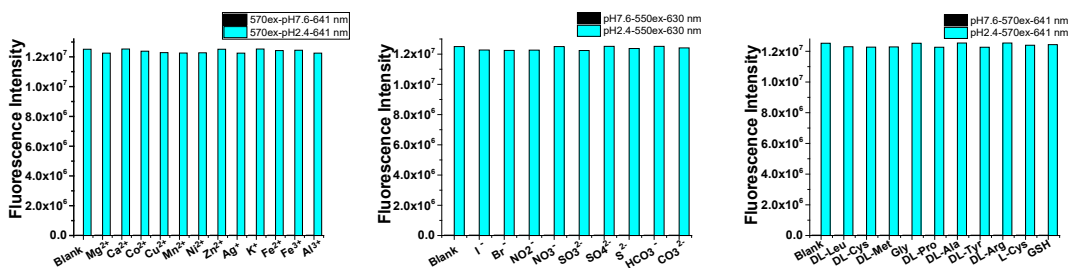
Figure S C.35. Rhodamine acceptor fluorescence intensity of probe **C** at 641 nm in buffers with pH 7.58 or 2.38 containing 50 µM different cations, anions, amino acids or biothiols under excitation at 570 nm.

11. Reversibility of probe fluorescence responses to pH changes
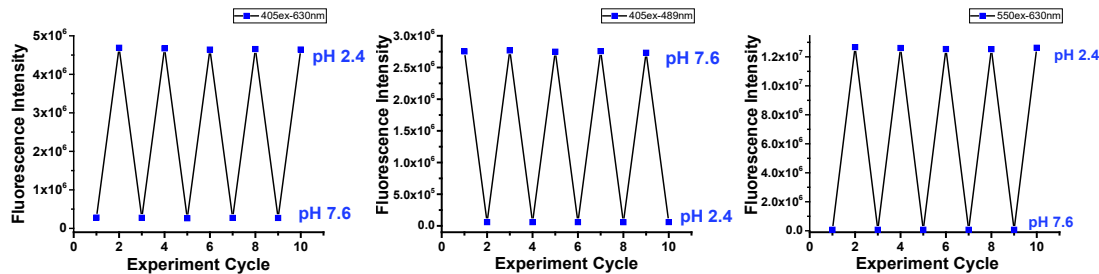
Figure S C.36. TPE donor (left) and rhodamine acceptor (middle and right) fluorescence responses of probes **A** to pH changes in 10 mM citrate buffers 2.4 and 7.6 under TPE excitation at 405 nm (left and middle) or rhodamine excitation at 550 nm (right).
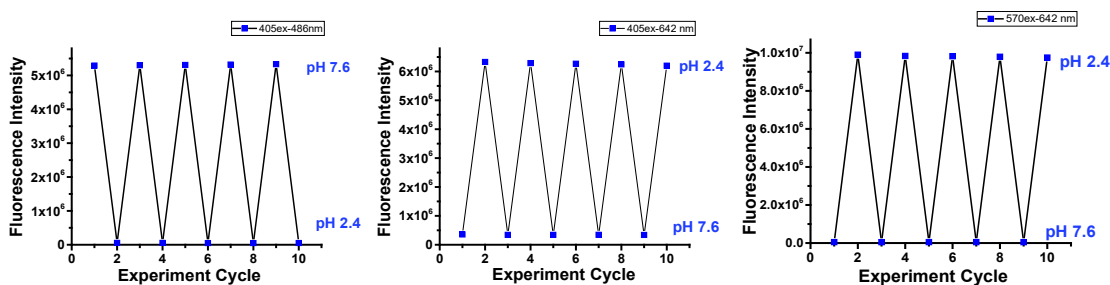
Figure S C.37. TPE donor (left) and rhodamine acceptor (middle and right) fluorescence responses of probe **B** to pH changes in 10 mM citrate buffers with pH 2.4 and 7.6 under TPE excitation at 405 nm (left and middle) or rhodamine excitation at 570 nm (right).
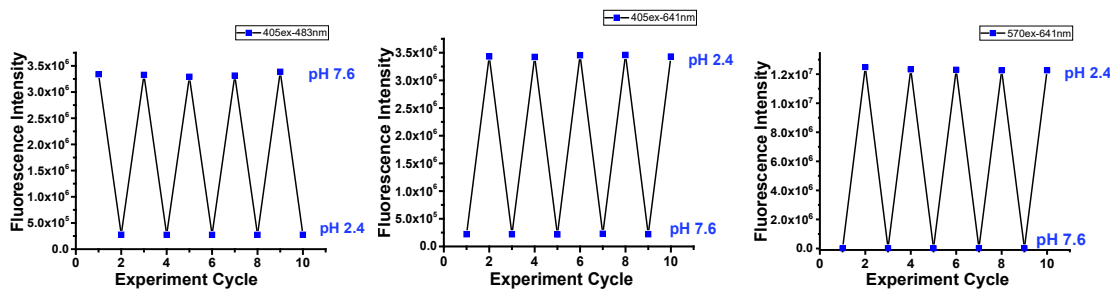
Figure S C.38. TPE donor (left) and rhodamine acceptor (middle and right) fluorescence responses of probe **C** to pH changes in 10 mM citrate buffers with pH 2.4 and 7.6 under TPE donor excitation at 405 nm (left and middle) or rhodamine excitation at 570 nm (right).

12. Photostability of the probes to pH changes
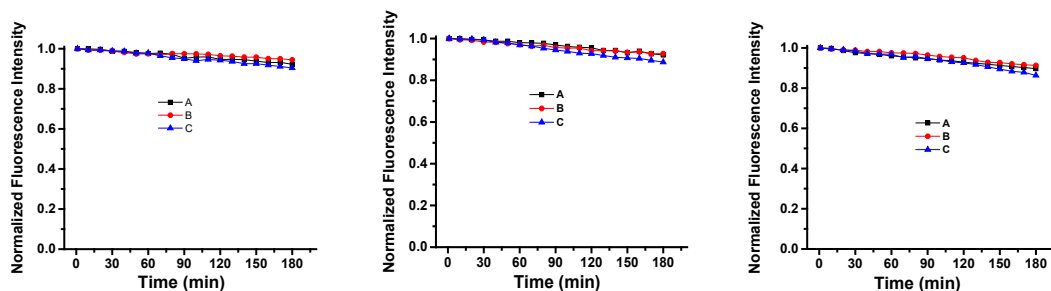
Figure S C.39. TPE donor fluorescence intensities at 489 nm, 486 nm and 483 nm (left) for probes **A**, **B**, and **C** under excitation at 405 nm versus time in a 10 mM citrate buffer with pH 7.6, respectively. Rhodamine fluorescence intensities at 630 nm, 642 nm, and 641 nm for probes **A**, **B** and **C** under TPE donor excitation at 405 nm (middle), and under rhodamine acceptor excitation at 550 nm, 570 nm and 570 nm (right) for probes **A**, **B**, and **C** versus time in a 10 mM citrate buffer with pH 2.4, respectively.

13. Cytotoxicity of the fluorescent probe.
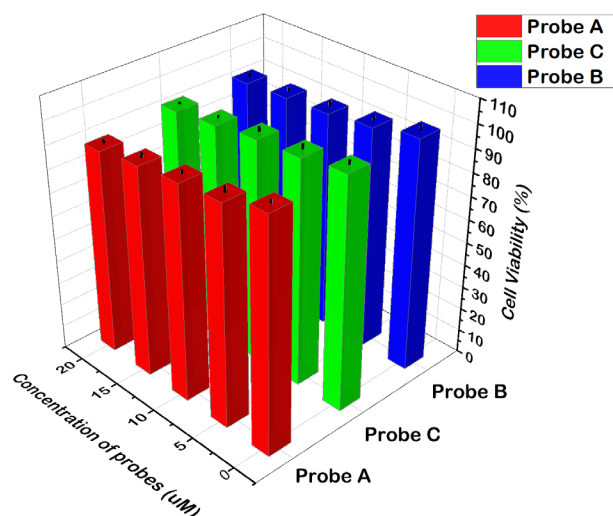
Figure S C.40. Cytotoxicity of probes **A**, **B**, and **C** determined by MTS assay. The HeLa cells were incubated with 0, 5, 10, 15, and 20 μM of probes **A**, **B**, and **C** for 48 h. The relative cell viability was normalized to untreated cells and the cell viability was obtained by measuring the absorbance at 490 nm, which has a linear relationship with the cell viability. The error bars indicate ± SD.

14. Cellular Imaging of the probes
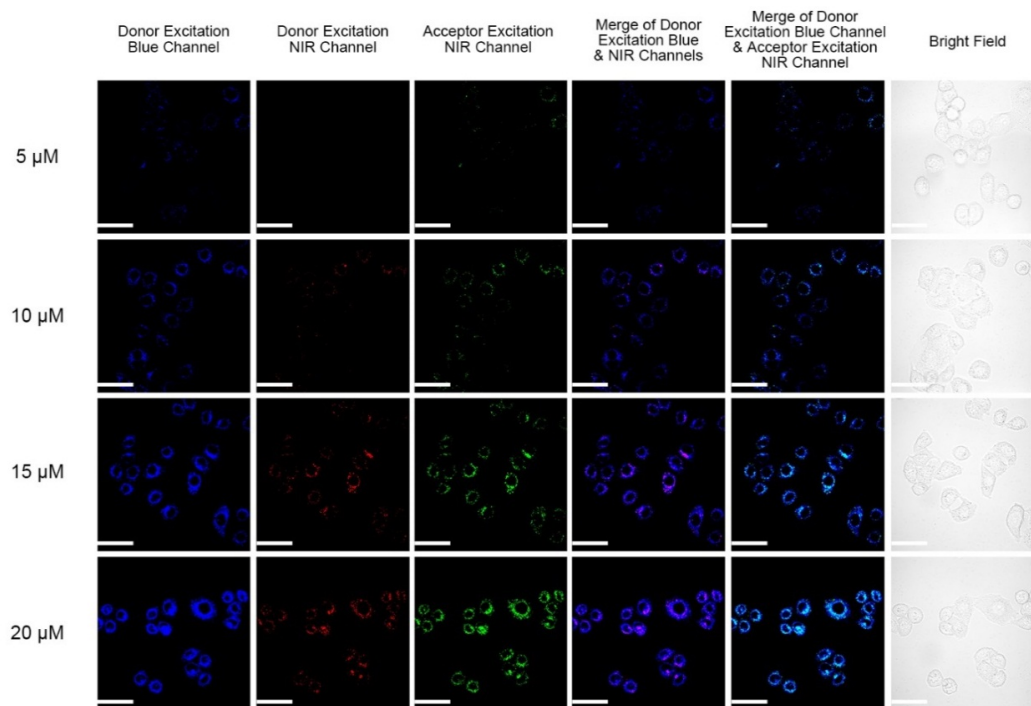
Figure S C.41. Cellular images of HeLa cells in 10 mM citrate pH 7.4 buffers containing probe **A** with different concentrations. The confocal fluorescence microscope was employed to obtain cellular images at 60× magnification. The blue channel of TPE donor fluorescence was collected from 475 to 525 nm, and the NIR channel (pseudo-colored as red for clarity) of rhodamine acceptor fluorescence in the second column was collected from 650 to 700 nm under excitation of TPE donor at 405 nm. The NIR channel (pseudo-colored as green for clarity) of rhodamine acceptor in the third column was collected from 650 to 700 nm under excitation of Rhodamine acceptor at 559 nm. Scale bar: 50 μM.
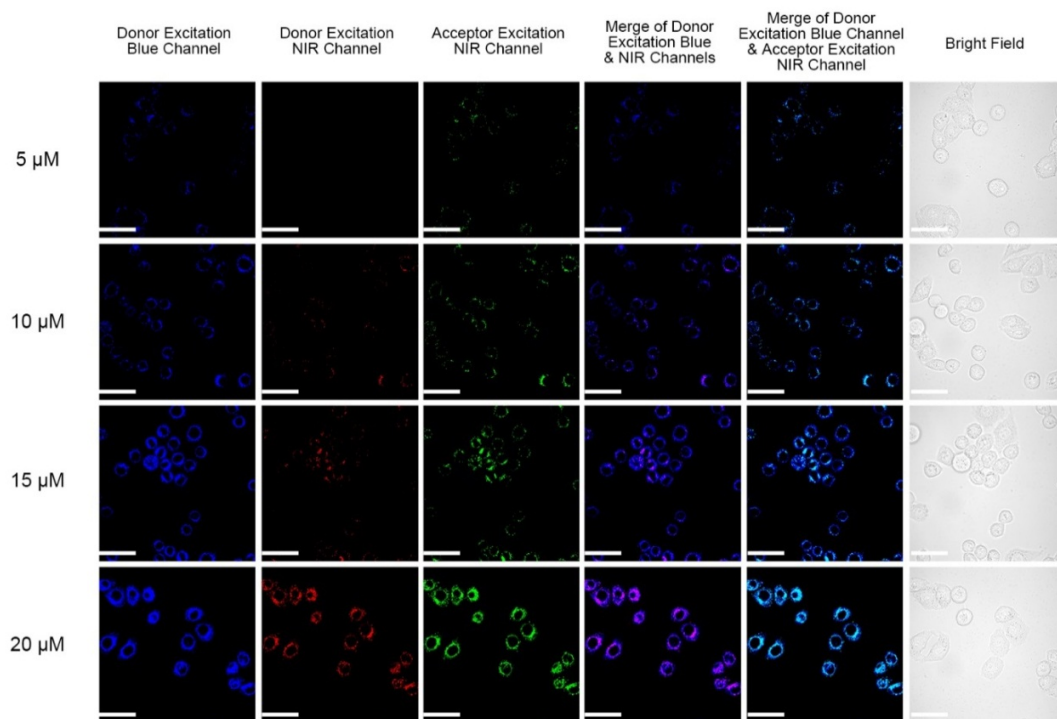
Figure S C.42. Cellular images of HeLa cells in 10 mM citrate pH 7.4 buffers containing probe **B** with different concentrations. The confocal fluorescence microscope was employed to obtain cellular images at 60× magnification. The blue channel of TPE donor fluorescence was collected from 475 to 525 nm, and the NIR channel (pseudo-colored as red for clarity) of rhodamine acceptor fluorescence in the second column was collected from 650 to 700 nm under excitation of TPE donor at 405 nm. The NIR channel (pseudo-colored as green for clarity) of rhodamine acceptor in the third column was collected from 650 to 700 nm under excitation of Rhodamine acceptor at 559 nm. Scale bar: 50 μM.
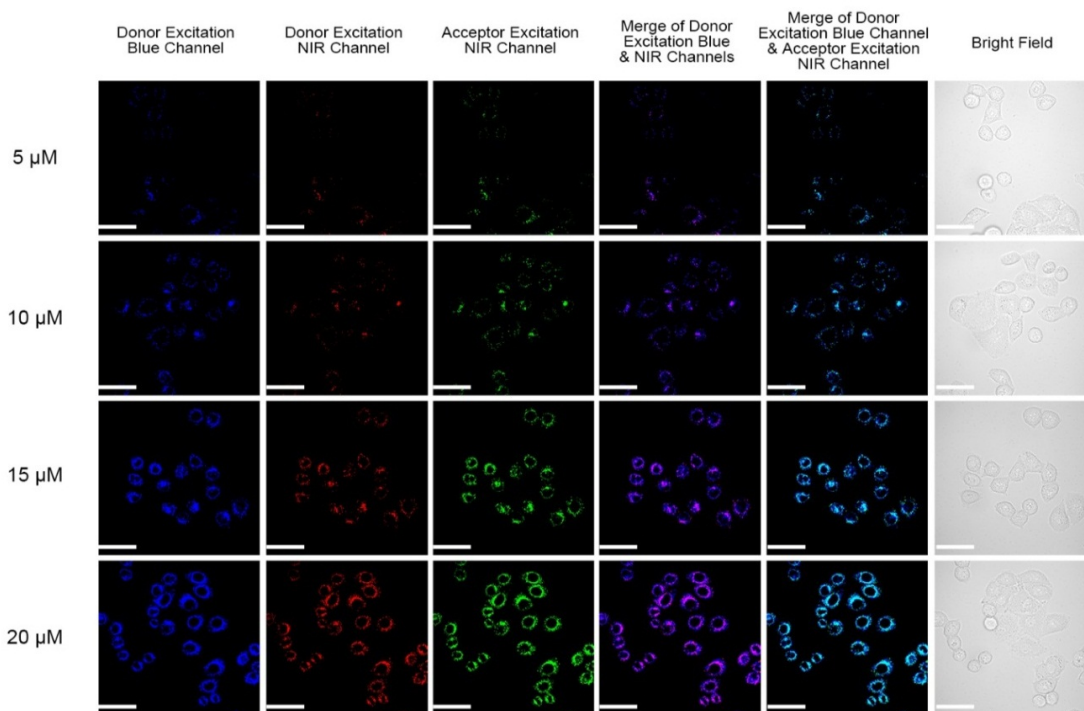
Figure S C.43. Cellular images of HeLa cells in 10 mM citrate pH 7.4 buffers containing probe **C** with different concentrations. The confocal fluorescence microscope was employed to obtain cellular images at 60× magnification. The blue channel of TPE donor fluorescence was collected from 475 to 525 nm, and the NIR channel (pseudo-colored as red for clarity) of rhodamine acceptor fluorescence in the second column was collected from 650 to 700 nm under excitation of TPE donor at 405 nm. The NIR channel (pseudo-colored as green for clarity) of rhodamine acceptor in the third column was collected from 650 to 700 nm under excitation of Rhodamine acceptor at 559 nm. Scale bar: 50 μM.

Near-infrared lysotracker
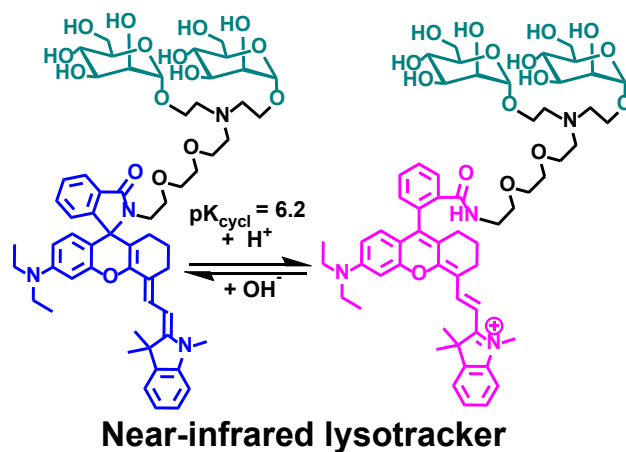
In order to investigate whether our probes as weak bases can be used to target lysosomes in live cells, we used a near-infrared fluorescent lysotacker to conduct colocalization correlation analysis. The Pearson's coefficients between donor excitation blue channel and near-infrared Lysotracker channel for probes **A**, **B** and **C** are 0.917, 0.896 and 0.934 respectively, indicating that our probes stay with near-infrared lysotracker together in lysosomes in live cells.
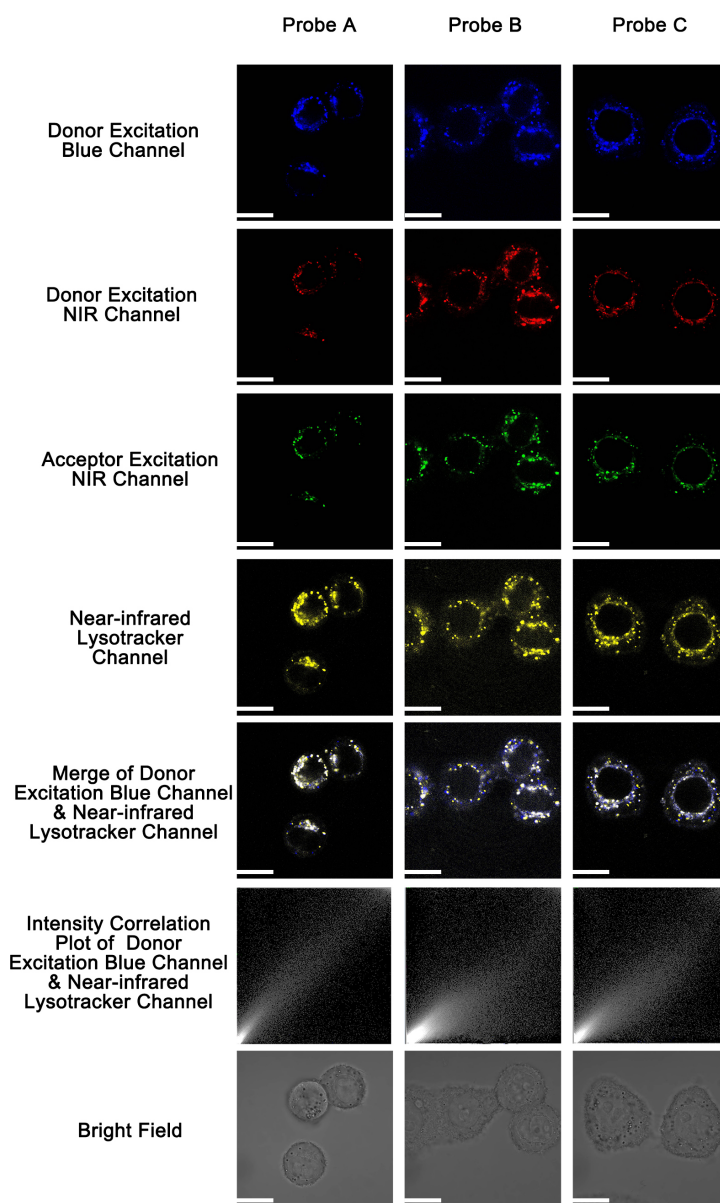
Figure S C.44. Fluorescence cellular images of HeLa Cells incubated with 10 µM near-infrared lysotracker and 15 µM probes **A**, **B** and **C**, respectively. The excitation of near-infrared lysotracker is at 635 nm and the fluorescence (pseudo-colored as yellow for clarity) was collect at the range of 725-775 nm. The blue channel of TPE donor fluorescence was collected from 475 to 525 nm, and the NIR channel (pseudo-colored as red for clarity) of rhodamine acceptor fluorescence in the second column was collected from 650 to 700 nm under excitation of TPE donor at 405 nm. The NIR channel (pseudo-colored as green for clarity) of rhodamine acceptor in the third column was collected from 650 to 700 nm under excitation of Rhodamine acceptor at 559 nm. Scale bar: 20 µM.
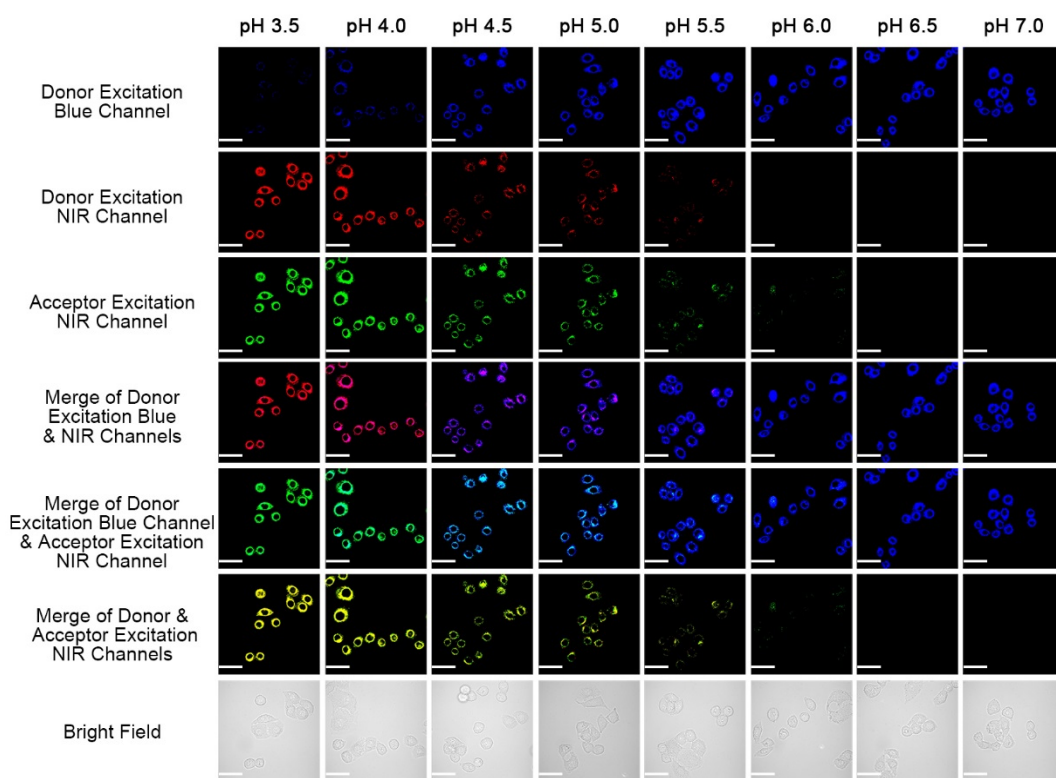
Figure S C.45: Cellular fluorescence images of 15 μM probes **A** incubated with HeLa cells in 10 mM citrate buffers having pH from 3.5 to 7.0 in the presence of 5 μg/mL nigericin. The blue channel in the first row was obtained from 475 to 525 nm, and two NIR channels (pseudo-colored as red and green for clarity) in the second and third rows were obtained from 650 to 700 nm under excitation of TPE donor and rhodamine acceptor at 405 nm and 559 nm, respectively. Confocal fluorescence microscope was employed to obtain fluorescence images at 60× magnification with scale bars of 50 μM.
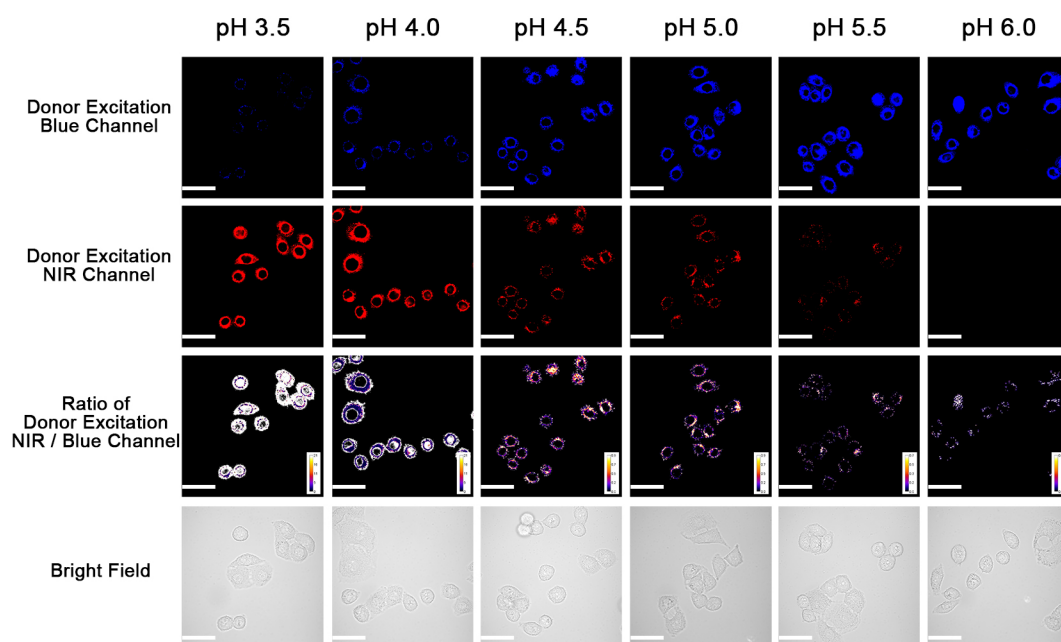
Figure S C.46: Cellular fluorescence images of 15 μM probes **A** incubated with HeLa cells in 10 mM citrate buffers having pH from 3.5 to 7.0 in the presence of 5 μg/mL nigericin. The blue channel in the first row was obtained from 475 to 525 nm, and NIR channel (pseudo-colored as red for clarity) in the second row were obtained from 650 to 700 nm under excitation of TPE donor at 405 nm. Confocal fluorescence microscope was employed to obtain fluorescence images at 60× magnification with scale bars of 50 μM. Ratiometric images (red channel/blue channel) in the third row.
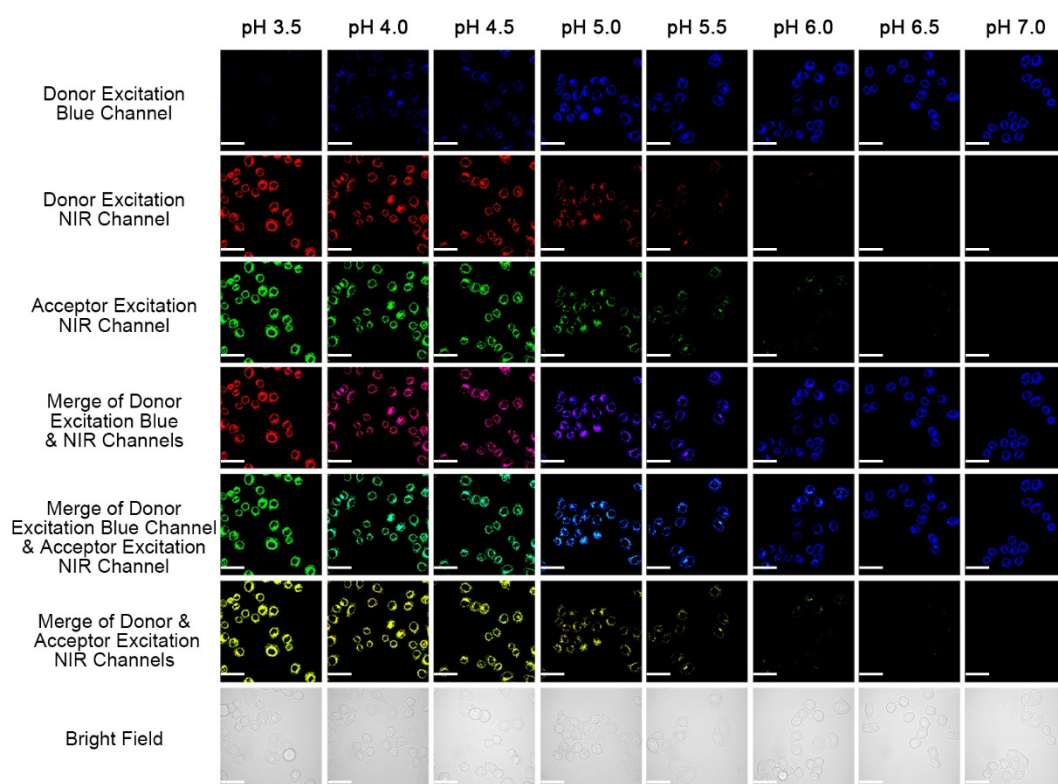
Figure S C.47: Cellular fluorescence images of 15 μM probes **B** incubated with HeLa cells in 10 mM citrate buffers having pH from 3.5 to 7.0 in the presence of 5 μg/mL nigericin. The blue channel in the first row was obtained from 475 to 525 nm, and two NIR channels (pseudo-colored as red and green for clarity) in the second and third rows were obtained from 650 to 700 nm under excitation of TPE donor and rhodamine acceptor at 405 nm and 559 nm, respectively. Confocal fluorescence microscope was employed to obtain fluorescence images at 60× magnification with scale bars of 50 μM.
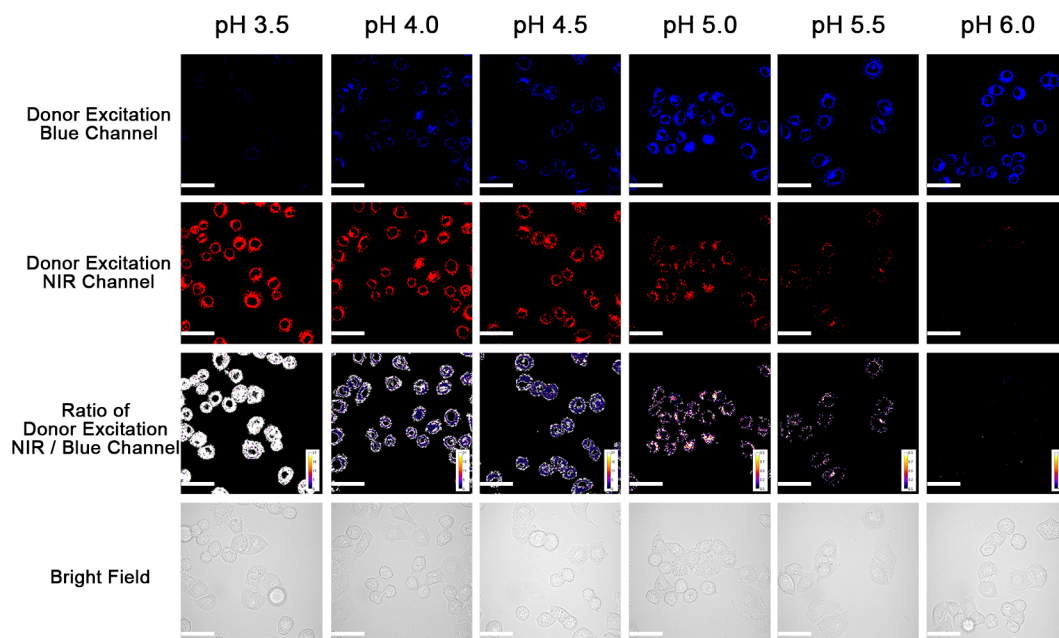
Figure S C.48: Cellular fluorescence images of 15 μM probes **B** incubated with HeLa cells in 10 mM citrate buffers having pH from 3.5 to 7.0 in the presence of 5 μg/mL nigericin. The blue channel in the first row was obtained from 475 to 525 nm, and NIR channel (pseudo-colored as red for clarity) in the second row were obtained from 650 to 700 nm under excitation of TPE donor at 405 nm. Confocal fluorescence microscope was employed to obtain fluorescence images at 60× magnification with scale bars of 50 μM. Ratiometric images (red channel/blue channel) in the third row.
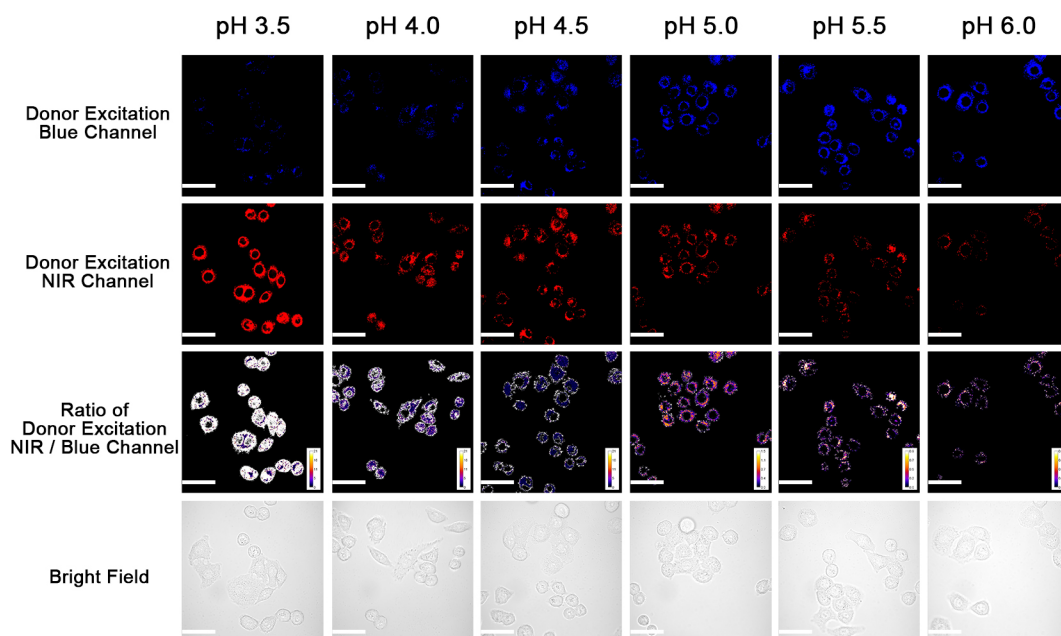
Figure S C.49: Cellular fluorescence images of 15 μM probes **C** incubated with HeLa cells in 10 mM citrate buffers having pH from 3.5 to 7.0 in the presence of 5 μg/mL nigericin. The blue channel in the first row was obtained from 475 to 525 nm, and NIR channel (pseudo-colored as red for clarity) in the second row were obtained from 650 to 700 nm under excitation of TPE donor at 405 nm. Confocal fluorescence microscope was employed to obtain fluorescence images at 60× magnification with scale bars of 50 μM. Ratiometric images (red channel/blue channel) in the third row.
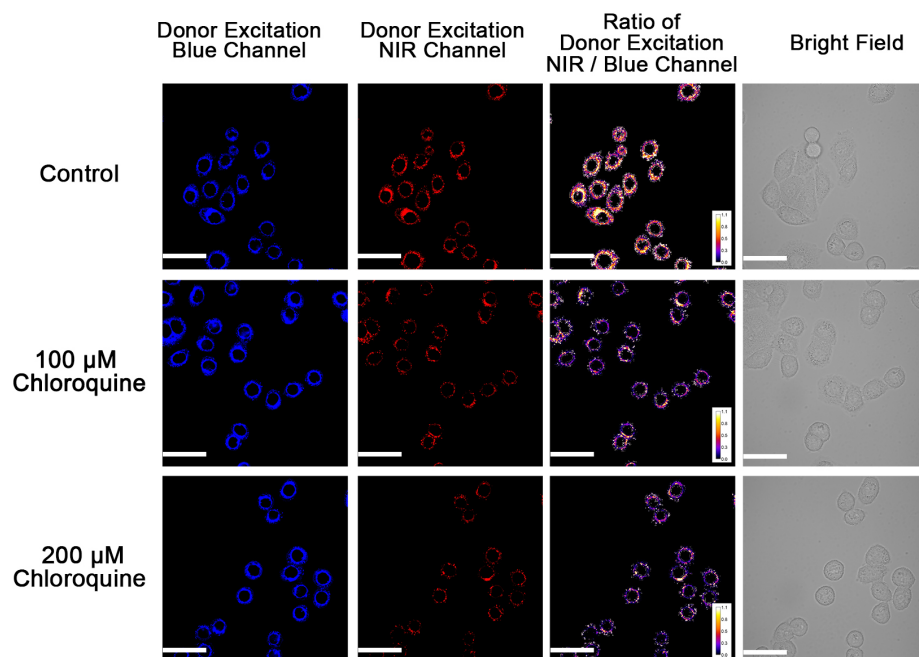
Figure S C.50: Cellular fluorescence images of 20 µM probes **C** incubated with HeLa cells in 10 mM citrate buffers with pH 7.4 in the absence and in the presence of 100 and 200 µM chloroquine. The blue channel in the first column was obtained from 475 to 525 nm, and NIR channel (pseudo-colored as red for clarity) in the second column was got from 650 to 700 nm under excitation of TPE donor at 405 nm. Confocal fluorescence microscope was used to acquire the images at 60× magnification with scale bars of 50 µM. Ratiometric images (red channel/blue channel) in the third row.

15. Probe Ratiometric fluorescence responses to intracellular pH changes
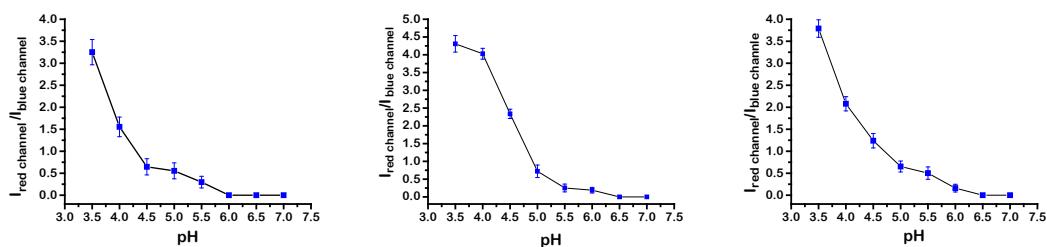
Figure S C.51. Cellular fluorescence ratio responses of TPE donor to rhodamine acceptor in probes **A** (left), **B** (middle), and **C** (left) to pH changes in 10 mM citrate buffers with pH ranging from 3.5 to 7.0 containing 5 µg/mL nigericin under TPE excitation at 405 nm. The fluorescence ratios of probes **A**, **B**, and **C** in HeLa live cells were obtained through statistical analysis of the confocal imaging data in Figures S45, S47, and 6.

254

16. Results of Theoretical Calculations

Probe A
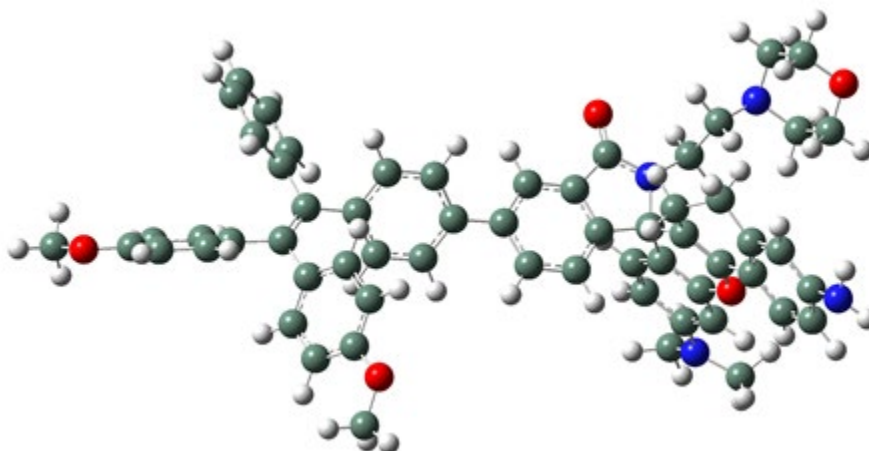
Figure S C.52. GaussView representation of Probe A.

Table S C.1. Computational results for Probe A.

a (Optimization completed)		
/home/rluck/calculation/liu/tbt/superior/a.log		
File Type	.log	
Calculation Type	FREQ	
Calculation Method	RTPSSh	
Basis Set	TZVP	
Charge	0	
Spin	Singlet	
Solvation	scrf=solvent=water	
E(RTPSSh)	-2916.356993	Hartree
RMS Gradient Norm	0.000002	Hartree/Bohr
Imaginary Freq		
Dipole Moment	9.117061	Debye
Point Group	C1	
Job cpu time:	10 days 21 hours 41 minutes 5...	

Table S C.2. Calculated atomic coordinates for Probe A.

Row	Symbol	X	Y	Z					
					25	O	2.681624	-3.5363	-0.88504
1	C	4.3909	-1.20242	4.159996	26	N	3.996241	-1.7904	-0.12772
2	C	5.461523	-0.3412	4.515407	27	C	-1.91904	-0.538	-0.02502
3	C	5.990225	0.483428	3.506905	28	C	6.962147	3.453873	-0.16885
4	C	5.451107	0.462108	2.223026	29	C	7.511411	4.464888	-0.94393
5	C	4.392679	-0.36943	1.866113	30	C	7.261104	4.516969	-2.32485
6	C	3.883864	-1.19819	2.875052	31	C	6.448747	3.521084	-2.89607
7	N	5.952318	-0.30237	5.802477	32	C	-2.77078	0.077594	0.905373
8	C	5.55878	-1.33593	6.752717	33	C	-4.15058	0.003102	0.774988
9	C	7.183815	0.427679	6.072388	34	C	-4.74454	-0.69122	-0.28976
10	C	3.849439	-0.41155	0.453747	35	C	-3.89234	-1.32616	-1.20617
11	C	2.333162	-0.26581	0.402523	36	C	-2.51164	-1.24233	-1.08389
12	C	1.746559	-1.40707	-0.13031	37	C	-6.22173	-0.80948	-0.41063
13	C	0.371738	-1.52688	-0.27984	38	C	-6.71997	-2.18126	-0.71071
14	C	-0.44694	-0.45864	0.113484	39	C	-7.06048	0.258573	-0.25931
15	C	0.161361	0.696302	0.646306	40	C	-8.52689	0.098809	-0.07901
16	C	1.541581	0.804812	0.795139	41	C	-6.57265	1.662382	-0.26736
17	C	2.811739	-2.39177	-0.44306	42	C	-7.63876	-2.40677	-1.74651
18	O	6.045239	1.323736	1.329598	43	C	-8.07448	-3.69344	-2.04842
19	C	5.530349	1.402334	0.054623	44	C	-7.60212	-4.78459	-1.31943
20	C	4.530809	0.625429	-0.4065	45	C	-6.68009	-4.57705	-0.29418
21	C	6.150071	2.464787	-0.73862	46	C	-6.23569	-3.29078	-0.00139
22	C	5.900914	2.506155	-2.12507	47	C	-9.4352	0.906448	-0.78572
23	C	5.096266	1.388615	-2.74304	48	C	-10.8034	0.774979	-0.61494
24	C	4.004331	0.87707	-1.80077	49	C	-11.3111	-0.16008	0.296424

50	C	-10.4273	-0.95557	1.031127	78	H	8.046042	0.00599	5.538082
51	C	-9.05498	-0.81974	0.834556	79	H	-0.05533	-2.44262	-0.67279
52	C	-5.67377	2.120361	-1.24622	80	H	-0.46373	1.534809	0.93193
53	C	-5.24317	3.436114	-1.27238	81	H	1.978595	1.709402	1.20385
54	C	-5.69739	4.3442	-0.30699	82	H	5.781751	0.562838	-2.97458
55	C	-6.60096	3.916383	0.669828	83	H	4.661043	1.711767	-3.69153
56	C	-7.03527	2.592616	0.670368	84	H	3.182253	1.604106	-1.75462
57	O	-5.21519	5.61707	-0.40792	85	H	3.578695	-0.04596	-2.20424
58	O	-12.6707	-0.21418	0.405009	86	H	7.162191	3.431784	0.895482
59	C	-13.228	-1.15995	1.325917	87	H	8.135261	5.223242	-0.48212
60	C	-5.66313	6.577275	0.556751	88	H	6.251973	3.544008	-3.96423
61	N	7.745245	5.563783	-3.09856	89	H	-2.3495	0.595482	1.760177
62	C	5.262894	-2.5066	-0.16234	90	H	-4.7826	0.474062	1.518864
63	C	5.913755	-2.51658	-1.55253	91	H	-4.31938	-1.87729	-2.03694
64	N	7.149781	-3.30738	-1.52378	92	H	-1.8857	-1.71463	-1.83324
65	C	7.491947	-3.93555	-2.80898	93	H	-8.00543	-1.5636	-2.3208
66	C	8.096711	-2.95703	-3.81167	94	H	-8.7792	-3.84548	-2.85902
67	O	9.259826	-2.32496	-3.25612	95	H	-7.94292	-5.78716	-1.55339
68	C	8.919984	-1.62063	-2.05281	96	H	-6.30355	-5.41905	0.276788
69	C	8.32028	-2.5696	-1.01715	97	H	-5.51301	-3.13971	0.793374
70	H	3.960278	-1.87265	4.890981	98	H	-9.0593	1.639778	-1.49077
71	H	6.817958	1.153094	3.694727	99	H	-11.4963	1.391193	-1.17661
72	H	3.066669	-1.87096	2.634545	100	H	-10.7911	-1.67077	1.757394
73	H	5.887127	-2.33714	6.443441	101	H	-8.3802	-1.43821	1.415124
74	H	6.007815	-1.10543	7.717076	102	H	-5.31852	1.432026	-2.00439
75	H	4.474305	-1.35014	6.882732	103	H	-4.55967	3.782396	-2.03937
76	H	7.079592	1.477599	5.787597	104	H	-6.9726	4.597832	1.424056
77	H	7.383187	0.388347	7.141735	105	H	-7.74179	2.276173	1.429996

106	H	-14.3063	-1.042	1.246631	116	H	5.224101	-2.99251	-2.25251
107	H	-12.9472	-2.18173	1.055394	117	H	6.061091	-1.4816	-1.8901
108	H	-12.9077	-0.94549	2.349393	118	H	8.224739	-4.72528	-2.60893
109	H	-5.16278	7.506952	0.295408	119	H	6.596976	-4.40378	-3.22635
110	H	-6.74688	6.712634	0.500198	120	H	8.431005	-3.4748	-4.7126
111	H	-5.37867	6.276824	1.56908	121	H	7.365231	-2.18798	-4.09892
112	H	7.824235	5.379021	-4.08925	122	H	9.847502	-1.17949	-1.68353
113	H	8.558183	6.040653	-2.73322	123	H	8.220379	-0.80804	-2.29407
114	H	5.92023	-2.04042	0.574591	124	H	9.080558	-3.30378	-0.73001
115	H	5.080071	-3.53781	0.147355	125	H	8.041502	-2.01347	-0.11903
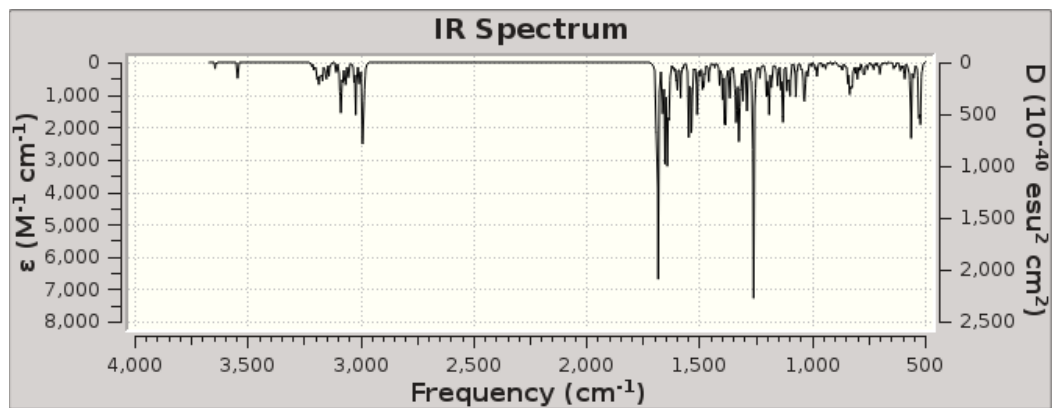
Figure S C.53. Calculated IR spectrum for probe A.
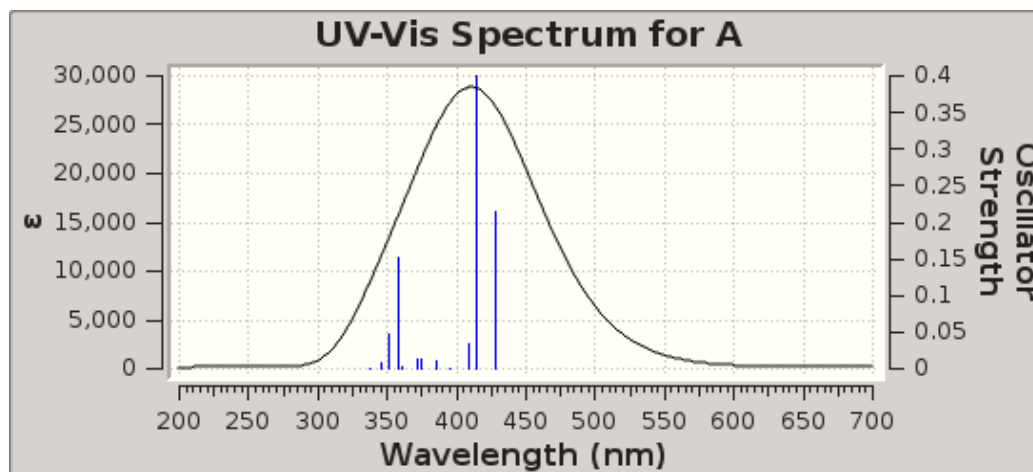
Figure S C.54. Calculated UV-Vis spectrum for probe A.

Table S C.3. Excitation energies and oscillator strengths listing for probe A**.**

Excitation energies and oscillator strengths:

Excited State   1:   Singlet-A   2.8945 eV 428.35 nm f=0.2150 <S**2>=0.000
   241 -> 243   -0.12251
   242 -> 243   0.69228
This state for optimization and/or second-order correction.
Total Energy, E(TD-HF/TD-DFT) = -2916.25062318
Copying the excited state density for this state as the 1-particle RhoCI density.

Excited State   2:   Singlet-A   2.9948 eV 414.00 nm f=0.3996 <S**2>=0.000
   240 -> 243   0.13591
   241 -> 243   0.67602
   242 -> 243   0.11861

Excited State   3:   Singlet-A   3.0338 eV 408.67 nm f=0.0350 <S**2>=0.000
   240 -> 243   0.68595
   241 -> 243   -0.13329

Excited State   4:   Singlet-A   3.1332 eV 395.72 nm f=0.0006 <S**2>=0.000
  239 -> 243   0.70267

Excited State   5:   Singlet-A   3.2140 eV 385.77 nm f=0.0100 <S**2>=0.000
  241 -> 244   -0.20476
  242 -> 244   0.66972

Excited State   6:   Singlet-A   3.3123 eV 374.31 nm f=0.0136 <S**2>=0.000
  240 -> 244   0.44997
  241 -> 244   0.50511
  242 -> 244   0.16993

Excited State   7:   Singlet-A   3.3399 eV 371.22 nm f=0.0141 <S**2>=0.000
  240 -> 244   0.53082
  241 -> 244   -0.44007
  242 -> 244   -0.11705

Excited State   8:   Singlet-A   3.4400 eV 360.42 nm f=0.0035 <S**2>=0.000
  239 -> 244   0.70041

Excited State   9:   Singlet-A   3.4600 eV 358.33 nm f=0.1515 <S**2>=0.000
  242 -> 245   0.68980

Excited State 10:   Singlet-A   3.5332 eV 350.91 nm f=0.0466 <S**2>=0.000
  241 -> 245   0.68529

Excited State 11:   Singlet-A   3.5891 eV 345.44 nm f=0.0076 <S**2>=0.000
  240 -> 245   0.67766
  242 -> 246   0.13444

Excited State 12:   Singlet-A   3.6731 eV 337.55 nm f=0.0007 <S**2>=0.000
  239 -> 245   0.67299
  239 -> 246   0.12757
  242 -> 246   0.14200

a-242 HOMO

a-243 LUMO

a-241 HOMO-1

a-244 LUMO+1

a-240 HOMO-2
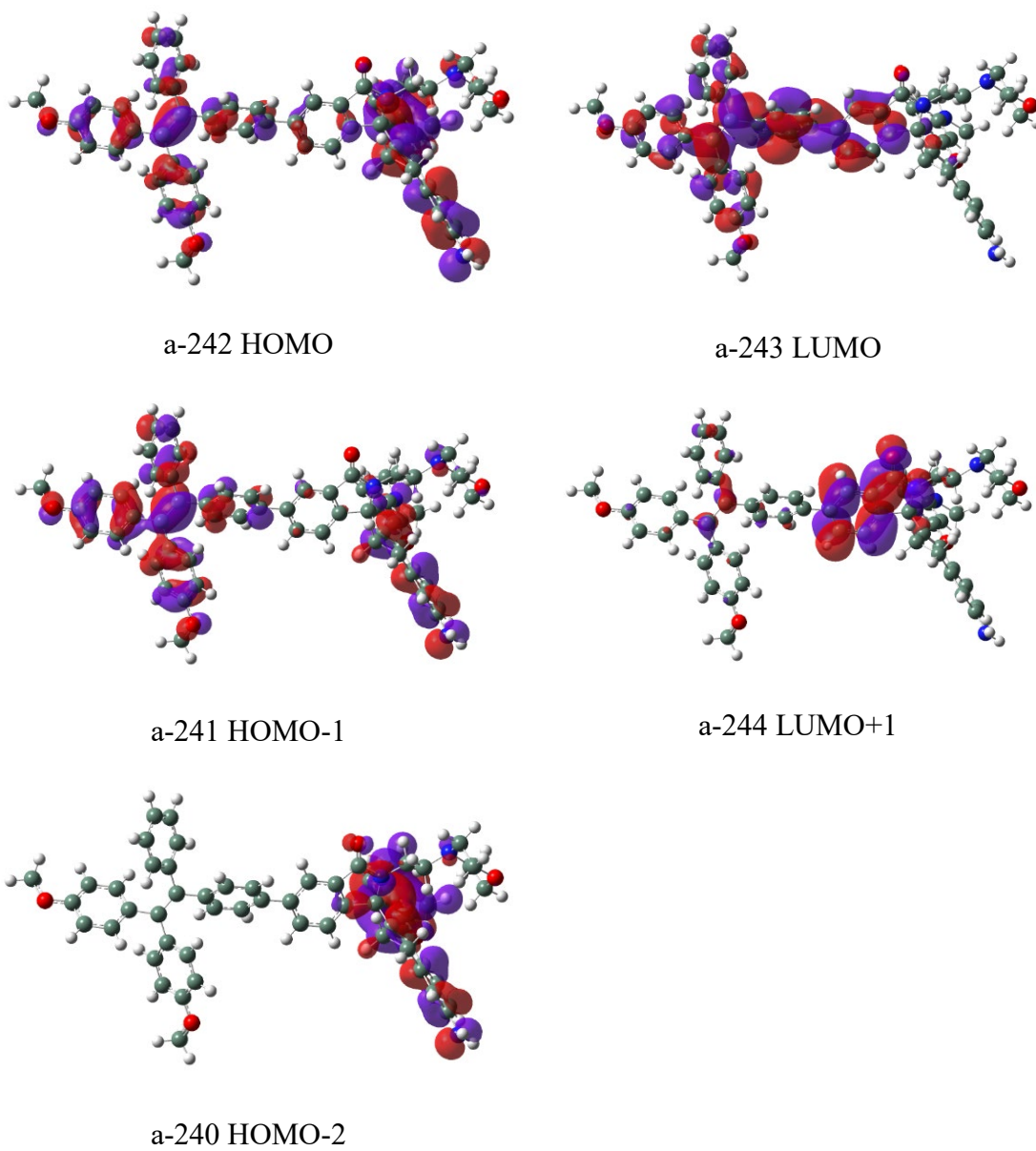
Figure S C.55. Drawings of the highest occupied and lowest unoccupied orbitals for probe A.

Probe AH⁺
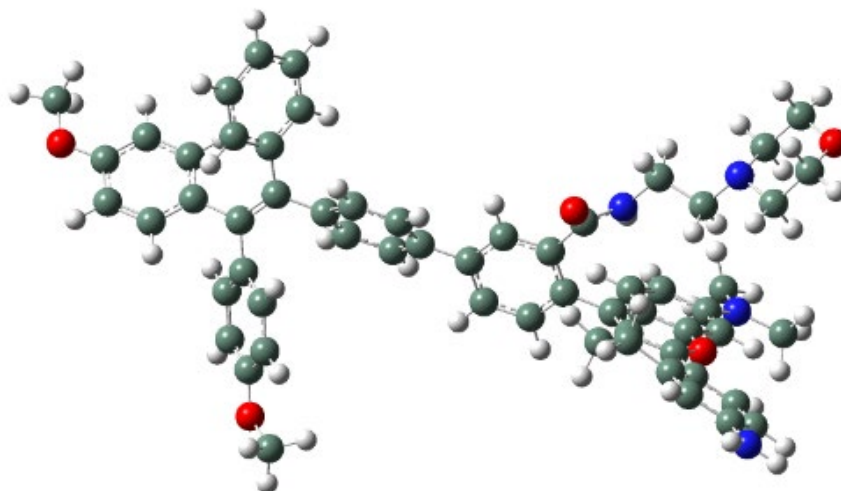
Figure S C.56. GaussView representation of probe AH⁺.

Table S C.4. Computational results for Probe AH⁺.

ah (Optimization completed)		
/home/rluck/calculation/liu/tbt/superior/ah.log		
File Type	.log	
Calculation Type	SP	
Calculation Method	RTPSSh	
Basis Set	TZVP	
Charge	1	
Spin	Singlet	
Solvation	scrf=solvent=water	
E(RTPSSh)	-2916.822560	Hartree
RMS Gradient Norm	0.000002	Hartree/Bohr
Imaginary Freq		
Dipole Moment	31.332553	Debye
Point Group	C1	
Job cpu time:	11 days 12 hours 43 minutes 1...	

Table S C.5. Calculated atomic coordinates for Probe AH⁺.

Row	Symbol	X	Y	Z					
Row	Symbol	X	Y	Z	26	N	-3.54544	2.024953	0.351055
1	C	-4.33857	-1.1402	4.072765	27	C	2.042035	0.030597	0.00528
2	C	-5.71452	-1.53456	4.088447	28	C	-7.81088	-2.56789	-1.68102
3	C	-6.35422	-1.75287	2.847251	29	C	-8.58187	-2.84267	-2.78218
4	C	-5.63934	-1.58576	1.682004	30	C	-8.1155	-2.51058	-4.08034
5	C	-4.2753	-1.21235	1.641254	31	C	-6.85109	-1.88937	-4.21238
6	C	-3.656	-0.98536	2.896357	32	C	2.947383	-0.51536	0.92836
7	N	-6.37906	-1.68965	5.257679	33	C	4.30944	-0.26951	0.827555
8	C	-7.78325	-2.09427	5.255152	34	C	4.829936	0.531132	-0.2008
9	C	-5.71174	-1.44702	6.537021	35	C	3.920682	1.09314	-1.11021
10	C	-3.64076	-1.06699	0.380845	36	C	2.558625	0.841438	-1.01611
11	C	-2.19223	-0.72501	0.320362	37	C	6.282604	0.834103	-0.29132
12	C	-1.72034	0.513319	-0.1502	38	C	6.61001	2.265564	-0.54554
13	C	-0.34802	0.736609	-0.25967	39	C	7.246375	-0.12481	-0.157
14	C	0.590273	-0.23212	0.113602	40	C	8.679865	0.209668	0.045927
15	C	0.106695	-1.4576	0.595122	41	C	6.93823	-1.57764	-0.20882
16	C	-1.25616	-1.69839	0.691428	42	C	7.495358	2.6336	-1.56932
17	C	-2.62757	1.643318	-0.56602	43	C	7.771323	3.972762	-1.8286
18	O	-6.32098	-1.78903	0.512723	44	C	7.169055	4.974464	-1.06777
19	C	-5.71614	-1.66974	-0.68653	45	C	6.278433	4.623848	-0.05372
20	C	-4.36389	-1.31188	-0.7866	46	C	5.993813	3.284454	0.19642
21	C	-6.54078	-1.95987	-1.81298	47	C	9.686599	-0.46688	-0.66514
22	C	-6.0728	-1.61305	-3.10969	48	C	11.02694	-0.17474	-0.47412
23	C	-4.76274	-0.87872	-3.23309	49	C	11.408	0.794865	0.462447
24	C	-3.76039	-1.33416	-2.17173	50	C	10.42674	1.461817	1.201622
25	O	-2.49439	2.191709	-1.66422	51	C	9.083224	1.165582	0.984619

263

52	C	7.495411	-2.4678	0.726005	80	H	-1.6057	-2.6658	1.034118
53	C	7.225707	-3.82548	0.680025	81	H	-4.95439	0.194852	-3.11472
54	C	6.403092	-4.34448	-0.32827	82	H	-4.34353	-1.01912	-4.23078
55	C	5.860452	-3.48324	-1.28634	83	H	-3.44436	-2.36258	-2.3876
56	C	6.130467	-2.11865	-1.21482	84	H	-2.86687	-0.7127	-2.20908
57	O	6.199555	-5.69368	-0.29973	85	H	-3.53935	1.569151	1.252528
58	O	12.74969	1.010123	0.589982	86	H	-8.17289	-2.83431	-0.69592
59	C	13.17891	1.995534	1.537642	87	H	-9.54775	-3.32149	-2.66893
60	C	5.362723	-6.26265	-1.31425	88	H	-6.49602	-1.62064	-5.20195
61	N	-8.86518	-2.7862	-5.16991	89	H	2.579129	-1.11353	1.75477
62	C	-4.4933	3.113553	0.136515	90	H	4.982797	-0.68854	1.566072
63	C	-5.90721	2.588958	-0.14269	91	H	4.290126	1.722133	-1.91263
64	N	-6.8576	3.685667	-0.33513	92	H	1.891165	1.26416	-1.75914
65	C	-7.26851	4.299554	0.93405	93	H	7.962468	1.859886	-2.16802
66	C	-8.21934	5.455725	0.664775	94	H	8.453082	4.235178	-2.63055
67	O	-9.37737	5.021708	-0.0558	95	H	7.385455	6.017985	-1.26838
68	C	-8.98484	4.418283	-1.29368	96	H	5.80206	5.395195	0.541933
69	C	-8.05252	3.239529	-1.06195	97	H	5.294703	3.021403	0.98308
70	H	-3.82258	-0.95741	5.004657	98	H	9.409409	-1.22507	-1.38937
71	H	-7.39362	-2.04007	2.782022	99	H	11.79525	-0.69051	-1.0389
72	H	-2.61469	-0.68867	2.92002	100	H	10.69387	2.200089	1.946648
73	H	-8.12205	-2.17785	6.284174	101	H	8.332648	1.685348	1.568829
74	H	-8.40467	-1.35458	4.741346	102	H	8.139393	-2.08337	1.509408
75	H	-7.90947	-3.06463	4.766174	103	H	7.646745	-4.50211	1.414991
76	H	-6.42758	-1.62483	7.334966	104	H	5.239874	-3.86018	-2.08899
77	H	-5.36054	-0.41404	6.609549	105	H	5.709457	-1.46221	-1.96776
78	H	-0.01389	1.703686	-0.61676	106	H	14.26443	2.008931	1.471521
79	H	0.801148	-2.24328	0.868791	107	H	12.78096	2.981954	1.283508

|									
108	H	12.87431	1.72218	2.551803					
109	H	5.329942	-7.32845	-1.09992	118	H	-7.76389	3.560185	1.588497
110	H	4.352998	-5.84513	-1.26802	119	H	-6.39085	4.681419	1.46015
111	H	5.78713	-6.0992	-2.30881	120	H	-7.70126	6.236783	0.091398
112	H	-8.54977	-2.54542	-6.09587	121	H	-8.58072	5.880882	1.601844
113	H	-9.77195	-3.21683	-5.08552	122	H	-8.48713	5.167158	-1.92514
114	H	-4.47765	3.752585	1.020975	123	H	-9.90336	4.0917	-1.78278
115	H	-4.13887	3.691322	-0.71585	124	H	-8.59214	2.451501	-0.50724
116	H	-6.2236	1.91381	0.670894	125	H	-7.74531	2.826732	-2.02662
117	H	-5.88116	2.001063	-1.06311	126	H	-4.86359	-2.12338	6.674356
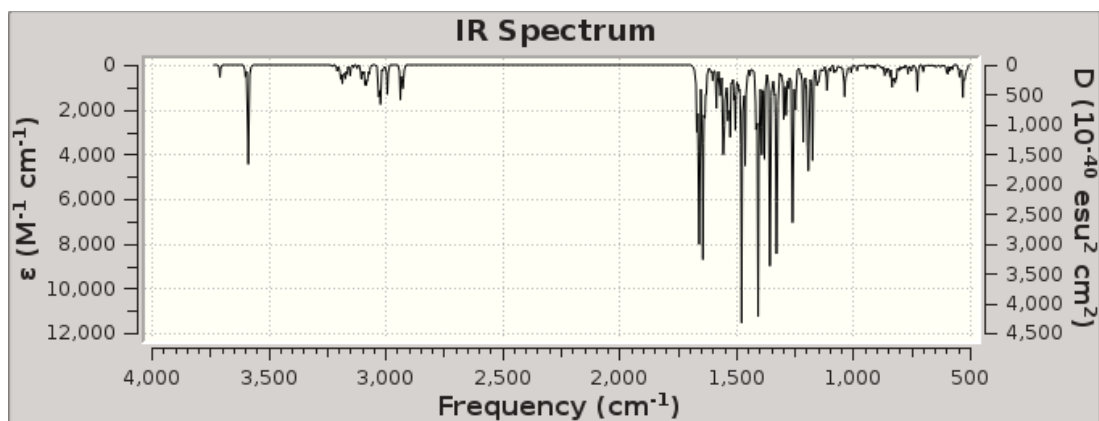
Figure S C.56. Calculated IR spectrum for probe AH$^+$.
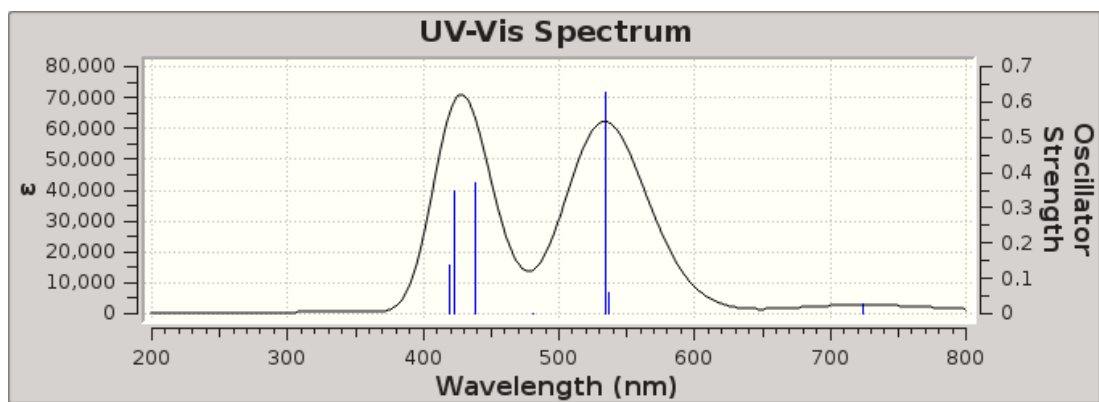
Figure S C.58. Calculated UV-Vis spectrum for probe AH$^+$.

266

Table S C.6. Excitation energies and oscillator strengths listing for Probe AH$^+$.

Excitation energies and oscillator strengths:

Excited State   1:   Singlet-A   1.7116 eV 724.39 nm f=0.0259 <S**2>=0.000
   242 -> 243   0.70674
This state for optimization and/or second-order correction.
Total Energy, E(TD-HF/TD-DFT) = -2916.75966126
Copying the excited state density for this state as the 1-particle RhoCI density.

Excited State   2:   Singlet-A   2.3081 eV 537.17 nm f=0.0593 <S**2>=0.000
   240 -> 243   0.67418
   241 -> 243   0.21064

Excited State   3:   Singlet-A   2.3219 eV 533.98 nm f=0.6285 <S**2>=0.000
   240 -> 243   -0.21284
   241 -> 243   0.66653

Excited State   4:   Singlet-A   2.5764 eV 481.23 nm f=0.0013 <S**2>=0.000
   239 -> 243   0.70672

Excited State   5:   Singlet-A   2.8321 eV 437.78 nm f=0.3725 <S**2>=0.000
   237 -> 243   -0.43324
   238 -> 243   0.50562
   242 -> 244   -0.19134

Excited State   6:   Singlet-A   2.9307 eV 423.05 nm f=0.3465 <S**2>=0.000
   237 -> 243   -0.40762
   238 -> 243   -0.12997
   242 -> 244   0.55416

Excited State   7:   Singlet-A   2.9582 eV 419.13 nm f=0.1376 <S**2>=0.000
   237 -> 243   0.36859
   238 -> 243   0.42430
   241 -> 245   0.10876
   242 -> 244   0.38404

AH$^+$-242 HOMO

AH$^+$-243 LUMO

AH$^+$-241 HOMO-1

AH$^+$-244 LUMO+1

AH$^+$-240 HOMO-2

AH$^+$-239 HOMO-3

AH+-238 HOMO-4

AH+-237 HOMO-4
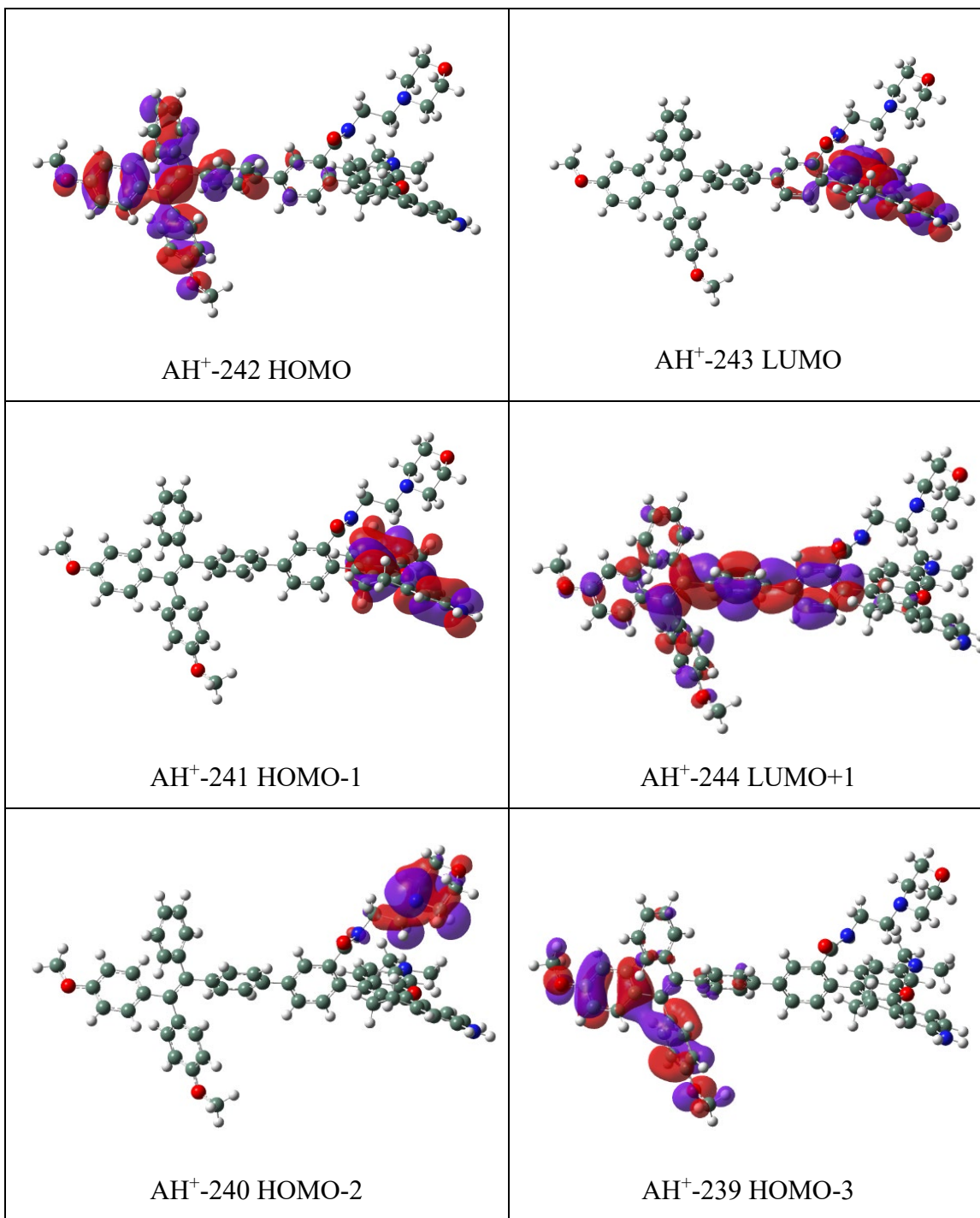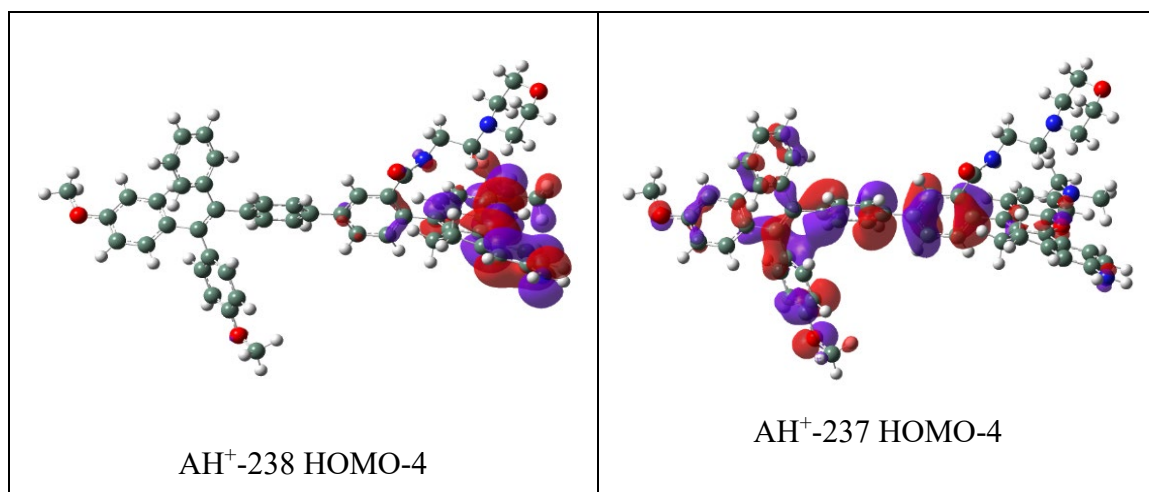
Figure S C.59. Drawings of the highest occupied and lowest unoccupied orbitals for probe AH+.

Probe B
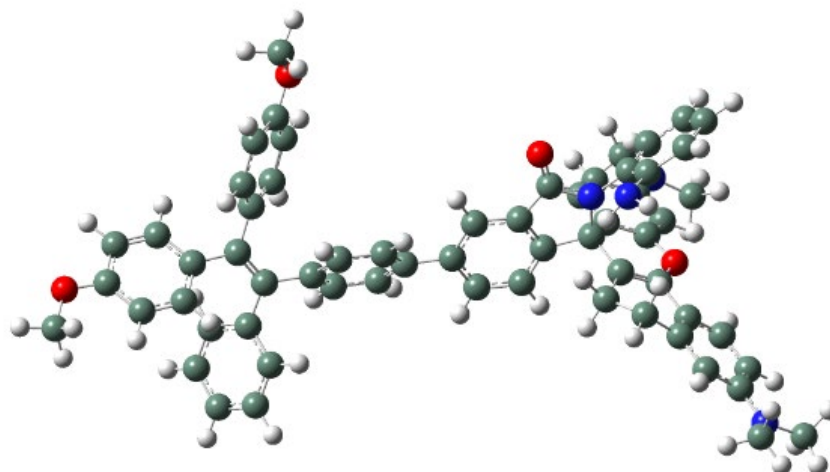
Figure S C.60. GaussView representation of probe B.

Table S C.7. Computational results for Probe B.

b (Optimization completed)		
/home/rluck/calculation/liu/tbt/superior/b.log		
File Type	.log	
Calculation Type	SP	
Calculation Method	RTPSSh	
Basis Set	TZVP	
Charge	0	
Spin	Singlet	
Solvation	scrf=solvent=water	
E(RTPSSh)	-2916.154120	Hartree
RMS Gradient Norm	0.000002	Hartree/Bohr
Imaginary Freq		
Dipole Moment	9.592948	Debye
Point Group	C1	
Job cpu time:	11 days 22 hours 13 minutes 5...	

270

Table S C.8. Calculated atomic coordinates for probe B.

Row	Symbol	X	Y	Z					
					26	N	3.656901	-1.57773	-1.09627
1	C	4.388261	-2.92305	3.055563	27	C	4.748394	-2.26798	-1.70735
2	C	5.730366	-2.64137	3.422316	28	C	-1.88053	0.27325	0.504173
3	C	6.396993	-1.63034	2.707441	29	C	7.845837	2.355731	0.454542
4	C	5.762037	-0.97562	1.65598	30	C	8.577584	3.475741	0.09212
5	C	4.45759	-1.26726	1.264322	31	C	8.173239	4.283367	-0.99584
6	C	3.789959	-2.25025	2.007815	32	C	7.020313	3.879774	-1.71158
7	N	6.355888	-3.33335	4.435153	33	N	8.863321	5.424736	-1.33859
8	C	5.569889	-4.19046	5.31463	34	C	8.552116	6.108518	-2.58732
9	C	7.652204	-2.87552	4.916949	35	C	10.15481	5.696289	-0.72052
10	C	3.826282	-0.59487	0.066447	36	C	5.126131	-1.95021	-3.03069
11	C	2.367387	-0.24356	0.312077	37	C	5.435248	-3.26116	-1.00585
12	C	1.527755	-0.94929	-0.53932	38	C	6.518709	-3.92421	-1.57306
13	C	0.147066	-0.80797	-0.49747	39	C	6.909436	-3.59624	-2.87175
14	C	-0.41422	0.082067	0.428442	40	C	6.221156	-2.63019	-3.59127
15	C	0.448971	0.794229	1.286127	41	N	4.402075	-1.04945	-3.79486
16	C	1.831689	0.639172	1.240706	42	C	-2.67935	0.202857	-0.64771
17	C	2.34127	-1.82837	-1.41283	43	C	-4.0543	0.379525	-0.58013
18	O	6.51238	-0.00338	1.036158	44	C	-4.69551	0.636327	0.641252
19	C	5.887511	0.81483	0.122075	45	C	-3.89322	0.728122	1.788845
20	C	4.642469	0.599562	-0.35053	46	C	-2.51884	0.540123	1.724617
21	C	6.694436	1.97585	-0.24646	47	C	-6.16191	0.870986	0.713853
22	C	6.294084	2.756282	-1.34894	48	C	-6.56951	2.044661	1.536379
23	C	5.106859	2.291366	-2.15773	49	C	-7.0684	0.071582	0.076458
24	C	4.043226	1.638024	-1.27238	50	C	-8.48946	0.46743	-0.1034
25	O	1.940839	-2.62772	-2.25691	51	C	-6.70523	-1.2566	-0.48269

271

52	C	-7.56601	1.930132	2.517044	80	H	-0.47952	-1.39468	-1.15965
53	C	-7.91805	3.018784	3.309227	81	H	0.024484	1.500546	1.990575
54	C	-7.28209	4.24809	3.137295	82	H	2.468167	1.203831	1.913078
55	C	-6.28209	4.374072	2.173735	83	H	5.461214	1.555049	-2.89087
56	C	-5.92247	3.281062	1.390378	84	H	4.678133	3.123541	-2.7208
57	C	-9.531	-0.4452	0.1398	85	H	3.535181	2.408315	-0.67631
58	C	-10.8582	-0.09116	-0.038	86	H	3.265417	1.185403	-1.89506
59	C	-11.1881	1.19181	-0.49384	87	H	8.175298	1.763041	1.299556
60	C	-10.1691	2.108127	-0.76883	88	H	9.463062	3.726098	0.66072
61	C	-8.84086	1.738921	-0.56941	89	H	6.68756	4.450117	-2.5698
62	C	-5.95234	-2.1836	0.258795	90	H	8.749493	5.481883	-3.46731
63	C	-5.64006	-3.43269	-0.25063	91	H	7.504082	6.417249	-2.60984
64	C	-6.0699	-3.79687	-1.53348	92	H	9.16719	7.004014	-2.65357
65	C	-6.83044	-2.89748	-2.28599	93	H	10.05906	5.756205	0.366403
66	C	-7.14818	-1.6513	-1.7503	94	H	10.90318	4.92978	-0.9622
67	O	-5.71028	-5.04438	-1.95438	95	H	10.51448	6.658749	-1.07958
68	O	-12.5197	1.449373	-0.64759	96	H	5.107133	-3.5083	-0.00433
69	C	-12.8968	2.751948	-1.11054	97	H	7.042218	-4.69032	-1.01348
70	C	-6.1372	-5.45602	-3.25887	98	H	7.752381	-4.10052	-3.33189
71	H	3.818013	-3.66805	3.592934	99	H	6.520486	-2.39035	-4.60659
72	H	7.406342	-1.33041	2.952599	100	H	4.911558	-0.60047	-4.54326
73	H	2.766807	-2.49981	1.746013	101	H	3.81786	-0.40801	-3.27777
74	H	5.055087	-4.96547	4.742114	102	H	-2.21543	0.038667	-1.61429
75	H	6.247131	-4.68296	6.009978	103	H	-4.64278	0.337259	-1.48926
76	H	4.823902	-3.62768	5.891171	104	H	-4.35689	0.931916	2.74786
77	H	7.602147	-1.87316	5.363441	105	H	-1.93734	0.581985	2.639156
78	H	8.009134	-3.57501	5.670576	106	H	-8.05988	0.975743	2.660018
79	H	8.380753	-2.85611	4.102559	107	H	-8.68583	2.905485	4.067188

272

| 108	H	-7.55747	5.096935	3.753447					
109	H	-5.77873	5.324762	2.033933	117	H	-7.18066	-3.15475	-3.27718
110	H	-5.13855	3.386595	0.648021	118	H	-7.7448	-0.96615	-2.34272
111	H	-9.29331	-1.44473	0.487093	119	H	-13.9836	2.742378	-1.1519
112	H	-11.655	-0.79689	0.167849	120	H	-12.5602	3.526703	-0.41591
113	H	-10.3941	3.098717	-1.14227	121	H	-12.4913	2.945606	-2.1076
114	H	-8.05992	2.456701	-0.79247	122	H	-5.74594	-6.46253	-3.38844
115	H	-5.61862	-1.92024	1.255819	123	H	-7.22862	-5.47257	-3.32653
116	H	-5.06968	-4.14506	0.334642	124	H	-5.72716	-4.79835	-4.03044
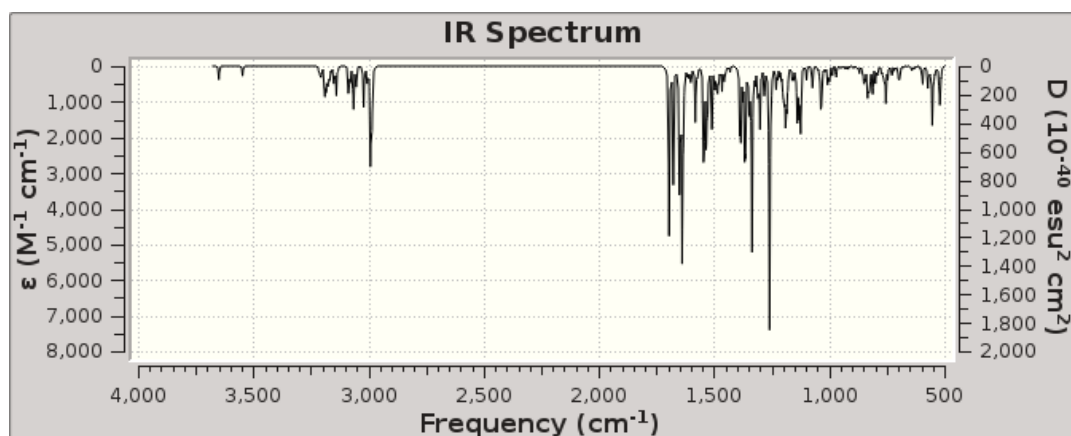
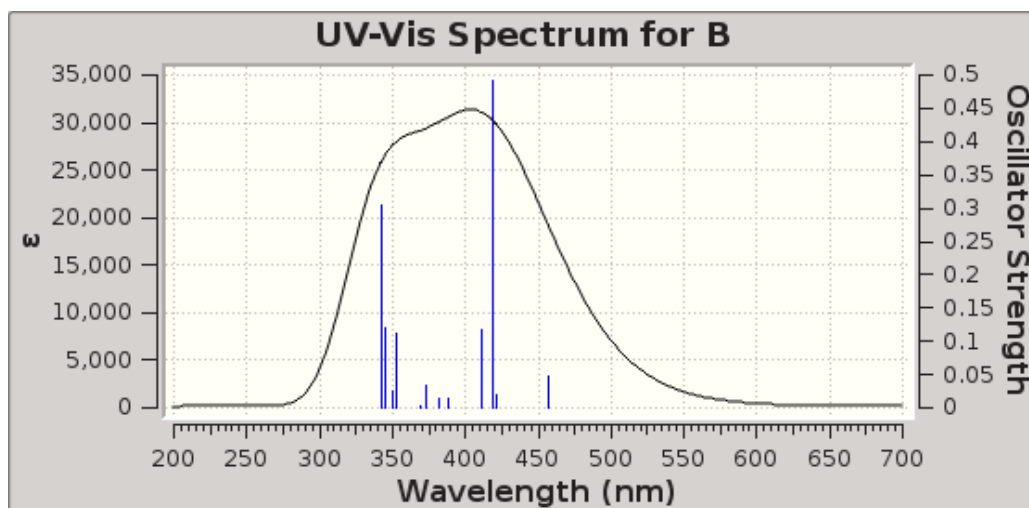**Figure S C.61.** Calculated IR spectrum for probe B.

**Figure S C.62.** Calculated UV-Vis spectrum for probe B.

Table S C.9. Excitation energies and oscillator strengths listing for probe B.

Excitation energies and oscillator strengths:

Excited State   1:   Singlet-A   2.7167 eV 456.39 nm f=0.0485 <S**2>=0.000
   243 -> 244   0.70097
This state for optimization and/or second-order correction.
Total Energy, E(TD-HF/TD-DFT) = -2916.05428490
Copying the excited state density for this state as the 1-particle RhoCI density.
Excited State   2:   Singlet-A   2.9426 eV 421.35 nm f=0.0192 <S**2>=0.000
   243 -> 245   0.69419
Excited State   3:   Singlet-A   2.9647 eV 418.21 nm f=0.4925 <S**2>=0.000
   241 -> 244   -0.19710
   242 -> 244   0.66539
Excited State   4:   Singlet-A   3.0196 eV 410.60 nm f=0.1179 <S**2>=0.000
   241 -> 244   0.66805
   242 -> 244   0.19858
Excited State   5:   Singlet-A   3.1965 eV 387.88 nm f=0.0147 <S**2>=0.000
   241 -> 245   -0.37463
   242 -> 245   0.58870
Excited State   6:   Singlet-A   3.2431 eV 382.31 nm f=0.0151 <S**2>=0.000
   241 -> 245   0.58607
   242 -> 245   0.38032
Excited State   7:   Singlet-A   3.3221 eV 373.22 nm f=0.0329 <S**2>=0.000
   243 -> 246   0.69120
Excited State   8:   Singlet-A   3.3548 eV 369.57 nm f=0.0021 <S**2>=0.000
   240 -> 244   0.69172
   240 -> 245   -0.11560
Excited State   9:   Singlet-A   3.5187 eV 352.35 nm f=0.1127 <S**2>=0.000
   242 -> 246   0.6833
Excited State 10:   Singlet-A   3.5446 eV 349.78 nm f=0.0242 <S**2>=0.000
   240 -> 244   0.11453
   240 -> 245   0.69051
Excited State 11:   Singlet-A   3.5934 eV 345.03 nm f=0.1201 <S**2>=0.000
   241 -> 246   0.60558
   241 -> 247   -0.11616
   243 -> 247   0.29956
Excited State 12:   Singlet-A   3.6197 eV 342.52 nm f=0.3053 <S**2>=0.000
   241 -> 246   -0.33094
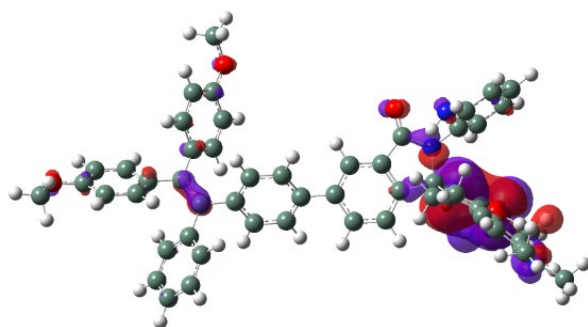   243 -> 247   0.55596
   243 -> 250   0.17836
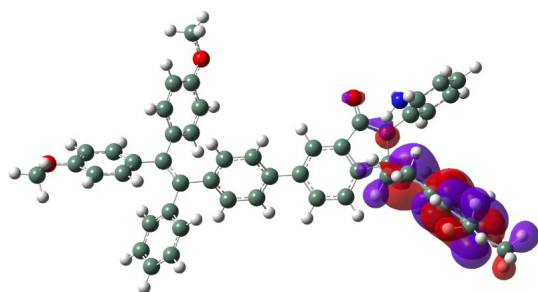
B-243 HOMO
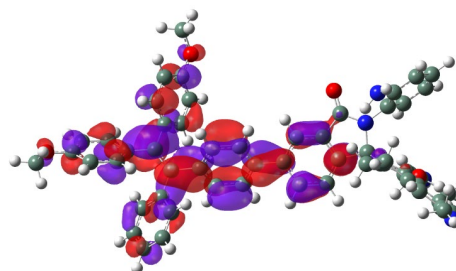
B-244 LUMO
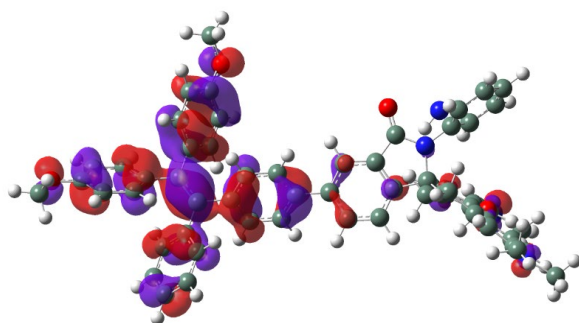
B-242 HOMO-1

B-241 HOMO-2

Figure S C.63. Drawings of the highest occupied and lowest unoccupied orbitals for probe B.
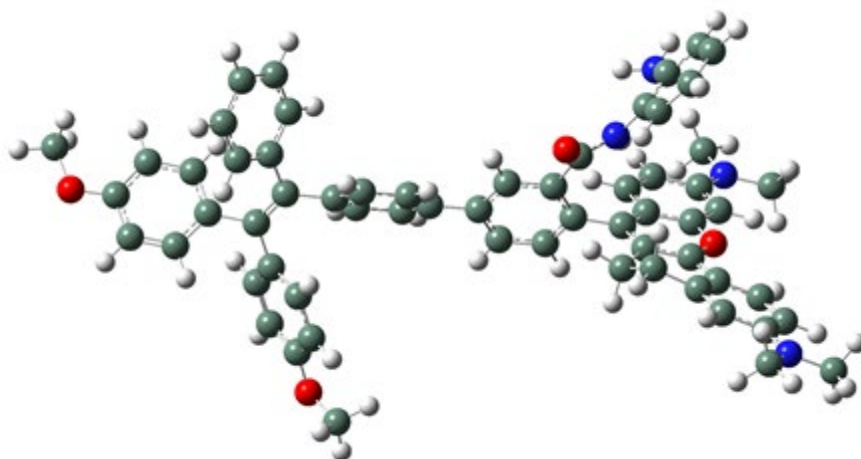
Probe BH⁺

Figure S C.64. GaussView representation of probe BH⁺.

Table S C.10. Computational results for Probe BH⁺.

bh (Optimization completed)		
/home/rluck/calculation/liu/tbt/superior/bh.log		
File Type	.log	
Calculation Type	SP	
Calculation Method	RTPSSh	
Basis Set	TZVP	
Charge	1	
Spin	Singlet	
Solvation	scrf=solvent=water	
E(RTPSSh)	-2916.620324	Hartree
RMS Gradient Norm	0.000002	Hartree/Bohr
Imaginary Freq		
Dipole Moment	32.324085	Debye
Point Group	C1	
Job cpu time:	11 days 11 hours 5 minutes 2...	

Table S C11. Calculated atomic coordinates for probe BH⁺.

Row	Symbol	X	Y	Z
1	C	4.325151	-1.8404	4.007804
2	C	5.71967	-1.60971	4.230199
3	C	6.416613	-0.81672	3.290569
4	C	5.737988	-0.29665	2.210891
5	C	4.357837	-0.4998	1.976561
6	C	3.679862	-1.30739	2.92398
7	N	6.349194	-2.13786	5.306546
8	C	5.621711	-2.96618	6.26822
9	C	7.775523	-1.897	5.513317
10	C	3.764311	0.079923	0.823308
11	C	2.299381	-0.07352	0.598481
12	C	1.750726	-0.82561	-0.45735
13	C	0.368585	-0.84169	-0.65135
14	C	-0.50634	-0.15174	0.193966
15	C	0.052206	0.579968	1.252449
16	C	1.425096	0.619388	1.445529
17	C	2.566482	-1.62582	-1.43719
18	O	6.473552	0.448005	1.328907
19	C	5.908642	1.018235	0.243936
20	C	4.543461	0.851018	-0.03775
21	C	6.784077	1.813987	-0.54799
22	C	6.348618	2.244365	-1.83058
23	C	5.016417	1.755652	-2.33789
24	C	3.995075	1.6377	-1.20558
25	O	2.319768	-1.59439	-2.64258
26	N	3.545901	-2.39985	-0.88596
27	C	4.490486	-3.20983	-1.55813
28	C	-1.96912	-0.19123	-0.02229
29	C	8.075059	2.187517	-0.10832
30	C	8.892465	2.970546	-0.88279
31	C	8.461067	3.426101	-2.16272
32	C	7.169861	3.029911	-2.60782
33	N	9.255604	4.21139	-2.92818
34	C	8.792638	4.69298	-4.22881
35	C	10.59205	4.589805	-2.46983
36	C	4.960141	-4.34672	-0.86552
37	C	4.993259	-2.89769	-2.82179
38	C	5.985052	-3.68871	-3.39549
39	C	6.481665	-4.79064	-2.70183
40	C	5.973811	-5.11383	-1.44762
41	N	4.464221	-4.62437	0.417723
42	C	-2.86208	-0.14384	1.05944
43	C	-4.23458	-0.17343	0.857326
44	C	-4.77822	-0.24918	-0.43423
45	C	-3.88323	-0.32068	-1.51286
46	C	-2.50983	-0.2829	-1.31332
47	C	-6.24658	-0.31721	-0.65675
48	C	-6.68659	-1.35303	-1.63352
49	C	-7.12748	0.510445	-0.01959
50	C	-8.59183	0.259119	-0.00992
51	C	-6.69128	1.730165	0.708658

52	C	-7.56344	-1.03293	-2.68058	80	H	-0.02228	-1.43564	-1.46885
53	C	-7.94496	-1.99341	-3.61246	81	H	-0.58911	1.150754	1.913757
54	C	-7.45908	-3.29721	-3.51699	82	H	1.834661	1.221802	2.248455
55	C	-6.57788	-3.62721	-2.48798	83	H	5.161881	0.770943	-2.79882
56	C	-6.1875	-2.66241	-1.56359	84	H	4.639951	2.421121	-3.11651
57	C	-9.50522	1.303396	-0.23809	85	H	3.733644	2.640956	-0.84598
58	C	-10.8727	1.084277	-0.21872	86	H	3.075656	1.18509	-1.57438
59	C	-11.3754	-0.19373	0.057748	87	H	3.597503	-2.43266	0.125714
60	C	-10.4877	-1.24228	0.315799	88	H	8.418918	1.864186	0.866321
61	C	-9.11565	-1.00615	0.276851	89	H	9.866351	3.249946	-0.50598
62	C	-7.20705	2.035422	1.980474	90	H	6.818896	3.33692	-3.58419
63	C	-6.81658	3.175202	2.6636	91	H	8.618341	3.861884	-4.91865
64	C	-5.90882	4.068089	2.079199	92	H	7.868409	5.267997	-4.12585
65	C	-5.40462	3.801329	0.802964	93	H	9.557389	5.339823	-4.6503
66	C	-5.79714	2.642259	0.137783	94	H	10.54083	5.18475	-1.55334
67	O	-5.58735	5.167202	2.821544	95	H	11.20843	3.70581	-2.28549
68	O	-12.7348	-0.31455	0.063534	96	H	11.06632	5.186221	-3.24457
69	C	-13.2873	-1.60768	0.339122	97	H	4.611268	-2.03149	-3.34313
70	C	-4.65803	6.101893	2.25936	98	H	6.369662	-3.43756	-4.37701
71	H	3.76439	-2.44965	4.702484	99	H	7.259035	-5.40751	-3.13844
72	H	7.472178	-0.60903	3.388846	100	H	6.344189	-5.9845	-0.91614
73	H	2.623507	-1.50212	2.785812	101	H	4.815814	-5.49327	0.80045
74	H	4.805088	-2.40642	6.732237	102	H	3.451928	-4.60943	0.483837
75	H	5.214744	-3.8619	5.790704	103	H	-2.47896	-0.11449	2.073668
76	H	6.314367	-3.27432	7.04675	104	H	-4.89993	-0.15362	1.712471
77	H	8.366613	-2.29966	4.685138	105	H	-4.27132	-0.38766	-2.52324
78	H	7.981921	-0.8269	5.608582	106	H	-1.85057	-0.30207	-2.17427
79	H	8.08138	-2.39209	6.430974	107	H	-7.94028	-0.01988	-2.7638

108	H	-8.61792	-1.72196	-4.41883	117	H	-7.20703	3.393756	3.651046
109	H	-7.75775	-4.04629	-4.24202	118	H	-4.71986	4.485347	0.318592
110	H	-6.19131	-4.63747	-2.40654	119	H	-5.4041	2.450051	-0.85401
111	H	-5.49656	-2.92674	-0.77015	120	H	-14.3661	-1.48005	0.286399
112	H	-9.13307	2.300218	-0.44798	121	H	-12.9646	-2.33818	-0.40799
113	H	-11.5689	1.892422	-0.41212	122	H	-13.0045	-1.94928	1.338793
114	H	-10.849	-2.23441	0.553615	123	H	-4.54052	6.8813	3.008788
115	H	-8.43816	-1.82622	0.484894	124	H	-3.69259	5.625598	2.066812
116	H	-7.91517	1.357779	2.444782	125	H	-5.04948	6.535082	1.334693
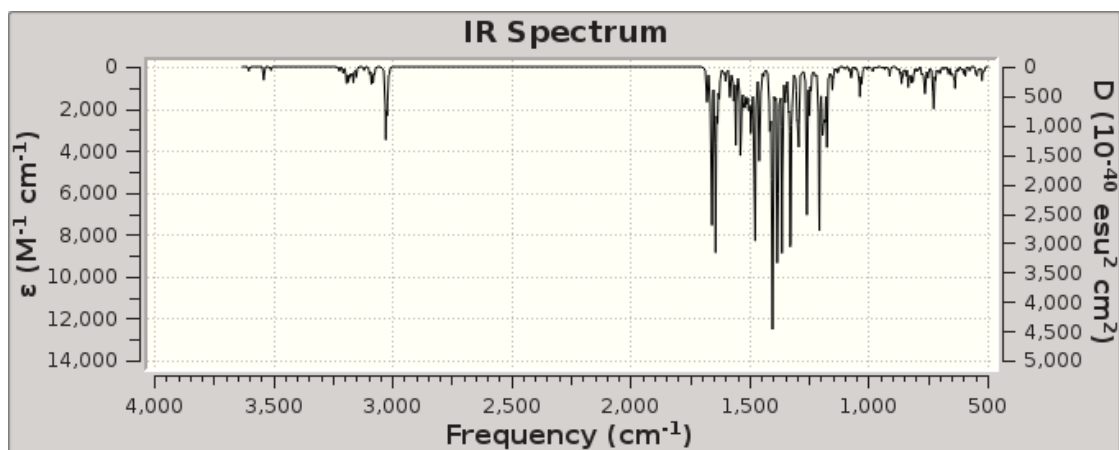
Figure S C.65. Calculated IR spectrum for probe BH$^+$.
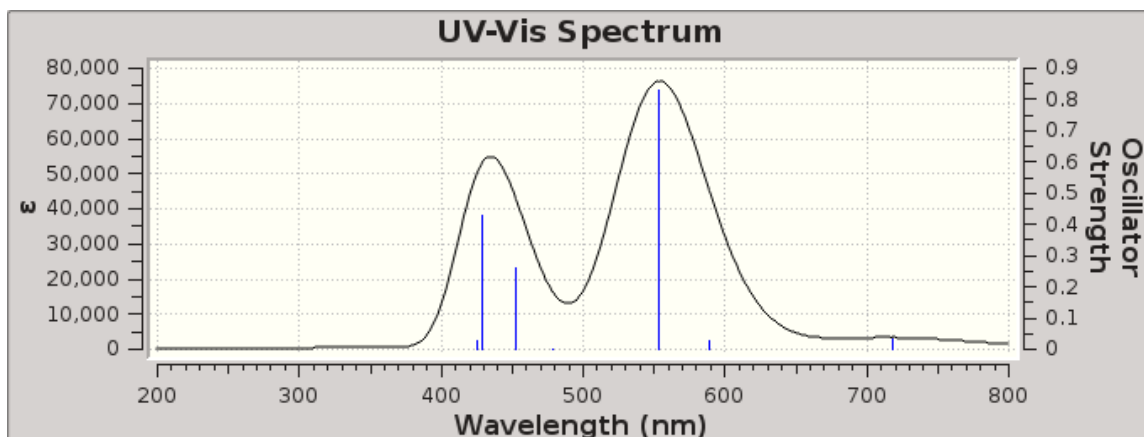
Figure S C.66. Calculated UV-Vis spectrum for probe BH$^+$.

Table S C.12. Excitation energies and oscillator strengths listing for probe BH$^+$.

Excited State   1:   Singlet-A   1.7268 eV 718.00 nm f=0.0317 <S**2>=0.000
   243 -> 244   0.70674
This state for optimization and/or second-order correction.
Total Energy, E(TD-HF/TD-DFT) = -2916.55686528
Copying the excited state density for this state as the 1-particle RhoCI density.
Excited State   2:   Singlet-A   2.1038 eV 589.33 nm f=0.0278 <S**2>=0.000
   241 -> 244   0.69547
   242 -> 244   -0.12533
Excited State   3:   Singlet-A   2.2389 eV 553.78 nm f=0.8284 <S**2>=0.000
   241 -> 244   0.12631
   242 -> 244   0.68934
Excited State   4:   Singlet-A   2.5909 eV 478.55 nm f=0.0018 <S**2>=0.000
   240 -> 244   0.70549
Excited State   5:   Singlet-A   2.7371 eV 452.98 nm f=0.2589 <S**2>=0.000
   238 -> 244   -0.16803
   239 -> 244   0.64657
   242 -> 247   0.10615
   243 -> 245   -0.11927
Excited State   6:   Singlet-A   2.8928 eV 428.59 nm f=0.4283 <S**2>=0.000
   237 -> 244   -0.25626
   243 -> 245   0.64761
Excited State   7:   Singlet-A   2.9162 eV 425.16 nm f=0.0292 <S**2>=0.000
   237 -> 244   0.53318
   238 -> 244   0.36334
   239 -> 244   0.17756
   243 -> 245   0.19666

BH$^+$-243 HOMO

BH$^+$-244 LUMO

BH$^+$-242 HOMO-1

BH$^+$-245 LUMO+1

BH$^+$-241 HOMO-2

BH$^+$-239 HOMO-4

BH$^+$-238 HOMO-5
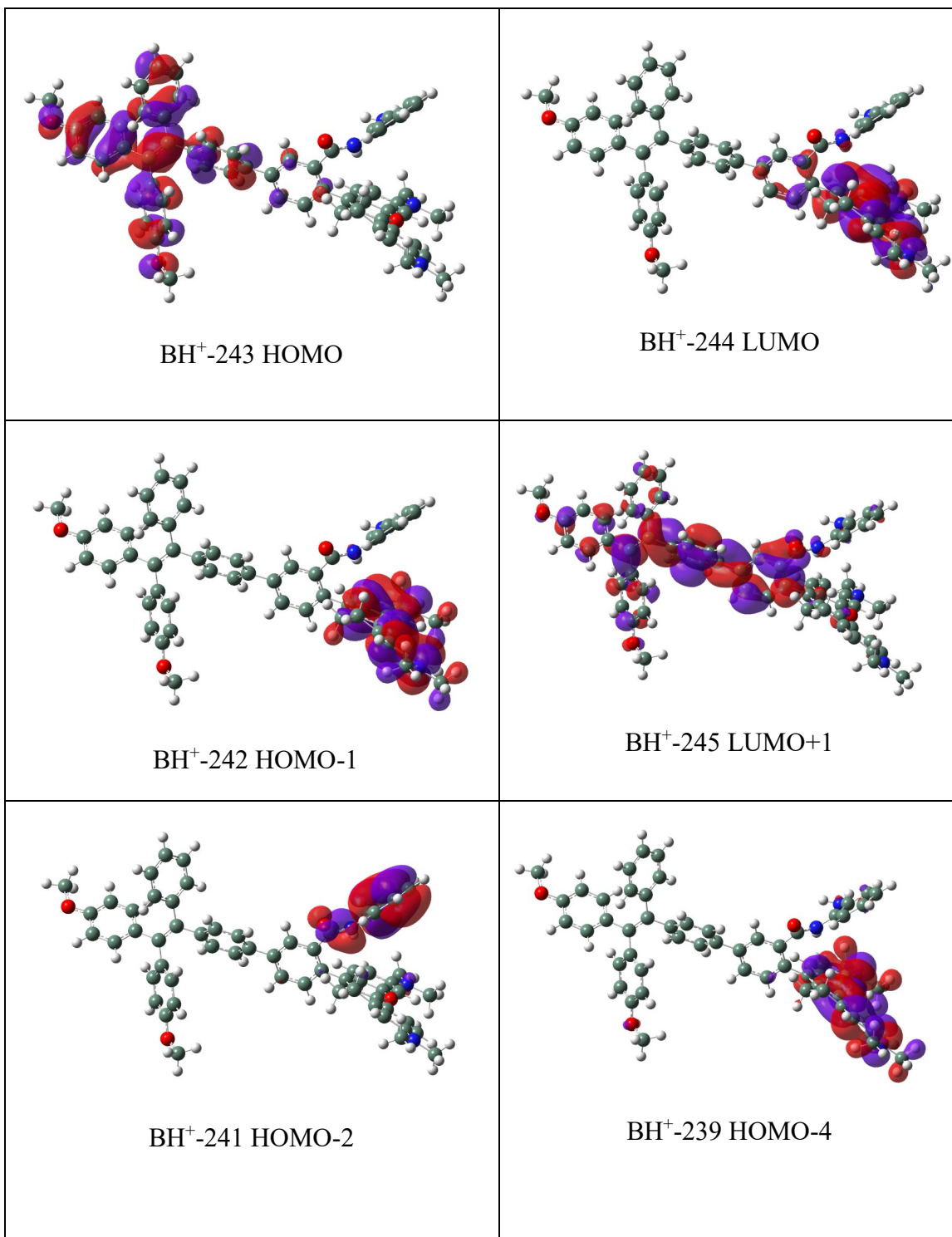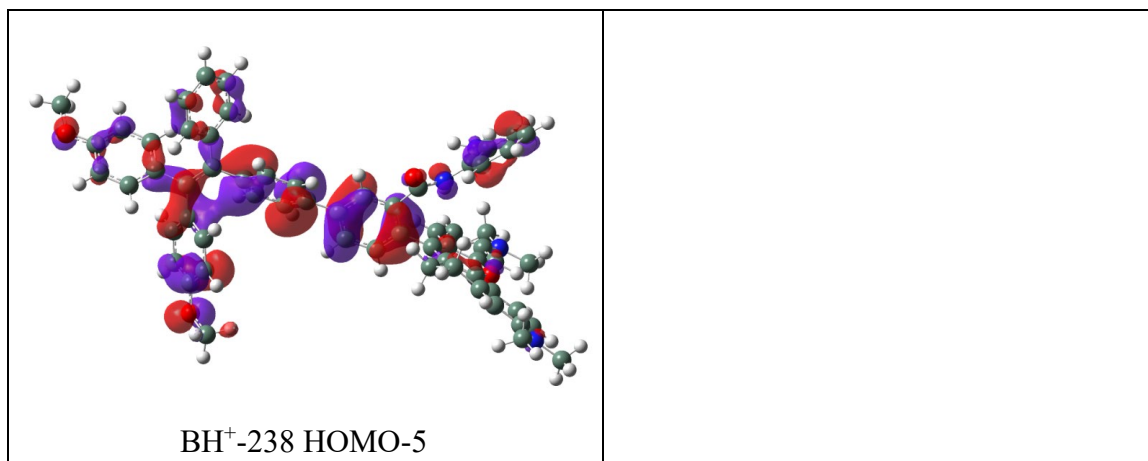
Figure S C.67. Drawings of the highest occupied and lowest unoccupied orbitals for probe BH$^+$.

Probe C
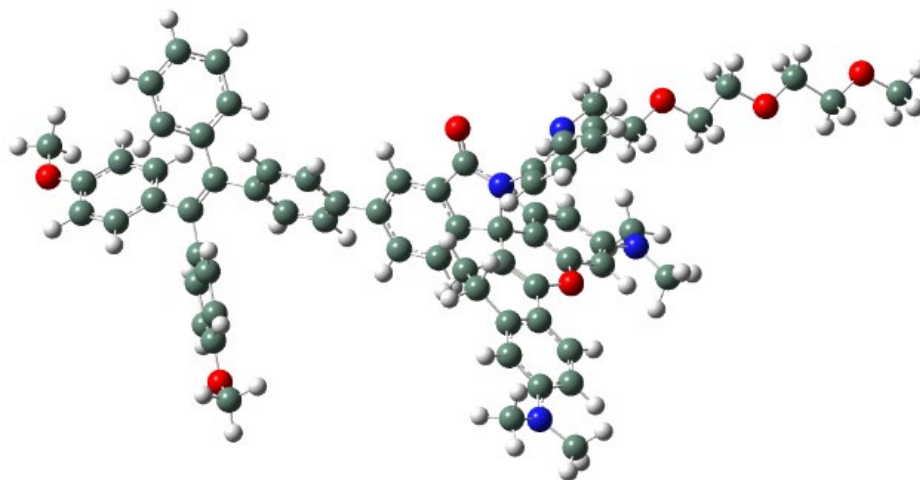
Figure S C.68. GaussView representation of probe C.

Table S C.13. Computational results for probe C**.**

c (Optimization completed)		
/home/rluck/calculation/liu/tbt/superior/c.log		
File Type	.log	
Calculation Type	SP	
Calculation Method	RTPSSh	
Basis Set	TZVP	
Charge	0	
Spin	Singlet	
Solvation	scrf=solvent=water	
E(RTPSSh)	-3417.150421	Hartree
RMS Gradient Norm	0.000001	Hartree/Bohr
Imaginary Freq		
Dipole Moment	11.356903	Debye
Point Group	C1	
Job cpu time:	17 days 16 hours 28 minutes	...

Table S C.14. Calculated atomic coordinates for probe C.

Row	Symbol	X	Y	Z					
					26	N	-2.54374	0.524267	1.919638
1	C	-3.7022	-1.45431	-1.90355	27	C	-3.76792	0.585025	2.656452
2	C	-4.85921	-0.81929	-2.42441	28	C	3.295078	-0.16786	0.470395
3	C	-5.12316	0.494292	-1.99692	29	C	-4.94282	5.150598	-0.96708
4	C	-4.29457	1.111964	-1.06477	30	C	-5.16879	6.517333	-1.01355
5	C	-3.18452	0.481055	-0.50758	31	C	-4.44092	7.399406	-0.18223
6	C	-2.90617	-0.81157	-0.9741	32	C	-3.5097	6.825067	0.716345
7	N	-5.69284	-1.46492	-3.31118	33	N	-4.61898	8.763313	-0.25122
8	C	-5.25429	-2.70809	-3.93491	34	C	-4.01925	9.621268	0.762672
9	C	-6.73906	-0.70752	-3.98565	35	C	-5.72617	9.30487	-1.02868
10	C	-2.33933	1.162846	0.544055	36	C	-4.62228	-0.54611	2.711727
11	C	-0.85514	0.887241	0.356813	37	C	-4.08101	1.736648	3.372265
12	C	-0.31799	0.242035	1.462353	38	C	-5.24262	1.826454	4.134895
13	C	1.02221	-0.11491	1.529311	39	C	-6.09126	0.722847	4.186491
14	C	1.858472	0.189992	0.446654	40	C	-5.79071	-0.4425	3.492224
15	C	1.30157	0.847689	-0.66935	41	N	-4.26875	-1.71276	2.073388
16	C	-0.04446	1.19778	-0.72721	42	C	-5.1365	-2.87145	1.956535
17	C	-1.38357	0.028136	2.470319	43	C	-6.26558	-2.69917	0.939686
18	O	-4.62566	2.410992	-0.75641	44	O	-7.05408	-3.88718	0.974599
19	C	-3.71366	3.162053	-0.04726	45	C	-8.12807	-3.8522	0.039526
20	C	-2.63702	2.640405	0.574892	46	C	-8.88173	-5.1637	0.16659
21	C	-4.00376	4.593291	-0.09006	47	O	-9.95276	-5.13155	-0.77186
22	C	-3.29161	5.457	0.764436	48	C	-10.7296	-6.32562	-0.74309
23	C	-2.35679	4.847119	1.781376	49	C	-11.8318	-6.17569	-1.77568
24	C	-1.6704	3.580785	1.259374	50	O	-12.606	-7.36916	-1.74922
25	O	-1.27297	-0.48519	3.581948	51	C	3.97256	-0.53554	-0.70256

52	C	5.320056	-0.86748	-0.67922	80	C	-13.6745	-7.3293	-2.68995
53	C	6.053083	-0.84962	0.516898	81	H	-3.42743	-2.44788	-2.22944
54	C	5.368877	-0.50636	1.692793	82	H	-5.95456	1.064029	-2.38808
55	C	4.023873	-0.16183	1.669152	83	H	-2.02649	-1.32642	-0.59946
56	C	7.486842	-1.24267	0.553591	84	H	-5.03118	-3.4632	-3.17799
57	C	7.850797	-2.18926	1.645014	85	H	-6.06527	-3.08578	-4.55496
58	C	8.401482	-0.7701	-0.34445	86	H	-4.36567	-2.57018	-4.56505
59	C	9.749471	-1.37501	-0.50304	87	H	-6.33324	0.077263	-4.63842
60	C	8.121387	0.38969	-1.23065	88	H	-7.32814	-1.39416	-4.59083
61	C	8.95217	-1.94467	2.478791	89	H	-7.40697	-0.24205	-3.25698
62	C	9.26708	-2.81212	3.520361	90	H	1.401661	-0.63971	2.398723
63	C	8.488029	-3.94577	3.750948	91	H	1.946005	1.10758	-1.50156
64	C	7.383672	-4.19599	2.937296	92	H	-0.44033	1.707186	-1.59888
65	C	7.06259	-3.32096	1.903448	93	H	-2.94763	4.596262	2.671469
66	C	10.89592	-0.56776	-0.60693	94	H	-1.60916	5.577673	2.098822
67	C	12.15586	-1.11952	-0.77016	95	H	-0.86996	3.854726	0.559089
68	C	12.30772	-2.50917	-0.8611	96	H	-1.18146	3.065383	2.091743
69	C	11.17976	-3.33157	-0.78825	97	H	-5.50679	4.501667	-1.62625
70	C	9.922643	-2.7593	-0.60885	98	H	-5.9089	6.899955	-1.70339
71	C	8.458583	0.355461	-2.59511	99	H	-2.9504	7.457078	1.394876
72	C	8.215444	1.436225	-3.42656	100	H	-4.41005	9.415994	1.768244
73	C	7.645638	2.606713	-2.90893	101	H	-2.93344	9.499321	0.781299
74	C	7.327181	2.675037	-1.54958	102	H	-4.23614	10.65762	0.510657
75	C	7.564986	1.572572	-0.73218	103	H	-5.65853	8.987068	-2.07202
76	O	7.450917	3.622791	-3.79929	104	H	-6.70389	8.997666	-0.634
77	O	13.58398	-2.96303	-1.02934	105	H	-5.66719	10.39144	-1.00419
78	C	13.77971	-4.37932	-1.12448	106	H	-3.38566	2.565097	3.335104
79	C	6.871294	4.837356	-3.30723	107	H	-5.47154	2.733097	4.681949

286

108	H	-7.00214	0.763052	4.774376	129	H	8.734373	-4.62269	4.561569
109	H	-6.46891	-1.28422	3.556161	130	H	6.768866	-5.07287	3.110022
110	H	-3.55885	-1.6145	1.361357	131	H	6.197441	-3.5202	1.280108
111	H	-4.51588	-3.71941	1.661757	132	H	10.79571	0.510343	-0.54472
112	H	-5.56063	-3.10841	2.935386	133	H	13.03579	-0.48939	-0.83315
113	H	-6.88452	-1.8276	1.189478	134	H	11.26568	-4.40678	-0.87719
114	H	-5.84912	-2.54833	-0.06383	135	H	9.055398	-3.40768	-0.56062
115	H	-8.79711	-3.00906	0.255861	136	H	8.906399	-0.54055	-3.0109
116	H	-7.74292	-3.73585	-0.98195	137	H	8.464179	1.39462	-4.48094
117	H	-8.21095	-6.00617	-0.0468	138	H	6.906305	3.574264	-1.1187
118	H	-9.26999	-5.27928	1.186963	139	H	7.320047	1.640658	0.321575
119	H	-10.1032	-7.19478	-0.98283	140	H	14.8518	-4.51709	-1.24532
120	H	-11.1638	-6.47507	0.254041	141	H	13.44269	-4.88283	-0.21402
121	H	-12.4581	-5.30589	-1.53529	142	H	13.25485	-4.78967	-1.99175
122	H	-11.3962	-6.02228	-2.77234	143	H	6.801609	5.496387	-4.16965
123	H	3.432082	-0.59255	-1.64114	144	H	5.873136	4.657006	-2.89837
124	H	5.812516	-1.16313	-1.59834	145	H	7.508123	5.293985	-2.54437
125	H	5.904739	-0.49025	2.635604	146	H	-14.2111	-8.27355	-2.60271
126	H	3.538598	0.135334	2.592486	147	H	-14.3596	-6.49995	-2.4736
127	H	9.55845	-1.06221	2.308853	148	H	-13.2947	-7.21969	-3.71354
128	H	10.1186	-2.59906	4.157821					

287
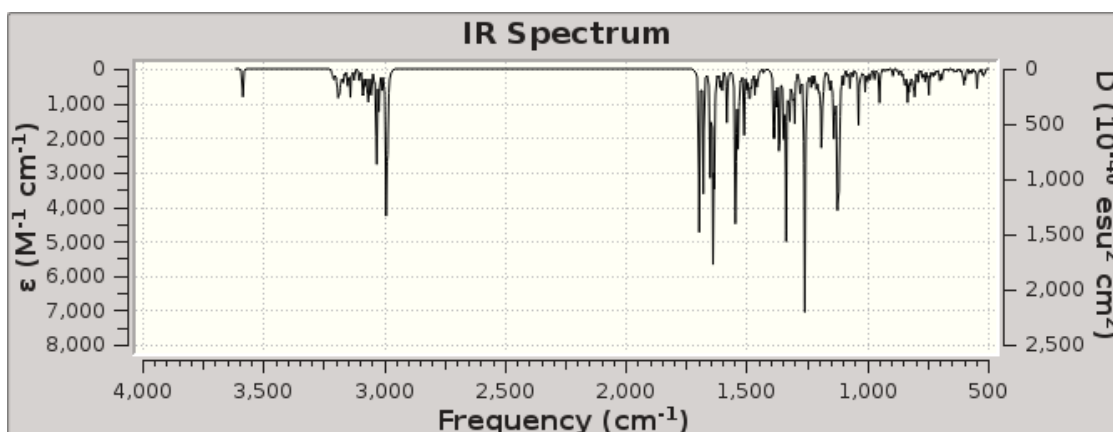
Figure S C.69. Calculated IR spectrum for probe C.
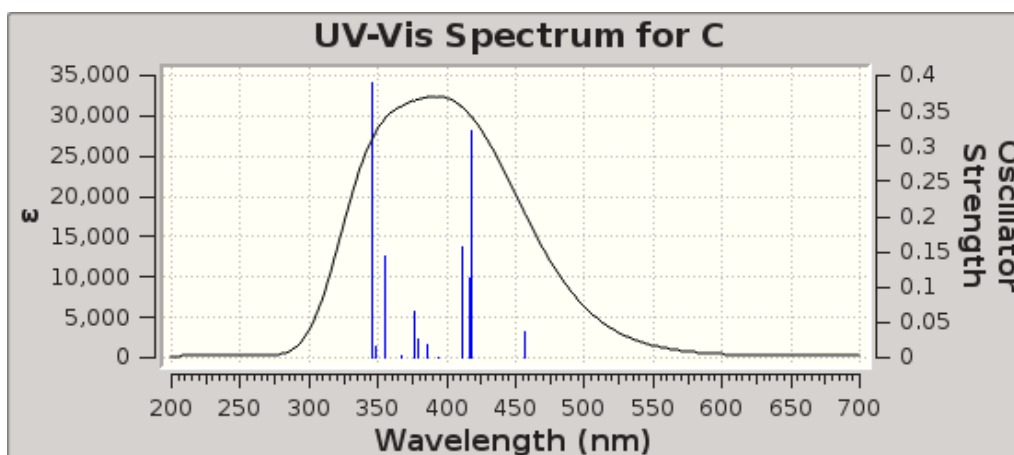
Figure S C.70. Calculated UV-Vis spectrum for probe C.

Table S C.15. Excitation energies and oscillator strengths listing for Probe C.

Excited State   1:   Singlet-A   2.7132 eV 456.97 nm f=0.0379 <S**2>=0.000
   283 -> 284   0.70141
This state for optimization and/or second-order correction.
Total Energy, E(TD-HF/TD-DFT) = -3417.05071481
Copying the excited state density for this state as the 1-particle RhoCI density.

Excited State 2:   Singlet-A   2.9645 eV 418.23 nm f=0.3210 <S**2>=0.000
   281 -> 284   -0.18114

```
282 -> 284      0.52811
283 -> 285     -0.42021


Excited State   3:      Singlet-A     2.9731 eV 417.01 nm  f=0.1115  <S**2>=0.000
  281 -> 284     -0.15062
  282 -> 284      0.39405
  283 -> 285      0.56025


Excited State   4:      Singlet-A     3.0166 eV 411.01 nm  f=0.1576  <S**2>=0.000
  281 -> 284      0.65473
  282 -> 284      0.23582


Excited State   5:      Singlet-A     3.1504 eV 393.55 nm  f=0.0008  <S**2>=0.000
  280 -> 284      0.69489
  280 -> 285     -0.11045


Excited State   6:      Singlet-A     3.2159 eV 385.53 nm  f=0.0185  <S**2>=0.000
  281 -> 285     -0.48219
  282 -> 285      0.49606


Excited State   7:      Singlet-A     3.2694 eV 379.23 nm  f=0.0254  <S**2>=0.000
  281 -> 285      0.48286
  282 -> 285      0.48728
  283 -> 286      0.12126


Excited State   8:      Singlet-A     3.2896 eV 376.89 nm  f=0.0650  <S**2>=0.000
  283 -> 286      0.68408


Excited State   9:      Singlet-A     3.3752 eV 367.34 nm  f=0.0017  <S**2>=0.000
  280 -> 284      0.10065
  280 -> 285      0.68817
  281 -> 285     -0.10477


Excited State  10:      Singlet-A     3.4948 eV 354.77 nm  f=0.1443  <S**2>=0.000
  282 -> 286      0.68413


Excited State  11:      Singlet-A     3.5582 eV 348.45 nm  f=0.0147  <S**2>=0.000
  281 -> 286      0.67130
  281 -> 287      0.10409
  283 -> 287      0.12999


Excited State  12:      Singlet-A     3.5884 eV 345.52 nm  f=0.3884  <S**2>=0.000
  281 -> 286     -0.14606
  283 -> 287      0.64387
  283 -> 291      0.15346
```

C-283 HOMO

C-284 LUMO

C-282 HOMO-1

C-285 LUMO+1

C-281 HOMO-2
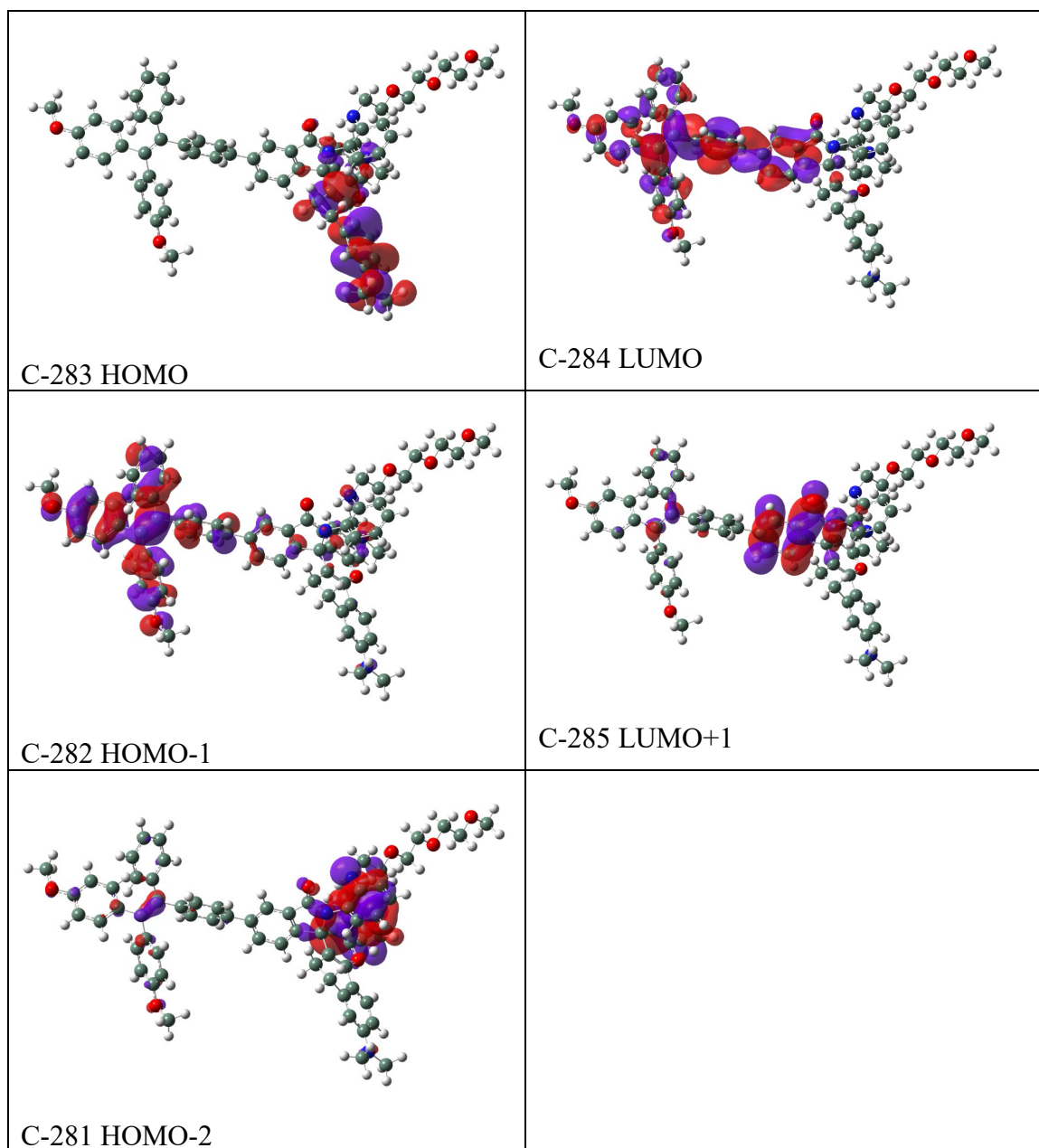
Figure S C.71. Drawings of the highest occupied and lowest unoccupied orbitals for probe C.

Probe CH⁺
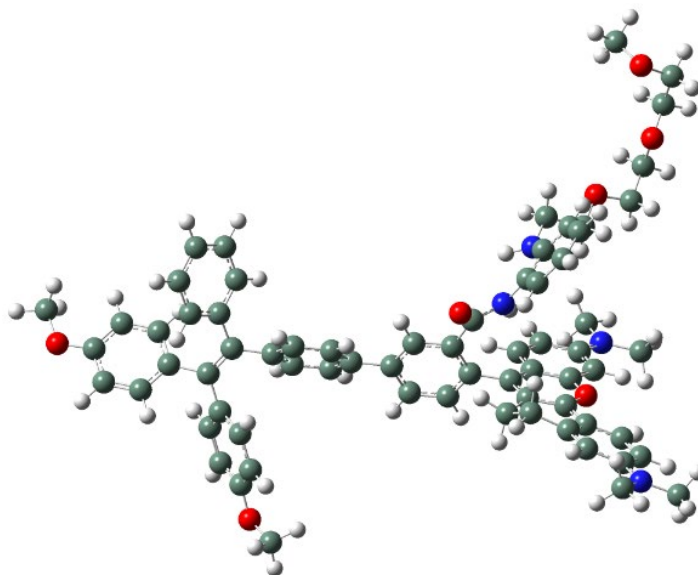
Figure S C.72. GaussView representation of probe CH⁺.

Table S C.16. Computational results for probe CH⁺.

ch (Optimization completed)		
/home/rluck/calculation/liu/tbt/superior/ch.log		
File Type	.log	
Calculation Type	SP	
Calculation Method	RTPSSh	
Basis Set	TZVP	
Charge	1	
Spin	Singlet	
Solvation	scrf=solvent=water	
E(RTPSSh)	-3417.616353	Hartree
RMS Gradient Norm	0.000001	Hartree/Bohr
Imaginary Freq		
Dipole Moment	30.539098	Debye
Point Group	C1	
Job cpu time:	16 days 23 hours 38 minutes ...	

Table S C.17. Calculated atomic coordinates for probe CH⁺.

Row	Symbol	X	Y	Z		Symbol	X	Y	Z
					26	N	2.669219	-0.12944	-1.39967
1	C	3.551294	-0.32012	3.438335	27	C	3.737972	-0.5412	-2.23462
2	C	4.854269	0.215185	3.689289	28	C	-3.17982	0.33298	-0.08959
3	C	5.265876	1.335808	2.932597	29	C	5.88842	5.284702	0.223626
4	C	4.410856	1.865539	1.99185	30	C	6.431923	6.390619	-0.37822
5	C	3.116182	1.358868	1.731024	31	C	5.822993	6.96012	-1.53456
6	C	2.72451	0.23189	2.496547	32	C	4.649675	6.337104	-2.04235
7	N	5.665729	-0.33906	4.62106	33	N	6.34546	8.058828	-2.12899
8	C	5.234821	-1.50673	5.389892	34	C	5.703238	8.642647	-3.30573
9	C	6.998534	0.212585	4.854915	35	C	7.570769	8.671617	-1.6164
10	C	2.325439	1.978295	0.726124	36	C	4.474849	-1.68051	-1.82829
11	C	0.937674	1.489625	0.485518	37	C	4.09114	0.159903	-3.38462
12	C	0.544387	0.800091	-0.67693	38	C	5.192582	-0.23528	-4.14007
13	C	-0.79531	0.448041	-0.85174	39	C	5.94832	-1.32939	-3.72782
14	C	-1.76994	0.734631	0.109161	40	C	5.598905	-2.04158	-2.58384
15	C	-1.36201	1.412336	1.267609	41	N	4.081094	-2.35851	-0.67561
16	C	-0.03756	1.782957	1.447083	42	C	4.752088	-3.57913	-0.2386
17	C	1.476421	0.406959	-1.79199	43	C	5.980295	-3.26053	0.608953
18	O	4.874958	2.938238	1.27969	44	O	6.626727	-4.49338	0.905682
19	C	4.11821	3.542889	0.339936	45	C	7.805953	-4.31079	1.68631
20	C	2.826928	3.08101	0.037835	46	C	8.469907	-5.6468	1.916804
21	C	4.711156	4.680806	-0.27556	47	O	9.027229	-6.12028	0.693773
22	C	4.103667	5.226772	-1.4386	48	C	9.647302	-7.39349	0.847316
23	C	2.913814	4.514727	-2.02916	49	C	10.19898	-7.84636	-0.49261
24	C	2.026064	3.906208	-0.94222	50	O	9.211693	-8.08655	-1.49394
25	O	1.14225	0.530388	-2.96961	51	C	-3.99017	-0.02608	0.998556

292

52	C	-5.31231	-0.40513	0.813247	80	C	8.474763	-9.2885	-1.28613
53	C	-5.88543	-0.4427	-0.46688	81	H	3.207597	-1.17952	3.996403
54	C	-5.06768	-0.10313	-1.55557	82	H	6.237658	1.789194	3.063958
55	C	-3.74793	0.286295	-1.37135	83	H	1.744233	-0.19818	2.331597
56	C	-7.28702	-0.89279	-0.6773	84	H	4.329164	-1.28904	5.962299
57	C	-7.46855	-1.87802	-1.78032	85	H	5.047317	-2.36354	4.736389
58	C	-8.32795	-0.43852	0.081659	86	H	6.026935	-1.76937	6.085907
59	C	-9.66296	-1.09093	0.076758	87	H	7.609971	0.160378	3.948982
60	C	-8.20784	0.747151	0.969595	88	H	6.938977	1.254493	5.183016
61	C	-8.45418	-1.69531	-2.76155	89	H	7.483018	-0.36911	5.634404
62	C	-8.5948	-2.59937	-3.81018	90	H	-1.06322	-0.09015	-1.75299
63	C	-7.75373	-3.7083	-3.90002	91	H	-2.09038	1.679138	2.024369
64	C	-6.76274	-3.8973	-2.93746	92	H	0.247286	2.33448	2.335927
65	C	-6.61521	-2.98575	-1.89599	93	H	3.280962	3.716521	-2.68574
66	C	-10.8401	-0.32495	0.010347	94	H	2.333024	5.198264	-2.65064
67	C	-12.0907	-0.92001	0.020244	95	H	1.53128	4.710955	-0.38393
68	C	-12.2054	-2.31234	0.124118	96	H	1.238107	3.304121	-1.39327
69	C	-11.0501	-3.09356	0.218967	97	H	2.813111	-0.26441	-0.40576
70	C	-9.80073	-2.47846	0.191813	98	H	6.360945	4.876653	1.108416
71	C	-8.71767	0.722676	2.279644	99	H	7.324021	6.834301	0.041161
72	C	-8.62224	1.82518	3.112387	100	H	4.174127	6.728202	-2.93205
73	C	-8.03166	3.007573	2.647662	101	H	5.706589	7.942128	-4.14616
74	C	-7.54291	3.065649	1.339332	102	H	4.670918	8.927717	-3.08587
75	C	-7.63384	1.941696	0.521605	103	H	6.254345	9.533758	-3.59378
76	O	-7.98914	4.044307	3.534211	104	H	7.433162	9.029599	-0.59215
77	O	-13.4764	-2.80948	0.135386	105	H	8.402655	7.96221	-1.63614
78	C	-13.6354	-4.22963	0.241411	106	H	7.823281	9.518628	-2.24862
79	C	-7.39213	5.271163	3.096412	107	H	3.503539	1.018967	-3.67777

108	H	5.460872	0.317501	-5.03254	129	H	-9.35845	-2.43426	-4.56275
109	H	6.816177	-1.64008	-4.29887	130	H	-7.86444	-4.41358	-4.71629
110	H	6.194661	-2.89613	-2.2892	131	H	-6.10115	-4.75471	-2.99951
111	H	3.078858	-2.38527	-0.54451	132	H	-5.8371	-3.13727	-1.15549
112	H	4.041286	-4.14735	0.36177	133	H	-10.7696	0.754741	-0.0639
113	H	5.04521	-4.21033	-1.08589	134	H	-12.9924	-0.32203	-0.04759
114	H	6.664567	-2.5955	0.065188	135	H	-11.1097	-4.16935	0.321707
115	H	5.675528	-2.75171	1.533166	136	H	-8.91295	-3.09499	0.27279
116	H	8.498034	-3.63131	1.171053	137	H	-9.1836	-0.18269	2.653068
117	H	7.549681	-3.86877	2.659195	138	H	-9.00367	1.791589	4.126606
118	H	9.260161	-5.52285	2.670663	139	H	-7.1019	3.972967	0.947287
119	H	7.736784	-6.36744	2.304064	140	H	-7.2574	2.001631	-0.49317
120	H	10.48237	-7.32808	1.560345	141	H	-14.7088	-4.40386	0.225329
121	H	8.925008	-8.11802	1.24715	142	H	-13.1654	-4.74013	-0.60388
122	H	10.8463	-7.06592	-0.89743	143	H	-13.2152	-4.60158	1.180086
123	H	10.80128	-8.75158	-0.33206	144	H	-7.45585	5.945275	3.947555
124	H	-3.57325	-0.0408	1.999661	145	H	-6.34428	5.120225	2.822147
125	H	-5.90891	-0.69541	1.670147	146	H	-7.94065	5.693187	2.249668
126	H	-5.47879	-0.1285	-2.55878	147	H	7.841777	-9.23492	-0.39323
127	H	-3.15824	0.576715	-2.23396	148	H	7.838902	-9.42044	-2.16129
128	H	-9.10745	-0.83231	-2.70096	149	H	9.149156	-10.1496	-1.19375

294
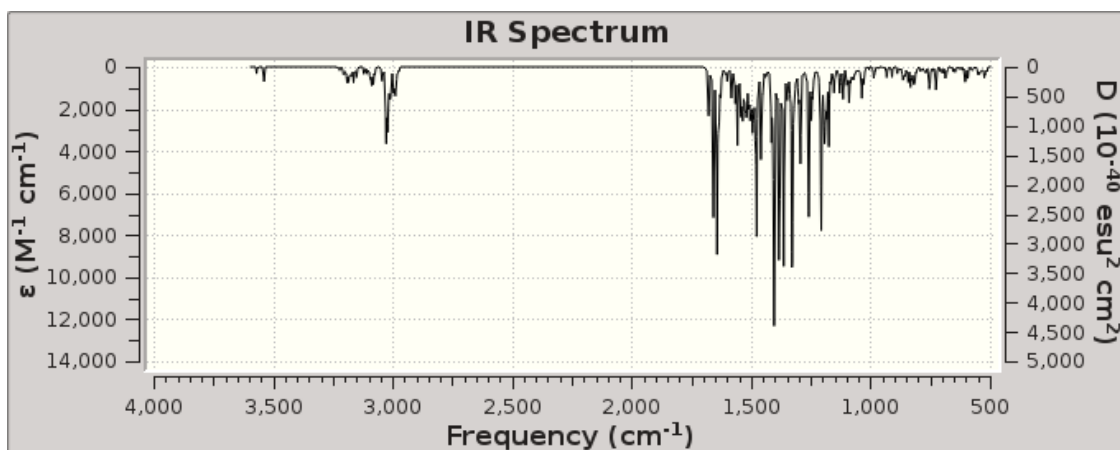
Figure S C.73. Calculated IR spectrum for probe CH$^+$.
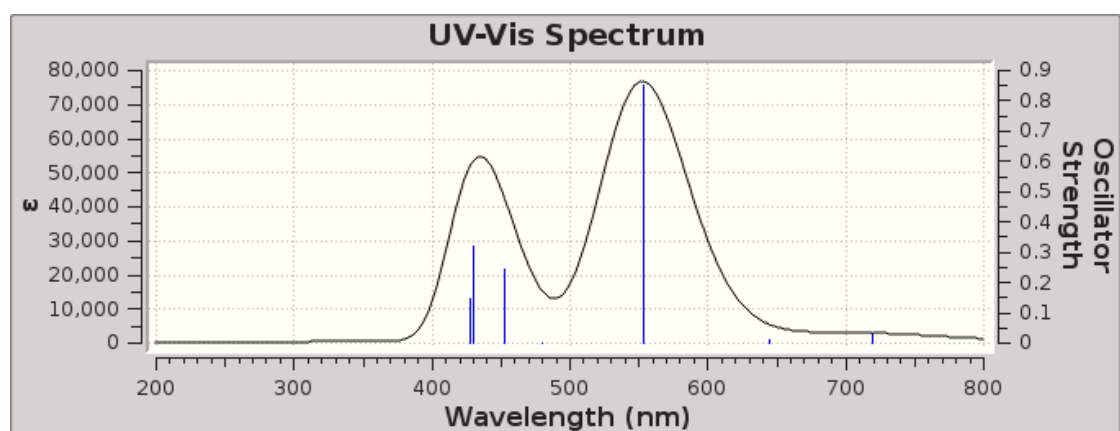
Figure S C.74. Calculated UV-Vis spectrum for probe CH$^+$.

Table S C.18. Excitation energies and oscillator strengths listing for Probe CH$^+$.

Excited State   1:   Singlet-A   1.7234 eV 719.42 nm f=0.0247 <S**2>=0.000
   283 -> 284   0.70674
This state for optimization and/or second-order correction.
Total Energy, E(TD-HF/TD-DFT) = -3417.55301986
Copying the excited state density for this state as the 1-particle RhoCI density.

Excited State   2:   Singlet-A   1.9224 eV 644.96 nm f=0.0124 <S**2>=0.000
   281 -> 284   0.68540
   282 -> 284   -0.17316

Excited State   3:   Singlet-A   2.2419 eV 553.02 nm f=0.8492 <S**2>=0.000
   281 -> 284   0.17173
   282 -> 284   0.67894

Excited State   4:   Singlet-A   2.5855 eV 479.54 nm f=0.0015 <S**2>=0.000
   280 -> 284   0.70620

Excited State   5:   Singlet-A   2.7365 eV 453.08 nm f=0.2433 <S**2>=0.000
   277 -> 284   -0.10817
   278 -> 284   -0.19676
   279 -> 284   0.63831
   282 -> 287   0.10278
   283 -> 285   -0.11238

Excited State   6:   Singlet-A   2.8850 eV 429.75 nm f=0.3205 <S**2>=0.000
   277 -> 284   -0.45476
   278 -> 284   -0.17219
   283 -> 285   0.50633

Excited State   7:   Singlet-A   2.9028 eV 427.12 nm f=0.1441 <S**2>=0.000
   277 -> 284   0.33398
   278 -> 284   0.36421
   279 -> 284   0.21488
   283 -> 285   0.43561

CH⁺-283 HOMO

CH⁺-284 LUMO

CH⁺-282 HOMO-1

CH⁺-285 LUMO+1

1 HOMO-2	CH$^+$-279 HOMO-4
CH$^+$-278 HOMO-5	CH$^+$-277 HOMO-6
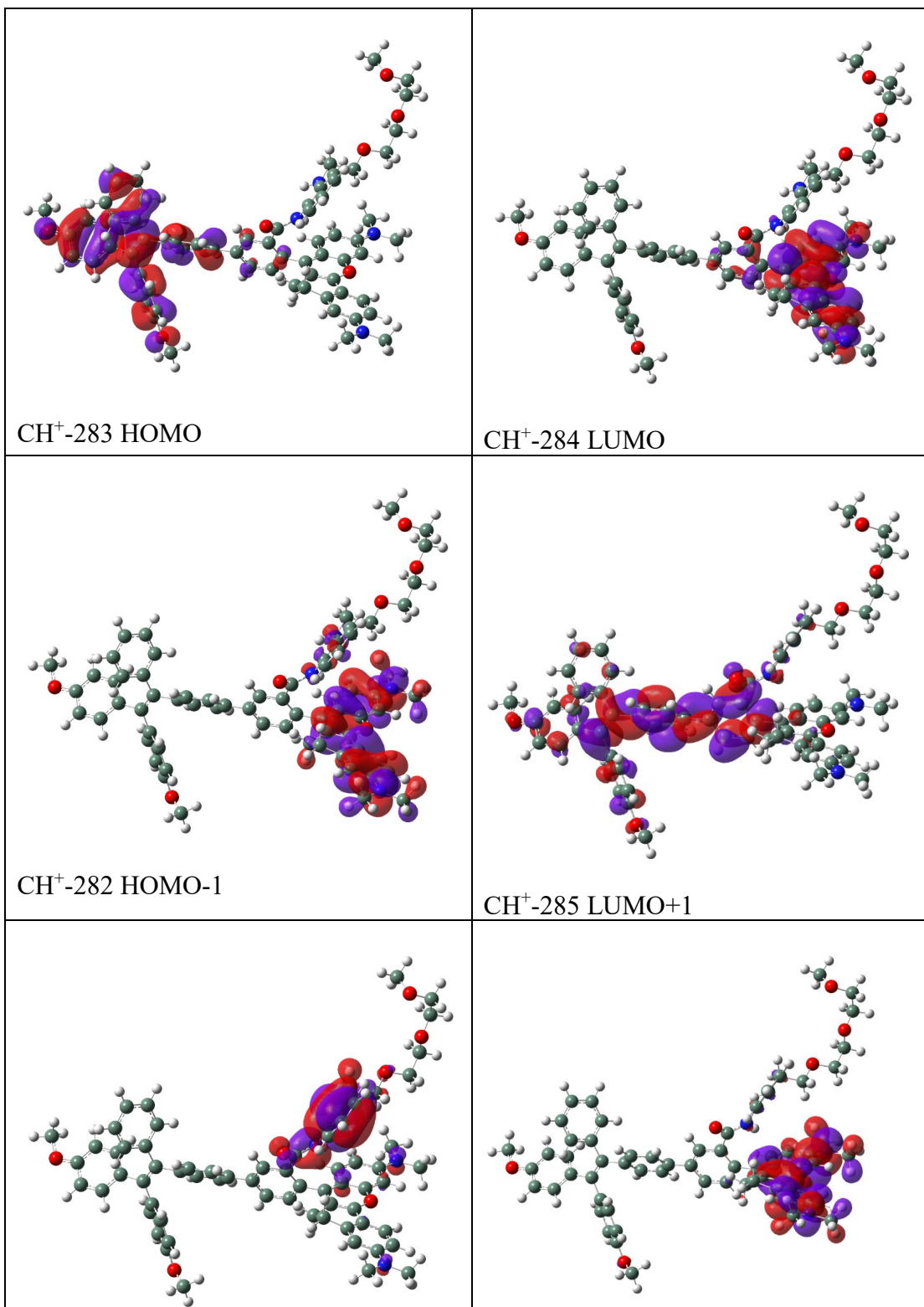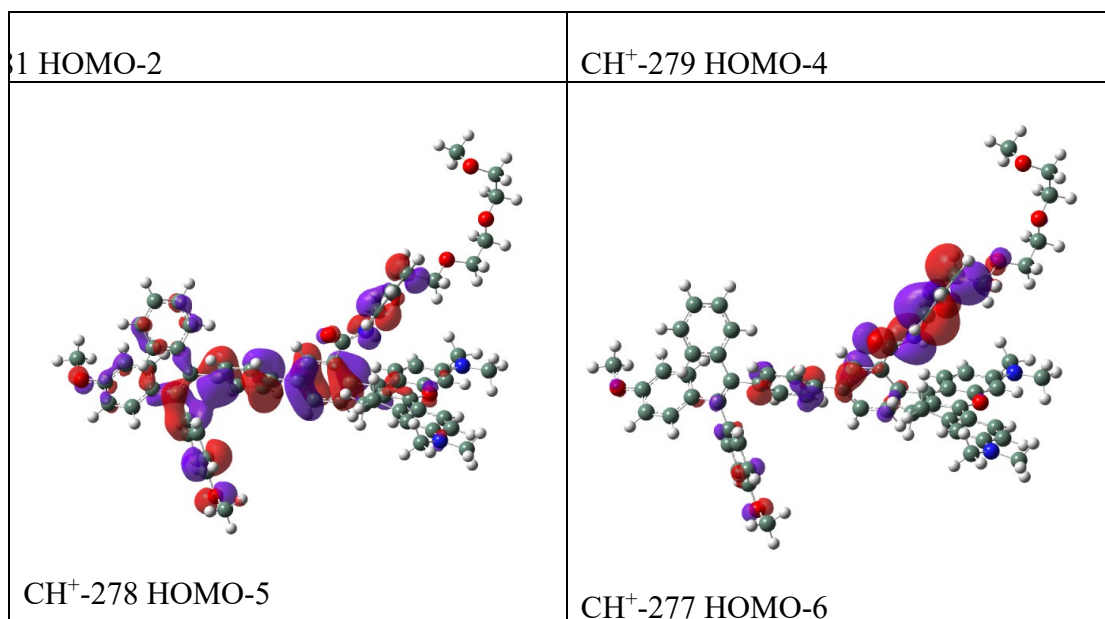
Figure S C.75. Drawings of the highest occupied and lowest unoccupied orbitals for probe CH$^+$.

Appendix D   Supporting Information for Chapter 5

1. Instruments and Materials

Solvents and reagents were obtained from Sigma-Aldrich or Fisher scientific. Column chromatographic purification was conducted on silica gel (200-300 mesh) obtained from Sigma-Aldrich while thin-layer chromatography (TLC) analysis was conducted in silica gel plates obtained from Sigma-Aldrich. Intermediates and the fluorescent probes were characterized by Varian Unity Inova NMR spectrophotometer at 400 MHz and 100 MHz to record ^{1}H NMR and ^{13}C NMR spectra in CDCl$_3$ solution. Absorption spectra were collected by employing Per-kin Elmer Lambda 35 UV/VIS spectrometer while fluorescence spectra were performed on Jobin Yvon Fluoromax-4 spectrofluorometer. Rhodol dye bearing formyl group (**3**) was prepared and characterized according to the reported procedure.

^{1}H and ^{13}C NMR spectra of probes A and B
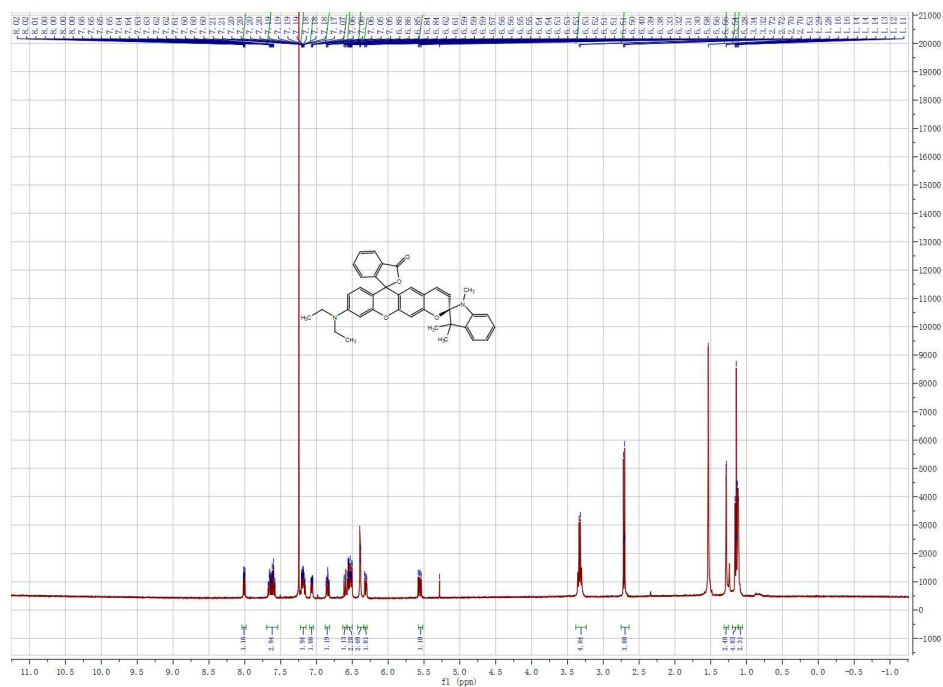
Figure S D.1. ^{1}H NMR spectrum of probe **A-3** in CDCl$_3$ solution.

299
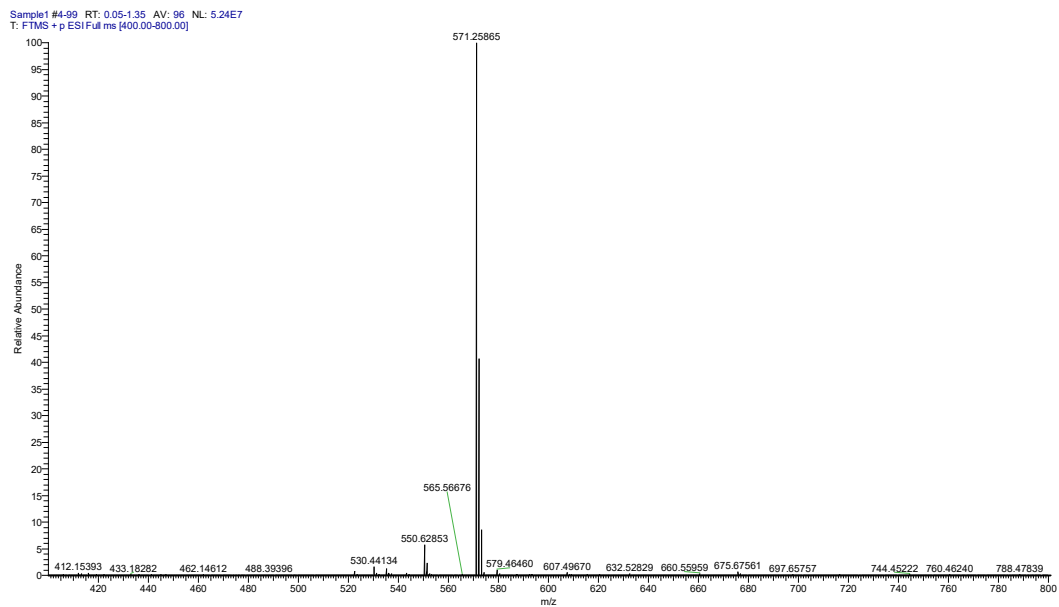
Figure S D.2. High-resolution mass spectrum of probe **A-3**

Figure S D.3. ^{13}C NMR spectrum of probe **A-3** in CDCl$_3$ solution.
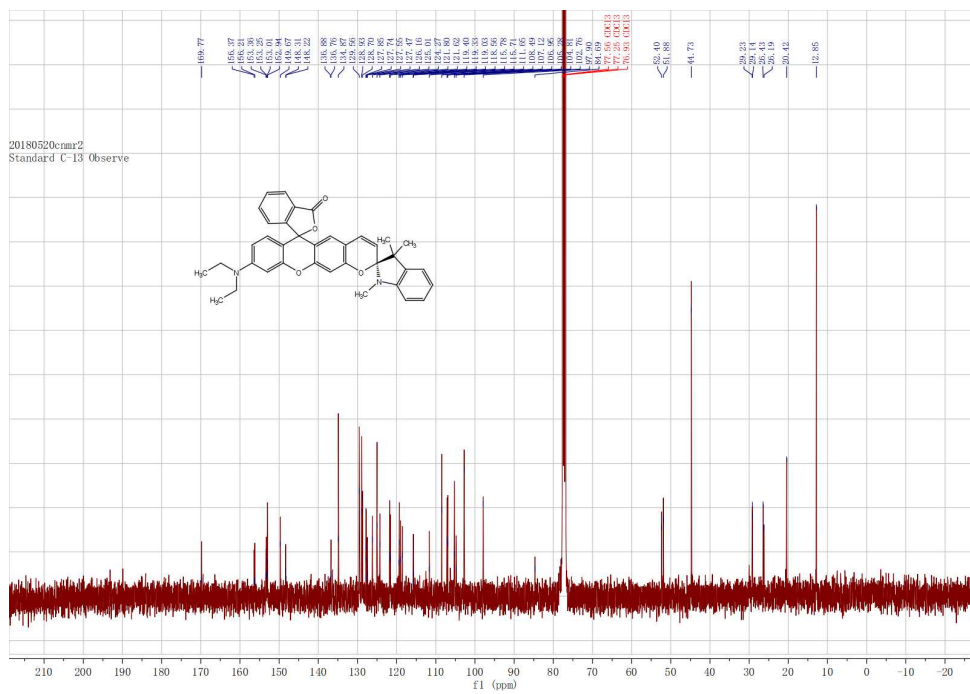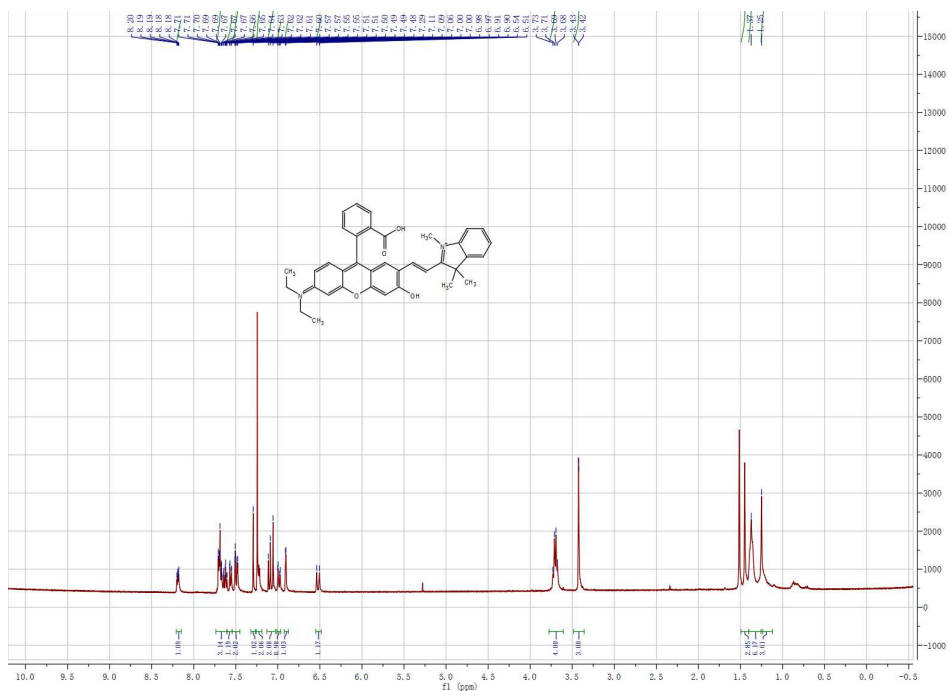
Figure S D.4. ^{1}H NMR spectrum of probe **A-1** in CDCl$_3$ and CF$_3$COOH solution
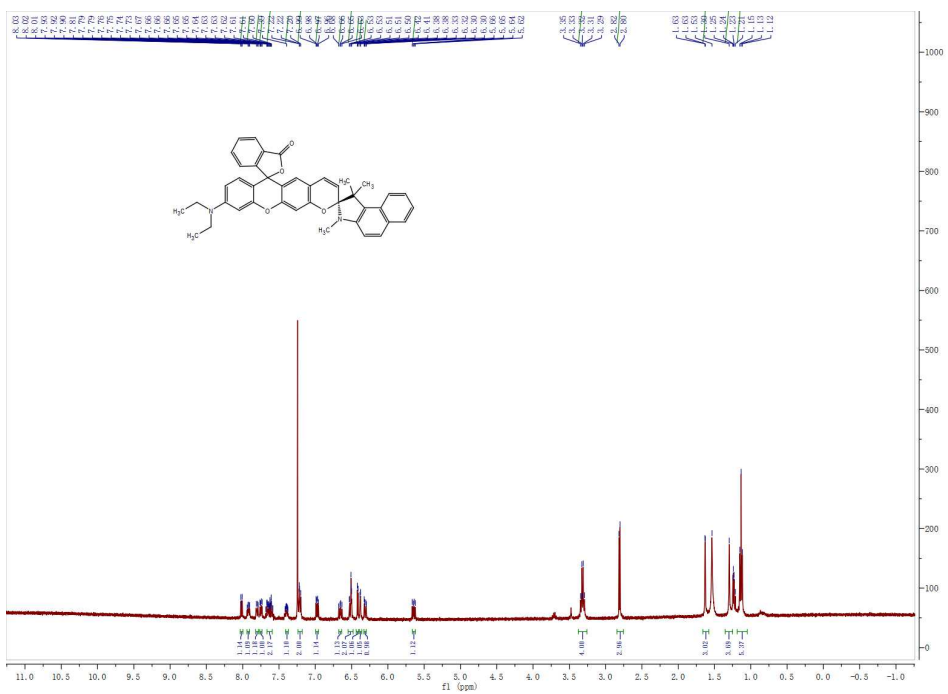
Figure S D.5. ^{1}H NMR spectrum of probe **B-3** in CDCl$_3$ solution

Figure S D.6. High-resolution mass spectrum of probe **B-3**.

Figure S D.7. ^{13}C NMR spectrum of probe **B-3** in CDCl$_3$ solution
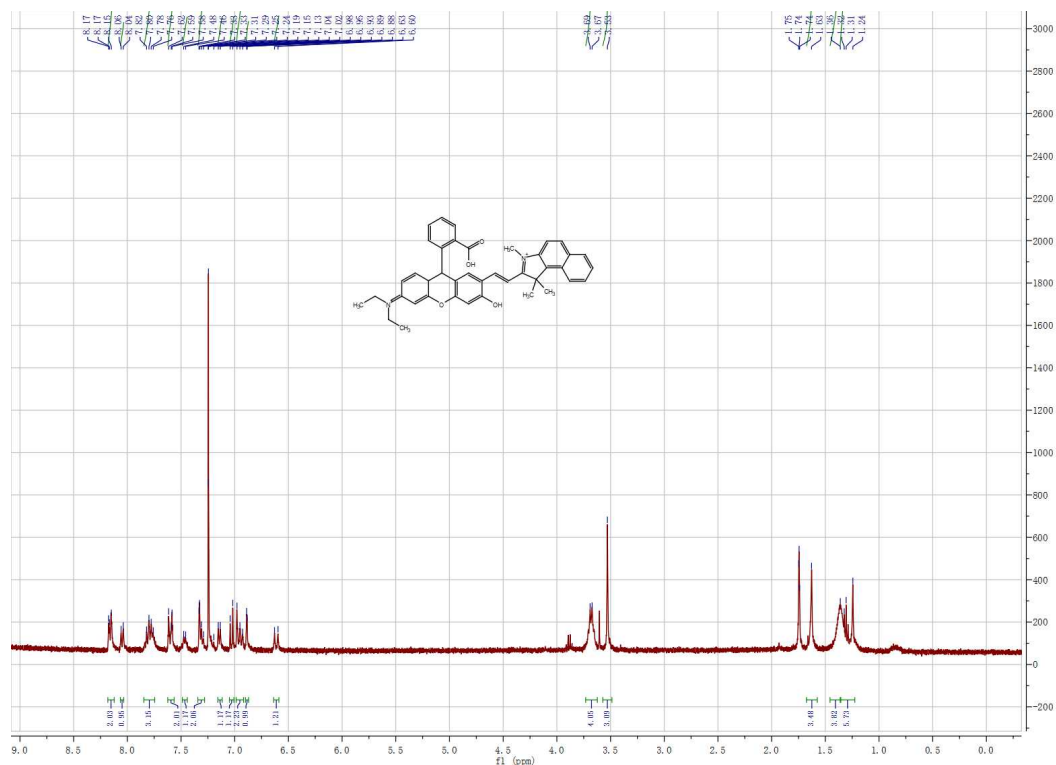
Figure S D.8. ^{1}HNMR spectrum of probe **B-1** in CDCl$_3$ and CF$_3$COOH solution

2. General information on the theoretical calculations

Chemdraw structures of probes **A**1-4 and **B**1-4, see below, were optimized initially with the MM2 functionality in Chem3D and then further with Avogadro. Optimization and frequency calculations were then conducted with the functional DFT/APFD and with basis sets at the 6-311+G(2d, p) level implemented using the Gaussian16 suite of programs. Imaginary frequencies were not obtained. The first six excited states were assessed on the basis of TD-DFT optimizations in a Polarizable Continuum Model (PCM) of water. Results were interpreted using GausView for all other data and figures. The diagrams and listings

of atomic positions from the calculations are listed sequentially for dyes A1-4 and B1-4

below and all data are within the PCM matrix of water.

Probe A-1   + OH⁻ / + H⁺   **Probe A-2**

Probe A-3   UV light / Heat   **Probe A-4**

Probe B-1   + OH⁻ / + H⁺   **Probe B-2**

Probe B-3   UV light / Heat   **Probe B-4**
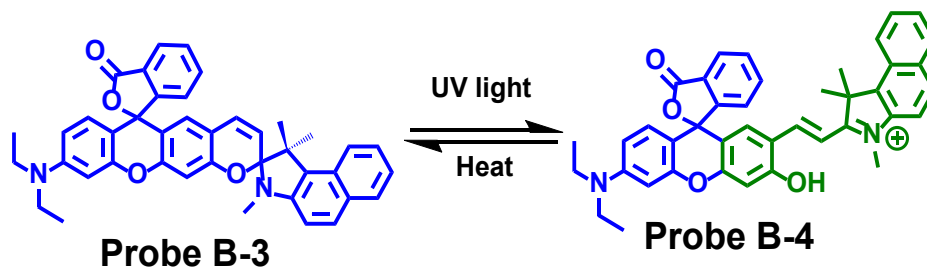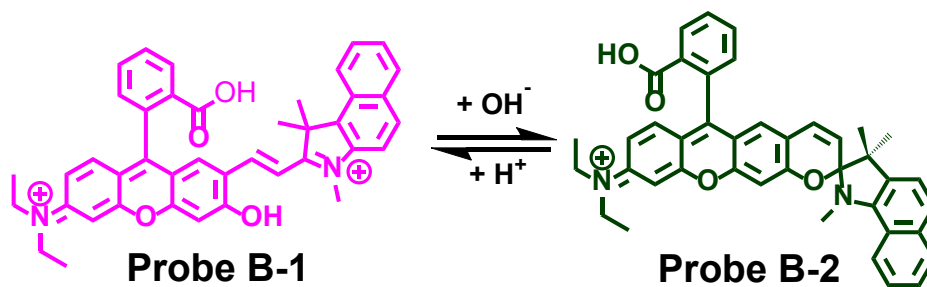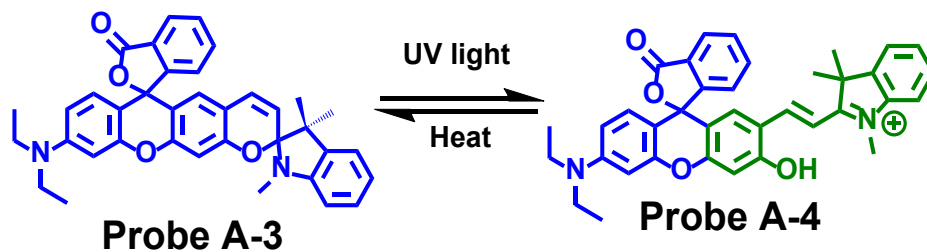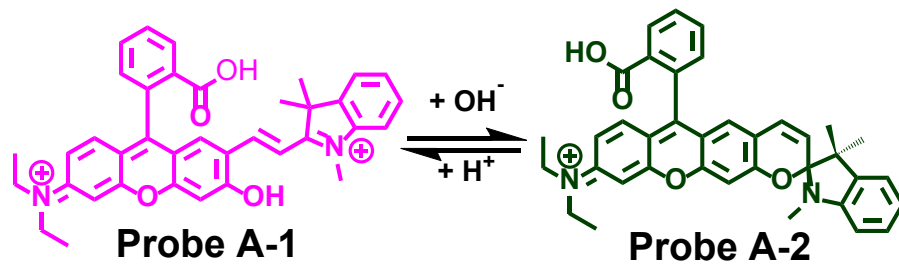
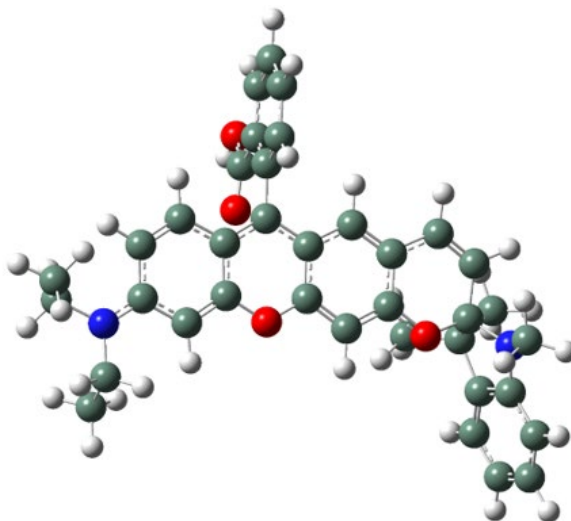## 2.1 Computation chemistry results of probe A1
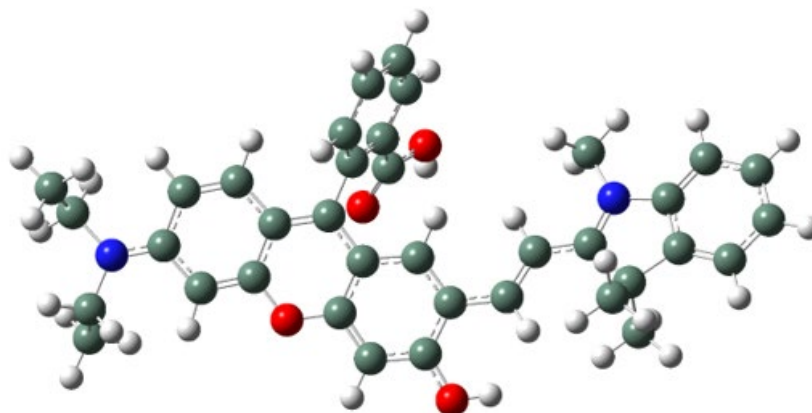
Figure S D.9. GaussView representation of probe **A-1**.

Table S D.1. Computa tional results for probe **A-1**.

rho3 (Optimization completed)		
/home/rluck/calculation/liu/rho/rho31.log		
File Type	.log	
Calculation Type	FREQ	
Calculation Method	RAPFD	
Basis Set	6-311+G(2d,p)	
Charge	2	
Spin	Singlet	
Solvation	scrf=solvent=water	
E(RAPFD)	-1840.787304	Hartree
RMS Gradient Norm	0.000001	Hartree/Bohr
Imaginary Freq	0	
Dipole Moment	4.002806	Debye
Polarizability (α)	876.781544	a.u.
Point Group	C1	
Job cpu time:	11 days 6 hours 11 minutes 2...	

Table S D.2. Calculated atomic coordinates for probe **A-1**.

Row	Symbol	X	Y	Z
1	C	1.923128	0.465063	-0.22397
2	C	3.292598	0.299713	-0.22652
3	C	3.842901	-1.013	-0.11155
4	O	3.037076	-2.09486	0.004049
5	C	1.69939	-1.95534	-0.00245
6	C	1.09427	-0.6869	-0.12684
7	C	0.952258	-3.10783	0.115768
8	C	-0.43193	-3.02597	0.117533
9	C	-1.08988	-1.76674	-0.01914
10	C	-0.29629	-0.6354	-0.14625
11	C	4.225938	1.373214	-0.30181
12	C	5.560959	1.157085	-0.28404
13	C	6.099165	-0.17442	-0.18842
14	C	5.185103	-1.25349	-0.09523
15	N	7.416342	-0.38031	-0.18703
16	C	8.386579	0.71328	-0.19284
17	C	8.745949	1.160878	-1.60165
18	C	8.181853	-2.2662	1.227941
19	C	7.991238	-1.72328	-0.18088
20	O	-0.13395	2.561225	2.851062
21	C	0.692018	1.926779	2.011816
22	C	0.661415	2.482585	0.638217
23	C	1.303186	1.79585	-0.40261
24	C	0.035381	3.699648	0.377114
25	C	0.04632	4.237908	-0.90043
26	C	0.686885	3.560497	-1.92877
27	C	1.311451	2.344878	-1.68031
28	O	1.388876	0.996277	2.35051
29	O	-1.0754	-4.18795	0.261476
30	C	-2.52905	-1.66854	-0.06444
31	C	-3.21945	-0.52378	0.148977
32	C	-4.62449	-0.38084	0.016179
33	N	-5.21058	0.782242	0.232091
34	C	-6.60321	0.705031	0.026032
35	C	-6.91453	-0.59432	-0.34592
36	C	-5.65708	-1.41692	-0.37439
37	C	-7.55559	1.701563	0.151626
38	C	-8.87183	1.344155	-0.11786
39	C	-9.20358	0.043956	-0.49487
40	C	-8.22422	-0.94013	-0.61168
41	C	-5.40495	-1.9668	-1.78717
42	C	-5.73997	-2.53802	0.675136
43	C	-4.53046	2.005997	0.630448
44	H	1.438391	-4.06967	0.220841
45	H	-0.76611	0.327461	-0.30136

| 46	H	3.843726	2.384241	-0.37824	63	H	1.800299	1.807529	-2.48544
47	H	6.228062	2.003905	-0.35802	64	H	-2.02782	-4.07554	0.346987
48	H	5.517573	-2.27572	0.013188	65	H	-3.08643	-2.56724	-0.3038
49	H	8.004105	1.539671	0.405989	66	H	-2.67138	0.363824	0.440218
50	H	9.271614	0.346616	0.330322	67	H	-7.30772	2.71394	0.445271
51	H	9.498838	1.950933	-1.56012	68	H	-9.65097	2.093188	-0.03199
52	H	9.155087	0.33159	-2.18333	69	H	-10.2392	-0.20426	-0.69951
53	H	7.871433	1.546996	-2.13004	70	H	-8.48991	-1.95012	-0.90489
54	H	8.638353	-3.25737	1.184959	71	H	-4.49499	-2.56524	-1.83587
55	H	8.83655	-1.61542	1.812102	72	H	-6.24378	-2.60404	-2.07207
56	H	7.228657	-2.35005	1.754449	73	H	-5.32608	-1.15631	-2.5137
57	H	7.365979	-2.38269	-0.78383	74	H	-4.83319	-3.14082	0.697233
58	H	8.94991	-1.65677	-0.69844	75	H	-5.90857	-2.12865	1.672538
59	H	-0.03782	2.153358	3.724784	76	H	-6.57549	-3.19387	0.425701
60	H	-0.45117	4.228067	1.187387	77	H	-4.06453	1.86951	1.605686
61	H	-0.44104	5.187416	-1.09108	78	H	-3.77878	2.270368	-0.1122
62	H	0.701322	3.974696	-2.93097	79	H	-5.25704	2.808368	0.694359
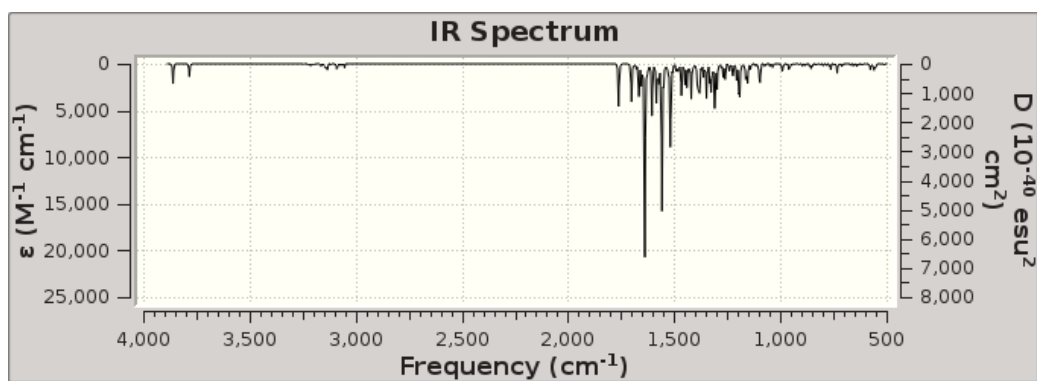
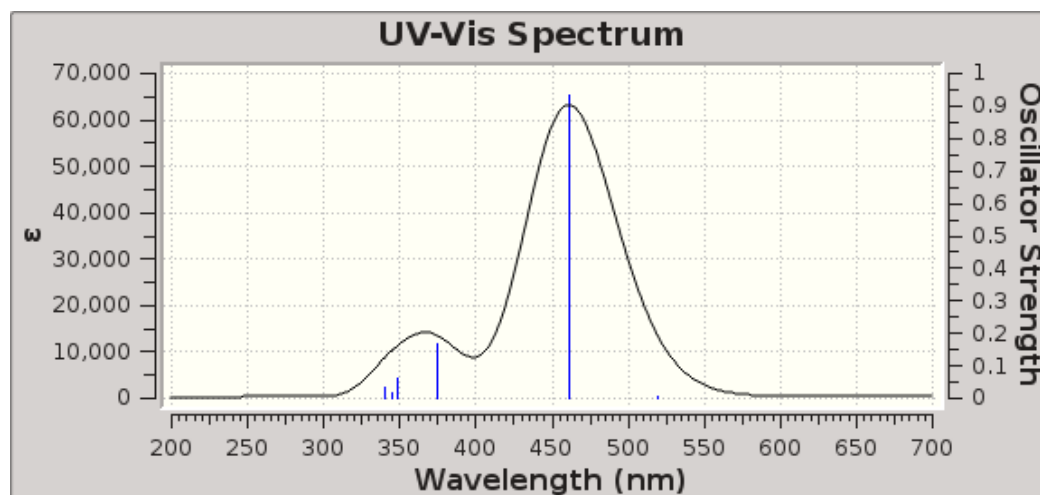**Figure S D.10**. Calculated IR spectrum for probe **A-1**.
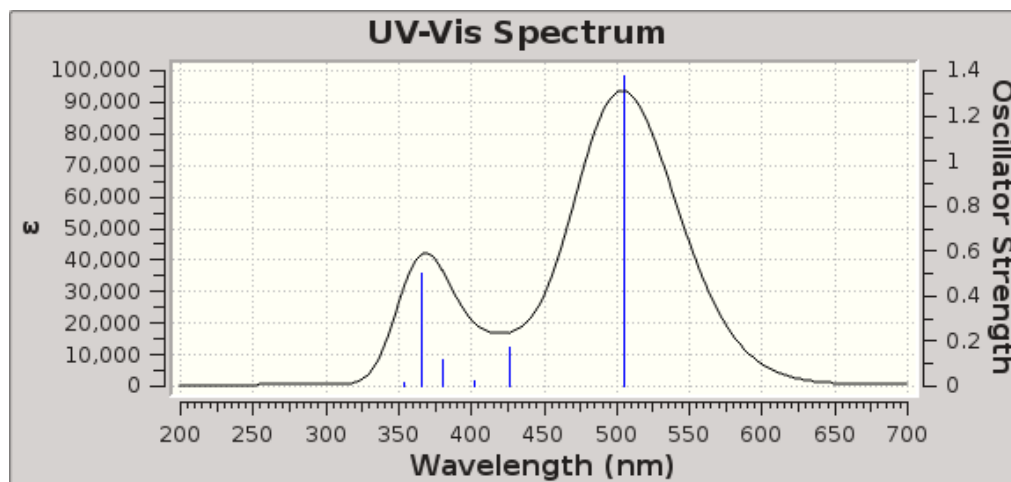
Figure S D.11. Calculated UV-Vis absorption spectrum for probe **A-1**.

Table S D.3. Excitation energies and oscillator strengths listing for probe **A-1**.

Excited State   1:   Singlet-A   2.4566 eV 504.70 nm f=1.3772 <S**2>=0.000

     151 -> 152   0.69276

This state for optimization and/or second-order correction.

Total Energy, E(TD-HF/TD-DFT) = -1840.69702978

Copying the excited state density for this state as the 1-particle RhoCI density.

Excited State   2:   Singlet-A   2.9061 eV 426.63 nm f=0.1695 <S**2>=0.000

     150 -> 152   -0.27211

     151 -> 153   0.64452

Excited State   3:   Singlet-A   3.0873 eV 401.59 nm f=0.0216 <S**2>=0.000

     149 -> 152   0.23264

     150 -> 152   0.59607

     151 -> 153   0.26470

Excited State   4:   Singlet-A   3.2615 eV 380.14 nm f=0.1162 <S**2>=0.000

     149 -> 152   0.61496

     149 -> 153   -0.14910

     150 -> 152   -0.18509

     150 -> 153   -0.22728

Excited State   5:   Singlet-A   3.3839 eV 366.39 nm f=0.5041 <S**2>=0.000

     149 -> 152   0.21349

     149 -> 153   0.11701

     150 -> 152   -0.12624

150 -> 153   0.63355

Excited State   6:   Singlet-A   3.5071 eV 353.53 nm f=0.0146 <S**2>=0.000

147 -> 152   0.21718

148 -> 152   0.63277

148 -> 153   0.16463
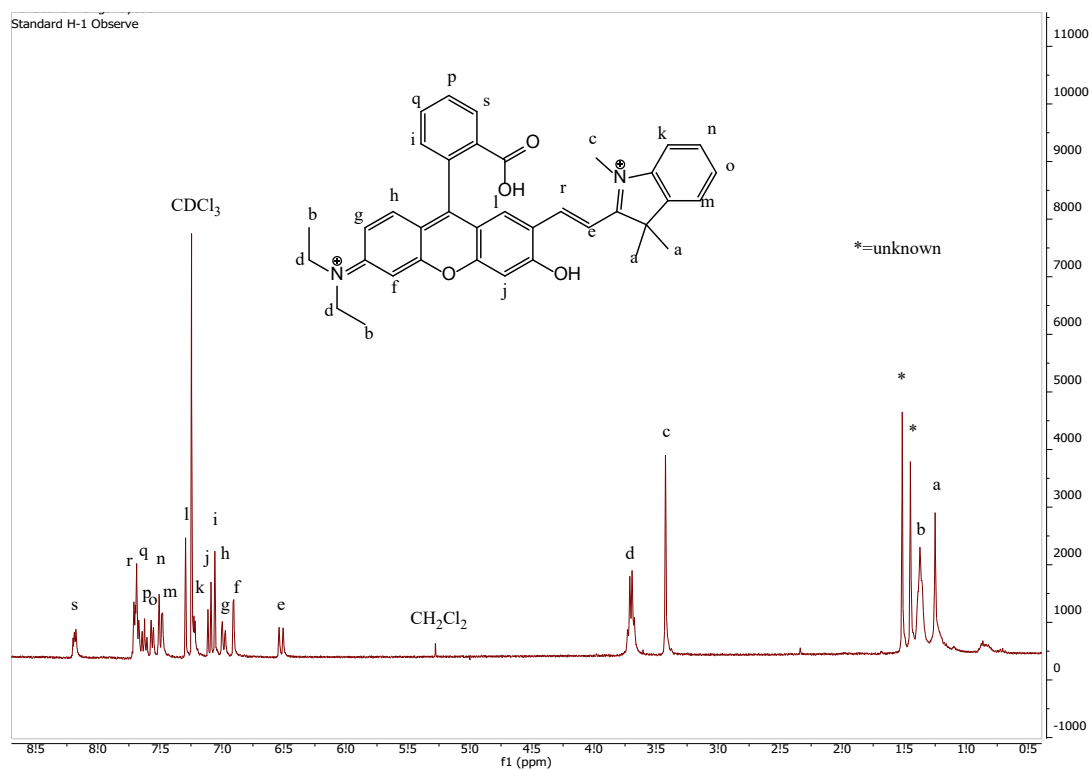
Figure S D.12. ^{1}H NMR spectrum of probe **A-1** in CDCl$_3$ with added CF$_3$COOH. The assignments are based on comparison to the calculated spectrum, Fig. S3, intensity of the peaks and the coupling patterns.
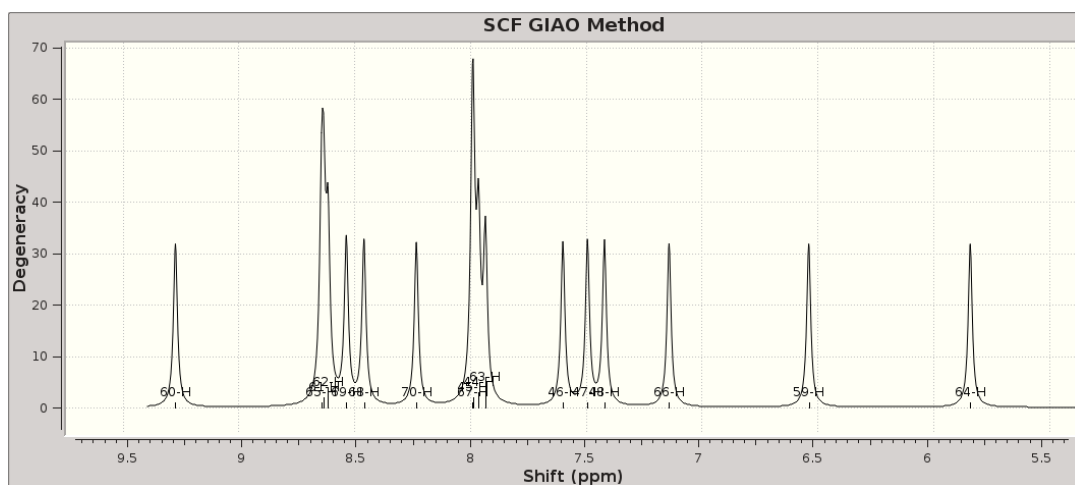
Figure S D.13. Calculated ^{1}H NMR spectrum of probe **A-1**.
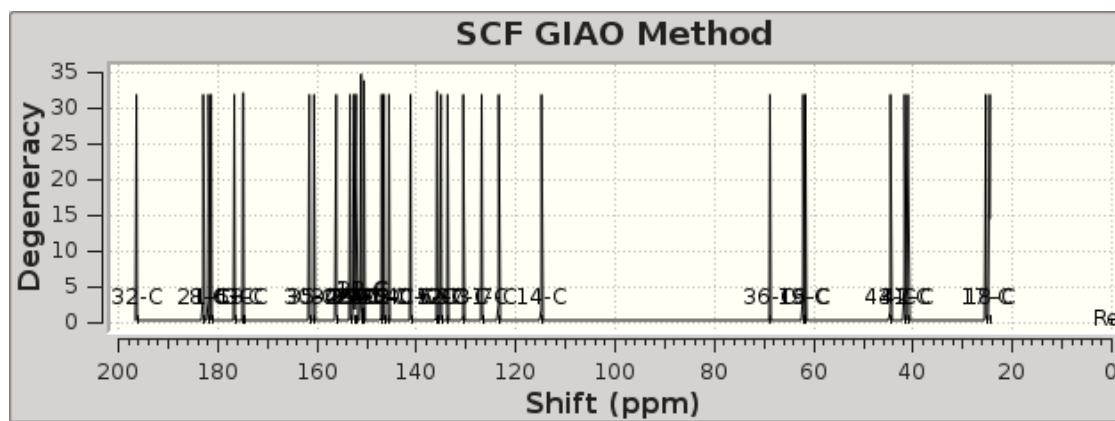
Figure S D.14. Calculated ^{13}C NMR spectrum of probe **A-1**.

2.2 Computation chemistry results for probe A-2

Figure S D.15. GaussView representation of probe **A-2**.

Table S D.4. Computational results for probe **A-2**.

rho4 (Optimization completed)		
/home/rluck/calculation/liu/rho/rho41.log		
File Type	.log	
Calculation Type	FREQ	
Calculation Method	RAPFD	
Basis Set	6-311+G(2d,p)	
Charge	1	
Spin	Singlet	
Solvation	scrf=solvent=water	
E(RAPFD)	-1840.353812	Hartree
RMS Gradient Norm	0.000002	Hartree/Bohr
Imaginary Freq		
Dipole Moment	14.479034	Debye
Point Group	C1	
Job cpu time:	11 days 12 hours 33 minutes ...	

Table S D.5. Calculated atomic coordinates for probe **A-2**.

Row	Symbol	X	Y	Z
1	C	2.041823	1.136871	-0.3738
2	C	2.998616	0.137601	-0.28735
3	C	2.585119	-1.22358	-0.26819
4	O	1.275026	-1.54691	-0.33968
5	C	0.333085	-0.58632	-0.43819
6	C	0.678343	0.782498	-0.46924
7	C	-0.97876	-1.01413	-0.49385
8	C	-1.98327	-0.06276	-0.57075
9	C	-1.68028	1.323325	-0.63043
10	C	-0.36631	1.718286	-0.5799
11	C	4.395264	0.37636	-0.18164
12	C	5.28481	-0.64054	-0.07388
13	C	4.852441	-2.01107	-0.06263
14	C	3.465777	-2.26558	-0.16305
15	N	5.739385	-3.00848	0.038394
16	C	5.338034	-4.40877	-0.04226
17	C	4.942136	-4.9816	1.311301
18	C	7.925317	-2.62148	-1.06743
19	C	7.166302	-2.77537	0.242226
20	O	2.002818	3.847538	2.929205
21	C	2.052119	2.896786	1.987805
22	C	2.432406	3.420272	0.65451
23	C	2.441887	2.560522	-0.45188
24	C	2.799915	4.755563	0.49115

Row	Symbol	X	Y	Z
25	C	3.173631	5.237143	-0.75323
26	C	3.183634	4.383482	-1.84825
27	C	2.819382	3.051946	-1.69676
28	O	1.810039	1.733008	2.21853
29	O	-3.23436	-0.50763	-0.62384
30	C	-2.78766	2.239582	-0.79423
31	C	-4.04598	1.805611	-0.74408
32	C	-4.39641	0.389079	-0.43631
33	N	-5.43172	-0.13145	-1.27683
34	C	-6.0504	-1.17734	-0.59545
35	C	-5.78179	-1.08365	0.771389
36	C	-4.94485	0.147105	1.012333
37	C	-6.84186	-2.19439	-1.10638
38	C	-7.3727	-3.12068	-0.20535
39	C	-7.11297	-3.0341	1.156825
40	C	-6.30796	-2.00217	1.652539
41	C	-5.86816	1.299331	1.430338
42	C	-3.83451	-0.02034	2.038272
43	C	-5.2177	-0.19989	-2.70376
44	H	-1.21886	-2.06949	-0.45907
45	H	-0.12413	2.774153	-0.63203
46	H	4.747234	1.40142	-0.19347
47	H	6.338364	-0.40734	-0.01244
48	H	3.064278	-3.26839	-0.13557
49	H	4.530543	-4.5084	-0.76913

50	H	6.186299	-4.9578	-0.45585					
51	H	4.670668	-6.03446	1.206999	65	H	-4.88278	2.478199	-0.88752
52	H	5.770102	-4.91288	2.020853	66	H	-7.03968	-2.28028	-2.16904
53	H	4.088285	-4.44768	1.734144	67	H	-7.99205	-3.92823	-0.58315
54	H	8.990801	-2.48479	-0.86926	68	H	-7.52948	-3.77031	1.836037
55	H	7.807385	-3.50909	-1.69355	69	H	-6.09867	-1.93109	2.715831
56	H	7.567846	-1.75805	-1.63307	70	H	-5.3031	2.222707	1.582059
57	H	7.303286	-1.90745	0.887852	71	H	-6.3563	1.039897	2.371979
58	H	7.546261	-3.63022	0.805334	72	H	-6.64396	1.480927	0.683202
59	H	1.75864	3.421207	3.764287	73	H	-4.26799	-0.12865	3.035115
60	H	2.795424	5.413795	1.350814	74	H	-3.22233	-0.89981	1.837837
61	H	3.458973	6.276883	-0.86734	75	H	-3.18866	0.862486	2.055779
62	H	3.475574	4.751472	-2.82588	76	H	-4.72136	0.713469	-3.03267
63	H	2.822829	2.383812	-2.55099	77	H	-4.60063	-1.0595	-2.99011
64	H	-2.56754	3.286196	-0.97833	78	H	-6.17801	-0.26701	-3.21683
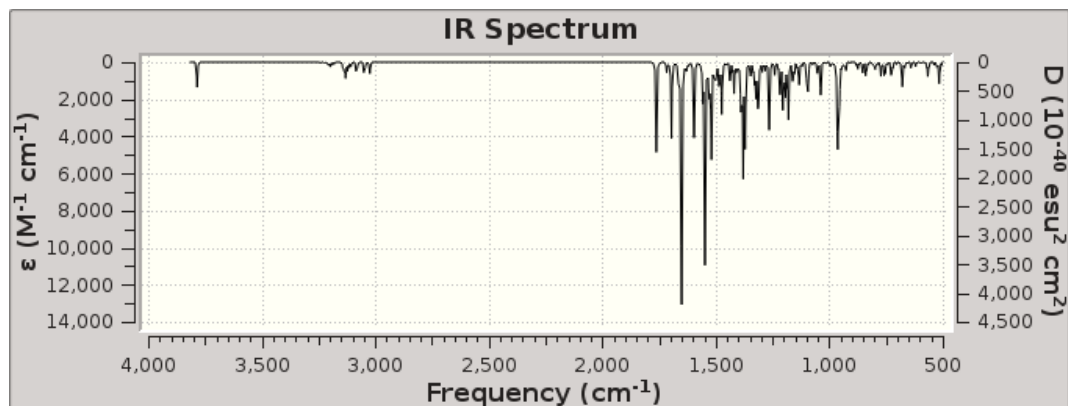
Figure S D.16. Calculated IR spectrum for probe **A-2**.

Figure S D.17. Calculated UV-Vis absorption spectrum for probe **A-2**.

315

Table S D.6. Excitation energies and oscillator strengths listing for probe **A-2**.

Excited State   1:   Singlet-A   2.3885 eV 519.10 nm f=0.0031 <S**2>=0.000

   151 -> 152   0.70575

This state for optimization and/or second-order correction.

Total Energy, E(TD-HF/TD-DFT) = -1840.26604005

Copying the excited state density for this state as the 1-particle RhoCI density.

Excited State   2:   Singlet-A   2.6866 eV 461.49 nm f=0.9322 <S**2>=0.000

   150 -> 152   0.69615

Excited State   3:   Singlet-A   3.3124 eV 374.30 nm f=0.1665 <S**2>=0.000

   147 -> 152   0.23665

   148 -> 152   0.33878

   149 -> 152   0.55277

Excited State   4:   Singlet-A   3.5564 eV 348.62 nm f=0.0598 <S**2>=0.000

   147 -> 152   0.31896

   148 -> 152   0.42841

   149 -> 152   -0.38572

   151 -> 153   -0.14333

   151 -> 154   -0.14975

Excited State   5:   Singlet-A   3.5928 eV 345.09 nm f=0.0154 <S**2>=0.000

    148 -> 152   0.14826

    149 -> 152   -0.12382

    151 -> 153   0.54869

    151 -> 154   0.37738

Excited State   6:   Singlet-A   3.6394 eV 340.67 nm f=0.0314 <S**2>=0.000

    150 -> 153   0.69406

    151 -> 154   -0.10270

2.3 Computation chemistry results for probe A-3
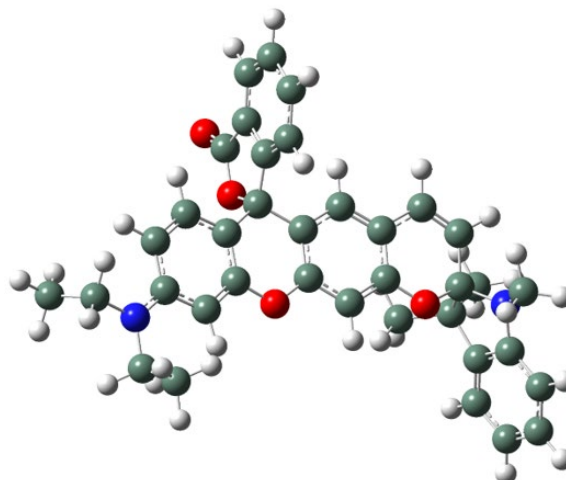
Figure S D.18. GaussView representation of probe **A-3**.

Table S D.7. Computational results for probe **A-3**.

rho1 (Optimization completed)		
/home/rluck/calculation/liu/rho/rho11.log		
File Type	.log	
Calculation Type	FREQ	
Calculation Method	RAPFD	
Basis Set	6-311+G(2d,p)	
Charge	0	
Spin	Singlet	
Solvation	scrf=solvent=water	
E(RAPFD)	-1839.905461	Hartree
RMS Gradient Norm	0.000005	Hartree/Bohr
Imaginary Freq	0	
Dipole Moment	8.463563	Debye
Polarizability (α)	671.816224	a.u.
Point Group	C1	
Job cpu time:	11 days 0 hours 16 minutes 4...	

Table S D.8. Calculated atomic coordinates for probe **A-3**

Row	Symbol	X	Y	Z	Row	Symbol	X	Y	Z
					25	C	-3.19522	4.996703	1.512049
Row	Symbol	X	Y	Z					
1	C	-2.05066	1.319086	-0.27765	26	C	-2.93463	3.926243	2.374992
2	C	-3.01022	0.1849	-0.13844	27	C	-2.55382	2.681015	1.888393
3	C	-2.57248	-1.13294	-0.07017	28	O	-2.12417	1.836892	-1.68181
4	O	-1.24712	-1.47043	-0.04101	29	O	3.2551	-0.4249	0.493126
5	C	-0.32106	-0.47972	0.04555	30	C	2.812834	2.326935	0.426861
6	C	-0.64226	0.874165	-0.02569	31	C	4.069354	1.884965	0.479413
7	C	0.991646	-0.9082	0.21392	32	C	4.416741	0.444421	0.285102
8	C	2.001662	0.029413	0.30442	33	N	5.420914	-0.01357	1.209374
9	C	1.711464	1.405327	0.254249	34	C	6.064862	-1.10386	0.634293
10	C	0.394222	1.796539	0.09149	35	C	5.860175	-1.10846	-0.7478
11	C	-4.39267	0.385375	-0.13819	36	C	5.040022	0.102533	-1.11323
12	C	-5.28901	-0.65578	-0.08152	37	C	6.829185	-2.08328	1.251321
13	C	-4.83645	-1.99836	-0.01361	38	C	7.398023	-3.07175	0.444219
14	C	-3.44673	-2.20479	-0.00376	39	C	7.201092	-3.08319	-0.93104
15	N	-5.71097	-3.04193	0.044175	40	C	6.422569	-2.08865	-1.53491
16	C	-5.25748	-4.41946	0.00262	41	C	5.987668	1.220797	-1.56658
17	C	-4.91507	-4.98243	1.377081	42	C	3.982471	-0.13797	-2.17955
18	C	-7.8424	-2.69691	-1.18632	43	C	5.13679	0.013305	2.624609
19	C	-7.14333	-2.83758	0.160406	44	H	1.21493	-1.96725	0.265948
20	O	-2.61286	3.744212	-2.75043	45	H	0.164696	2.857532	0.055068
21	C	-2.49278	3.132858	-1.71438	46	H	-4.773	1.400827	-0.19741
22	C	-2.69715	3.59162	-0.33198	47	H	-6.34716	-0.43326	-0.10604
23	C	-2.44011	2.535374	0.517006	48	H	-3.01648	-3.1936	0.079428
24	C	-3.07884	4.84036	0.139004	49	H	-6.05369	-5.01144	-0.45661

50	H	-4.40272	-4.49777	-0.67419					
51	H	-4.1138	-4.41025	1.850711					
52	H	-5.78659	-4.94988	2.036268					
53	H	-4.59008	-6.02315	1.296425					
54	H	-8.91884	-2.56356	-1.04898	66	H	7.996789	-3.85025	0.906992
55	H	-7.45966	-1.83733	-1.74174	67	H	7.645531	-3.86621	-1.53629
56	H	-7.68712	-3.58938	-1.79835	68	H	6.261939	-2.09434	-2.60909
57	H	-7.55055	-3.69313	0.705938	69	H	5.434298	2.133031	-1.8046
58	H	-7.33588	-1.96663	0.791531	70	H	6.517662	0.89873	-2.46557
59	H	-3.27663	5.657288	-0.54626	71	H	6.728967	1.451978	-0.79823
60	H	-3.4907	5.955004	1.925033	72	H	4.463877	-0.33309	-3.14092
61	H	-3.03269	4.073338	3.445528	73	H	3.347605	-0.99041	-1.93713
62	H	-2.3535	1.853449	2.560315	74	H	3.350228	0.746341	-2.3008
63	H	2.592379	3.385202	0.529917	75	H	4.626585	0.946324	2.865687
64	H	4.903958	2.559403	0.627476	76	H	4.503725	-0.82504	2.938672
65	H	6.977975	-2.09373	2.325445	77	H	6.070193	-0.01818	3.188839
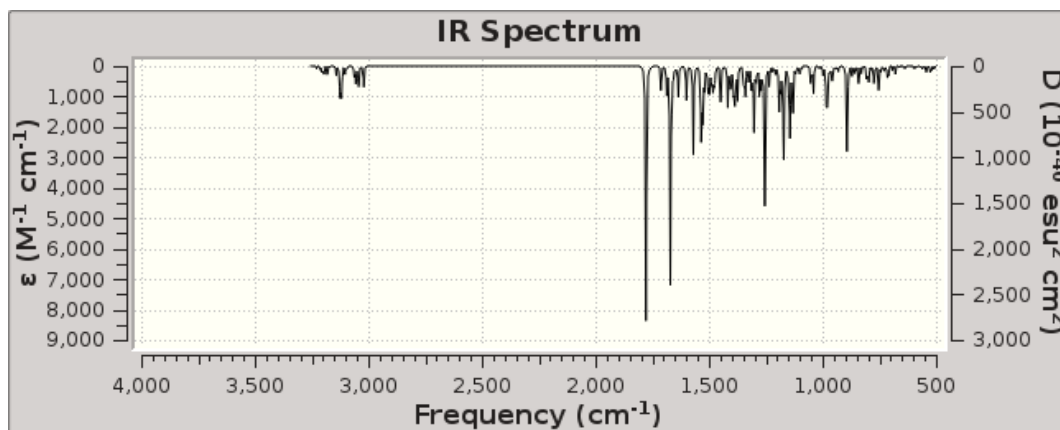
Figure S D.19. Calculated IR spectrum for probe **A-3**.
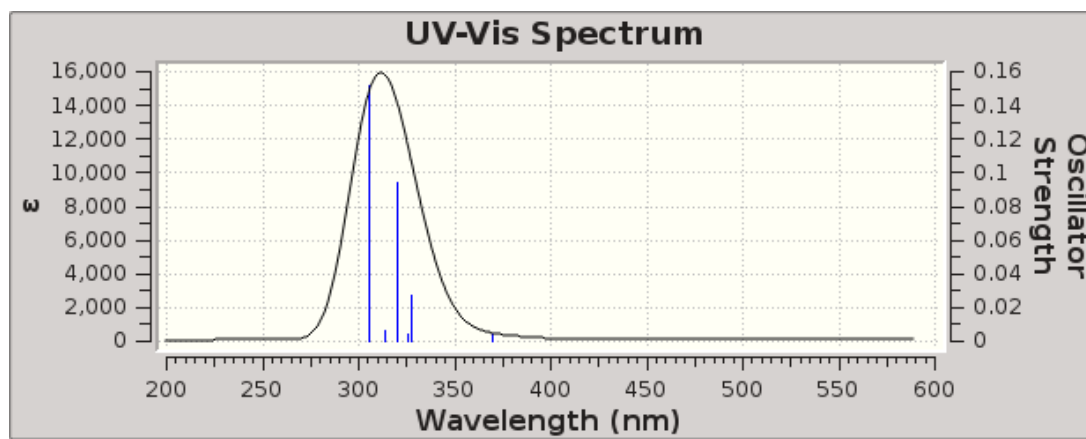
Figure S D.20. Calculated UV-Vis absorption spectrum for probe **A-3**.

Table S D.9. Excitation energies and oscillator strengths listing for probe **A-3**.

Excited State   1:   Singlet-A   3.3573 eV 369.30 nm f=0.0039 <S**2>=0.000

    151 -> 152   0.70135

This state for optimization and/or second-order correction.

Total Energy, E(TD-HF/TD-DFT) = -1839.78208145

Copying the excited state density for this state as the 1-particle RhoCI density.

Excited State   2:   Singlet-A   3.7855 eV 327.52 nm f=0.0269 <S**2>=0.000

    149 -> 152   0.62192

    150 -> 152   0.29049

    150 -> 153   0.13600

Excited State   3:   Singlet-A   3.8116 eV 325.28 nm f=0.0040 <S**2>=0.000

    149 -> 152   -0.30897

    150 -> 152   0.51527

    150 -> 153   0.35426

Excited State   4:   Singlet-A   3.8700 eV 320.37 nm f=0.0938 <S**2>=0.000

    151 -> 153   0.68809

Excited State   5:   Singlet-A   3.9541 eV 313.56 nm f=0.0066 <S**2>=0.000

   150 -> 152   -0.38325

   150 -> 153   0.58237

Excited State   6:   Singlet-A   4.0591 eV 305.45 nm f=0.1520 <S**2>=0.000

   151 -> 154   0.66700

   151 -> 155   0.14807

   151 -> 157   -0.10347
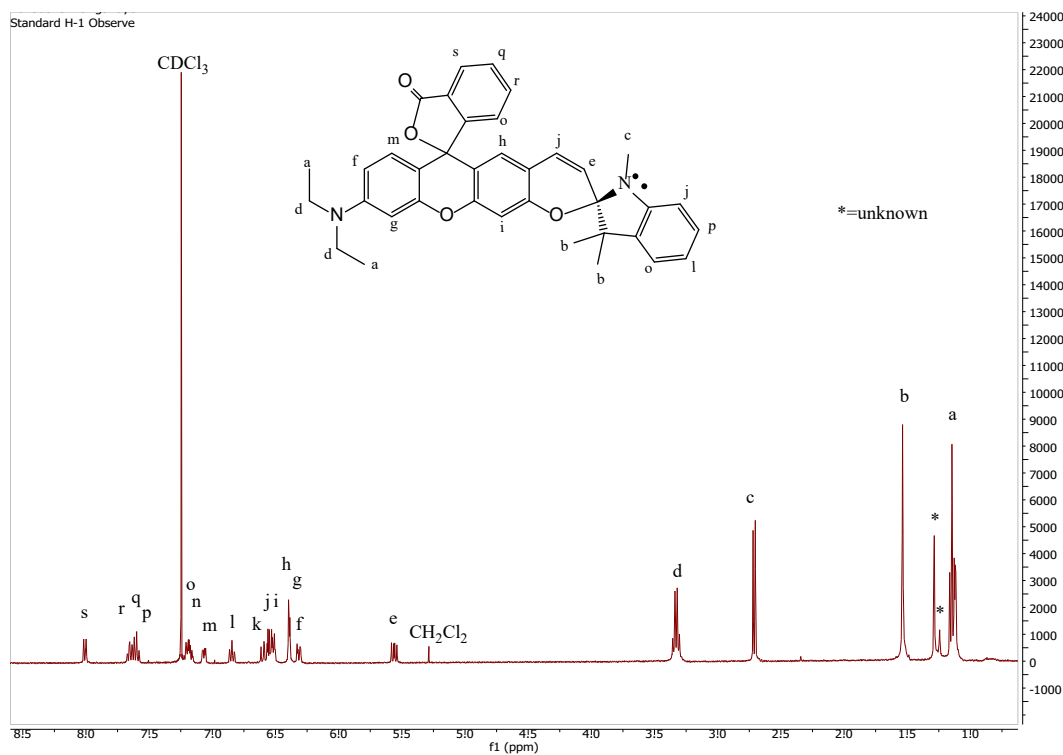
Figure S D.21. ^{1}H NMR spectrum of probe **A-3** in CDCl$_3$. The assignments are based on comparison to the calculated spectrum, Fig. S1, intensity of the peaks and the coupling patterns.
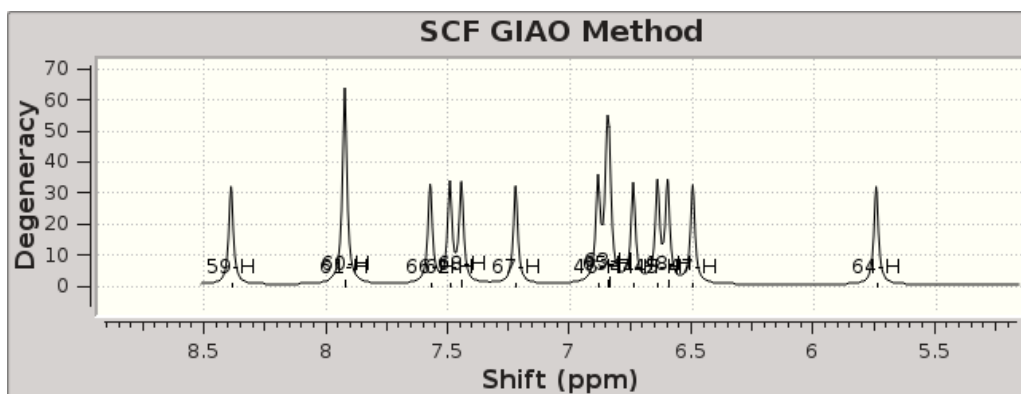
Figure S D.22. Calculated ^{1}H NMR spectrum of probe **A-3**.
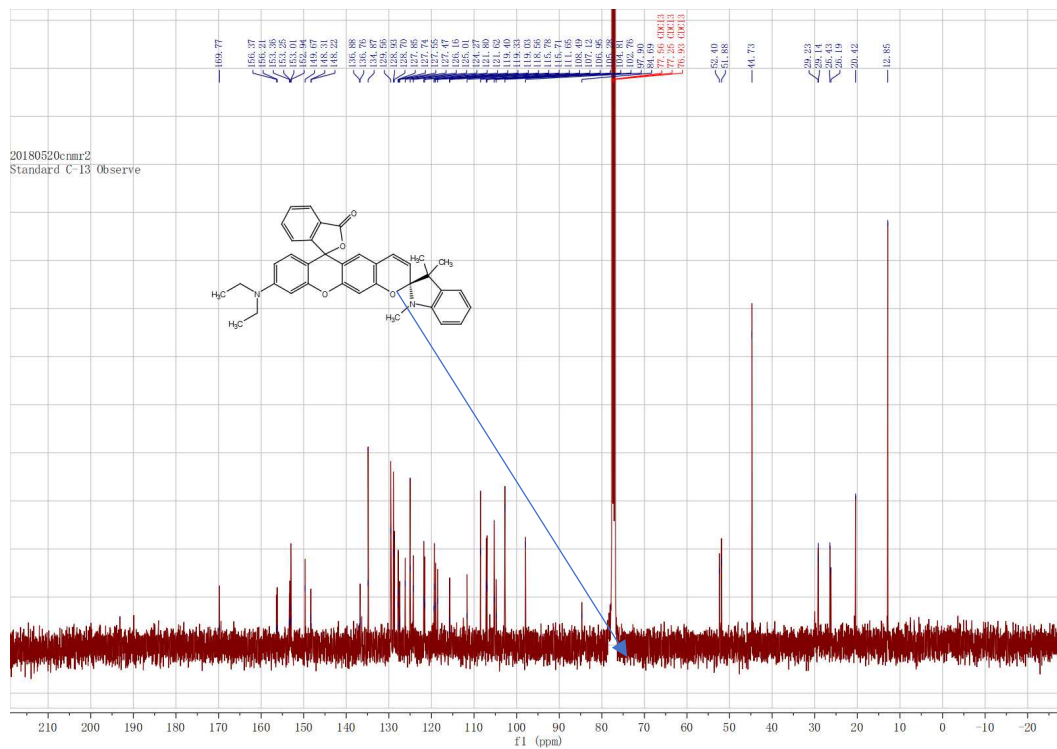
Figure S D.23. ^{13}C NMR spectrum of probe **A-3** in CDCl$_3$.
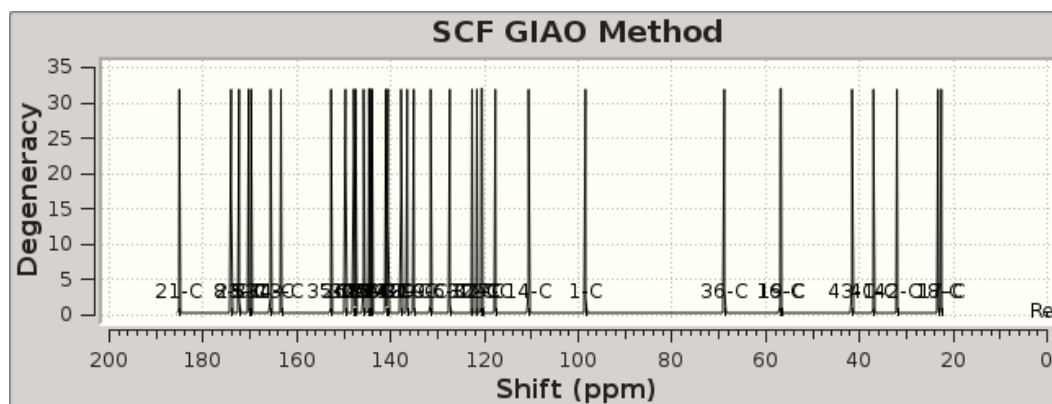
Figure S D.24. Calculated ^{13}C NMR spectrum of probe **A-3**. Note the resonance at 98 ppm.

2.4 Computation chemistry results for probe A-4
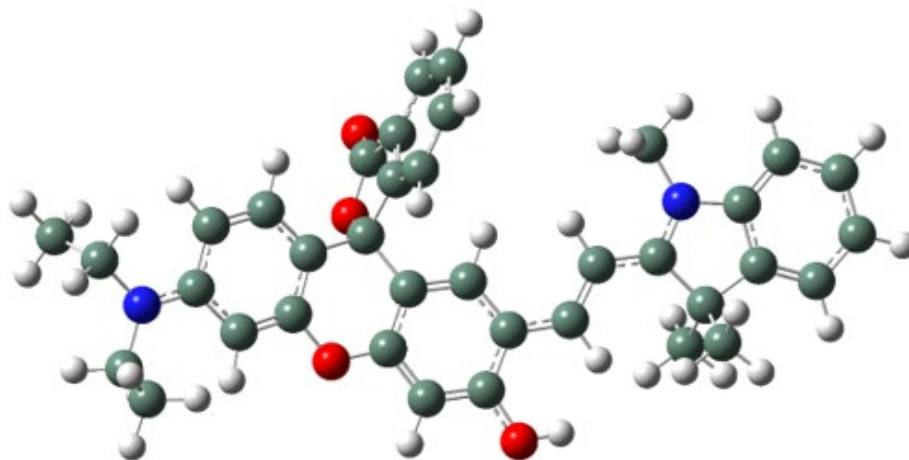
Figure S D.25. GaussView representation of probe **A-4**.

Table S D.10. Computational results for probe **A-4**.

rho2 (Optimization completed)		
/home/rluck/calculation/liu/rho/rho21.log		
File Type	.log	
Calculation Type	FREQ	
Calculation Method	RAPFD	
Basis Set	6-311+G(2d,p)	
Charge	1	
Spin	Singlet	
Solvation	scrf=solvent=water	
E(RAPFD)	-1840.346120	Hartree
RMS Gradient Norm	0.000002	Hartree/Bohr
Imaginary Freq	0	
Dipole Moment	17.633786	Debye
Polarizability (α)	779.110295	a.u.
Point Group	C1	
Job cpu time:	10 days 3 hours 23 minutes 4...	

Table S D.11. Calculated atomic coordinates for probe **A-4**.

Row	Symbol	X	Y	Z	Row	Symbol	X	Y	Z
					25	C	-1.24762	1.911156	1.80964
1	C	-1.86167	0.642709	-0.38582	26	O	1.200428	-4.09706	-0.11708
2	C	-3.30313	0.333729	-0.15969	27	C	2.60613	-1.52501	-0.0799
3	C	-3.77351	-0.97348	-0.167	28	C	3.308805	-0.36178	-0.00451
4	O	-2.93832	-2.0599	-0.2847	29	C	4.716505	-0.2827	0.040926
5	C	-1.60732	-1.8687	-0.252	30	N	5.335721	0.886203	0.121019
6	C	-1.01957	-0.59427	-0.25095	31	C	6.735641	0.730032	0.137925
7	C	-0.8317	-3.01586	-0.21135	32	C	7.023552	-0.6249	0.07062
8	C	0.547976	-2.92289	-0.15913	33	C	5.738489	-1.40379	0.008873
9	C	1.182843	-1.64953	-0.14045	34	C	7.717781	1.70276	0.207252
10	C	0.351127	-0.52083	-0.18978	35	C	9.037386	1.262346	0.207508
11	C	-4.26074	1.339009	-0.00885	36	C	9.345242	-0.09483	0.140866
12	C	-5.60209	1.064546	0.118584	37	C	8.335638	-1.05323	0.071551
13	C	-6.07448	-0.27275	0.106687	38	C	5.615411	-2.30759	1.246807
14	C	-5.11229	-1.28921	-0.03381	39	C	5.666442	-2.20407	-1.30094
15	N	-7.39843	-0.56179	0.230781	40	C	4.67544	2.179705	0.183381
16	C	-7.89803	-1.91914	0.108707	41	C	-1.15065	2.390152	-1.78946
17	C	-7.8904	-2.6828	1.427527	42	O	-1.69074	1.151651	-1.77712
18	C	-8.93203	1.113979	-0.77602	43	O	-0.92499	2.982696	-2.81691
19	C	-8.38797	0.468272	0.492317	44	H	-1.30692	-3.98924	-0.20971
20	C	-0.92351	2.808325	-0.39809	45	H	0.803264	0.463787	-0.192
21	C	-1.34538	1.792711	0.434616	46	H	-3.93481	2.37475	-0.00461
22	C	-0.38382	3.988518	0.094294	47	H	-6.29432	1.890131	0.212194
23	C	-0.2796	4.116692	1.471218	48	H	-5.37986	-2.33685	-0.01849
24	C	-0.70844	3.087808	2.317043	49	H	-8.91678	-1.85718	-0.28284

| 50	H	-7.32037	-2.44956	-0.65258					
51	H	-6.87872	-2.7647	1.831955	65	H	2.772114	0.577843	0.021353
52	H	-8.2856	-3.69256	1.288828	66	H	7.489727	2.760217	0.257439
53	H	-8.51013	-2.17565	2.171638	67	H	9.837538	1.99228	0.260043
54	H	-9.40018	0.365967	-1.42127	68	H	10.38339	-0.4083	0.142304
55	H	-8.13526	1.59838	-1.3455	69	H	8.580065	-2.10894	0.019036
56	H	-9.6843	1.868352	-0.53072	70	H	4.687059	-2.87864	1.247451
57	H	-9.20128	0.001238	1.05401	71	H	6.447053	-3.01428	1.252951
58	H	-7.96152	1.22021	1.160489	72	H	5.65819	-1.71823	2.164434
59	H	-0.05761	4.774626	-0.57762	73	H	4.742808	-2.77742	-1.38159
60	H	0.136824	5.021205	1.900755	74	H	5.73865	-1.54327	-2.16658
61	H	-0.61733	3.212668	3.390915	75	H	6.502298	-2.90511	-1.33311
62	H	-1.57786	1.115675	2.468704	76	H	4.124534	2.362485	-0.73918
63	H	2.154135	-3.98544	-0.06019	77	H	3.997742	2.210011	1.035959
64	H	3.187346	-2.43912	-0.0978	78	H	5.4252	2.954011	0.30552
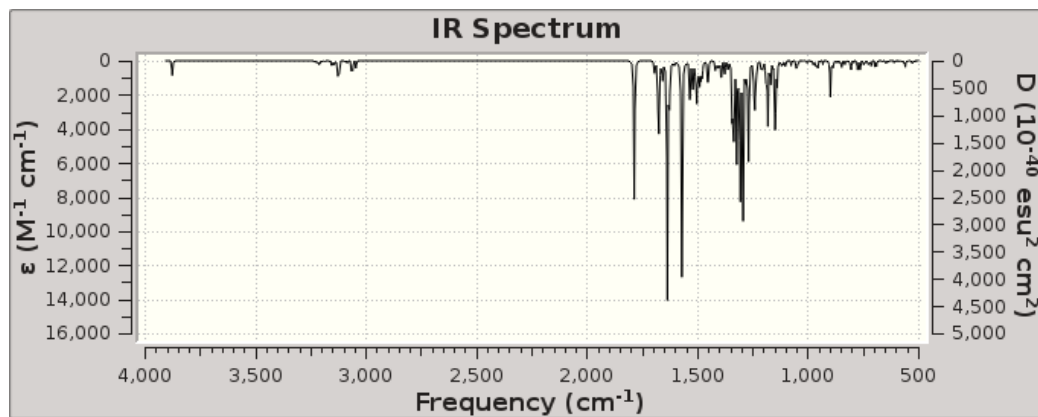
Figure S D.26. Calculated IR spectrum for probe **A-4**.
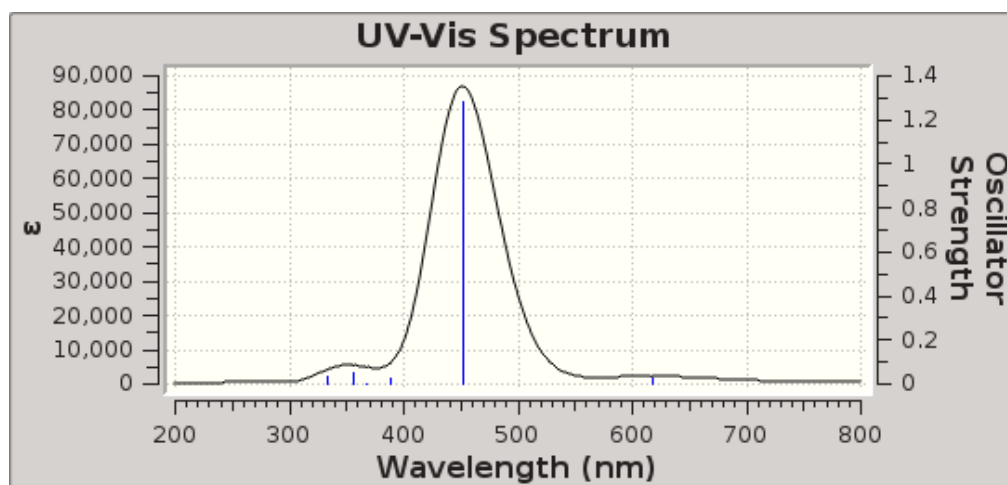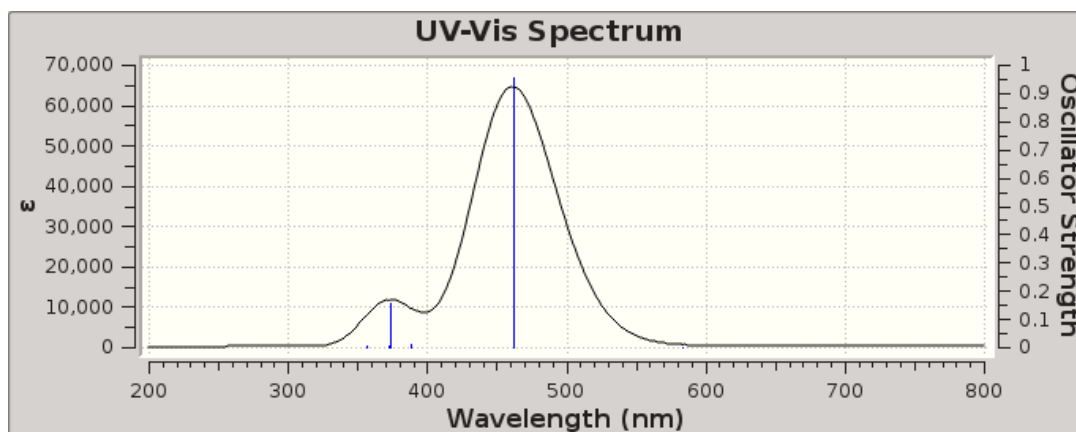

Figure S D.27. Calculated UV-Vis spectrum for probe **A-4**.

Table S D.12. Excitation energies and oscillator strengths listing for probe **A-4**.

Excited State   1:   Singlet-A   2.0073 eV 617.68 nm f=0.0270 <S**2>=0.000

   151 -> 152   0.70564

This state for optimization and/or second-order correction.

Total Energy, E(TD-HF/TD-DFT) = -1840.27235749

Copying the excited state density for this state as the 1-particle RhoCI density.

Excited State   2:   Singlet-A   2.7424 eV 452.10 nm f=1.2826 <S**2>=0.000

   150 -> 152   0.70360

Excited State   3:   Singlet-A   3.1876 eV 388.96 nm f=0.0286 <S**2>=0.000

   148 -> 152   0.27589

   149 -> 152   0.64134

Excited State   4:   Singlet-A   3.3705 eV 367.85 nm f=0.0027 <S**2>=0.000

   151 -> 153   0.70300

Excited State   5:   Singlet-A   3.4801 eV 356.27 nm f=0.0520 <S**2>=0.000

   148 -> 152   0.64083

   149 -> 152   -0.27457

Excited State   6:   Singlet-A   3.7134 eV 333.88 nm f=0.0350 <S**2>=0.000

   147 -> 152   0.69038

5 Computation chemistry results for probe B-1

Figure S D.28. GaussView representation of probe **B-1**.
Table S D.13. Computational results for probe **B-1**.

rho7 (Optimization completed)		
/home/rluck/calculation/liu/rho/rho71.log		
File Type	.log	
Calculation Type	FREQ	
Calculation Method	RAPFD	
Basis Set	6-311+G(2d,p)	
Charge	2	
Spin	Singlet	
Solvation	scrf=solvent=water	
E(RAPFD)	-1994.342891	Hartree
RMS Gradient Norm	0.000002	Hartree/Bohr
Imaginary Freq	0	
Dipole Moment	5.741626	Debye
Polarizability (α)	943.471828	a.u.
Point Group	C1	
Job cpu time:	14 days 4 hours 51 minutes 2...	

Table S D.14. Calculated atomic coordinates for probe **B-1**.

Row	Symbol	X	Y	Z		Row	Symbol	X	Y	Z
1	C	-2.70922	-0.40399	-0.45236		24	C	-0.37492	-3.38814	-0.49201
2	C	-4.0739	-0.34191	-0.24412		25	C	-0.69049	-3.94215	-1.72426
3	C	-4.6839	0.915668	0.051705		26	C	-1.67282	-3.35834	-2.51169
4	O	-3.9393	2.040477	0.155843		27	C	-2.3393	-2.22296	-2.0687
5	C	-2.60612	1.997811	-0.02137		28	O	-1.55654	-1.12528	1.997447
6	C	-1.94859	0.794328	-0.35021		29	O	0.055798	4.378296	0.188343
7	C	-1.9211	3.18557	0.132259		30	C	1.605342	1.992112	-0.48885
8	C	-0.54283	3.200591	-0.01667		31	C	2.347185	0.897184	-0.21771
9	C	0.163865	2.0101	-0.3495		32	C	3.763015	0.771094	-0.31911
10	C	-0.56708	0.85074	-0.53594		33	N	4.569235	1.394505	-1.14485
11	C	-4.94197	-1.47178	-0.26841		34	C	5.913384	1.027823	-0.90551
12	C	-6.27327	-1.35231	-0.0601		35	C	5.952022	0.095907	0.101705
13	C	-6.8762	-0.07147	0.19794		36	C	4.546072	-0.16891	0.562241
14	C	-6.02451	1.058431	0.260254		37	C	7.046613	1.518593	-1.56795
15	N	-8.19283	0.041538	0.377503		38	C	8.256174	1.013785	-1.17382
16	C	-9.0886	-1.11345	0.402779		39	C	8.361463	0.043878	-0.14549
17	C	-9.58587	-1.49031	-0.9847		40	C	7.188492	-0.43462	0.520145
18	C	-8.8863	1.761047	2.02168		41	C	4.315915	0.206256	2.035663
19	C	-8.84099	1.337675	0.560651		42	C	4.10097	-1.61548	0.269749
20	O	0.515341	-1.93163	1.687235		43	C	4.199271	2.283027	-2.23195
21	C	-0.7526	-1.71267	1.312222		44	C	9.623019	-0.4611	0.240344
22	C	-1.047	-2.25878	-0.03514		45	C	9.730108	-1.39588	1.236806
23	C	-2.03864	-1.66407	-0.83019		46	C	8.574997	-1.86605	1.89353
						47	C	7.334459	-1.39841	1.546179

48	H	-2.44993	4.093987	0.392402	67	H	-3.08663	-1.74979	-2.69607
49	H	-0.05246	-0.04375	-0.86363	68	H	1.016172	4.311021	0.143891
50	H	-4.51434	-2.44842	-0.45986	69	H	2.102696	2.910848	-0.78394
51	H	-6.88872	-2.23958	-0.10091	70	H	1.858432	0.034137	0.222265
52	H	-6.39945	2.044101	0.494847	71	H	6.97946	2.268403	-2.34625
53	H	-8.58814	-1.9497	0.890801	72	H	9.16619	1.36129	-1.6515
54	H	-9.92553	-0.84467	1.049822	73	H	4.893184	-0.45284	2.683575
55	H	-10.2802	-2.3305	-0.91571	74	H	4.623217	1.235289	2.229672
56	H	-10.1097	-0.6537	-1.45292	75	H	3.261549	0.10073	2.296596
57	H	-8.75874	-1.78085	-1.63633	76	H	4.730852	-2.31074	0.824273
58	H	-9.4008	2.719827	2.115002	77	H	3.068012	-1.77666	0.582965
59	H	-9.42449	1.026109	2.624718	78	H	4.191213	-1.8467	-0.79291
60	H	-7.88125	1.869072	2.435243	79	H	4.867319	2.098794	-3.07005
61	H	-8.33538	2.081087	-0.0566	80	H	3.17781	2.069325	-2.5373
62	H	-9.8508	1.244177	0.157011	81	H	4.289734	3.322932	-1.9172
63	H	0.624783	-1.58639	2.586741	82	H	10.50872	-0.0941	-0.26866
64	H	0.38575	-3.83983	0.133221	83	H	10.70418	-1.7769	1.524391
65	H	-0.16916	-4.82859	-2.06757	84	H	8.670146	-2.60487	2.682174
66	H	-1.92038	-3.78079	-3.47932	85	H	6.462323	-1.77195	2.066896
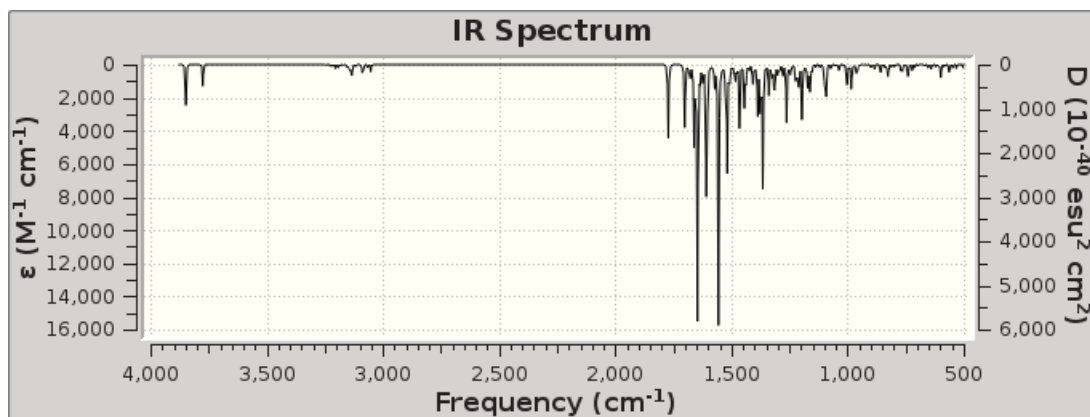
Figure S D.29. Calculated IR spectrum for probe **B-1**.
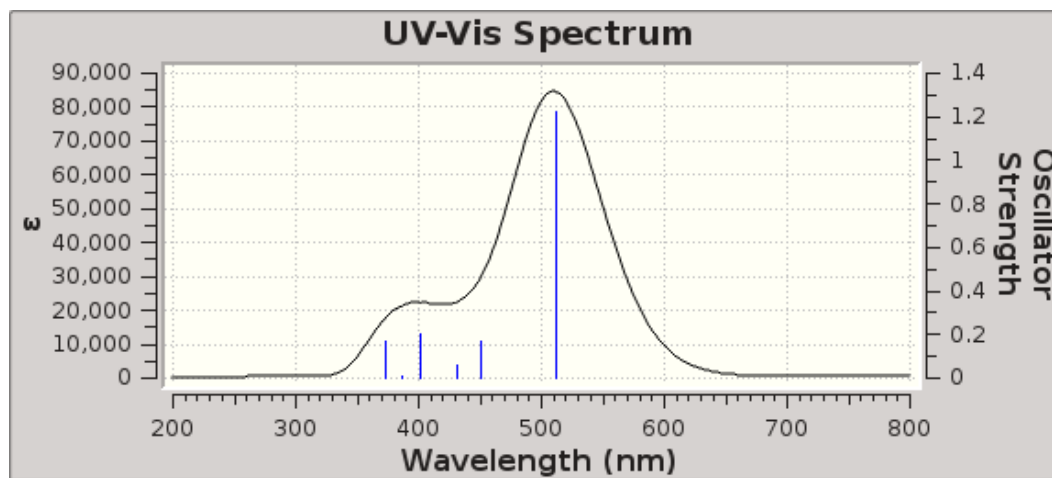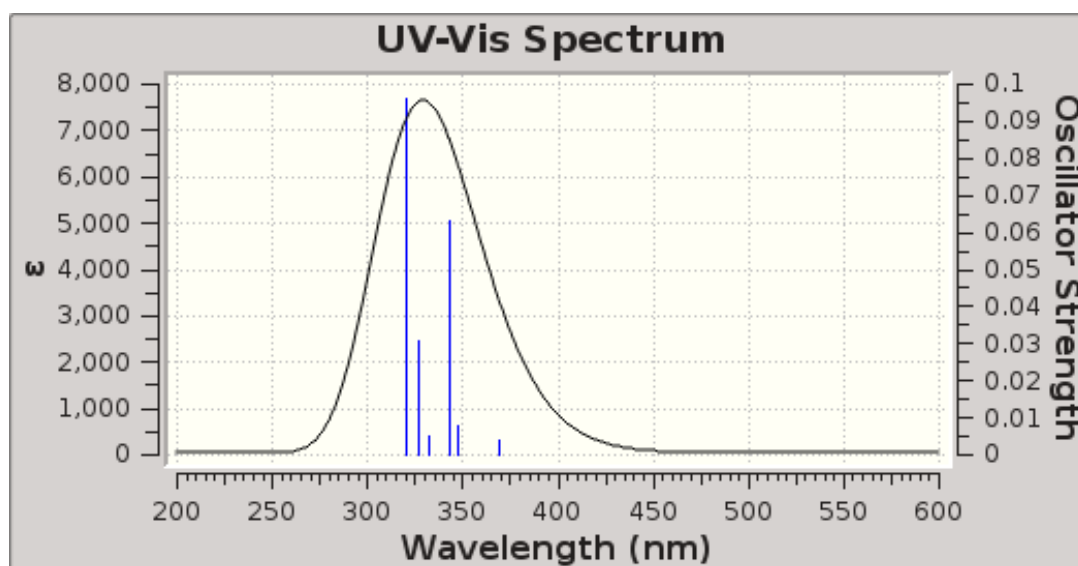

Figure S D.30. Calculated UV-Vis absorption spectrum for probe **B-1**.

Table S D.15. Excitation energies and oscillator strengths listing for probe **B-1**

Excited State   1:   Singlet-A   2.4209 eV 512.14 nm f=1.2210 <S**2>=0.000

   164 -> 165   0.68398

This state for optimization and/or second-order correction.

Total Energy, E(TD-HF/TD-DFT) = -1994.25392211

Copying the excited state density for this state as the 1-particle RhoCI density.

Excited State   2:   Singlet-A   2.7532 eV 450.32 nm f=0.1683 <S**2>=0.000

   163 -> 165   0.67002

   163 -> 166   -0.15090

Excited State   3:   Singlet-A   2.8780 eV 430.79 nm f=0.0598 <S**2>=0.000

   164 -> 166   0.69149

Excited State   4:   Singlet-A   3.0848 eV 401.92 nm f=0.2057 <S**2>=0.000

   163 -> 165   0.16529

   163 -> 166   0.67549

Excited State   5:   Singlet-A   3.2012 eV 387.31 nm f=0.0057 <S**2>=0.000

   161 -> 165   -0.38862

   162 -> 165   0.56258

Excited State   6:   Singlet-A   3.3287 eV 372.47 nm f=0.1692 <S**2>=0.000

    161 -> 165   0.53322

    162 -> 165   0.34736

    162 -> 166   -0.26314
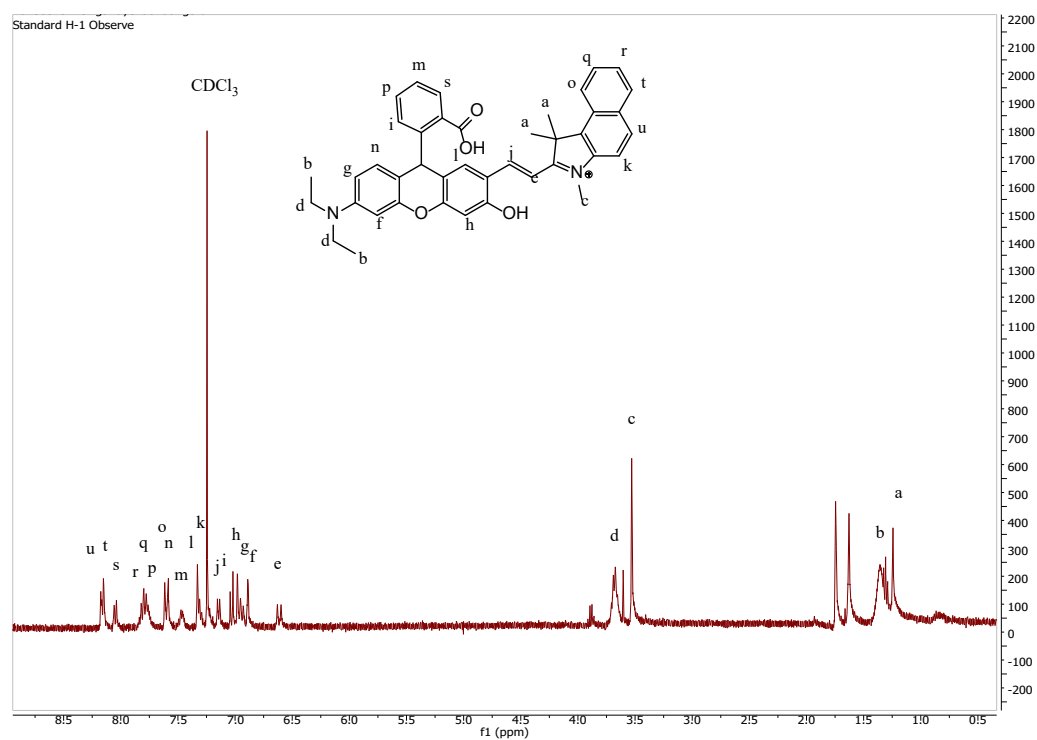
Figure S D.31. ^{1}H NMR spectrum of probe **B-1** in CDCl$_3$ with added CF$_3$COOH. The assignments are based on comparison to the calculated spectrum, Fig. S6, intensity of the peaks and the coupling patterns.
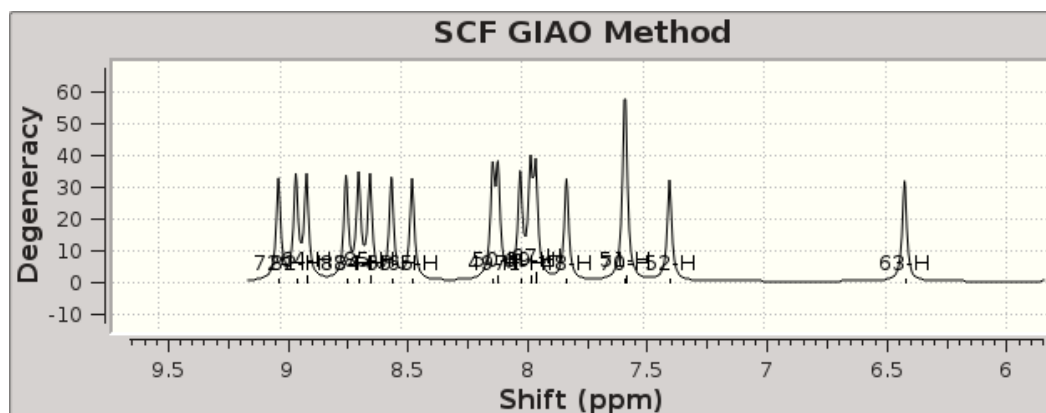
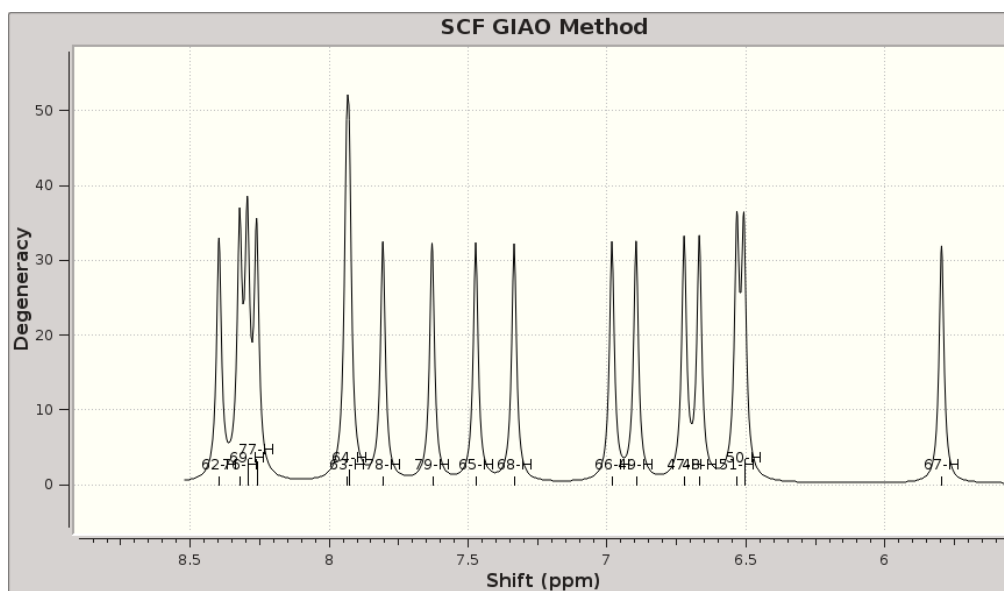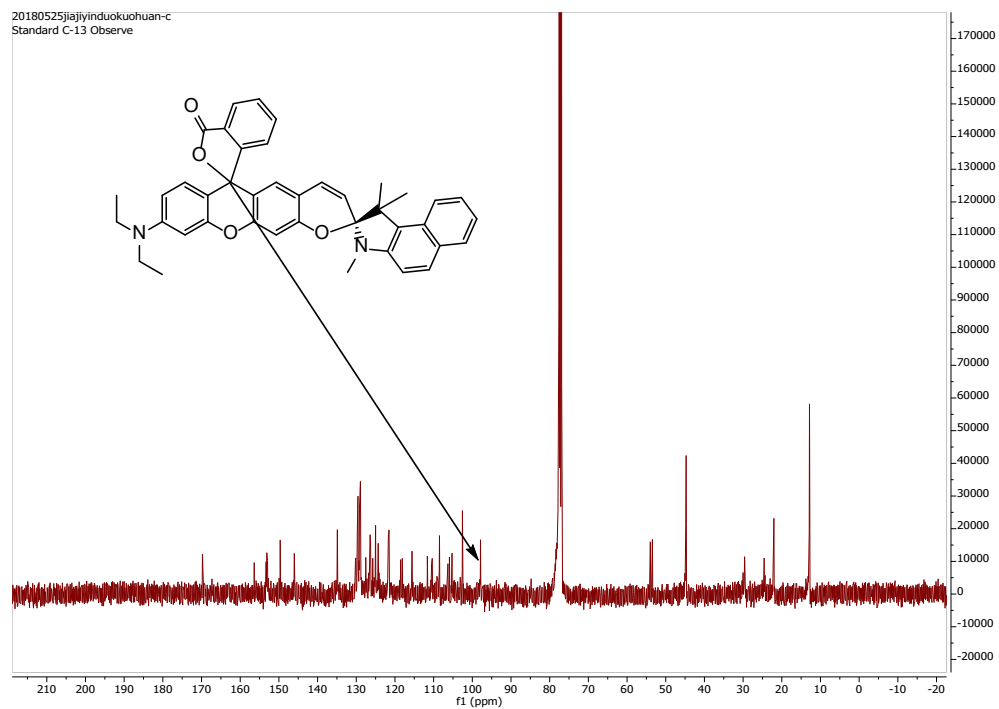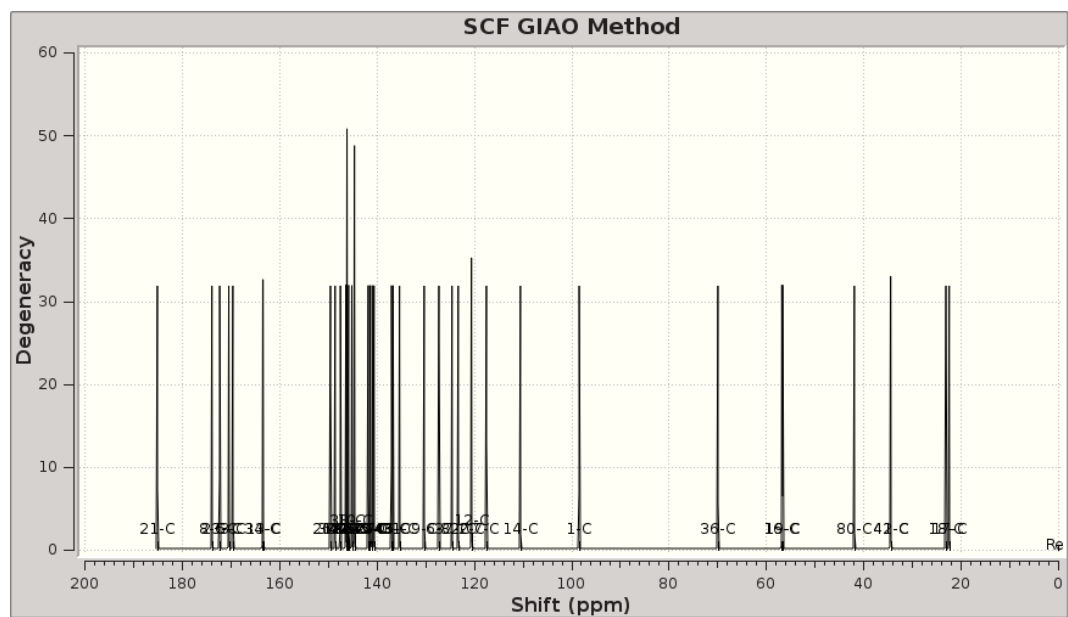**Figure S D.32**. Calculated ^{1}H NMR spectrum of probe **B-1**.
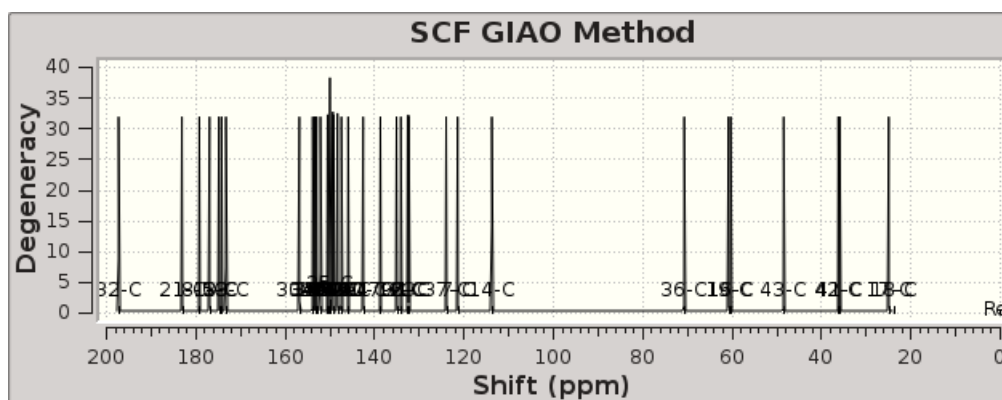
Figure S D.33. Calculated ^{13}C NMR spectrum of probe **B-1**.
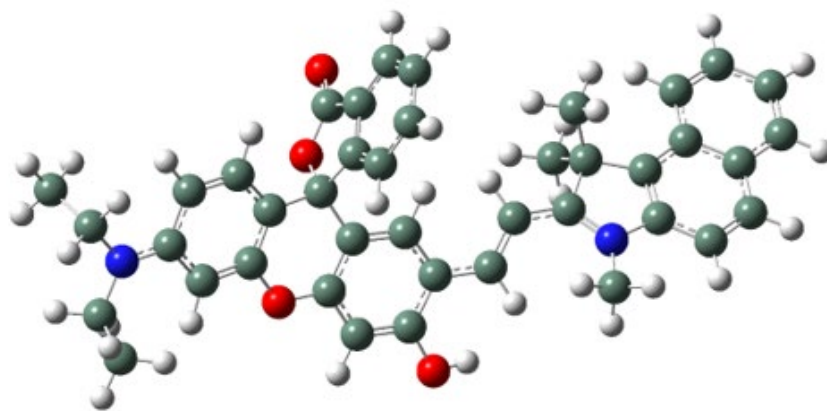
2.6 Computation chemistry results for probe B-2
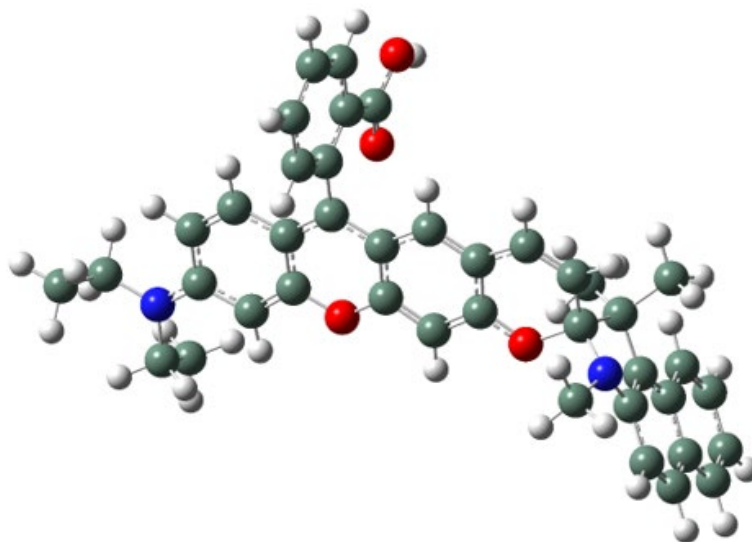
Figure S D.34. GaussView representation of probe **B-2**.

rho8 (Optimization completed)		
/home/rluck/calculation/liu/rho/rho81.log		
File Type	.log	
Calculation Type	FREQ	
Calculation Method	RAPFD	
Basis Set	6-311+G(2d,p)	
Charge	1	
Spin	Singlet	
Solvation	scrf=solvent=water	
E(RAPFD)	-1993.909127	Hartree
RMS Gradient Norm	0.000005	Hartree/Bohr
Imaginary Freq		
Dipole Moment	17.610537	Debye
Point Group	C1	
Job cpu time:	16 days 0 hours 0 minutes 54...	

Table S D.16. Computational results for probe **B-2**

Table S 17. Calculated atomic coordinates for probe **B-2**.

Row	Symbol	X	Y	Z
1	C	2.815289	1.112226	-0.24953
2	C	3.640949	-0.00094	-0.21638
3	C	3.071157	-1.29615	-0.36537
4	O	1.739919	-1.44742	-0.54102
5	C	0.92532	-0.37336	-0.59033
6	C	1.429278	0.939006	-0.45709
7	C	-0.41999	-0.62901	-0.76734
8	C	-1.29911	0.441789	-0.80444
9	C	-0.83347	1.778928	-0.69693
10	C	0.510768	2.0022	-0.52823
11	C	5.045632	0.051941	-0.00892
12	C	5.801398	-1.07232	0.035761
13	C	5.212908	-2.37325	-0.12745
14	C	3.815363	-2.44375	-0.32629
15	N	5.969327	-3.47707	-0.09328
16	C	5.413083	-4.80147	-0.34869
17	C	4.867257	-5.45856	0.911197
18	C	8.247149	-3.24378	-1.04587
19	C	7.398945	-3.44258	0.201621
20	O	2.766219	3.522986	3.276692
21	C	2.822724	2.647105	2.265719
22	C	3.370899	3.234449	1.020401
23	C	3.382768	2.476796	-0.15825
24	C	3.89747	4.52567	1.013571

Row	Symbol	X	Y	Z
25	C	4.431969	5.063373	-0.14634
26	C	4.444424	4.310751	-1.31306
27	C	3.921987	3.024011	-1.3174
28	O	2.4613	1.496556	2.374226
29	O	-2.58501	0.15944	-0.97753
30	C	-1.81281	2.836174	-0.81949
31	C	-3.1126	2.558632	-0.90881
32	C	-3.65264	1.172256	-0.81757
33	N	-4.6211	0.877117	-1.82636
34	C	-5.4334	-0.14311	-1.33849
35	C	-5.34195	-0.23961	0.0348
36	C	-4.39938	0.842572	0.521625
37	C	-6.27787	-0.97173	-2.09628
38	C	-7.04375	-1.89559	-1.43155
39	C	-7.00331	-2.01546	-0.0241
40	C	-6.1399	-1.16056	0.737149
41	C	-3.39528	0.468645	1.608025
42	C	-5.23196	2.048645	0.9778
43	C	-6.15124	-1.29152	2.150183
44	C	-6.95183	-2.21604	2.768375
45	C	-7.78832	-3.0676	2.014867
46	C	-7.80948	-2.96313	0.648966
47	C	-4.22294	0.920584	-3.21574
48	H	-0.78313	-1.64501	-0.85934
49	H	0.87732	3.02011	-0.45356

| 50 | H | 5.515116 | 1.021505 | 0.110604 | | | | | |
51	H	6.868166	-0.97733	0.180721	68	H	-1.46137	3.862404	-0.85565
52	H	3.298626	-3.38721	-0.42831	69	H	-3.85034	3.342943	-1.02517
53	H	4.647723	-4.72516	-1.12257	70	H	-6.31972	-0.89006	-3.17639
54	H	6.216149	-5.405	-0.77623	71	H	-7.70037	-2.55599	-1.99006
55	H	4.057231	-4.86976	1.347164	72	H	-2.58556	1.204477	1.632709
56	H	4.480708	-6.45297	0.677073	73	H	-3.86126	0.485381	2.593425
57	H	5.650935	-5.56728	1.664669	74	H	-2.96181	-0.51837	1.446789
58	H	9.30763	-3.25835	-0.78437	75	H	-5.86635	1.750672	1.815011
59	H	8.065374	-4.03929	-1.77243	76	H	-4.5897	2.867296	1.313177
60	H	8.025358	-2.28849	-1.52699	77	H	-5.8775	2.413558	0.175822
61	H	7.597108	-2.67134	0.946382	78	H	-5.52117	-0.64854	2.750383
62	H	7.643064	-4.39207	0.682142	79	H	-6.94393	-2.29464	3.851087
63	H	2.411276	3.057374	4.048588	80	H	-8.41328	-3.79691	2.519589
64	H	3.89057	5.104036	1.928874	81	H	-8.45382	-3.6078	0.057747
65	H	4.840553	6.067618	-0.1386	82	H	-3.58301	1.789658	-3.3701
66	H	4.861281	4.723047	-2.22557	83	H	-3.67504	0.021777	-3.52047
67	H	3.925797	2.435565	-2.22839	84	H	-5.10279	1.03388	-3.84989
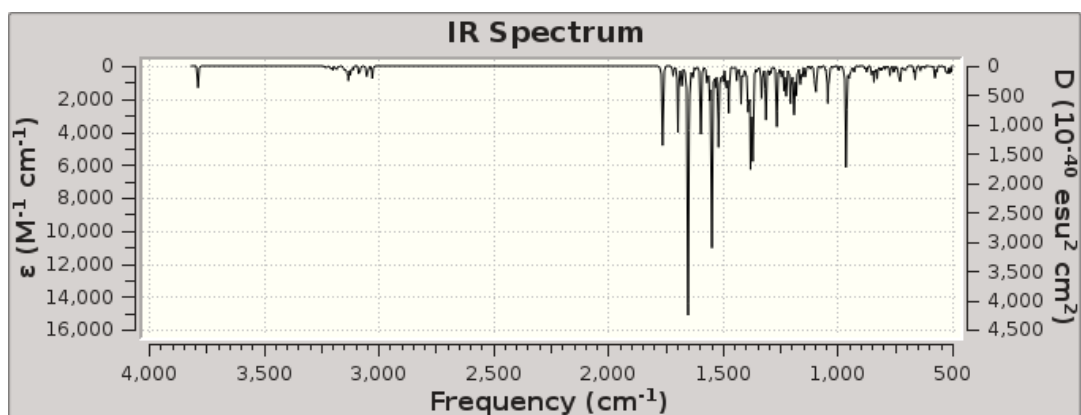
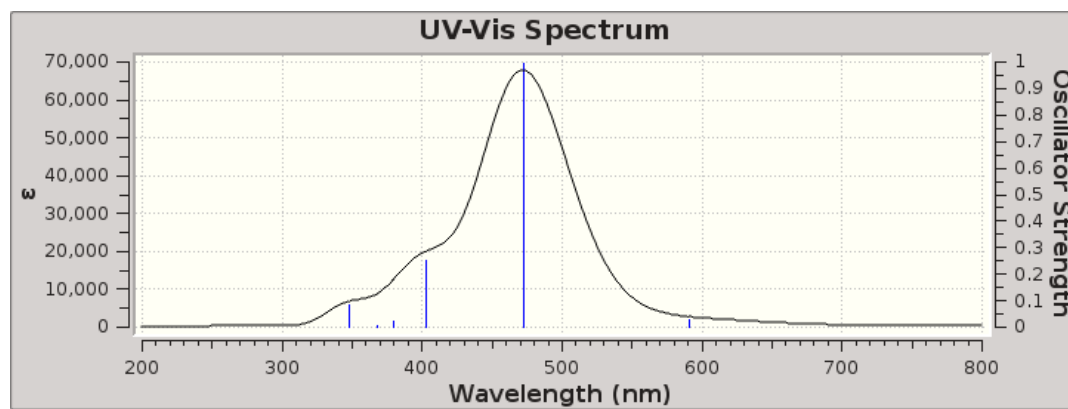**Figure S D.35**. Calculated IR spectrum for probe **B-2**.

Figure S D.36. Calculated UV-Vis spectrum for probe **B-2**.

Table S D.18. Excitation energies and oscillator strengths listing for probe **B-2**.

Excited State   1:   Singlet-A   2.1250 eV 583.45 nm f=0.0024 <S**2>=0.000

  164 -> 165   0.70582

This state for optimization and/or second-order correction.

Total Energy, E(TD-HF/TD-DFT) = -1993.83102978

Copying the excited state density for this state as the 1-particle RhoCI density.

Excited State   2:   Singlet-A   2.6864 eV 461.52 nm f=0.9549 <S**2>=0.000

  163 -> 165   0.69632

Excited State   3:   Singlet-A   3.1940 eV 388.18 nm f=0.0098 <S**2>=0.000

  161 -> 165   0.15999

  162 -> 165   0.67985

Excited State   4:   Singlet-A   3.3234 eV 373.06 nm f=0.1542 <S**2>=0.000

  160 -> 165   -0.26744

  161 -> 165   0.59564

  162 -> 165   -0.18120

  164 -> 166   -0.12387

Excited State   5:   Singlet-A   3.3311 eV 372.21 nm f=0.0056 <S**2>=0.000

  161 -> 165   0.10907

  164 -> 166   0.61093

  164 -> 167   -0.31905

Excited State   6:   Singlet-A   3.4727 eV 357.03 nm f=0.0060 <S**2>=0.000

  164 -> 166   0.33193

  164 -> 167   0.61531

2.7 Computation results Data for probe B-3
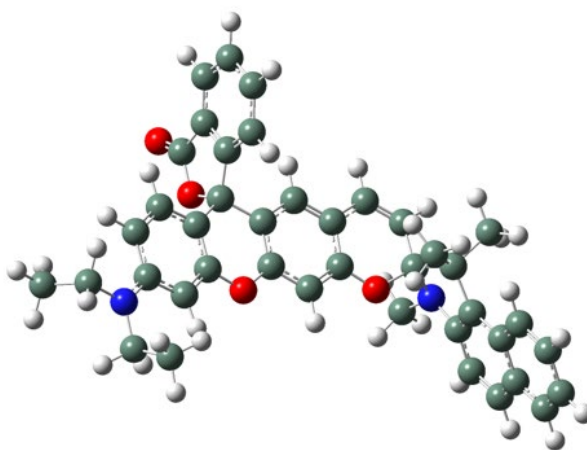
Figure S D.37. GaussView representation of probe **B-3**.

Table S D.19. Computational results for probe **B-3**.

rho511 (Optimization completed)		
/home/rluck/calculation/liu/rho/rho511.log		
File Type	.log	
Calculation Type	FREQ	
Calculation Method	RAPFD	
Basis Set	6-311+G(2d,p)	
Charge	0	
Spin	Singlet	
Solvation	scrf=solvent=water	
E(RAPFD)	-1993.460751	Hartree
RMS Gradient Norm	0.000006	Hartree/Bohr
Imaginary Freq	0	
Dipole Moment	7.268882	Debye
Polarizability (α)	755.282606	a.u.
Point Group	C1	
Job cpu time:	13 days 14 hours 58 minutes	...

Table S D.20. Calculated atomic coordinates for probe **B-3**.

Row	Symbol	X	Y	Z
1	C	2.88412	-1.32468	-0.22192
2	C	3.644424	-0.0438	-0.13385
3	C	3.050676	1.175371	-0.44073
4	O	1.725561	1.2916	-0.76009
5	C	0.927115	0.197718	-0.64883
6	C	1.412878	-1.07508	-0.35603
7	C	-0.43101	0.43358	-0.83432
8	C	-1.32068	-0.61703	-0.72017
9	C	-0.8647	-1.91632	-0.43165
10	C	0.493367	-2.11559	-0.25554
11	C	5.001911	-0.01307	0.194105
12	C	5.730714	1.152842	0.209896
13	C	5.119777	2.39348	-0.10526
14	C	3.752039	2.369272	-0.4259
15	N	5.827088	3.558316	-0.09288
16	C	5.235796	4.813422	-0.51714
17	C	4.519253	5.551611	0.607554
18	C	8.209883	3.342795	-0.76456
19	C	7.207898	3.613283	0.351295
20	O	4.282943	-4.02849	-1.96715
21	C	3.856703	-3.26973	-1.12799
22	C	3.792666	-3.43481	0.332176
23	C	3.223371	-2.30012	0.871566
24	C	4.202549	-4.5007	1.12131
25	C	4.018588	-4.38879	2.491294
26	C	3.440894	-3.23848	3.040315
27	C	3.035913	-2.17858	2.237217
28	O	3.337869	-2.06629	-1.44246
29	O	-2.62284	-0.34895	-0.92568
30	C	-1.85038	-2.97272	-0.3745
31	C	-3.152	-2.6994	-0.46643
32	C	-3.67513	-1.30371	-0.56404
33	N	-4.69262	-1.16148	-1.56913
34	C	-5.48079	-0.0742	-1.21154
35	C	-5.33723	0.229357	0.127859
36	C	-4.37691	-0.77294	0.735584
37	C	-6.35132	0.639146	-2.05376
38	C	-7.08936	1.659472	-1.50941
39	C	-6.9963	1.990019	-0.13876
40	C	-6.10654	1.252259	0.71039
41	C	-5.19291	-1.88914	1.401392
42	C	-3.33286	-0.24457	1.714726
43	C	-6.06598	1.595351	2.087329
44	C	-7.77484	3.034458	0.412666
45	C	-6.84109	2.608542	2.587849
46	C	-7.70314	3.343659	1.745522

47	H	-0.78412	1.434875	-1.0506					
48	H	0.850648	-3.11825	-0.03969	66	H	-1.50655	-3.99756	-0.27052
49	H	5.502645	-0.94643	0.433703	67	H	-3.8987	-3.4837	-0.44629
50	H	6.783699	1.10489	0.451965	68	H	-6.43352	0.396146	-3.1071
51	H	3.200568	3.27316	-0.64636	69	H	-7.76416	2.233731	-2.13732
52	H	6.041057	5.43431	-0.91876	70	H	-4.53896	-2.65498	1.827021
53	H	4.558603	4.628776	-1.35509	71	H	-5.79114	-1.4658	2.211091
54	H	4.100269	6.493603	0.243799	72	H	-5.87209	-2.3644	0.689894
55	H	3.704014	4.951359	1.01842	73	H	-2.89696	0.697323	1.38155
56	H	5.211594	5.780917	1.42194	74	H	-3.76213	-0.09735	2.706171
57	H	9.233828	3.414314	-0.38803	75	H	-2.52833	-0.97789	1.825231
58	H	8.069992	2.344857	-1.18694	76	H	-5.41579	1.04484	2.754292
59	H	8.094586	4.069617	-1.57304	77	H	-8.43942	3.587662	-0.2452
60	H	7.374814	4.608928	0.771138	78	H	-6.79311	2.848934	3.645469
61	H	7.351202	2.915872	1.180214	79	H	-8.30745	4.145496	2.156797
62	H	4.648456	-5.38363	0.676715	80	C	-4.3463	-1.41181	-2.94971
63	H	4.323738	-5.19723	3.146653	81	H	-5.24857	-1.61333	-3.52859
64	H	3.30743	-3.17462	4.11522	82	H	-3.71199	-2.29744	-2.99567
65	H	2.589118	-1.28832	2.666467	83	H	-3.80931	-0.57191	-3.40535
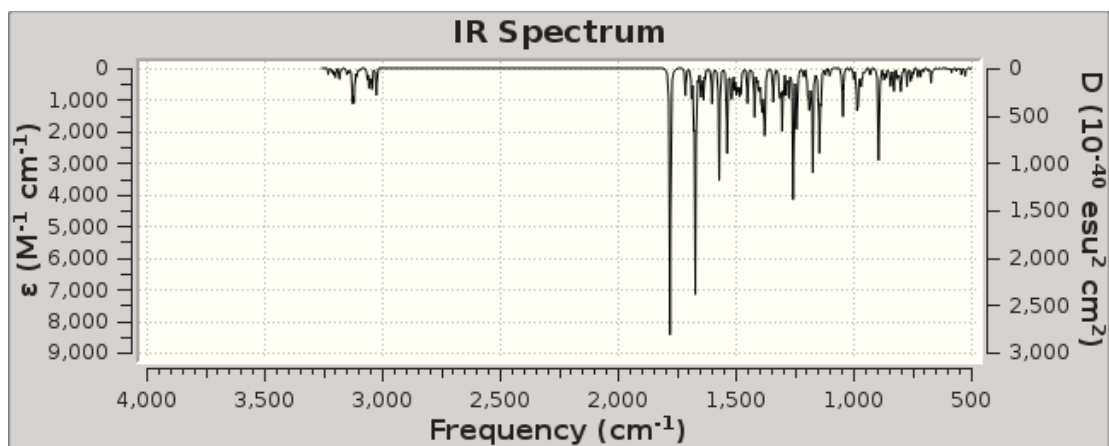
Figure S D.38. Calculated IR spectrum for probe **B-3**.

Figure S D.39. Calculated UV-Vis spectrum for probe **B-3**.

Table S D.21. Excitation energies and oscillator strengths listing for probe **B-3**.

Excitation energies and oscillator strengths:

Excited State   1:   Singlet-A   3.3573 eV 369.30 nm f=0.0040 <S**2>=0.000

   163 -> 165   0.69522

This state for optimization and/or second-order correction.

Total Energy, E(TD-HF/TD-DFT) = -1993.33737366

Copying the excited state density for this state as the 1-particle RhoCI density.

Excited State   2:   Singlet-A   3.5640 eV 347.88 nm f=0.0078 <S**2>=0.000

   164 -> 165   0.61190

   164 -> 166   -0.21397

   164 -> 167   0.25810

Excited State   3:   Singlet-A   3.6168 eV 342.80 nm f=0.0632 <S**2>=0.000

   164 -> 165   0.16932

   164 -> 166   0.64689

   164 -> 167   0.15246

Excited State   4:   Singlet-A   3.7256 eV 332.79 nm f=0.0050 <S**2>=0.000

   164 -> 165   -0.29485

   164 -> 167   0.62500

Excited State   5:   Singlet-A   3.7929 eV 326.89 nm f=0.0306 <S**2>=0.000

   162 -> 165   0.69553

Excited State   6:   Singlet-A   3.8663 eV 320.68 nm f=0.0962 <S**2>=0.000

   163 -> 166   -0.24835

   163 -> 167   0.64182
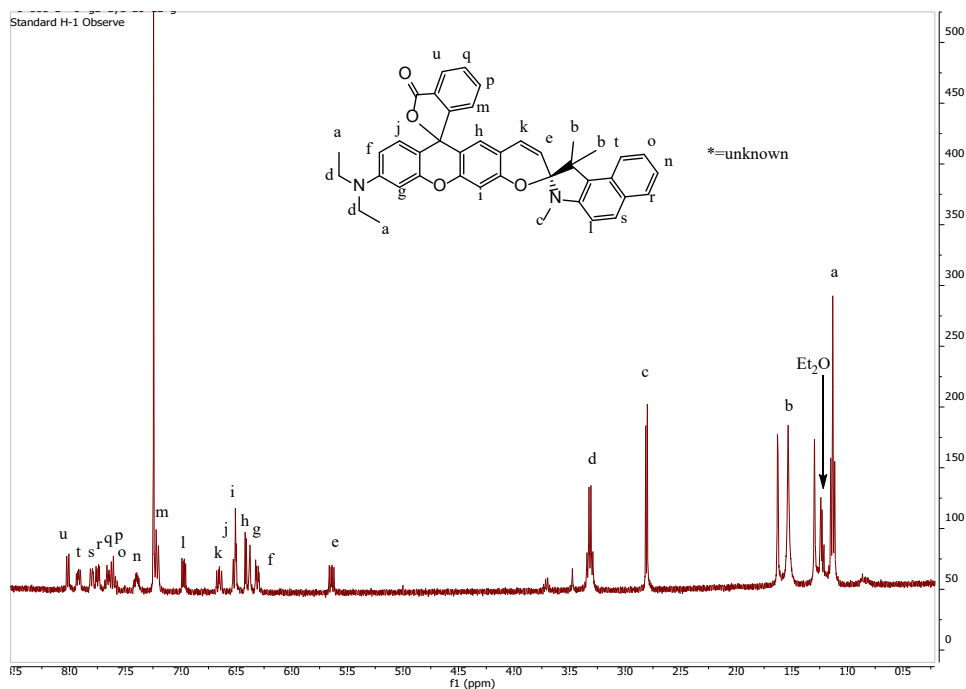
Figure S D.40. ^{1}H NMR spectrum of probe **B-3** in CDCl$_3$. The assignments are based on comparison to the calculated spectrum, Fig. S4, intensity of the peaks and the coupling patterns.

Figure S D.41. Calculated ^{1}H NMR spectrum of probe **B-3**.

Figure S D.42. ^{13}C NMR spectrum of probe **B-3** in CDCl$_3$.

Figure S D.43. Calculated ^{13}C NMR spectrum of probe **B-3**.

350

2.8 Computation chemistry results for probe B-4

Figure S D.44. GaussView representation of probe **B-4**.

Table S D.22. Computational results for probe **B-4**.

rho6 (Optimization completed)		
/home/rluck/calculation/liu/rho/rho61.log		
File Type	.log	
Calculation Type	FREQ	
Calculation Method	RAPFD	
Basis Set	6-311+G(2d,p)	
Charge	1	
Spin	Singlet	
Solvation	scrf=solvent=water	
E(RAPFD)	-1993.900504	Hartree
RMS Gradient Norm	0.000006	Hartree/Bohr
Imaginary Freq		
Dipole Moment	17.269069	Debye
Point Group	C1	
Job cpu time:	12 days 1 hours 17 minutes 1...	

Table S D.23. Calculated atomic coordinates for probe **B-4**.

Row	Symbol	X	Y	Z		Row	Symbol	X	Y	Z
1	C	2.589271	-0.63561	-0.20606		25	C	2.039666	-1.42804	2.218165
2	C	4.057327	-0.38992	-0.10996		26	O	-0.18992	4.262774	-0.66426
3	C	4.60223	0.863858	-0.35802		27	C	-1.71752	1.854703	-0.04958
4	O	3.828355	1.969211	-0.61769		28	C	-2.51144	0.755044	-0.09511
5	C	2.489049	1.871726	-0.50533		29	C	-3.91393	0.718691	0.106437
6	C	1.829029	0.658156	-0.27057		30	N	-4.64974	1.529586	0.838611
7	C	1.785305	3.059766	-0.63092		31	C	-6.01892	1.196507	0.733882
8	C	0.407034	3.064587	-0.51578		32	C	-6.15583	0.09006	-0.06584
9	C	-0.29566	1.860301	-0.25171		33	C	-4.79018	-0.33495	-0.53066
10	C	0.457664	0.685903	-0.1459		34	C	-7.09268	1.868118	1.334062
11	C	4.960836	-1.41878	0.165097		35	C	-8.34418	1.363364	1.102691
12	C	6.320898	-1.21845	0.185403		36	C	-8.54907	0.217201	0.295225
13	C	6.869777	0.06422	-0.07012		37	C	-7.43571	-0.44563	-0.31257
14	C	5.963422	1.105505	-0.33842		38	C	-4.63383	-0.27183	-2.05788
15	N	8.213614	0.279733	-0.05137		39	C	-4.39515	-1.71588	0.025636
16	C	8.785778	1.562686	-0.41599		40	C	-4.1852	2.569904	1.73729
17	C	8.885973	2.531021	0.75667		41	C	1.695715	-2.56318	-1.21456
18	C	9.594302	-1.63959	-0.81576		42	O	2.30659	-1.38454	-1.46468
19	C	9.151692	-0.75573	0.343779		43	O	1.373079	-3.32036	-2.09812
20	C	1.530923	-2.69797	0.240381		44	C	-9.85131	-0.28489	0.074188
21	C	2.058815	-1.57479	0.842495		45	C	-10.0542	-1.39111	-0.70859
22	C	0.958771	-3.72772	0.974432		46	C	-8.95774	-2.04408	-1.30766
23	C	0.933244	-3.58991	2.354117		47	C	-7.68077	-1.58471	-1.11659
24	C	1.469262	-2.45152	2.966333		48	H	2.315893	3.98394	-0.82539
						49	H	-0.05371	-0.24451	0.07463

352

50	H	4.574739	-2.41521	0.357697					
51	H	6.967426	-2.06216	0.384678	68	H	-2.19389	2.814156	0.124275
52	H	6.293001	2.121005	-0.51083	69	H	-2.08301	-0.18927	-0.41162
53	H	9.77939	1.370566	-0.82934	70	H	-6.95051	2.752305	1.942907
54	H	8.204622	1.998001	-1.23292	71	H	-9.20981	1.848946	1.541018
55	H	9.332299	3.476409	0.437157	72	H	-5.28435	-1.00572	-2.53313
56	H	7.901332	2.743953	1.179624	73	H	-4.89873	0.717427	-2.43526
57	H	9.509962	2.113085	1.55103	74	H	-3.60463	-0.49177	-2.34696
58	H	10.31275	-2.38971	-0.47463	75	H	-5.07111	-2.47749	-0.36264
59	H	8.74373	-2.15953	-1.26296	76	H	-3.38135	-1.98246	-0.27794
60	H	10.07263	-1.04282	-1.59688	77	H	-4.45283	-1.73081	1.115381
61	H	10.0177	-0.25672	0.786637	78	H	-4.82304	2.573374	2.618607
62	H	8.714374	-1.35509	1.145896	79	H	-3.16415	2.350629	2.041392
63	H	0.549082	-4.60231	0.481324	80	H	-4.23338	3.546158	1.253925
64	H	0.495502	-4.36933	2.968102	81	H	-10.6911	0.223325	0.537869
65	H	1.437987	-2.36767	4.047601	82	H	-11.0584	-1.76798	-0.87073
66	H	2.453642	-0.54725	2.696832	83	H	-9.1278	-2.91861	-1.92679
67	H	-1.14687	4.180466	-0.72801	84	H	-6.85572	-2.10149	-1.58949

353
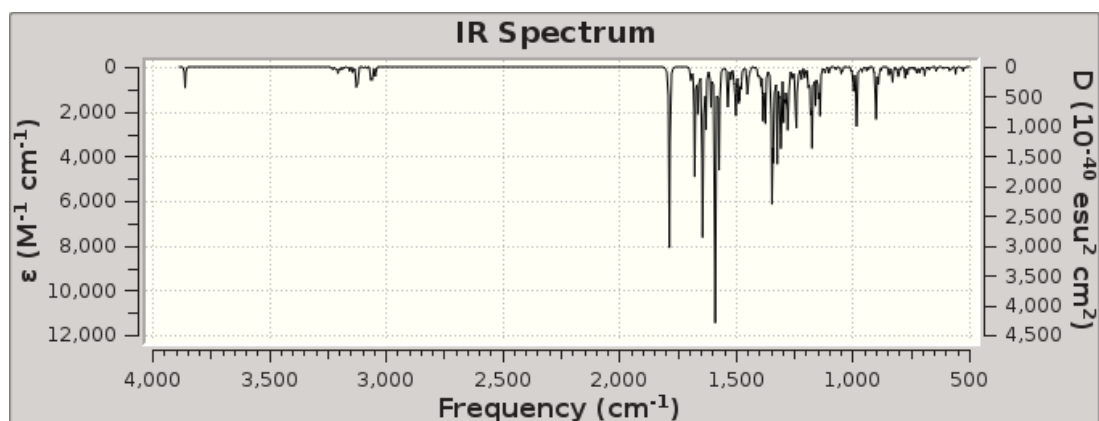
Figure S D.45. Calculated IR spectrum for probe **B-4**.

Figure S D.46. Calculated UV-Vis absorption spectrum for probe **B-4**.

Table S D.24. Excitation energies and oscillator strengths listing for probe **B-4**.

Excited State   1:   Singlet-A   2.0994 eV 590.56 nm f=0.0277 <S**2>=0.000

  164 -> 165   0.70554

This state for optimization and/or second-order correction.

Total Energy, E(TD-HF/TD-DFT) = -1993.82335416

Copying the excited state density for this state as the 1-particle RhoCI density.

Excited State   2:   Singlet-A   2.6216 eV 472.93 nm f=0.9939 <S**2>=0.000

  163 -> 165   0.70299

Excited State   3:   Singlet-A   3.0763 eV 403.03 nm f=0.2487 <S**2>=0.000

  162 -> 165   0.68913

Excited State   4:   Singlet-A   3.2638 eV 379.88 nm f=0.0247 <S**2>=0.000

  160 -> 165   -0.13600

  161 -> 165   0.67850

Excited State   5:   Singlet-A   3.3687 eV 368.05 nm f=0.0032 <S**2>=0.000

  164 -> 166   -0.46091

  164 -> 167   0.53075

Excited State   6:   Singlet-A   3.5603 eV 348.24 nm f=0.0850 <S**2>=0.000

  160 -> 165   0.67491

  161 -> 165   0.12121

  162 -> 165   0.10146

A-1 HOMO (LCAO #151)

A- A-1 LUMO (LCAO #152)

A-2 HOMO-1 (LCAO #150)

A-2 LUMO (LCAO #152)

A-2 HOMO (LCAO #151)
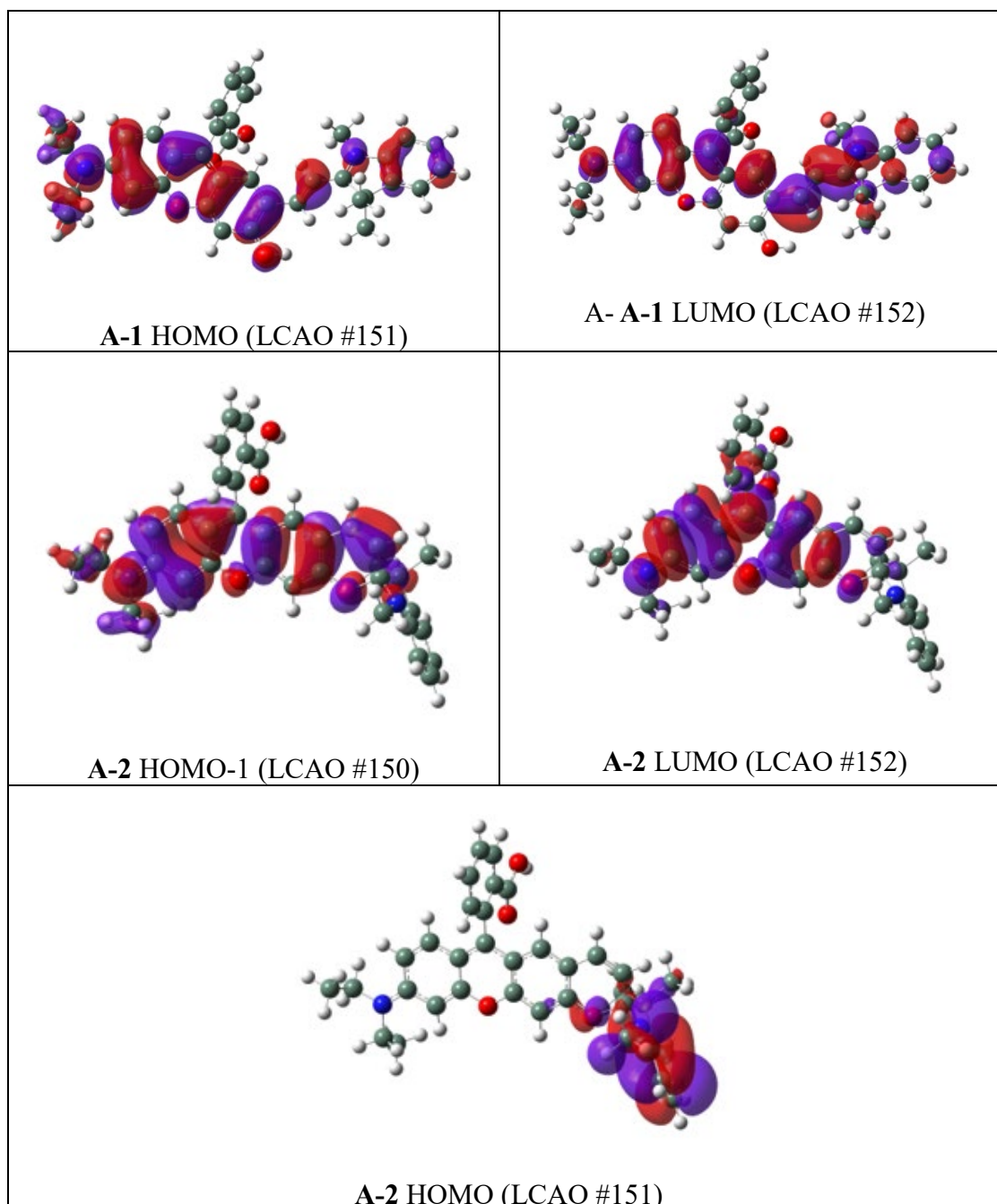
Figure S D.47. LCAO for various levels for **A-1** and **A-2** involved with the transitions noted as Excited State 1 for **A-1** and Excited State 2 for **A-2** in Tables S9 and S11 respectively.

B-1 HOMO (LCAO #164)

B-1 LUMO (LCAO #165)

B-2 HOMO-1 (LCAO #163)

B-2 LUMO (LCAO #165)

B-2 HOMO (LCAO #164)
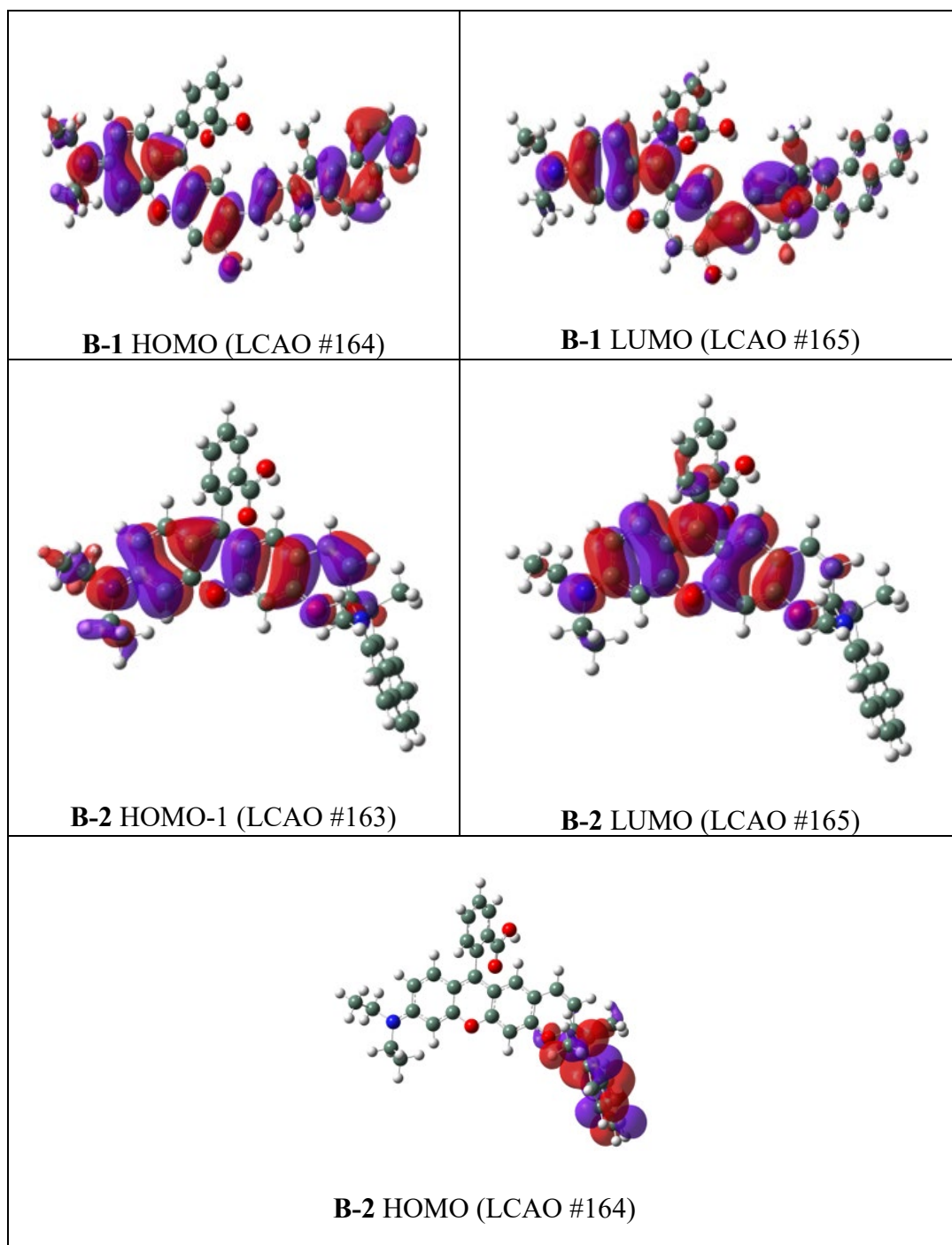
Figure S D.48. LCAO for various levels for **B-1** and **B-2** involved with the transitions noted as Excited State 1 for **B-1** and Excited State 2 for **B-2** in Tables S20 and S23 respectively.

Table S D.25. Calculated Excitation state energies (nm) from different functionals corresponding to the experimentally obtained data. *

Molecule	Expt	APFD	B3P86	B3LYP	CAM-B3LYP	PBEPBE	M06	M052X
A-1	609	505	517	517	441	655	496	439
A-2	535	462	468	468	424	529	456	422
B-1	622	512	527	528	438	670	506	437
B-2	535	462	468	469	424	527	455	422

* Information on these functionals is available on the Gaussian website at http://gaussian.com/dft/

3. Calculation of Fluorescence Quantum Yields of the Probes

Fluorescence quantum yields of the probes were calculated according to literature using the equation below. ϕ represents fluorescence quantum yield. I_x is integration of sample's fluorescence spectra at specific excitation wavelength. A is the absorbance at the specific excited wavelength while the absorbances at the wavelength of excitation is optimally kept in between 0.02 and 0.05. η is the refractive index of solvents which were used for optical measurements, and the subscripts x and st stand for the probe and a reference compound of known fluorescence quantum yield, respectively.

$$\phi_x = \phi_{st} \frac{\eta_x^2 \, A_{st} I_x}{\eta_{st}^2 \, A_x I_{st}}$$

Rhodamine 6G with fluorescence quantum yield of 95.0% in ethanol was used as standard to calculate quantum yields of 450 nm excitation parts. A near-infrared rhodamine dye (Standard) with a fluorescence quantum yield 22.6% in pH 7.4 PBS buffer with 10% ethanol was used to determine quantum yields of 600 nm excitation parts.

Standard:

4. Determination of pK$_a$ by fluorometric titration

The constant K_a of probes were obtained by fluorometric titration as a function of pH using the fluorescence spectra. The expression of the steady-state fluorescence intensity F as a function of the proton concentration has been extended for the case of a n=1 complex between H^+ and a fluorescent probe, which is expressed by the equation below.

$$F = \frac{F_{min}[H^+]^n + F_{max}K_a}{K_a + [H^+]^n}$$

F_{min} and F_{max} are the fluorescence intensities at maximal and minimal H^+ concentrations, respectively, and n is apparent stoichiometry of H^+ binding to the probe which affects the fluorescent change. Nonlinear fitting of equation expressed above to the fluorescence titration data recoded as a function of H^+ concentration with K_a and n as free adjustable parameters yields the estimated apparent constant of K_a.

Figure S D.49. Plot curve of fluorescence intensity of probe **A** (5 μM) versus pH under excitation at 600 nm with three repeated experiments.
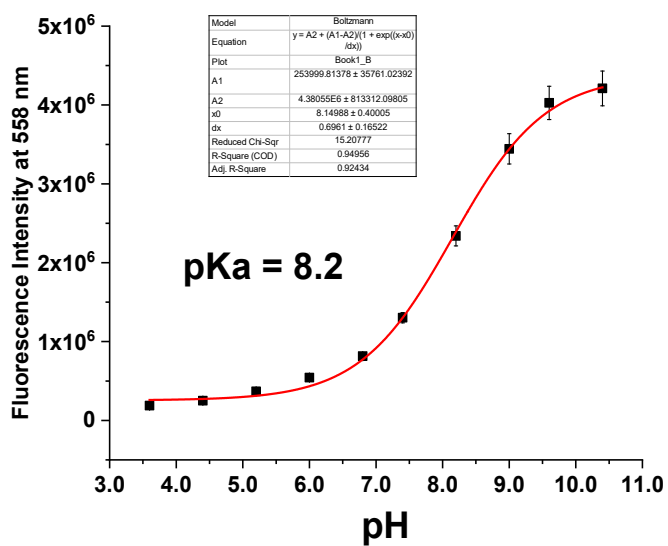
Figure S D.50. Plot curve of fluorescence intensity of 5 μM probe **A** versus pH under excitation at 480 nm with three repeated experiments.
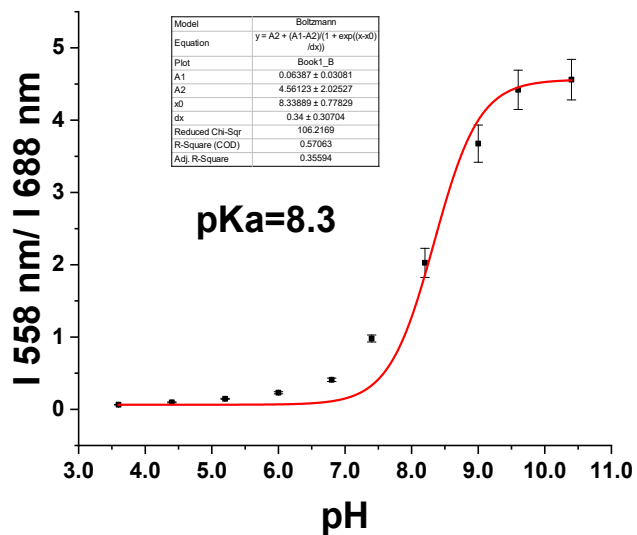
Figure S D.51. Plot curve of fluorescence intensity ratio of 5 μM probe **A** versus pH under excitation at 480 nm with three repeated experiments.

Figure S D.52. Plot curve of fluorescence intensity of 5 μM probe **B** versus pH under excitation at 600 nm with three repeated experiments.

Figure S D.53. Plot curve of fluorescence intensity of 5 μM probe **B** versus pH under excitation at 480 nm with three repeated experiments.

Model	Boltzmann
Equation	y = A2 + (A1-A2)/(1 + exp((x-x0)/dx))
Plot	B
A1	0.35814
A2	5.03431
x0	7.01914
dx	1.25214
Reduced Chi-Sqr	0.10431
R-Square(COD)	0.99983
Adj. R-Square	0.99974

pKa=7.0
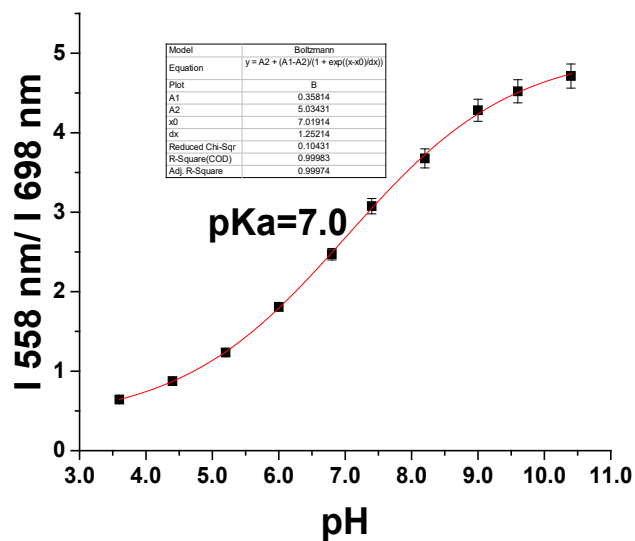
Figure S D.54. Plot curve of fluorescence intensity ratio of 5 µM probe **B** versus pH under excitation at 480 nm with three repeated experiments.

Trifloroacetic acid
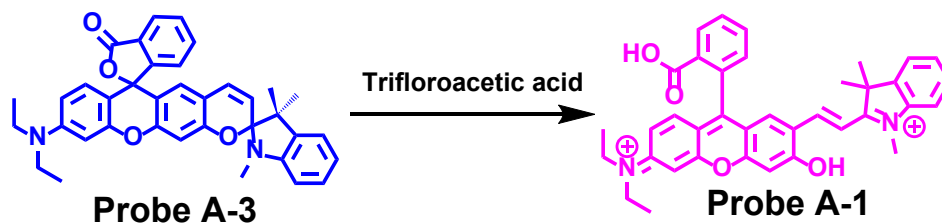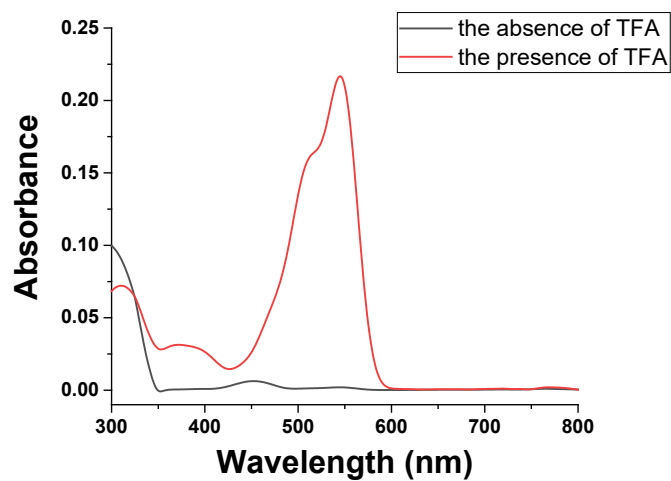
Probe A-3

Probe A-1

Figure S D.55. UV-Vis absorption spectra of 5 µM probe **A** in DMSO solution in the absence and presence of trifluoroacetic acid (TFA).
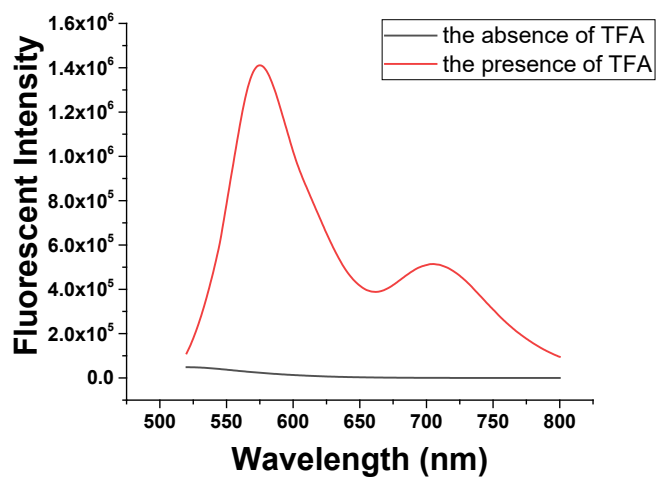
Figure S D.56. Fluorescence spectra of 5 µM probe **A** in DMSO solution in the absence and presence of trifluoroacetic acid (TFA) under excitation of 480 nm.
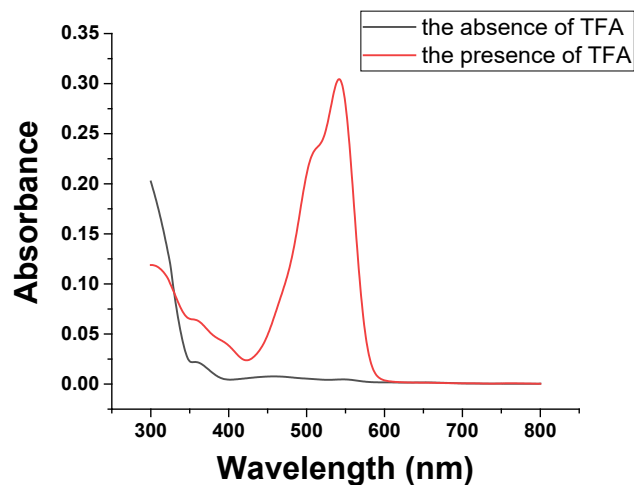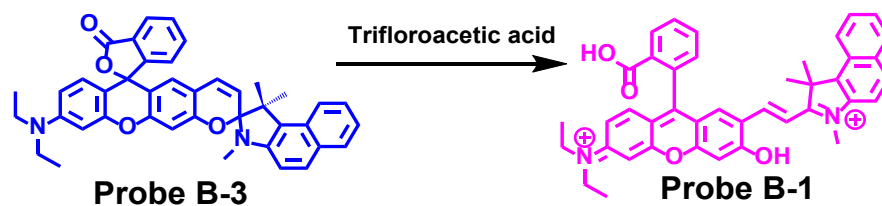
Figure S D.57. UV-Vis absorption spectra of 5 µM probe **B** in DMSO solution in the absence and presence of trifluoroacetic acid (TFA).
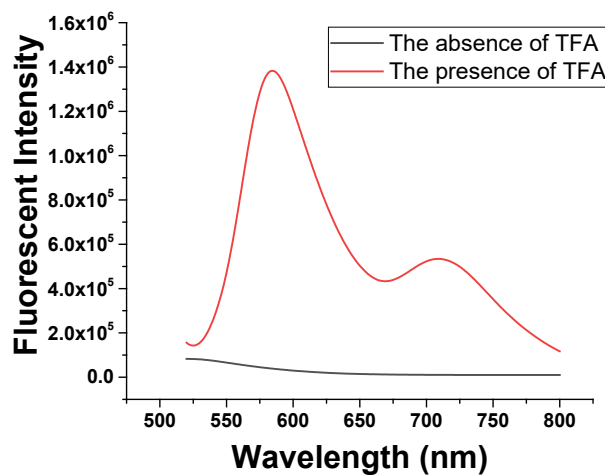
Figure S D.58. Fluorescence spectra of 5 µM probe **B** in DMSO solution in the absence and presence of trifluoroacetic acid (TFA) under excitation of 480 nm.

5. Selectivity of probes A and B to pH over different cations, anions and amino acids.
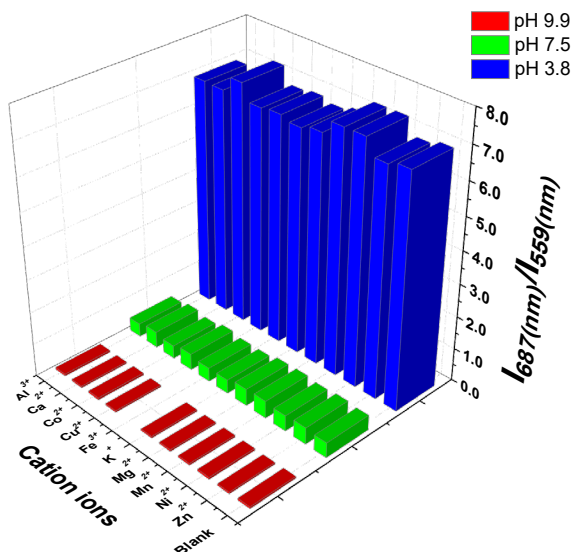
Figure S D.59. Fluorescence intensities of 5 μM probe **A** in the absence and presence of different cations (100 μM) in pH 3.8, 7.5 and 9.9 buffers under excitation at 480 nm.
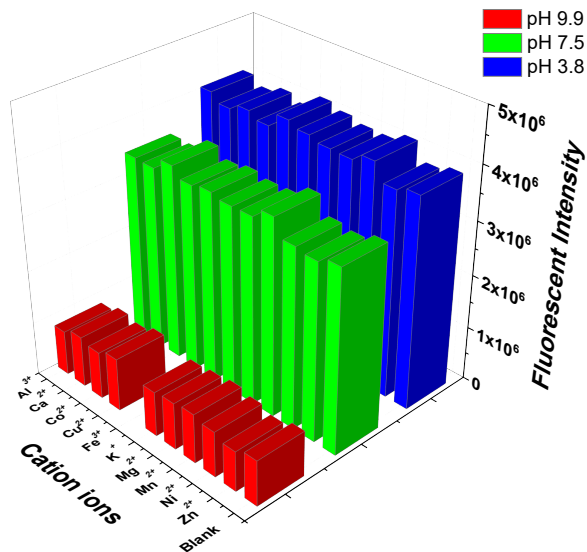
Figure S D.60. Fluorescence intensities of 5 μM probe **A** in the absence and presence of different cations (100 μM) in pH 3.8, 7.5 and 9.9 buffers under excitation at 600 nm.
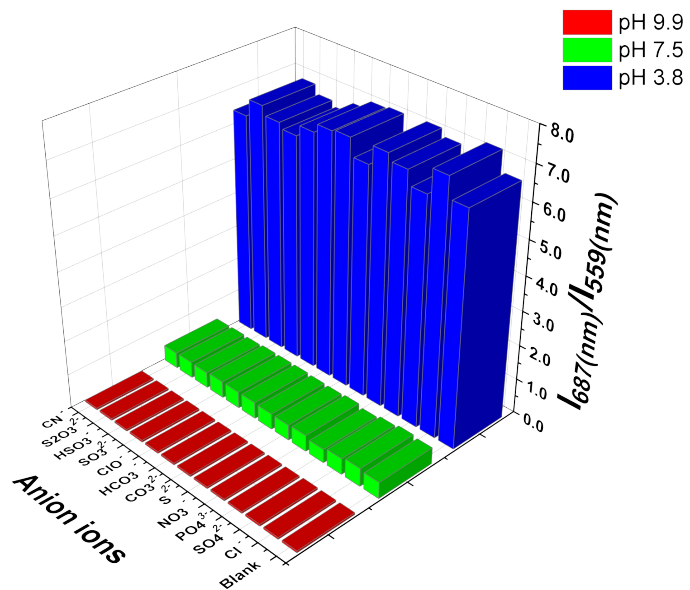
Figure S D.61. Fluorescence intensities of 5 µM probe **A** in the absence and presence of different anions (100 µM) in pH 3.8, 7.5 and 9.9 buffers under excitation at 480 nm.
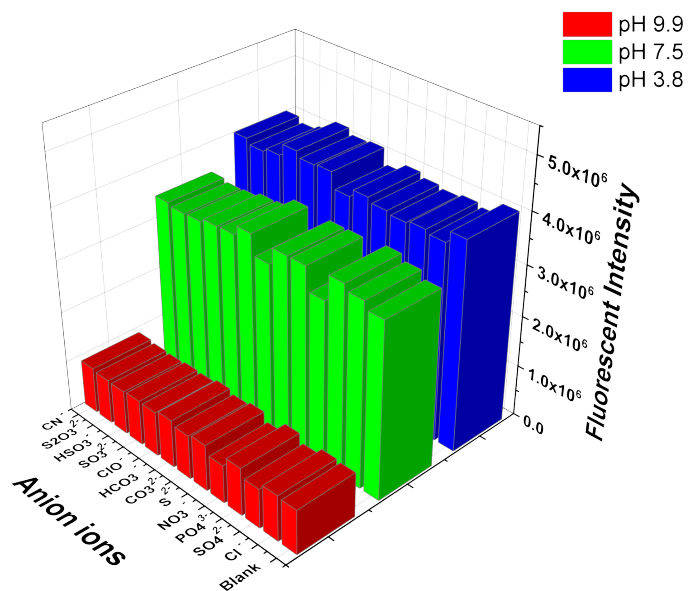
Figure S D.62. Fluorescence intensities of 5 µM probe **A** in the absence and presence of different anions (100 µM) in pH 3.8, 7.5 and 9.9 buffers under excitation at 600 nm.
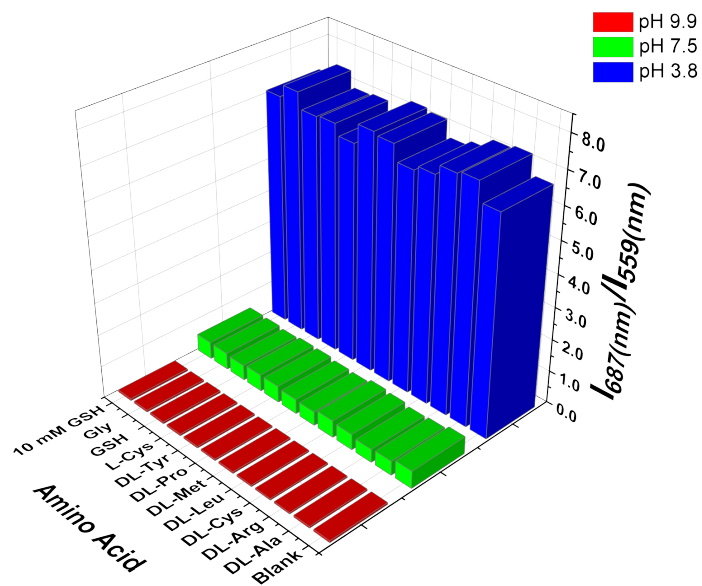
Figure S D.63. Fluorescence intensities of 5 µM probe **A** in the absence and presence of different amino acids (100 µM) in pH 3.8, 7.5 and 9.9 buffers under excitation at 480 nm.
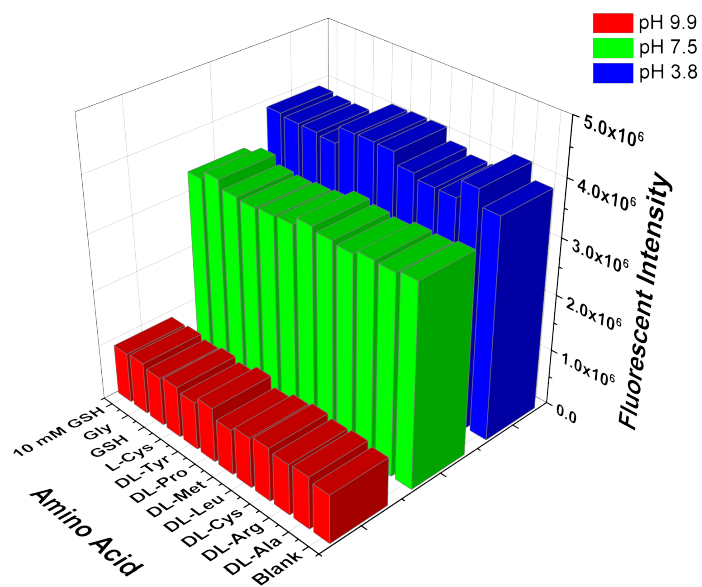
Figure S D.64. Fluorescence intensities of probe A (5 µM) in the absence and presence of different amino acids (100 µM) in pH 3.8, 7.5 and 9.9 buffers under excitation at 600 nm.
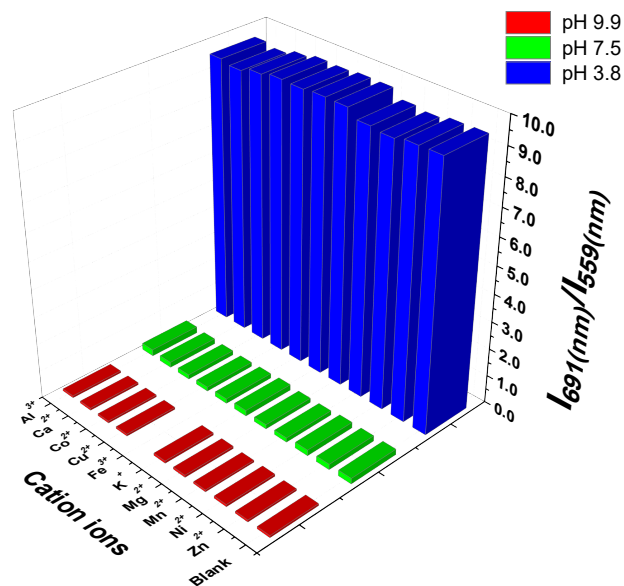
Figure S D.65. Fluorescence intensities of 5 μM probe **B** in the absence and presence of different cations (100 μM) in pH 3.8, 7.5 and 9.9 buffers under excitation at 480 nm.
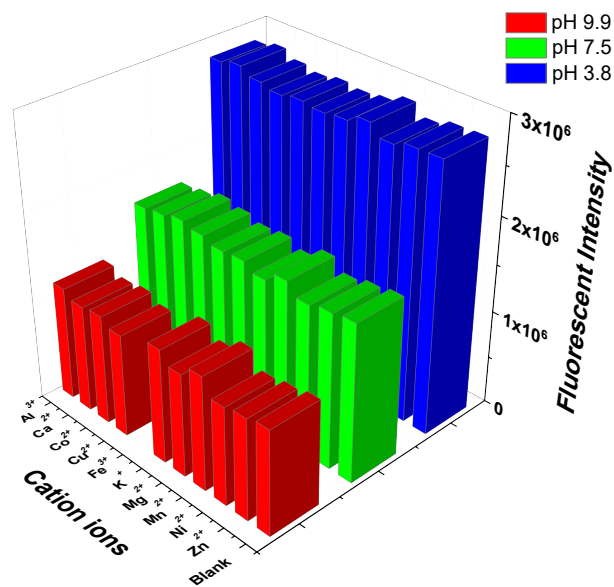
Figure S D.66. Fluorescence intensities of 5 μM probe **B** in the absence and presence of different cations (100 μM) in pH 3.8, 7.5 and 9.9 buffers under excitation at 600 nm.
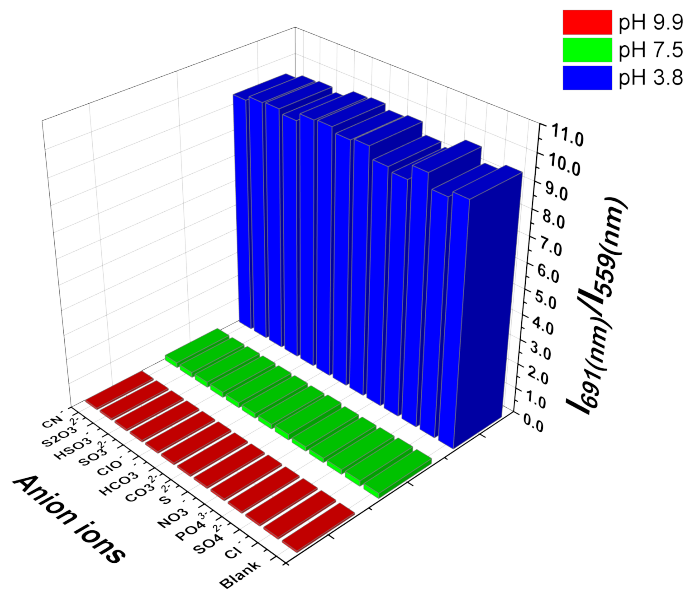
Figure S D.67. Fluorescence intensities of 5 μM probe **B** in the absence and presence of different anions (100 μM) in pH 3.8, 7.5 and 9.9 buffers under excitation at 480 nm.
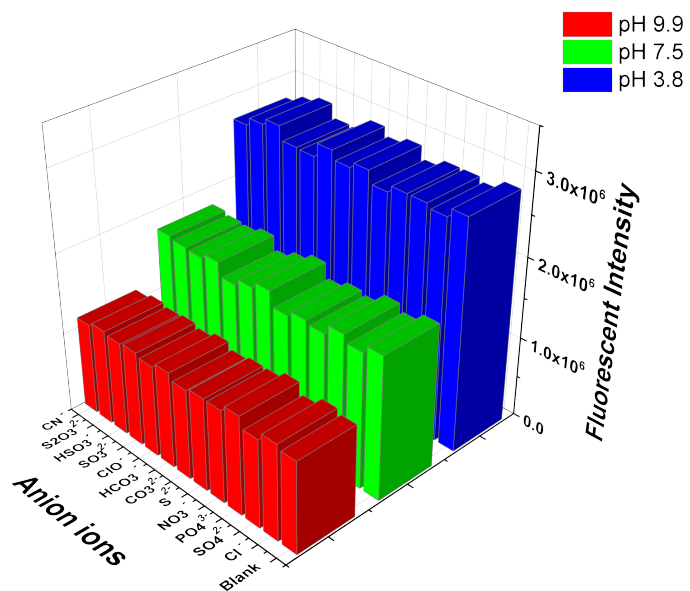
Figure S D.68. Fluorescence intensities of 5 μM probe **B** in the absence and presence of different cations (100 μM) in pH 3.8, 7.5 and 9.9 buffers under excitation at 600 nm.
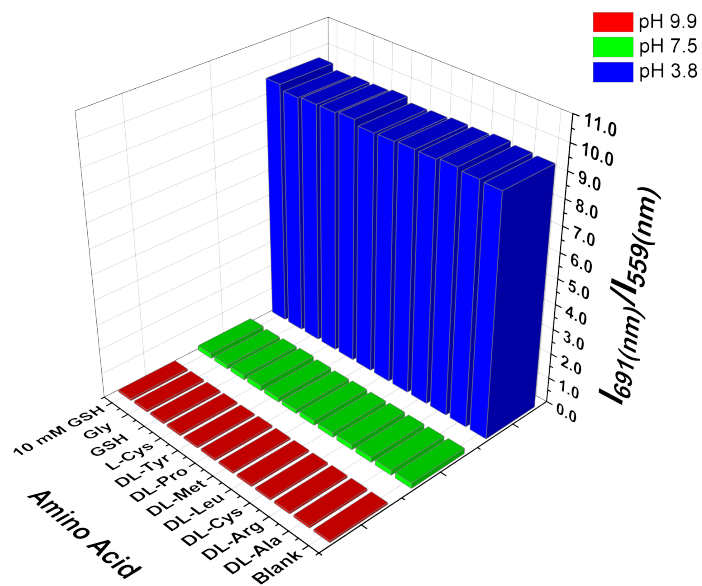
Figure S D.69. Fluorescence intensities of 5 μM probe **B** in the absence and presence of different amino acids (100 μM) in pH 3.8, 7.5 and 9.9 buffers under excitation at 480 nm.
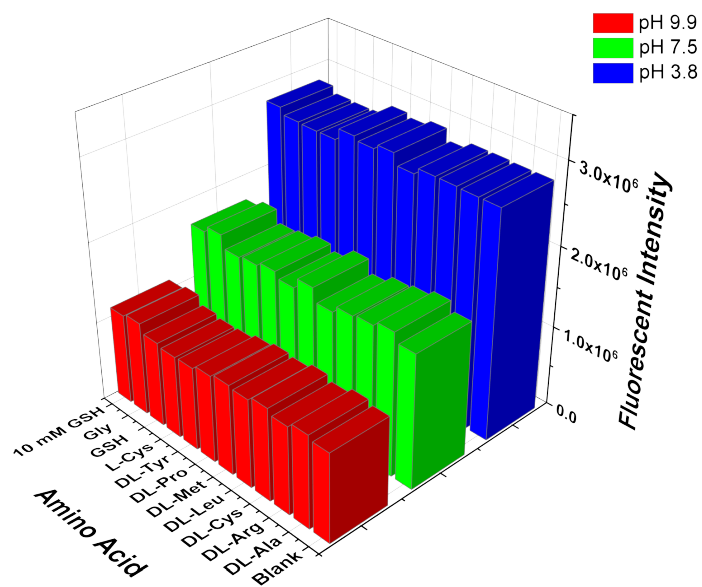
Figure S D.70. Fluorescence intensities of 5 μM probe **B** in the absence and presence of different amino acids (100 μM) in pH 3.8, 7.5 and 9.9 buffers under excitation at 600 nm.
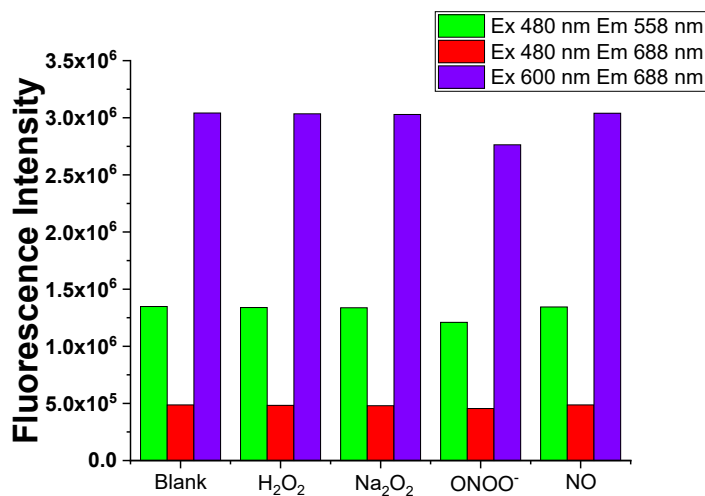
Figure S D.71. Fluorescence intensities of 5 μM probe **A** in the absence and presence of 50 μM reactive oxygen and nitrogen species including 100 μM hydrogen peroxide in pH 7.4 buffer under excitation at 480 nm or 600 nm.
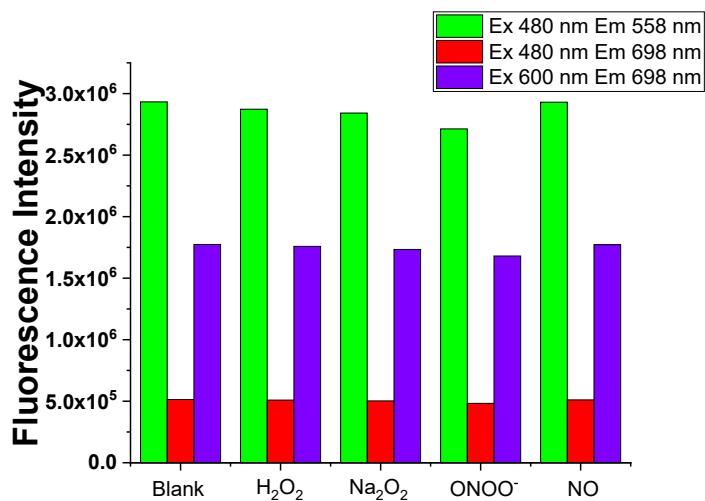
Figure S D.72. Fluorescence intensities of 5 μM probe **B** in the absence and presence of 50 μM reactive oxygen and nitrogen species including 100 μM hydrogen peroxide in pH 7.4 buffer under excitation at 480 nm or 600 nm.

6. Reversible fluorescence responses of probes A and B to pH changes.
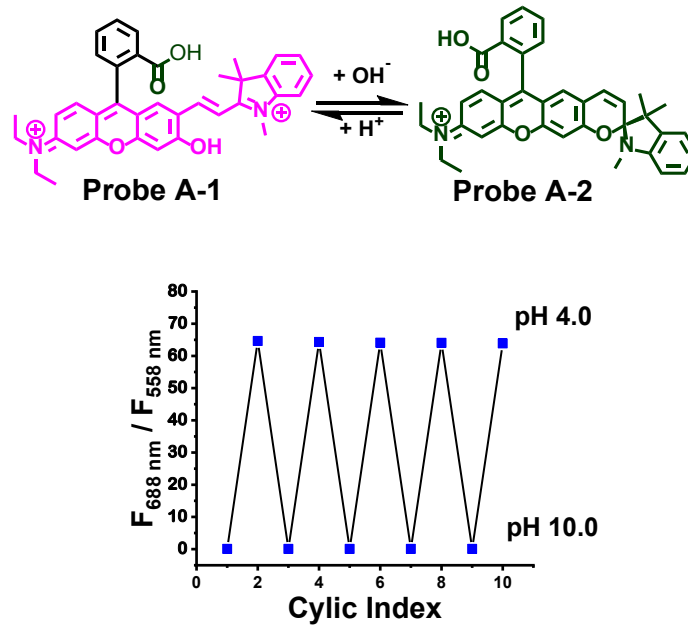
Figure S D.73. Fluorescence responses of 5 µM probe **A** in solution containing 30 % of ethanol under pH changes between 4.0 and 10.0 under excitation at 480 nm
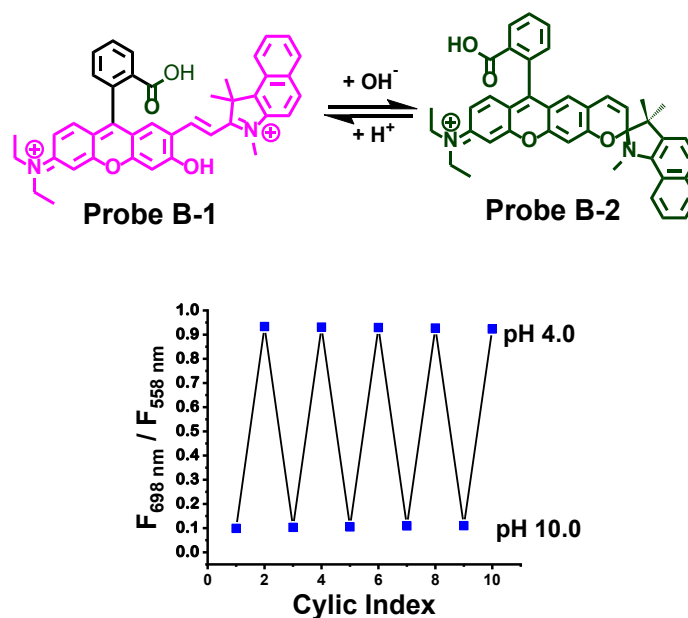
Figure S D.74. Fluorescence responses of 5 µM probe **B** in solution containing 30 % of ethanol between 4.0 and 10.0 under excitation at 480 nm

7. Photoswitch Properties of probes A and B

Probe A-3 → UV light → **Probe A-4**
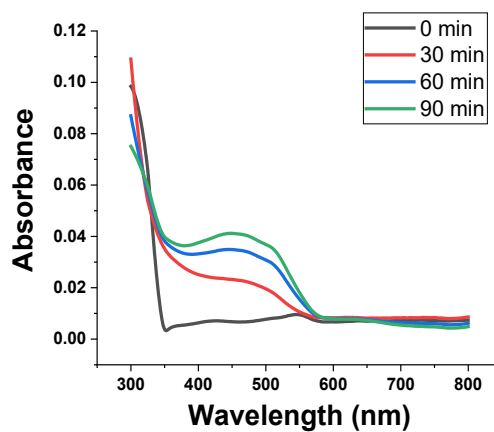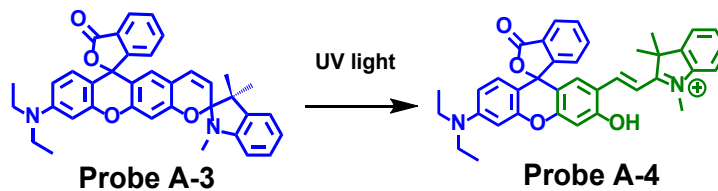
Figure S D.75. UV-Vis absorption spectra of 5 µM probe **A** in DMSO under UV light (254 nm).

Probe A-3 → UV light → **Probe A-4**
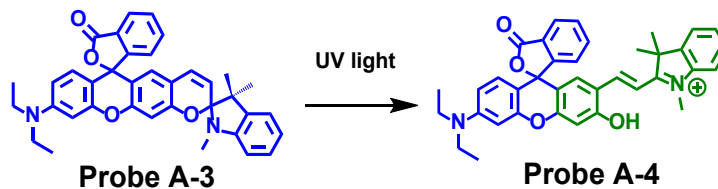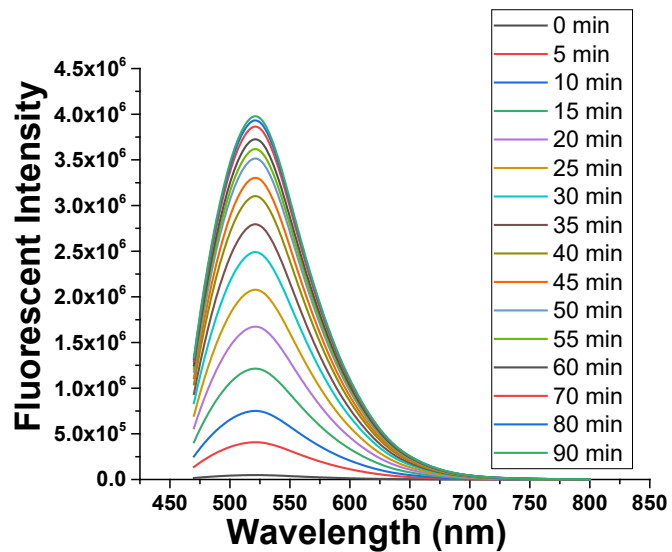
Figure S D.76. Fluorescent spectra of 5 µM probe **A** in DMSO under UV light (254 nm) at different times under excitation at 450 nm.

Equation	$y = a + b*x$
Plot	B
Weight	No Weighting
Intercept	0.02276 ± 0.0204
Slope	-0.02945 ± 0.0011
Residual Sum of Squares	0.00448
Pearson's r	-0.99633
R-Square (COD)	0.99267
Adj. R-Square	0.99121
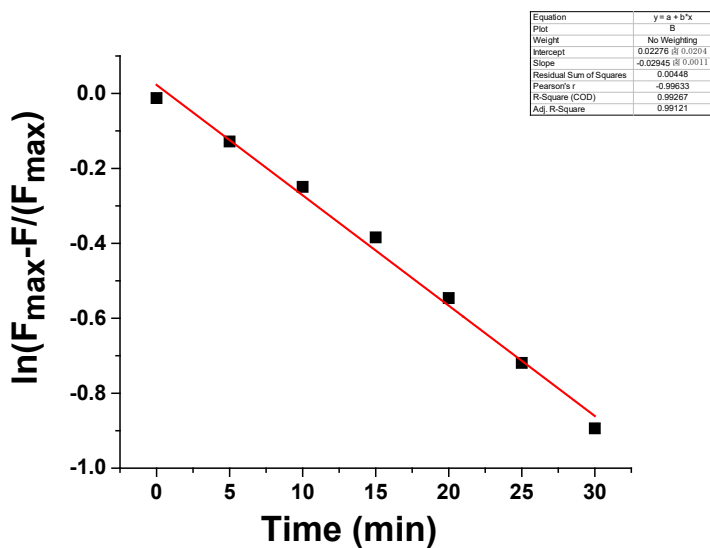
Figure S D.77. Fluorescence intensity of 5 µM probe **A** in DMSO under UV light (254 nm) to open the ring under excitation at 450 nm.
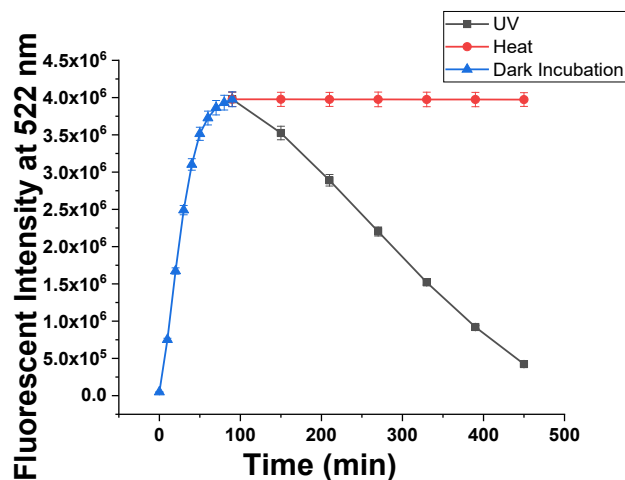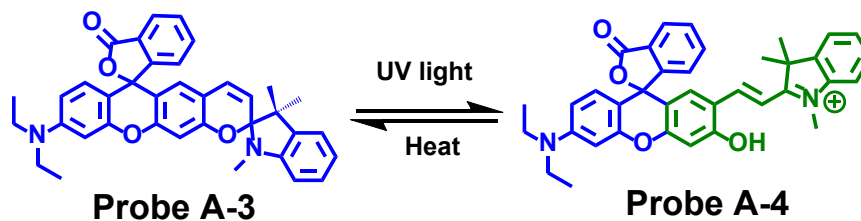
Figure S D.78. Fluorescence intensities of 5 µM probe **A** at 522 nm in DMSO under UV light (254 nm), heat (80 °C) or under dark incubation conditions with three repeated experiments.
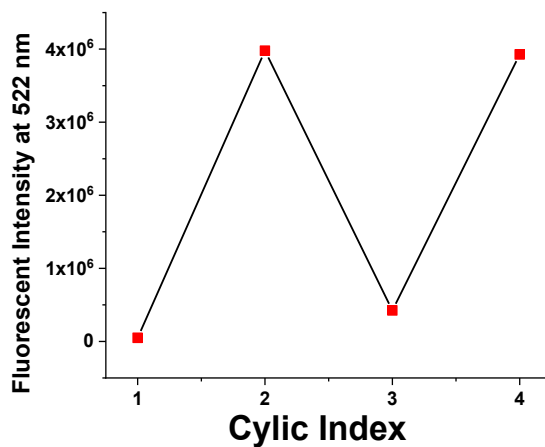
Figure S D.79. Photochemical reversibility of 5 µM probe **A** in DMSO under UV light (254 nm) and heat (80 °C).
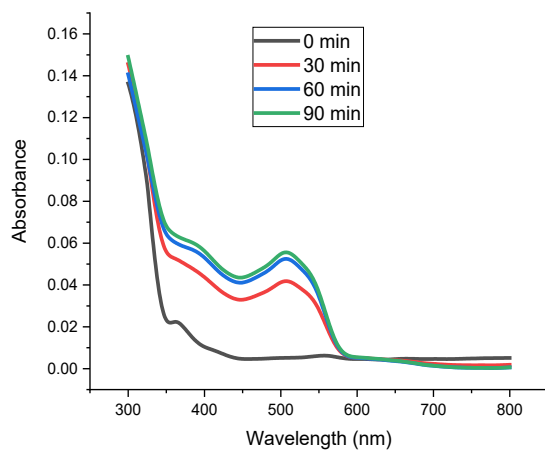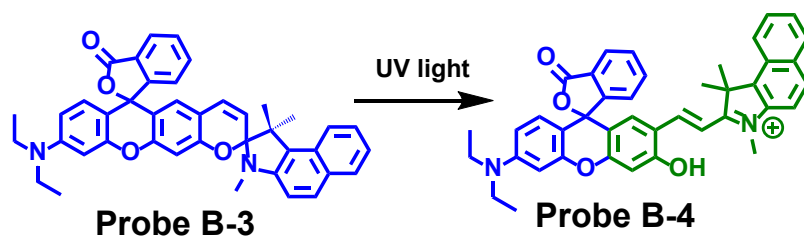
Figure S D.80. UV-Vis absorption spectra of 5 µM probe **B** in DMSO using UV light (254 nm).
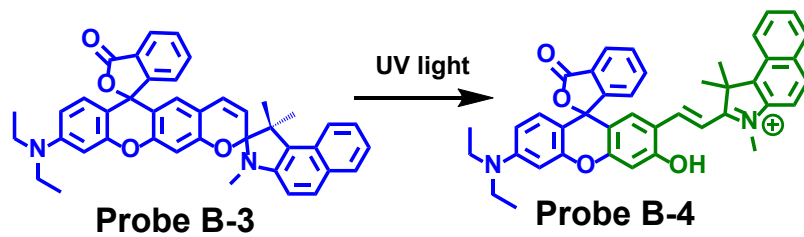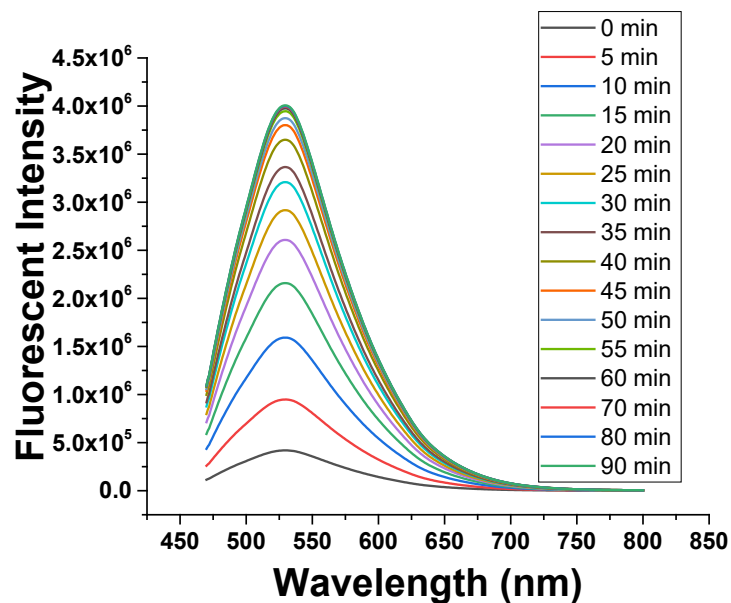
Figure S D.81. Fluorescent spectra of 5 µM probe **B** in DMSO under UV light (254 nm) to open the ring under excitation at 450 nm.
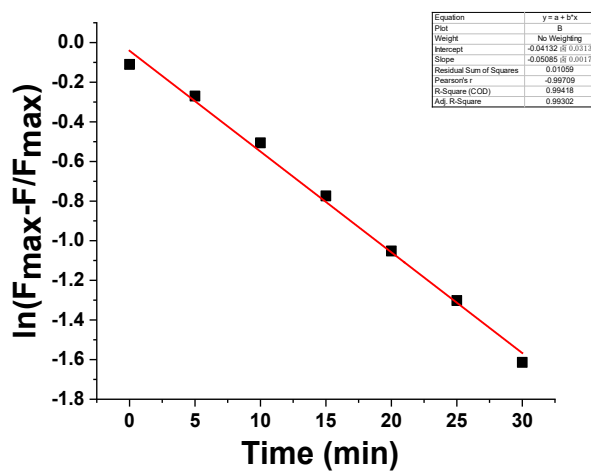
Figure S D.82. Fluorescence intensity of 5 µM probe **B** in DMSO under UV light (254 nm) to open the ring under excitation at 450 nm.

Probe B-3 → **Probe B-4**
(UV light / Heat)
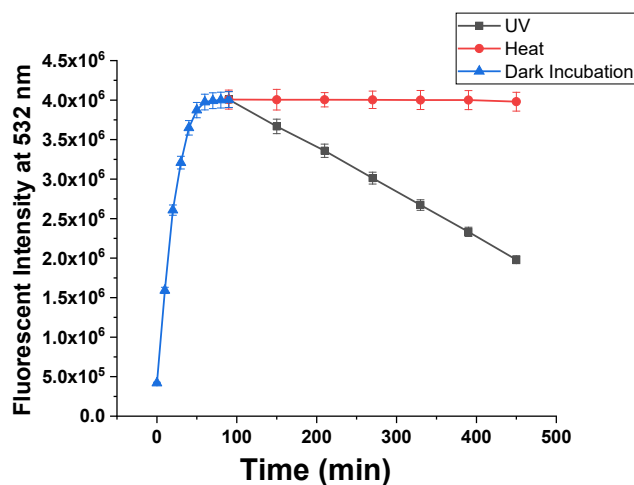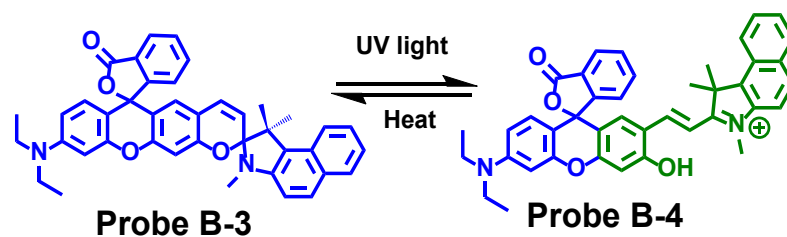
Figure S D.83. Fluorescence intensites of 5 µM probe **A** at 522 nm in DMSO under UV light (254 nm), heat (80 °C) or in dark incubation condition with three repeated experiments.
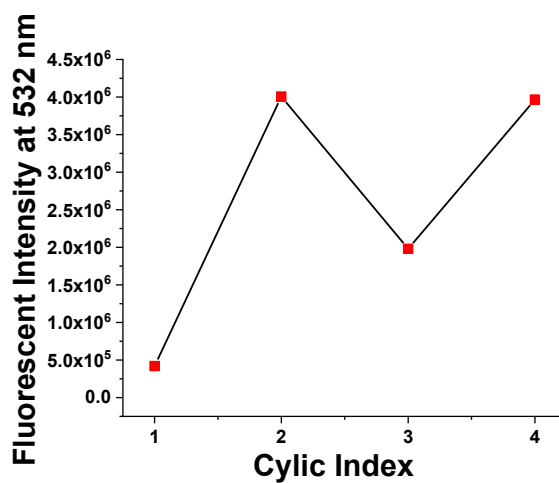
Figure S D.84. Photochemical reversibility of 5 µM probe **A** in DMSO under UV light (254 nm) and heat (80 °C).
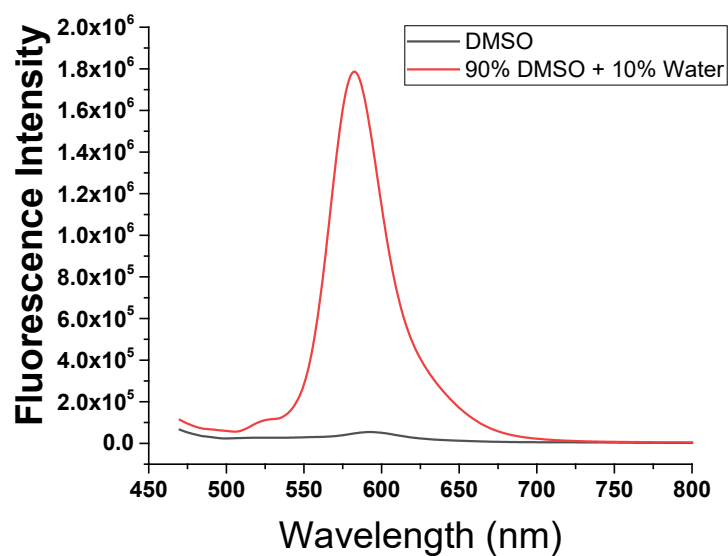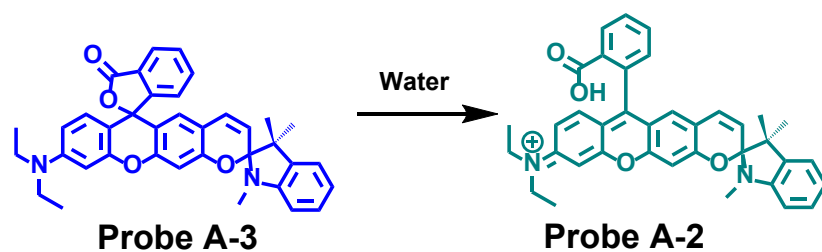
Figure S D.85. Fluorescence spectra of probe **A** in DMSO solution in the absence and presence of 10% water.
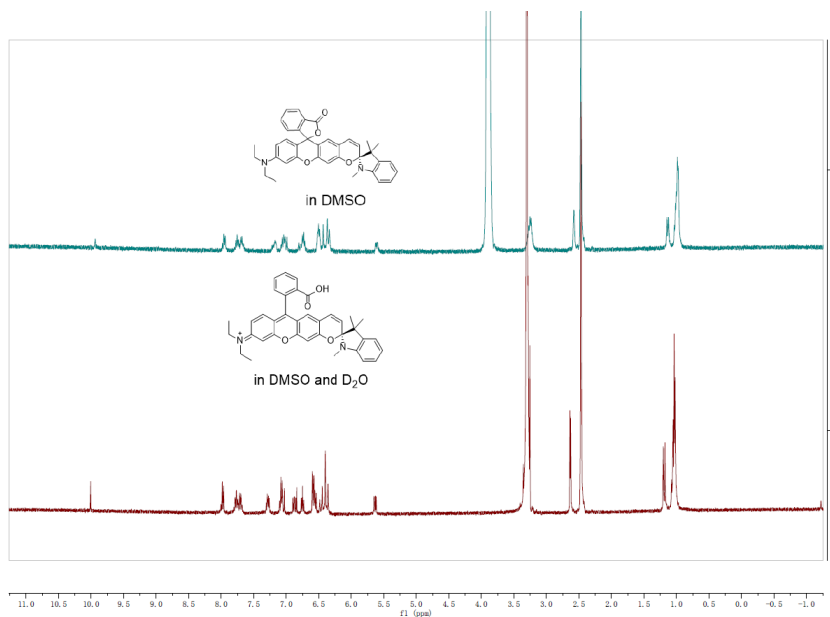
Figure S D.86. ^{1}H NMR spectra of probe **A** in DMSO-d$_6$ solution in the absence and presence of D$_2$O.
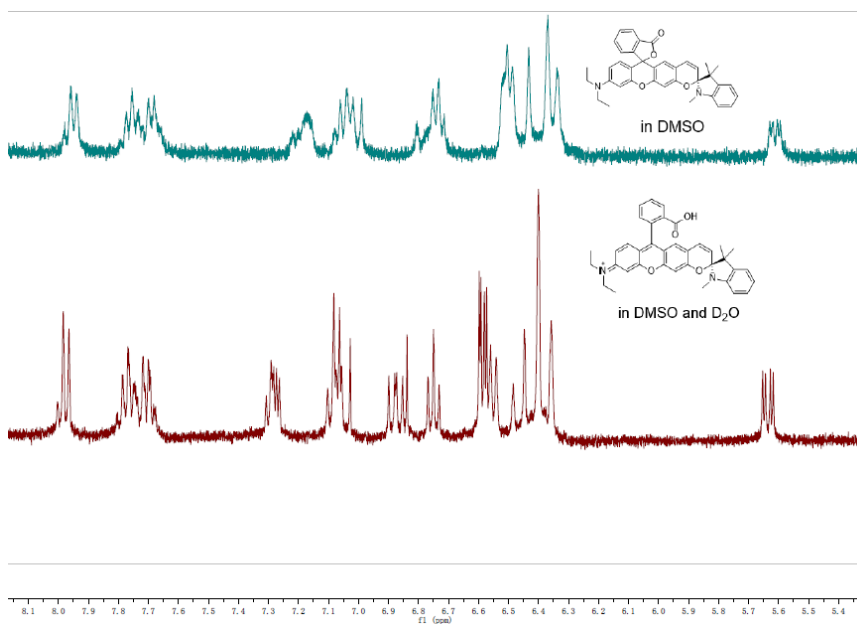
Figure S D.87. Enlarged partial ^{1}H NMR spectra of probe **A** in DMSO-d$_6$ solution in the absence and presence of D$_2$O from Figure S85.

8. Photostability of the probes
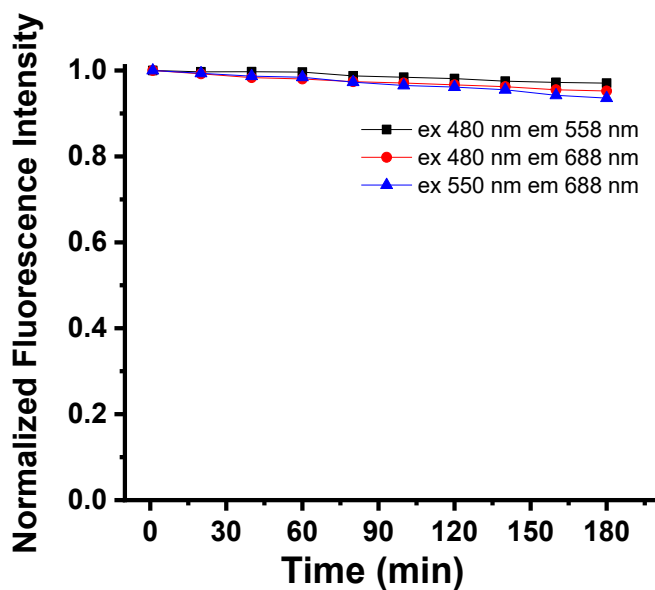
Figure S D.88. Photostability of probe **A** in pH 7.6 buffer under excitation of 480 nm and 550 nm with three repeated experiments.
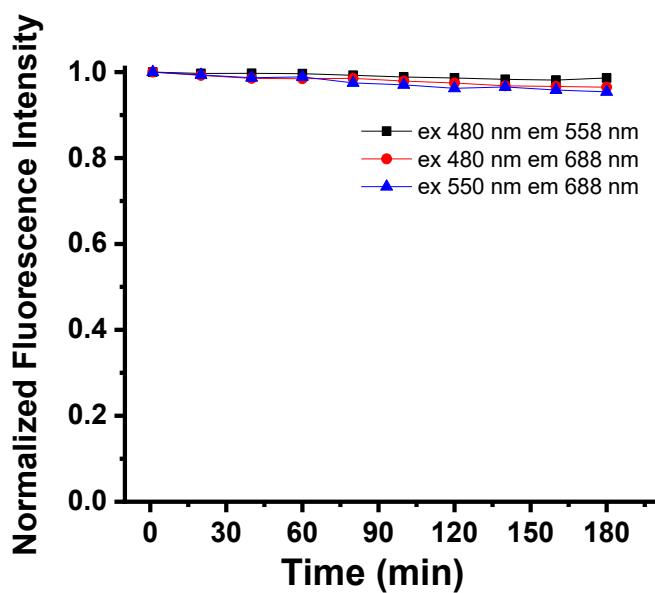
Figure S D.89. Photostability of probe **A** in pH 4.0 buffer under excitation of 480 nm and 550 nm with three repeated experiments.
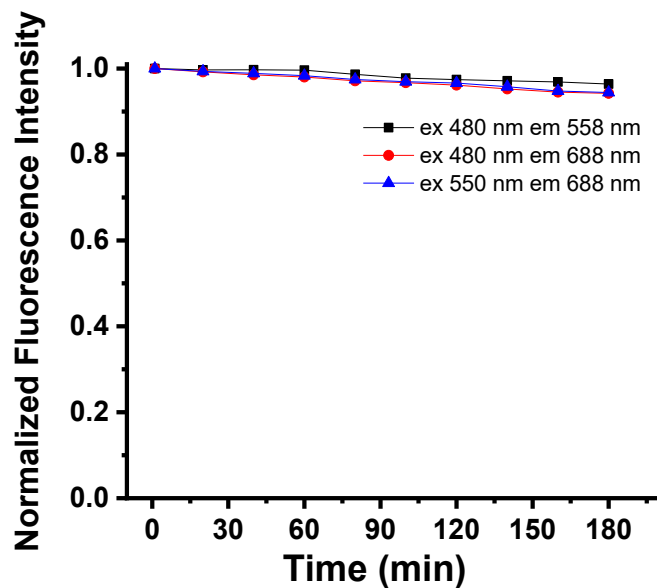
Figure S D.90. Photostability of probe **B** in pH 7.6 buffer under excitation of 480 nm and 550 nm with three repeated experiments.
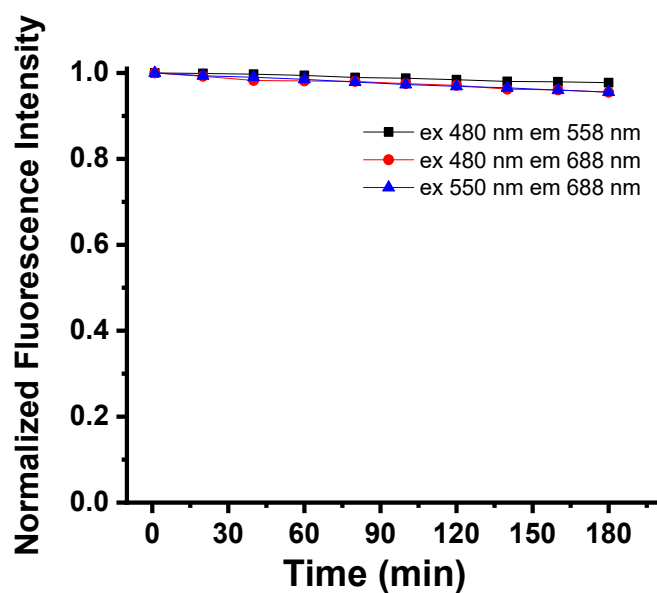
Figure S D.91. Photostability of probe **B** in pH 4.0 buffer under excitation of 480 nm and 550 nm with three repeated experiments.

9. Cell culture and cell imaging procedures

9.1 Cell culture and MTT cytotoxicity assay
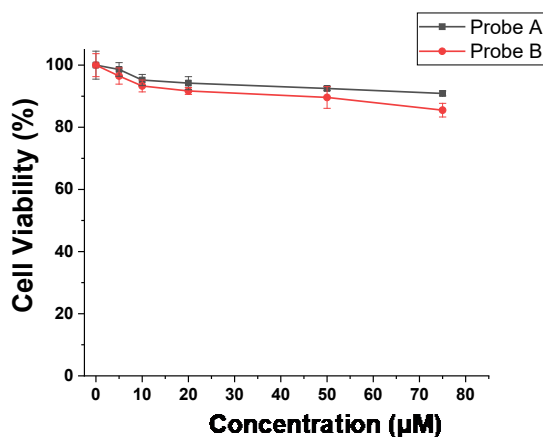
Figure S D.92. Cell cytotoxicity of probes **A** and **B** with 5, 10, 20, 50, 75 µM by MTT assay with three repeated experiments.

9.2 Confocal Microscopy imaging applications
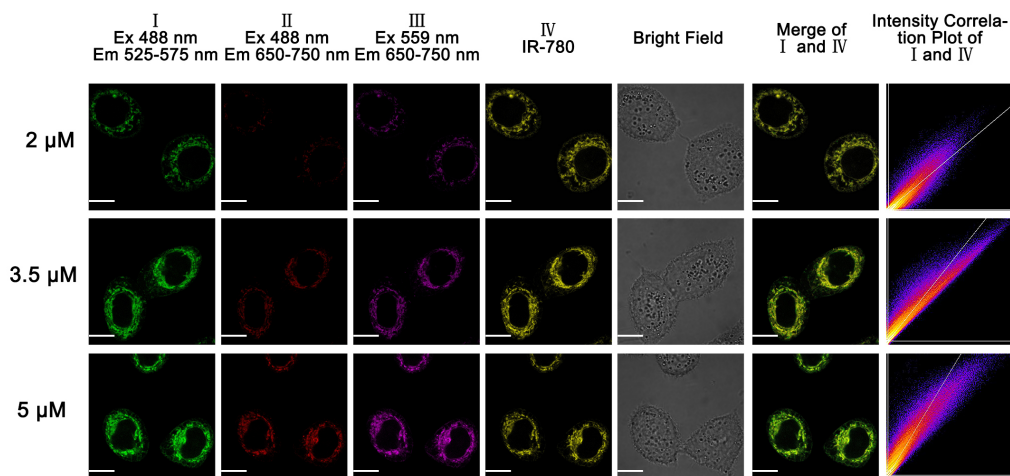
Figure S93. Fluorescence imaging of HeLa cells with 5 µM probe **B** (Ex 488 nm and 559 nm), 5 µM cyanine dye (IR-780) (upper, Ex 635 nm) in the presence of fetal bovine serum at 30-min incubation. Scale bar: 20 µm.

Cellular fluorescence intensity of probe **B** in HeL cells increases with probe concentration. high Pearson correlation coefficients of probe with cyanine dye (IR-780) further confirms that the probe **B** selectively stains mitochondria (Figure S92).
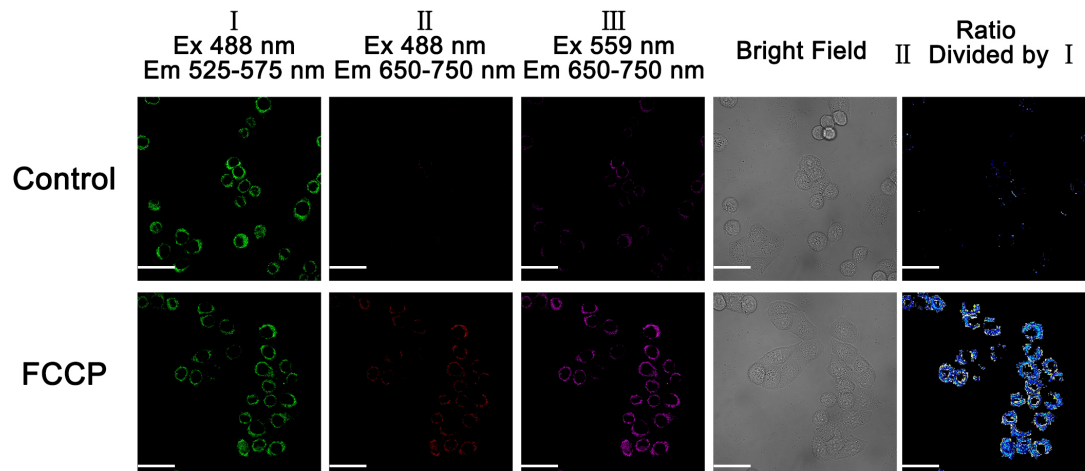
Figure S D.94. Fluorescence imaging of HeLa cells with 2.5 µM probe **B** (Ex 448 nm and 559 nm) in normal media at 20-min incubation before and after FCCP treatment. FCCP treatment was conducted as follows: Cells was incubated with 20 µM probe **B** for 20-min in normal medium, and further incubated with FCCP for 5 minutes. Cells were washed before we conducted confocal imaging. Scale bar: 50 µm

HeLa cells were seeded in 35 mm confocal glass bottom dishes (MatTek) with 1×10^5 cells per dish and cultured for 24 h. After HeLa cells were incubated with 3 µM probe **A** or 2.5 µM probe **B** for 20 min, the cells were washed with PBS buffer three times, and then further incubated with 3 µM of FCCP for 20 min. The cells were washed with PBS before the cellular fluorescence imaging was conducted.

In order to further confirm that the probes accumulate in mitochondria in live cells selectively, we further treat HeLa cells with an uncoupler of mitochondrial oxidative phosphorylation, FCCP (carbonyl cyanide 4-(trifluoromethoxy) phenylhydrazone). Upon further 20 min-incubation of HeLa cells in PBS buffer containing FCCP after the cells were incubated with probe **B** for 30 minutes in normal cell culture media, cellular visible fluorescence decreases and near-infrared fluorescence increases with dramatic color of ratio images from extremely weakly green to bluish green for probe **B** (Figure S94). These results indicate that FCCP treatment disrupts the mitochondrial membrane potential, and leads to apparent acidification of mitochondria, further confirming that the probe stays in mitochondria before FCCP treatment.
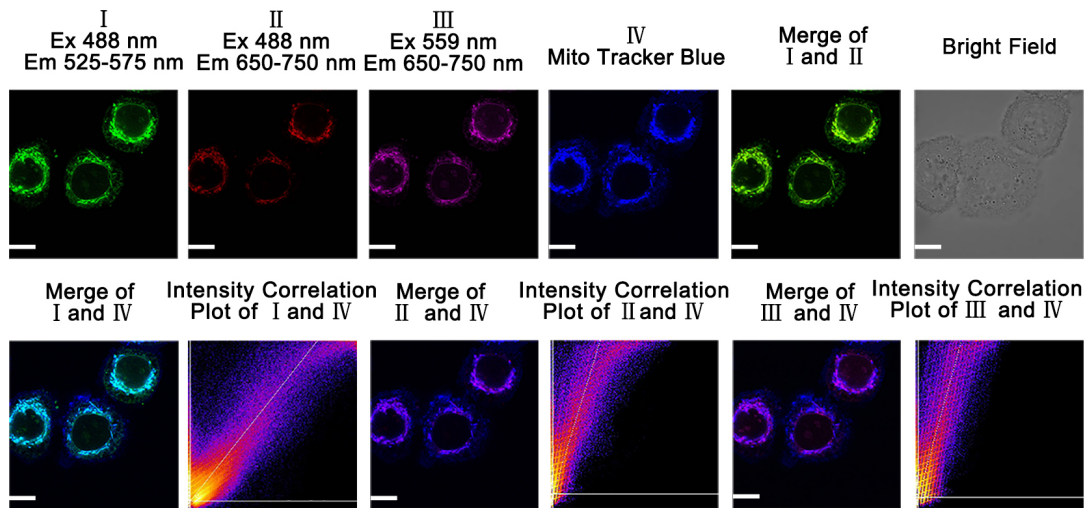
Figure S D.95. Fluorescence imaging of HeLa cells with 5 µM probe **A** and 10 µM Mito Tracker blue (Ex 405 nm) in normal medium containing fetal bovine serum under 30-min cell incubation with the probe and Mito Tracker blue. Scale bar: 20 µm. Pearson correlation coefficient between channel Ⅰ and channel Ⅳ: 0.93. Pearson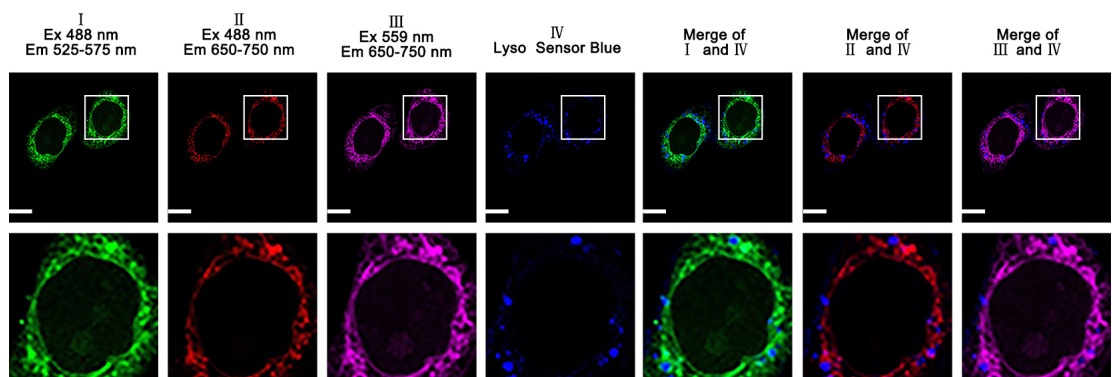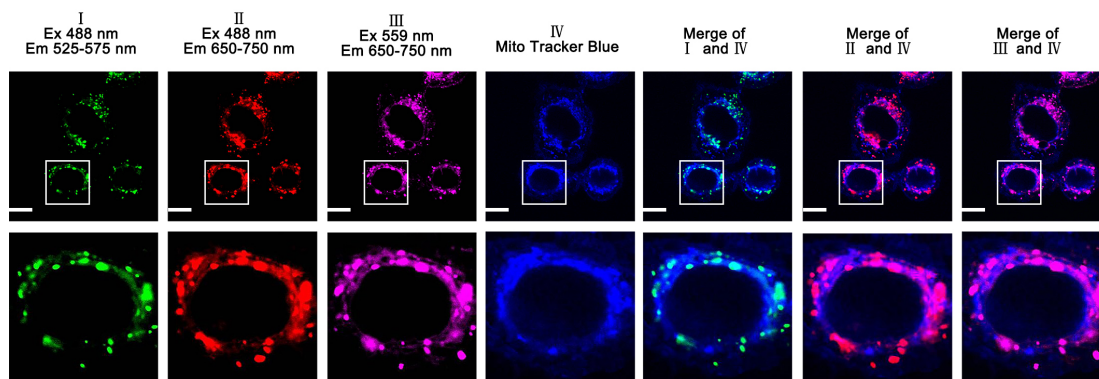 correlation coefficient between channel Ⅱ and channel Ⅳ: 0.90. Pearson correlation coefficient between channel Ⅲ and channel Ⅳ: 0.92.
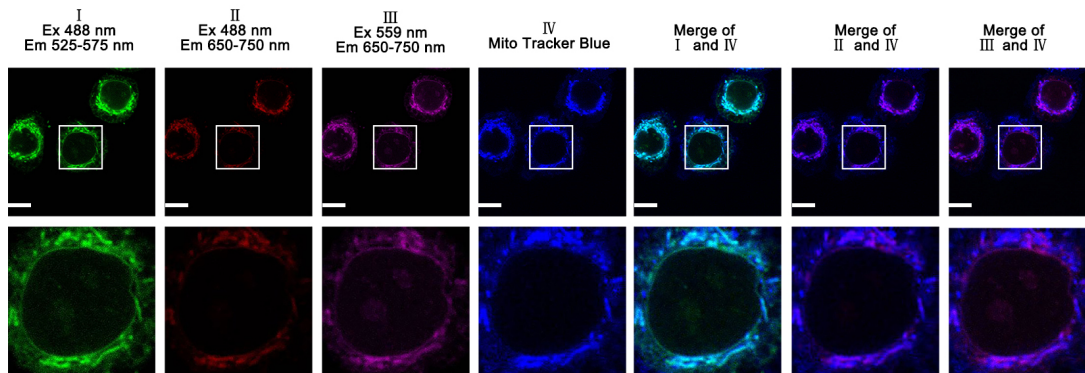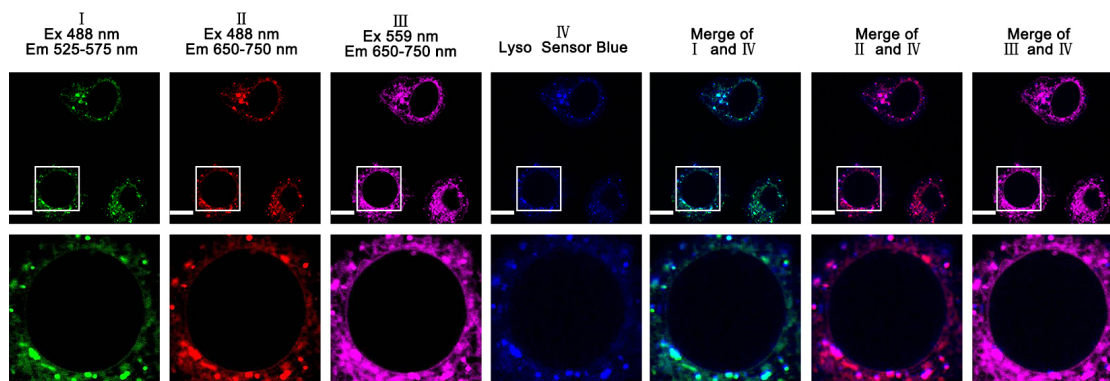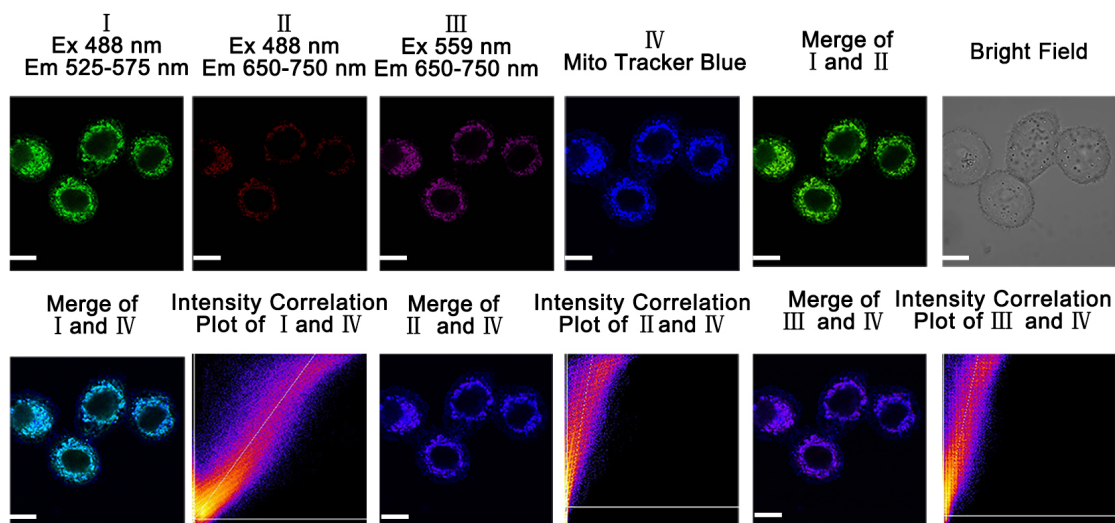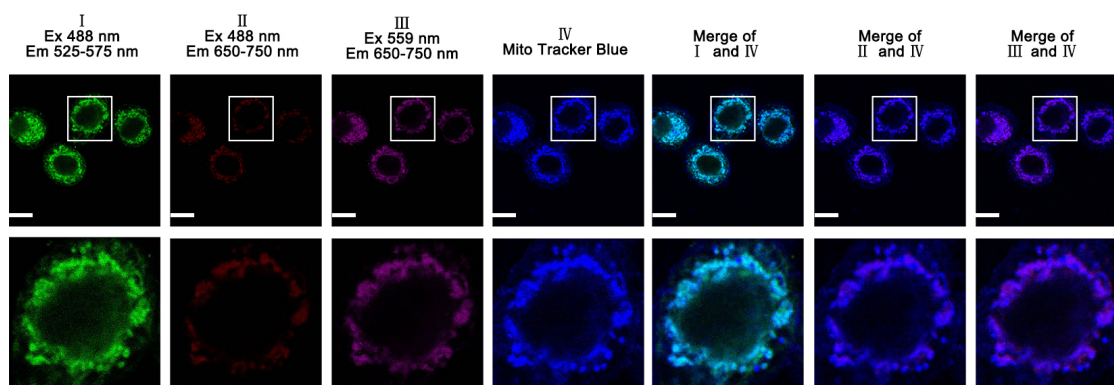

Figure S D.96. Enlarged fluorescence imaging of HeLa cells with 5 µM probe **A** and 10 µM Mito Tracker blue (Ex 405 nm) in normal medium containing fetal bovine serum under 30-min cell incubation with probe **A** and Mito Tracker blue. Scale bar: 20 µm.
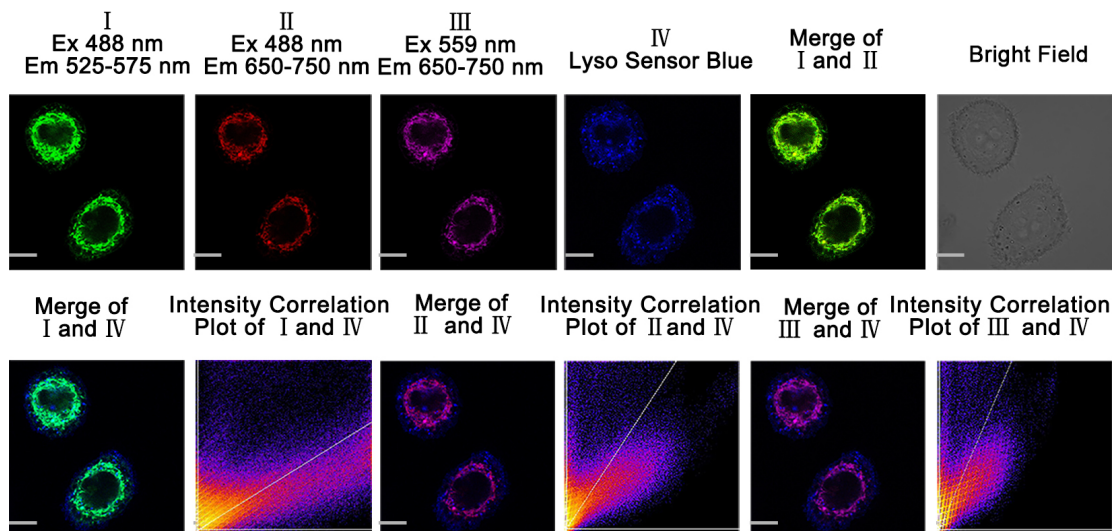
Figure S D.97. Fluorescence imaging of HeLa cells with 5 µM probe **A** and 10 µM Lysosensor blue (Ex 405 nm) in normal medium containing fetal bovine serum at 30-min incubation of probe **A** and Lysosensor blue. Scale bar: 20 µm. Pearson correlation coefficient between channel Ⅰ and channel Ⅳ: 0.67. Pearson correlation coefficient between channel Ⅱ and channel Ⅳ: 0.55. Pearson correlation coefficient between channel Ⅲ and channel Ⅳ: 0.53.
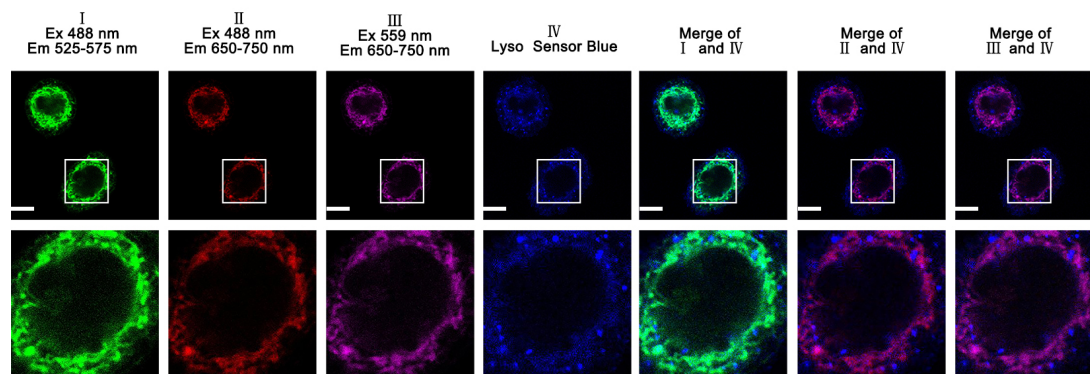
Figure S D.98. Enlarged fluorescence imaging of HeLa cells with 5 µM probe **A** and 10 µM Lysosensor blue (Ex 405 nm) in normal medium containing fetal bovine serum under 30-min incubation of probe **A** and Lysosensor blue with HeLa cells. Scale bar: 20 µm.

387
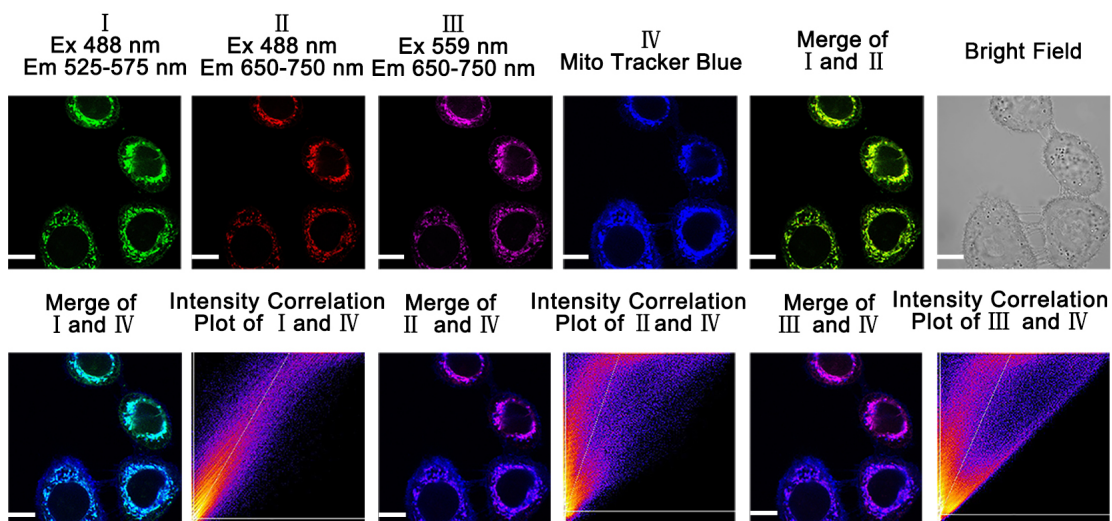
Figure S D.99. Fluorescence imaging of HeLa cells with 5 µM probe **A** and 10 µM Mito Tracker blue (Ex 405 nm) in normal medium containing fetal bovine serum at 2-h incubation of probe **A** and Mito Tracker blue. Scale bar: 20 µm. Pearson correlation coefficient between channel Ⅰ and channel Ⅳ: 0.95. Pearson correlation coefficient between channel Ⅱ and channel Ⅳ: 0.89. Pearson correlation coefficient between channel Ⅲ and channel Ⅳ: 0.91.
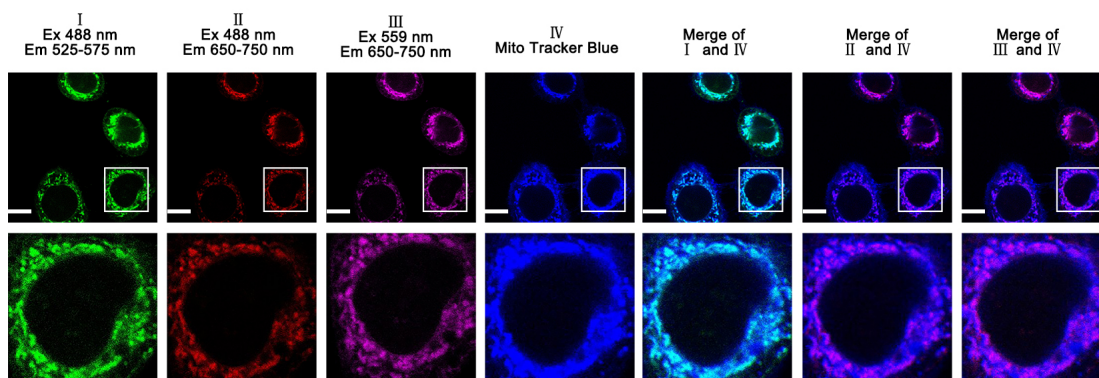
Figure S D.100. Enlarged fluorescence imaging of HeLa cells with 5 µM probe **A** and 10 µM Mito Tracker blue (Ex 405 nm) in normal medium containing fetal bovine serum at 2-h incubation of probe **A** and Mito Tracker blue with HeLa cells. Scale bar: 20 µm.
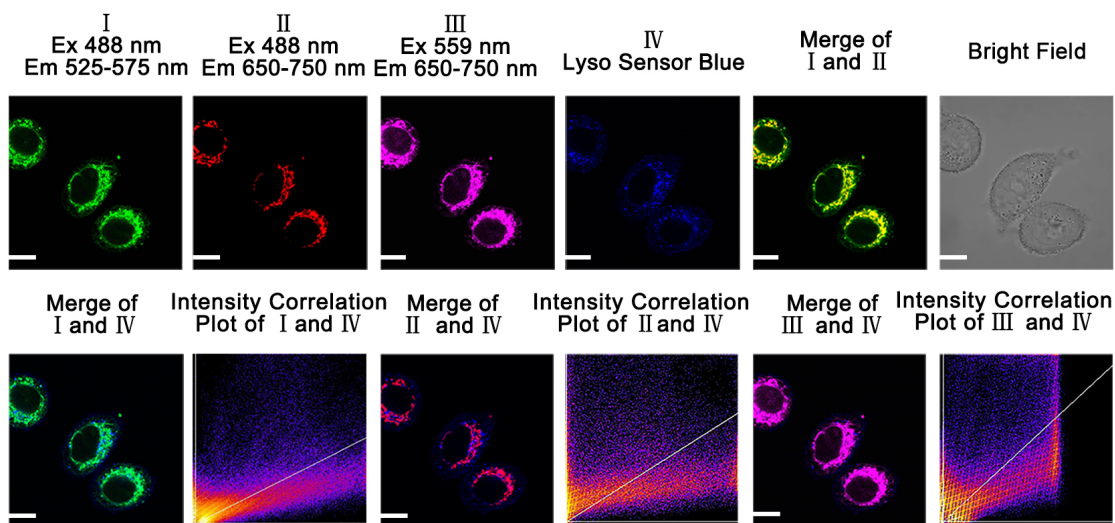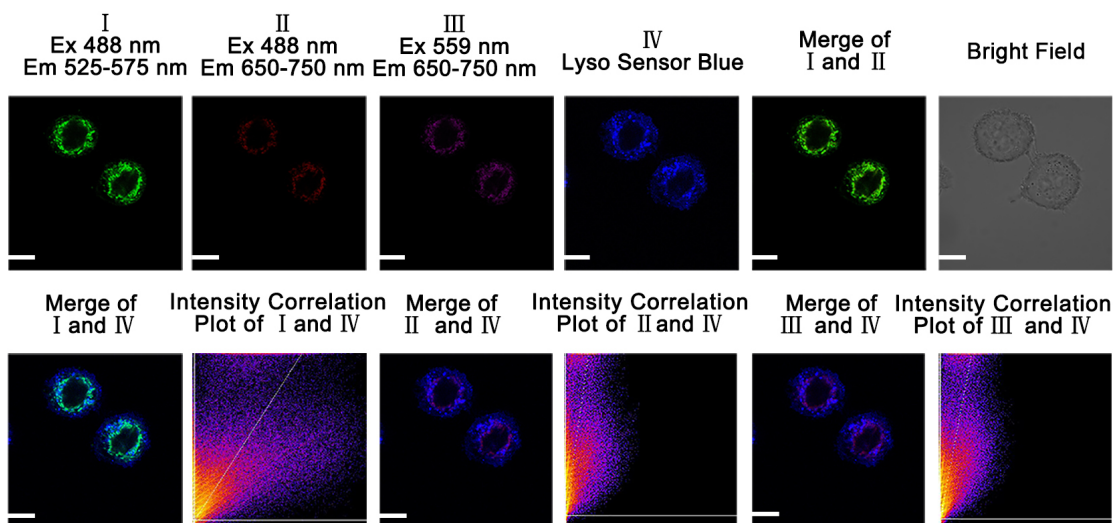
Figure S D.101. Fluorescence imaging of HeLa cells with 5 μM probe **A** and 10 μM Lysosensor blue (Ex 405 nm) in normal medium containing fetal bovine serum at 2-h incubation of probe **A** and Lysosensor blue. Scale bar: 20 μm. Pearson correlation coefficient between channel Ⅰ and channel Ⅳ: 0.69. Pearson correlation coefficient between channel Ⅱ and channel Ⅳ: 0.61. Pearson correlation coefficient between channel Ⅲ and channel Ⅳ: 0.66.
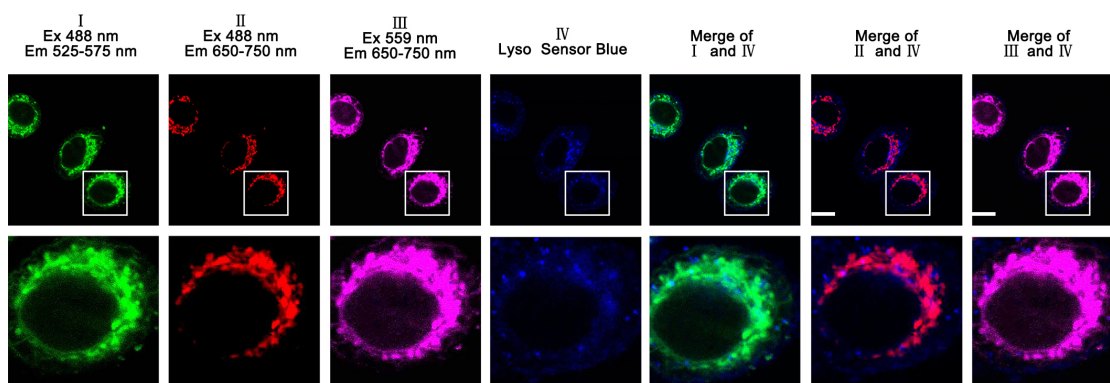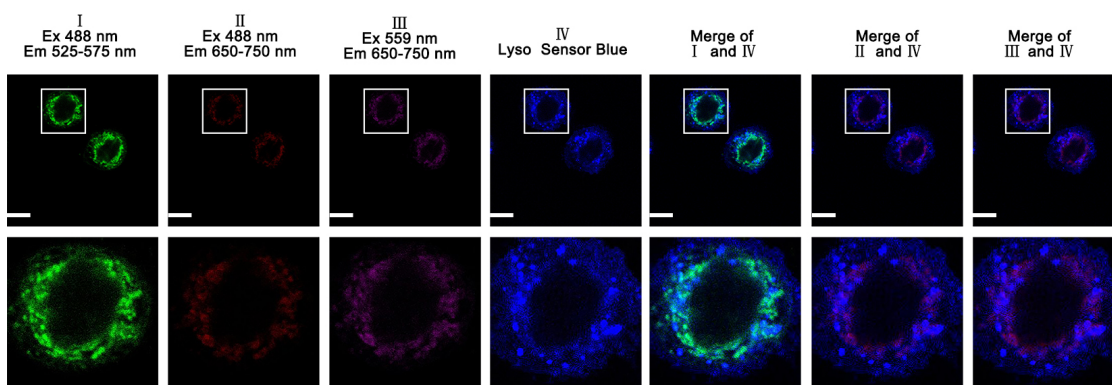

Figure S D.102. Enlarged fluorescence imaging of HeLa cells with 5 μM probe **A** and 10 μM Lysosensor blue (Ex 405 nm) in normal medium containing fetal bovine serum at 2-h incubation of probe **A** and Lysosensor blue with HeLa cells. Scale bar: 20 μm.
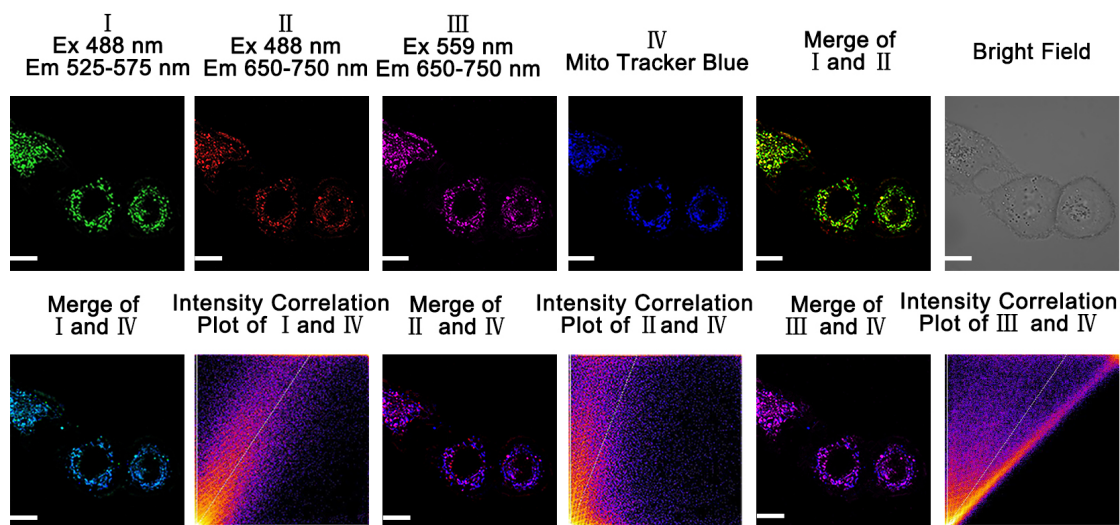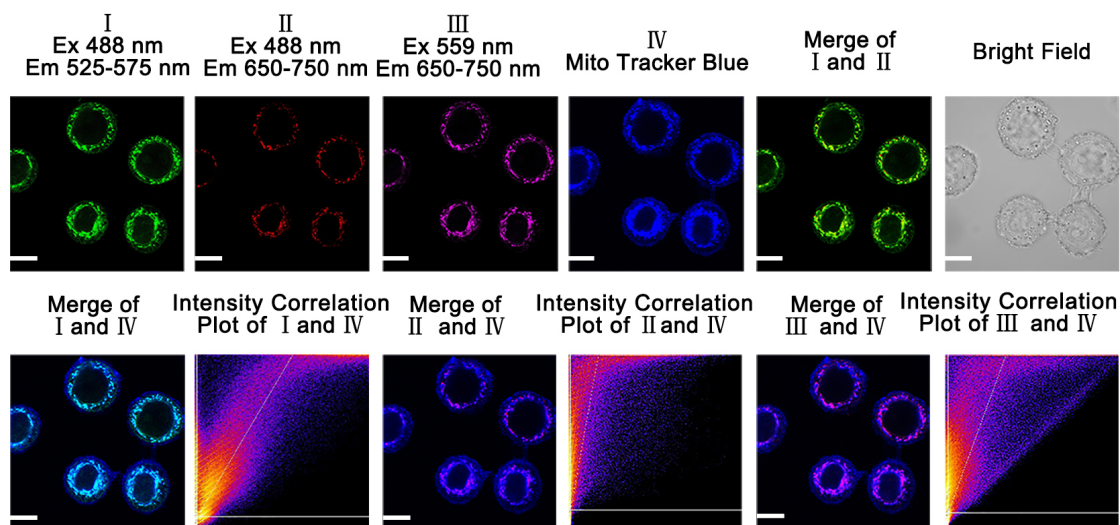
Figure S D.103. Fluorescence imaging of HeLa cells with 5 µM probe **A** and 10 µM Mito Tracker blue (Ex 405 nm) in serum-free medium at 30-min incubation of probe **A** and Mito Tracker blue with HeLa cells. Scale bar: 20 µm. Pearson correlation coefficient between channel Ⅰ and channel Ⅳ: 0.92. Pearson correlation coefficient between channel Ⅱ and channel Ⅳ: 0.88. Pearson correlation coefficient between channel Ⅲ and channel Ⅳ: 0.89.
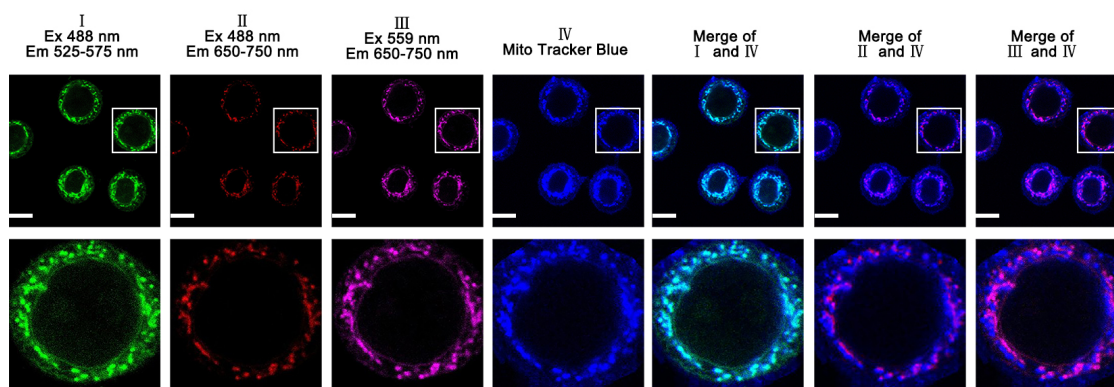

Figure S D.104. Enlarged fluorescence imaging of HeLa cells with 5 µM probe **A** and 10 µM Mito Tracker blue (Ex 405 nm) in serum-free medium at 30-min incubation of probe **A** and Mito Tracker blue with HeLa cells. Scale bar: 20 µm.

390

Figure S D.105. Fluorescence imaging of HeLa cells with 5 µM probe **A** and 10 µM Lysosensor blue (Ex 405 nm) in serum-free medium at 30-min incubation of probe **A** and Lysosensor blue with HeLa cells. Scale bar: 20 µm. Pearson correlation coefficient between channel Ⅰ and channel Ⅳ: 0.44. Pearson correlation coefficient between channel Ⅱ and channel Ⅳ: 0.51. Pearson correlation coefficient between channel Ⅲ and channel Ⅳ: 0.48.

Figure S D.106. Enlarged fluorescence imaging of HeLa cells with 5 µM probe **A** and 10 µM Lysosensor blue (Ex 405 nm) in serum-free medium at 30-min incubation of probe **A** and Lysosensor blue with HeLa cells. Scale bar: 20 µm
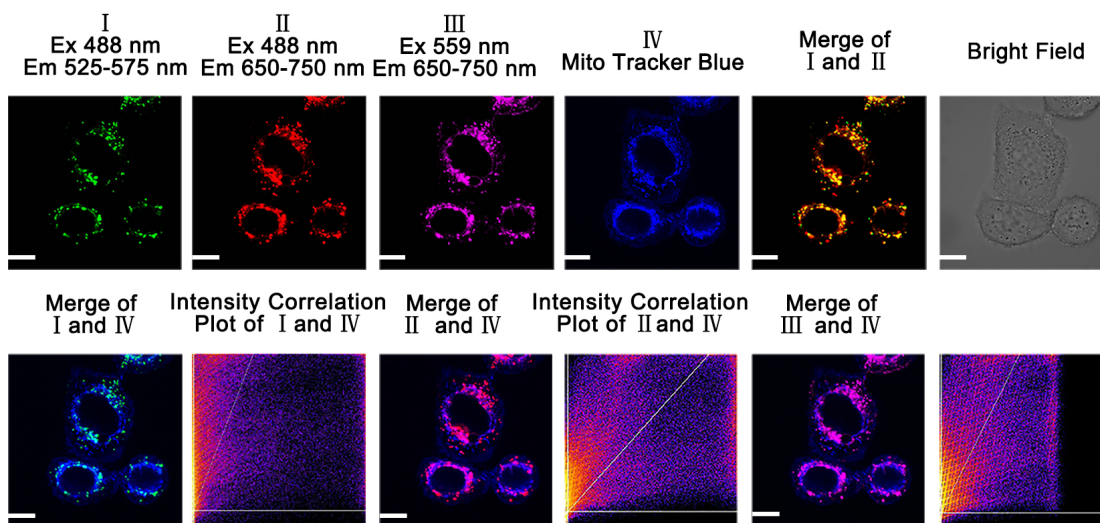
Figure S D.107. Fluorescence imaging of HeLa cells with 5 µM probe **A** and 10 µM Mito Tracker blue (Ex 405 nm) in serum-free medium at 2-h incubation of probe A and Mito Tracker blue with HeLa cells. Scale bar: 20 µm. Pearson correlation coefficient between channel Ⅰ and channel Ⅳ: 0.49. Pearson correlation coefficient between channel Ⅱ and channel Ⅳ: 0.57. Pearson correlation coefficient between channel Ⅲ and channel Ⅳ: 0.62.
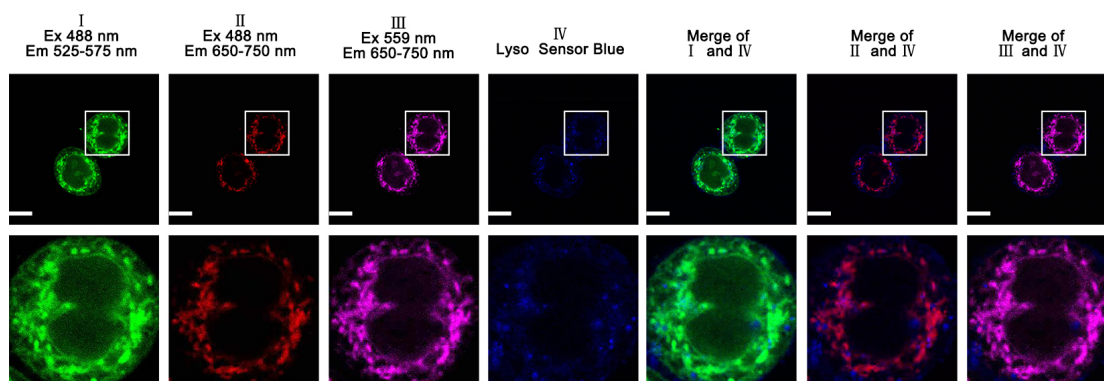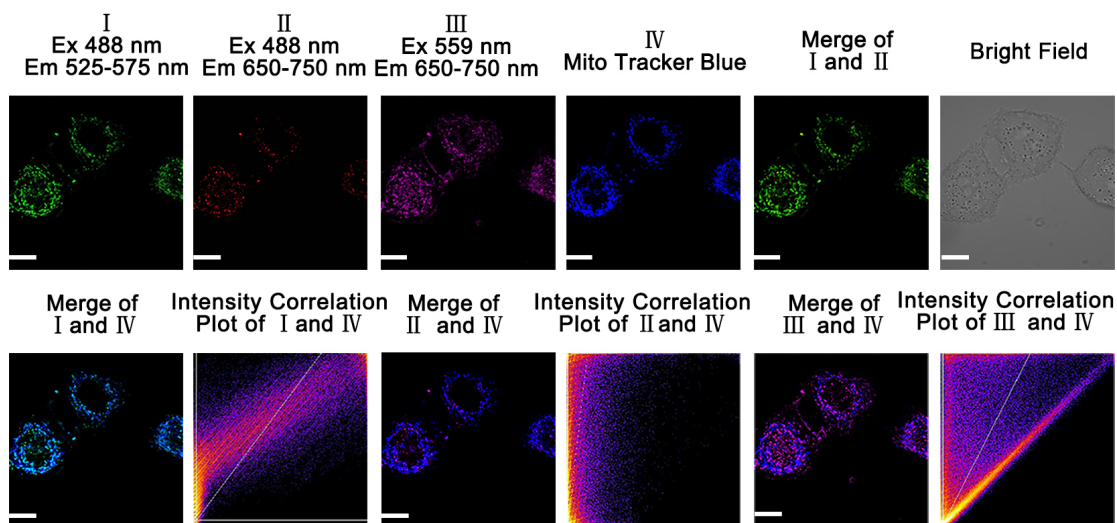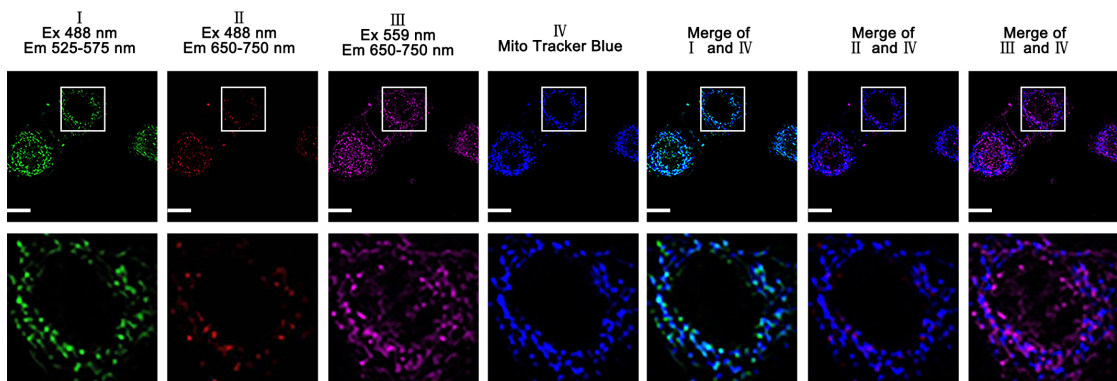

Figure S D.108. Enlarged fluorescence imaging of HeLa cells with 5 µM probe **A** and 10 µM Mito Tracker blue (Ex 405 nm) in serum-free medium at 2-h incubation of probe **A** and Mito Tracker blue with HeLa cells. Scale bar: 20 µm
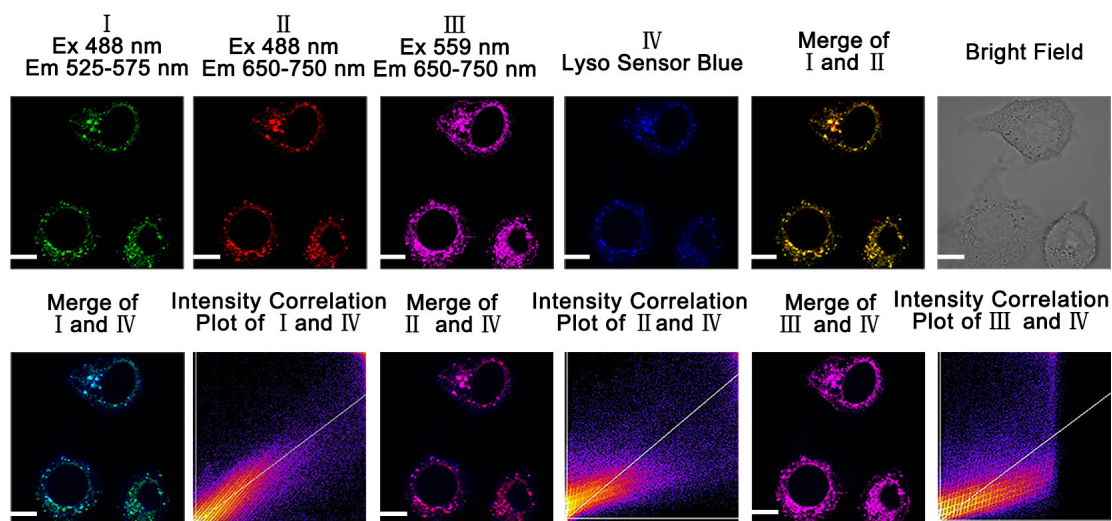
Figure S D.109. Fluorescence imaging of HeLa cells with 5 µM probe **A** and 10 µM Lysosensor blue (Ex 405 nm) in serum-free medium at 2-h incubation of probe A and Lysosensor blue with HeLa cells. Scale bar: 20 µm. Pearson correlation coefficient between channel Ⅰ and channel Ⅳ: 0.93. Pearson correlation coefficient between channel Ⅱ and channel Ⅳ: 0.92. Pearson correlation coefficient between channel Ⅲ and channel Ⅳ: 0.93.
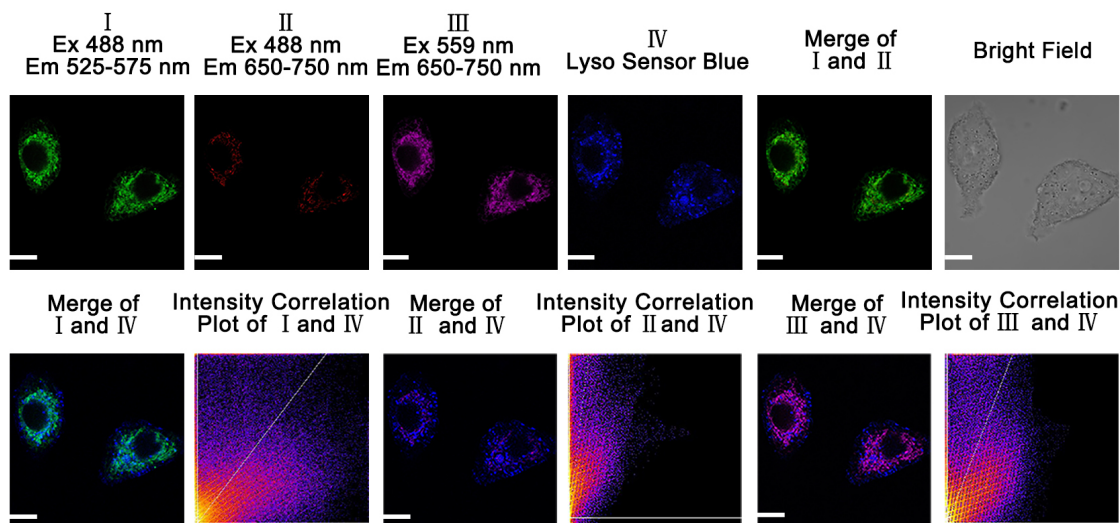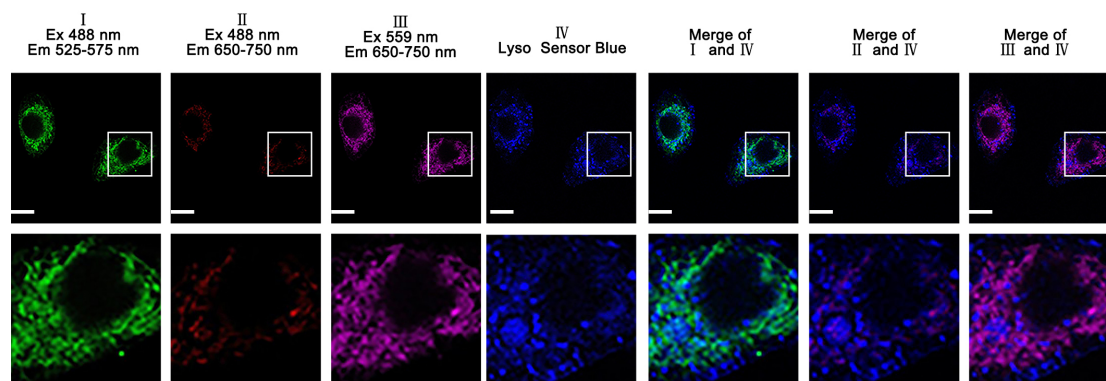

Figure S D.110. Enlarged fluorescence imaging of HeLa cells with 5 µM probe **A** and 10 µM Lysosensor blue (Ex 405 nm) in serum-free medium at 2-h incubation of probe **A** and Lysosensor blue with HeLa cells. Scale bar: 20 µm

Figure S D.111. Fluorescence imaging of HeLa cells with 5 µM probe **B** and 10 µM Mito Tracker blue (Ex 405 nm) in normal medium containing fetal bovine serum at 30-min incubation of probe **B** and Mito Tracker blue with HeLa cells. Scale bar: 20 µm. Pearson correlation coefficient between channel Ⅰ and channel Ⅳ: 0.97. Pearson correlation coefficient between channel Ⅱ and channel Ⅳ: 0.92. Pearson correlation coefficient between channel Ⅲ and channel Ⅳ: 0.95.

Figure S D.112. Enlarged fluorescence imaging of HeLa cells with 5 µM probe **B** and 10 µM Mito Tracker blue (Ex 405 nm) in normal medium containing fetal bovine serum at 30-min incubation of probe **B** and Mito Tracker blue. Scale bar: 20 µm.

Figure S D.113. Fluorescence imaging of HeLa cells with 5 µM probe **B** and 10 µM Lysosensor blue (Ex 405 nm) in normal medium containing fetal bovine serum at 30-min incubation of probe **B** and Lysosensor blue with HeLa cells. Scale bar: 20 µm. Pearson correlation coefficient between channel Ⅰ and channel Ⅳ: 0.35. Pearson correlation coefficient between channel Ⅱ and channel Ⅳ: 0.44. Pearson correlation coefficient between channel Ⅲ and channel Ⅳ: 0.38.

Figure S D.114. Enlarged fluorescence imaging of HeLa cells with 5 µM probe **B** and 10 µM Lysosensor blue (Ex 405 nm) in normal medium containing fetal bovine serum at 30-min incubation of probe **B** and Lysosensor blue with HeLa cells. Scale bar: 20 µm.

Figure S D.115. Fluorescence imaging of HeLa cells with 5 µM probe **B** and 10 µM Mito Tracker blue (Ex 405 nm) in the presence of fetal bovine serum at 2-h incubation of probe **B** and Mito Tracker blue with HeLa cells. Scale bar: 20 µm. Pearson correlation coefficient between channel Ⅰ and channel Ⅳ: 0.94. Pearson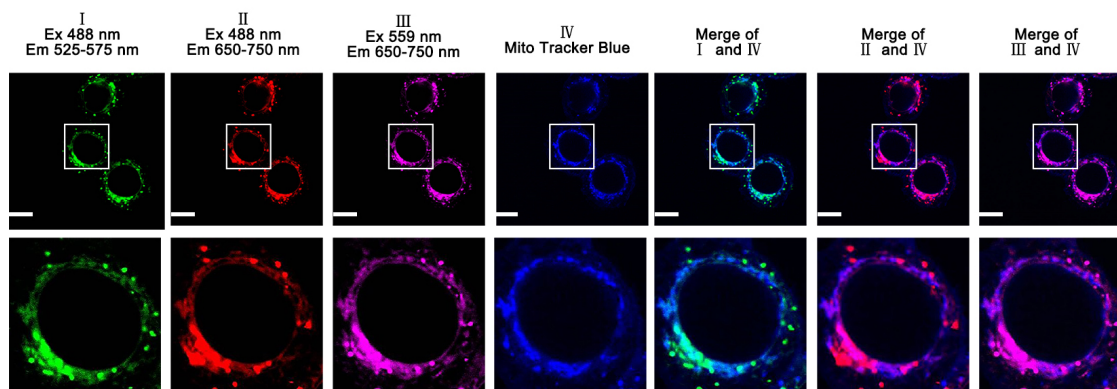 correlation coefficient between channel Ⅱ and channel Ⅳ: 0.90. Pearson correlation coefficient between channel Ⅲ and channel Ⅳ: 0.93.

Figure S D.116. Enlarged fluorescence imaging of HeLa cells with 5 µM probe **B** and 10 µM Mito Tracker blue (Ex 405 nm) in normal medium containing fetal bovine serum at 2-h incubation of probe **B** and Mito Tracker blue with HeLa cells. Scale bar: 20 µm.
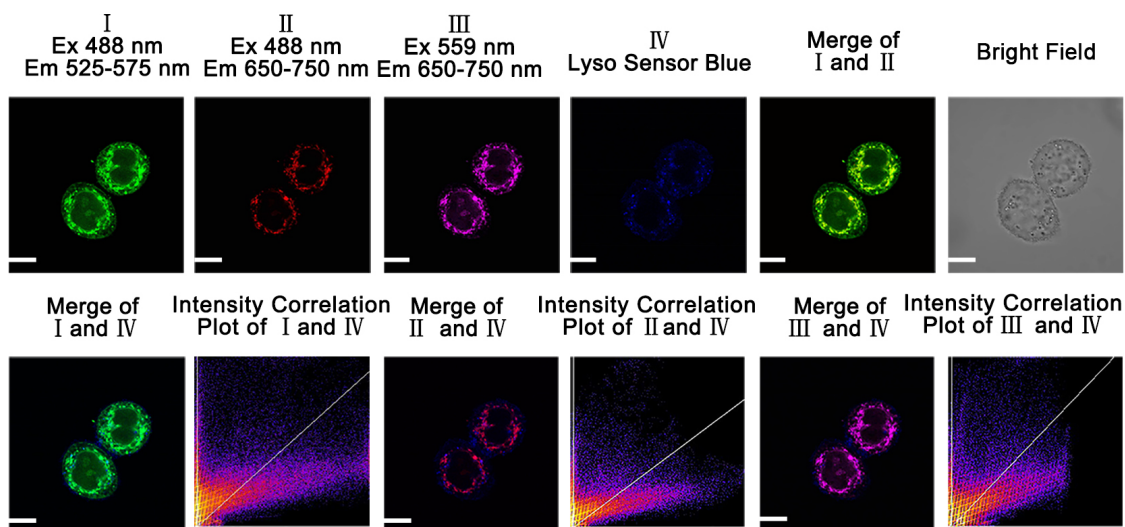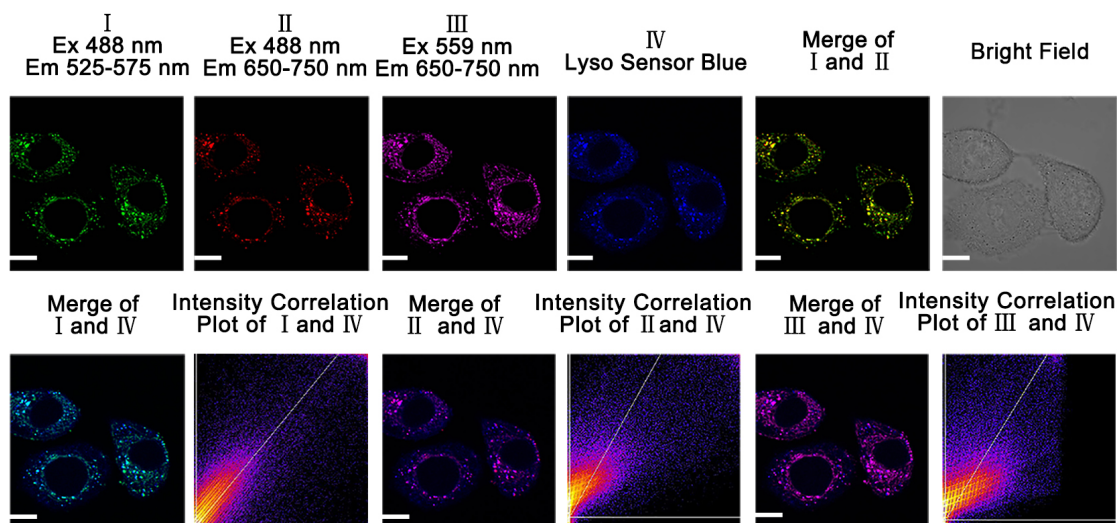
Figure S D.117. Fluorescence imaging of HeLa cells with 5 µM probe **B** and 10 µM Lysosensor blue (Ex 405 nm) in normal medium containing fetal bovine serum at 2-h incubation of probe **B** and Lysosensor with HeLa cells. Scale bar: 20 µm. Pearson correlation coefficient between channel Ⅰ and channel Ⅳ: 0.51. Pearson correlation coefficient between channel Ⅱ and channel Ⅳ: 0.50. Pearson correlation coefficient between channel Ⅲ and channel Ⅳ: 0.55.

Figure S D.118. Enlarged fluorescence imaging of HeLa cells with 5 µM probe **B** and 10 µM Lysosensor blue (Ex 405 nm) in normal medium containing fetal bovine serum at 2-h incubation of probe **B** and Lysosesnor blue with HeLa cells. Scale bar: 20 µm.

Figure S D.119. Fluorescence imaging of HeLa cells with 5 µM probe **B** and 10 µM Mito Tracker blue (Ex 405 nm) in serum-free medium at 30-min incubation of probe **B** and Mito Tracker blue with HeLa cells. Scale bar: 20 µm. Pearson correlation coefficient between channel Ⅰ and channel Ⅳ: 0.91. Pearson correlation coefficient between channel Ⅲ and channel Ⅳ: 0.88.

Figure S D.120. Enlarged fluorescence imaging of HeLa cells with 5 µM probe **B** and 10 µM Mito Tracker blue (Ex 405 nm) in serum-free medium at 30-min incubation of probe **B** and Mito Tracker blue with HeLa cells. Scale bar: 20 µm

398

Figure S D.121. Fluorescence imaging of HeLa cells with 5 µM probe **B** and 10 µM Lysosensor blue (Ex 405 nm) in serum-free medium at 30-min incubation of probe **B** and Lysosensor blue with HeLa cells. Scale bar: 20 µm. Pearson correlation coefficient between channel Ⅰ and channel Ⅳ: 0.46. Pearson correlation coefficient between channel Ⅲ and channel Ⅳ: 0.51.

Figure S D.122. Enlarged fluorescence imaging of HeLa cells with 5 µM probe **B** and 10 µM Lysosensor blue (Ex 405 nm) in serum-free medium at 30-min incubation of probe **B** and Lysosensor blue with HeLa cells. Scale bar: 20 µm
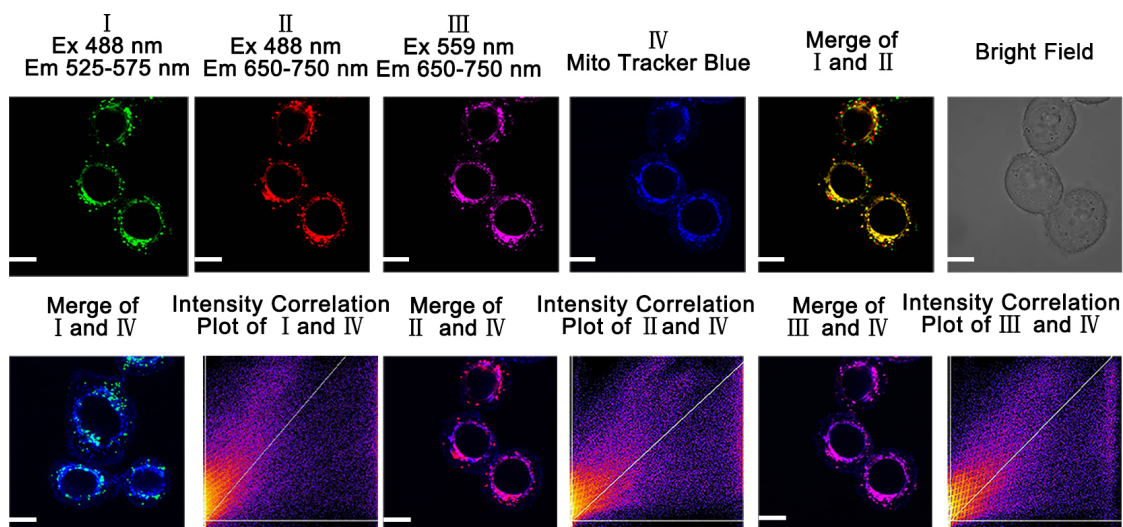
Figure S D.123. Fluorescence imaging of HeLa cells with 5 µM probe **B**, 10 µM Mito Tracker blue (Ex 405 nm) in serum-free medium at 2-h incubation of probe **B** and Mito Tracker blue with HeLa cells. Scale bar: 20 µm. Pearson correlation coefficient between channel Ⅰ and channel Ⅳ: 0.58. Pearson correlation coefficient between channel Ⅱ and channel Ⅳ: 0.56. Pearson correlation coefficient between channel Ⅲ and channel Ⅳ: 0.53.

Figure S D.124. Enlarged fluorescence imaging of HeLa cells with 5 µM probe **B** and 10 µM Mito Tracker blue (Ex 405 nm) in serum-free medium at 2-h incubation of probe **B** and Mito Tracker blue with HeLa cells. Scale bar: 20 µm

Figure S D.125. Fluorescence imaging of HeLa cells with 5 µM probe **B** and 10 µM Lysosensor blue (Ex 405 nm) in serum-free medium at 2-h incubation. Scale bar: 20 µm. Pearson correlation coefficient between channel Ⅰ and channel Ⅳ: 0.93. Pearson correlation coefficient between channel Ⅱ and channel Ⅳ: 0.91. Pearson correlation coefficient between channel Ⅲ and channel Ⅳ: 0.91.
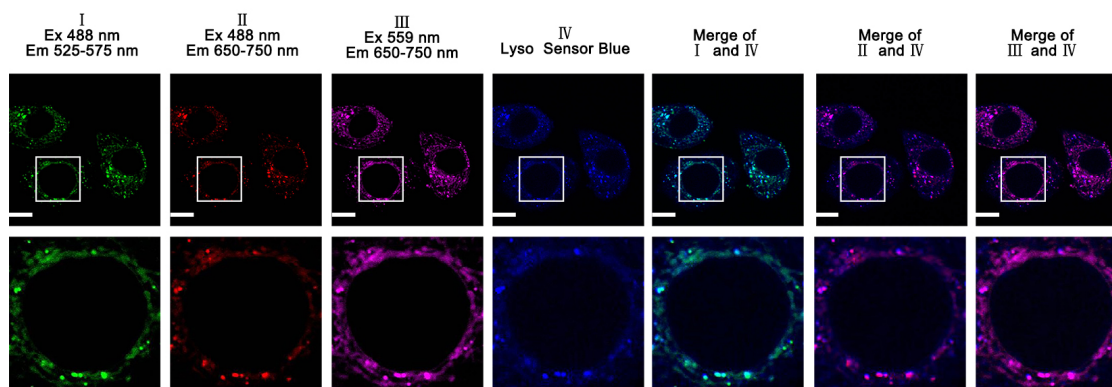

**Figure S D.126**. Enlarged fluorescence imaging of HeLa cells with 5 µM probe **B**, 10 µM Lysosensor blue (Ex 405 nm) in serum-free medium at 2-h incubation of probe B and Lysosensor blue with HeLa cells. Scale bar: 20 µm
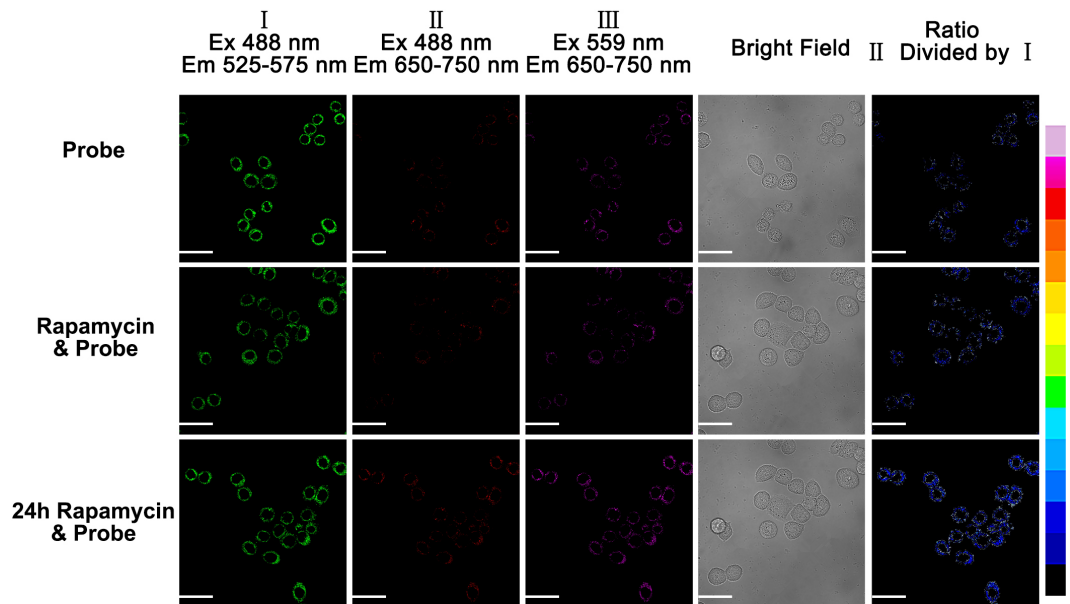
Figure S D.127. Fluorescence images of HeLa cells incubated with 3.5 µM probe **B** and rapamycin (100 nM) in the full normal culture media with 10-minute incubation time with probe **B** under excitation of 488 nm and 559 nm with scale bars of 50 µm. Images from upper to lower: probe **B** only (upper), probe **A** and rapamycin (middle), cells incubated with rapamycin for 24 h and then further incubated with probe **A** (lower).
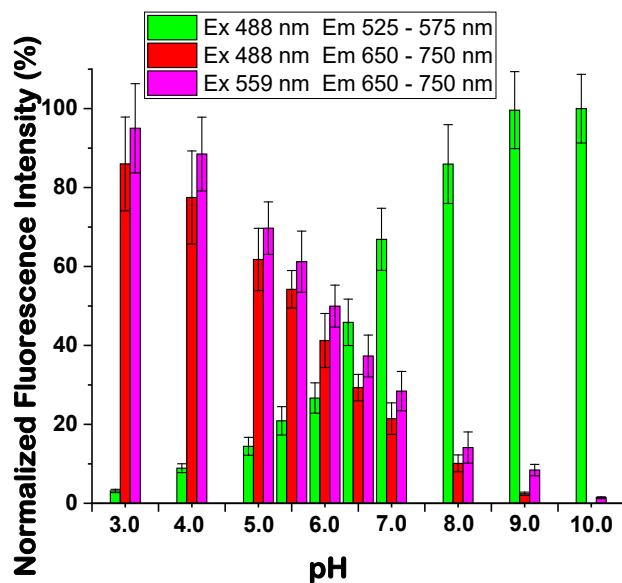
Figure S D.128. Statistical analysis of the confocal imaging data in **Fig. 12** generates from fluorescence intensities of Channel I, II, and III of probe **A** in HeLa live cells.
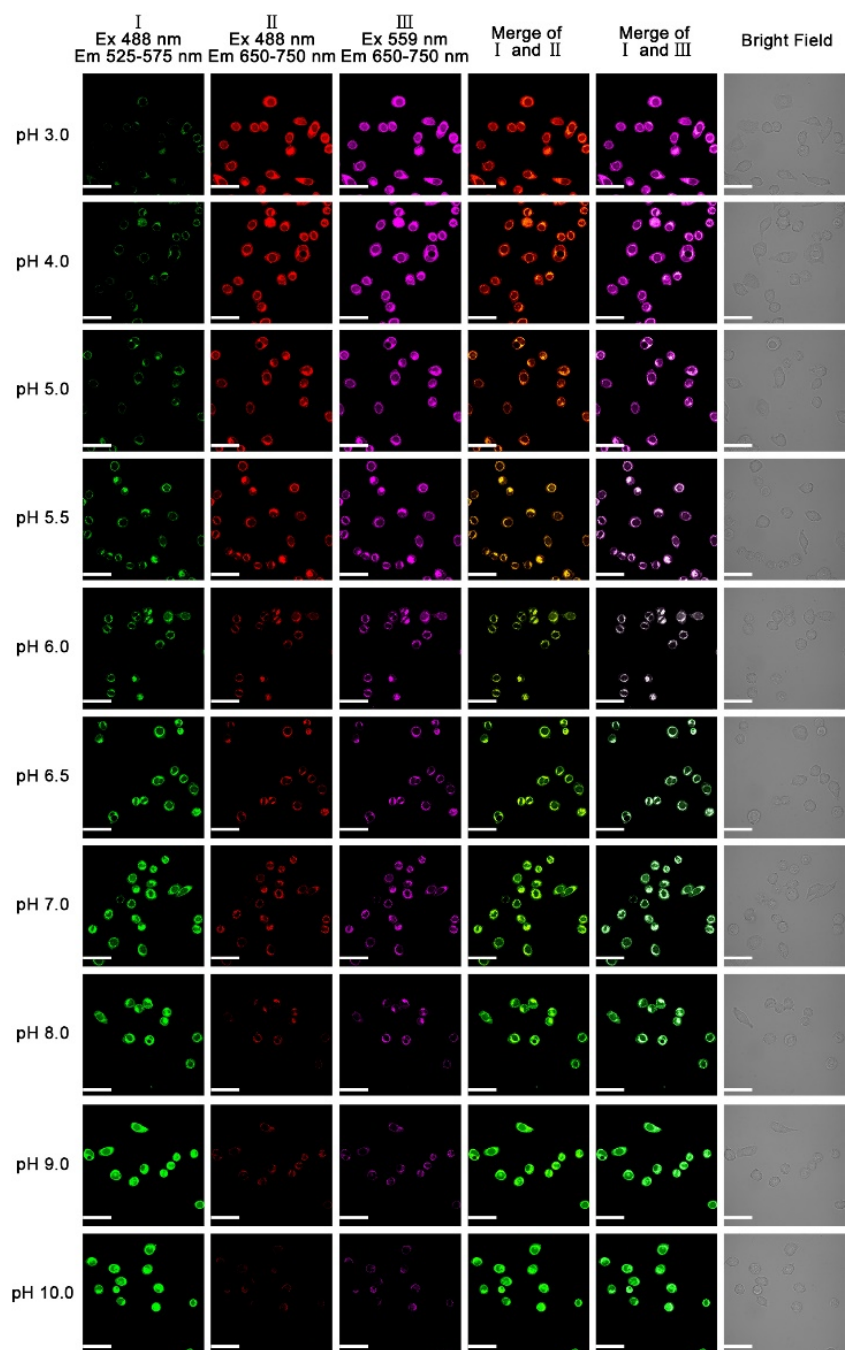
Figure S D.129. Fluorescence images of HeLa cells incubated with 10 μM probe **B** in different pH buffers containing 5 μM nigericin. Scale bar: 50 μm.
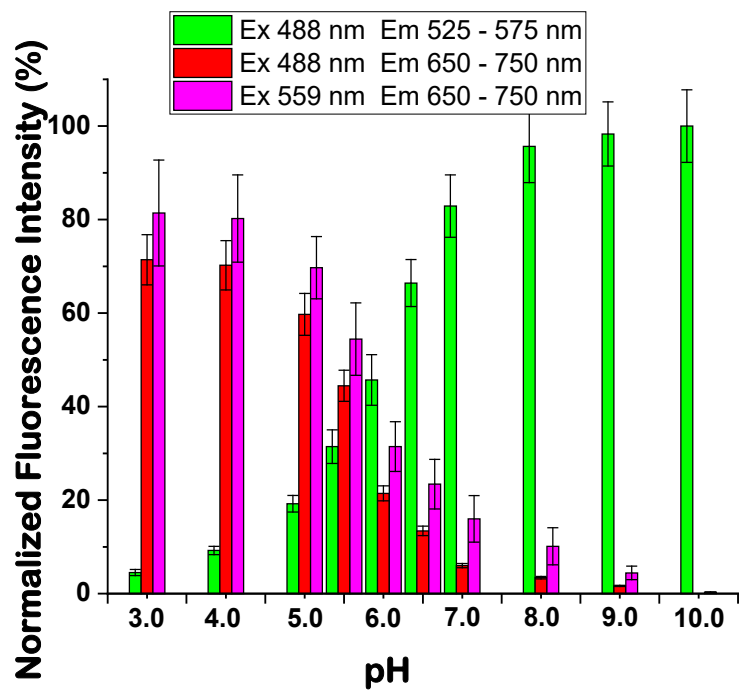
Figure S D.130. Statistical analysis of the confocal imaging data in **Fig. S129** generates from fluorescence intensities of Channel I, II, and III of probe **B** in HeLa live cells.
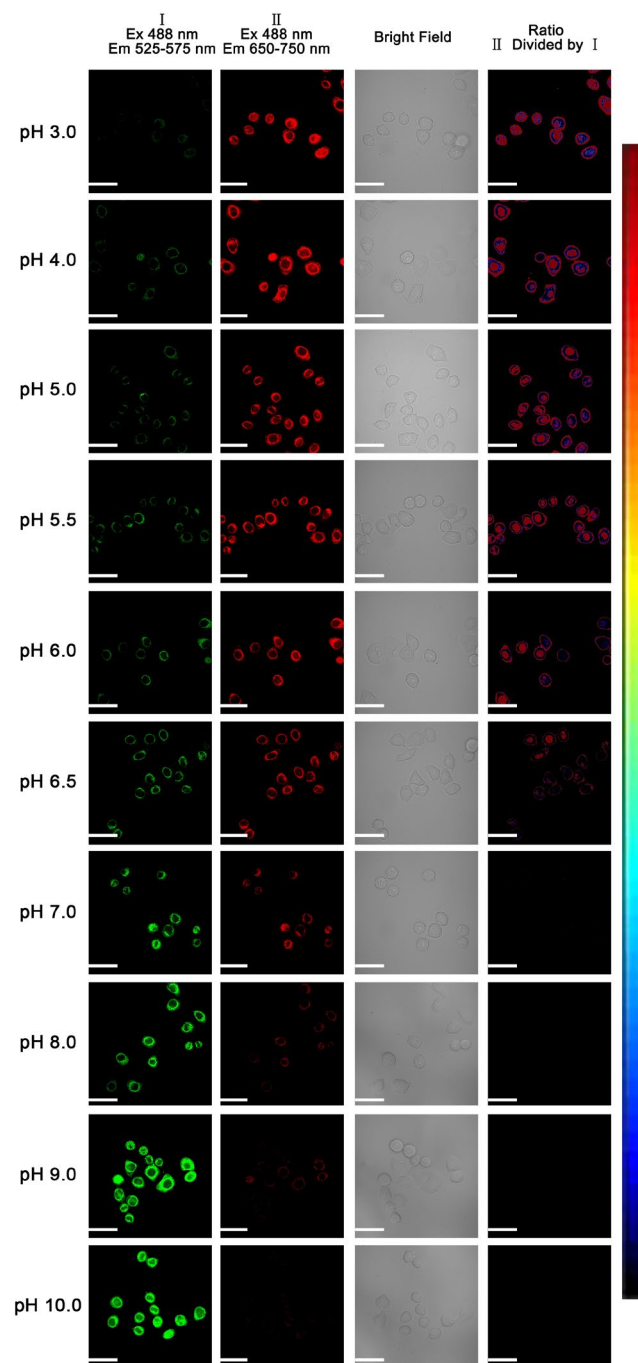
Figure S D.131. Ratio fluorescence images of HeLa cells incubated with 10 µM probe **A** in different pH buffers containing 5 µM nigericin. Scale bar: 50 µm.
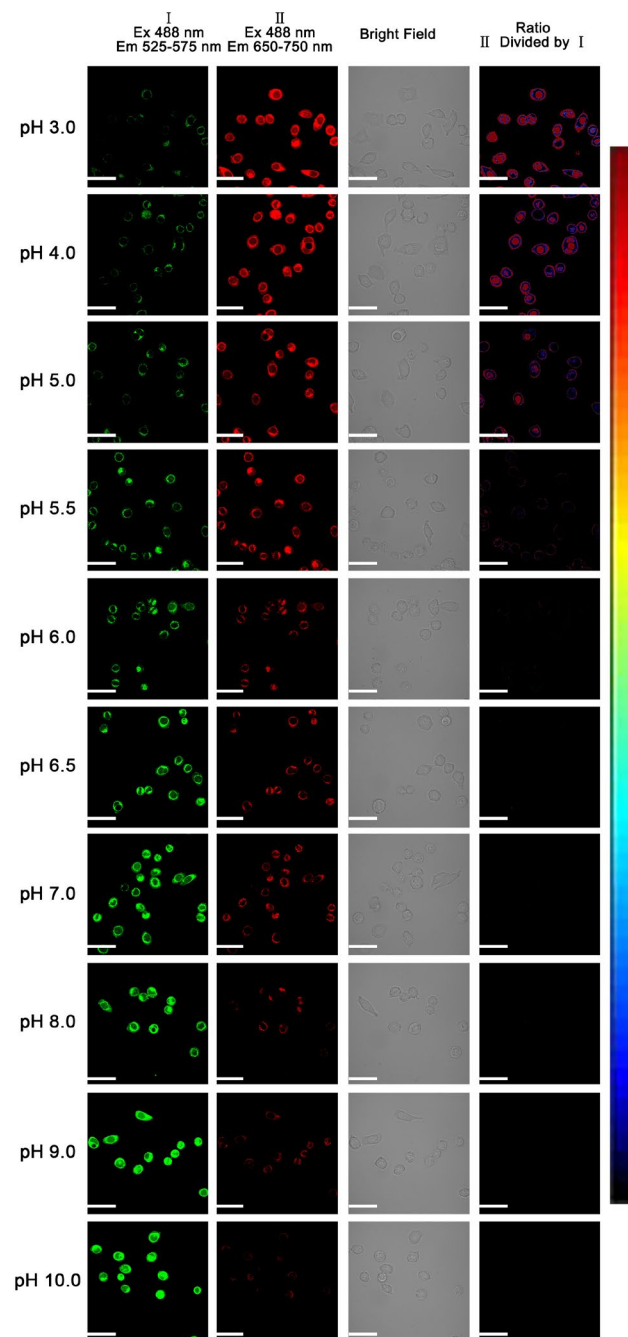
Figure S D.132. Ratio fluorescence images of HeLa cells incubated with 10 µM probe **B** in different pH buffers containing 5 µM nigericin. Scale bar: 50 µm.
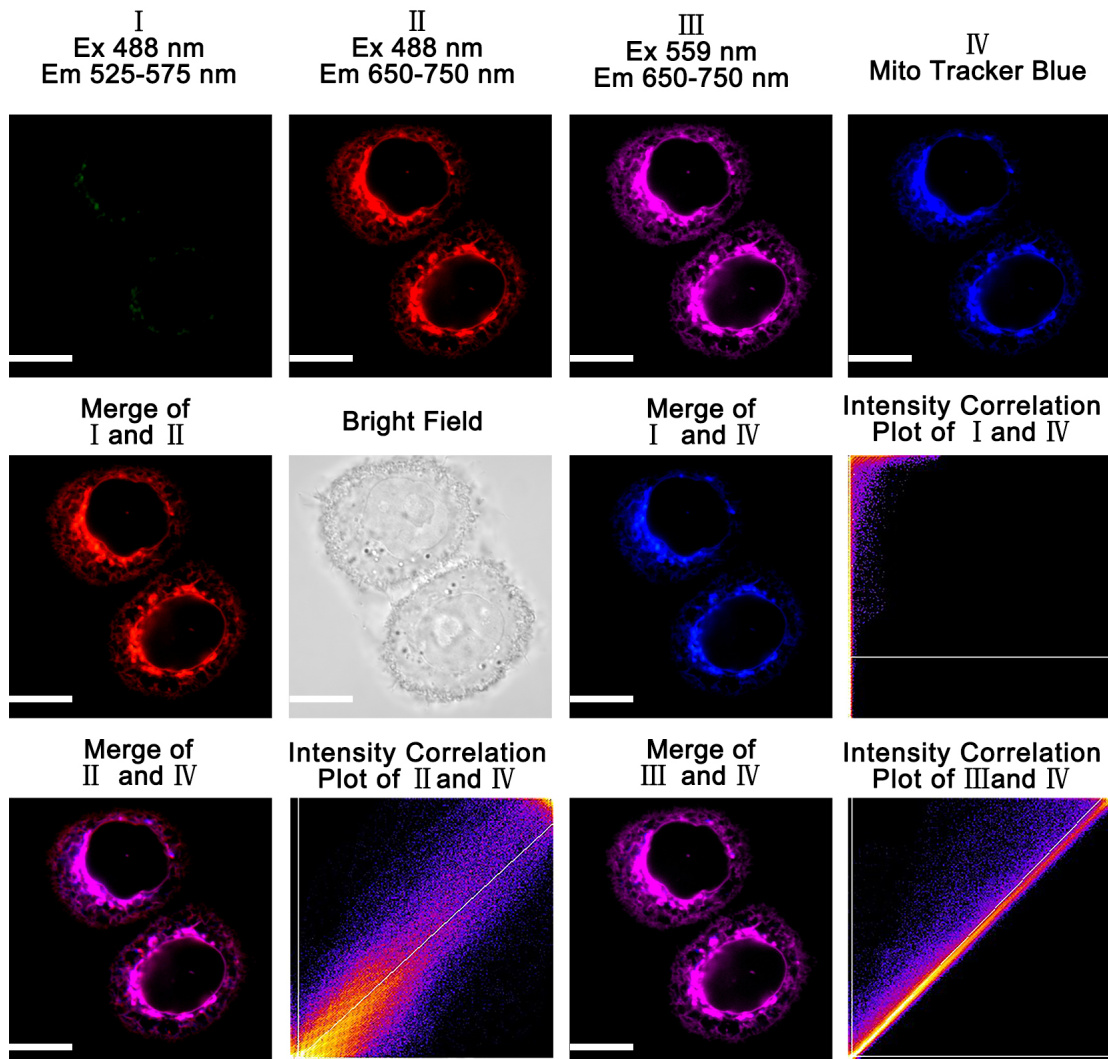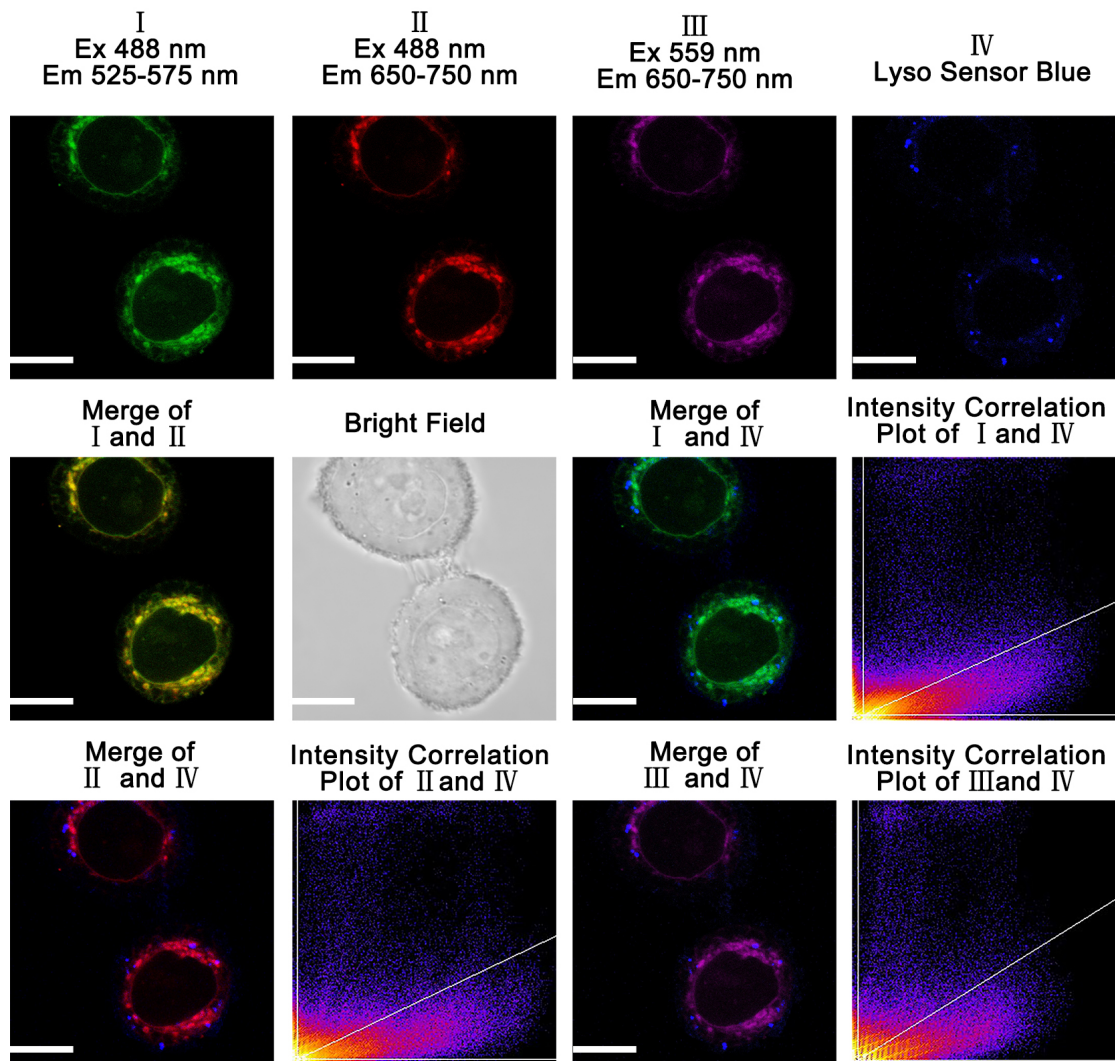
Figure S D.133. Fluorescence images of 5 µM probe **A** incubated with HeLa cells in pH 5.0 buffer containing 5 µM nigericin and 10 µM Mito Tracker blue (Ex 405 nm). Scale bar: 10 µm. Pearson correlation coefficient between channel II and channel IV: 0.93. Pearson correlation coefficient between channel III and channel IV: 0.96.
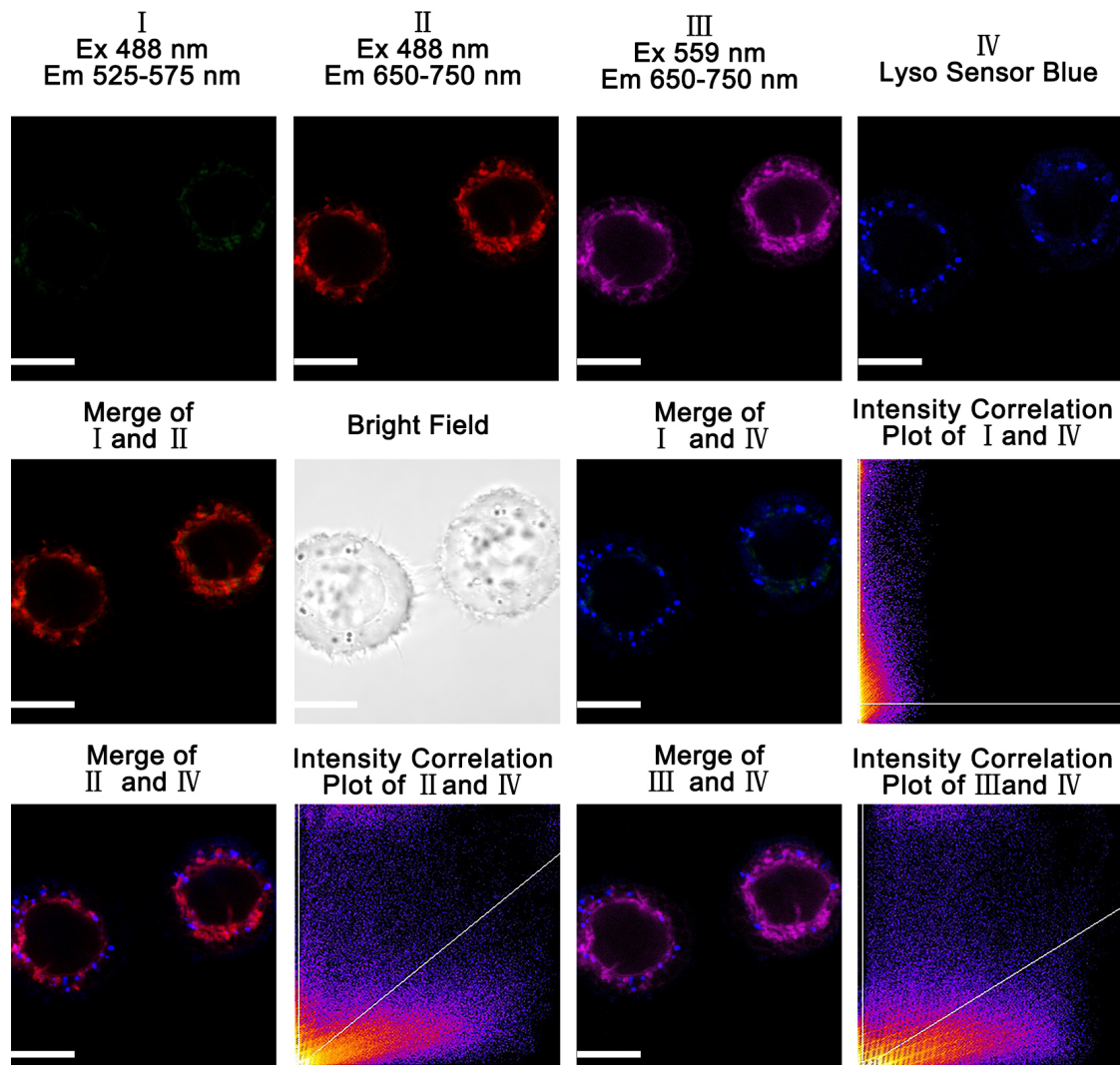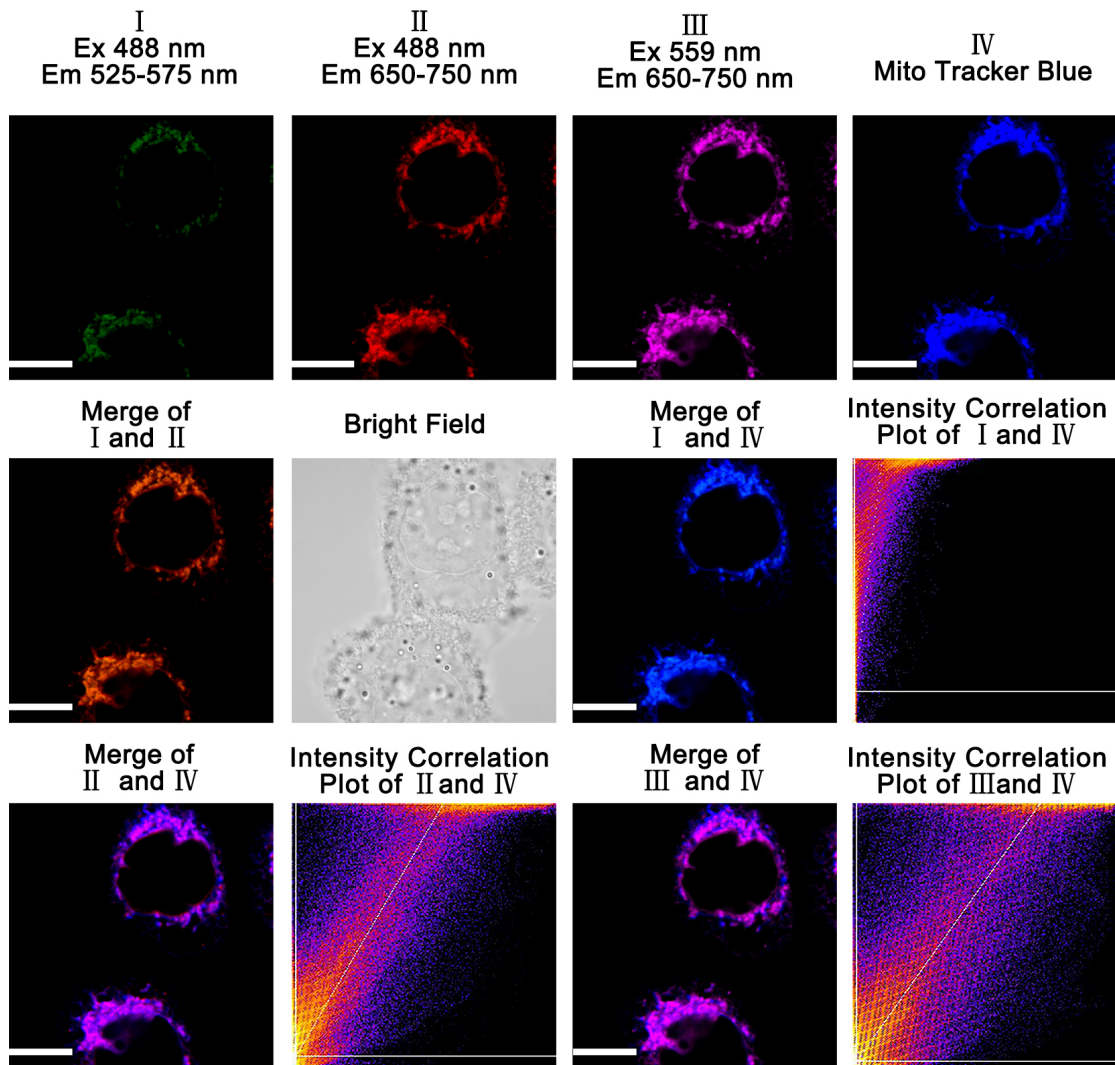
Figure S D.134. Fluorescence images of 5 µM probe **A** incubated with HeLa cells in pH 5.0 buffer containing 5 µM nigericin and 10 µM Lysosensor blue (Ex 405 nm). Scale bar: 10 µm. Pearson correlation coefficient between channel II and channel IV: 0.35. Pearson correlation coefficient between channel III and channel IV: 0.39.
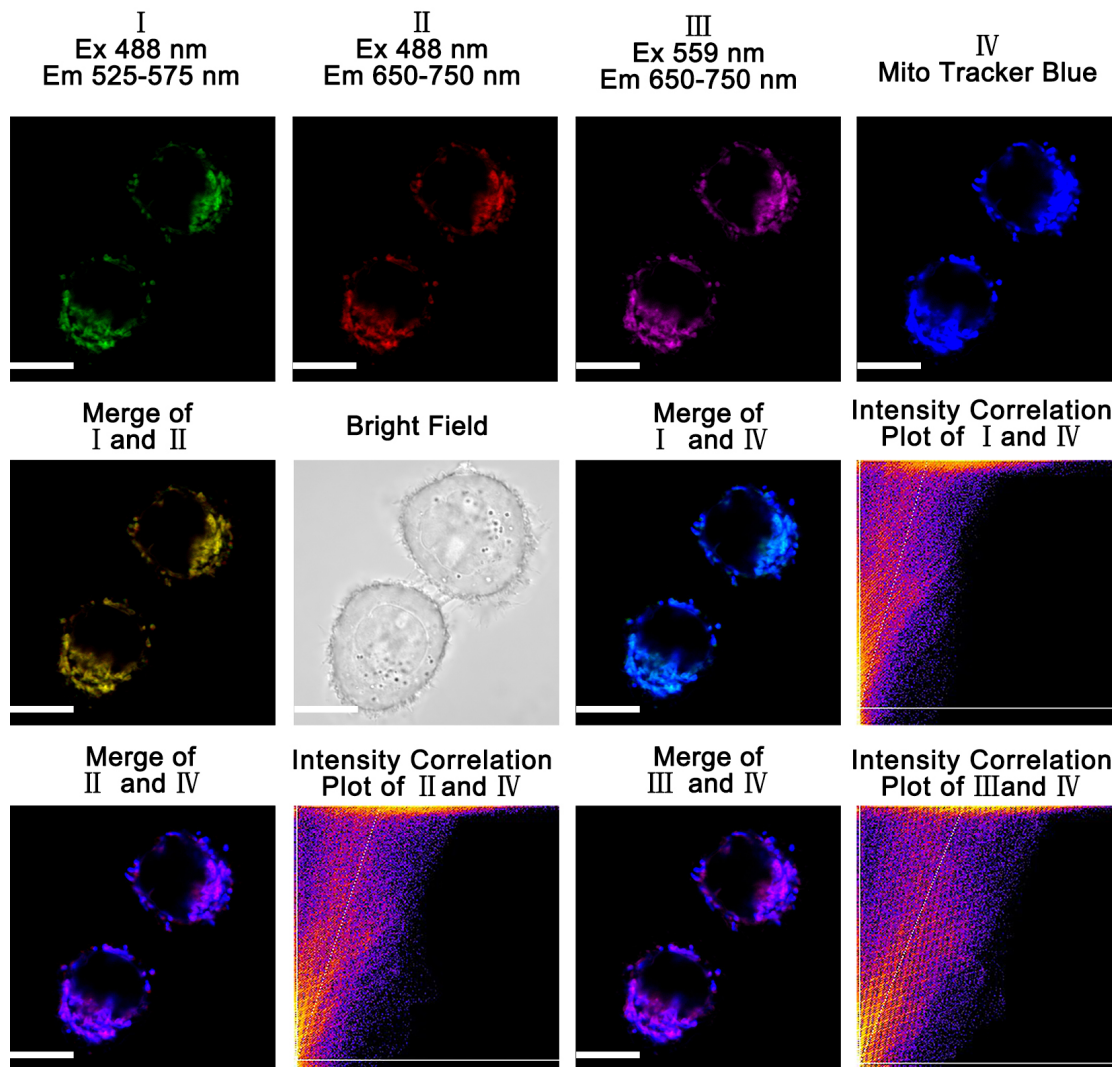
Figure S D.135. Fluorescence images of 5 µM probe **A** incubated with HeLa cells in pH 6.0 buffer containing 5 µM nigericin and 10 µM Mito Tracker blue (Ex 405 nm). Scale bar: 10 µm. Pearson correlation coefficient between channel I and channel IV: 0.92. Pearson correlation coefficient between channel II and channel IV: 0.88. Pearson correlation coefficient between channel III and channel IV: 0.91.
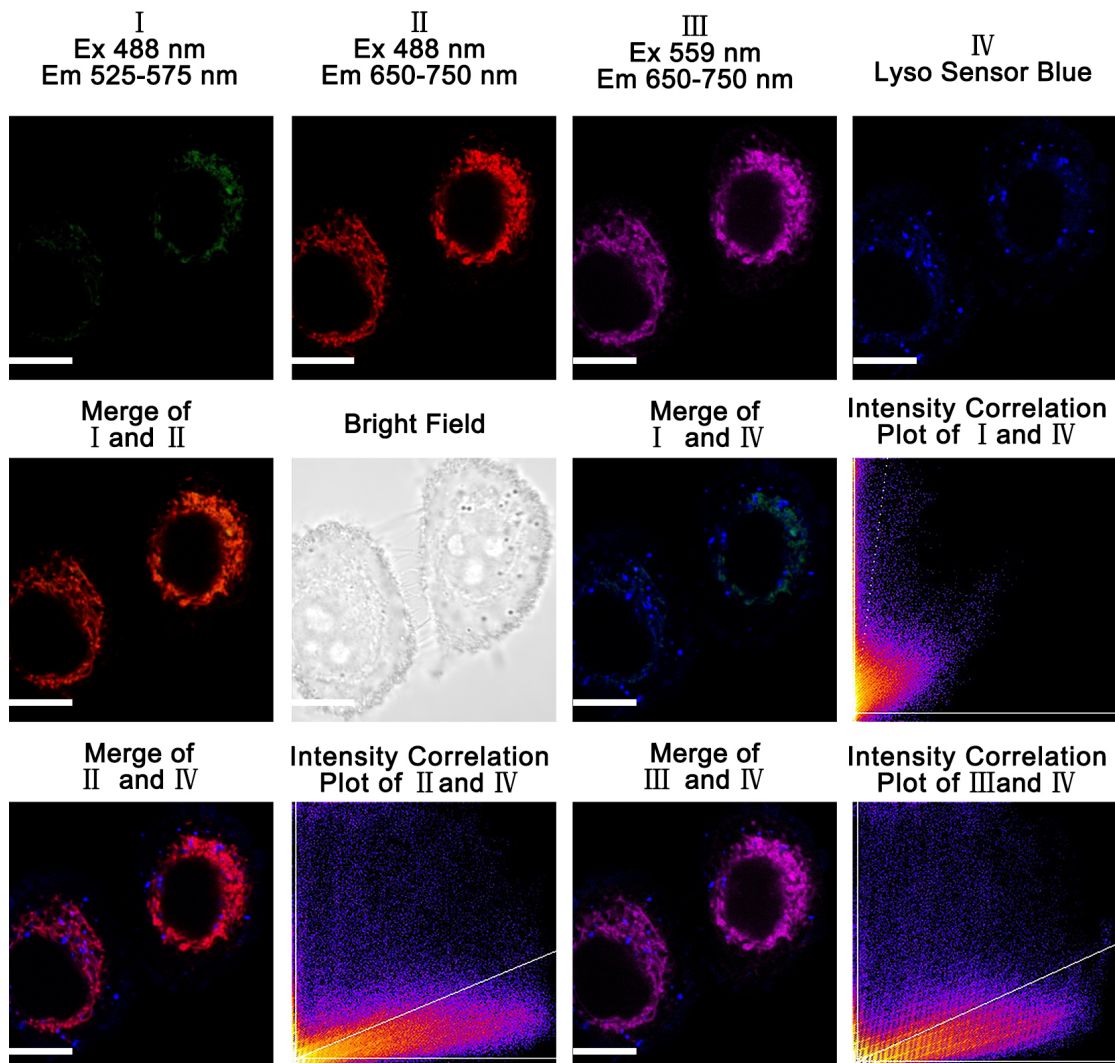
Figure S D.136. Fluorescence images of 5 µM probe **A** incubated with HeLa cells in pH 6.0 buffer containing 5 µM nigericin and 10 µM Lysosensor blue (Ex 405 nm). Scale bar: 10 µm. Pearson correlation coefficient between channel I and channel IV: 0.51. Pearson correlation coefficient between channel II and channel IV: 0.50. Pearson correlation coefficient between channel III and channel IV: 0.55.
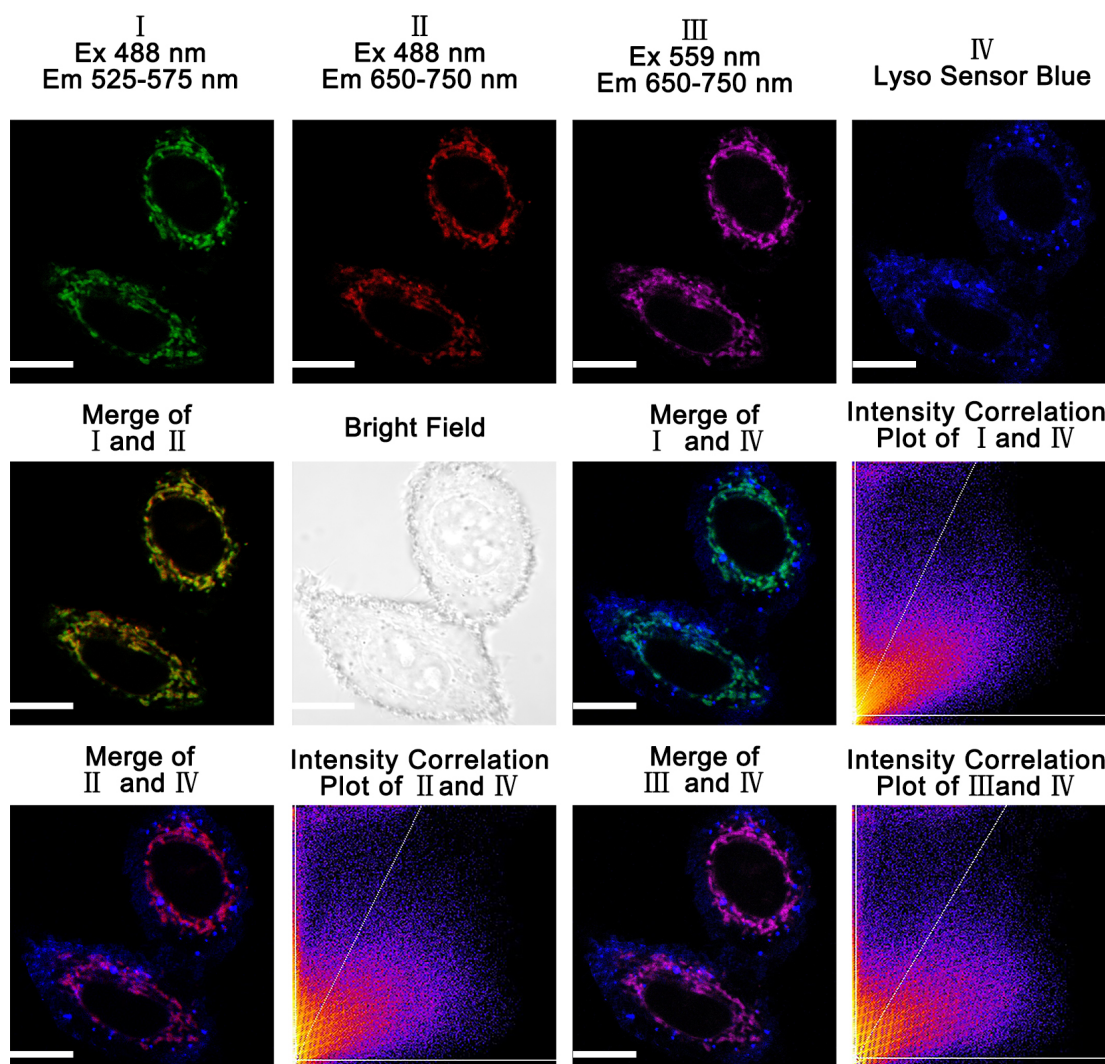
Figure S D.137. Fluorescence images of 5 µM probe **B** incubated with HeLa cells in pH 5.0 buffer containing 5 µM nigericin and 10 µM Mito Tracker blue (Ex 405 nm). Scale bar: 10 µm. Pearson correlation coefficient between channel I and channel IV: 0.88. Pearson correlation coefficient between channel II and channel IV: 0.95. Pearson correlation coefficient between channel III and channel IV: 0.96.

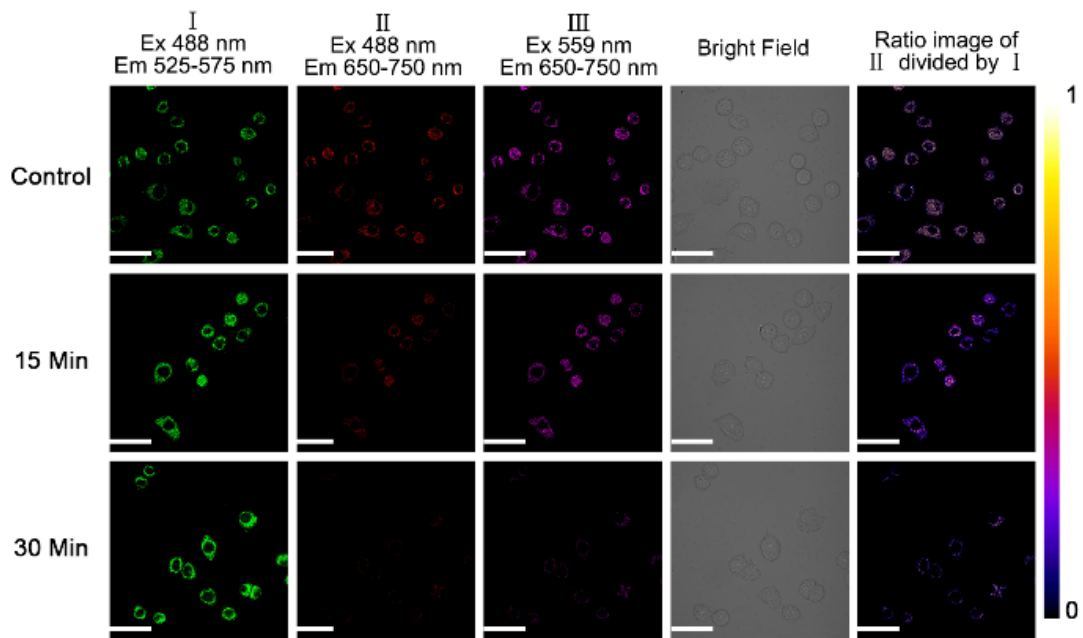**Figure S D.138.** Fluorescence images of 5 µM probe **B** incubated with HeLa cells in pH 5.0 buffer containing 5 µM nigericin and 10 µM Lysosensor blue (Ex 405 nm). Scale bar: 10 µm. Pearson correlation coefficient between channel I and channel IV: 0.46. Pearson correlation coefficient between channel II and channel IV: 0.53. Pearson correlation coefficient between channel III and channel IV: 0.50.

Figure S D.139. Fluorescence images of 5 µM probe **B** incubated with HeLa cells in pH 6.0 buffers containing 5 µM nigericin and 10 µM Lysosensor blue (Ex 405 nm). Scale bar: 10 µm. Pearson correlation coefficient between channel I and channel IV: 0.51. Pearson correlation coefficient between channel II and channel IV: 0.50. Pearson correlation coefficient between channel III and channel IV: 0.55.

Figure S D.140. Fluorescence images of HeLa cells incubated with 5 µM probe **A** under treatment of 100 µM H_2O_2 with different times. Scale bar: 50 µm.
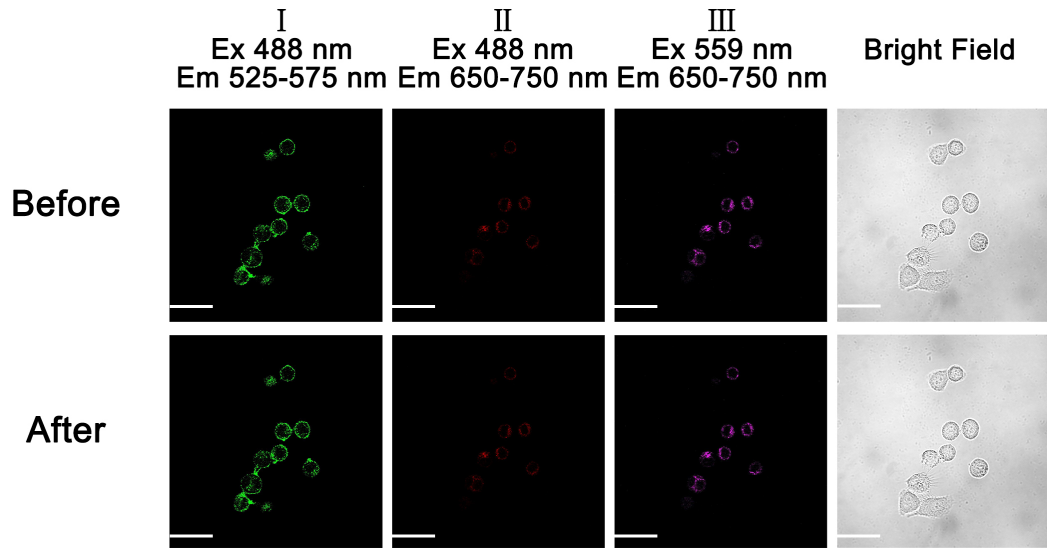
Figure S D.141. Fluorescence images of HeLa cells incubated with 3 µM probe **A** before and after photobleach by confocal microscopy in 240 seconds. Scale bar: 50 µm.
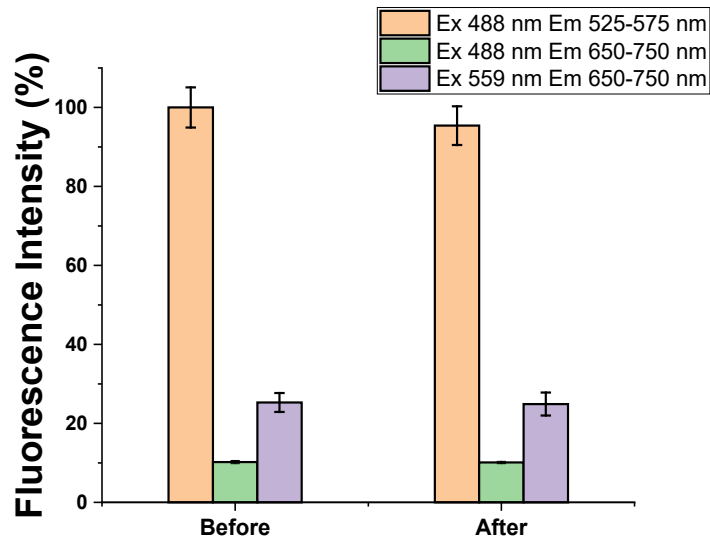

Figure S D.142. Statistical analysis of the confocal imaging data in **Fig. S141** generated from fluorescence intensities of Channel I, II, and III of probe **A** in HeLa live cells before and after photobleaching studies in HeLa cells.
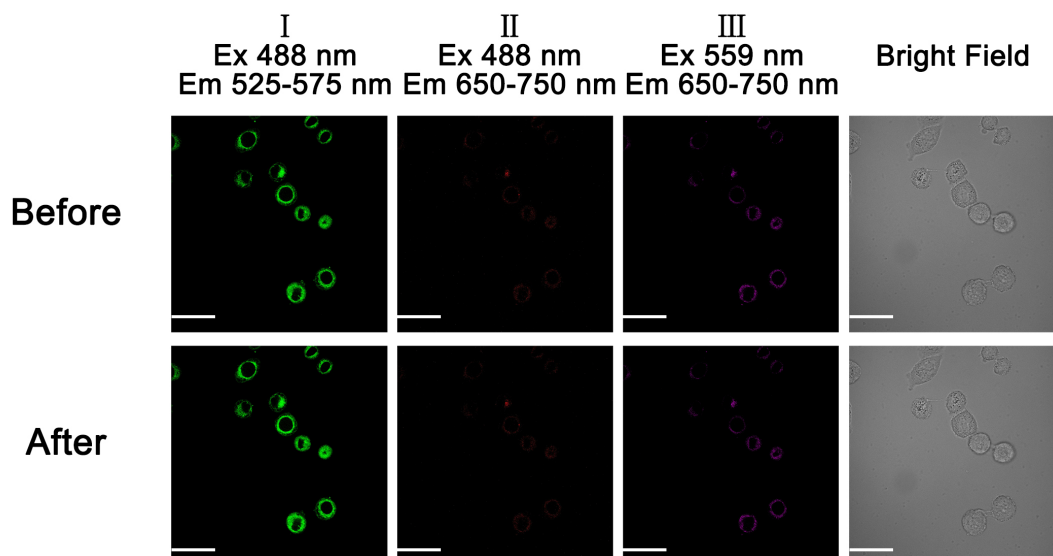
Figure S D.143. Fluorescence images of HeLa cells incubated with 3.5 µM probe **B** before and after photobleach by confocal microscopy in 240 seconds. Scale bar: 50 µm.
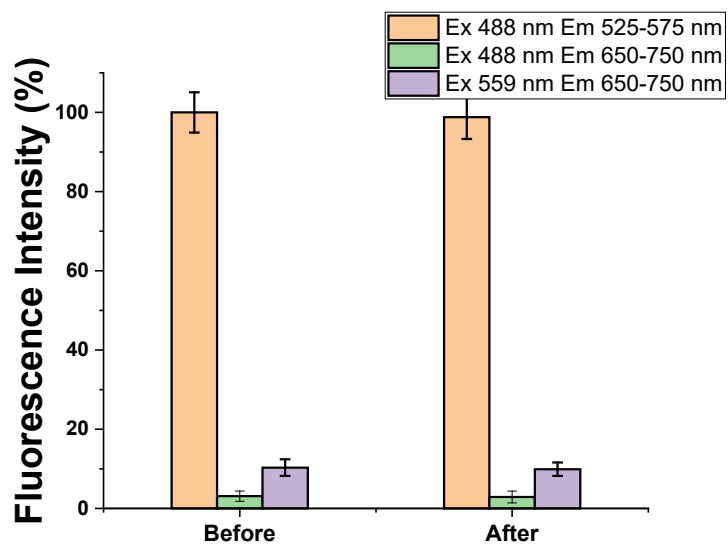

Figure S D.144. Statistical analysis of the confocal imaging data in **Fig. S143** generated from fluorescence intensities of Channel I, II, and III of probe **B** in HeLa live cells before and after photobleaching studies in HeLa cells.
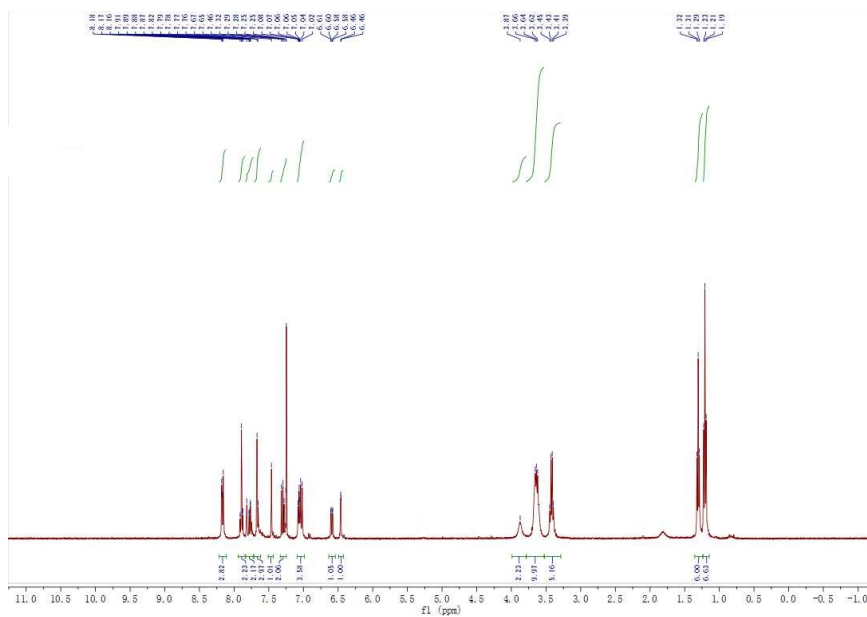
Appendix E   Supporting Information for Chapter 6

1. ^{1}H, ^{13}C NMR and HR-MS spectra of compound 3 and probe A

Figure S E.1. ^{1}H NMR of compound **3** in CDCl$_3$.

Figure S E.2. ^{13}C NMR of compound **3** in CDCl$_3$.

Figure S E.3. ^{1}H NMR of probe **A** in CDCl$_3$.
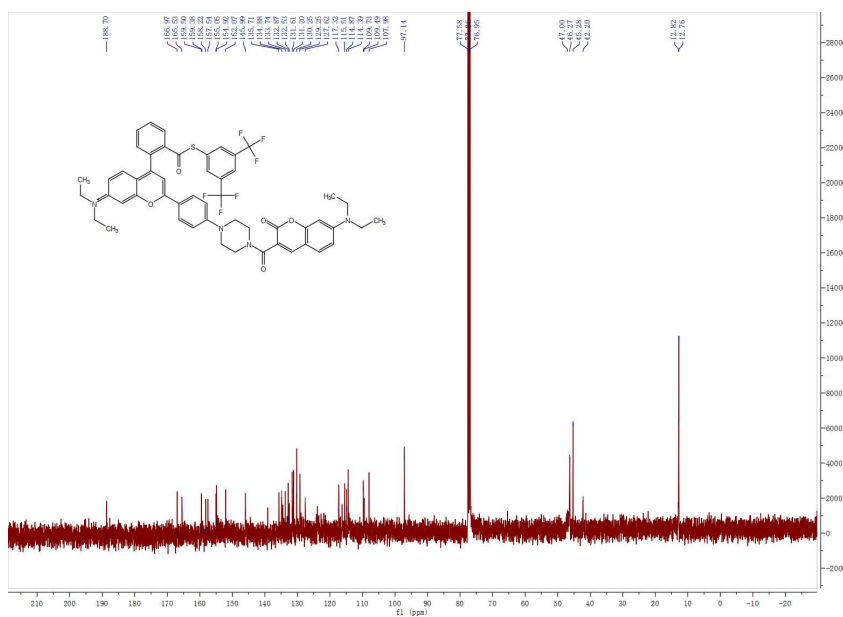

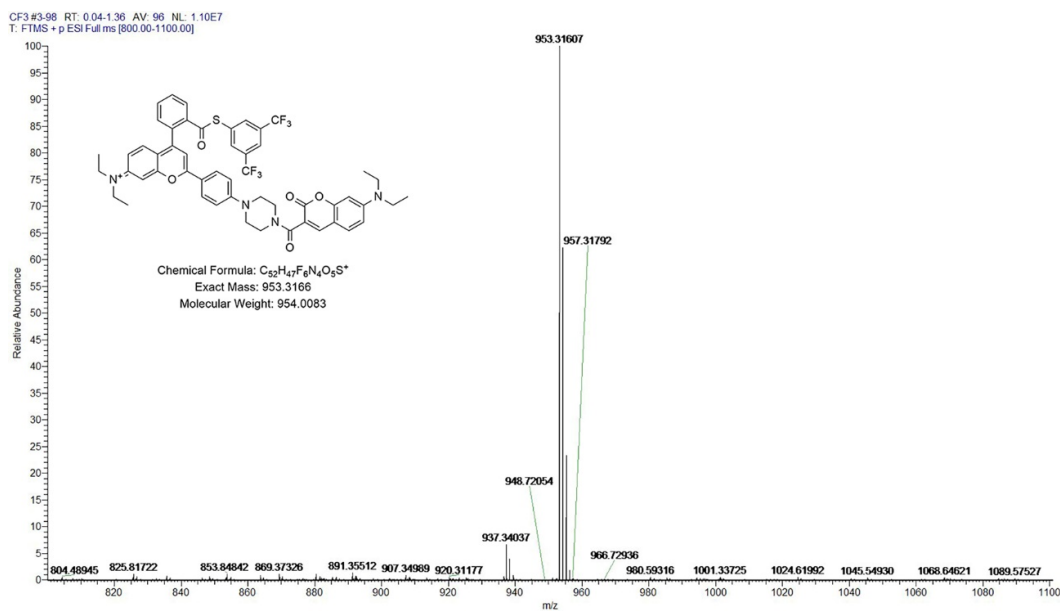**Figure S E.4.** ^{13}C NMR of probe **A** in CDCl$_3$.

Figure S E.5. HRMS of probe **A**.

2. Absorption and fluorescence spectra of 5 μM probe A in the absence and presence of various concentrations of Hcy at excitation of 440 nm.
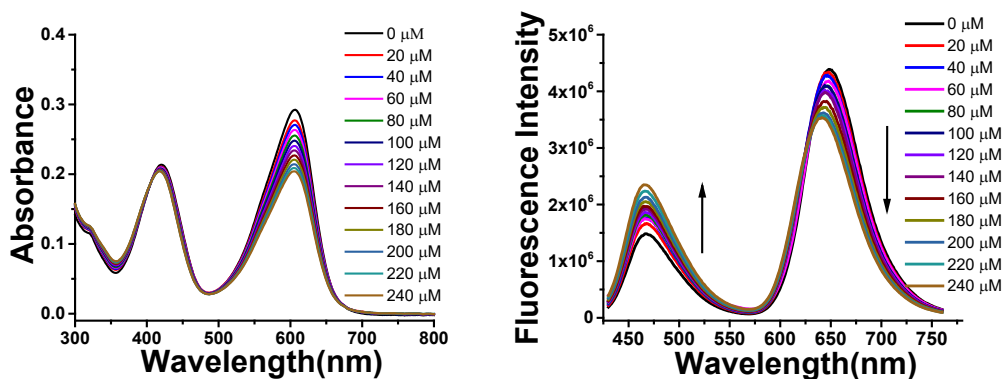

Figure S E.6. Absorption (left) and fluorescence (right) spectra of 5 μM probe **A** in the absence and presence of various concentrations of Hcy in pH 7.4 buffer containing 30% ethanol at excitation of 440 nm.

3. Fluorescence spectra of probe A responds to cysteine and homocysteine and kinetic plot under the excitation at 560 nm
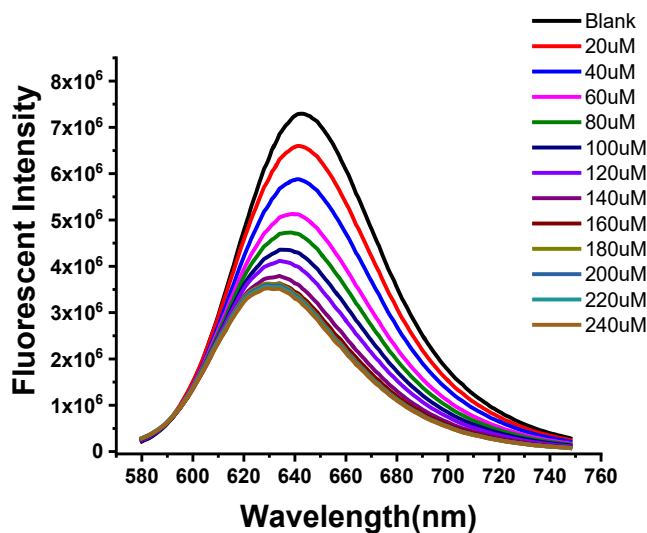

Figure S E.7. Probe **A** (5 µM) responses to different concentrations of cysteine in pH 7.4 buffer containing 30% ethanol under the excitation at 560 nm.
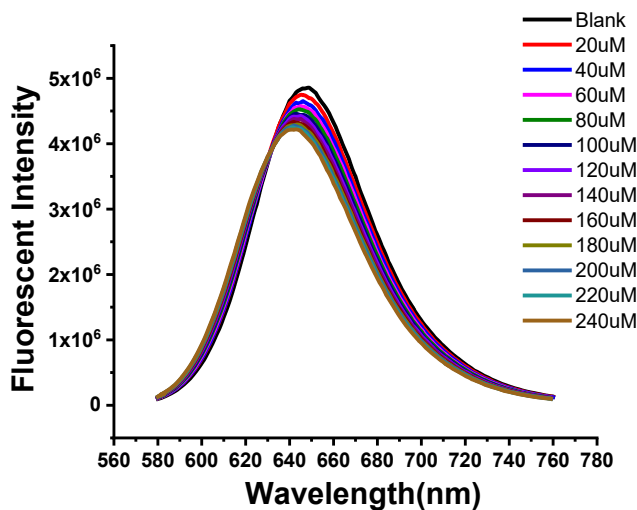

Figure S E.8. Probe **A** (5 µM) responses to different concentrations of homocysteine in pH 7.4 buffer containing 30% ethanol under the excitation at 560 nm.

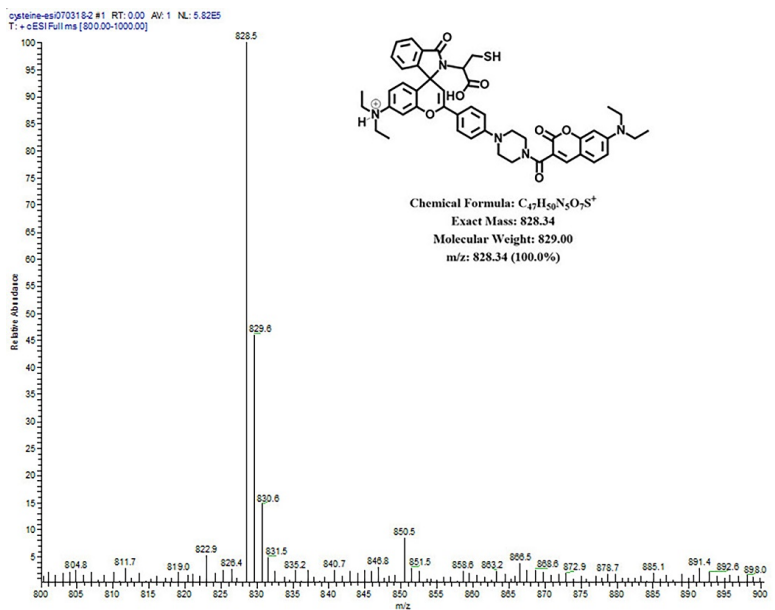# 4. ESI-MS data of reaction products of probe A with cysteine, Hcy and GSH.

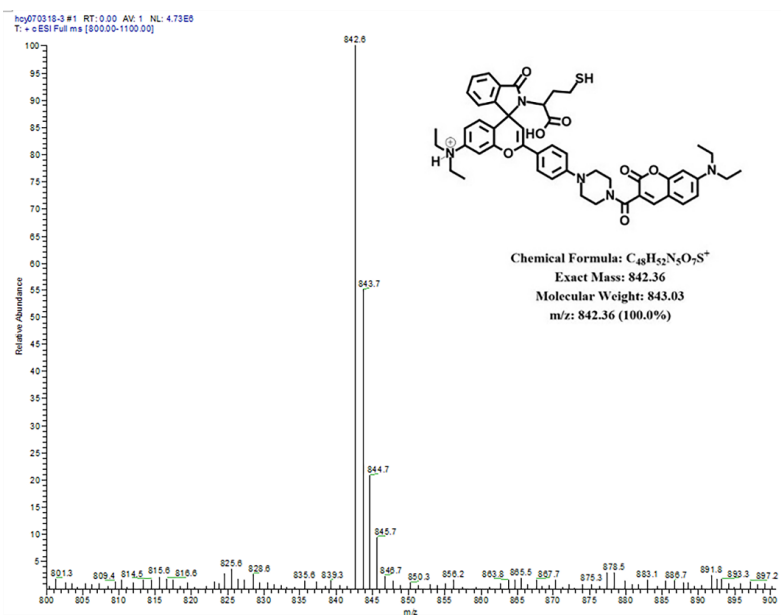**Figure S E.9.** ESI-MS data of reaction product of probe **A** with cysteine.

Figure S E.10. ESI-MS data of reaction product of probe **A** with Hcy (homocysteine).
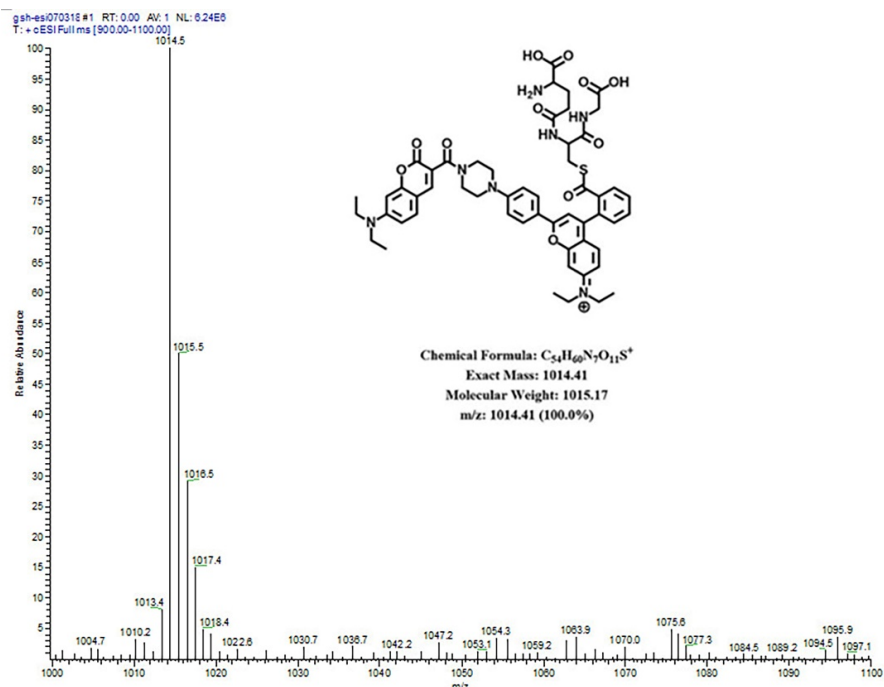
Figure S E.11. ESI-MS data of reaction product of probe **A** with GSH (glutathione).

5. General information and results on the theoretical calculations

Chemdraw structures of probes **A**, **A-1** and **A-3**, were optimized initially with the MM2 functionality in Chem3D and then further with Avogadro. Optimization and frequency calculations were then conducted with the exchange correlation (xc) functional DFT/TPSSH and with atoms defined at the split-valence triple-ζ plus polarization function (TZVP) implemented, using the Gaussian 16 suite of programs. Imaginary frequencies were not obtained. The first ten excited states were assessed on the basis of TD-DFT optimizations in a Polarizable Continuum Model (PCM) of water. Results were interpreted using GausView for all other data and figures. The diagrams and listings of atomic positions from the calculations are listed sequentially for probes **A**, **A-1** and **A-3** below and all data are within the PCM matrix of water.
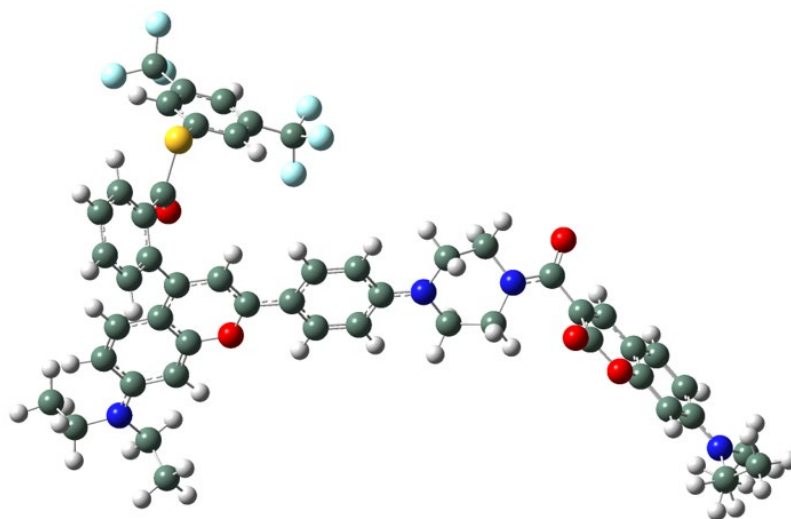
Figure S E.12. Drawing of probe **A** with atoms represented as spheres of arbitrary size (H-white, C-grey, N-blue and O-red) using the GaussView program.

Table S E.1. Results of the refinement for probe **A**.

fluorafreqnoraman (Optimization completed)		
/storage/liu/fluor/tps/ftpa.log		
File Type	.log	
Calculation Type	FREQ	
Calculation Method	RTPSSh	
Basis Set	TZVP	
Charge	1	
Spin	Singlet	
Solvation	scrf=solvent=water	
E(RTPSSh)	-3603.381746	Hartree
RMS Gradient Norm	0.000002	Hartree/Bohr
Imaginary Freq		
Dipole Moment	21.778773	Debye
Point Group	C1	
Job cpu time:	11 days 9 hours 15 minutes 5...	

Table S E.2. Atomic coordinates for probe **A**.

Row	Symbol	X	Y	Z
1	C	7.438733	2.640189	4.153357
2	C	6.420746	2.881185	3.234085
3	C	5.986783	1.879071	2.363297
4	C	6.601434	0.609803	2.426103
5	C	7.621813	0.379354	3.355258
6	C	8.042047	1.388258	4.213898
7	C	4.840283	2.176106	1.464323
8	C	4.950073	3.130207	0.42979
9	C	3.800254	3.408884	-0.34999
10	O	2.616446	2.775516	-0.07808
11	C	2.501936	1.861529	0.912877
12	C	3.614933	1.55886	1.691082
13	C	6.134074	3.81514	0.058341
14	C	6.150263	4.711443	-0.97377
15	C	4.970619	4.998399	-1.73802
16	C	3.783714	4.310588	-1.38888
17	N	4.999283	5.888115	-2.75785
18	C	3.825298	6.133383	-3.60784
19	C	6.199066	6.673286	-3.08732
20	C	2.89721	7.213996	-3.05161
21	C	7.132662	5.961399	-4.06641
22	C	-6.36233	-2.36582	1.08633
23	C	-7.64097	-1.63038	0.829923
24	O	-6.33088	-3.60345	1.012244
25	C	-8.39918	-1.98707	-0.25753
26	C	-9.64888	-1.39066	-0.52254
27	C	-10.1279	-0.42081	0.382457
28	O	-9.39534	-0.10512	1.49779
29	C	-8.15861	-0.68454	1.790846
30	O	-7.65003	-0.34535	2.84511
31	C	-10.4643	-1.67575	-1.64081
32	C	-11.6643	-1.04122	-1.83424
33	C	-12.1406	-0.0591	-0.90901
34	C	-11.3307	0.23316	0.215398
35	N	-13.3302	0.570966	-1.10537
36	C	-13.7959	1.642609	-0.21728
37	C	-14.2307	0.219729	-2.21106
38	C	-13.9346	0.987119	-3.50039
39	C	-14.5781	1.128957	0.992851
40	C	6.216271	-0.45186	1.457268
41	O	5.82905	-0.2418	0.330624
42	S	6.352554	-2.142	2.144314
43	C	5.919545	-3.0902	0.688294
44	C	6.926808	-3.64331	-0.0987
45	C	6.582058	-4.40638	-1.2125
46	C	5.247841	-4.6245	-1.54244
47	C	4.252846	-4.06853	-0.74321

48	C	4.579092	-3.30234	0.373078	72	H	8.841402	1.197476	4.919584
49	C	1.189711	1.297919	1.038639	73	H	3.51756	0.83514	2.486605
50	C	0.154158	1.646525	0.14163	74	H	7.048282	3.614964	0.602962
51	C	-1.1039	1.103135	0.246548	75	H	7.084636	5.191681	-1.22575
52	C	-1.41531	0.163091	1.267356	76	H	2.851492	4.474345	-1.90896
53	C	-0.37551	-0.18101	2.17457	77	H	3.290514	5.194043	-3.75592
54	C	0.87839	0.368434	2.057334	78	H	4.205007	6.433181	-4.58605
55	N	-2.65782	-0.37638	1.366807	79	H	6.720712	6.935623	-2.16642
56	C	-3.78047	0.133094	0.568486	80	H	5.845934	7.610434	-3.52113
57	C	-5.10435	-0.20615	1.244565	81	H	2.495756	6.929857	-2.07673
58	N	-5.24584	-1.65553	1.381064	82	H	2.060641	7.367178	-3.73753
59	C	-4.01843	-2.4024	1.67572	83	H	3.428184	8.162326	-2.94229
60	C	-2.96544	-1.48257	2.279699	84	H	7.514371	5.029376	-3.64437
61	C	2.804537	-4.26003	-1.11394	85	H	7.982136	6.608086	-4.29907
62	C	7.668739	-5.04469	-2.03918	86	H	6.613651	5.729514	-4.9992
63	F	8.794282	-4.29584	-2.06472	87	H	-8.02052	-2.7444	-0.93642
64	F	7.28741	-5.23829	-3.32142	88	H	-10.1243	-2.4107	-2.36234
65	F	8.024868	-6.26181	-1.55218	89	H	-12.2439	-1.28142	-2.71389
66	F	2.596146	-5.42016	-1.77558	90	H	-11.6345	0.94657	0.967636
67	F	2.354284	-3.26584	-1.92287	91	H	-14.4288	2.297913	-0.81898
68	F	1.998506	-4.26759	-0.0283	92	H	-12.9399	2.242105	0.097503
69	H	7.756665	3.43324	4.819845	93	H	-15.2443	0.441027	-1.87098
70	H	5.939189	3.85164	3.204282	94	H	-14.1903	-0.85741	-2.37996
71	H	8.11371	-0.58584	3.380026	95	H	-14.0107	2.064634	-3.33636

96	H	-14.6565	0.70689	-4.27171	106	H	-0.5661	-0.86106	2.993024
97	H	-12.9314	0.766449	-3.87136	107	H	1.626594	0.081157	2.785405
98	H	-15.4573	0.563926	0.674174	108	H	-3.75472	-0.28162	-0.44551
99	H	-14.9155	1.972548	1.600282	109	H	-3.70743	1.219531	0.49816
100	H	-13.9609	0.480108	1.617798	110	H	-5.91491	0.173716	0.624511
101	H	7.966069	-3.47586	0.15322	111	H	-5.16671	0.279519	2.221317
102	H	4.987287	-5.22075	-2.40708	112	H	-3.63294	-2.86808	0.763088
103	H	3.801726	-2.87869	0.995702	113	H	-4.24948	-3.19989	2.382786
104	H	0.355229	2.347411	-0.65812	114	H	-2.06641	-2.07539	2.438566
105	H	-1.85179	1.382245	-0.48269	115	H	-3.29821	-1.10128	3.251492

A-248 (HOMO)

A-249 (LUMO)

A-247

A 250
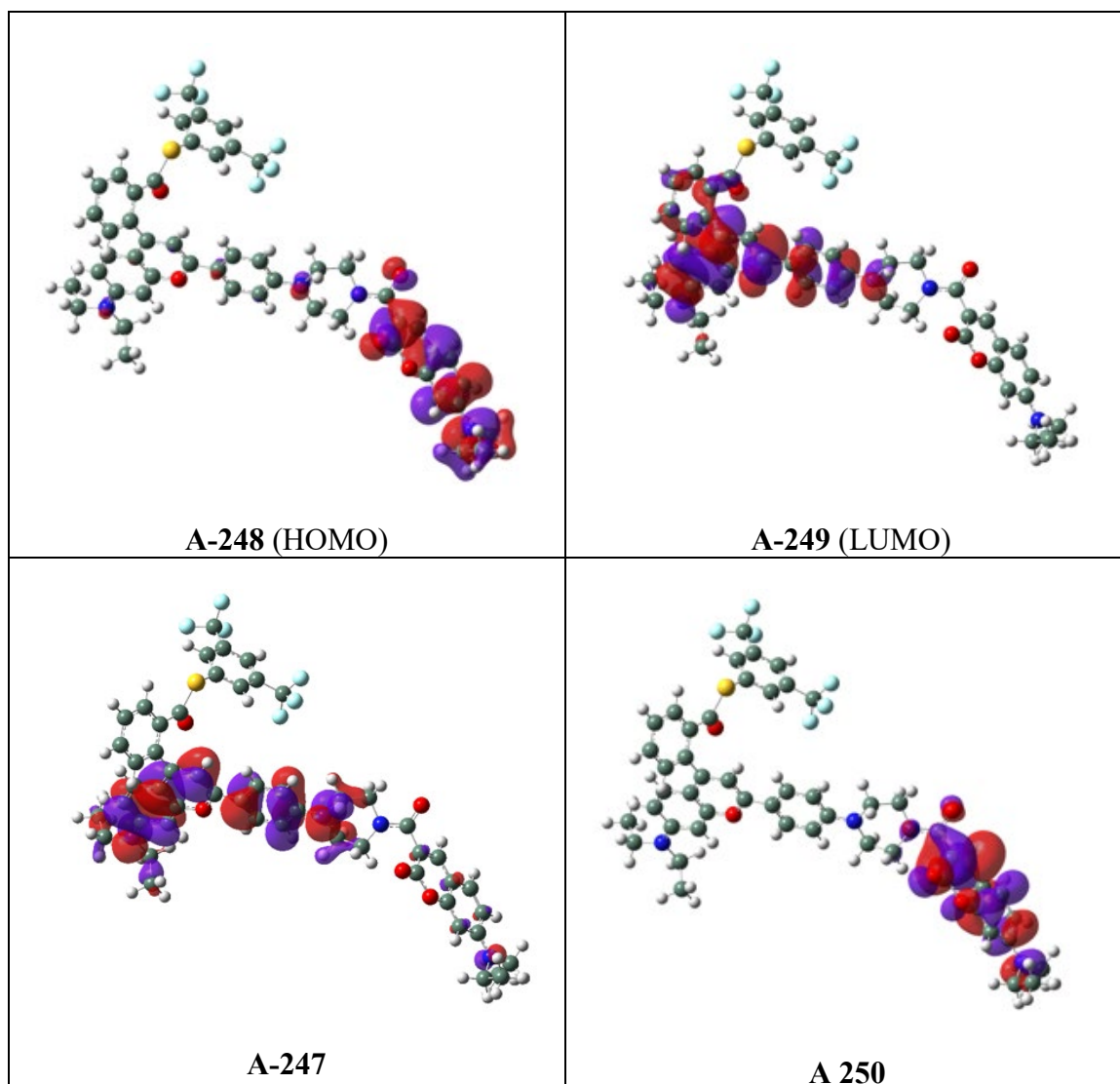
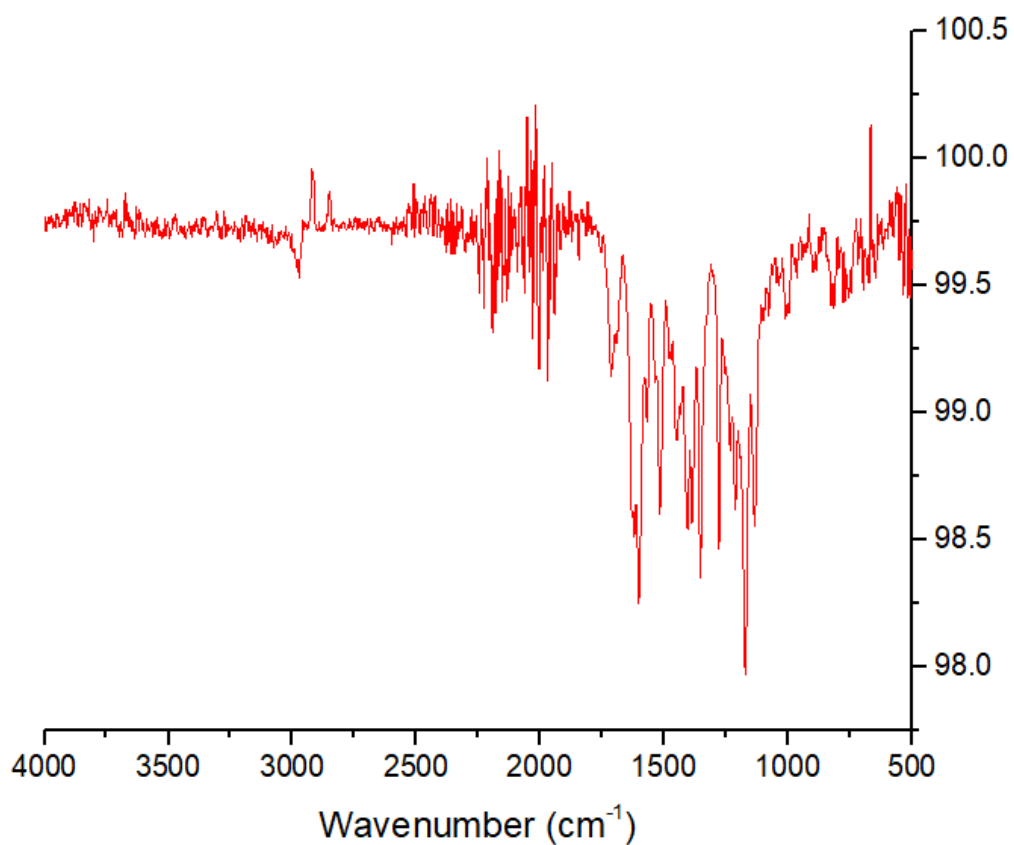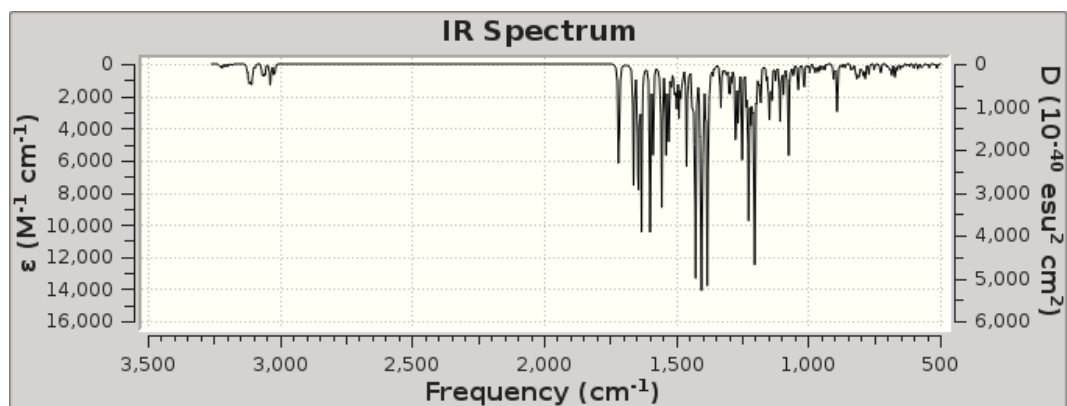**Figure S E.13.** LCAO for orbitals 247, 248, 249, 250 in Probe **A**.

Figure S E.14. Calculated (top) FTIR spectrum of Probe **A** in water. Experimental solid FTIR of probe **A** on the bottom.
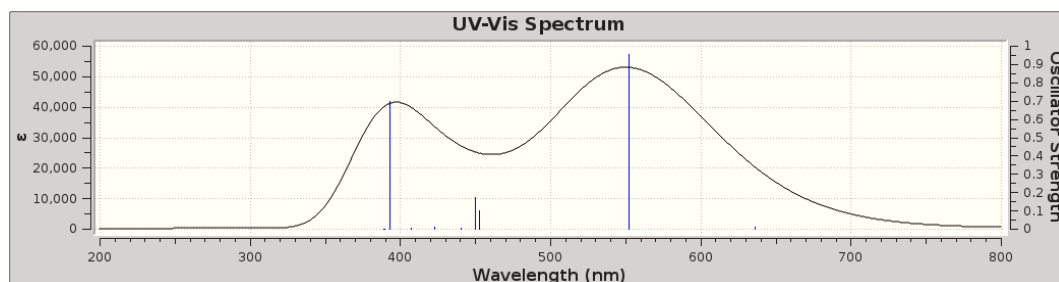
Figure S E.15. Calculated UV-Vis spectrum for Probe **A**

Table S E.3. Excitation energies and oscillator strength for Probe **A**
Excited state symmetry could not be determined.
 Excited State   1:   Singlet-?Sym   1.9498 eV 635.89 nm f=0.0104 <S**2>=0.000
    248 -> 249   0.70016
 This state for optimization and/or second-order correction.
 Total Energy, E(TD-HF/TD-DFT) = -3603.31009246
 Copying the excited state density for this state as the 1-particle RhoCI density.

 Excited state symmetry could not be determined.
 Excited State   2:   Singlet-?Sym   2.2447 eV 552.34 nm f=0.9574 <S**2>=0.000
    247 -> 249   0.69231

 Excited state symmetry could not be determined.
 Excited State   3:   Singlet-?Sym   2.7386 eV 452.74 nm f=0.1022 <S**2>=0.000
    246 -> 249   0.60523
    247 -> 250   -0.29098
    247 -> 254   -0.11868
    248 -> 250   -0.14956

429

Excited state symmetry could not be determined.
Excited State 4: Singlet-?Sym 2.7566 eV 449.77 nm f=0.1736 <S**2>=0.000
   246 -> 249   0.30711
   247 -> 250   0.54114
   248 -> 250   0.30517

Excited state symmetry could not be determined.
Excited State 5: Singlet-?Sym 2.8142 eV 440.57 nm f=0.0078 <S**2>=0.000
   247 -> 250   -0.33860
   248 -> 250   0.61970

Excited state symmetry could not be determined.
Excited State 6: Singlet-?Sym 2.9316 eV 422.92 nm f=0.0099 <S**2>=0.000
   247 -> 251   0.67641
   248 -> 251   0.19930

Excited state symmetry could not be determined.
Excited State 7: Singlet-?Sym 3.0432 eV 407.41 nm f=0.0047 <S**2>=0.000
   245 -> 249   0.70413

Excited state symmetry could not be determined.
Excited State 8: Singlet-?Sym 3.1555 eV 392.92 nm f=0.7003 <S**2>=0.000
   247 -> 251   -0.19870
   248 -> 251   0.66474

Excited state symmetry could not be determined.
Excited State 9: Singlet-?Sym 3.1841 eV 389.38 nm f=0.0008 <S**2>=0.000
   247 -> 252   0.44059
   248 -> 252   0.54023

Excited state symmetry could not be determined.
Excited State 10: Singlet-?Sym 3.1863 eV 389.12 nm f=0.0004 <S**2>=0.000
   247 -> 253   0.46243
   248 -> 253   0.52227
SavETr: write IOETrn= 770 NScale= 10 NData= 16 NLR=1 NState= 10 LETran= 190.
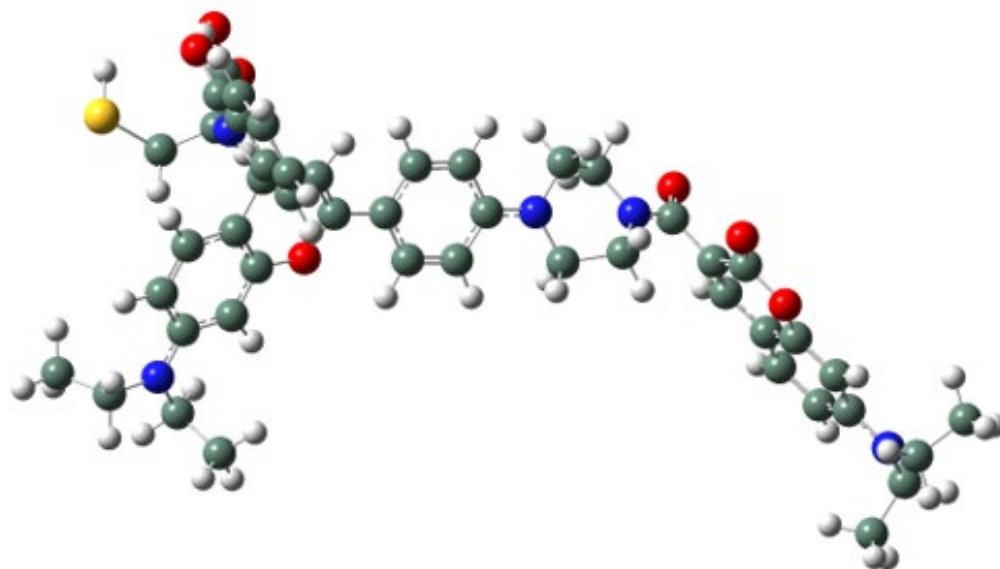The selected state is a singlet.

Figure S E.16. Drawing of probe A-1 with atoms represented as spheres of arbitrary size (H-white, C-grey, N-blue and O-red) using the GaussView program

Table S E.4. Results of the refinement for probe A-1

fluorafreqnoraman (Optimization completed)		
/storage/liu/fluor/tps/ftpb.log		
File Type	.log	
Calculation Type	FREQ	
Calculation Method	RTPSSh	
Basis Set	TZVP	
Charge	0	
Spin	Singlet	
Solvation	scrf=solvent=water	
E(RTPSSh)	-3020.131328	Hartree
RMS Gradient Norm	0.000007	Hartree/Bohr
Imaginary Freq		
Dipole Moment	24.624128	Debye
Point Group	C1	
Job cpu time:	10 days 15 hours 40 minutes 5...	

Table S E.5. Atomic coordinates for probe A-1.

Row	Symbol	X	Y	Z					
					24	O	-6.40069	-2.9747	-2.48849
1	C	6.578016	-1.08012	4.655974	25	C	-8.18004	-0.82447	-1.61937
2	C	5.920049	-0.54972	3.54588	26	C	-9.30464	-0.16341	-1.08291
3	C	6.265946	-1.03363	2.291706	27	C	-9.54282	-0.27474	0.302401
4	C	7.233049	-2.02195	2.157315	28	O	-8.70785	-1.03382	1.081371
5	C	7.89194	-2.56306	3.257691	29	C	-7.59194	-1.70604	0.577348
6	C	7.553996	-2.07485	4.516316	30	O	-6.97525	-2.38568	1.379165
7	C	5.699577	-0.64654	0.937731	31	C	-10.2146	0.62351	-1.82371
8	C	5.883969	0.812934	0.610262	32	C	-11.2793	1.246189	-1.22394
9	C	4.84642	1.571417	0.070121	33	C	-11.5119	1.124836	0.182516
10	O	3.589481	1.05103	-0.15626	34	C	-10.6054	0.337784	0.933559
11	C	3.317844	-0.23121	0.259591	35	N	-12.5676	1.745068	0.776091
12	C	4.259672	-1.02752	0.800504	36	C	-12.777	1.69768	2.227957
13	C	7.099126	1.482461	0.817096	37	C	-13.5686	2.496777	0.008237
14	C	7.281132	2.809433	0.486162	38	C	-13.1892	3.962409	-0.20925
15	C	6.220973	3.572424	-0.07732	39	C	-13.5726	0.473575	2.685148
16	C	4.991135	2.912296	-0.2683	40	C	7.375957	-2.36217	0.732779
17	N	6.387573	4.891032	-0.41421	41	N	6.550548	-1.54942	0.029662
18	C	5.332836	5.651505	-1.08605	42	C	1.907564	-0.58069	0.059062
19	C	7.626613	5.614681	-0.12172	43	C	0.927335	0.412139	-0.09012
20	C	4.338057	6.305101	-0.12329	44	C	-0.41046	0.094158	-0.25671
21	C	8.684517	5.489766	-1.22074	45	C	-0.84428	-1.25153	-0.28404
22	C	-6.18685	-2.28012	-1.48264	46	C	0.147312	-2.25139	-0.13983
23	C	-7.31421	-1.53943	-0.83038	47	C	1.480021	-1.91715	0.02001

48	N	-2.17082	-1.56644	-0.44884	72	H	-7.9885	-0.75947	-2.68574
49	C	-3.20997	-0.54349	-0.33421	73	H	-10.0587	0.737936	-2.89086
50	C	-4.53919	-1.18502	0.049823	74	H	-11.9377	1.850754	-1.83097
51	N	-4.94145	-2.16143	-0.96392	75	H	-10.7285	0.182822	1.995584
52	C	-3.86145	-2.93855	-1.58379	76	H	-13.3105	2.610648	2.499537
53	C	-2.62254	-2.93374	-0.69694	77	H	-11.8089	1.743366	2.730136
54	H	6.328934	-0.71688	5.646692	78	H	-14.5041	2.433876	0.567538
55	H	5.164696	0.218871	3.663477	79	H	-13.744	1.993877	-0.94398
56	H	8.641603	-3.33553	3.132786	80	H	-13.0493	4.472751	0.746678
57	H	8.047007	-2.46676	5.398305	81	H	-13.9854	4.473538	-0.75637
58	H	3.975685	-2.01033	1.152408	82	H	-12.2648	4.051026	-0.78409
59	H	7.934851	0.931689	1.236735	83	H	-14.5571	0.453043	2.211807
60	H	8.251632	3.256406	0.650568	84	H	-13.7144	0.508047	3.768309
61	H	4.123346	3.424835	-0.65902	85	H	-13.0524	-0.45361	2.435747
62	H	4.813826	4.99721	-1.79057	86	H	1.218403	1.455248	-0.07701
63	H	5.825071	6.4205	-1.68595	87	H	-1.12205	0.898976	-0.38742
64	H	8.024715	5.274389	0.836613	88	H	-0.12545	-3.29848	-0.14108
65	H	7.357583	6.664797	0.013811	89	H	2.20251	-2.72048	0.11085
66	H	3.821348	5.556548	0.481368	90	H	-3.3212	0.021937	-1.26837
67	H	3.588982	6.869527	-0.68527	91	H	-2.93883	0.160793	0.455983
68	H	4.850419	6.99556	0.551297	92	H	-5.29899	-0.40727	0.113048
69	H	8.98429	4.449346	-1.36465	93	H	-4.45868	-1.66384	1.028811
70	H	9.572251	6.069632	-0.9537	94	H	-3.61999	-2.52314	-2.56759
71	H	8.301567	5.870318	-2.17097	95	H	-4.20421	-3.96355	-1.73059

433

103	H	9.028386	-2.03426	-2.92861	96	H	-1.84174	-3.47749	-1.22876
104	H	7.511698	-3.63845	-1.05421	97	H	-2.82271	-3.46818	0.240624
105	O	8.09862	-3.27005	0.269991	98	C	7.304518	-0.52433	-2.15483
106	C	6.331274	-1.47252	-1.41648	99	C	6.190549	-2.79064	-2.20789
107	H	6.973829	-0.42696	-3.18855	100	O	6.941979	-3.83065	-1.88901
108	H	7.25415	0.455271	-1.68265	101	O	5.435759	-2.81971	-3.16291
109	H	5.345657	-1.01179	-1.51938	102	S	9.089525	-0.95188	-2.12521

434

| A-1 217 (HOMO-2) | A-1 220 (LUMO) |
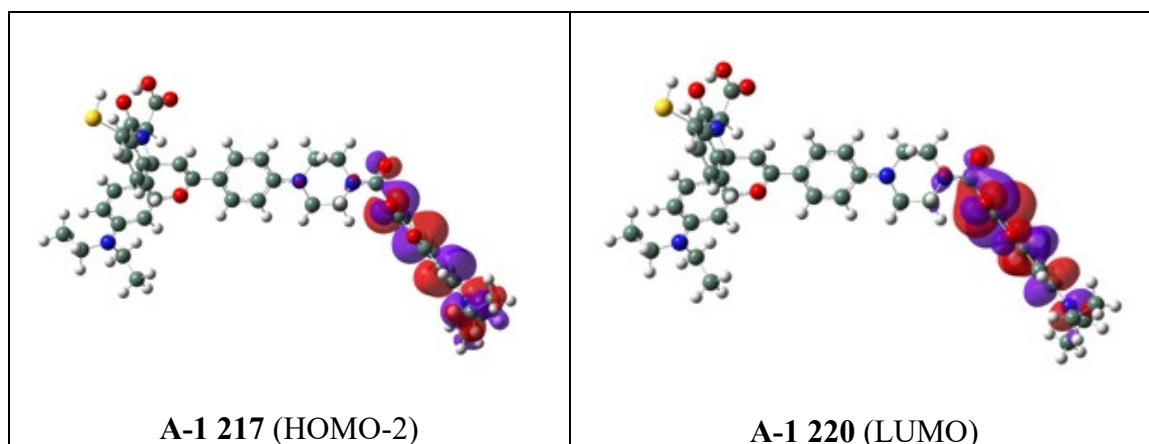
Figure S E.17. LCAO for orbitals 217 and 220 in probe A-1.
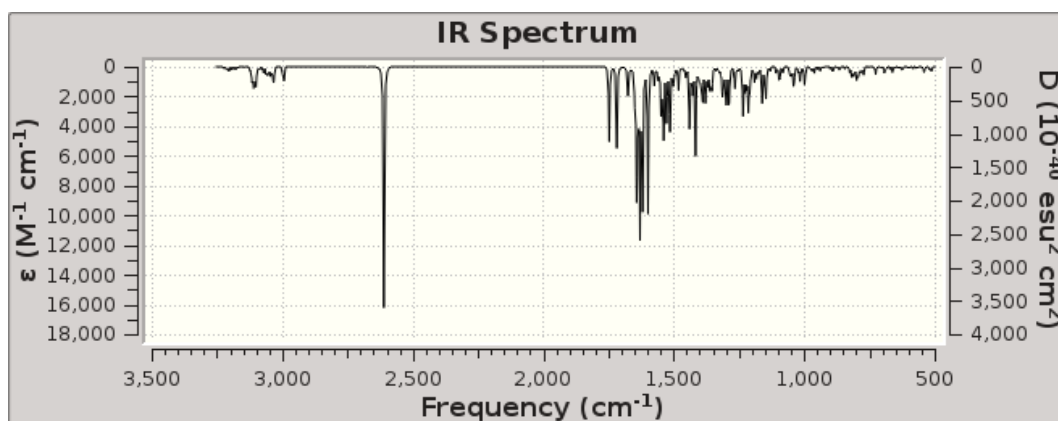
Figure S E.18. Calculated FTIR spectrum of probe A-1 in water.
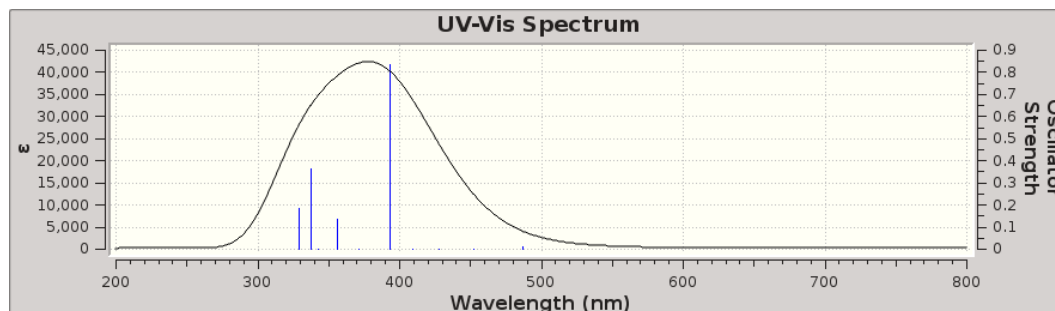
Figure S E.19. Calculated UV-Vis spectrum for probe A-1.

Table S E.6. Excitation Energies and Oscillator Strengths for A-1.

Excited state symmetry could not be determined.
Excited State   1:   Singlet-?Sym   2.5462 eV 486.94 nm f=0.0104 <S**2>=0.000
   218 -> 220   -0.15053
   219 -> 220   0.68994
This state for optimization and/or second-order correction.
Total Energy, E(TD-HF/TD-DFT) = -3020.03775633
Copying the excited state density for this state as the 1-particle RhoCI density.

Excited state symmetry could not be determined.
Excited State   2:   Singlet-?Sym   2.7411 eV 452.31 nm f=0.0023 <S**2>=0.000
   218 -> 220   0.68940
   219 -> 220   0.15238

Excited state symmetry could not be determined.
Excited State   3:   Singlet-?Sym   2.8970 eV 427.97 nm f=0.0005 <S**2>=0.000

218 -> 221   0.10148
219 -> 221   0.69920

Excited state symmetry could not be determined.
Excited State   4:   Singlet-?Sym   3.0264 eV 409.67 nm f=0.0001 <S**2>=0.000
  218 -> 221   0.69707

Excited state symmetry could not be determined.
Excited State   5:   Singlet-?Sym   3.1544 eV 393.05 nm f=0.8335 <S**2>=0.000
  217 -> 220   0.69430

Excited state symmetry could not be determined.
Excited State   6:   Singlet-?Sym   3.3425 eV 370.93 nm f=0.0000 <S**2>=0.000
  217 -> 221   0.70599

Excited state symmetry could not be determined.
Excited State   7:   Singlet-?Sym   3.4785 eV 356.43 nm f=0.1338 <S**2>=0.000
  218 -> 222   0.42247
  219 -> 222   0.56006

Excited state symmetry could not be determined.
Excited State   8:   Singlet-?Sym   3.6232 eV 342.20 nm f=0.0019 <S**2>=0.000
  216 -> 220   0.70369

Excited state symmetry could not be determined.
Excited State   9:   Singlet-?Sym   3.6702 eV 337.81 nm f=0.3622 <S**2>=0.000
  218 -> 222   0.52062
  219 -> 222   -0.36282
  219 -> 223   -0.25490
  219 -> 226   -0.11106

Excited state symmetry could not be determined.
Excited State 10:   Singlet-?Sym   3.7705 eV 328.83 nm f=0.1823 <S**2>=0.000
  214 -> 220   -0.17825
  218 -> 222   0.14149
  218 -> 223   0.15879
  219 -> 222   -0.14349
  219 -> 223   0.61968
SavETr: write IOETrn=   770 NScale= 10 NData= 16 NLR=1 NState=   10 LETran=
190.
The selected state is a singlet.

437
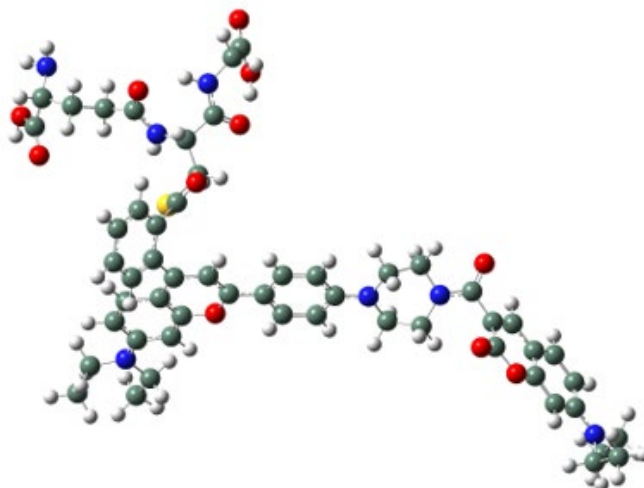
Figure S E.20. Drawing of probe A-3 with atoms represented as spheres of arbitrary size (H-white, C-grey, N-blue and O-red), using the GaussView program.

Table S E.7. Results of the refinement for probe A-3.

fluorafreqnoraman (Optimization completed)		
/storage/liu/fluor/tps/ftpc.log		
File Type	.log	
Calculation Type	FREQ	
Calculation Method	RTPSSh	
Basis Set	TZVP	
Charge	1	
Spin	Singlet	
Solvation	scrf=solvent=water	
E(RTPSSh)	-3704.076265	Hartree
RMS Gradient Norm	0.000001	Hartree/Bohr
Imaginary Freq	0	
Dipole Moment	32.375864	Debye
Polarizability (α)	1286.898600	a.u.
Point Group	C1	
Job cpu time:	14 days 18 hours 35 minutes ...	

Table S E.8. Atomic coordinates for probe A-3.

Row	Symbol	X	Y	Z
1	C	6.883011	4.096321	2.275537
2	C	5.837672	4.156518	1.360652
3	C	5.286071	2.989017	0.817475
4	C	5.815461	1.744805	1.213183
5	C	6.853843	1.694041	2.149348
6	C	7.391732	2.862754	2.673875
7	C	4.083243	3.106886	-0.04325
8	C	4.08393	3.883405	-1.22568
9	C	2.871455	4.006382	-1.9463
10	O	1.734401	3.39184	-1.49179
11	C	1.725291	2.638287	-0.36899
12	C	2.902124	2.493013	0.361019
13	C	5.21014	4.525611	-1.79827
14	C	5.115714	5.24694	-2.95615
15	C	3.875417	5.374758	-3.66519
16	C	2.743591	4.730082	-3.11068
17	N	3.791768	6.069755	-4.82913
18	C	2.468472	6.208926	-5.47641
19	C	4.920749	6.883545	-5.30512
20	C	2.491577	6.817932	-6.87101
21	C	5.023594	8.243609	-4.61288
22	C	-7.00029	-1.60519	1.219853
23	C	-8.30857	-0.89745	1.050926
24	O	-6.96553	-2.84352	1.279848
25	C	-9.19975	-1.37254	0.120861
26	C	-10.4783	-0.80212	-0.04515
27	C	-10.842	0.270362	0.795445
28	O	-9.97262	0.707774	1.761249
29	C	-8.70449	0.156022	1.956327
30	C	-11.4312	-1.20896	-1.00605
31	C	-12.651	-0.59174	-1.11358
32	C	-13.009	0.495553	-0.25493
33	C	-12.0608	0.910212	0.711878
34	N	-14.2183	1.108582	-0.36524
35	C	-14.5705	2.279618	0.446424
36	C	-15.2528	0.640763	-1.29678
37	C	-15.1325	1.253797	-2.69275
38	C	-15.1794	1.916317	1.802001
39	C	5.364962	0.43102	0.658158
40	O	5.087103	-0.5249	1.355415
41	S	5.399372	0.345796	-1.13828
42	C	5.854008	-2.41941	-1.21557
43	C	5.230732	-3.82852	-1.24894
44	C	0.44757	2.072601	-0.05342
45	C	-0.68112	2.310559	-0.87155
46	C	-1.91007	1.77036	-0.57888
47	C	-2.09576	0.942986	0.563427

48	C	-0.96057	0.705125	1.386862	72	H	-13.3389	-0.92847	-1.87581
49	C	0.262102	1.252638	1.083704	73	H	-15.2843	2.864166	-0.13726
50	N	-3.31015	0.408315	0.850352	74	H	-13.6856	2.906093	0.571689
51	C	-4.52012	0.819687	0.126243	75	H	-16.2152	0.907089	-0.8553
52	C	-5.75835	0.555803	0.976017	76	H	-15.2267	-0.44883	-1.34531
53	N	-5.86336	-0.86955	1.288144	77	H	-15.1951	2.343546	-2.64445
54	C	-4.59937	-1.57849	1.51216	78	H	-15.946	0.892425	-3.32688
55	C	-3.50003	-0.59856	1.900598	79	H	-14.1841	0.984964	-3.1629
56	H	7.289467	5.01343	2.685322	80	H	-16.0881	1.323794	1.672088
57	H	5.413418	5.116232	1.090172	81	H	-15.4403	2.827618	2.346026
58	H	7.249087	0.72881	2.442861	82	H	-14.4786	1.341098	2.410659
59	H	8.20308	2.809542	3.390011	83	H	-0.57784	2.924437	-1.75682
60	H	1.814944	6.802859	-4.82629	84	H	-2.73492	1.963529	-1.2507
61	H	2.035649	5.208448	-5.54843	85	H	-4.59642	0.29221	-0.83118
62	H	4.796507	7.016493	-6.37691	86	H	-4.47185	1.891119	-0.07367
63	H	5.839825	6.311478	-5.17859	87	H	-4.31086	-2.1301	0.611542
64	H	2.83664	7.853272	-6.87392	88	H	-4.73734	-2.30296	2.315251
65	H	1.467245	6.81014	-7.24973	89	H	-2.58023	-1.16831	2.020453
66	H	3.106267	6.234113	-7.55941	90	H	-3.73163	-0.11924	2.858103
67	H	4.121985	8.836793	-4.78144	91	H	-1.05066	0.109824	2.284591
68	H	5.877151	8.795241	-5.01451	92	H	1.088269	1.046294	1.752478
69	H	5.163916	8.130225	-3.53561	93	O	4.06089	-4.02982	-1.62454
70	H	-8.90681	-2.20592	-0.50974	94	N	6.04722	-4.81226	-0.85345
71	H	-11.1834	-2.02605	-1.67471	95	C	5.611643	-6.19667	-0.68323

96	C	5.30025	-6.93816	-1.98911
97	H	4.707723	-6.21269	-0.06566
98	H	6.399859	-6.73577	-0.16648
99	O	8.482264	-3.30657	-1.03001
100	C	11.52671	-1.79644	-3.76767
101	H	7.014482	-4.5585	-0.64281
102	O	4.392452	-6.3613	-2.78249
103	O	5.804179	-8.00288	-2.27667
104	H	4.091766	-5.49456	-2.3736
105	C	4.768225	-1.35883	-1.36478
106	H	6.35646	-2.30362	-0.25343
107	H	4.314798	-1.38481	-2.35553
108	H	3.990911	-1.52092	-0.6207
109	C	8.14841	-2.71515	-2.0673
110	H	6.615363	-1.87718	-3.13755
111	N	6.876062	-2.28577	-2.25039
112	C	9.11638	-2.45334	-3.20001
113	H	8.661763	-1.80118	-3.94915
114	H	9.323028	-3.416	-3.67732

115	N	11.82495	-3.13535	-4.28696
116	H	12.52404	-3.07557	-5.02167
117	H	12.23729	-3.68821	-3.53975
118	C	11.15146	-0.82943	-4.88223
119	O	10.51099	0.188641	-4.72163
120	O	11.66472	-1.18554	-6.07739
121	H	11.43094	-0.49576	-6.7234
122	C	10.43418	-1.85748	-2.69136
123	H	10.80811	-2.468	-1.8663
124	H	10.26764	-0.85022	-2.305
125	H	12.40519	-1.31963	-3.30129
126	H	1.768928	4.781	-3.57132
127	H	6.008615	5.719236	-3.33802
128	H	6.170023	4.441294	-1.30493
129	H	2.882857	1.91726	1.274259
130	O	-8.06657	0.60931	2.890606
131	H	-6.63643	0.861913	0.409052
132	H	-5.72235	1.148067	1.893386
133	H	-12.2686	1.709112	1.408739

A-3 268 (HOMO)

A-3 269 (LUMO)

A-3 267

A-3 270

A-3 263
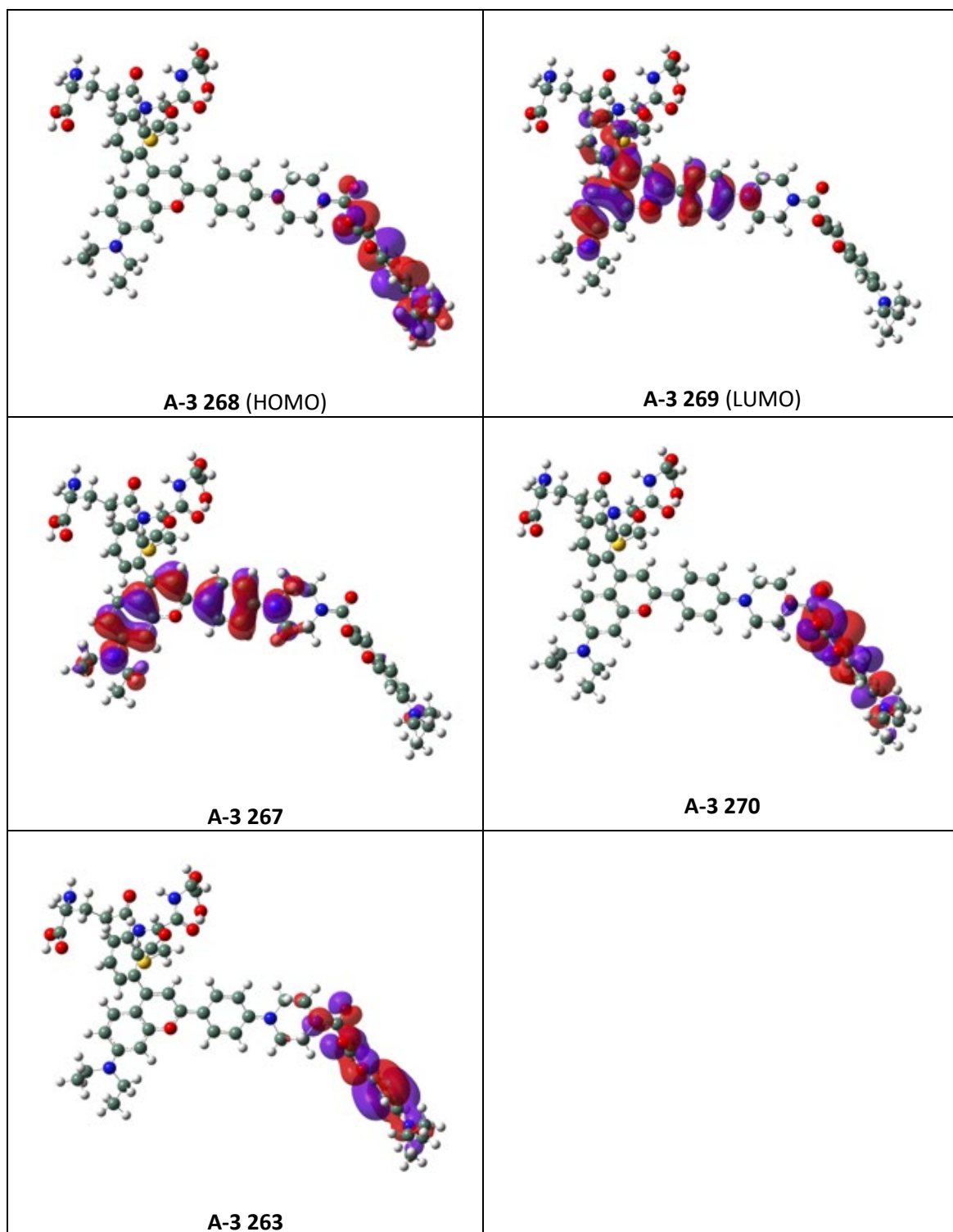
Figure S E.21. LCAO for orbitals 217 and 220 in probe A-3.
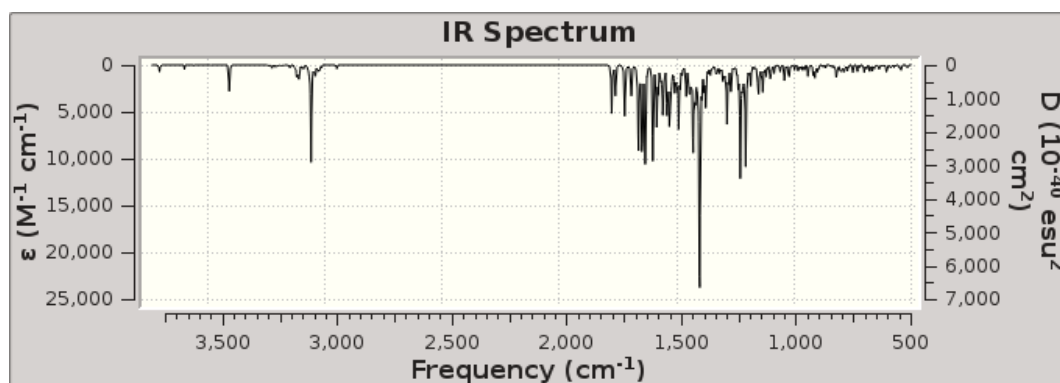
Figure S E.22. Calculated FTIR spectrum of probe A-3 in water.
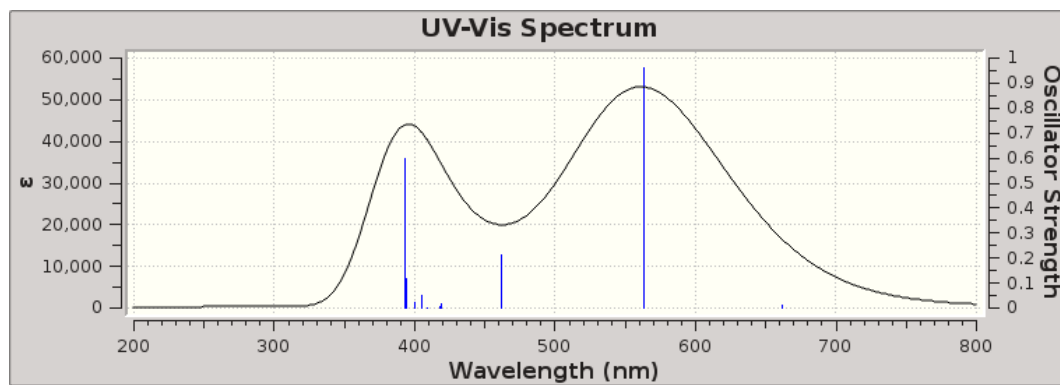
Figure S E.23. Calculated UV-Vis spectrum for probe A-3.

Table S E.9. Excitation Energies and Oscillator Strengths for A-3.

Excited state symmetry could not be determined.
Excited State   1:   Singlet-?Sym   1.8737 eV 661.70 nm f=0.0093 <S**2>=0.000
    268 -> 269   0.70361
This state for optimization and/or second-order correction.
Total Energy, E(TD-HF/TD-DFT) = -3704.00740701
Copying the excited state density for this state as the 1-particle RhoCI density.

Excited state symmetry could not be determined.
Excited State   2:   Singlet-?Sym   2.2005 eV 563.43 nm f=0.9594 <S**2>=0.000
    267 -> 269   0.69801

Excited state symmetry could not be determined.
Excited State   3:   Singlet-?Sym   2.6834 eV 462.05 nm f=0.2103 <S**2>=0.000
    266 -> 269   0.67999
    267 -> 272   -0.13570

Excited state symmetry could not be determined.
Excited State   4:   Singlet-?Sym   2.9575 eV 419.22 nm f=0.0163 <S**2>=0.000
    267 -> 270   0.68044
    268 -> 270   -0.17861

Excited state symmetry could not be determined.
Excited State   5:   Singlet-?Sym   2.9659 eV 418.03 nm f=0.0039 <S**2>=0.000
    265 -> 269   0.70254

Excited state symmetry could not be determined.
Excited State   6:   Singlet-?Sym   3.0342 eV 408.63 nm f=0.0000 <S**2>=0.000
    264 -> 269   0.70699

Excited state symmetry could not be determined.
Excited State   7:   Singlet-?Sym   3.0621 eV 404.90 nm f=0.0521 <S**2>=0.000
    267 -> 271   0.52658
    268 -> 271   -0.46241

Excited state symmetry could not be determined.
Excited State   8:   Singlet-?Sym   3.1013 eV 399.79 nm f=0.0199 <S**2>=0.000
    267 -> 271   0.45986
    268 -> 271   0.53431

Excited state symmetry could not be determined.

Excited State   9:   Singlet-?Sym   3.1484 eV 393.80 nm f=0.1149 <S**2>=0.000
   263 -> 269   0.63811
   268 -> 270   -0.27793

Excited state symmetry could not be determined.
Excited State 10:   Singlet-?Sym   3.1561 eV 392.84 nm f=0.5966 <S**2>=0.000
   263 -> 269   0.29375
   267 -> 270   0.16080
   268 -> 270   0.60974
 SavETr: write IOETrn=   770 NScale= 10 NData= 16 NLR=1 NState=   10 LETran= 190.
 The selected state is a singlet

6. Kinetic and thermodynamic study

(a)

$K = -0.08572 \pm 0.00622$

(b)

$K = -0.07364 \pm 0.00630$
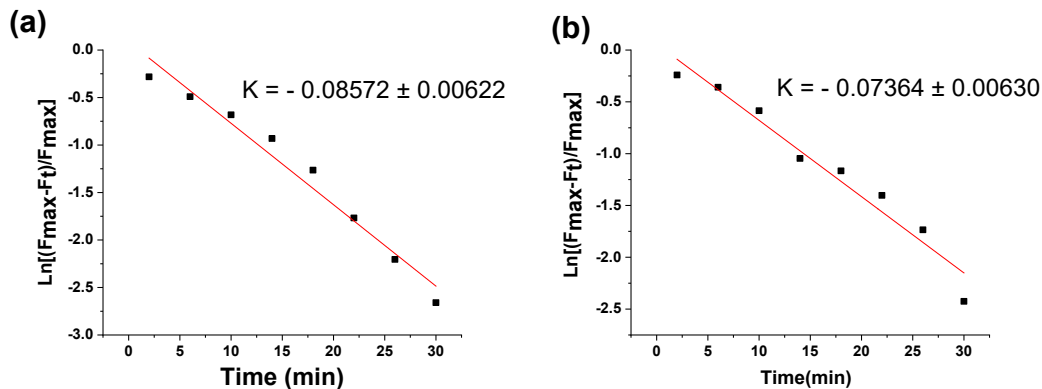
Figure S E.24. The pseudo first-order kinetic plot of the reaction of probe **A** (5 μM) to 20 equiv. of Cys (a) or Hcy (b) in pH 7.4 buffer containing 30% ethanol under the excitation of 440 nm.

(a)

$Y = 0.00118X + 0.35253$

$R = 0.99473$

(b)
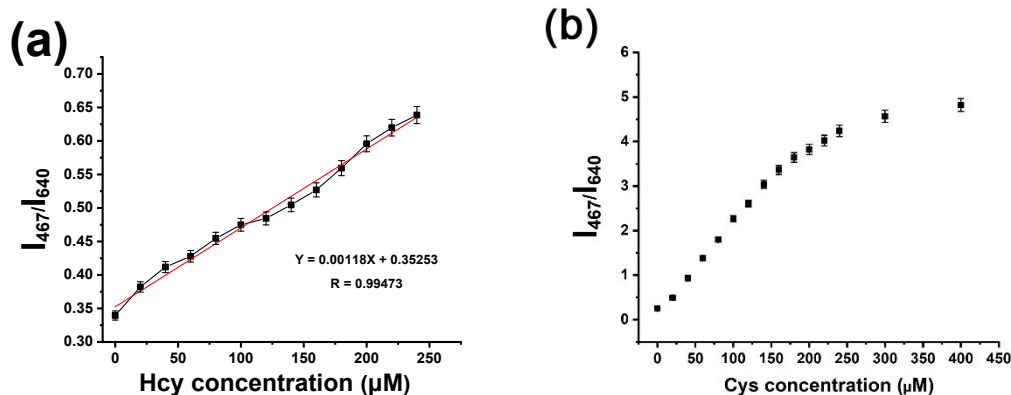
Figure S E.25. (a) Linear relationship of the fluorescence intensity ratio of the rhodamine acceptor to the coumarin donor fluorescence to Hcy concentration in pH 7.4 buffers containing 30% ethanol at excitation of 440 nm for 20 min. (b) Relationship of the fluorescence intensity ratio of the rhodamine acceptor to the coumarin donor fluorescence to Cys concentration in pH 7.4 buffers containing 30% ethanol at excitation of 440 nm for 20 min.

7. Selectivity of probe A:
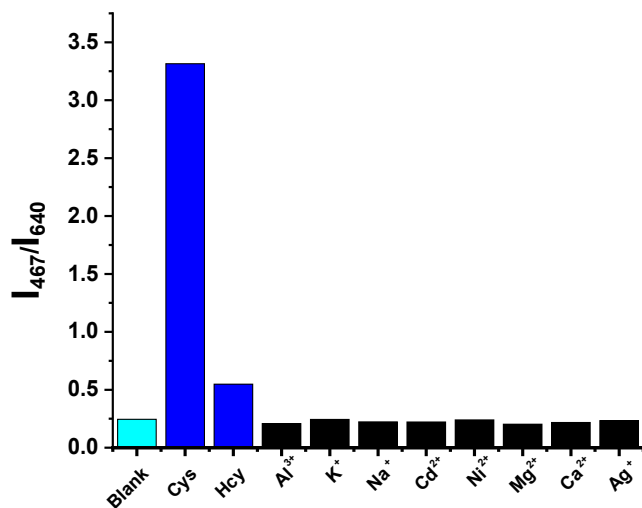
Figure S E.26. Probe **A** (5 µM) in the absence and presence of various of metal ions (200 µM) in buffer solutions.
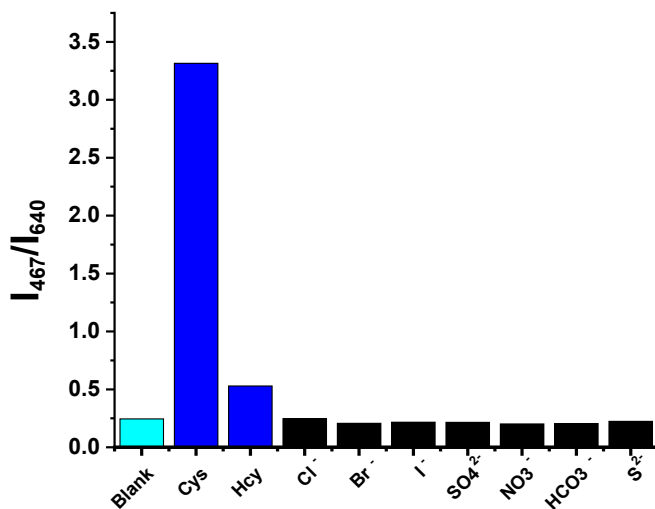
Figure S E.27. Probe **A** (5 µM) in the absence and presence of various of anions (200 µM) in buffer solutions
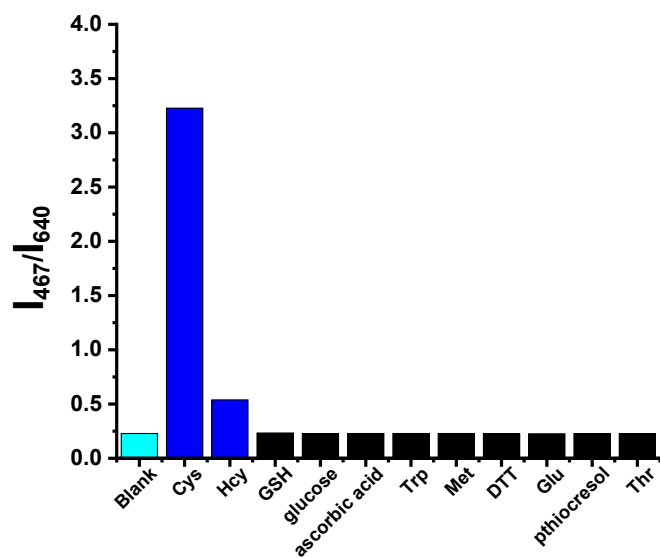
Figure S E.28. Probe **A** (5 μM) in the absence and presence of various of amino acids (200 μM) in buffer solutions.

8. Photostability of probe A
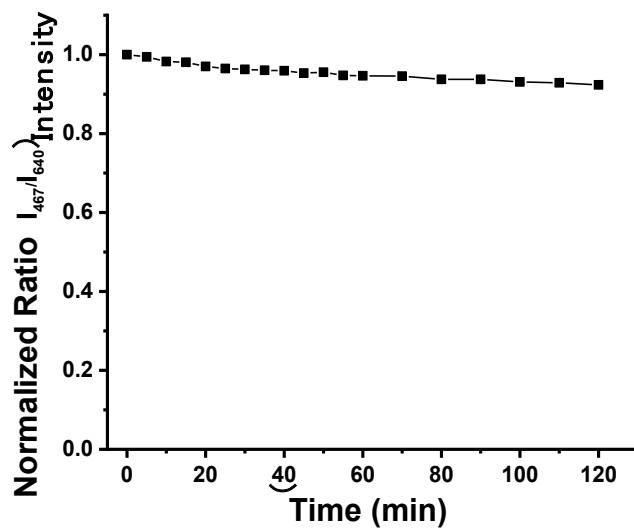
Figure S E.29. Probe **A** (5 μM) photostability under the excitation at 400 nm.
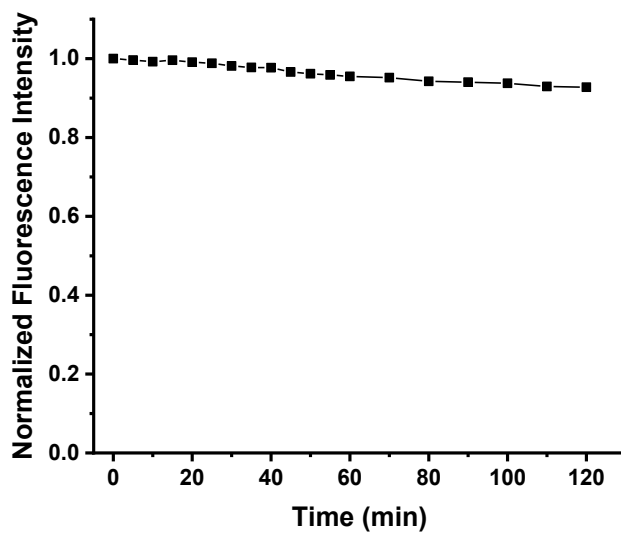
Figure S E.30. Probe **A** (5 μM) photostability under the excitation at 560 nm.

9. pH effect on probe A
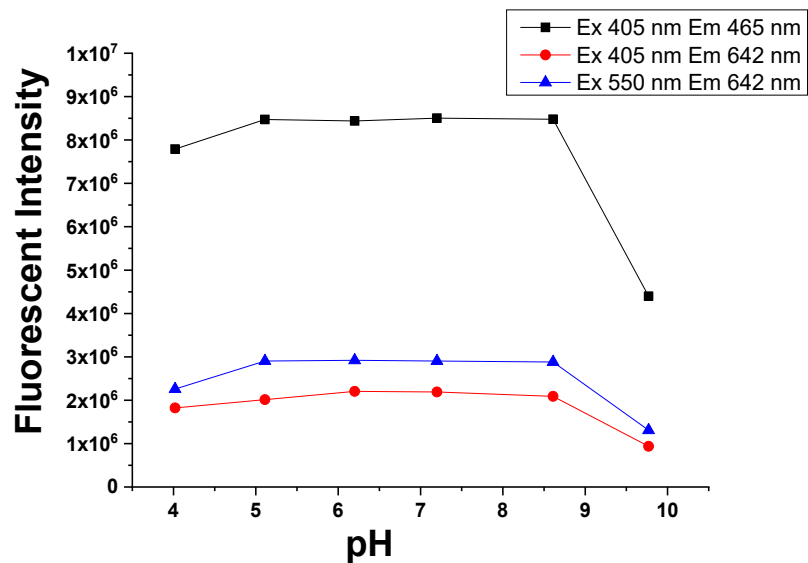
Figure S E.31. pH effect on probe **A** (5 µM) under the excitation at 405 nm or 560 nm in the absence of cysteine.
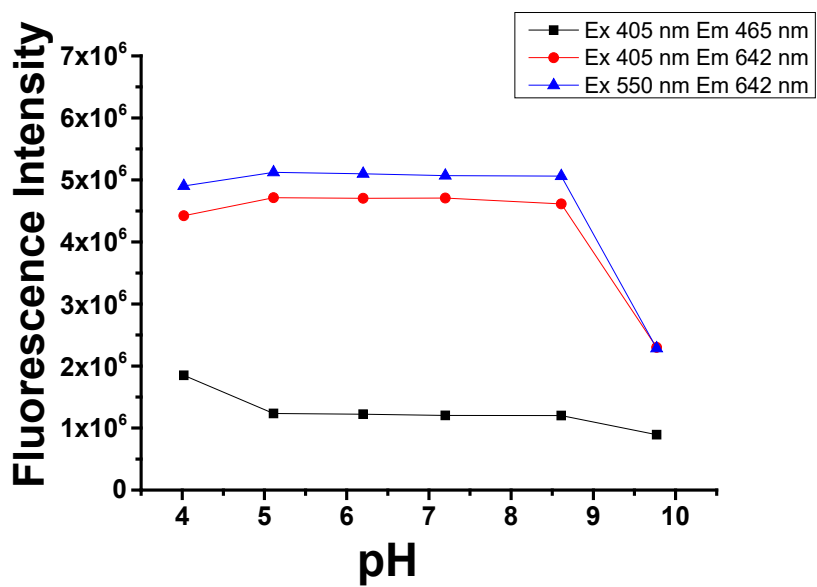
Figure S E.32. pH effect on probe **A** (5 µM) under the excitation at 405 nm or 560 nm in the presence of Cys (500 µM)

10. Cell Viability Assay
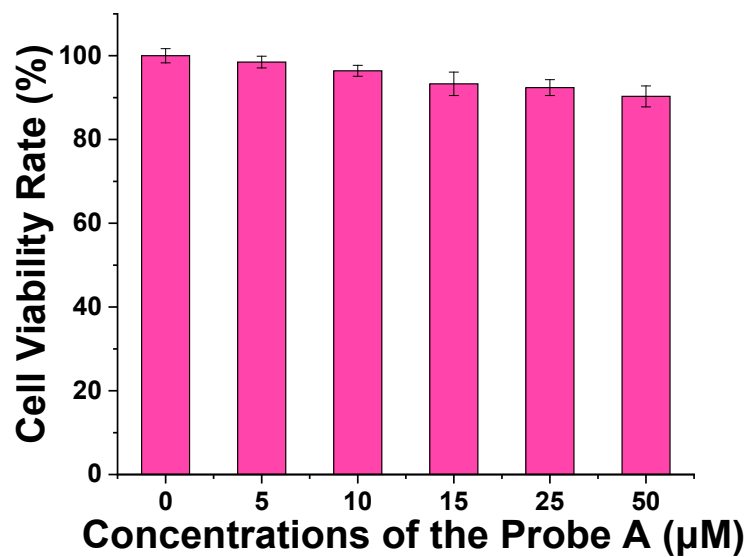
Figure S E.33. Cytotoxicity of probe **A** (5, 10, 15, 25, 50 μM) by MTT assay.

11. Ratiometric fluorescence imaging of HeLa cells with 10 µM probe A in the absence and presence of different concentrations of cysteine
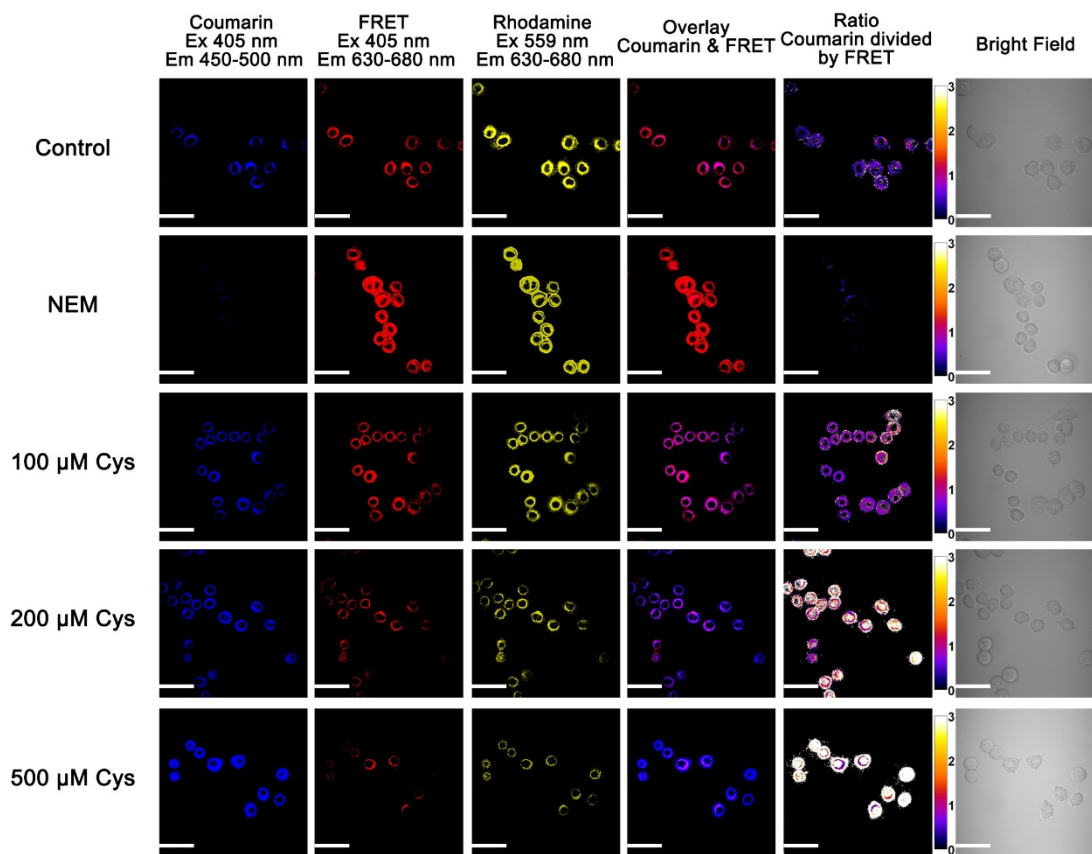
Figure S E.34. Fluorescence imaging of HeLa cells with 10 µM probe A in the absence and presence of different concentrations of Cys or under NEM treatment. Scale bar: 50 µm. Ratiometric images were obtained by using the ImageJ.

12. Fluorescence imaging of HeLa cells with 10 μM probe A in the absence and presence of different concentrations of Hcy
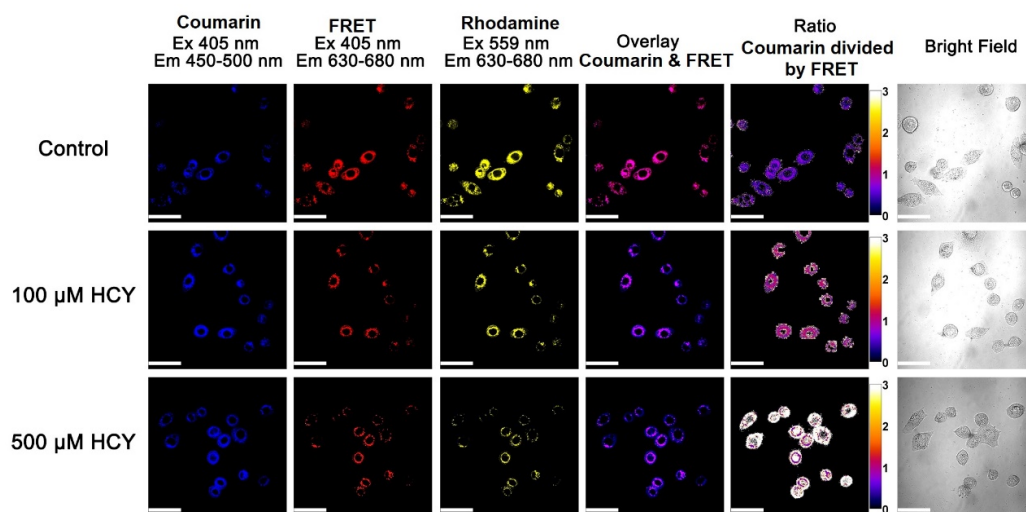
Figure S E.35. Fluorescence imaging of HeLa cells with 10 μM probe **A** in the absence and presence of different concentrations of Hcy. Scale bar: 50 μm.

13. Statistical analysis of the confocal imaging of the larvae in Fig 8
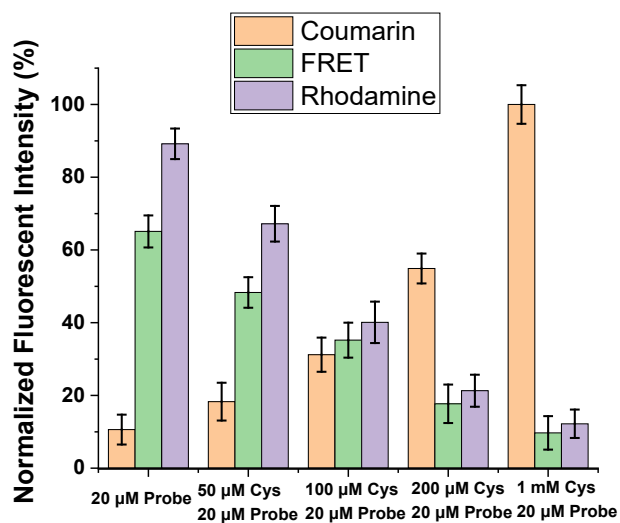
Figure S E.36. Fluorescence intensity of probe **A** in the Drosophila melanogaster first-instar larvae obtained from statistical analysis of the confocal imaging in Fig 8.

14. Fluorescence imaging of Drosophila melanogaster first-instar larvae with 20 μM probe A in the presence of 50 μM cysteine before and after hydrogen peroxide treatment
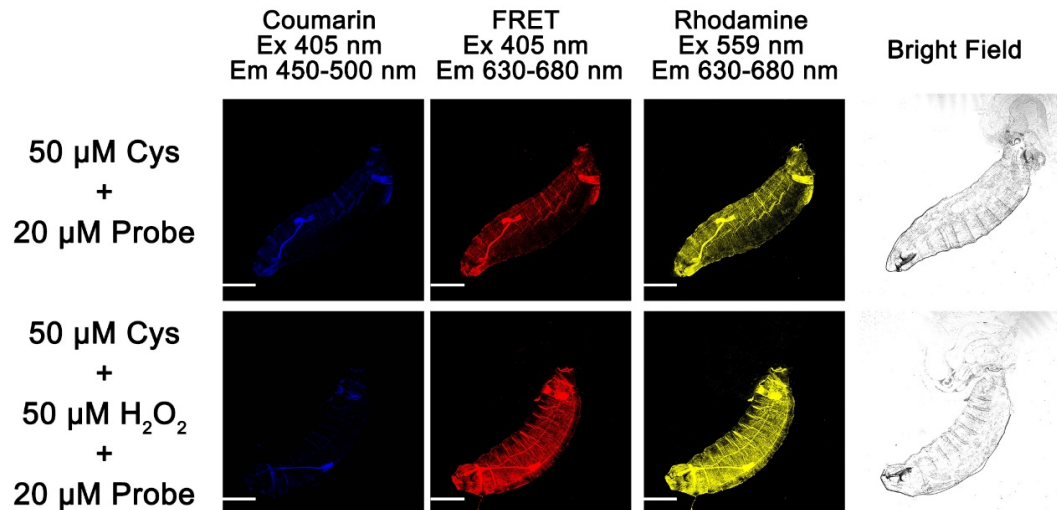
Figure S E.37. Fluorescence imaging of Drosophila melanogaster first-instar larvae with 20 μM probe **A** in the presence of 50 μM cysteine before and after hydrogen peroxide treatment. Scale bar: 200 μm

Copyright documentation

This letter is for chapter 2 and 4

Publication contents permission from Royal Society of Chemistry (RSC)

This letter is for chapter 5

Publication contents reuse permission from American Chemistry Society (ACS)

American Chemical Society's Policy on Theses and Dissertations

If your university requires you to obtain permission, you must use the RightsLink permission system.
See RightsLink instructions at http://pubs.acs.org/page/copyright/permissions.html.

This is regarding request for permission to include **your** paper(s) or portions of text from **your** paper(s) in your thesis. Permission is now automatically granted; please pay special attention to the **implications** paragraph below. The Copyright Subcommittee of the Joint Board/Council Committees on Publications approved the following:

Copyright permission for published and submitted material from theses and dissertations
ACS extends blanket permission to students to include in their theses and dissertations their own articles, or portions thereof, that have been published in ACS journals or submitted to ACS journals for publication, provided that the ACS copyright credit line is noted on the appropriate page(s).

Publishing **implications** of electronic publication of theses and dissertation material
Students and their mentors should be aware that posting of theses and dissertation material on the Web prior to submission of material from that thesis or dissertation to an ACS journal <u>may</u> affect publication in that journal. Whether Web posting is considered prior publication may be evaluated on a case-by-case basis by the journal's editor. If an ACS journal editor considers Web posting to be "prior publication", the paper will not be accepted for publication in that journal. If you intend to submit your unpublished paper to ACS for publication, check with the appropriate editor prior to posting your manuscript electronically.

Reuse/Republication of the Entire Work in Theses or Collections: Authors may reuse all or part of the Submitted, Accepted or Published Work in a thesis or dissertation that the author writes and is required to submit to satisfy the criteria of degree-granting institutions. Such reuse is permitted subject to the ACS' "Ethical Guidelines to Publication of Chemical Research" (http://pubs.acs.org/page/policy/ethics/index.html); the author should secure written confirmation (via letter or email) from the respective ACS journal editor(s) to avoid potential conflicts with journal prior publication*/embargo policies. Appropriate citation of the Published Work must be made. If the thesis or dissertation to be published is in electronic format, a direct link to the Published Work must also be included using the ACS Articles on Request author-directed link − see http://pubs.acs.org/page/policy/articlesonrequest/index.html

* Prior publication policies of ACS journals are posted on the ACS website at
http://pubs.acs.org/page/policy/prior/index.html

If your paper has **not** yet been published by ACS, please print the following credit line on the first page of your article: "Reproduced (or 'Reproduced in part') with permission from [JOURNAL NAME], in press (or 'submitted for publication'). Unpublished work copyright [CURRENT YEAR] American Chemical Society." Include appropriate information.

If your paper has already been published by ACS and you want to include the text or portions of the text in your thesis/dissertation, please print the ACS copyright credit line on the first page of your article: "Reproduced (or 'Reproduced in part') with permission from [FULL REFERENCE CITATION.] Copyright [YEAR] American Chemical Society." Include appropriate information.

Submission to a Dissertation Distributor: If you plan to submit your thesis to <u>UMI or to another dissertation distributor</u>, you should not include the unpublished ACS paper in your thesis if the thesis will be disseminated electronically, until ACS has published your paper. After publication of the paper by ACS, you may release the <u>entire</u> thesis (**not the individual ACS article by itself**) for electronic dissemination through the distributor; ACS's copyright credit line should be printed on the first page of the ACS paper.

10/10/03, 01/15/04, 06/07/06, 04/07/10, 08/24/10, 02/28/11

456

This letter is for Chapter 3.

Copyright Clearance Center RightsLink®   🏠 Home   ❓ Help   ✉ Email Support   👤 Shuai Xia ⌄

Fluorescent probes based on π-conjugation modulation between hemicyanine and coumarin moieties for ratiometric detection of pH changes in live cells with visible and near-infrared channels

Author:
Shuai Xia,Jianbo Wang,Jianheng Bi,Xiao Wang,Mingxi Fang,Tyler Phillips,Aslan May,Nathan Conner,Marina Tanasova,Fen-Tair Luo,Haiying Liu

Publication: Sensors and Actuators B: Chemical

Publisher: Elsevier

Date: 15 July 2018

© 2018 Elsevier B.V. All rights reserved.

BACK   CLOSE WINDOW

This letter is for Chapter 5.

Copyright Clearance Center

RightsLink®

Home　　Help　　Email Support　　Shuai Xia ⌄

Near-Infrared Hybrid Rhodol Dyes with Spiropyran Switches for Sensitive Ratiometric Sensing of pH Changes in Mitochondria and Drosophila melanogaster First-Instar Larvae

ACS Publications
Most Trusted. Most Cited. Most Read.

Author: Yibin Zhang, Shuai Xia, Logan Mikesell, et al

Publication: ACS Applied Bio Materials

Publisher: American Chemical Society

Date: Nov 1, 2019

Copyright © 2019, American Chemical Society

Quick Price Estimate

This service provides permission for reuse only. If you do not have a copy of the portion you are using, you may copy and paste the content and reuse according to the terms of your agreement. Please be advised that obtaining the content you license is a separate transaction not involving RightsLink.

Permission for this particular request is granted for print and electronic formats, and translations, at no charge. Figures and tables may be modified. Appropriate credit should be given. Please print this page for your records and provide a copy to your publisher. Requests for up to 4 figures require only this record. Five or more figures will generate a printout of additional terms and conditions. Appropriate credit should read: "Reprinted with permission from {COMPLETE REFERENCE CITATION}. Copyright {YEAR} American Chemical Society." Insert appropriate information in place of the capitalized words.

I would like to... ⑦	reuse in a Thesis/Dissertation ▾	Will you be translating? ⑦	No ▾
Requestor Type ⑦	Author (original work) ▾	Select your currency	USD - $ ▾
Portion ⑦	Full article ▾	Quick Price	Click Quick Price
Format ⑦	Print ▾		

QUICK PRICE　　CONTINUE

To request permission for a type of use not listed, please contact the publisher directly.

This letter is for Chapter 6.

Copyright Clearance Center | RightsLink®

A FRET-Based Near-Infrared Fluorescent Probe for Ratiometric Detection of Cysteine in Mitochondria

Author: Shuai Xia, Yibin Zhang, Mingxi Fang, et al

Publication: ChemBioChem

Publisher: John Wiley and Sons

Date: Jun 14, 2019

© 2019 Wiley-VCH Verlag GmbH & Co. KGaA, Weinheim

Order Completed

Thank you for your order.

This Agreement between shuai xia ("You") and John Wiley and Sons ("John Wiley and Sons") consists of your license details and the terms and conditions provided by John Wiley and Sons and Copyright Clearance Center.

Your confirmation email will contain your order number for future reference.

License Number	4743770626376
License date	Jan 07, 2020

🖶 Printable Details

☑ Licensed Content

Licensed Content Publisher	John Wiley and Sons
Licensed Content Publication	ChemBioChem
Licensed Content Title	A FRET-Based Near-Infrared Fluorescent Probe for Ratiometric Detection of Cysteine in Mitochondria
Licensed Content Author	Shuai Xia, Yibin Zhang, Mingxi Fang, et al
Licensed Content Date	Jun 14, 2019
Licensed Content Volume	20
Licensed Content Issue	15
Licensed Content Pages	9

▦ Order Details

Type of use	Dissertation/Thesis
Requestor type	Author of this Wiley article
Format	Print and electronic
Portion	Full article
Will you be translating?	No

📄 About Your Work

Title of your thesis / dissertation	Ratiometric near-infrared fluorescent probes for the sensitive detection of intracellular pH and bio-thiols in live cells
Expected completion date	Jan 2020
Expected size (number of pages)	20

📁 Additional Data

459

Requestor Location

shuai xia
47751 Us Highway 41 Apt 8

Requestor Location

HOUGHTON, MI 49931
United States
Attn: shuai xia

Tax Details

Publisher Tax ID   EU826007151

$ Price

Total   0.00 USD

Would you like to purchase the full text of this article? If so, please continue on to the content ordering system located here: Purchase PDF
If you click on the buttons below or close this window, you will not be able to return to the content ordering system.

Total: 0.00 USD

CLOSE WINDOW   ORDER MORE